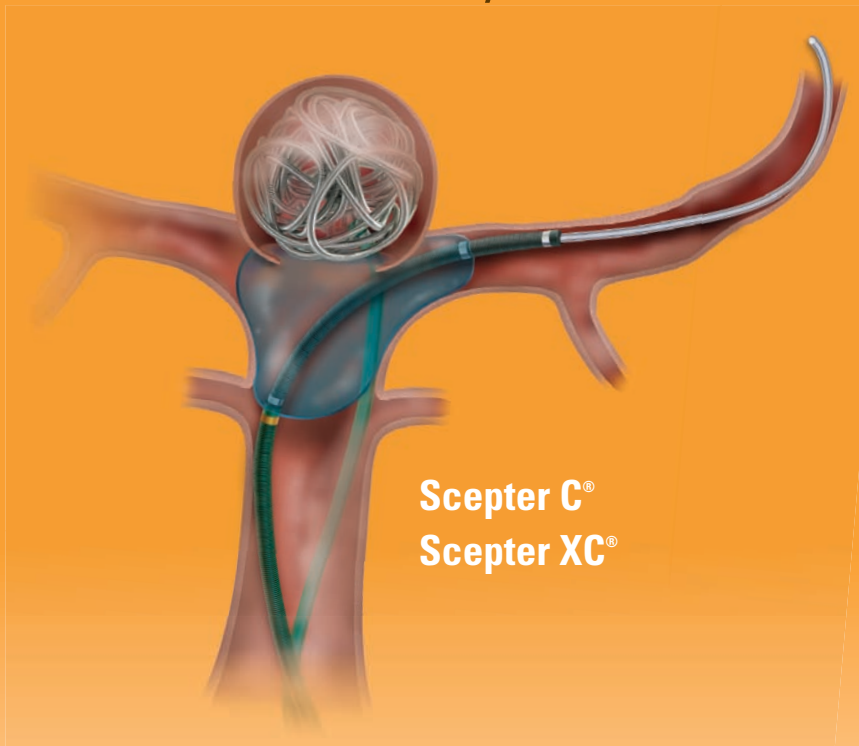


Versatility

by MicroVention



Scepter C®
Scepter XC®

Scepter
Occlusion Balloon
Catheter

REDEFINING DELIVERABILITY, VERSATILITY AND CONTROL

MicroVention has developed two occlusion balloon catheters. **Scepter C®** compliant balloon is designed for reliable vessel occlusion yet conforms to vessel anatomy. **Scepter XC®** x-tra compliant balloon conforms to extremely complex anatomies where neck coverage is more challenging.

• Used with



For more information or a product demonstration,
contact your local MicroVention representative:



MicroVention, Inc.

Worldwide Headquarters

1311 Valencia Avenue

Tustin, CA 92780 USA

MicroVention UK Limited

MicroVention Europe, S.A.R.L.

MicroVention Deutschland GmbH

PH +1.714.247.8000

PH +44 (0) 191 258 6777

PH +33 (1) 39 21 77 46

PH +49 211 210 798-0

BARRICADE™ COIL SYSTEM

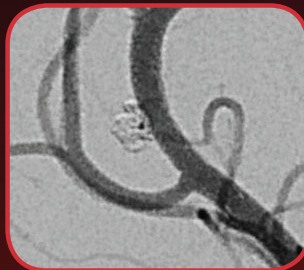
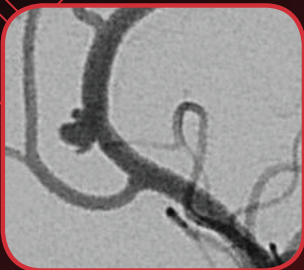
COILS THAT PERFORM

Cost Analysis of Cerebral Aneurysms Treated with the Barricade Coil System, A Retrospective Review

22 Patients Treated ♦ 114 Total Barricade Coils Used ♦ 8.2mm Mean Aneurysm Size

RIGHT PERICALLOSAL ANEURYSM

LEFT ICA TERMINUS ANEURYSM



PRE-TREATMENT

POST-TREATMENT

PRE-TREATMENT

POST-TREATMENT

“ I have successfully treated a wide range of aneurysms with the Barricade Coil System. I am impressed with the overall performance of the coils and the realized cost savings.”

-Yince Loh, M.D.

COILS THAT SAVE \$

\$110,000*
SAVED

Images and data courtesy of Yince Loh, M.D., Seattle, WA

* Estimated savings in this case, data on file.

The Barricade Coil System is intended for the endovascular embolization of intracranial aneurysms and other neurovascular abnormalities such as arteriovenous malformations and arteriovenous fistulae. The System is also intended for vascular occlusion of blood vessels within the neurovascular system to permanently obstruct blood flow to an aneurysm or other vascular malformation and for arterial and venous embolizations in the peripheral vasculature. Refer to the instructions for use for complete product information.

18 TECHNOLOGY DRIVE #169, IRVINE CA 92618 | p: 949.788.1443 | f: 949.788.1444
WWW.BLOCKADEMEDICAL.COM

MKTG-050 Rev. A



Smooth and stable.

Target Detachable Coils deliver consistently smooth deployment and exceptional microcatheter stability. Designed to work seamlessly together for framing, filling and finishing. Target Coils deliver the high performance you demand.

For more information, please visit www.strykerneurovascular.com/Target or contact your local Stryker Neurovascular sales representative.



Target®
DETACHABLE COILS

The Foundation of the ASNR Symposium 2017: *Discovery and Didactics* April 22-23, 2017

ASNR 55th Annual Meeting: *Diagnosis and Delivery* April 24-27, 2017



Long Beach Convention & Entertainment Center © Long Beach Convention & Visitors Bureau

Jacqueline A. Bello, MD, FACR
ASNR 2017 Program Chair/President-Elect

Programming developed in cooperation with and appreciation of the...

American Society of Functional Neuroradiology (ASFNR)
Kirk M. Welker, MD

American Society of Head and Neck Radiology (ASHNR)
Rebecca S. Cornelius, MD, FACR

American Society of Pediatric Neuroradiology (ASPNR)
Susan Palasis, MD

American Society of Spine Radiology (ASSR)
Joshua A. Hirsch, MD, FACR, FSIR

Society of NeuroInterventional Surgery (SNIS)
Blaise W. Baxter, MD

American Society of Neuroradiology (ASNR)
Health Policy Committee
Robert M. Barr, MD, FACR

Computer Sciences & Informatics (CSI) Committee
John L. Go, MD, FACR

Research Scientist Committee
Dikoma C. Shungu, PhD and Timothy, P.L. Roberts, PhD

The International Hydrocephalus Imaging Working Group (IHIWG)/CSF Flow Group
William G. Bradley, Jr., MD, PhD, Harold L. Rekate, MD and Bryn A. Martin, PhD



ASNR 55th Annual Meeting

c/o American Society of Neuroradiology
800 Enterprise Drive, Suite 205 • Oak Brook, Illinois 60523-4216
Phone: 630-574-0220 • Fax: 630 574-0661 • www.asnr.org/2017



ASFNR ASHNR ASPNR ASSR SNIS

THE FOUNDATION OF THE ASNR



Come to the beach! Please join us in Long Beach, California, April 22-27, 2017, for the 55th Annual Meeting of the ASNR. Known for its 5.5 miles of Pacific Ocean waterfront, this southern California beach resort boasts a blend of city sophistication and seaside serenity. ASNR is delighted to provide a “4D” focus for this meeting, as depicted by our meeting logo: **Discovery and Didactics** for The Foundation of the ASNR Symposium 2017: **Diagnosis and Delivery** for the ensuing Annual Meeting Program.

Centered on Discovery and Didactics, the symposium will feature sessions on “What’s New?” in the role neuroimaging plays defining CNS disease mechanisms and how to best prepare for “What’s Next?” for our subspecialty in terms of training, teaching, and leading the process of lifelong learning. The annual meeting programming will address best practices in Diagnosis and Delivery, as we strive to provide value, promote quality in better health and care and consider cost. Our discussions will consider how to navigate the changing landscape of healthcare reform and reimbursement as subspecialists in a field that is changing at an equally “fast forward” pace!



Hyatt Regency Long Beach
© Hyatt Regency Long Beach



Westin Long Beach
© The Westin Long Beach



American Society of Head & Neck Radiology

Comprehensive Head and Neck Imaging: 50 Years of Progress

September 7 - 11, 2016

Hyatt Regency Washington on Capitol Hill
Washington, D.C.

29.25 AMA PRA Category 1 Credit(s)TM

Four sessions of the meeting program will be submitted for SAM qualification.

**Hands-on US and US-Guided Biopsy Seminar
Saturday, September 10, 2016**

Separate Registration Required
Registration is Limited to 20 Attendees Per Session.

Not accredited for AMA PRA Category 1 Credit(s)TM

Please contact Educational Symposia at 813-806-1000 or ASHNR@edusymp.com or visit www.ASHNR.org for additional information.



AMA Preferred Provider Offers and Services



AMA Preferred Provider Offers and Services

Special offers that fit you and your practice's needs.

Which savings would benefit you the most? Discounts on pharmaceuticals, medical supplies and equipment? Or on travel, practice financing, and financial and insurance services? Now physicians can save in all of these professional and personal categories and more through the AMA Preferred Provider Offers and Services program.

Please activate your 2016 AMA membership by calling **(800) 262-3211** or visit **ama-assn.org/go/join**.



* Subsidiary of the American Medical Association.

AXS Catalyst™ Distal Access Catheter

See package insert for complete indications, complications, warnings, and instructions for use.

INTENDED USE/INDICATIONS FOR USE

The AXS Catalyst Distal Access Catheter is indicated for use in facilitating the insertion and guidance of appropriately sized interventional devices into a selected blood vessel in the peripheral and neurovascular systems. The AXS Catalyst Distal Access Catheter is also indicated for use as a conduit for retrieval devices.

CONTRAINDICATIONS

None known.

ADVERSE EVENTS

Potential adverse events associated with the use of catheters or with the endovascular procedures include, but are not limited to: access site complications, allergic reaction, aneurysm perforation, aneurysm rupture, death, embolism (air, foreign body, plaque, thrombus), hematoma, hemorrhage, infection, ischemia, neurological deficits, pseudoaneurysm, stroke, transient ischemic attack, vasospasm, vessel dissection, vessel occlusion, vessel perforation, vessel rupture, and vessel thrombosis.

WARNING

Contents supplied sterile using an ethylene oxide (EO) process. Do not use if sterile barrier is damaged. If damage is found, call your Stryker Neurovascular representative. For single use only. Do not reuse, reprocess or resterilize. Reuse, reprocessing or resterilization may compromise the structural integrity of the device and/or lead to device failure which, in turn, may result in patient injury, illness or death. Reuse, reprocessing or resterilization may also create a risk of contamination of the device and/or cause patient infection or cross-infection, including, but not limited to, the transmission of infectious disease(s) from one patient to another.

Contamination of the device may lead to injury, illness or death of the patient. After use, dispose of product and packaging in accordance with hospital, administrative and/or local government policy.

- Limited testing has been performed with solutions such as contrast media, and saline. The use of these catheters for delivery of solutions other than the types that have been tested for compatibility is not recommended.
- Not intended for use with power injectors.
- If flow through catheter becomes restricted, do not attempt to clear catheter lumen by infusion. Doing so may cause catheter damage or patient injury. Remove and replace catheter.

- Never advance or withdraw an intravascular device against resistance until the cause of the resistance is determined by fluoroscopy. Movement of the device against resistance could dislodge a clot, perforate a vessel wall, or damage the device.

PRECAUTIONS

- Carefully inspect all devices prior to use. Verify size, length, and condition are suitable for the specific procedure. Do not use a device that has been damaged in any way. Damaged device may cause complications.
- To control the proper introduction, movement, positioning and removal of the catheter within the vascular system, users should employ standard clinical angiographic and fluoroscopic practices and techniques throughout the interventional procedure.
- Use the product prior to the "Use By" date printed on the label.
- To prevent thrombus formation and contrast media crystal formation, maintain a constant infusion of appropriate flush solution through catheter lumen.
- Torquing the catheter may cause damage which could result in kinking or separation of the catheter shaft.

Trevo® XP ProVue Retrievers

See package insert for complete indications, complications, warnings, and instructions for use.

INDICATIONS FOR USE

The Trevo Retriever is intended to restore blood flow in the neurovasculature by removing thrombus in patients experiencing ischemic stroke within 8 hours of symptom onset. Patients who are ineligible for intravenous tissue plasminogen activator (IV t-PA) or who fail IV t-PA therapy are candidates for treatment.

COMPLICATIONS

Procedures requiring percutaneous catheter introduction should not be attempted by physicians unfamiliar with possible complications which may occur during or after the procedure. Possible complications include, but are not limited to, the following: air embolism; hematoma or hemorrhage at puncture site; infection; distal embolization; pain/headache; vessel spasm, thrombosis, dissection, or perforation; emboli; acute occlusion; ischemia; intracranial hemorrhage; false aneurysm formation; neurological deficits including stroke; and death.

COMPATIBILITY

3x20mm retrievers are compatible with Trevo® Pro 14 Microcatheters (REF 90231) and Trevo® Pro 18 Microcatheters (REF 90238). 4x20mm retrievers are compatible with Trevo® Pro 18

Microcatheters (REF 90238). 4x30mm retrievers are compatible with Excelsior® XT-27® Microcatheters (150cm x 6cm straight REF 275081) and Trevo® Pro 18 Microcatheters (REF 90238). 6x25mm Retrievers are compatible with Excelsior® XT-27® Microcatheters (150cm x 6cm straight REF 275081). Compatibility of the Retriever with other microcatheters has not been established. Performance of the Retriever device may be impacted if a different microcatheter is used.

Balloon Guide Catheters (such as Merci® Balloon Guide Catheter and FlowGate® Balloon Guide Catheter) are recommended for use during thrombus removal procedures.

Retrievers are compatible with the Abbott Vascular DOC® Guide Wire Extension (REF Z2260).

Retrievers are compatible with Boston Scientific RHV (Ref 421242).

WARNINGS

- Contents supplied STERILE, using an ethylene oxide (EO) process. Nonpyrogenic.
- To reduce risk of vessel damage, adhere to the following recommendations:
 - Take care to appropriately size Retriever to vessel diameter at intended site of deployment.
 - Do not perform more than six (6) retrieval attempts in same vessel using Retriever devices.
 - Maintain Retriever position in vessel when removing or exchanging Microcatheter.
- To reduce risk of kinking/fracture, adhere to the following recommendations:
 - Immediately after unsheathing Retriever, position Microcatheter tip marker just proximal to shaped section. Maintain Microcatheter tip marker just proximal to shaped section of Retriever during manipulation and withdrawal.
 - Do not rotate or torque Retriever.
 - Use caution when passing Retriever through stented arteries.
- Do not resterilize and reuse. Structural integrity and/or function may be impaired by reuse or cleaning.
- The Retriever is a delicate instrument and should be handled carefully. Before use and when possible during procedure, inspect device carefully for damage. Do not use a device that shows signs of damage. Damage may prevent device from functioning and may cause complications.
- Do not advance or withdraw Retriever against resistance or significant vasospasm. Moving or torquing device against resistance or significant vasospasm may result in damage to vessel or device. Assess cause of resistance

using fluoroscopy and if needed resheath the device to withdraw.

- If Retriever is difficult to withdraw from the vessel, do not torque Retriever. Advance Microcatheter distally, gently pull Retriever back into Microcatheter, and remove Retriever and Microcatheter as a unit. If undue resistance is met when withdrawing the Retriever into the Microcatheter, consider extending the Retriever using the Abbott Vascular DOC guidewire extension (REF Z2260) so that the Microcatheter can be exchanged for a larger diameter catheter such as a DAC® catheter. Gently withdraw the Retriever into the larger diameter catheter.
- Administer anti-coagulation and anti-platelet medications per standard institutional guidelines.

PRECAUTIONS

- Prescription only – device restricted to use by or on order of a physician.
- Store in cool, dry, dark place.
- Do not use open or damaged packages.
- Use by "Use By" date.
- Exposure to temperatures above 54°C (130°F) may damage device and accessories. Do not autoclave.
- Do not expose Retriever to solvents.
- Use Retriever in conjunction with fluoroscopic visualization and proper anti-coagulation agents.
- To prevent thrombus formation and contrast media crystal formation, maintain a constant infusion of appropriate flush solution between guide catheter and Microcatheter and between Microcatheter and Retriever or guidewire.
- Do not attach a torque device to the shaped proximal end of DOC® Compatible Retriever. Damage may occur, preventing ability to attach DOC® Guide Wire Extension.



Stryker Neurovascular
47900 Bayside Parkway
Fremont, CA 94538

strykerneurovascular.com

Date of Release: MAY/2016

EX_EN_US

Copyright © 2016 Stryker
NV00020190_AA

Target® Detachable Coil

See package insert for complete indications, contraindications, warnings and instructions for use.

INTENDED USE / INDICATIONS FOR USE

Target Detachable Coils are intended to endovascularly obstruct or occlude blood flow in vascular abnormalities of the neurovascular and peripheral vessels.

Target Detachable Coils are indicated for endovascular embolization of:

- Intracranial aneurysms
- Other neurovascular abnormalities such as arteriovenous malformations and arteriovenous fistulae
- Arterial and venous embolizations in the peripheral vasculature

CONTRAINDICATIONS

None known.

POTENTIAL ADVERSE EVENTS

Potential complications include, but are not limited to: allergic reaction, aneurysm perforation and rupture, arrhythmia, death, edema, embolus, headache, hemorrhage, infection, ischemia, neurological/intracranial sequelae, post-embolization syndrome (fever, increased white blood cell count, discomfort), TIA/stroke, vasospasm, vessel occlusion or closure, vessel perforation, dissection, trauma or damage, vessel rupture, vessel thrombosis. Other procedural complications including but not limited to: anesthetic and contrast media risks, hypotension, hypertension, access site complications.

WARNINGS

- Contents supplied STERILE using an ethylene oxide (EO) process. Do not use if sterile barrier is damaged. If damage is found, call your Stryker Neurovascular representative.
- For single use only. Do not reuse, reprocess or resterilize. Reuse, reprocessing or resterilization may compromise the structural integrity of the device and/or lead to device failure which, in turn, may result in patient injury, illness or death. Reuse, reprocessing or resterilization may also create a risk of contamination of the device and/or cause patient infection or cross-infection, including, but not limited to, the transmission of infectious disease(s) from one patient to another. Contamination of the device may lead to injury, illness or death of the patient.

- After use, dispose of product and packaging in accordance with hospital, administrative and/or local government policy.

• This device should only be used by physicians who have received appropriate training in interventional neuroradiology or interventional radiology and preclinical training on the use of this device as established by Stryker Neurovascular.

- Patients with hypersensitivity to 316LVM stainless steel may suffer an allergic reaction to this implant.
- MR temperature testing was not conducted in peripheral vasculature, arteriovenous malformations or fistulae models.

The safety and performance characteristics of the Target Detachable Coil System (Target Detachable Coils, InZone Detachment Systems, delivery systems and accessories) have not been demonstrated with other manufacturer's devices (whether coils, coil delivery devices, coil detachment systems, catheters, guidewires, and/or other accessories). Due to the potential incompatibility of non Stryker Neurovascular devices with the Target Detachable Coil System, the use of other manufacturer's device(s) with the Target Detachable Coil System is not recommended.

- To reduce risk of coil migration, the diameter of the first and second coil should never be less than the width of the ostium.
- In order to achieve optimal performance of the Target Detachable Coil System and to reduce the risk of thromboembolic complications, it is critical that a continuous infusion of appropriate flush solution be maintained between a) the femoral sheath and guiding catheter, b) the 2-tip microcatheter and guiding catheters, and c) the 2-tip microcatheter and Stryker Neurovascular guidewire and delivery wire. Continuous flush also reduces the potential for thrombus formation on, and crystallization of infusate around, the detachment zone of the Target Detachable Coil.
- Do not use the product after the "Use By" date specified on the package.
- Reuse of the flush port/dispenser coil or use with any coil other than the original coil may result in contamination of, or damage to, the coil.
- Utilization of damaged coils may affect coil delivery to, and stability inside, the vessel or aneurysm, possibly resulting in coil migration and/or stretching.
- The fluoro-saver marker is designed for use with a Rotating Hemostatic Valve (RHV). If used without an RHV, the distal end of the coil may be beyond the alignment

marker when the fluoro-saver marker reaches the microcatheter hub.

- If the fluoro-saver marker is not visible, do not advance the coil without fluoroscopy.
- Do not rotate delivery wire during or after delivery of the coil. Rotating the Target Detachable Coil delivery wire may result in a stretched coil or premature detachment of the coil from the delivery wire, which could result in coil migration.
- Verify there is no coil loop protrusion into the parent vessel after coil placement and prior to coil detachment. Coil loop protrusion after coil placement may result in thromboembolic events if the coil is detached.
- Verify there is no movement of the coil after coil placement and prior to coil detachment. Movement of the coil after coil placement may indicate that the coil could migrate once it is detached.
- Failure to properly close the RHV compression fitting over the delivery wire before attaching the InZone® Detachment System could result in coil movement, aneurysm rupture or vessel perforation.
- Verify repeatedly that the distal shaft of the catheter is not under stress before detaching the Target Detachable Coil. Axial compression or tension forces could be stored in the 2-tip microcatheter causing the tip to move during coil delivery. Microcatheter tip movement could cause the aneurysm or vessel to rupture.
- Advancing the delivery wire beyond the microcatheter tip once the coil has been detached involves risk of aneurysm or vessel perforation.
- The long term effect of this product on extravascular tissues has not been established so care should be taken to retain this device in the intravascular space.

Damaged delivery wires may cause detachment failures, vessel injury or unpredictable distal tip response during coil deployment. If a delivery wire is damaged at any point during the procedure, do not attempt to straighten or otherwise repair it. Do not proceed with deployment or detachment. Remove the entire coil and replace with undamaged product.

- After use, dispose of product and packaging in accordance with hospital, administrative and/or local government policy.

CAUTIONS / PRECAUTIONS

- Federal Law (USA) restricts this device to sale by or on the order of a physician.
- Besides the number of InZone Detachment System units needed to complete the case, there must be an extra

InZone Detachment System unit as back up.

- Removing the delivery wire without grasping the introducer sheath and delivery wire together may result in the detachable coil sliding out of the introducer sheath.
- Failure to remove the introducer sheath after inserting the delivery wire into the RHV of the microcatheter will interrupt normal infusion of flush solution and allow back flow of blood into the microcatheter.
- Some low level overhead light near or adjacent to the patient is required to visualize the fluoro-saver marker; monitor light alone will not allow sufficient visualization of the fluoro-saver marker.
- Advance and retract the Target Detachable Coil carefully and smoothly without excessive force. If unusual friction is noticed, slowly withdraw the Target Detachable Coil and examine for damage. If damage is present, remove and use a new Target Detachable Coil. If friction or resistance is still noted, carefully remove the Target Detachable Coil and microcatheter and examine the microcatheter for damage.
- If it is necessary to reposition the Target Detachable Coil, verify under fluoroscopy that the coil moves with a one-to-one motion. If the coil does not move with a one-to-one motion or movement is difficult, the coil may have stretched and could possibly migrate or break. Gently remove both the coil and microcatheter and replace with new devices.
- Increased detachment times may occur when:
 - Other embolic agents are present.
 - Delivery wire and microcatheter markers are not properly aligned.
 - Thrombus is present on the coil detachment zone.
- Do not use detachment systems other than the InZone Detachment System.
- Increased detachment times may occur when delivery wire and microcatheter markers are not properly aligned.
- Do not use detachment systems other than the InZone Detachment System.



Stryker Neurovascular
47900 Bayside Parkway
Fremont, CA 94538

strykerneurovascular.com

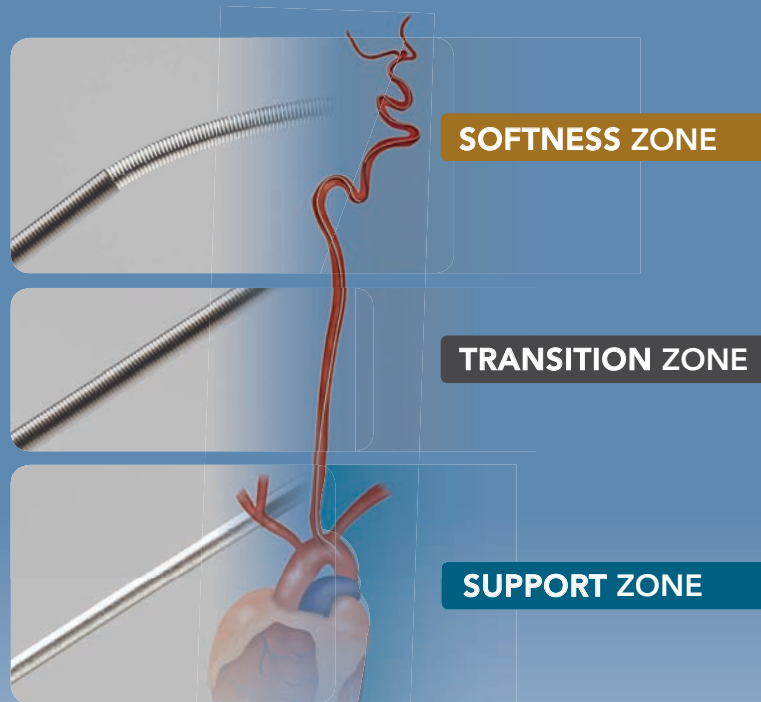
Date of Release: MAR/2016

EX_EN_US

Copyright © 2016 Stryker
NV00018669_AA

Advanced

by MicroVention



ENHANCED CONTROL TO MAXIMIZE COIL PERFORMANCE

The V-Trak® Advanced Coil System, the next generation to power the performance of our most technically advanced line of coils. Offering the optimal combination of support and flexibility.

microvention.com

MICROVENTION, V-Trak, Scepter C, Scepter XC and Headway are registered trademarks of MicroVention, Inc. Scientific and clinical data related to this document are on file at MicroVention, Inc. Refer to Instructions for Use, contraindications and warnings for additional information. Federal (USA) law restricts this device for sale by or on the order of a physician. © 2015 MicroVention, Inc. 5/15

CE
0297

Take on tortuosity.

The **AXS Catalyst™ Distal Access Catheter** family is designed for easy navigation in challenging cases.



AXS Catalyst 6

DISTAL ACCESS CATHETER

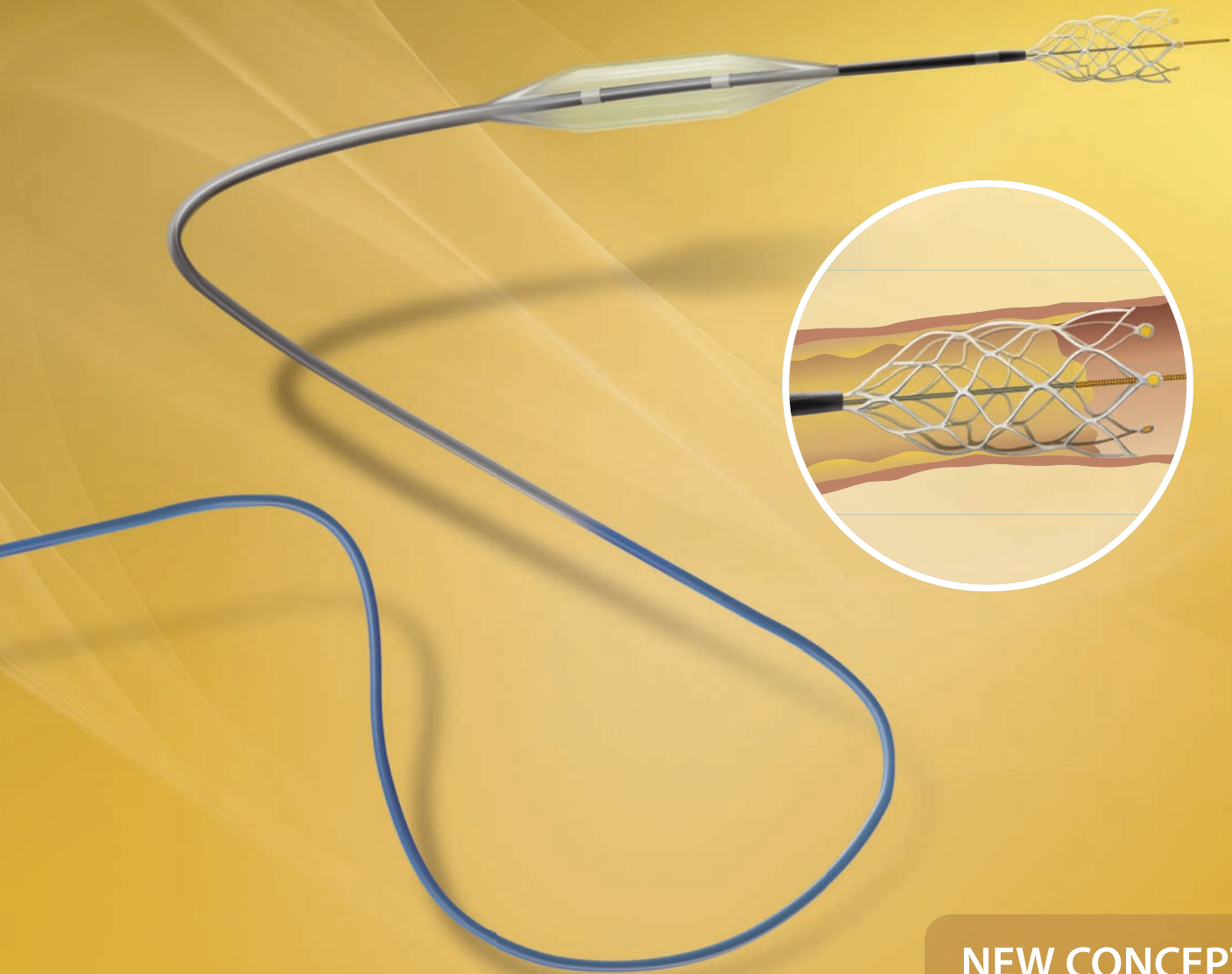
for rapid revascularization with
Trepo[®] XP ProVue Retriever

AXS Catalyst 5

DISTAL ACCESS CATHETER

for flow diversion support

CREDO[®] Stent with **NeuroSpeed[®] PTA Balloon Catheter**



Not for sale within the territory of the United States

NEW CONCEPT

- One access – two options
- Timesaving and effective

CREDO[®] Stent only available within **ASSISTENT – Acandis Stenting of Intracranial STENosis-regisTry**



Simplify the MOC Process



Manage your CME Credits Online

CMEgateway.org

Available to Members of Participating Societies

American Board of Radiology (ABR)
American College of Radiology (ACR)
American Roentgen Ray Society (ARRS)
American Society of Neuroradiology (ASNR)
Commission on Accreditation of Medical
Physics Educational Programs, Inc. (CAMPEP)
Radiological Society of North America (RSNA)
Society of Interventional Radiology (SIR)
SNM
The Society for Pediatric Radiology (SPR)

It's Easy and Free!

Log on to CME Gateway to:

- View or print reports of your CME credits from multiple societies from a single access point.
- Print an aggregated report or certificate from each participating organization.
- Link to SAMs and other tools to help with maintenance of certification.

American Board of Radiology (ABR) participation!

By activating ABR in your organizational profile, your MOC-fulfilling CME and SAM credits can be transferred to your own personalized database on the ABR Web site.

Sign Up Today!

go to CMEgateway.org

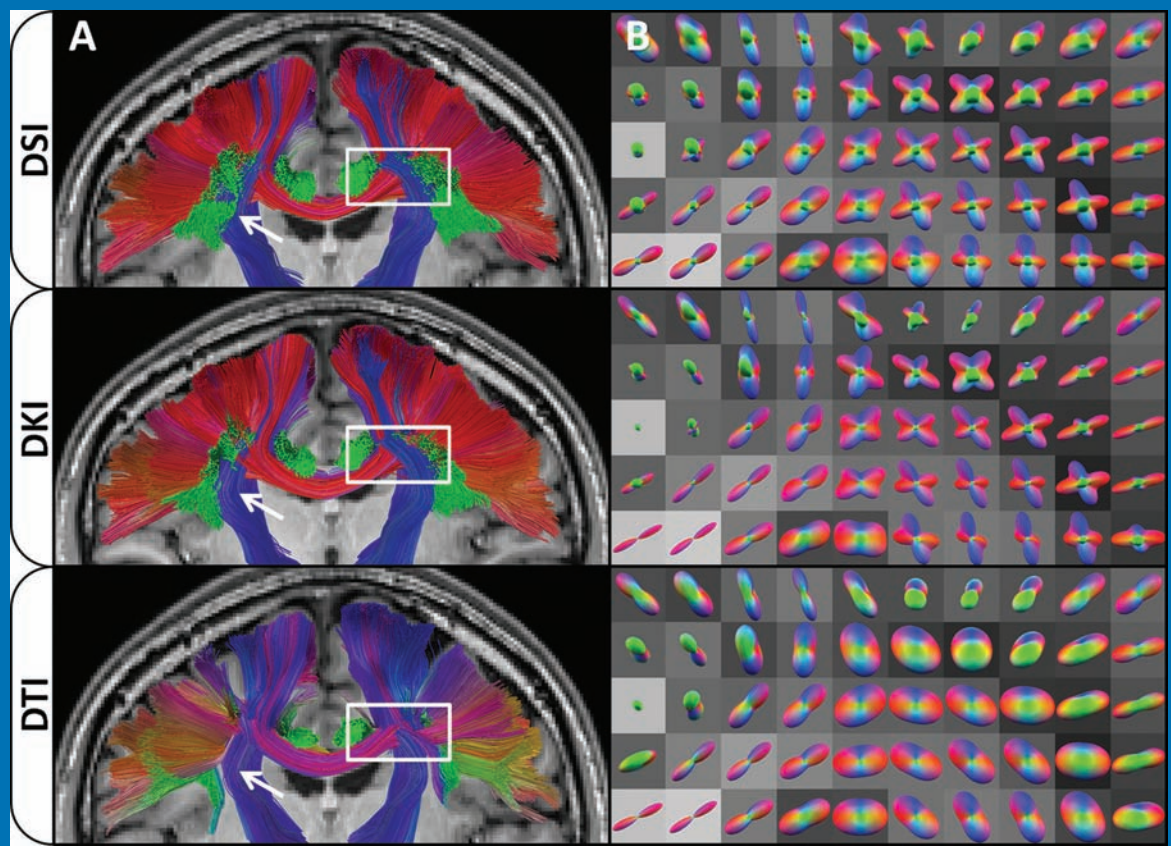
AJNR

AMERICAN JOURNAL OF NEURORADIOLOGY

JULY 2016
VOLUME 37
NUMBER 7
WWW.AJNR.ORG

THE JOURNAL OF DIAGNOSTIC AND
INTERVENTIONAL NEURORADIOLOGY

Comparison of DTI, DKI, and diffusion spectrum imaging
of white matter
Non-RVU-generating activities of academic neuroradiologists
Atypical presentations of intracranial hypotension
Official Journal ASNR • ASFNR • ASHNR • ASPNR • ASSR



Official Journal:

American Society of Neuroradiology
American Society of Functional Neuroradiology
American Society of Head and Neck Radiology
American Society of Pediatric Neuroradiology
American Society of Spine Radiology

EDITOR-IN-CHIEF

Jeffrey S. Ross, MD

Professor of Radiology, Department of Radiology,
Mayo Clinic College of Medicine, Phoenix, Arizona

SENIOR EDITORS

Harry J. Cloft, MD, PhD

Professor of Radiology and Neurosurgery,
Department of Radiology, Mayo Clinic College of
Medicine, Rochester, Minnesota

Thierry A.G.M. Huisman, MD

Professor of Radiology, Pediatrics, Neurology, and
Neurosurgery, Chairman, Department of Imaging
and Imaging Science, Johns Hopkins Bayview,
Director, Pediatric Radiology and Pediatric
Neuroradiology, Johns Hopkins Hospital,
Baltimore, Maryland

C.D. Phillips, MD, FACR

Professor of Radiology, Weill Cornell Medical
College, Director of Head and Neck Imaging,
New York-Presbyterian Hospital, New York,
New York

Pamela W. Schaefer, MD

Clinical Director of MRI and Associate Director of
Neuroradiology, Massachusetts General Hospital,
Boston, Massachusetts, Associate Professor,
Radiology, Harvard Medical School, Cambridge,
Massachusetts

Charles M. Strother, MD

Professor of Radiology, Emeritus, University of
Wisconsin, Madison, Wisconsin

Jody Tanabe, MD

Professor of Radiology and Psychiatry,
Chief of Neuroradiology,
University of Colorado, Denver, Colorado

STATISTICAL SENIOR EDITOR

Bryan A. Comstock, MS

Senior Biostatistician,
Department of Biostatistics,
University of Washington, Seattle, Washington

EDITORIAL BOARD

Ashley H. Aiken, *Atlanta, Georgia*
A. James Barkovich, *San Francisco, California*
Walter S. Bartynski, *Charleston, South Carolina*
Barton F. Branstetter IV, *Pittsburgh, Pennsylvania*
Jonathan L. Brisman, *Lake Success, New York*
Julie Bykowski, *San Diego, California*
Donald W. Chakeres, *Columbus, Ohio*
Asim F. Choudhri, *Memphis, Tennessee*
Alessandro Cianfoni, *Lugano, Switzerland*
Colin Derdeyn, *St. Louis, Missouri*
Rahul S. Desikan, *San Francisco, California*
Richard du Mesnil de Rochemont, *Frankfurt, Germany*
Clifford J. Eskey, *Hanover, New Hampshire*
Massimo Filippi, *Milan, Italy*
David Fiorella, *Cleveland, Ohio*
Allan J. Fox, *Toronto, Ontario, Canada*
Christine M. Glastonbury, *San Francisco, California*
John L. Go, *Los Angeles, California*
Wan-Yuo Guo, *Taipei, Taiwan*
Rakesh K. Gupta, *Lucknow, India*
Lotfi Hacein-Bey, *Sacramento, California*
David B. Hackney, *Boston, Massachusetts*
Christopher P. Hess, *San Francisco, California*
Andrei Holodny, *New York, New York*
Benjamin Huang, *Chapel Hill, North Carolina*
George J. Hunter, *Boston, Massachusetts*
Mahesh V. Jayaraman, *Providence, Rhode Island*
Valerie Jewells, *Chapel Hill, North Carolina*
Timothy J. Kaufmann, *Rochester, Minnesota*
Kenneth F. Layton, *Dallas, Texas*
Ting-Yim Lee, *London, Ontario, Canada*
Michael M. Lell, *Erlangen, Germany*
Michael Lev, *Boston, Massachusetts*
Karl-Olof Lovblad, *Geneva, Switzerland*
Franklin A. Marden, *Chicago, Illinois*
M. Gisele Matheus, *Charleston, South Carolina*
Joseph C. McGowan, *Merion Station, Pennsylvania*
Kevin R. Moore, *Salt Lake City, Utah*
Christopher J. Moran, *St. Louis, Missouri*
Takahisa Mori, *Kamakura City, Japan*
Suresh Mukherji, *Ann Arbor, Michigan*
Amanda Murphy, *Toronto, Ontario, Canada*
Alexander J. Nemeth, *Chicago, Illinois*
Laurent Pierot, *Reims, France*
Jay J. Pillai, *Baltimore, Maryland*
Whitney B. Pope, *Los Angeles, California*
M. Judith Donovan Post, *Miami, Florida*
Tina Young Poussaint, *Boston, Massachusetts*
Joana Ramalho, *Lisbon, Portugal*

Otto Rapalino, *Boston, Massachusetts*
Álex Rovira-Cañellas, *Barcelona, Spain*
Paul M. Ruggieri, *Cleveland, Ohio*
Zoran Rumboldt, *Rijeka, Croatia*
Amit M. Saindane, *Atlanta, Georgia*
Erin Simon Schwartz, *Philadelphia, Pennsylvania*
Aseem Sharma, *St. Louis, Missouri*
J. Keith Smith, *Chapel Hill, North Carolina*
Maria Vittoria Spampinato, *Charleston, South Carolina*
Gordon K. Sze, *New Haven, Connecticut*
Krishnamoorthy Thamburaj, *Hershey, Pennsylvania*
Kent R. Thielen, *Rochester, Minnesota*
Cheng Hong Toh, *Taipei, Taiwan*
Thomas A. Tomsick, *Cincinnati, Ohio*
Aquila S. Turk, *Charleston, South Carolina*
Willem Jan van Rooij, *Tilburg, Netherlands*
Arastoo Vossough, *Philadelphia, Pennsylvania*
Elysa Widjaja, *Toronto, Ontario, Canada*
Max Wintermark, *Charlottesville, Virginia*
Ronald L. Wolf, *Philadelphia, Pennsylvania*
Kei Yamada, *Kyoto, Japan*

EDITORIAL FELLOW

Daniel S. Chow, *San Francisco, California*

SPECIAL CONSULTANTS TO THE EDITOR

AJNR Blog Editor

Neil Lall, *Denver, Colorado*

Case of the Month Editor

Nicholas Stence, *Aurora, Colorado*

Case of the Week Editors

Juan Pablo Cruz, *Santiago, Chile*
Sapna Rawal, *Toronto, Ontario, Canada*

Classic Case Editor

Sandy Cheng-Yu Chen, *Taipei, Taiwan*

Facebook Editor

Peter Yi Shen, *Sacramento, California*

Health Care and Socioeconomics Editor

Pina C. Sanelli, *New York, New York*

Physics Editor

Greg Zaharchuk, *Stanford, California*

Podcast Editor

Yvonne Lui, *New York, New York*

Twitter Editor

Ryan Fitzgerald, *Little Rock, Arkansas*

YOUNG PROFESSIONALS

ADVISORY COMMITTEE

Asim K. Bag, *Birmingham, Alabama*
Anna E. Nidecker, *Sacramento, California*
Peter Yi Shen, *Sacramento, California*

Founding Editor

Juan M. Taveras

Editors Emeriti

Mauricio Castillo, Robert I. Grossman,
Michael S. Huckman, Robert M. Quencer

Managing Editor

Karen Halm

Electronic Publications Manager

Jason Gantenberg

Executive Director, ASNIR

James B. Gantenberg

Director of Communications, ASNIR

Angelo Artemakis

AJNR

AMERICAN JOURNAL OF NEURORADIOLOGY

JULY 2016
VOLUME 37
NUMBER 7
WWW.AJNR.ORG

Publication Preview at www.ajnr.org features articles released in advance of print. Visit www.ajnrblog.org to comment on AJNR content and chat with colleagues and AJNR's News Digest at <http://ajnrdigest.org> to read the stories behind the latest research in neuroimaging.

1191 **PERSPECTIVES** *A. Gordhan*

REVIEW ARTICLE

 1192 **Gadolinium-Based Contrast Agent Accumulation and Toxicity: An Update** *J. Ramalho, et al.*

PATIENT SAFETY
ADULT BRAIN

PATIENT SAFETY

  1199 **Full Dose-Reduction Potential of Statistical Iterative Reconstruction for Head CT Protocols in a Predominantly Pediatric Population** *A.E. Mirro, et al.*

PEDIATRICS

ACADEMIC PERSPECTIVES

 1206 **Non-Relative Value Unit-Generating Activities Represent One-Fifth of Academic Neuroradiologist Productivity** *M. Wintermark, et al.*

GENERAL CONTENTS

   1209 **Quantitative Susceptibility Mapping in Cerebral Cavernous Malformations: Clinical Correlations** *H. Tan, et al.*

ADULT BRAIN

     1216 **Mapping the Orientation of White Matter Fiber Bundles: A Comparative Study of Diffusion Tensor Imaging, Diffusional Kurtosis Imaging, and Diffusion Spectrum Imaging** *G.R. Glenn, et al.*

ADULT BRAIN

  1223 **Iron and Non-Iron-Related Characteristics of Multiple Sclerosis and Neuromyelitis Optica Lesions at 7T MRI** *S. Chawla, et al.*

ADULT BRAIN

   1231 **Assessment of Collateral Status by Dynamic CT Angiography in Acute MCA Stroke: Timing of Acquisition and Relationship with Final Infarct Volume** *I.R. van den Wijngaard, et al.*

ADULT BRAIN

 1237 **Improving Perfusion Measurement in DSC-MR Imaging with Multiecho Information for Arterial Input Function Determination** *A.T. Newton, et al.*

ADULT BRAIN
PEDIATRICS
FUNCTIONAL

1244 **Time-of-Flight MR Angiography for Detection of Cerebral Hyperperfusion Syndrome after Superficial Temporal Artery-Middle Cerebral Artery Anastomosis in Moyamoya Disease** *K. Sato, et al.*

ADULT BRAIN
PEDIATRICS
EXTRACRANIAL
VASCULAR

AJNR (Am J Neuroradiol ISSN 0195-6108) is a journal published monthly, owned and published by the American Society of Neuroradiology (ASNR), 800 Enterprise Drive, Suite 205, Oak Brook, IL 60523. Annual dues for the ASNR include \$170.00 for journal subscription. The journal is printed by Cadmus Journal Services, 5457 Twin Knolls Road, Suite 200, Columbia, MD 21045; Periodicals postage paid at Oak Brook, IL and additional mailing offices. Printed in the U.S.A. POSTMASTER: Please send address changes to American Journal of Neuroradiology, P.O. Box 3000, Denville, NJ 07834, U.S.A. Subscription rates: nonmember \$380 (\$450 foreign) print and online, \$305 online only; institutions \$440 (\$510 foreign) print and basic online, \$875 (\$940 foreign) print and extended online, \$365 online only (basic), extended online \$790; single copies are \$35 each (\$40 foreign). Indexed by PubMed/Medline, BIOSIS Previews, Current Contents (Clinical Medicine and Life Sciences), EMBASE, Google Scholar, HighWire Press, Q-Sensei, RefSeek, Science Citation Index, and SCI Expanded. Copyright © American Society of Neuroradiology.

	1249	Comparison of CSF Distribution between Idiopathic Normal Pressure Hydrocephalus and Alzheimer Disease <i>S. Yamada, et al.</i>	ADULT BRAIN
	1256	Atypical Presentations of Intracranial Hypotension: Comparison with Classic Spontaneous Intracranial Hypotension <i>A.A. Capizzano, et al.</i>	ADULT BRAIN
	1262	Quantitative Assessment of Circumferential Enhancement along the Wall of Cerebral Aneurysms Using MR Imaging <i>S. Omodaka, et al.</i>	ADULT BRAIN
	1267	Evaluating Permeability Surface-Area Product as a Measure of Blood-Brain Barrier Permeability in a Murine Model <i>E.K. Weidman, et al.</i>	ADULT BRAIN
	1275	Multicenter Prospective Trial of Stent Placement in Patients with Symptomatic High-Grade Intracranial Stenosis <i>P. Gao, et al.</i>	INTERVENTIONAL ADULT BRAIN
	1281	Endovascular Management of Tandem Occlusion Stroke Related to Internal Carotid Artery Dissection Using a Distal to Proximal Approach: Insight from the RECAST Study <i>G. Marnat, et al.</i>	INTERVENTIONAL EXTRACRANIAL VASCULAR
	1289	Hemodynamic and Anatomic Variations Require an Adaptable Approach during Intra-Arterial Chemotherapy for Intraocular Retinoblastoma: Alternative Routes, Strategies, and Follow-Up <i>E. Bertelli, et al.</i>	INTERVENTIONAL PEDIATRICS EXTRACRANIAL VASCULAR
	1296	Prediction of Stent-Retriever Thrombectomy Outcomes by Dynamic Multidetector CT Angiography in Patients with Acute Carotid T or MCA Occlusions <i>K.M. Thierfelder, et al.</i>	INTERVENTIONAL ADULT BRAIN
	1303	C-Arm Conebeam CT Perfusion Imaging in the Angiographic Suite: A Comparison with Multidetector CT Perfusion Imaging <i>K. Niu, et al.</i>	INTERVENTIONAL ADULT BRAIN
	1310	Thinner Regions of Intracranial Aneurysm Wall Correlate with Regions of Higher Wall Shear Stress: A 7T MRI Study <i>R. Blankena, et al.</i>	INTERVENTIONAL ADULT BRAIN
	1318	Inflow Jet Patterns of Unruptured Cerebral Aneurysms Based on the Flow Velocity in the Parent Artery: Evaluation Using 4D Flow MRI <i>K. Futami, et al.</i>	INTERVENTIONAL
	1324	The Impact of Middle Turbinate Concha Bullosa on the Severity of Inferior Turbinate Hypertrophy in Patients with a Deviated Nasal Septum <i>C.M. Tomblinson, et al.</i>	HEAD & NECK
	1331	Vestibular Aqueduct Measurements in the 45° Oblique (Pöschl) Plane <i>A.F. Juliano, et al.</i>	HEAD & NECK PEDIATRICS
	1338	Brain Injury in Neonates with Complex Congenital Heart Disease: What Is the Predictive Value of MRI in the Fetal Period? <i>M. Brossard-Racine, et al.</i>	PEDIATRICS
	1347	Whole-Brain DTI Assessment of White Matter Damage in Children with Bilateral Cerebral Palsy: Evidence of Involvement beyond the Primary Target of the Anoxic Insult <i>F. Arrigoni, et al.</i>	PEDIATRICS
	1354	Decreased Superior Sagittal Sinus Diameter and Jugular Bulb Narrowing Are Associated with Poor Clinical Outcome in Vein of Galen Arteriovenous Malformation <i>G. Saliou, et al.</i>	PEDIATRICS
	1359	Development of the Fetal Vermis: New Biometry Reference Data and Comparison of 3 Diagnostic Modalities—3D Ultrasound, 2D Ultrasound, and MR Imaging <i>E. Katorza, et al.</i>	PEDIATRICS
	1367	A Novel Methodology for Applying Multivoxel MR Spectroscopy to Evaluate Convection-Enhanced Drug Delivery in Diffuse Intrinsic Pontine Gliomas <i>D.I. Guisado, et al.</i>	PEDIATRICS
	1374	Imaging Signs in Spontaneous Intracranial Hypotension: Prevalence and Relationship to CSF Pressure <i>P.G. Kranz, et al.</i>	SPINE ADULT BRAIN

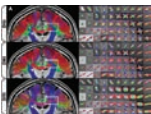
1379 The “Hyperdense Paraspinal Vein” Sign: A Marker of CSF-Venous Fistula **SPINE**

P.G. Kranz, et al.

1382 **35 YEARS AGO IN AJNR**

BOOK REVIEWS R.M. Quencer, Section Editor

Please visit www.ajnrblog.org to read and comment on Book Reviews.



Effects of diffusion orientation distribution function on WM tractography are shown for diffusion spectrum imaging (*top*), DKI (*middle*), and DTI (*bottom*) overlaid on an MPRAGE image for anatomic reference. DTI fibers prematurely terminate or merge distinct tracts because crossing fibers are not detected.



Indicates Editor's Choices selection



Indicates Fellows' Journal Club selection



Indicates open access to non-subscribers at www.ajnr.org



Indicates article with supplemental on-line table



Indicates article with supplemental on-line photo



Indicates article with supplemental on-line video



Evidence-Based Medicine Level 1



Evidence-Based Medicine Level 2



Title: Percussive Bliss.

What comes out of the drum? Music!
And there is a dance no hands or feet dance.
No fingers play it, no ears hear it,
Because the Enlightened One is the ear, and the one listening too.
The great doors remain closed,
But the spring fragrance is inside anyway,
And no one sees what takes place there.
Men and women who have escaped from
The gross part of their brain will understand
This poem.

—Kabir (16th century poet)

Ajeet Gordhan, MD, Neurointerventional Radiology, Bloomington Radiology, St Joseph Medical Center, Bloomington, Illinois

Gadolinium-Based Contrast Agent Accumulation and Toxicity: An Update

J. Ramalho, R.C. Semelka, M. Ramalho, R.H. Nunes, M. AlObaidy, and M. Castillo



ABSTRACT

SUMMARY: In current practice, gadolinium-based contrast agents have been considered safe when used at clinically recommended doses in patients without severe renal insufficiency. The causal relationship between gadolinium-based contrast agents and nephrogenic systemic fibrosis in patients with renal insufficiency resulted in new policies regarding the administration of these agents. After an effective screening of patients with renal disease by performing either unenhanced or reduced-dose-enhanced studies in these patients and by using the most stable contrast agents, nephrogenic systemic fibrosis has been largely eliminated since 2009. Evidence of in vivo gadolinium deposition in bone tissue in patients with normal renal function is well-established, but recent literature showing that gadolinium might also deposit in the brain in patients with intact blood-brain barriers caught many individuals in the imaging community by surprise. The purpose of this review was to summarize the literature on gadolinium-based contrast agents, tying together information on agent stability and animal and human studies, and to emphasize that low-stability agents are the ones most often associated with brain deposition.

ABBREVIATIONS: DN = dentate nuclei; GBCA = gadolinium-based contrast agent; NSF = nephrogenic systemic fibrosis

Gadolinium-based contrast agents (GBCAs) have been widely used in clinical MR imaging studies since the initial FDA approval of gadopentetate dimeglumine (Magnevist; Bayer HealthCare Pharmaceuticals, Wayne, New Jersey) in 1988. To date, 9 GBCAs are available for clinical use in 1 or more regions of the world (Table 1), and it is estimated that >200 million doses have been administered worldwide.¹

All GBCAs approved for clinical use have been considered to have a wide safety margin when used at relatively low doses (0.1–0.3 mmol/kg) in patients with normal renal function. The accumulated safety record is excellent, with serious adverse reactions occurring in roughly 0.03% of all administrations.^{2,3} These adverse reactions are more common in patients with history of asthma, allergies, and renal insufficiency and in patients injected at faster rates.^{1,4,5}

GBCAs had an exceptional safety reputation from 1988 to 2006, to the point that in 2004 and 2005 GBCAs were recom-

mended as a substitute for iodine-based contrast media in patients with renal failure for CT and in interventional studies.^{6–9}

In 2006, the association between the administration of GBCAs and the development of nephrogenic systemic fibrosis (NSF) in patients with renal insufficiency was described.^{10,11} NSF is a debilitating and potentially life-threatening disease characterized by widespread progressive tissue fibrosis that results from the deposition of fibroblasts and collagen. It predominantly involves the skin but may also affect other organs such as the lungs, liver, heart, and muscles.

The exact pathophysiology of NSF remains unknown, but the dissociation of gadolinium ions from their chelating ligands has been accepted as the primary etiology, which is more likely to occur in patients with renal failure than in those with normal renal function because the excretion rate is reduced in the former, allowing time for the chelates to disassociate in vivo. Most cases of NSF reported in the literature have been associated with administration of nonionic, linear gadodiamide (Omniscan; GE Healthcare, Piscataway, New Jersey),¹² though reports also described substantial incidents with another nonionic linear agent, gadoversetamide (OptiMARK; Covidien, Irvine, California), and with an ionic linear agent, gadopentetate dimeglumine (Magnevist).^{13–17}

Since mid-2009, no new cases of NSF have been reported. This finding reflects the use of more stable GBCAs and limiting the use of GBCAs in patients with renal failure. As a result, from 2009 to 2014, confidence in the safety profile of GBCAs has been largely

From the Departments of Neuroradiology (J.R., R.H.N., M.C.) and Radiology (R.C.S., M.R., R.H.N., M.A.), University of North Carolina Hospital, Chapel Hill, North Carolina; Centro Hospitalar de Lisboa Central (J.R.), Lisbon, Portugal; Hospital Garcia de Orta (M.R.), Almada, Portugal; Santa Casa de Misericórdia de São Paulo (R.H.N.), São Paulo, Brazil; and King Faisal Specialist Hospital and Research Center (M.A.), Riyadh, Saudi Arabia.

Please address correspondence to Joana Ramalho, MD, University of North Carolina Hospital at Chapel Hill, Room 3326 Old Infirmary Building, Manning Dr, Chapel Hill, NC 27599-7510; e-mail: Joana-Ramalho@netcabo.pt

Indicates open access to non-subscribers at www.ajnr.org

<http://dx.doi.org/10.3174/ajnr.A4615>

Table 1: Gadolinium-based contrast agents currently approved for clinical use: biochemical properties

Chemical Structure	Trade Name	Thermodynamic Stability Constant	Conditional Stability Constant	Elimination Pathway
Linear				
Nonionic				
Gadodiamide	Omniscan, 0.5 mmol/mL	16.8	14.9	Renal
Gadoversetamide	OptiMARK, 0.5 mmol/mL	16.6	15	Renal
Ionic				
Gadopentetate dimeglumine	Magnevist, 0.5 mmol/mL	22.1	17.7	Renal
Gadobenate dimeglumine	MultiHance, 0.5 mmol/mL	22.6	18.4	93% Renal 3% Biliary
Gadoxetic acid disodium	Primovist, 0.25 mmol/mL	23.5	NA	50% Renal 50% Biliary
Gadofosveset trisodium	Vasovist, 0.25 mmol/mL ^a	22	NA	91% Renal 9% Biliary
Macrocyclic				
Nonionic				
Gadoteridol	ProHance, 0.5 mmol/mL	22.8	17.1	Renal
Gadobutrol	Gadavist, 0.5 mmol/mL	21.8	NA	Renal
Ionic				
Gadoterate meglumine	Dotarem, 0.5 mmol/mL	25.4	19	Renal

Note:—NA indicates not applicable.

^a Bayer Schering Pharma.

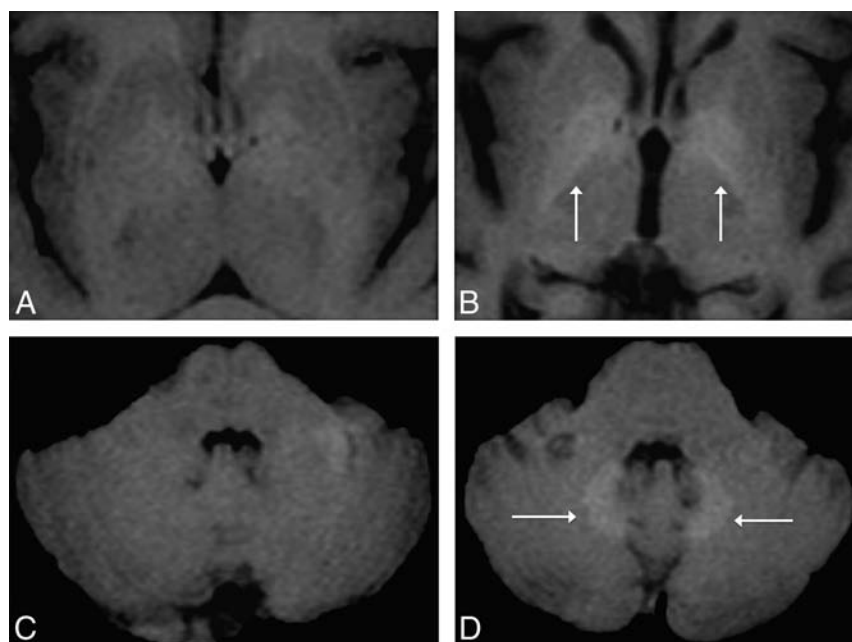


FIG 1. Axial MR images in a 51-year-old woman with parkinsonism. Unenhanced T1-weighted MR imagings of the first (A and C) and fifth (3 years later; B and D) gadolinium-enhanced MR imagings performed with a nonionic linear GBCA (Omniscan) at the level of the basal ganglia (A and B) and the level of the dentate nuclei of the cerebellum (C and D). The images show progressively increased T1 signal of the globi pallidi and dentate nuclei (white arrows, B and D), undetectable on the first MR imaging.

restored. However, in the past 2 years, numerous studies regarding gadolinium deposition in neural tissues in patients with normal renal function have been published.

This deposition was first postulated by MR imaging studies in which progressively increased signal intensity in the globi pallidi and/or dentate nuclei (DN) on unenhanced T1-weighted images in patients with normal renal function was related to multiple administrations of GBCAs. As with NSF, the agent most associated with this finding was gadodiamide (Omniscan) (Fig 1),¹⁸⁻²¹ but it has also been shown with gadopentetate dimeglumine (Magnevist).^{18,22}

inductively coupled plasma mass spectroscopy. They also showed a dose-dependent relationship between intravenous gadodiamide administrations and subsequent neural tissue deposition that was independent of renal function. Kanda et al²⁷ confirmed neural tissue deposition in 5 patients with normal renal function who had received gadopentetate dimeglumine (Magnevist), gadodiamide (Omniscan), or gadoteridol (ProHance; Bracco Diagnostics, Princeton, New Jersey) in varying combinations.

Confirming human studies, an animal study²⁸ also demonstrated that repeated administrations of linear gadodiamide (Omniscan) to

T1 hyperintensity in the DN was previously described in the progressive subtype of multiple sclerosis and was associated with increased clinical disability, lesion load, and brain atrophy.²³ Similar findings were also reported with brain irradiation.²⁴ From the perspective of our current understanding, none of these studies considered the number of contrast-enhanced MR imaging studies performed in their analyses, raising the question of whether these findings reflect gadolinium deposition rather than a primary disease manifestation, as demonstrated recently by Adin et al²⁵ in a study with 184 subjects who were treated with brain irradiation.

A study by McDonald et al²⁶ was the first to document that the high signal in the neural tissues reflected deposited gadolinium. In brain specimens from postmortem examinations of 13 subjects who underwent at least 4 MR imaging examinations with gadodiamide (Omniscan), the presence of gadolinium was histologically confirmed by using

healthy rats was associated with progressive and persistent T1 signal hyperintensity in the DN and with histologic gadolinium deposits in the cerebellum, in contrast to those who received the macrocyclic agent gadoterate meglumine (Dotarem; Guerbet, Aulnay-sous-Bois, France), in whom no effects were observed.

The more stable macrocyclic GBCAs, such as gadoteridol (ProHance),²² and gadoterate meglumine (Dotarem),^{28,29} were not associated with substantial MR imaging changes or even brain deposition in the case of gadoterate meglumine (Dotarem),²⁸ supporting the concept that gadolinium accumulation varies depending on the stability of the agent used. Gadobenate dimeglumine (MultiHance; Bracco Diagnostics), an agent of intermediate stability, was associated with fewer MR imaging changes compared with the linear gadodiamide (Omniscan) and was only appreciated in the DN.²¹ Recently, Weberling et al³⁰ suggested that this agent releases less gadolinium than gadopentetate dimeglumine (Magnevist) but more than gadoterate meglumine (Dotarem). Most surprising, a more stable macrocyclic agent, gadobuterol (Gadavist; Bayer Schering Pharma, Berlin, Germany), has also been shown to result in brain deposition.³¹ These findings suggest that all GBCAs should be evaluated individually, despite their molecular structures.

Gadolinium-Based Contrast Agents: In Vitro Stability, Pharmacokinetics, and Biodistribution

GBCAs are used as MR imaging contrast agents because of their excellent paramagnetic properties. Gadolinium is a rare earth element and one of the 15 metallic atoms in the lanthanide series. On the periodic table, its symbol is Gd, and its atomic number is 64. Free gadolinium (Gd^{3+}) is toxic in humans, and to be used in vivo, it must be chelated to organic ligands.³²

Depending on the ligand structure, GBCAs can be classified in 2 major groups: macrocyclic molecules, in which the Gd^{3+} is caged in the preorganized cavity of the ligand; and linear or open chain molecules, in which the ligand is not fully closed. From a chemical structure perspective, each category may be further subclassified, according to their charges, into ionic and nonionic.^{33,34}

Frenzel et al³³ reported that under physiologic conditions (human serum, at 37°C), GBCAs can be divided into 3 distinct stability classes: nonionic linear, ionic linear, and macrocyclic. Macrocyclic chelates are more stable than linear chelates, and ionic linear chelates are more stable than the nonionic linear ones.

The dissociation of Gd^{3+} from its ligand is an equilibrium process defined by 2 distinct and independent parameters: kinetic and thermodynamic stabilities.

Kinetic stability of a gadolinium complex is characterized by its dissociation rate, which describes how fast a resting equilibrium is reached and thus how fast Gd^{3+} is released from a gadolinium complex.³³ If the kinetic stability is high, the dissociation rate is considerably slower than the elimination rate from the body, and the release of Gd^{3+} becomes negligible during the in vivo residence time of the gadolinium complex. A simple way to understand kinetic stability is the speed at which the chelated gadolinium agent dissociates. At present, kinetic stability of GBCAs is reported for a pH of 1 (hence, we prefer to designate these values as “pH 1, kinetic stability”), in large part, because the

kinetic stability of some of the macrocyclic agents would need to be expressed in terms of months or years at a pH of 7.4.

Thermodynamic stability reflects the energy required for the metalloligand to release the Gd^{3+} ion. When thermodynamic stability is high, the chelate less readily releases the free Gd^{3+} ion. A simple way to understand thermodynamic stability is that it represents the final equilibrium state between chelated and unchelated gadolinium. Thermodynamic stability is also determined at a pH of 1, but a more appropriate measure when considering an in vivo environment is to calculate it at the physiologic pH of 7.4,^{4,33} which is termed “conditional stability” (we prefer the term “pH 7, thermodynamic stability”).

Other factors, including the concentration of competing ions or ligands and the interaction times between the gadolinium chelates and the competitors,^{35,36} contribute to the stability of GBCAs.⁴

In vivo, the gadolinium complex is surrounded by a variety of competitors, which have the potential to interact with either the Gd^{3+} or the ligand. Different endogenous cations (eg, Fe^{3+} , Mg^{2+} , Cu^{2+} , Zn^{2+} , or Ca^{2+}) compete with Gd^{3+} ions for the ligand, and endogenous anions (eg, phosphate, carbonate, hydroxide) compete for the Gd^{3+} ions. This competition may destabilize the gadolinium complex in biologic fluids and shift the dissociation equilibrium toward its free components. The components do not exist as free ions but bind to other agents rapidly. This exchange process is termed “transmetallation.”^{1,33,37-39} Most often, if the ligand releases Gd^{3+} ions, they quickly rebind. On the basis of the availability of other cations and the affinity of the ligand to them, the ligand may bind to another cation.^{4,33} The same phenomenon is experienced by the anionic component.

GBCAs are also classified according to their biodistribution as extracellular, combined extracellular-intracellular, and blood-pool agents. An intravenously administered chelate rapidly equilibrates in the intravascular and interstitial fluid compartments (extracellular compartment). Depending on its structure, the complex may also be distributed in the intracellular compartment (including the liver and kidneys) by passive diffusion or specific uptake processes.⁴⁰ Most GBCAs in clinical use are nonspecific extracellular contrast agents, which, like iodine-based contrast agents, are cleared almost exclusively by the kidneys. Combined extracellular-intracellular agents are distributed into the extracellular and intracellular compartments of hepatocytes; therefore, they are also described as “hepatocyte-specific agents.” These agents (gadobenate dimeglumine [MultiHance] and gadoxetic acid/gadoxetate disodium [Primovist/Eovist; Bayer Schering Pharma]) when taken up by hepatocytes are excreted into the bile ducts, thus exhibiting dual-elimination routes (renal and biliary). The biliary route is an important pathway of elimination of contrast if the kidneys are functioning poorly.^{32,41} With normally functioning kidneys, most of the administered dose of GBCAs, regardless of which agent was given, should be eliminated in <2 hours after injection and >95% by 24 hours. However, patients with renal impairment have reduced GBCA elimination, and the Gd complex remains inside the body for extended periods, allowing dissociation to occur.^{4,33} In this setting, GBCAs with dual elimination (biliary and renal) have an alternative elimination

pathway, which helps decrease the gadolinium burden in the body.

Gadolinium Toxicity

Most of the known toxicity of the free Gd^{3+} ion is related to 2 properties: its insolubility at physiologic pH, resulting in very slow systemic excretion; and an ionic radius close to that of Ca^{2+} ($Gd^{3+} = 107.8$ pm and $Ca^{2+} = 114$ pm) that allows Gd^{3+} to compete biologically with Ca^{2+} .^{3,34}

Gadolinium is a well-known blocker of many types of voltage-gated calcium channels at very low concentrations, and consequently, it can inhibit physiologic processes such as contraction of smooth, skeletal, and cardiac muscles; transmission of nerve impulses; and blood coagulation. It also inhibits the activity of certain enzymes such as Ca^{2+} -activated- Mg^{2+} -adenosine triphosphatase, some dehydrogenases and kinases, and glutathione S-transferases. It also acts as an agonist on the calcium-sensing receptors.⁴² Gadolinium may also increase the expression of some cytokines,⁴³ inhibit mitochondrial function, and induce oxidative stress.^{44,45}

Major lesions related to single-dose administration of gadolinium chloride (0.07–0.35 mmol/kg) in rats consist of mineral deposition in capillary beds, phagocytosis of minerals by macrophage-like cells, hepatocellular and splenic necrosis followed by dystrophic mineralization, decreased platelet numbers, and increased coagulation times.⁴⁶ Gadolinium is also a potent inhibitor of the reticuloendothelial system.^{34,47} All GBCAs and gadolinium chloride have been found to stimulate fibroblast proliferation in tissues taken from healthy subjects.^{48–51} This last process may be a major factor responsible for NSF because proliferation of CD34+ fibroblasts is the hallmark histologic feature of this disease.^{52,53}

Gadolinium Retention and Tissue Deposition

Several studies describe a complex pharmacokinetic behavior after intravenous administration of GBCA. Even in patients with normal renal function, *in vivo* clinical exposure to gadolinium chelates results in gadolinium incorporation into body tissues such as bone matrix^{54–56} or brain tissues.^{26,27} As early as 1991, Rocklage et al⁵⁷ stated, “Minute amounts of chelated or unchelated metals are likely to remain in the body for an extended period and could possibly result in a toxic effect.”

Gibby et al⁵⁴ used inductivity coupled plasma atomic emission spectroscopy to quantify gadolinium deposition in the bones of patients who underwent total hip arthroplasty after an injection of 0.1 mmol/kg of gadodiamide (Omniscan) or gadoteridol (ProHance) no less than 3 days and not more than 8 days before the operation. The authors found that Omniscan resulted in 2.5 times the amount of gadolinium deposition as ProHance. In a follow-up study, White et al⁵⁵ confirmed these findings by using a more sensitive analytic method and reported that Omniscan deposited 4 times more than did ProHance.

Later, Darrach et al⁵⁶ also analyzed bone tissue. The authors confirmed that gadolinium incorporates into bone and is retained for >8 years. However, no differences were observed in bone gadolinium concentration between patients dosed with Omniscan ($n = 6$) and ProHance ($n = 5$). It is difficult to explain the different findings between these 2 groups, and perhaps the small

number of patients may have affected the results of Darrach et al. Other researchers have previously estimated that approximately 1% of the injected gadolinium from each dose of the evaluated GBCAs could be released from the contrast agent and deposited in the bones, including in patients with normal kidney function.⁵⁸

The methods of gadolinium sequestration and deposition remain poorly understood. Little is known about the levels of gadolinium required to induce tissue structural changes and to achieve clinical significance in humans. Recently, Christensen et al⁵² analyzed the skin of 13 patients with NSF and found significant differences in the amounts of gadolinium in affected-versus-unaaffected regions. Gadolinium was also present in unaffected skin. The authors also found elevated gadolinium concentration in the skin of 2 healthy individuals months after the GBCA exposure. These findings suggest that there may be a threshold level for gadolinium required for the development of disease.⁵²

Regarding brain tissue deposition, Xia et al⁵⁹ used scanning electron microscopy with energy dispersive x-ray spectroscopy to evaluate gadolinium deposition within brain tumor tissues that had blood-brain barrier disruption and found that gadolinium deposition occurred in patients without severe renal disease. Deposition of gadolinium in the cerebellum was also reported in a patient who developed NSF after several administrations of Omniscan.⁶⁰ Gadolinium deposition in neural tissues in patients with intact blood-brain barrier and normal renal function was only recently established by McDonald et al,²⁶ followed by Kanda et al.²⁷ Postmortem brain specimens from the 2 studies showed no obvious gadolinium-mediated histologic changes²⁶ or macroscopic changes²⁷ in areas of gadolinium deposition.

Another intriguing finding is the nonuniform gadolinium deposition in neural structures. Among all sampled neuroanatomic locations (globi pallidi, thalami, DN, and pons), McDonald et al²⁶ found that the DN contained the highest median concentrations of elemental gadolinium, followed by the globi pallidi. Confirming this finding, Kanda et al²⁷ found that the DN and globi pallidi showed significantly higher gadolinium concentrations than the other evaluated brain regions (ie, cerebellar white matter, frontal lobe cortex, and frontal lobe white matter).

Similar MR imaging signal-intensity changes in the dentate and/or deep gray nuclei are seen in patients with multiple sclerosis, neurofibromatosis, hypoparathyroidism, manganism, inherited metabolic disorders, and Fahr disease, suggesting that these areas are particularly susceptible to metal deposition^{18,19,26,61}; but these anatomic preferences remain poorly understood.

In bone and other tissues, gadolinium deposition can be explained, in part, by the presence of fenestrated capillary systems, in combination with the analogous nature of Gd and Ca. However, neural tissue deposition with an otherwise intact blood-brain barrier as reported by McDonald et al²⁶ and Kanda et al²⁷ is not clearly understood. Kanda et al²⁷ found that gadolinium was prominently clustered in large foci within the endothelial wall but 18%–42% of gadolinium appeared to have crossed the blood-brain barrier and was deposited into the neural tissue interstitium.

It also remains unclear whether the gadolinium present in tissues, including neuronal tissues, is present in a chelated or unchelated state. Dissociated gadolinium often binds to phosphates or

Table 2: Summary of the results of the “Survey of Chronic Effects of Retained Gadolinium from Contrast MRIs”^{67,a}

Symptoms	Percentage (%) ^b
Pain: ache (dull, continuous pain), burning, numbness, tingling, or pricking sensations (paraesthesia), deep bone pain, and electric-like feelings	100% ^c
Pain location: extremities (feet, legs, hands, arms), hips, joints, and ribs	
Muscle symptoms: twitching and weakness	88%
Ocular symptoms: worsening vision, dry and bloodshot eyes	76%
Dermal changes: discoloration, rash, skin lesions (ulcers, papules, macules, nodules, or other lesions), tight skin, thickened tissue	71%
Cognitive symptoms: brain fog, difficulty concentrating	65%
ENT symptoms: ringing in ears, swallowing and voice problems	65%
Low body temperature, hair loss, and itchy skin	59%
Balance problems	53%
Swelling of extremities	53%

Note:—ENT indicates ear, nose, and throat.

^aData obtained directly from the survey.

^bPercentage of patients who reported the symptoms.

^cHighest priority chronic symptom in 59%.

carbonates in vivo, but it may also bind to proteins or other macromolecules and may also be taken up by macrophages or similar immune cells. Phosphate- and carbonate-bound gadolinium is considered insoluble and thought to not generate increased T1 signal.⁶² Tissue gadolinium deposits have often been associated with the presence of calcium, phosphorus, and sometimes iron or zinc.^{58,63,64} It is likely that chelated, protein-bound, insoluble, and intramacrophage gadolinium may all be present in different proportions depending on the type of GBCA. Future studies are needed to investigate in detail the behavior of GBCA molecules taken up in brain areas associated with T1 high signal intensity.²⁸

Clinical Significance of Gadolinium Deposition

The retention of gadolinium is important clinically. Gadolinium is not a naturally occurring biologic constituent, and once within the tissues of animals, it persists for long periods.⁵⁴ Additionally, heavy metals are known to be toxic.

The risks associated with the administration of weaker chelate GBCAs to patients with severely impaired kidney function are well-documented, and NSF is the result. As described in this review, the published literature, most of which is recent, indicates that some gadolinium from each dose given may remain in the body of all patients regardless of their renal function. The long-term and cumulative effects of retained gadolinium are, at present, unknown in patients with normal renal function.

Preclinical safety studies performed on animals failed to reveal any neurologic effects of chelated gadolinium when given intravenously.⁶⁰ There is, however, proof of gadolinium toxicity in the brain when administered by the intraventricular route in rats⁶⁵ and also by the intravenous route after blood-brain barrier disruption.⁶⁶

It is conceivable that patients may be adversely affected by retained gadolinium, especially in the brain. Despite being a difficult-to-prove cause-effect relationship, an MR imaging gadolinium-toxicity support group has been created. This group reported symptoms that they considered consistent with what is known about the toxic effects of gadolinium. In a recent survey performed in 17 patients, an association between chronic effects and GBCA exposure was suggested.⁶⁷ Although no specific conclusions can be drawn from the survey, the results indicated that the

symptoms appeared within 1 month after the last contrast-enhanced MR imaging and chronic pain was present in all 17 subjects (Table 2).

We recommend future investigations to evaluate a possible relation between gadolinium retention and clinical symptoms in subjects with normal renal function.

CONCLUSIONS

All GBCAs probably deposit in vivo in humans to some degree. At present, it is unclear why only the weaker chelates appear to result in meaningful clinical disease such as NSF, despite the fact that more stable GBCAs also show deposition. This presumably reflects the concentration of gadolinium deposited in tissues, though it is likely that the molecular state of the administered and deposited gadolinium strongly influences both deposition and clinical manifestations.

Recent literature confirms that gadolinium deposition occurs in the human brain after multiple gadolinium contrast administrations, despite an intact blood-brain barrier and normal renal function. On MR imaging, this accumulation is seen as increased signal intensity within the DN and globi pallidi on T1-weighted images. Gadolinium-associated findings gleaned from in vitro, animal, and human studies suggest that the greatest deposition and most deleterious effects are associated with GBCAs with the lowest stability. The ultimate significance of this deposition in subjects with normal renal function, in their brain and elsewhere, remains to be determined. Careful evaluation, especially in children, is recommended when administering GBCAs.

Recent literature confirms that gadolinium deposition occurs in the human brain after multiple gadolinium contrast administrations, despite an intact blood-brain barrier and normal renal function. On MR imaging, this accumulation is seen as increased signal intensity within the DN and globi pallidi on T1-weighted images. Gadolinium-associated findings gleaned from in vitro, animal, and human studies suggest that the greatest deposition and most deleterious effects are associated with GBCAs with the lowest stability. The ultimate significance of this deposition in subjects with normal renal function, in their brain and elsewhere, remains to be determined. Careful evaluation, especially in children, is recommended when administering GBCAs.

REFERENCES

1. Hao D, Ai T, Goerner F, et al. **MRI contrast agents: basic chemistry and safety.** *J Magn Reson Imaging* 2012;36:1060–71 [CrossRef Medline](#)
2. Bleicher AG, Kanal E. **Assessment of adverse reaction rates to a newly approved MRI contrast agent: review of 23,553 administrations of gadobenate dimeglumine.** *AJR Am J Roentgenol* 2008;191:W307–11 [CrossRef Medline](#)
3. Kanal E, Tweedle MF. **Residual or retained gadolinium: practical implications for radiologists and our patients.** *Radiology* 2015;275:630–34 [CrossRef Medline](#)
4. Ersoy H, Rybicki FJ. **Biochemical safety profiles of gadolinium-based extracellular contrast agents and nephrogenic systemic fibrosis.** *J Magn Reson Imaging* 2007;26:1190–97 [CrossRef Medline](#)
5. Lin SP, Brown JJ. **MR contrast agents: physical and pharmacologic basics.** *J Magn Reson Imaging* 2007;25:884–99 [CrossRef Medline](#)
6. Gierada DS, Bae KT. **Gadolinium as a CT contrast agent: assessment in a porcine model.** *Radiology* 1999;210:829–34 [CrossRef Medline](#)
7. Quinn AD, O'Hare NJ, Wallis FJ, et al. **Gd-DTPA: an alternative contrast medium for CT.** *J Comput Assist Tomogr* 1994;18:634–36 [CrossRef Medline](#)
8. Henson JW, Nogueira RG, Covarrubias DJ, et al. **Gadolinium-enhanced CT angiography of the circle of Willis and neck.** *AJNR Am J Neuroradiol* 2004;25:969–72 [Medline](#)
9. Bonvento MJ, Moore WH, Button TM, et al. **CT angiography with gadolinium-based contrast media.** *Acad Radiol* 2006;13:979–85 [CrossRef Medline](#)

10. Grobner T. Gadolinium: a specific trigger for the development of nephrogenic fibrosing dermopathy and nephrogenic systemic fibrosis? *Nephrol Dial Transplant* 2005;21:1104–08 CrossRef Medline
11. Marckmann P. Nephrogenic systemic fibrosis: suspected causative role of gadodiamide used for contrast-enhanced magnetic resonance imaging. *J Am Soc Nephrol* 2006;17:2359–62 CrossRef Medline
12. Thomsen HS. Nephrogenic systemic fibrosis: history and epidemiology. *Radiol Clin North Am* 2009;47:827–31, vi CrossRef Medline
13. Broome DR. Nephrogenic systemic fibrosis associated with gadolinium based contrast agents: a summary of the medical literature reporting. *Eur J Radiol* 2008;66:230–34 CrossRef Medline
14. Abujudeh HH, Kaewlai R, Kagan A, et al. Nephrogenic systemic fibrosis after gadopentetate dimeglumine exposure: case series of 36 patients. *Radiology* 2009;253:81–89 CrossRef Medline
15. Wertman R, Altun E, Martin DR, et al. Risk of nephrogenic systemic fibrosis: evaluation of gadolinium chelate contrast agents at four American universities. *Radiology* 2008;248:799–806 CrossRef Medline
16. Hope TA, Herfkens RJ, Denianke KS, et al. Nephrogenic systemic fibrosis in patients with chronic kidney disease who received gadopentetate dimeglumine. *Invest Radiol* 2009;44:135–39 CrossRef Medline
17. Fretellier N, Idée JM, Guerret S, et al. Clinical, biological, and skin histopathologic effects of ionic macrocyclic and nonionic linear gadolinium chelates in a rat model of nephrogenic systemic fibrosis. *Invest Radiol* 2011;46:85–93 CrossRef Medline
18. Kanda T, Ishii K, Kawaguchi H, et al. High signal intensity in the dentate nucleus and globus pallidus on unenhanced T1-weighted MR images: relationship with increasing cumulative dose of a gadolinium-based contrast material. *Radiology* 2014;270:834–41 CrossRef Medline
19. Errante Y, Cirimele V, Mallio CA, et al. Progressive increase of T1 signal intensity of the dentate nucleus on unenhanced magnetic resonance images is associated with cumulative doses of intravenously administered gadodiamide in patients with normal renal function, suggesting dechelation. *Invest Radiol* 2014;49:685–90 CrossRef Medline
20. Quattrocchi CC, Mallio CA, Errante Y, et al. Gadodiamide and dentate nucleus T1 hyperintensity in patients with meningioma evaluated by multiple follow-up contrast-enhanced magnetic resonance examinations with no systemic interval therapy. *Invest Radiol* 2015;50:470–72 CrossRef Medline
21. Ramalho J, Castillo M, Alobaidy M, et al. High signal intensity in globus pallidus and dentate nucleus on unenhanced T1-weighted MR images: evaluation of two linear gadolinium-based contrast agents. *Radiology* 2015;276:836–44 CrossRef Medline
22. Kanda T, Osawa M, Oba H, et al. High signal intensity in dentate nucleus on unenhanced T1-weighted MR images: association with linear versus macrocyclic gadolinium chelate administration. *Radiology* 2015;275:803–09 CrossRef Medline
23. Roccatagliata L, Vuolo L, Bonzano L, et al. Multiple sclerosis: hyperintense dentate nucleus on unenhanced T1-weighted MR images is associated with the secondary progressive subtype. *Radiology* 2009;251:503–10 CrossRef Medline
24. Kasahara S, Miki Y, Kanagaki M, et al. Hyperintense dentate nucleus on unenhanced T1-weighted MR images is associated with a history of brain irradiation. *Radiology* 2011;258:222–28 CrossRef Medline
25. Adin ME, Kleinberg L, Vaidya D, et al. Hyperintense dentate nuclei on T1-weighted MRI: relation to repeat gadolinium administration. *AJNR Am J Neuroradiol* 2015;36:1859–65 CrossRef Medline
26. McDonald RJ, McDonald JS, Kallmes DF, et al. Intracranial gadolinium deposition after contrast-enhanced MR imaging. *Radiology* 2015;275:772–82 CrossRef Medline
27. Kanda T, Fukusato T, Matsuda M, et al. Gadolinium-based contrast agent accumulates in the brain even in subjects without severe renal dysfunction: evaluation of autopsy brain specimens with inducively coupled plasma mass spectroscopy. *Radiology* 2015;276:228–32 CrossRef Medline
28. Robert P, Lehericy S, Grand S, et al. T1-weighted hypersignal in the deep cerebellar nuclei after repeated administrations of gadolinium-based contrast agents in healthy rats: difference between linear and macrocyclic agents. *Invest Radiol* 2015;50:473–80 CrossRef Medline
29. Radbruch A, Weberling LD, Kieslich PJ, et al. Gadolinium retention in the dentate nucleus and globus pallidus is dependent on the class of contrast agent. *Radiology* 2015;275:783–91 CrossRef Medline
30. Weberling LD, Kieslich PJ, Kickingereder P, et al. Increased signal intensity in the dentate nucleus on unenhanced T1-weighted images after gadobenate dimeglumine administration. *Invest Radiol* 2015;50:743–48 CrossRef Medline
31. Stojanov DA, Aracki-Trenkic A, Vojinovic S, et al. Increasing signal intensity within the dentate nucleus and globus pallidus on unenhanced T1W magnetic resonance images in patients with relapsing-remitting multiple sclerosis: correlation with cumulative dose of a macrocyclic gadolinium-based contrast agent, gadobutrol. *Eur Radiol* 2015 Jun 25. [Epub ahead of print] Medline
32. de Campos RO, Herédia V, Ramalho M, et al. Application of gadolinium based contrast agents in abdominal magnetic resonance imaging: important considerations. In: Thompson CC, ed. *Gadolinium: Compounds, Production and Applications*. New York: Nova Science Publishers; 2009:chap 5
33. Frenzel T, Lengsfeld P, Schirmer H, et al. Stability of gadolinium-based magnetic resonance imaging contrast agents in human serum at 37 degrees C. *Invest Radiol* 2008;43:817–28 CrossRef Medline
34. Idée JM, Port M, Robic C, et al. Role of thermodynamic and kinetic parameters in gadolinium chelate stability. *J Magn Reson Imaging* 2009;30:1249–58 CrossRef Medline
35. Prince MR, Erel HE, Lent RW, et al. Gadodiamide administration causes spurious hypocalcemia. *Radiology* 2003;227:639–46 CrossRef Medline
36. Laurent S, Elst LV, Copoix F, et al. Stability of MRI paramagnetic contrast media: a proton relaxometric protocol for transmetallation assessment. *Invest Radiol* 2001;36:115–22 CrossRef Medline
37. Tweedle MF, Wedeking P, Kumar K. Biodistribution of radiolabeled, formulated gadopentetate, gadoteridol, gadoterate, and gadodiamide in mice and rats. *Invest Radiol* 1995;30:372–80 CrossRef Medline
38. Tweedle MF, Hagan JJ, Kumar K, et al. Reaction of gadolinium chelates with endogenously available ions. *Magn Reson Imaging* 1991;9:409–15 CrossRef Medline
39. Corot C, Idée JM, Hentsch AM, et al. Structure-activity relationship of macrocyclic and linear gadolinium chelates: investigation of transmetallation effect on the zinc-dependent metalloproteinase angiotensin-converting enzyme. *J Magn Reson Imaging* 1998;8:695–702 CrossRef Medline
40. Aime S, Caravan P. Biodistribution of gadolinium-based contrast agents, including gadolinium deposition. *J Magn Reson Imaging* 2009;30:1259–67 CrossRef Medline
41. Altun E, Semelka RC, Cakit C. Nephrogenic systemic fibrosis and management of high-risk patients. *Acad Radiol* 2009;16:897–905 CrossRef Medline
42. Quarles LD, Hartle JE 2nd, Middleton JP, et al. Aluminum-induced DNA synthesis in osteoblasts: mediation by a G-protein coupled cation sensing mechanism. *J Cell Biochem* 1994;56:106–17 CrossRef Medline
43. Palasz A, Czekaj P. Toxicological and cytophysiological aspects of lanthanides action. *Acta Biochim Pol* 2000;47:1107–14 Medline
44. Feng X, Xia Q, Yuan L, et al. Impaired mitochondrial function and oxidative stress in rat cortical neurons: implications for gadolinium-induced neurotoxicity. *Neurotoxicology* 2010;31:391–98 CrossRef Medline
45. Xia Q, Feng X, Huang H, et al. Gadolinium-induced oxidative stress triggers endoplasmic reticulum stress in rat cortical neurons. *J Neurochem* 2011;117:38–47 CrossRef Medline

46. Spencer AJ, Wilson SA, Batchelor J, et al. **Gadolinium chloride toxicity in the rat.** *Toxicol Pathol* 1997;25:245–55 CrossRef Medline
47. Idée JM, Port M, Medina C, et al. **Possible involvement of gadolinium chelates in the pathophysiology of nephrogenic systemic fibrosis: a critical review.** *Toxicology* 2008;248:77–88 CrossRef Medline
48. Piera-Velazquez S, Louneva N, Fertala J, et al. **Persistent activation of dermal fibroblasts from patients with gadolinium-associated nephrogenic systemic fibrosis.** *Ann Rheum Dis* 2010;69:2017–23 CrossRef Medline
49. Bhagavathula N, Dame MK, DaSilva M, et al. **Fibroblast response to gadolinium: role for platelet-derived growth factor receptor.** *Invest Radiol* 2010;45:769–77 CrossRef Medline
50. Edward M, Quinn JA, Burden AD, et al. **Effect of different classes of gadolinium-based contrast agents on control and nephrogenic systemic fibrosis-derived fibroblast proliferation.** *Radiology* 2010;256:735–43 CrossRef Medline
51. Varani J, DaSilva M, Warner RL, et al. **Effects of gadolinium-based magnetic resonance imaging contrast agents on human skin in organ culture and human skin fibroblasts.** *Invest Radiol* 2009;44:74–81 CrossRef Medline
52. Christensen KN, Lee CU, Hanley MM, et al. **Quantification of gadolinium in fresh skin and serum samples from patients with nephrogenic systemic fibrosis.** *J Am Dermatol* 2011;64:91–96 CrossRef Medline
53. Cowper SE, Bucala R, Leboit PE. **Nephrogenic fibrosing dermopathy/nephrogenic systemic fibrosis: setting the record straight.** *Semin Arthritis Rheum* 2006;35:208–10 CrossRef Medline
54. Gibby WA, Gibby KA, Gibby WA. **Comparison of Gd DTPA-BMA (Omniscan) versus Gd HP-DO3A (ProHance) retention in human bone tissue by inductively coupled plasma atomic emission spectroscopy.** *Invest Radiol* 2004;39:138–42 CrossRef Medline
55. White GW, Gibby WA, Tweedle MF. **Comparison of Gd(DTPA-BMA) (Omniscan) versus Gd(HP-DO3A) (ProHance) relative to gadolinium retention in human bone tissue by inductively coupled plasma mass spectroscopy.** *Invest Radiol* 2006;41:272–78 CrossRef Medline
56. Darrah TH, Prutsman-Pfeiffer JJ, Poreda RJ, et al. **Incorporation of excess gadolinium into human bone from medical contrast agents.** *Metallomics* 2009;1:479–88 CrossRef Medline
57. Rocklage SM, Worah D, Kim SH. **Metal ion release from paramagnetic chelates: what is tolerable?** *Magn Reson Med* 1991;22:216–21; discussion 229–32 CrossRef Medline
58. Abraham JL, Thakral C, Skov L, et al. **Dermal inorganic gadolinium concentrations: evidence for in vivo transmetallation and long-term persistence in nephrogenic systemic fibrosis.** *Br J Dermatol* 2008;158:273–80 Medline
59. Xia D, Davis RL, Crawford JA, et al. **Gadolinium released from MR contrast agents is deposited in brain tumors: in situ demonstration using scanning electron microscopy with energy dispersive X-ray spectroscopy.** *Acta Radiol* 2010;51:1126–36 CrossRef Medline
60. Sanyal S, Marckmann P, Scherer S, et al. **Multiorgan gadolinium (Gd) deposition and fibrosis in a patient with nephrogenic systemic fibrosis: an autopsy-based review.** *Nephrol Dial Transplant* 2011;26:3616–26 CrossRef Medline
61. Ogi S, Fukumitsu N, Tsuchida D, et al. **Imaging of bilateral striopallidodentate calcinosis.** *Clin Nucl Med* 2002;27:721–24 CrossRef Medline
62. Fretellier N, Idée JM, Dencausse A, et al. **Comparative in vivo dissociation of gadolinium chelates in renally impaired rats: a relaxometry study.** *Invest Radiol* 2011;46:292–300 CrossRef Medline
63. Schroeder JA, Weingart C, Coras B, et al. **Ultrastructural evidence of dermal gadolinium deposits in a patient with nephrogenic systemic fibrosis and end-stage renal disease.** *Clin J Am Soc Nephrol* 2008;3:968–75 CrossRef Medline
64. Thakral C, Abraham JL. **Gadolinium-induced nephrogenic systemic fibrosis is associated with insoluble Gd deposits in tissues: in vivo transmetallation confirmed by microanalysis.** *J Cutan Pathol* 2009;36:1244–54 CrossRef Medline
65. Ray DE, Holton JL, Nolan CC, et al. **Neurotoxic potential of gadodiamide after injection into the lateral cerebral ventricle of rats.** *AJNR Am J Neuroradiol* 1998;19:1455–62 Medline
66. Roman-Goldstein SM, Barnett PA, McCormick CI, et al. **Effects of gadopentetate dimeglumine administration after osmotic blood-brain barrier disruption: toxicity and MR imaging findings.** *AJNR Am J Neuroradiol* 1991;12:885–90 Medline
67. Gadolinium Toxicity: A Survey of the Chronic Effects of Retained Gadolinium from Contrast MRIs. <https://gdtoxicity.files.wordpress.com/2014/09/gd-symptom-survey.pdf>. Accessed September 1, 2015

Full Dose-Reduction Potential of Statistical Iterative Reconstruction for Head CT Protocols in a Predominantly Pediatric Population

A.E. Mirro, S.L. Brady, and R.A. Kaufman



ABSTRACT

BACKGROUND AND PURPOSE: A statistical iterative reconstruction algorithm provides an effective approach to reduce patient dose by compensating for increased image noise in CT due to reduced radiation output. However, after a point, the degree to which a statistical iterative algorithm is used for image reconstruction changes the image appearance. Our aim was to determine the maximum level of statistical iterative reconstruction that can be used to establish dose-reduced head CT protocols in a primarily pediatric population while maintaining similar appearance and level of image noise in the reconstructed image.

MATERIALS AND METHODS: Select head examinations (brain, orbits, sinus, maxilla, and temporal bones) were investigated. Dose-reduced head protocols using an adaptive statistical iterative reconstruction were compared for image quality with the original filtered back-projection reconstructed protocols in a phantom by using the following metrics: image noise frequency (change in perceived appearance of noise texture), image noise magnitude, contrast-to-noise ratio, and spatial resolution. Dose-reduction estimates were based on CT dose index values. Patient volume CT dose index and image noise magnitude were assessed in 737 pre- and post-dose-reduced examinations.

RESULTS: Image noise texture was acceptable for up to 60% adaptive statistical iterative reconstruction for the soft reconstruction kernel (at both 100 and 120 kV[peak]) and up to 40% adaptive statistical iterative reconstruction for the standard reconstruction kernel. Implementation of 40% and 60% adaptive statistical iterative reconstruction led to an average reduction in the volume CT dose index of 43% for brain, 41% for orbit, 30% for maxilla, 43% for sinus, and 42% for temporal bone protocols for patients between 1 month and 26 years of age, while maintaining an average noise magnitude difference of 0.1% (range, -3% to 5%), improving the contrast-to-noise ratio of low-contrast soft-tissue targets and the spatial resolution of high-contrast bony anatomy, compared with filtered back-projection.

CONCLUSIONS: The methodology in this study demonstrates maximizing patient dose reduction and maintaining image quality by using statistical iterative reconstruction for a primarily pediatric population undergoing head CT examinations.

ABBREVIATIONS: ASIR = adaptive statistical iterative reconstruction; CNR = contrast-to-noise ratio; CTDI_{vol} = volume CT dose index; FBP = filtered back-projection; IR = iterative reconstruction; MTF = modulation transfer function; NPS = noise power spectrum

Use of statistical iterative reconstruction (IR) has been demonstrated as an effective method for lowering radiation exposure in thoracic and abdominal-pelvic CT.¹⁻⁸ Recently, several studies have investigated a reduced dose in head CT by using statistical IR⁹⁻¹⁴; however, only 2 studies examined a pediatric

population.^{10,11} These studies investigated the effect of statistical IR on image quality by using metrics such as noise magnitude, by measuring the interpixel variation or SD within an ROI. Measuring noise magnitude is simple but does not fully describe the effect that statistical IR algorithms have on the texture or the appearance of the pixelated noise, as has been reported previously.^{2,15,16}

Current St Jude Children's Research Hospital examinations for the chest and abdomen-pelvis are performed on a LightSpeed VCT-XTe (GE Healthcare, Milwaukee, Wisconsin) and incorporate adaptive statistical iterative reconstruction (ASIR; GE Healthcare),^{1,2} but protocols involving the head (brain, orbits, sinus, maxilla, and temporal bone) are reconstructed by using filtered back-projection (FBP). The purpose of this study was to implement the maximum level of statistical IR for dose-reduced head protocols by using ASIR in a primarily pediatric population while maintaining a similar image-noise magnitude. Fourier-

Received October 6, 2015; accepted after revision January 5, 2016.

From the Department of Biomedical Engineering (A.E.M.), Washington University, St. Louis, Missouri; and Department of Diagnostic Imaging (A.E.M., S.L.B., R.A.K.), St Jude Children's Research Hospital, Memphis, Tennessee.

This work was supported by American Lebanese Syrian Associated Charities and National Cancer Institute R25E grant 5R25CA23944.

Please address correspondence to Samuel Brady, PhD, Department of Diagnostic Imaging, St Jude Children's Research Hospital, 262 Danny Thomas Pl, Memphis, TN 38105; e-mail: samuel.brady@stjude.org

Indicates open access to non-subscribers at www.ajnr.org

<http://dx.doi.org/10.3174/ajnr.A4754>

Table 1: Head CT examination parameters^a

Patient Age (yr)	A or H	Rotation (sec)	Collimation (mm)	Section (mm)	Reconstruction Kernel	kVp	Pre-ASIR (mA)	Post-ASIR (mA)
Brain								
0–2 ^b	A	0.5	20	5	Soft and bone	100	280	150
2–5		1					200	120
6–10							220	130
11–18							240	140
≥19						120	200	105
Sinus								
≥19	H	0.5	40	2.5	Soft and bone	120	NI = 7.5	155
0–18						100	220	130
Orbits								
0–18 ^c	H ^d	0.5	20	1.25	Standard and bone	100	240	155
Temporal bone								
≥19	H	1	20	1.25	Standard and bone	120	250	150
2–18		0.5				120	400	230
Maxillary bone								
≥19	H ^d	0.5	20	2.5	Standard and bone	120	NI = 7.5	NI = 9.25
0–18	H					100	300	180

Note:—A indicates axial; H, helical; NI, Noise Index; SFOV, scan FOV.

^a All protocols were imaged with a SFOV using “Head” unless otherwise indicated. All helical acquisitions were scanned with a pitch of 0.984 unless otherwise indicated.

^b SFOV used “Ped Head.”

^c SFOV used “Small Head.”

^d Pitch = 0.516.

based image quality metrics, such as noise power spectrum (NPS) and modulation transfer function (MTF), were used to fully characterize the effects of ASIR on noise and spatial resolution. Dose-reduction estimates are based on a comparison of pre- and post-dose-reduced examination volume CT dose index (CTDI_{vol}) values.

MATERIALS AND METHODS

Head CT Image Quality Analyzed in a Phantom

To determine the maximum possible level of statistical IR and tube current (ie, milliamperere) reduction, we analyzed image quality from an ASIR reconstruction and compared it with image quality from the original head protocols by using FBP. Image quality was assessed in a phantom on the basis of the measured change of image noise frequency (ie, change in the perceived appearance of noise texture as quantified by calculating the NPS), image noise magnitude (ie, calculated by using the SD of an ROI), contrast-to-noise ratio (CNR), and spatial resolution (calculated by using MTF).

The NPS was calculated by using a 20-cm diameter uniform water phantom (Quality Assurance Phantom; GE Healthcare). The water phantom was scanned to produce twelve 2.5-mm images by using tube potential (ie, kilovolt[peak]) and other acquisition factors from the original head protocols (Table 1). The images were averaged, and the center of the averaged image was used to calculate a single NPS curve.² Initially, the uniform water phantom was imaged at the CTDI_{vol} and milliamperere or, in the case of tube current–modulated examinations, the Noise Index value recorded for the original clinical FBP protocol. To produce a series of noisier images, we decremented the milliamperere setting in steps of 10 milliampereres until the original CTDI_{vol} was decreased by ~70% (eg, for the brain protocol for individuals older than 19 years of age, the initial CTDI_{vol} and milliamperere was 36.6 mGy and 200 mA; both were decremented to 10.04 mGy and 60 mA); for head scan techniques imaged by using tube current

modulation, the Noise Index value was incremented² (thus allowing a lower milliamperere) in steps of 3. All other acquisition parameters were held constant (Table 1). Each milliamperere-reduced image was reconstructed by using the soft, standard, and bone reconstruction kernels at every level of ASIR (0%–100%, in which 0% ASIR represents 100% FBP). Image noise magnitude, variance, and NPS were calculated by using a script written in Matlab (R2014b; MathWorks, Natick, Massachusetts).

The NPS of dose-reduced statistical IR data was grouped according to similar amplitudes (ie, the measure of noise variance) by reconstruction kernel type (ie, soft, standard, or bone), and kilovolt peak level (ie, 100 and 120). From these matched NPS curves, the shift in mean NPS frequency was calculated at each level of ASIR reconstruction. The texture of the image noise as it appeared in reconstructed images changed as the mean of the NPS curve shifted along the abscissa; thus, shifts in mean NPS frequency were associated with changes in image-noise texture (Fig 1) as has been shown in previous studies.^{2,16}

A literature search was conducted to determine the level of acceptable shift in mean NPS frequency in lieu of a receiver operating characteristic test performed by radiologists at St Jude Children’s Research Hospital. Acceptable changes in perceived noise texture determined by a single institutional receiver operating characteristic would not be generalizable, whereas a literature search represented a multi-institutional consensus. The resulting literature search indicated for soft-tissue reconstruction kernels, typical of body imaging (ie, the standard kernel), an average implementation of 40% ASIR reconstruction,^{1–3,6–8,17–19} correlated with an acceptable change in perceived image noise texture or mean NPS frequency shift of 25% (range, 16%–40%).^{2,4,5,20,21} No level of acceptable shift in mean NPS frequency was reported for the soft reconstruction kernel typical for brain CT. The tolerance of 25% reported for the standard reconstruction kernel was adopted for the soft reconstruction kernel.

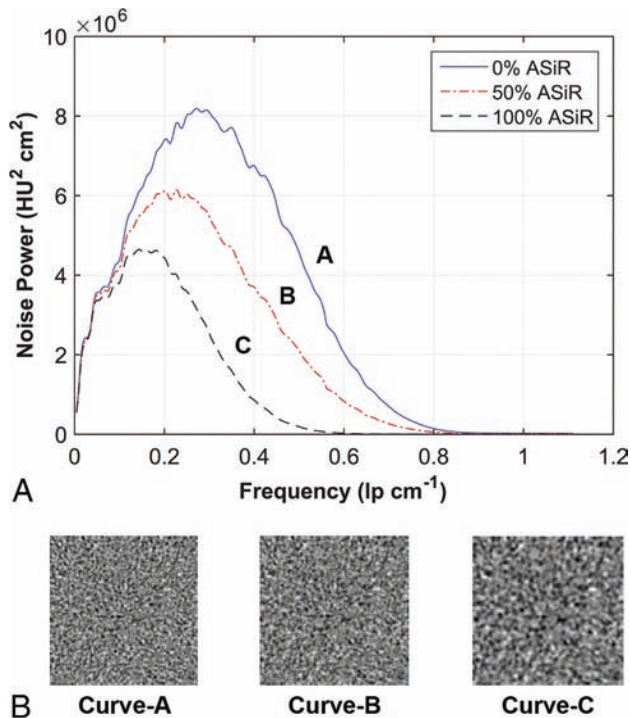


FIG 1. Texture of image noise as it appears in reconstructed images changes as the mean of the NPS curve shifts along the abscissa; shifts in mean NPS frequency are associated with changes in the appearance of image noise texture. *A*, NPS curves of the standard reconstruction kernel are reconstructed at 3 levels of ASiR. *B*, A corresponding ROI of 128×128 pixels from the center of a water phantom shows the appearance of the noise texture as it correlates with a 32% shift in NPS mean frequency along the abscissa from curve A to B and a 52% shift in curve A to C.

Images of low-contrast targets were acquired to qualitatively compare noise texture. The low contrast targets were imaged at multiple milliamperage-reduced, ASiR-reconstructed levels and were compared with the original full-dose protocol by using FBP. Images of low-contrast targets were acquired with the soft and standard reconstruction kernels by using a Catphan 700 phantom (The Phantom Laboratory, Salem, New York), and the CNR of the 3-mm-diameter target was calculated. Additionally, a qualitative assessment of a low-contrast target was performed on a diagnostic-quality display (Dome S3c; NDS Surgical Imaging, San Jose, California) under reading room ambient light control (ie, illuminance average ~ 20 lx).

Fine-detailed spatial resolution was evaluated for the bone reconstruction kernel by calculating the MTF from images of high-contrast targets by using the Catphan 700 phantom. FBP and milliamperage-reduced statistical IR images were used to image the phantom. Twelve scans of the first test module were acquired and averaged. The Fourier transform of the derivative of an ensemble of 1D edge spread functions sampled radially across the bone circular boundary insert was used to calculate the MTF.²²

The percentage difference between milliamperage values from the FBP image and the matched NPS curve reconstructed with statistical IR was used to determine new dose-reduced milliamperage settings for all head protocols. All changes to protocols were reviewed by the chief neuroradiologist before implementation.

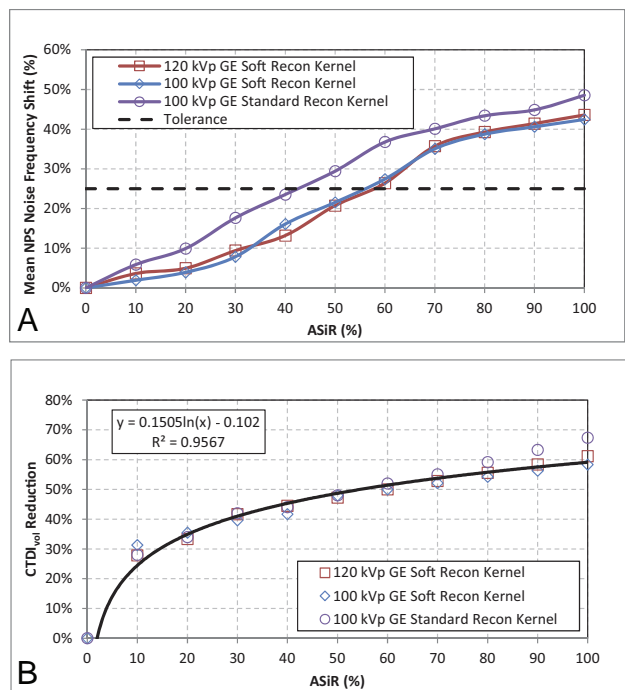


FIG 2. Dose-reduced ASiR protocols compare the mean NPS frequency shift (*A*) as a function of the level of ASiR reconstruction. An acceptable tolerance for the appearance of noise texture in the reconstructed image is reported in the literature,^{4,5,20,21} based on a 25% shift of NPS noise frequency (*dashed line*). *B*, Corresponding reductions of $CTDI_{vol}$ for the protocols by using ASiR are plotted and fit by using a log-regression function.

Image Quality and Dosimetry Analyzed from Patient Examinations

The institutional review board at St Jude Children's Research Hospital deemed this quality-assurance analysis exempt from obtaining informed consent. All data were managed in compliance with the Health Insurance Portability and Accountability Act. Head protocols were selected on the basis of each patient's age, which was obtained immediately prior to the examination. Pre-dose-reduced examination $CTDI_{vol}$ values were analyzed from June 2013 to 2014. Post-dose-reduced values were analyzed from June 2014 to 2015.

Reconstructed image-noise magnitude from pre- and post-dose-reduced patient examination images was assessed on the basis of an ROI analysis. Multiple ROIs were placed in regions of uniformity within the brain and averaged; the locations varied depending on the examination type. Image noise analysis was only for images reconstructed with soft-tissue reconstruction kernels (ie, soft or standard).

RESULTS

Head CT Image Quality Analyzed in a Phantom

Eleven NPSs (1 FBP, 10 ASiR spectra) were calculated for the soft reconstruction kernel (at both 100 and 120 kVp) and the standard reconstruction kernel (100 kVp). The percentage shift in mean NPS frequency for each spectrum was plotted as a function of the level of ASiR (Fig 2*A*) with its accompanying reduction in $CTDI_{vol}$ (Fig 2*B*). The shift of mean NPS frequency (ie, noise texture) was impacted mostly by selection of the reconstruction kernel, and not the level of kilovolt (peak). On the basis of the reported^{4,5,20,21}

25% threshold for acceptable change in perceived noise texture (dashed line in Fig 2A), an implementation of 60% ASiR was chosen for the soft reconstruction kernel and 40% ASiR was chosen for the standard reconstruction kernel; the data for the standard reconstruction kernel agree with those in previous publications.^{3,6-8,17-19} Dose-reduced NPS curves for the soft reconstruction kernel were calculated for up to 60% ASiR and, for the standard reconstruction kernel, up to 40% ASiR (Fig 3). The overall noise magnitude and variance for the dose-reduced ASiR spectra were matched to the original FBP noise amplitude to a mean (± 1 SD) of 4.8 ± 0.4 HU, 4.1 ± 0.3 HU, and 5.7 ± 0.5 HU for protocols acquired with the soft reconstruction kernel at 100 kVp (Fig 3A) and 120 kVp (Fig 3B) and the standard reconstruction kernel at 100 kVp (Fig 3C), respectively.

The visual assessment of low-contrast targets demonstrates a slight degradation in lesion boundary sharpness with the ASiR reconstruction (Fig 4). However, for images reconstructed with the soft reconstruction kernel, CNR improved with the increasing level of ASiR reconstruction. The smallest low-contrast target (3 mm) acquired at 100 kVp had a CNR calculated to be 1.2 at 0% ASiR and 2.4 at 60% ASiR. For targets acquired at 120 kVp, the CNR was calculated to be 1.7 at 0% ASiR and 2.3 at 60% ASiR. For targets acquired with the standard reconstruction kernel, the CNR improved up to the level of 30% ASiR; the CNR was 1.4 at 0% ASiR and 1.9 at 30% ASiR; however, the CNR was only 1.8 at 40% ASiR, a slight decrease from 30% ASiR.

For image-quality measurements of the bone reconstruction kernel, the dose-reduced NPS demonstrated an overall average reduction in noise variance by 26% (range, 7%–36%) compared with non-dose-reduced FBP protocols. Additionally, spatial resolution calculated for the dose-reduced 60% ASiR protocol improved by an average of 26% (range, 24%–30%) compared at the 50% MTF level and 113% (range, 101%–123%) at the 10% MTF level.

Image Quality and Dosimetry Analyzed from Patient Examinations

The total number of pre-dose-reduced examinations analyzed was 376 (242 male); the mean age was 9.6 ± 6.2 years (1 month to 24 years). The number of examinations analyzed per protocol was the following: 220 brain, 11 orbit, 98 sinus, 37 maxilla, and 10 temporal bone examinations. The total number of post-dose-reduced examinations analyzed was 361 (212 male); the mean age was 10.7 ± 6.6 years (1 month to 26 years). The number of examinations analyzed per protocol was the following: 193 brain, 3 orbit, 127 sinus, 35 maxilla, and 3 temporal bone examinations. Lowering the protocol milliamperage (Table 1) and implementing 40% or 60% ASiR for image noise control resulted in lowered $CTDI_{vol}$ values as shown in Fig 3B. The percentage reduction in $CTDI_{vol}$ for all examinations is shown in Table 2. The image noise magnitude from the dose-reduced patient examinations was shown to change by an average difference of 0.1% (range, -3% to 5%) compared with the original FBP patient examinations (Table 2).

DISCUSSION

The purpose of this study was to implement the maximum level of statistical IR that could be used to establish dose-reduced pediatric head protocols (ie, brain, orbit, sinus, maxilla, and temporal

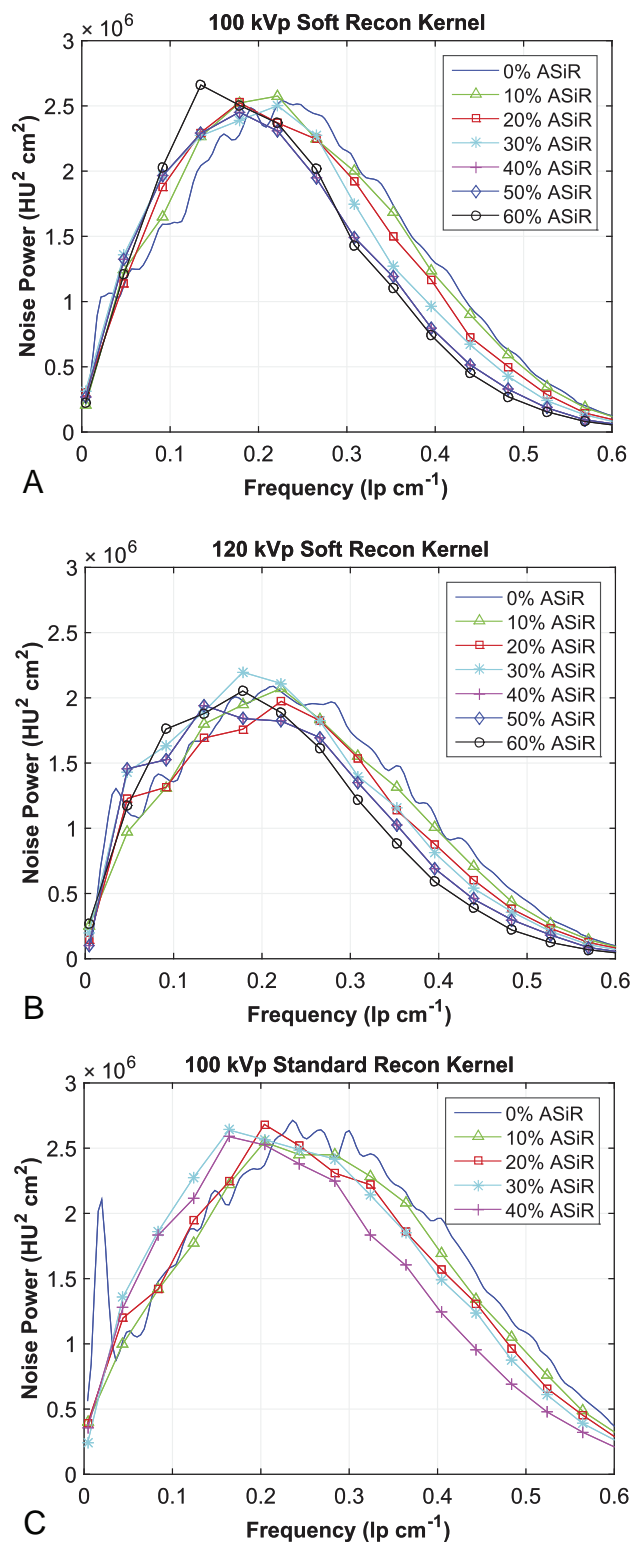


FIG 3. Noise power spectra acquired with the soft reconstruction kernel at 100 kVp from 240 to 120 mA (A), with the soft reconstruction kernel at 120 kVp from 200 to 110 mA (B), and the standard reconstruction kernel at 100 kVp from 250 to 140 mA (C). The calculated spectra are reconstructed at 0%–60% ASiR (soft reconstruction kernel) and at 0%–40% ASiR (standard reconstruction kernel).

bone) while maintaining acceptable image quality. The use of NPS to evaluate image quality is a departure from the more commonly used metrics of CNR, SNR, and SD as previously reported.¹¹⁻¹⁴

Using NPS allowed the definition of acceptable image quality to be based on the results from multiple published observer studies instead of a single-institute analysis; thus, the results of this analysis will be more generalizable across pediatric imaging institutions. The results of this study provide a more in-depth description of image appearance and noise texture and demonstrate a methodic approach for the application of the highest possible dose reduction by using statistical IR while maintaining a similar noise magnitude in the reconstructed image.

Images acquired with higher levels of statistical IR can appear overly smooth, leading to concerns about the visibility of anatomic structures. This change in image appearance is likely a visual manifestation of a shift in the spatial frequency distribution of the image noise. By measuring the mean frequency of the NPS curves, the image noise texture produced by ASIR for the dose-reduced protocols could be compared with the image texture produced by the original FBP protocols, allowing the selection of acceptable change in noise texture. While the dose-reduced protocols did result in changes in the spatial frequency, these shifts were similar to the reported tolerance for soft-tissue imaging in

the body^{4,5,20,21} and were not detrimental for image diagnosis as determined by the radiologists at our institution.

In 1 clinical example, image noise magnitude was measured in 2 axial brain examinations of a 16-kg (3-year-old) patient, performed approximately 6 months apart. The first scan (Fig 5A) was acquired with the original institutional protocol, and the second (Fig 5B), with the dose-reduced protocol at 60% ASIR. Noise texture appearance was slightly coarser, but the noise magnitude, as measured by the SD of a 1-cm² ROI, was 3.8 HU in the pre-ASIR image and 4.0 HU in the post-ASIR image. The pre-ASIR image was acquired at 200 mA, and the post-ASIR image, at 120 mA (both at 100 kVp); all other scan parameters were constant with a minor difference in gantry tilt angle to align with the orbitomeatal line. The change in milliampererepresented a decrease in CTDI_{vol} from 25.1 to 15.0 mGy, a dose reduction of 40%.

A comparison of radiation dose reduction between FBP and dose-reduced ASIR brain protocols with previously published studies follows. By implementing 30% ASIR reconstruction, Kilic et al¹¹ reported a reduction of an adult brain protocol of 35% (CTDI_{vol}, 59.4–38.6 mGy), whereas the current study achieved a

48% dose reduction from 36.6 to 18.9 mGy in a population of patients 19 years of age or older, using 60% ASIR. For pediatric brain scans, Vorona et al⁹ reported a reduction of 22% (CTDI_{vol}, 28.8–22.4 mGy) for patients 3–18 years of age by using 20% ASIR, compared with the average reduction of 40% (CTDI_{vol}, 26.5–15.8 mGy) in the current study for the same age range by using 60% ASIR. Also, for pediatric brain scans, McKnight et al,¹⁰ using 30% ASIR, reported a reduction of CTDI_{vol} of 28% (30.0–21.5 mGy) for patients 3–12 years of age and 48% (49.9–25.7 mGy) for patients older than 12 years of age, compared with the 40% (25.2–15.3 mGy) and 45% (32.9–18.0 mGy) dose reduction reported in the current study using 60% ASIR, respectively. Percentage reductions are relative to the initial

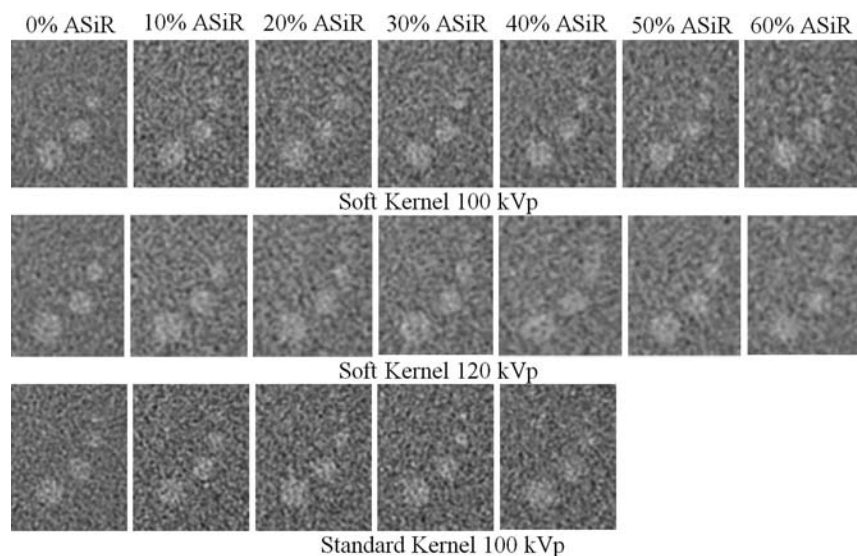


FIG 4. Images of the 3-, 5-, 7-, and 9-mm low-contrast targets in the Catphan 700 phantom are acquired with FBP and dose-reduced ASIR reconstruction up to 60% ASIR for the soft reconstruction kernels at both 100 and 120 kVp and up to 40% for the standard reconstruction kernel at 100 kVp.

Table 2: Original and dose-reduced CTDI_{vol} and noise values for all head protocols

Patient Age Category	Protocol	CTDI _{vol} (mGy)			Noise (HU)		
		Original	Dose-Reduced	Difference	Original	Dose-Reduced	Difference
0–23 mo	Brain	15.0 ± 0.7	8.0 ± 0.4	–47%	4.4 ± 1.0	4.2 ± 0.7	–3%
2–5 yr	Brain	24.1 ± 0.9	14.6 ± 0.6	–39%	4.2 ± 0.7	4.1 ± 0.7	–3%
6–10 yr	Brain	26.3 ± 1.3	15.9 ± 0.4	–40%	4.1 ± 0.5	4.2 ± 0.6	4%
11–18 yr	Brain	29.1 ± 0.9	17.0 ± 0.5	–42%	4.4 ± 0.6	4.5 ± 0.6	3%
≥ 19 yr	Brain	36.6 ± 0.8	18.9 ± 0.5	–48%	4.3 ± 0.6	4.4 ± 0.4	3%
0–18 yr	Maxilla	19.4 ± 0.0	11.5 ± 0.1	–41%	11.2 ± 2.8	11.6 ± 1.6	3%
≥19 yr	Maxilla	22.8 ± 0.0	18.7 ± 0.2	–18%	9.6 ± 1.4	9.2 ± 1.7	–3%
0–18 yr	Orbits	26.9 ± 8.0	15.8 ± 0.5	–41%	7.5 ± 1.2	7.2 ± 0.1	–4%
0–18 yr	Sinus	13.1 ± 0.0	7.2 ± 0.3	–45%	8.5 ± 1.2	8.9 ± 1.1	5%
≥19 yr	Sinus	22.8 ± 0.0	13.7 ± 0.1	–40%	8.3 ± 0.9	8.2 ± 0.6	–1%
2–18 yr	Temporal	40.7 ± 0.0	22.8 ± 0.0	–44%	9.3 ± 1.4	9.2 ± 1.2	–2%
≥19 yr ^a	Temporal	49.9 ± 0.0	29.7 ± 0.0	–40%	9.3 ± 1.0		

^a No dose-reduced patient examinations were available for comparison. Dose-reduced CTDI_{vol} value is calculated on the basis of scan parameters. Dose difference is a theoretic calculation.

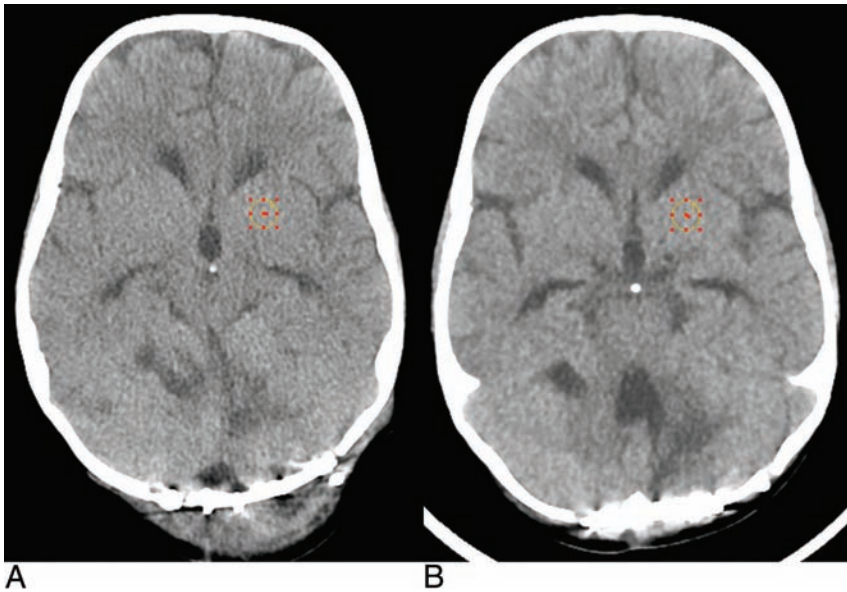


FIG 5. A 3-year-old boy with scans 6 months apart. *A*, The original brain protocol is acquired at 200 mA and 100 kVp with a CTDI_{vol} of 25.1 mGy by using FBP. *B*, The patient is re-examined postsurgery with the dose-reduced brain protocol by using 60% ASIR, 120 mA, and 100 kVp, with a CTDI_{vol} of 15.0 mGy. Both examinations were acquired by using the GE Healthcare soft reconstruction kernel.

CTDI_{vol} calculated by using FBP reconstruction. Similarities in dose reduction between the current study and other previous studies, despite differences in the level of statistical IR implementation, are due to differences in the initial FBP CTDI_{vol} values.

In the current study, the statistical IR technique ASIR was used to mitigate increased image noise from the reductions of tube current, allowing reduced patient examination radiation dose. The use of ASIR is only available on GE Healthcare scanners. Other statistical IR algorithms are available for use with other CT manufacturers and may be used for potential head CT dose-reduction purposes. The implementation of these statistical IR algorithms will be subtly different; thus, the description of image noise texture and the amount of dose reduction reported in the current study may not be identical to those in other scanners using statistical IR algorithms for dose-reduced head CT. However, the principles outlined in the methodology of this study are universal, namely the need to analyze both image noise magnitude (ie, by using traditional ROI analysis) and the visual perception of the noise texture (ie, by using Fourier analysis techniques such as NPS) for a more complete understanding of the impact on reconstructed patient image quality from statistical IR. The use of Fourier image-quality metrics, such as NPS and MTF, will allow a more detailed analysis and customization of a statistical IR algorithm, despite the application.

CONCLUSIONS

Substantial dose reduction can be achieved at higher levels of ASIR reconstruction than previously reported for head CT protocols. An analysis of the effects on the perceived appearance of noise texture from implementation of statistical IR was performed. In this study, it was shown that an implementation of 60% ASIR (soft reconstruction kernel) and 40% ASIR (standard reconstruction kernel) will produce acceptable changes in image

noise texture in the reconstructed image as defined in the scientific literature and may be used for greater dose reduction. Head CT images acquired with the soft and standard reconstruction kernels demonstrated an overall improvement of CNR of the image. For all head protocols, the average reduction in CTDI_{vol} was 43% for the brain, 41% for orbits, 30% for the maxilla, 43% for the sinus, and 42% for the temporal bone.

ACKNOWLEDGMENTS

The authors acknowledge Zoltan Patay, MD, PhD, for his advice and expertise.

Disclosures: Amy E. Mirro, Samuel L. Brady—*RELATED: Grant:* National Cancer Institute.* Robert A. Kaufman—*RELATED: Grant:* Pediatric Oncology Education students are supported in part by grant R25CA23944 from the National Cancer Institute.* *Comments:* This funds partial support of the summer student Pediatric Oncology Education program at St. Jude, which helped to support the coauthor Amy E. Mirro, an undergraduate student at Washington University in St. Louis. *Money paid to the institution.

REFERENCES

- Brady S, Moore B, Yee B, et al. **Pediatric CT: implementation of ASIR for substantial radiation dose reduction while maintaining pre-ASIR image noise.** *Radiology* 2014;270:223–31 [CrossRef Medline](#)
- Brady SL, Yee BS, Kaufman RA. **Characterization of adaptive statistical iterative reconstruction algorithm for dose reduction in CT: a pediatric oncology perspective.** *Med Phys* 2012;39:5520–31 [CrossRef Medline](#)
- Hara AK, Paden RG, Silva AC, et al. **Iterative reconstruction technique for reducing body radiation dose at CT: feasibility study.** *AJR Am J Roentgenol* 2009;193:764–71 [CrossRef Medline](#)
- Hong SS, Lee JW, Seo JB, et al. **Evaluation of image quality and radiation dose by adaptive statistical iterative reconstruction technique level for chest CT examination.** *Radiat Prot Dosimetry* 2013; 157:163–71 [CrossRef Medline](#)
- Sagara Y, Hara AK, Pavlicek W, et al. **Abdominal CT: comparison of low-dose CT with adaptive statistical iterative reconstruction and routine-dose CT with filtered back projection in 53 patients.** *AJR Am J Roentgenol* 2010;195:713–19 [CrossRef Medline](#)
- Singh S, Kalra MK, Gilman MD, et al. **Adaptive statistical iterative reconstruction technique for radiation dose reduction in chest CT: a pilot study.** *Radiology* 2011;259:565–73 [CrossRef Medline](#)
- Singh S, Kalra MK, Hsieh J, et al. **Abdominal CT: comparison of adaptive statistical iterative and filtered back projection reconstruction techniques.** *Radiology* 2010;257:373–83 [CrossRef Medline](#)
- Vorona GA, Ceschin RC, Clayton BL, et al. **Reducing abdominal CT radiation dose with the adaptive statistical iterative reconstruction technique in children: a feasibility study.** *Pediatr Radiol* 2011;41: 1174–82 [CrossRef Medline](#)
- Vorona GA, Zucconi G, Sutcavage T, et al. **The use of adaptive statistical iterative reconstruction in pediatric head CT: a feasibility study.** *AJNR Am J Neuroradiol* 2013;34:205–11 [CrossRef Medline](#)
- McKnight CD, Watcharotone K, Ibrahim M, et al. **Adaptive statistical iterative reconstruction: reducing dose while preserving image quality in the pediatric head CT examination.** *Pediatr Radiol* 2014; 44:997–1003 [CrossRef Medline](#)
- Kilic K, Erbas G, Guryildirim M, et al. **Lowering the dose in head CT using adaptive statistical iterative reconstruction.** *AJNR Am J Neuroradiol* 2011;32:1578–82 [CrossRef Medline](#)

12. Korn A, Fenchel M, Bender B, et al. **Iterative reconstruction in head CT: image quality of routine and low-dose protocols in comparison with standard filtered back-projection.** *AJNR Am J Neuroradiol* 2012;33:218–24 CrossRef Medline
13. Niu YT, Mehta D, Zhang ZR, et al. **Radiation dose reduction in temporal bone CT with iterative reconstruction technique.** *AJNR Am J Neuroradiol* 2012;33:1020–26 CrossRef Medline
14. Rapalino O, Kamalian S, Kamalian S, et al. **Cranial CT with adaptive statistical iterative reconstruction: improved image quality with concomitant radiation dose reduction.** *AJNR Am J Neuroradiol* 2012;33:609–15 CrossRef Medline
15. Samei E, Richard S. **Assessment of the dose reduction potential of a model-based iterative reconstruction algorithm using a task-based performance metrology.** *Med Phys* 2015;42:314–23 CrossRef Medline
16. Solomon J, Samei E. **Quantum noise properties of CT images with anatomical textured backgrounds across reconstruction algorithms: FBP and SAFIRE.** *Med Phys* 2014;41:091908 CrossRef Medline
17. Cornfeld D, Israel G, Detroy E, et al. **Impact of adaptive statistical iterative reconstruction (ASIR) on radiation dose and image quality in aortic dissection studies: a qualitative and quantitative analysis.** *AJR Am J Roentgenol* 2011;196:W336–40 CrossRef Medline
18. Flicek KT, Hara AK, Silva AC, et al. **Reducing the radiation dose for CT colonography using adaptive statistical iterative reconstruction: a pilot study.** *AJR Am J Roentgenol* 2010;195:126–31 CrossRef Medline
19. Leipsic J, Nguyen G, Brown J, et al. **A prospective evaluation of dose reduction and image quality in chest CT using adaptive statistical iterative reconstruction.** *AJR Am J Roentgenol* 2010;195:1095–99 CrossRef Medline
20. Marin D, Nelson RC, Schindera ST, et al. **Low-tube-voltage, high-tube-current multidetector abdominal CT: improved image quality and decreased radiation dose with adaptive statistical iterative reconstruction algorithm—initial clinical experience.** *Radiology* 2010;254:145–53 CrossRef Medline
21. Miéville FA, Gudinchet F, Brunelle F, et al. **Iterative reconstruction methods in two different MDCT scanners: physical metrics and 4-alternative forced-choice detectability experiments—a phantom approach.** *Phys Med* 2013;29:99–110 CrossRef Medline
22. Richard S, Husarik DB, Yadava G, et al. **Towards task-based assessment of CT performance: system and object MTF across different reconstruction algorithms.** *Med Phys* 2012;39:4115–22 CrossRef Medline

Non-Relative Value Unit–Generating Activities Represent One-Fifth of Academic Neuroradiologist Productivity

 M. Wintermark,  M. Zeineh,  G. Zaharchuk,  A. Srivastava, and  N. Fischbein



ABSTRACT

BACKGROUND AND PURPOSE: A neuroradiologist's activity includes many tasks beyond interpreting relative value unit–generating imaging studies. Our aim was to test a simple method to record and quantify the non-relative value unit–generating clinical activity represented by consults and clinical conferences, including tumor boards.

MATERIALS AND METHODS: Four full-time neuroradiologists, working an average of 50% clinical and 50% academic activity, systematically recorded all the non-relative value unit–generating consults and conferences in which they were involved during 3 months by using a simple, Web-based, computer-based application accessible from smartphones, tablets, or computers. The number and type of imaging studies they interpreted during the same period and the associated relative value units were extracted from our billing system.

RESULTS: During 3 months, the 4 neuroradiologists working an average of 50% clinical activity interpreted 4241 relative value unit–generating imaging studies, representing 8152 work relative value units. During the same period, they recorded 792 non-relative value unit–generating study reviews as part of consults and conferences (not including reading room consults), representing 19% of the interpreted relative value unit–generating imaging studies.

CONCLUSIONS: We propose a simple Web-based smartphone app to record and quantify non-relative value unit–generating activities including consults, clinical conferences, and tumor boards. The quantification of non-relative value unit–generating activities is paramount in this time of a paradigm shift from volume to value. It also represents an important tool for determining staffing levels, which cannot be performed on the basis of relative value unit only, considering the importance of time spent by radiologists on non-relative value unit–generating activities. It may also influence payment models from medical centers to radiology departments or practices.

ABBREVIATION: RVU = relative value unit

Radiologists' productivity is typically evaluated on the basis of the number of imaging studies they interpret or procedures they perform. The amount of work input for each imaging study or procedure is captured by the professional component of a relative value unit (RVU). The professional component work RVU is currently the accepted basis for measuring work output by radiologists.¹

In January 2015, 2 ambitious goals were set by the Department of Health and Human Services that will significantly impact radiology: One-half of all Medicare payment to hospitals and physicians will be based on alternative payment models (ie, Account-

able Care Organizations) by 2018; and 85% of all fee-for-service payments will be tied to quality or value by 2016, with 90% by 2018.² Shifting from fee-for-service reimbursement in Medicare to a pay-for-performance model has long been an aspiration of the Department of Health and Human Services. However, this is the first time the Department of Health and Human Services has set explicit numeric goals for alternative payment models and value-based payments.³ Radiology has much to do to prepare for the transition from the current fee-for-service payment schedule to new value-based reimbursement systems because it has historically not measured its added value to patient care and not communicated it in easily understood terms to all stakeholders. This includes quantifying all activities in which radiologists are engaged that clearly add value to patient care but do not generate RVUs.

One of the key non-RVU–generating activities in which neuroradiologists engage with their referring clinical colleagues is providing expertise during consults and a variety of clinical con-

Received October 6, 2015; accepted after revision December 14.

From the Departments of Radiology (M.W., M.Z., G.Z., N.F.), Neuroradiology Section, and Radiology (A.S.), Stanford University, Stanford, California.

Please address correspondence to Max Wintermark, MD, MAS, MBA, Department of Radiology, Stanford University School of Medicine, 300 Pasteur Dr, S047, Stanford, CA 94305; e-mail: max.wintermark@gmail.com; @StanfordNRAD

<http://dx.doi.org/10.3174/ajnr.A4701>

Neuroradiologists Initials

Number of studies to be recorded

List all patient accession number(s)

Check all that apply

CT MRI PET

Check all that apply

Brain Neck Spine

Mutually Exclusive

1-on-1
 Conference
 EPIC
 Email/Phone

Requesting Service

Neurology
 Neurosurgery
 E.N.T
 Neuro-Oncology
 Pediatrics
 Psychiatry
 Trauma
 Medicine
 E.D.
 Radiation Oncology
 Other

FIG 1. User interface of our simple, Web-based smartphone app to record our non-RVU-generating consults.

ferences, including tumor boards. While most radiologists are involved in such activities, the exact effort represented by this activity has typically not been quantified; this feature has made it difficult to assess the exact value of the activity. In this study, we propose a simple method to quantify the activity represented by consults and clinical conferences, including tumor boards, and to estimate the radiologist's time consumed.

MATERIALS AND METHODS

We designed a simple, Web-based app (Fig 1) by using REDcap software (<http://project-redcap.org/>). This app was accessible from smartphones, tablets, or computers and allowed radiologists, in a few clicks and several seconds, to record the following information for each consult or clinical conference: radiologist's initials, number of studies reviewed in that encounter, technique (CT, MR imaging, PET), anatomic region (brain, neck, spine), type of encounter (1-on-1 in-person consultations, e-mail/phone consultations, consultation request through the electronic medical record, conferences), and requesting service (Neurology, Neurosurgery, Otolaryngology Head and Neck Surgery, Neuro-Oncology, Pediatrics, Psychiatry, Trauma, Medicine, Radiation Oncology, Emergency Department, other). Tumor boards were counted under "conferences," but a number

of clinical conferences were given that were not tumor boards (epilepsy conference, stroke conference, and so forth). Only the cases actually shown during conferences were counted.

Four full-time neuroradiologists, working an average of 50% clinical and 50% nonclinical activities, systematically recorded all non-RVU-generating consults and conferences for 3 months. The number and type of imaging studies they interpreted during the same period and the associated RVUs were extracted from our billing system. The 50% nonclinical activity encompassed funded research, teaching, and administrative activities.

Of note, we did not count reading room consults (ie, the phone calls, consults, and communication of results for imaging studies being interpreted in the reading room). If an inpatient study was reviewed after it was interpreted by a neuroradiologist different from the one who signed the report for this study, it was included in the non-RVU count. The non-RVU count included non-RVU-generating consults that occurred during clinical and academic days and off-hours.

RESULTS

During 3 months (January–March 2015), the 4 neuroradiologists working an average of 50% clinical activity (4 times 0.5 clinical full-time equivalents or 2 clinical full-time equivalents) and interpreted 4241 RVU-generating imaging studies, representing 8152 work RVUs. During the same period, they recorded 792 non-RVU-generating study reviews as part of consults and conferences. This represented 19% (792/4241) of the number of RVU-generating imaging studies (Table 1) or an equivalent of 1549 work RVUs. The 19% was relatively constant for each of the 4 neuroradiologists and indicated that the neuroradiologists with less academic time and reading more RVUs also performed more non-RVU-generating consults and conferences. If we used the 2013 Medical Group Management Association statistics (median salary per RVU = \$53.34, <http://www.mgma.com/industry-data/all-data-resources/benchmarking-tools-from-mgma-surveys>), this translated into \$82,617 for 2 clinical full-time equivalents or \$41,308 per year for 1 clinical full-time equivalent. If we used the 2013 Association of Administrators in Academic Radiology statistics (median salary per RVU = \$45.16), this translated into \$69,953 for 2 clinical full-time equivalents or \$34,976 per year for 1 clinical full-time equivalent. Again, this did not include the reading room consults as explained above because these were considered the postimaging acquisition component of the RVUs associated with these imaging studies rather than non-RVU-generating activities.

Slightly more than half of non-RVU-generating encounters were clinical working conferences, including tumor boards (Table 2). The rest represented a mix of 1-on-1 encounters, e-mails, phone calls, text messages, pages, and electronic medical record consults, in which a physician would contact a specific radiologist and request image review and discussion. Sixty-eight percent of the conferences and consults involved individuals who were already patients of our institution; 32% involved outside imaging studies. PET studies are typically read by the nuclear medicine department, but the non-RVU-generating consults and conferences included 8% of PET studies.

Table 1: Modality and anatomic region for RVU-generating and non-RVU-generating imaging studies

RVU-Generating Activity		Non-RVU-Generating Activity		RVU/Non-RVU Ratio
n = 4241	Studies	n = 792	Studies	19%
2271 (55%)	CT	251 (32%)	CT	11%
1970 (45%)	MRI	474 (60%)	MRI	24%
0 (0%)	PET	67 (8%)	PET	
1987 (51%)	Brain	433 (55%)	Brain	22%
998 (21%)	Neck	235 (30%)	Neck	24%
1256 (28%)	Spine	124 (16%)	Spine	10%

Table 2: Type of encounter for the non-RVU-generating activities

Non-RVU-Generating Activities	
n = 792	Studies
437 (55%)	Conferences
78 (10%)	1-on-1
218 (28%)	E-mail/phone
59 (7%)	Electronic medical record consults
541 (68%)	Internal patients
251 (32%)	Outside studies

DISCUSSION

Our study describes an easy-to-implement method to record non-RVU-generating activities performed by clinically active academic neuroradiologists. During a 3-month representative time frame, non-RVU-generating studies comprised 19% of the volume of the RVU-generating imaging studies, a significant fraction of the clinical effort of our neuroradiologists. This finding is in line with the results of a survey conducted in Ireland that showed that approximately one-third of radiologists' time is engaged in activities not easily counted in study numbers.⁴ Differences in absolute numbers could relate to our study having involved only 4 radiologists in 1 section of 1 academic institution. Most interesting, the 19% ratio of non-RVU activities to RVU reads was relatively constant for each of the 4 neuroradiologists and indicated that the neuroradiologists reading the most RVUs also performed the most non-RVU-generating consults and conferences. This indication suggests that our findings may hold independent of the academic time received by the neuroradiologists and may be representative of other neuroradiology sections at other academic institutions or in private practice.

We did not track the amount of time spent on individual consults or in preparing for conferences or tumor boards; hence, the time could be even greater, given the detailed interactions that often take place for each consult as well as follow-up communications and other postconsultation tasks. In addition, recording time accurately is a difficult task. We used RVUs as the basis for our recording because we wanted a very simple recording system that would not add significant burden or consume a significant amount of time for the participating radiologists. There had been prior attempts to record times, and the time measurements were variable and unreliable. The RVU recording is more representative, probably also because our activity is typically measured in RVUs.

Outside studies typically require at least as much effort as consults on internal patient imaging studies. There is growing literature suggesting that such outside consults can and should be paid for.⁵⁻⁷

We did not count managerial, teaching and research activities, peer-review, and so forth, which are other important non-RVU activities in academic practices. Others⁸ have proposed systems to measure such types of non-RVU activities.

Finally, we focused our attention on neuroradiology and did not examine other radiology subspecialties.

CONCLUSIONS

We developed a simple Web-based smartphone app to record and quantify non-RVU-generating activities, including consults, clinical conferences, and tumor boards, and we report the results of our consultation tracking via this app for 3 months. The quantification of non-RVU-generating activities is paramount in this time of a paradigm shift from volume to value. It also represents an important tool for determining staffing levels, which cannot be performed solely on the basis of RVUs, considering the value brought to the institution by radiologists involved in non-RVU-generating consult activities. Studies such as this may influence payment models from medical centers to radiology departments or practices.

Disclosures: Max Wintermark—UNRELATED: Board Membership: GE Healthcare and National Football League Advisory Board. Greg Zaharchuk—UNRELATED: Grants/Grants Pending: National Institutes of Health,* GE Healthcare.* *Money paid to the institution.

REFERENCES

- Lu Y, Zhao S, Chu PW, et al. **An update survey of academic radiologists' clinical productivity.** *J Am Coll Radiol* 2008;5:817–26 CrossRef Medline
- Burwell SM. **Setting value-based payment goals: HHS efforts to improve U.S. health care.** *N Engl J Med* 2015;372:897–99 CrossRef Medline
- Burleson J. **Quality and the physician value-based payment program.** *Radiol Manage* 2014;36:14–20; quiz 22–23 Medline
- Brady AP. **Measuring Consultant Radiologist workload: method and results from a national survey.** *Insights Imaging* 2011;2:247–60 CrossRef Medline
- Jeffers AB, Saghir A, Camacho M. **Formal reporting of second-opinion CT interpretation: experience and reimbursement in the emergency department setting.** *Emerg Radiol* 2012;19:187–93 CrossRef Medline
- Zan E, Yousem DM, Carone M, et al. **Second-opinion consultations in neuroradiology.** *Radiology* 2010;255:135–41 CrossRef Medline
- Briggs G, Flynn P, Worthington M, et al. **The role of specialist neuroradiology second opinion reporting: is there added value?** *Clin Radiol* 2008;63:791–95 CrossRef Medline
- Mezrich R, Nagy PG. **The academic RVU: a system for measuring academic productivity.** *J Am Coll Radiol* 2007;4:471–78 CrossRef Medline

Quantitative Susceptibility Mapping in Cerebral Cavernous Malformations: Clinical Correlations

H. Tan, L. Zhang, A.G. Mikati, R. Girard, O. Khanna, M.D. Fam, T. Liu, Y. Wang, R.R. Edelman, G. Christoforidis, and I.A. Awad



ABSTRACT

BACKGROUND AND PURPOSE: Quantitative susceptibility mapping has been shown to assess iron content in cerebral cavernous malformations. In this study, our aim was to correlate lesional iron deposition assessed by quantitative susceptibility mapping with clinical and disease features in patients with cerebral cavernous malformations.

MATERIALS AND METHODS: Patients underwent routine clinical scans in addition to quantitative susceptibility mapping on 3T systems. Data from 105 patients met the inclusion criteria. Cerebral cavernous malformation lesions identified on susceptibility maps were cross-verified by T2-weighted images and differentiated on the basis of prior overt hemorrhage. Mean susceptibility per cerebral cavernous malformation lesion ($\bar{\chi}_{\text{lesion}}$) was measured to correlate with lesion volume, age at scanning, and hemorrhagic history. Temporal rates of change in $\bar{\chi}_{\text{lesion}}$ were evaluated in 33 patients.

RESULTS: Average $\bar{\chi}_{\text{lesion}}$ per patient was positively correlated with patient age at scanning ($P < .05$, 4.1% change with each decade of life). Cerebral cavernous malformation lesions with prior overt hemorrhages exhibited higher $\bar{\chi}_{\text{lesion}}$ than those without ($P < .05$). Changes in $\bar{\chi}_{\text{lesion}}$ during 3- to 15-month follow-up were small in patients without new hemorrhage between the 2 scans (bias = -0.0003 ; 95% CI, -0.06 – 0.06).

CONCLUSIONS: The study revealed a positive correlation between mean quantitative susceptibility mapping signal and patient age in cerebral cavernous malformation lesions, higher mean quantitative susceptibility mapping signal in hemorrhagic lesions, and minimum longitudinal quantitative susceptibility mapping signal change in clinically stable lesions. Quantitative susceptibility mapping has the potential to be a novel imaging biomarker supplementing conventional imaging in cerebral cavernous malformations. The clinical significance of such measures merits further study.

ABBREVIATIONS: CCM = cerebral cavernous malformation; QSM = quantitative susceptibility mapping; $\bar{\chi}_{\text{lesion}}$ = mean susceptibility per cerebral cavernous malformation lesion; $\bar{\chi}_{\text{patient}}$ = lesional mean susceptibility per patient

Cerebral cavernous malformation (CCM) is a common hemorrhagic vascular anomaly of the human brain, affecting >1 million Americans.¹ Patients with CCMs are subject to 1%–5% annual risk and an estimated $\geq 30\%$ lifetime risk of hemorrhage, epilepsy, seizure, and other neurologic sequelae.^{2–4} The clinical consequences of CCM remain unpredictable, and currently there

is no known treatment to alter the course of this disease besides surgery.

Iron deposition related to hemorrhage within CCM lesions is a recognized hallmark of disease activity.^{5–7} Recently, therapeutic changes in lesion burden have been found with experimental drugs in animal models, in which a major phenotypic effect of the therapy was a decrease in iron deposition in lesions treated by immunohistochemistry.⁶ Lesional iron was therefore hypothesized to be a marker for disease progression and a relevant therapeutic target. It would be essential to determine whether the dis-

Received August 3, 2015; accepted after revision January 4, 2016.

From the Department of Surgery (Neurosurgery) (H.T., L.Z., A.G.M., R.G., O.K., M.D.F., I.A.A.), University of Chicago Medicine and Biological Sciences, University of Chicago, Chicago, Illinois; MedImageMetric (T.L.), New York, New York; Department of Radiology (Y.W.), Weill Cornell Medical College, New York, New York; Department of Biomedical Engineering (Y.W.), Cornell University, Ithaca, New York; Department of Radiology (R.R.E.), NorthShore University HealthSystem, Evanston, Illinois; Department of Radiology (R.R.E.), Feinberg School of Medicine, Northwestern University, Chicago, Illinois; and Department of Radiology (G.C.), Pritzker School of Medicine, University of Chicago, Chicago, Illinois.

This project was funded, in part, by the Collaborative and Translational Studies Award through the Institute of Translational Medicine at the University of Chicago (UL1 TR000430) and the Bill and Judy Davis Research Fund in Neurovascular Research.

Please address correspondence to Huan Tan, PhD, Department of Surgery, Section of Neurosurgery, SBRI J328, 5841 South Maryland Ave, MC 3026, Chicago, IL 60637; e-mail: htan@surgery.bsd.uchicago.edu

Indicates open access to non-subscribers at www.ajnr.org

Indicates article with supplemental on-line appendix.

Indicates article with supplemental on-line photo.

<http://dx.doi.org/10.3174/ajnr.A4724>

ease severity and beneficial effect on iron can also be quantified by a method suitable for clinical studies. The current evaluation of CCM disease burden in humans primarily relies on lesion count and size with MR imaging, in great part due to the imaging of susceptibility effects caused by the iron-rich blood breakdown by-products. Modern MR imaging techniques, such as susceptibility-weighted imaging,⁸ can offer accurate lesion counts⁹; however, they lack the ability to quantify lesional iron deposition, particularly in larger clinically concerning lesions. The continuing investigation of experimental CCM therapies is in need of a quantitative technique for a more accurate and sensitive assessment of outcomes and a potential biomarker of novel therapies.

Quantitative susceptibility mapping (QSM) is a noninvasive MR imaging technique that has the potential to estimate lesional iron content by quantifying the magnetic susceptibility of local tissues.^{10,11} The initial feasibility of QSM in CCM was previously demonstrated in a small cohort of patients.¹² Most important, QSM as a means to quantify lesional iron in CCM was validated by mass spectroscopy by using excised human lesion specimens.¹² However, to our knowledge, iron burden and its evolution in relation to disease progression have not been established. Novel discoveries relating iron content and the clinical features of the disease and changes in iron accumulation with time will offer valuable information in understanding the disease pathophysiology and assisting in the development of potential interventions.

In this study, we answer those questions by applying QSM to a large cohort of patients with CCMs as a part of the routine clinical examination. We tested the following hypotheses: 1) The average CCM susceptibility per patient is correlated with age, 2) lesions with previous hemorrhagic events have higher susceptibility, and 3) changes in lesional susceptibility ($\bar{\chi}_{\text{lesion}}$) in a short time (<2 years) are insignificant in patients who were clinically stable (ie, asymptomatic, no bleeds); other changes in QSM with time may reflect new bleeding or recovery from hemorrhage. The goal of this study was to extend from the initial feasibility¹² to explore QSM for a clinical measure of the disease severity and correlate lesion-specific behaviors during disease progression.

MATERIALS AND METHODS

Study Design

Clinical features of the CCM disease and prior lesion behaviors were correlated with QSM-derived iron measurements. A sub-cohort of patients underwent serial QSM measurements, and longitudinal assessment of QSM was correlated with clinical lesion behavior in these cases. In addition, QSM was spatially correlated to the T1- and T2-weighted imaging characteristics of lesions based on blood breakdown products. The iron sources that contribute to the QSM signal are complex. In the context of the preliminary evidence¹² that demonstrated that the mean QSM signal was directly proportional to the actual iron concentration in CCM lesions by mass spectroscopy, the terms “mean susceptibility” and “iron concentration” will be used interchangeably in this article.

Patients

This study enrolled 105 consecutive patients (mean age, 39 years; range, 3–76 years) scheduled for routine clinical evaluation and

Clinical information of the included patients

Information	
No. of patients included in analysis	95
Mean age at first scan/range (yr)	40/3–76
Male/female	34:61
No. of sporadic/familial CCMs	39/56

MR imaging for CCM disease from February 2012 to December 2014. Inclusion criteria for enrollment were the presence of known CCM disease and the absence of other unrelated neurologic pathology. The imaging study took place at the University of Chicago and NorthShore University HealthSystem. Both institutional review boards approved the study, and written informed consent was obtained from each patient.

A total of 175 scans including follow-up imaging were obtained in 105 patients. Thirty-seven scans (21%) were excluded from the final analysis due to excessive imaging artifacts because of motion and/or medical implants and the absence of lesions (eg, the scan occurred after the lesion was resected). As a result, the final analysis included 138 scans from 95 patients (96 scans in 69 patients at University of Chicago and 42 scans in 26 patients at NorthShore University HealthSystem). Among those 95 patients, 33 (22 at University of Chicago and 11 at NorthShore University HealthSystem) underwent at least 1 follow-up scan. The time between the repeat scans ranged from 91 to 455 days, with an average of 359 days.

For cross-sectional analyses, the first QSM of those who had multiple scans was used. A clinical summary of the included patients is shown in the Table.

Imaging Environment and Data Acquisition

Imaging was performed on 3T MR imaging systems. Sixty-nine patients were imaged at the University of Chicago (Achieva; Philips Healthcare, Best, the Netherlands) with an 8-channel phased array head coil, while 26 patients were imaged at NorthShore University HealthSystem (Magnetom Verio; Siemens, Erlangen, Germany) with a 12-channel phased array head coil (inter-scanner calibration was performed with satisfactory result, see On-line Appendix). Follow-up scans for patients were obtained on the same units as the ones used at their initial visits.

A 3D, T2*-weighted, multiecho, spoiled gradient-echo sequence was used for QSM data acquisition with the following common parameters: 8 TEs with uniform spacing, flip angle of 15°, and a parallel acceleration of a factor 2. The following parameters are system-specific: Philips Achieva: TE, 5.6–51 ms; FOV, 224 mm; acquisition matrix, 224 × 224; slab-encoding thickness, 1 mm; TR, 66 ms; Siemens Verio: TE, 3.6–45 ms; FOV, 240 mm; acquisition matrix, 256 × 256; slab-encoding thickness, 1.5 mm; TR, 55 ms.

Data Reconstruction

QSM images were reconstructed by using a morphology-enabled dipole inversion algorithm,^{10,13} which generates the local susceptibility distribution by inverting the estimated tissue field map with prior information from the magnitude images. The tissue field map was obtained by removing the background field induced by large susceptibility sources (ie, air/tissue in-

terface) from the field map derived from the gradient-echo phase images.¹⁴ Image reconstruction was performed locally on a dedicated workstation (Intel Core i7 2.7 GHz, 16 GB RAM; Intel, Santa Clara, California) with an average processing time of 8 minutes.

Data Analysis

Extraction of Clinical Parameters. The electronic medical records of the patients were reviewed by 1 experienced clinician (with >20 years of experience in the care of CCM), and de-identified clinical information was collected and stored in a data base before initiating the correlations. Hemorrhage associated with CCM was defined according to the criteria of Al-Shahi Salman et al.¹⁵ Briefly, hemorrhage due to CCM requires both acute or subacute onset of symptoms accompanied by imaging evidence of acute or subacute lesional or extralesional hemorrhage. Cases were classified as familial or sporadic on the basis of lesion count, family history, and/or identified mutations by using genetic screening.^{9,16}

Inclusion Criteria for Lesion Analysis. Lesions were selected from the 138 scans with acceptable image quality. Because sporadic cases often only contain a solitary lesion, all lesions in sporadic cases were included. In familial cases, the number of lesions can be innumerable with many small punctate lesions. Hence, we only included lesions with a maximum cross-diameter of ≥ 5 mm¹⁷ on the corresponding T2-weighted images that were of higher clinical significance. A total of 407 lesions (64 from 64 scans in 39 patients with sporadic CCM and 343 from 74 scans in 56 patients with familial CCM) were included in the final analysis.

Lesion Susceptibility and Volume Measurements. CCM lesions appeared hyperintense on the QSM maps and were cross-verified with SWI and T2-weighted images. Lesion segmentation was performed by using ImageJ software (National Institute of Health, Bethesda, Maryland) by experienced scientists and physicians with high intra- and interobserver consistency demonstrated previously.¹⁸ The final ROI defined for each lesion was 3D by aggregating 2D ROI cross-multiple sections. Mean susceptibility ($\bar{\chi} = \sum \chi_{ROI} / N$, where N is the number of pixels within the 3D ROI) was then calculated per lesion ($\bar{\chi}_{lesion}$) and averaged across all lesions per patient ($\bar{\chi}_{patient}$). Lesion volume was computed as the product of the total number of pixels in the 3D ROI and the voxel size.

Correlation Analyses. We performed correlation analysis between $\bar{\chi}_{lesion}$ (proportional to lesional iron concentration¹²) and a set of clinical parameters consisting of patients' basic characteristics and the CCM disease features. Specific parameters from basic characteristics included patient sex and age at scanning, which provide an estimation of the duration of lesion presence. Often lesion genesis can occur before the lesion becomes symptomatic; we assumed that older patients were more likely to have had the lesion for a longer duration. Parameters from the disease feature included lesional volume, sporadic versus familial, and hemorrhagic history. In patients with follow-up scans, we assessed changes with time in $\bar{\chi}_{lesion}$ in the same lesions.

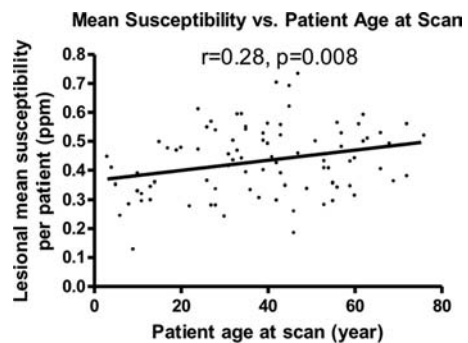


FIG 1. Lesional mean susceptibility per patient (parts per million) is positively correlated with patient age at scanning.

Spatial Correlation Based on Conventional MR Imaging Features. Spatial correlation of imaging features between QSM and conventional MR imaging sequences was conducted in 20 randomly selected lesions in our cohort. Each lesion was spatially segmented by an experienced neuroradiologist (with >20 years of experience) on the basis of the signal intensity on the conventional T1- and T2-weighted images as different blood breakdown products.¹⁹ We identified 4 types of blood by-products: deoxygenated hemoglobin, intra-/extracellular methemoglobin, and hemosiderin. A category of “unknown” was used to describe all other depositions within the lesion. The susceptibility of each blood by-product was empirically determined as high (>1.4 ppm), medium (between 0.6 and 1.4 ppm), or low (<0.6 ppm). The distribution of susceptibility measurements across different blood types was analyzed.

Statistical Analysis

The Pearson correlation and Student t test were applied to explore the correlations and comparisons made between $\bar{\chi}_{lesion}$ and continuous or dichotomous clinical factors, respectively. The Bland-Altman plot was used to assess the changes in patients with repeat scans. Receiver operating characteristic analysis was applied to express the diagnostic accuracy of QSM identifying lesions with prior hemorrhages in cases with familial CCM. Statistical analyses were performed by using GraphPad Prism 4 software (GraphPad Software, San Diego, California), and all reported P values were 2-sided and were considered statistically significant at $P < .05$.

RESULTS

Correlations with Patients' Basic Characteristics

We found a linear, positive correlation between patient age at scanning and the $\bar{\chi}_{patient}$ ($P < .05$, Fig 1), suggesting that older lesions have a higher iron concentration. The average change in $\bar{\chi}_{patient}$ was small (estimated to be 4.8% per decade of life); this finding may imply a slow, progressive iron deposition. $\bar{\chi}_{patient}$ was not significantly different between sexes. Furthermore, there was no correlation between $\bar{\chi}_{patient}$ in symptomatic patients and years since initial symptom onset.

Correlations with Clinical Features of the Disease

Sporadic and Familial CCM and Lesion Volume. We did not find a significant difference in $\bar{\chi}_{patient}$ between patients with sporadic and familial CCM. No correlation was found between $\bar{\chi}_{lesion}$ and

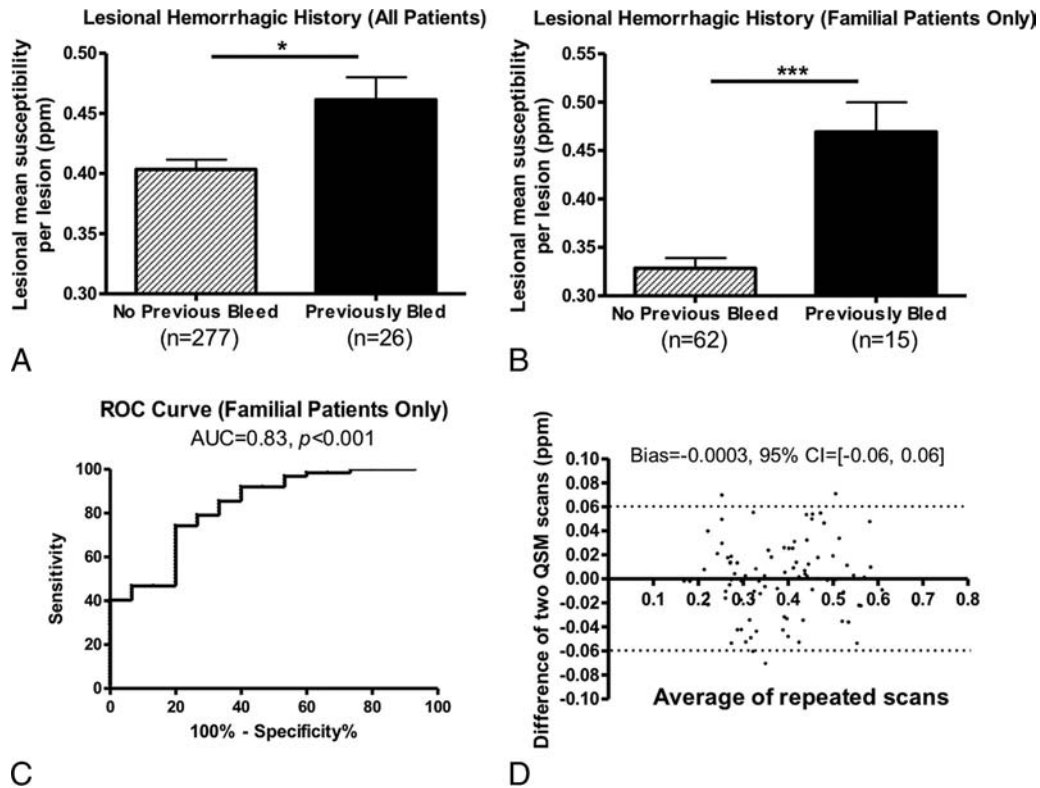


FIG 2. A, Mean susceptibility comparison between lesions with and without prior hemorrhages in all patients. B, Mean susceptibility comparison between lesions with and without prior hemorrhages only in patients with familial CCM. C, Receiver operating characteristics analysis indicates that QSM is a good differentiator of lesions with and without prior hemorrhage in cases with familial CCM. D, A Bland-Altman plot of the repeat QSM measurements. Changes in susceptibility were small in clinically stable patients within a short follow-up.

lesion volume, indicating that lesional iron concentration is independent of lesion volume.

Hemorrhagic and Nonhemorrhagic Lesions. CCM lesions in patients with both sporadic and familial CCMs with previous overt hemorrhages were found to have significantly higher iron concentrations. $\bar{\chi}_{\text{lesion}}$ in 26 lesions that previously bled at least once was significantly higher than that in lesions ($n = 277$) that had no history of prior CCM hemorrhages ($P < .05$, Fig 2A). The 95% confidence interval for the difference between patients with and without overt hemorrhage was 0.39–0.50. This result suggests that CCM lesions with prior symptomatic bleeds have more iron or iron-containing products.

The difference in $\bar{\chi}_{\text{lesion}}$ between hemorrhagic and nonhemorrhagic cases was more prominent in patients with familial CCM ($P < .01$, Fig 2B). Considering lesions with prior hemorrhagic events as the true-positive group and the remaining lesions as the true-negative group in our data, we performed receiver operating characteristic analysis as a measure of the overall discriminative performance of QSM—that is, the overall ability to identify lesions with prior bleeds ahead of those without. The area under curve was 0.83, suggesting that QSM had a good accuracy in identifying prior hemorrhage of a lesion (Fig 2C).

When we controlled for lesion volume, the difference in $\bar{\chi}_{\text{lesion}}$ was not significant between hemorrhagic and nonhemorrhagic lesions. This finding suggests that the effect of prior hemorrhages on lesional iron concentration is mediated, at least in part, by lesion volume.

Longitudinal Changes in Lesional Susceptibility

Changes in $\bar{\chi}_{\text{lesion}}$ were small among 33 patients in the short term (mean, 300 ± 125 days; median, 360 days). The bias for changes in mean susceptibility was -0.0003 (95% confidence interval, $-0.06-0.06$), shown in the Bland-Altman plot (Fig 2D). Among the 33 patients, lesions from 20 patients were clinically stable without historical symptoms (bias = -0.003 ; 95% CI, $-0.064-0.058$); 5 patients had a CCM-related hemorrhage within 6 months before the first QSM (bias = -0.015 ; 95% CI, $-0.033-0.064$); and 8 patients had a CCM-related hemorrhage >6 months before the first QSM (bias = 0.23 ; 95% CI, $-0.044-0.075$). None of the patients experienced a hemorrhage between their first and second QSM scans. In the same cohort, no significant correlation was found between changes in $\bar{\chi}_{\text{lesion}}$ and changes in lesion volume, indicating that changes in lesional iron concentration can occur independent of changes in lesion volume.

Impact of an Operation and Recent Hemorrhage on QSM

In 1 patient with sporadic CCM (a 41-year-old woman), the lesion located in the right frontal lobe was removed surgically before the second QSM scan. The success of the operation was reflected on the QSM image, where only residual iron deposition was seen at the edge of the old lesion (Fig 3A).

One patient with sporadic CCM (a 28-year-old woman), in whom the CCM lesion bled 3 months before her first QSM scan in September, had a rebleed in the same lesion in October. A second QSM scan was obtained in December, and an increase in both $\bar{\chi}_{\text{lesion}}$

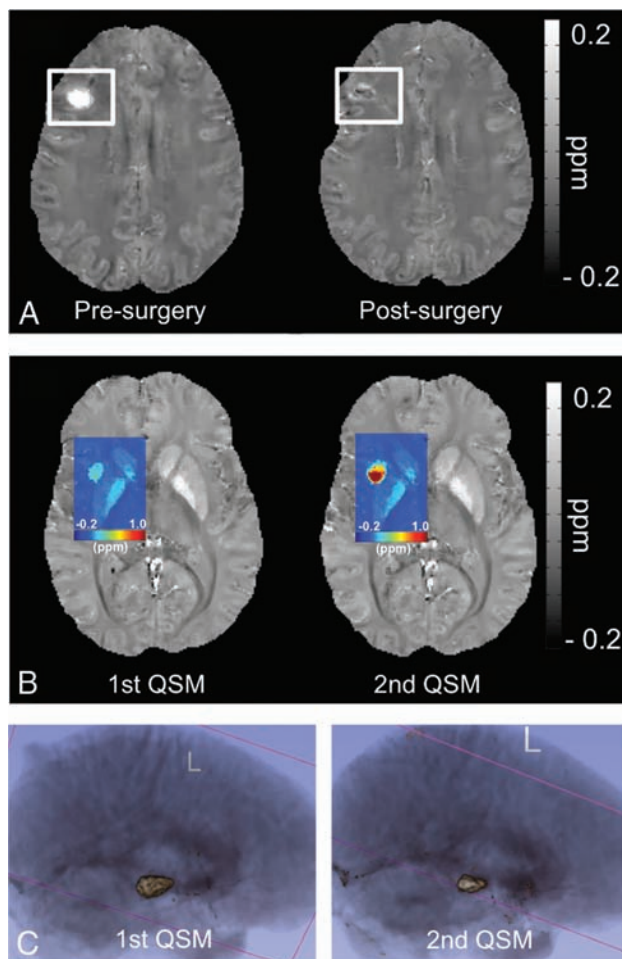


FIG 3. Each subfigure exhibits a separate CCM case. *A*, QSM map depicts the appearance of a CCM lesion before and after the operation. *B*, A colorized QSM map depicting a big increase in iron deposition in the same CCM lesion in a short time, after 2 recent overt hemorrhages. *C*, 3D rendering of a CCM lesion in repeat scans after a known hemorrhage, depicting the shrinkage in overall lesion volume during the short-term recovery period in a patient following a hemorrhage, but with increased mean susceptibility.

(from 0.1751 to 0.4659 ppm) and lesion volume (from 519 to 932 mm³) was observed (Fig 3*B*). We suspect that the increase in lesional iron deposition was related to the 2 overt hemorrhages in such a short timeframe. One other patient with familiar CCM (a 2-year-old boy) had a hemorrhage 11 months after the first QSM scan with a second QSM follow-up 2 months later. However, no significant change was observed in the lesion that bled ($\bar{\chi}_{\text{lesion, 1st QSM}} = 0.4966$ ppm, first lesion volume = 3960 mm³; $\bar{\chi}_{\text{lesion, 2nd QSM}} = 0.4765$ ppm, second lesion volume = 3919 mm³).

One other case worth noting was a 59-year-old patient with sporadic CCM who underwent her first QSM scan 14 days after the lesion bled, and a second QSM scan was performed 35 days after that. Although both the lesion volume and the total susceptibility decreased from 2165 to 1242 mm³ and from 1130 to 723 ppm × mm³, respectively (Fig 3*C*), $\bar{\chi}_{\text{lesion}}$ increased slightly from 0.4298 to 0.4791 ppm. This change suggests that the human body does not effectively remove the iron products associated with hemorrhage during the natural recovery progress. Furthermore, this case illustrates that changes in lesion volume do not necessarily reflect a concomitant change in lesional iron concentration.

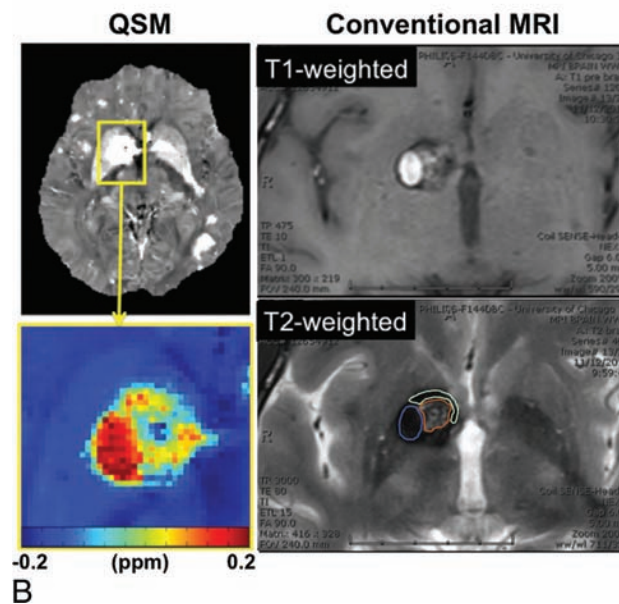
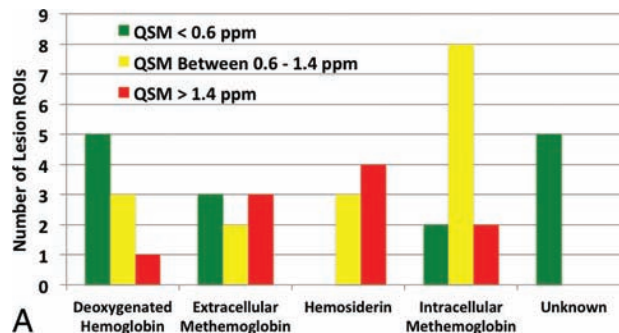


FIG 4. Spatial comparison results between QSM and conventional MR imaging. *A*, Susceptibility distribution of different blood breakdown by-products within CCM lesions. *B*, Illustration of blood breakdown by-product identification and correlation with the corresponding QSM measurements. ROIs for different blood by-products are shown in the T2-weighted image with color (blue, intracellular methemoglobin; brown, intracellular methemoglobin and hemosiderin; cyan, hemosiderin).

Overall, of the 3 patients with follow-up QSM after recent hemorrhages in a longitudinal study, 2 had an interval increase in lesional iron concentrations without an increase in lesion volume and a third had nearly 2.5-fold increase in lesional iron concentration, with only an 80% increase in lesion volume. This finding shows that increased iron concentration in CCM lesions can occur after hemorrhage, independent of lesion volume.

Spatial Correlation with Conventional MRI

All CCM lesions revealed hypointense signal compared with normal brain parenchyma on QSM. A total of 41 ROIs were identified from 20 randomly selected CCM lesions, consisting of 9 deoxygenated hemoglobin, 8 extracellular methemoglobin, 12 intracellular methemoglobin, 7 hemosiderin, and 5 unknown regions. The signal intensities for deoxygenated hemoglobin, extracellular methemoglobin, and intracellular methemoglobin spanned the full spectrum (low to high) on the QSM images, whereas hemosiderin exhibited medium and high intensities, and the unidentified regions exhibited low intensities (Fig 4*A*). In particular, hemosiderin demonstrated the most homogeneous signal distri-

bution on QSM, while the other blood by-product regions exhibited both homogeneous and heterogeneous signal distributions. An example of the spatial correlation between QSM and the conventional T1 and T2 images is shown in Fig 4B.

DISCUSSION

Our previous investigation¹² demonstrated the proof of concept that QSM can quantify lesional iron deposition in CCM. In the current study, we aimed to evaluate the relationship between iron burden by using QSM and the clinical features of the CCM disease in a larger clinical population.

Because the total iron content measured by QSM in CCM lesions is inherently related to the lesion size (ie, larger lesions contain more iron deposition¹²), we sought to assess lesional mean susceptibility, a measurement proportional to the lesional iron concentration, as the metric to assess lesional iron burden. The results have confirmed the hypothesis that lesions in older patients had higher iron burden. We used age at scanning as an estimate for the duration of lesion presence because lesion genesis is unknowable in most cases. Other studies have analyzed bleed risk and other natural history features on the basis of similar years of exposure since birth.^{3,20} Aging itself may be a factor in this observation, given the increasing evidence to show that older brains are associated with increased iron.²¹ This observation supports the conservation of mass hypothesis, with QSM signal reflecting lesional permeability as demonstrated in a previous study,¹⁸ now also reflected by iron accumulation with time.

No correlation was found between lesional iron concentration and lesion volume. This finding confirmed our initial observation in the prior feasibility study.¹² Changes in lesional volume and iron concentration may be 2 independent indicators of different aspects of disease activities, which will be further examined in a future prospective longitudinal investigation.

We found that lesions with prior overt hemorrhages were shown to have a higher iron concentration than those without. Even though the observation was predominately in cases of familial CCM, it still indicates that hemorrhages were related to iron depositions within CCM lesions, and it confirmed that the human body lacks an effective mechanism to clear the residual iron products from a CCM during recovery. The receiver operating characteristic analysis suggests that QSM might identify prior bleeding events in cases of familial CCM with a good sensitivity measure. This aspect of the QSM application is important, especially when a patient's medical history is unknown or when patients do not present for medical evaluation after unknowingly experiencing a hemorrhage. While the mean iron concentration in bled lesions was higher than ones without bleeds in cases with sporadic CCM, it did not reach statistical significance. This outcome may be related to the small sample size of sporadic bleeds.

Our cross-sectional data showed that the hemorrhagic effect on the lesional iron concentration was mediated, at least in part, by lesion volume in cross-sectional observations. This cohort may not have included a sufficient number of hemorrhagic cases in all volume strata. Our data from the longitudinal study in patients with repeat QSM scans after recent hemorrhage showed a manifest increase in lesional iron concentrations independent of lesional volume. To fully evaluate whether QSM offers an added

measure beyond lesion size, a higher number of patients with hemorrhage with repeat scans are required.

The longitudinal results in cases with repeat QSM studies revealed little temporal change in lesional iron for up to 15 months in clinically stable lesions (Fig 2D). Lesions included in the analysis consist of those without any prior hemorrhages and those with prior hemorrhage in the chronic stage before the first QSM. In both scenarios, the susceptibility signal within the lesion remained relatively unchanged at short-term follow-up. The observation of minimum change in stable CCM lesions and increased susceptibility signal associated with overt hemorrhages may indicate that lesional iron concentration increases only in the presence of recent bleeds. This hypothesis will be subject to more rigorous testing in a larger longitudinal study.

We found that there was a large variation (estimated range, 0.4–1.9 ppm) in the susceptibility signal within regions of different blood breakdown products (eg, deoxygenated hemoglobin, intracellular methemoglobin, extracellular methemoglobin). Hemosiderin, however, consistently exhibited a higher mean susceptibility value (>1.0 ppm). This could be the result of hemosiderin crystallization generating superparamagnetism.²² The heterogeneity and variation of susceptibility values in deoxygenated hemoglobin, intracellular methemoglobin, and extracellular methemoglobin suggest that there might be other contributing susceptibility sources. Overall, we believe that the spatial distribution of the lesional susceptibility does offer additional information beyond that from conventional MRI, the details of which require further investigation.

Limitations of this study include lesional iron content, which may be underestimated due to partial volume effects because other susceptibility sources such as diamagnetic myelin were not accounted for. This study was not powered to detect the effects of lesional iron content in patients recovering from or with recent bleeds, though the ongoing study is currently accumulating additional data to power future studies in relation to ongoing CCM lesion activity. The classification of blood by-products based on Bradley¹⁹ was overly simplified. Differentiating various blood products was a difficult task, and some ROI regions contained spatially heterogeneous signal distribution on conventional MRI. Those regions were likely to contain a variety of blood iron products, and they were classified according to the predominant signal appearances. In addition, we did not specifically examine cases of CCM associated with seizures, in which QSM may reflect lesional epileptogenicity, and this will be addressed in future studies. While the data in this study were not enough to establish the clinical utility of QSM, we postulate that QSM may still be used as a potential imaging biomarker to supplement information from conventional imaging and to calibrate experimental therapies in future clinical trials targeted at reducing lesional iron deposition in CCM.

CONCLUSIONS

We demonstrated in the current study the following: 1) lesional mean susceptibility was positively correlated with patient age, 2) lesions with prior symptomatic bleeding have higher mean susceptibility than those without, and 3) changes in lesional susceptibility were minimal in clinically stable CCM lesions. Addition-

ally, in a limited number of observations, there was a significant increase in lesional mean susceptibility in association with new clinical hemorrhage, motivating further the prospective longitudinal investigation already underway. The findings in this study will be hypothesis-generating for future investigations that will help guide and design human trials for potential treatments.

ACKNOWLEDGMENTS

The authors thank Eugene Dunkle and Dr Wei Li for assisting with data collection and the Center for Advanced Imaging at NorthShore University HealthSystem for providing the scanning time and equipment for the study.

Disclosures: Huan Tan—*RELATED*: The project was funded in part by the Collaborative and Translational Studies Award through the Institute of Translational Medicine at the University of Chicago (UL1 TR000430) and by the Bill and Judy Davis Research Fund in Neurovascular Research*; *OTHER RELATIONSHIPS*: Drs Tian Liu and Yi Wang have filed patents related to QSM technology. Dr Tian Liu is an employee of MedImageMetric in New York. Tian Liu—*RELATED*: Grant: MedImageMetric.* *Comments*: National Institutes of Health grant 1R43 EB015293-01; *UNRELATED*: Patents (planned, pending, or issued): I am listed as an inventor on patent applications related to QSM. Yi Wang—*RELATED*: Grant: National Institutes of Health R01NS072370*; *UNRELATED*: Patents (planned, pending, or issued): I am one of the inventors of QSM; *Stock/Stock Options*: MedImageMetric, *Comments*: interested in QSM commercialization. Robert R. Edelman—*UNRELATED*: Grants/Grants Pending: National Institutes of Health, Siemens Healthcare; Patents (planned, pending, or issued): Non-contrast MR angiography; *Royalties*: Siemens Healthcare. Gregory Christoforidis—*RELATED*: Grant: National Institutes of Health.* Issam A. Awad—*RELATED*: Grant: National Institutes of Health/National Institute of Neurological Disorders and Stroke.* Davis Research Fund in Neurovascular Surgery Research*; *UNRELATED*: *Expert Testimony*: legal expert testimony, unrelated to subject of research; *Grants/Grants Pending*: National Institutes of Health/National Institute of Neurological Disorders and Stroke.* *Money paid to the institution.

REFERENCES

- Barrow D, Krisht A, AANS Publications Committee. **Cavernous malformation and hemorrhage**. In: Awad IA, Barrow D, eds. *Cavernous Malformations*. Park Ridge: American Association of Neurological Surgeons; 1993:65–80
- Bruner JM, Tien RD, McLendon RE. **Tumors of vascular origin**. In: Bigner DD, McLendon RE, Bruner JM, et al, eds. *Russell and Rubinstein's Pathology of Tumors of the Nervous System*. London: Arnold; 1998:239–93
- Robinson JR, Awad IA, Little JR. **Natural history of the cavernous angioma**. *J Neurosurg* 1991;75:709–14 CrossRef Medline
- Robinson JR Jr, Awad IA, Magdinec M, et al. **Factors predisposing to clinical disability in patients with cavernous malformations of the brain**. *Neurosurgery* 1993;32:730–35; discussion 735–36 CrossRef Medline
- McDonald DA, Shenkar R, Shi C, et al. **A novel mouse model of cerebral cavernous malformations based on the two-hit mutation hypothesis recapitulates the human disease**. *Hum Mol Genet* 2011; 20:211–22 CrossRef Medline
- McDonald DA, Shi C, Shenkar R, et al. **Fasudil decreases lesion burden in a murine model of cerebral cavernous malformation disease**. *Stroke* 2012;43:571–74 CrossRef Medline
- Shenkar R, Venkatasubramanian PN, Zhao JC, et al. **Advanced magnetic resonance imaging of cerebral cavernous malformations, part I: high-field imaging of excised human lesions**. *Neurosurgery* 2008; 63:782–89; discussion 789 CrossRef Medline
- Haacke EM. **Susceptibility weighted imaging (SWI)**. *Z Med Phys* 2006;16:237 CrossRef Medline
- de Champfleury NM, Langlois C, Ankenbrandt WJ, et al. **Magnetic resonance imaging evaluation of cerebral cavernous malformations with susceptibility-weighted imaging**. *Neurosurgery* 2011;68: 641–47; discussion 647–48 CrossRef Medline
- Liu T, Liu J, de Rochefort L, et al. **Morphology enabled dipole inversion (MEDI) from a single-angle acquisition: comparison with COSMOS in human brain imaging**. *Magn Reson Med* 2011;66: 777–83 CrossRef Medline
- Schweser F, Deistung A, Lehr BW, et al. **Quantitative imaging of intrinsic magnetic tissue properties using MRI signal phase: an approach to in vivo brain iron metabolism?** *Neuroimage* 2011;54: 2789–807 CrossRef Medline
- Tan H, Liu T, Wu Y, et al. **Evaluation of iron content in human cerebral cavernous malformation using quantitative susceptibility mapping**. *Invest Radiol* 2014;49:498–504 CrossRef Medline
- Liu T, Wisnieff C, Lou M, et al. **Nonlinear formulation of the magnetic field to source relationship for robust quantitative susceptibility mapping**. *Magn Reson Med* 2013;69:467–76 CrossRef Medline
- Liu T, Khalidov I, de Rochefort L, et al. **A novel background field removal method for MRI using projection onto dipole fields (PDF)**. *NMR Biomed* 2011;24:1129–36 CrossRef Medline
- Al-Shahi Salman R, Berg MJ, Morrison L, et al; Angioma Alliance Scientific Advisory Board. **Hemorrhage from cavernous malformations of the brain: definition and reporting standards—Angioma Alliance Scientific Advisory Board**. *Stroke* 2008;39:3222–30 CrossRef Medline
- Abdulrauf SI, Kaynar MY, Awad IA. **A comparison of the clinical profile of cavernous malformations with and without associated venous malformations**. *Neurosurgery* 1999;44:41–46; discussion 46–47 CrossRef Medline
- Campbell PG, Jabbour P, Yadla S, et al. **Emerging clinical imaging techniques for cerebral cavernous malformations: a systematic review**. *Neurosurg Focus* 2010;29:E6 CrossRef Medline
- Mikati AG, Tan H, Shenkar R, et al. **Dynamic permeability and quantitative susceptibility: related imaging biomarkers in cerebral cavernous malformations**. *Stroke* 2014;45:598–601 CrossRef Medline
- Bradley WG Jr. **MR appearance of hemorrhage in the brain**. *Radiology* 1993;189:15–26 CrossRef Medline
- Shenkar R, Shi C, Rebeiz T, et al. **Exceptional aggressiveness of cerebral cavernous malformation disease associated with PDCD10 mutations**. *Genet Med* 2015;17:188–96 CrossRef Medline
- Zecca L, Youdim MB, Riederer P, et al. **Iron, brain ageing and neurodegenerative disorders**. *Nat Rev Neurosci* 2004;5:863–73 CrossRef Medline
- Richter GW. **Electron microscopy of hemosiderin; presence of ferritin and occurrence of crystalline lattices in hemosiderin deposits**. *J Biophys Biochem Cytol* 1958;4:55–58 CrossRef Medline

Mapping the Orientation of White Matter Fiber Bundles: A Comparative Study of Diffusion Tensor Imaging, Diffusional Kurtosis Imaging, and Diffusion Spectrum Imaging

G.R. Glenn, L.-W. Kuo, Y.-P. Chao, C.-Y. Lee, J.A. Helpert, and J.H. Jensen



ABSTRACT

BACKGROUND AND PURPOSE: White matter fiber tractography relies on fiber bundle orientation estimates from diffusion MR imaging. However, clinically feasible techniques such as DTI and diffusional kurtosis imaging use assumptions, which may introduce error into in vivo orientation estimates. In this study, fiber bundle orientations from DTI and diffusional kurtosis imaging are compared with diffusion spectrum imaging as a criterion standard to assess the performance of each technique.

MATERIALS AND METHODS: For each subject, full DTI, diffusional kurtosis imaging, and diffusion spectrum imaging datasets were acquired during 2 independent sessions, and fiber bundle orientations were estimated by using the specific theoretic assumptions of each technique. Angular variability and angular error measures were assessed by comparing the orientation estimates. Tractography generated with each of the 3 reconstructions was also examined and contrasted.

RESULTS: Orientation estimates from all 3 techniques had comparable angular reproducibility, but diffusional kurtosis imaging decreased angular error throughout the white matter compared with DTI. Diffusion spectrum imaging and diffusional kurtosis imaging enabled the detection of crossing-fiber bundles, which had pronounced effects on tractography relative to DTI. Diffusion spectrum imaging had the highest sensitivity for detecting crossing fibers; however, the diffusion spectrum imaging and diffusional kurtosis imaging tracts were qualitatively similar.

CONCLUSIONS: Fiber bundle orientation estimates from diffusional kurtosis imaging have less systematic error than those from DTI, which can noticeably affect tractography. Moreover, tractography obtained with diffusional kurtosis imaging is qualitatively comparable with that of diffusion spectrum imaging. Because diffusional kurtosis imaging has a shorter typical scan time than diffusion spectrum imaging, diffusional kurtosis imaging is potentially more suitable for a variety of clinical and research applications.

ABBREVIATIONS: b0 = image in DWI dataset with no diffusion weighting; DKI = diffusional kurtosis imaging; dPDF = diffusion displacement probability distribution function; dODF = diffusion orientation distribution function; DSI = diffusion spectrum imaging; FA = fractional anisotropy

White matter fiber tractography is used clinically to visualize functionally important WM tracts and aid neurosurgeons during presurgical planning.^{1,2} Tractography is also an important research tool for studying structural connectivity because tractography is currently the only noninvasive technique for in vivo mapping of anatomic neural connections in the human brain.³ However, tractography relies on fiber bundle orientation estimates

derived from particular DWI techniques, which may have inherent methodologic limitations, potentially resulting in clinically misleading information.^{4,5}

Of the several proposed DWI methods for estimating the orientation of WM fiber bundles, a common approach uses the diffusion orientation distribution function (dODF), which quantifies the relative degree of diffusion mobility along a given

Received September 2, 2015; accepted after revision December 30.

From the Center for Biomedical Imaging (G.R.G., C.-Y.L., J.A.H., J.H.J.), Department of Neurosciences (G.R.G., J.A.H.), and Department of Radiology and Radiological Science (G.R.G., C.-Y.L., J.A.H., J.H.J.), Medical University of South Carolina, Charleston, South Carolina; Institute of Biomedical Engineering and Nanomedicine (L.-W.K.), National Health Research Institutes, Miaoli County, Taiwan; and Graduate Institute of Medical Mechatronics (Y.-P.C.), Chang Gung University, Taoyuan, Taiwan.

This work was supported by the National Institutes of Health research grant T32GM008716 (to P. Halushka), the Litwin Foundation (to J.A.H.), and grants NHRI-BN-104-PP-06 and MOST-103-2221-E-400-001 (to L.-W.K.).

Please address correspondence to J.H. Jensen, PhD, Center for Biomedical Imaging, Department of Radiology and Radiological Science, Medical University of South Carolina, 96 Jonathan Lucas, MSC 323, Charleston, SC 29425-0323; e-mail: jense@musc.edu; L.-W. Kuo, PhD, Institute of Biomedical Engineering and Nanomedicine, National Health Research Institutes, 35 Keyan Rd, Zhunan Town, Miaoli County, Taiwan 35053; e-mail: lwkuo@nhri.org.tw

 Indicates open access to non-subscribers at www.ajnr.org

 Indicates article with supplemental on-line table and appendix.

 Indicates article with supplemental on-line photos.

 Indicates article with supplemental on-line video.

<http://dx.doi.org/10.3174/ajnr.A4714>

direction from physical properties of water diffusion.⁶⁻⁹ Diffusion of water is assumed to be least restricted parallel to the orientation of WM fiber bundles, resulting in local maxima of the dODF. The dODF may be defined by

$$\Psi(\mathbf{n}) = \frac{1}{Z} \int_0^\infty r^\alpha P(r\mathbf{n}, t) dr,$$

where \mathbf{n} is a normalized orientation vector, r is a radial displacement magnitude, $P(r\mathbf{n}, t)$ is the diffusion displacement probability distribution function (dPDF) for diffusion displacement $r\mathbf{n}$ over a diffusion time t , α is a constant radial weighting power, and Z is a normalization constant.

Several distinct techniques exist for reconstructing the dODF from DWI data, which differ in their theoretic assumptions and optimal experimental implementation. These include DTI, which assumes that the diffusion of water can be completely described by Gaussian (normal) diffusion¹⁰⁻¹²; diffusional kurtosis imaging (DKI), which extends the DTI model to account for non-Gaussian diffusion effects¹³⁻¹⁶; Q-ball imaging, which applies the Funk transform to DWI data from high-angular-resolution diffusion-weighted imaging^{6,7}; and diffusion spectrum imaging (DSI).^{8,9}

In contrast to other methods, DSI quantifies the dODF by using an exact (in the narrow gradient pulse limit) Fourier transform relationship between the DWI signal and the dPDF. To accomplish this requires a dense sampling of q -space with relatively high maximum b -values. Thus, DSI effectively characterizes complex intravoxel microarchitecture without the need for intricate tissue models or ancillary approximations, though it tends to have more demanding data-acquisition requirements than alternative methods. Due to its rigorous mathematic formulation and comprehensive description of intravoxel diffusion dynamics, DSI may be considered a reference standard for validating other dODF techniques for in vivo experiments.¹⁷ Nonetheless, even the exact dODF may not give the precise orientation of WM fiber bundles, reflecting the complex and subtle relationship between diffusion and microstructure.

The DTI dODF has the same information as the diffusion tensor ellipsoid, and the global maximum of the DTI dODF gives the direction identical to the principal eigenvector of the diffusion tensor.^{7,16} Although efficient in terms of image-acquisition time, DTI is not capable of directly resolving intravoxel fiber crossings,¹⁰⁻¹² which can lead to increased errors in orientation estimates from regions with complex tissue architecture.^{5,18}

The motivation for considering the kurtosis dODF is 2-fold. First, there have been a considerable number of prior studies using DKI to investigate neuropathology, including stroke,¹⁹⁻²³ Alzheimer disease,²⁴⁻²⁸ cancer,²⁹⁻³¹ and numerous others.³² Therefore, a tractography method that is compatible with DKI can be of value. Second, DKI shares some of the practical advantages of DTI that make it particularly attractive for clinical settings, such as small maximum b -values and protocol options with relatively short scan times.^{14,21,33} For example, in clinical settings, a whole-brain DKI dataset with good image quality may be acquired in approximately 7 minutes,²¹ and respectable whole-brain DKI tractography has been demonstrated with acquisition times as short as 5.3 minutes.³³ Moreover, DKI inherently provides mea-

asures of the diffusion and kurtosis tensors as well as all the corresponding tensor-derived quantitative measures (eg, mean diffusivity and mean kurtosis), which are of interest for characterizing tissue microstructure.³⁴

In this study, dODFs derived from DSI, DKI, and DTI by using in vivo human measurements are directly compared, particularly with regard to their estimates of fiber bundle orientation. The errors intrinsic to the dODF orientations from DTI and DKI are calculated using the DSI orientations as benchmarks. In addition, the intrasubject variabilities of dODF orientation estimates are calculated across independent sessions for all 3 methods. A primary goal of this study is to assess the degree to which the DKI dODF approximates the DSI dODF and improves the DTI dODF. Tractography results are also compared qualitatively for the 3 dODF reconstruction techniques.

MATERIALS AND METHODS

The study was approved by the institutional review board at the National Health Research Institutes (Taiwan), and informed consent was obtained from all participants before enrollment in the study. Experiments were performed on 3 healthy volunteers on a 3T MR imaging system (Tim Trio; Siemens, Erlangen, Germany); and for each participant, 2 full DSI and DKI datasets were obtained, with the DTI dataset being taken as a subset of the DKI dataset. Angular variabilities in the orientation estimates were quantified as the absolute, voxelwise angular difference for each reconstruction between repeat scans, and for DKI and DTI, angular errors were quantified as the absolute, voxelwise angular differences from the corresponding DSI scan. For each subject, T1-weighted magnetization-prepared rapid acquisition of gradient echo images were also acquired for anatomic reference. The experimental design is illustrated in Fig 1, and the angular variability and error measures are illustrated in Fig 2. A detailed description of our image-acquisition protocol and image-analysis steps is given in the On-line Appendix.

The angular error estimates, as quantified in this study, include contributions from both random and systematic errors. Random error may result from thermal noise, incomplete q -space sampling distributions, and physiologic effects such as pulsatile flow and bulk subject motion, while systematic errors arise from the approximations inherent to the DTI and DKI dODFs. Although it is difficult to rigorously isolate the random and systematic components of the angular error, a rough index of systematic error is given by the difference between the angular error and angular variability for a given reconstruction because the angular variability is a measure of random error. We used this heuristic approach as a practical means of comparing systematic errors for the DTI and DKI dODFs.

Fiber-tracking results were assessed qualitatively by looking at the reconstructed tracts in specific regions with complex fiber bundle geometries and over the whole brain (On-line Video). To aid the qualitative assessment, a color-encoding scheme was used, in which each individual tract was colored by its overall displacement from the starting point to the ending point of the tract, with red indicating a left-right displacement, blue indicating an inferior-superior displacement, and green indicating an anteroposterior displacement. Similar colors represent similar overall trajec-

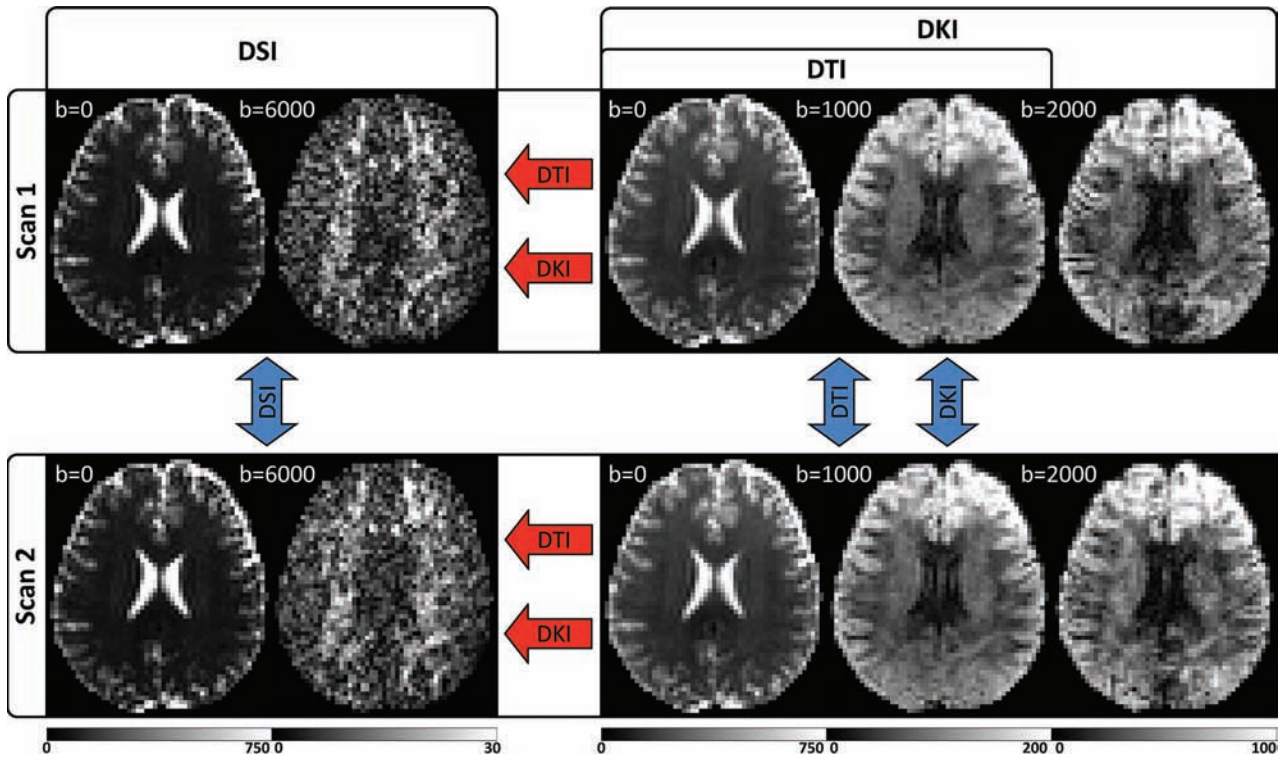


FIG 1. Experimental design illustrated with sample images from a single subject. For each subject, 2 separate scans are obtained, which include independent DSI and DKI acquisitions optimized for the respective reconstructions. The DTI reconstruction is calculated from a subset of the DKI acquisition and is fully independent of the DSI scan but not the DKI scan. Angular variability is calculated between scans (*blue arrows*), and angular error is calculated for DKI and DTI in reference to the corresponding DSI scan (*red arrows*). Units for the *b*-value are second/square millimeter, and the signal intensity ranges for each image are given by the corresponding color bar (in arbitrary units). DWIs from the highest *b*-value for each acquisition are given to illustrate the range of diffusion-weighting applied.

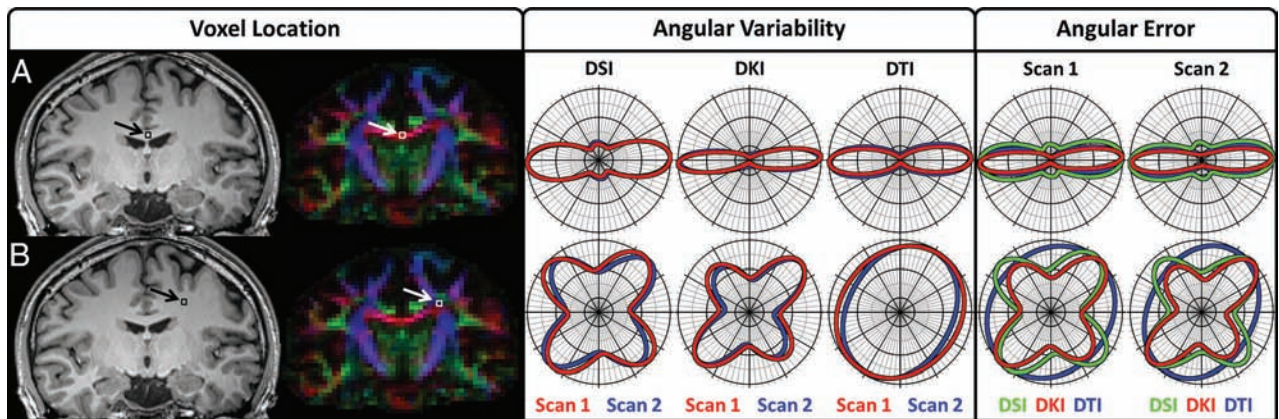


FIG 2. Polar 2D dODF cross-section plots illustrate angular variability and angular error measures. Row *A* illustrates dODFs taken from a single voxel in the corpus callosum where 1 predominant fiber bundle orientation is expected, and row *B* illustrates dODFs taken from a single voxel where multiple fiber bundles are expected to occur between cortical projections from the corpus callosum and the ascending and descending fiber bundles in the corona radiata. The “Voxel Location” tab illustrates the location of the voxels overlaid on the corresponding section from the MPRAGE image and the FA color map for anatomic reference; the “Angular Variability” tab illustrates angular variability measures, which are taken between scans for each reconstruction; and the “Angular Error” tab illustrates the angular error measures, which are taken relative to the corresponding DSI dODF for each scan. The section plane for the polar plots is rotated to contain the first and second largest orientations of the DSI dODF, because DSI is used as a reference. For visualization, each dODF is scaled to a maximum value of 1.

ories, whereas differing colors indicate tracts following different overall trajectories.

RESULTS

Summary statistics for each subject and ROI are given in the On-line Table. DTI has the lowest angular variability in both the inclusive and conservative WM ROIs as well as the single fiber bun-

dle ROI, while DSI has the lowest angular variability in both the 2 and ≥ 3 crossing-fibers ROIs. Conversely, DKI has the highest angular variability in all ROIs, with the exception of the ≥ 3 crossing-fibers ROI, where DTI has the highest angular variability. However, the angular variabilities for all reconstructions are comparable within each of the ROIs, differing by, at most, 2.1° in the single fiber bundle ROI (On-line Table, “Single-fiber ROI”). On

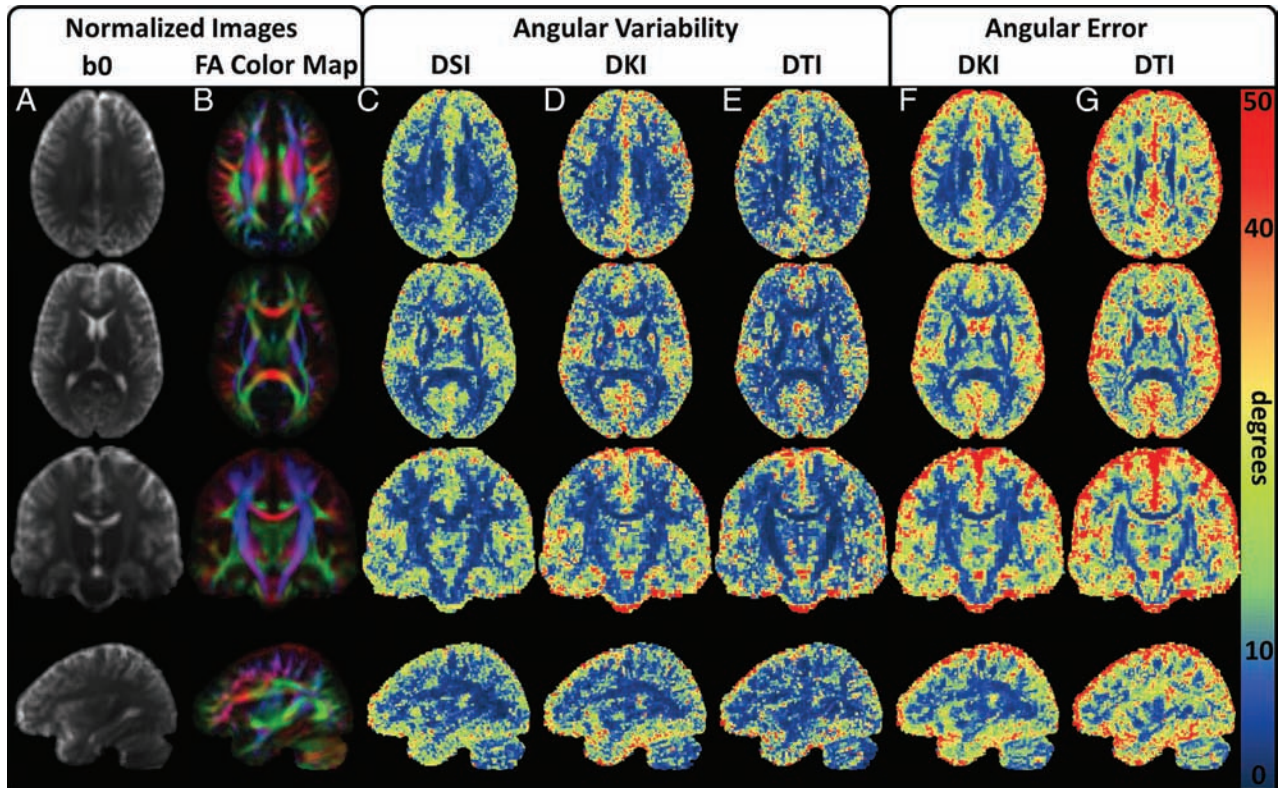


FIG 3. Group mean angular variability and angular error maps illustrate dODF performance. A and B, Mean of the normalized b0 and FA color map images, respectively, from all DKI acquisitions. These are included for anatomic reference and to help validate the normalization procedure. The rows illustrate representative transverse, coronal, and sagittal orientations. C–E, Angular variability for the DSI, DKI, and DTI reconstructions, respectively. All 3 techniques demonstrate similar angular variability in the white matter regions. F and G, Angular error for the DKI and DTI reconstructions, respectively. Angular error measures increase in regions with low FA, though the angular error for the DKI reconstruction is relatively consistent throughout the WM. The angular error is higher for the DTI reconstruction in the WM, particularly in regions where complex fiber bundle geometries may be present.

the other hand, DKI consistently improves angular error compared with DTI in all ROIs. Moreover, the DKI systematic errors are all substantially smaller than the DTI systematic errors, consistent with a higher degree of accuracy for the DKI dODFs.

For the ROIs tested, dODF performance measures are influenced by the fractional anisotropy (FA) value, with the smaller angular variability and angular error for regions with higher FA. Conversely, the occurrence of crossing fibers increased angular variability and angular error in dODF-derived orientation estimates. However, the accuracy of the DKI dODF is less affected than the DTI-derived dODF in crossing-fiber regions. Properties of the dODF reconstructions are explored further in On-line Figs 1 and 2.

Mean normalized parameter maps are given in Fig 3 to illustrate the group-wise performance of the dODF reconstructions. All 3 of the reconstruction techniques demonstrate similar angular variability throughout the WM, but DTI shows improvement in angular variability in regions with high FA (eg, note the corpus callosum and corticospinal tracts in rows 2 and 3, which show high FA contrast). The DKI angular error estimates are relatively consistent throughout the WM, whereas the DTI angular error estimates show distinct WM regions where the angular error deteriorates. When one compares these regions with the normalized FA color maps, it is likely that these regions represent voxels with more complex fiber bundle geometries owing to influences from

multiple fiber bundle orientations within a voxel (eg, note the intersecting regions between the corpus callosum and corona radiata, which are apparent in rows 1 and 3).

Exemplary tractography results are given in Fig 4. A cross-sectional view of the fiber tracts has been selected to highlight the effects of interactions that occur in regions with complex tissue architecture. This particular section contains noticeable influences from the corpus callosum, which is mainly along the left-right orientation, and the corticospinal tracts (among others), which are mainly along the inferosuperior orientation. This section also shows effects from the superior longitudinal fasciculus and the cingulum bundle, which are mainly oriented along the anteroposterior direction. In the tractography panels for DSI and DKI, the corpus callosum can be seen crossing through the corona radiata as it passes from one hemisphere to the next. However, these trajectories are obscured by the DTI dODFs, with the corpus callosum tracts either being prematurely truncated or swept into the corticospinal tracts. It can also be seen from these images that the DSI dODF approximation is more sensitive at detecting multiple peaks (note the extent of the superior longitudinal fasciculus fibers indicated by the white arrows and the predominance of green lobes in the respective 3D dODF renderings). DTI is not capable of directly resolving crossing fibers; this scenario markedly affects tractography through complex regions such as those

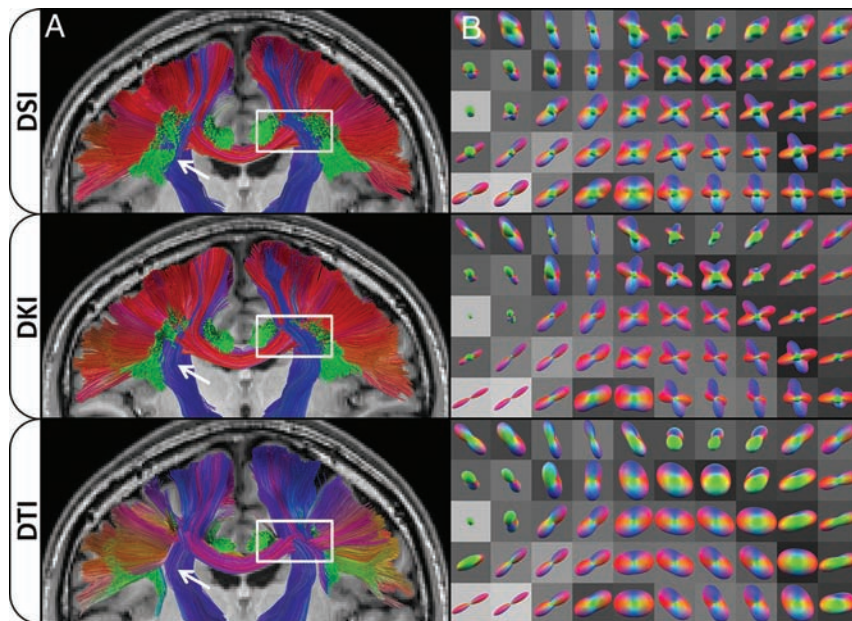


FIG 4. Effects of dODF reconstructions on WM tractography. Column A shows a coronal cross-section through the fiber tracts identified with DSI, DKI, and DTI, respectively, overlaid on the corresponding section from the MPRAGE image for anatomic reference. The color encoding is used to represent the overall displacement of the end points of each tract with 1 color being applied per tract, where red represents an overall left-right orientation, blue represents an overall inferior-superior orientation, and green represents an overall anterior-posterior orientation. DSI is the most sensitive technique for detecting fibers (*white arrows*); however, DSI and DKI are fairly similar in both the color, which illustrates the overall trajectory, and distribution of fibers identified. Column B shows selected dODFs with the same coloring scheme as the fibers in column A, overlaid on the corresponding FA image from the DTI scan. The region shown in column B is demarcated by the *white box* in the corresponding images in column A. DTI fibers are conspicuously affected in this region because the dODFs cannot detect crossing fibers; this feature causes fibers to prematurely terminate or meld anatomically distinct tracts. This cross-section was chosen to demonstrate interactions that occur among the corpus callosum, corona radiata, superior longitudinal fasciculus, and cingulum bundle and their effect on dODFs and subsequent tractography.

shown in Fig 4. Full-brain tractography results are compared in the On-line Video.

DISCUSSION

In this study, we have used DSI as a reference standard to assess the angular error in orientation estimates from DKI and DTI and quantified the intrasubject angular variability of WM fiber bundle orientation estimates from DTI, DKI, and DSI. We have focused primarily on comparing the estimated fiber orientations that the dODFs identify, because these are the inputs needed for constructing tractography. However, these are only approximations for the true fiber orientations, which are, in general, not known, even if the dODF is measured exactly.

A primary motivation for this study is to help assess the potential of DKI tractography for data obtained with clinical MR imaging scanners. By estimating both the diffusion and kurtosis tensors, DKI more fully characterizes diffusion in complex neural tissue than conventional DTI; this feature, theoretically, should improve tractography. Our experimental results support this proposition because both the angular and systematic errors are markedly lower for DKI (On-line Table and Fig 3). Moreover, tractography generated with DKI is qualitatively much more similar to that obtained with DSI than is DTI tractography (Fig 4 and On-line Video). Given that DKI, in comparison with DTI, also

provides several additional diffusion measures (eg, mean kurtosis) that are sensitive to neuropathologic changes associated with a variety of diseases,¹⁹⁻³² there are potentially compelling advantages to DKI vis-à-vis DTI.

Overall, the angular variability estimates are comparable for all 3 reconstructions in all ROIs, differing by, at most, 2.1° in the single-fiber ROI (On-line Table, “Single-fiber ROI”). However, DKI tends to have increased angular variability compared with both DTI and DSI in all ROIs except for the ROI with ≥ 3 crossing-fiber bundles. Although the precise origin of the increased angular variability of DKI is unclear, this could result from a trade-off between estimation error from incomplete q -space sampling distributions and subject motion. DTI, for example, requires the shortest acquisition time, which may result in the lowest contributions of subject motion to angular variability. DSI, on the other hand, uses a large number of diffusion-encoding vectors to characterize diffusion dynamics, which could have lower angular variability from the dODF reconstruction but an increased likelihood of subject motion. DKI is also known to be sensitive to reconstruction artifacts resulting from Gibbs ringing^{35,36} and noise bias,³⁷

though these are also expected to affect DSI.

To acquire high-quality, whole-brain DSI and DKI datasets for evaluation, we optimized our protocol for high SNR rather than a short acquisition time. Consequently, the total scan time used in this study was relatively long compared with typical clinical protocols. To improve scan efficiency, one or more of several different strategies may be used. For example, there has been a successful effort to reduce the q -space sampling burden of DSI, including decreasing the q -space sampling density by sampling fewer points,^{38,39} sampling only one-half of the q -space by assuming symmetry of the q -space data,^{40,41} or sampling only a quarter of the q -space by using compressed sensing.⁴² The acquisition time can also be reduced with simultaneous multisection EPI,⁴³⁻⁴⁷ while stronger diffusion-encoding gradients can be used to reduce the TE to improve the SNR.⁴⁷ Although DSI may show the largest improvement in acquisition time, these considerations are generally applicable to DKI as well. There may be an increase in the angular error and variability if SNR is reduced, as may occur with accelerated acquisition schemes,⁴⁵ or if sparse q -space sampling schemes are used.⁴⁰ Nevertheless, DKI may be presumed to have shorter typical scan times than DSI because DKI requires only the second and fourth cumulants of the dPDF,⁴⁸ while DSI uses the full dPDF with the inherent greater data-acquisition burden. A

valuable follow-up study would be to quantitatively investigate the differences in the orientation estimates by using protocols with acquisition times that are more suitable for routine clinical scanning.

A variety of alternative techniques can resolve the orientations of crossing-fiber bundles for tractography. Compared with several other dODF reconstructions, the kurtosis dODF has been shown to have a comparable or improved resolving power⁴⁹; however, numeric simulations indicate that the kurtosis dODF may sometimes have a greater angular error than other dODFs for larger fiber-crossing angles.^{16,49} Fiber bundle orientations can also be estimated from directional diffusional kurtosis estimates provided by DKI without estimating the dODF directly,⁵⁰ or the white matter fiber bundles may be modeled mathematically and used to estimate a model-dependent fiber orientation distribution function—for example, by using fiber ball imaging⁵¹ or constrained spherical deconvolution.^{52,53} Because none of these techniques are directly analogous to the dODF, they were not included in the present study. In addition, model-based approaches make detailed assumptions about the relationship between WM and the DWI signal that have yet to be fully validated. Nevertheless, the directional diffusional kurtosis approach has been shown to increase fiber detection through the corpus callosum,⁵⁰ and constrained spherical deconvolution can be highly sensitive to crossing fibers.^{18,54}

To summarize, in this study we acquired, from 3 healthy volunteers, a unique dataset with 6 full DSI and DKI acquisitions, to quantify dODF performance measures from DTI, DKI, and DSI. In general, DKI substantially decreases the error of dODF orientation estimates relative to DTI. Moreover, DKI enables the detection of crossing fibers, which results in pronounced improvement relative to DTI for tractography throughout regions with complex fiber bundle geometries.^{15,16,33,36} Indeed, our results indicate that the tractography obtained with DKI is qualitatively quite comparable with that for DSI, despite DKI sampling a much smaller portion of q -space. With enhanced tractography relative to DTI and shorter typical scan times than DSI, DKI-based tractography is potentially advantageous, particularly in clinical settings where time considerations are crucial. However, further study will be needed to more fully investigate the comparative utility of DKI-based tractography.

CONCLUSIONS

The higher order information provided by the kurtosis tensor enables DKI to directly resolve crossing fibers and improves the accuracy of DKI relative to DTI for tractography. Both DKI and DTI are capable of mapping the single predominant fiber bundle orientation, but the angular error of DTI deteriorates in regions with complex fiber orientations due to its theoretic limitation under the assumption of Gaussian diffusion. DSI, DKI, and DTI all have comparable angular variabilities; however, DKI has decreased angular error in the dODF fiber orientation estimates relative to DTI. Unlike DTI, DKI is thus able to generate white matter fiber tractography comparable with that of DSI, and due to its shorter typical scan time than DSI, DKI is potentially more suitable for a variety of clinical and research applications.

Disclosures: Li-Wei Kuo—RELATED: Grant: NHRI-BN-104-PP-06*; MOST-103-2221-E-400-001.* Joseph A. Helpert—RELATED: Grant: Litwin Foundation*; UNRELATED: Grants/Grants Pending: National Institutes of Health.* Jens H. Jensen—RELATED: Grant: Litwin Foundation.* Comments: I have partial salary support from this grant; UNRELATED: Patents (planned, pending or issued) and Royalties: US Patent 881706. Comments: I am a coinventor on a patent that covers one of the imaging methods investigated in this article (DKI). The patent is owned by my former employer (New York University), but I could be entitled to royalties at some point. To date, I have not received royalties from this patent. *Money paid to the institution.

REFERENCES

1. Romano A, D'Andrea G, Minniti G, et al. **Pre-surgical planning and MR-tractography utility in brain tumour resection.** *Eur Radiol* 2009;19:2798–808 CrossRef Medline
2. Mormina E, Longo M, Arrigo A, et al. **MRI tractography of cortico-spinal tract and arcuate fasciculus in high-grade gliomas performed by constrained spherical deconvolution: qualitative and quantitative analysis.** *AJNR Am J Neuroradiol* 2015;36:1853–58 CrossRef Medline
3. Lazar M. **Mapping brain anatomical connectivity using white matter tractography.** *NMR Biomed* 2010;23:821–35 CrossRef Medline
4. Tournier JD, Mori S, Leemans A. **Diffusion tensor imaging and beyond.** *Magn Reson Med* 2011;65:1532–56 CrossRef Medline
5. Farquharson S, Tournier JD, Calamante F, et al. **White matter fiber tractography: why we need to move beyond DTI.** *J Neurosurg* 2013;118:1367–77 CrossRef Medline
6. Tuch DS, Reese TG, Wiegell MR, et al. **Diffusion MRI of complex neural architecture.** *Neuron* 2003;40:885–95 CrossRef Medline
7. Tuch DS. **Q-ball imaging.** *Magn Reson Med* 2004;52:1358–72 CrossRef Medline
8. Wedeen VJ, Hagmann P, Tseng WY, et al. **Mapping complex tissue architecture with diffusion spectrum magnetic resonance imaging.** *Magn Reson Med* 2005;54:1377–86 CrossRef Medline
9. Wedeen VJ, Wang RP, Schmahmann JD, et al. **Diffusion spectrum magnetic resonance imaging (DSI) tractography of crossing fibers.** *Neuroimage* 2008;41:1267–77 CrossRef Medline
10. Basser PJ, Mattiello J, LeBihan D. **Estimation of the effective self-diffusion tensor from the NMR spin echo.** *J Magn Reson* 1994;103:247–54 CrossRef Medline
11. Basser PJ, Pierpaoli C. **Microstructural and physiological features of tissues elucidated by quantitative-diffusion-tensor-MRI.** *J Magn Reson B* 1996;111:209–19 CrossRef Medline
12. Basser PJ, Pajevic S, Pierpaoli C, et al. **In vivo fiber tractography using DT-MRI data.** *Magn Reson Med* 2000;44:625–32 Medline
13. Jensen JH, Helpert JA, Ramani A, et al. **Diffusional kurtosis imaging: the quantification of non-Gaussian water diffusion by means of magnetic resonance imaging.** *Magn Reson Med* 2005;53:1432–40 CrossRef Medline
14. Jensen JH, Helpert JA. **MRI quantification of non-Gaussian water diffusion by kurtosis analysis.** *NMR Biomed.* 2010;23:698–710 CrossRef Medline
15. Lazar M, Jensen JH, Xuan L, et al. **Estimation of the orientation distribution function from diffusional kurtosis imaging.** *Magn Reson Med* 2008;60:774–81 CrossRef Medline
16. Jensen JH, Helpert JA, Tabesh A. **Leading non-Gaussian corrections for diffusion orientation distribution function.** *NMR Biomed* 2014;27:202–11 CrossRef Medline
17. Hagmann P, Jonasson L, Maeder P, et al. **Understanding diffusion MR imaging techniques: from scalar diffusion-weighted imaging to diffusion tensor imaging and beyond.** *Radiographics* 2006;26(suppl 1):S205–23 CrossRef Medline
18. Jeurissen B, Leemans A, Tournier JD, et al. **Investigating the prevalence of complex fiber configurations in white matter tissue with diffusion magnetic resonance imaging.** *Hum Brain Mapp* 2013;34:2747–66 CrossRef Medline
19. Jensen JH, Falangola MF, Hu C, et al. **Preliminary observations of increased diffusional kurtosis in human brain following recent cerebral infarction.** *NMR Biomed* 2011;24:452–57 CrossRef Medline
20. Fung SH, Roccatagliata L, Gonzalez RG, et al. **MR diffusion imaging**

- in ischemic stroke. *Neuroimaging Clin N Am* 2011;21:345–77, xi CrossRef Medline
21. Hui ES, Fieremans E, Jensen JH, et al. **Stroke assessment with diffusional kurtosis imaging.** *Stroke* 2012;43:2968–73 CrossRef Medline
 22. Grinberg F, Ciobanu L, Farrher E, et al. **Diffusion kurtosis imaging and log-normal distribution function imaging enhance the visualization of lesions in animal stroke models.** *NMR Biomed* 2012;25:1295–304 CrossRef Medline
 23. Umesh Rudrapatna S, Wieloch T, Beirup K, et al. **Can diffusion kurtosis imaging improve the sensitivity and specificity of detecting microstructural alterations in brain tissue chronically after experimental stroke? Comparisons with diffusion tensor imaging and histology.** *Neuroimage* 2014;97:363–73 CrossRef Medline
 24. Falangola MF, Jensen JH, Tabesh A, et al. **Non-Gaussian diffusion MRI assessment of brain microstructure in mild cognitive impairment and Alzheimer's disease.** *Magn Reson Imaging* 2013;31:840–46 CrossRef Medline
 25. Benitez A, Fieremans E, Jensen JH, et al. **White matter tract integrity metrics reflect the vulnerability of late-myelinating tracts in Alzheimer's disease.** *Neuroimage Clin* 2013;9:64–71 CrossRef Medline
 26. Fieremans E, Benitez A, Jensen JH, et al. **Novel white matter tract integrity metrics sensitive to Alzheimer disease progression.** *AJNR Am J Neuroradiol* 2013;34:2105–12 CrossRef Medline
 27. Vanhoutte G, Pereson S, Delgado Y Palacios R, et al. **Diffusion kurtosis imaging to detect amyloidosis in an APP/PS1 mouse model for Alzheimer's disease.** *Magn Reson Med* 2013;69:1115–21 CrossRef Medline
 28. Gong NJ, Wong CS, Chan CC, et al. **Correlations between microstructural alterations and severity of cognitive deficiency in Alzheimer's disease and mild cognitive impairment: a diffusional kurtosis imaging study.** *Magn Reson Imaging* 2013;31:688–94 CrossRef Medline
 29. Raab P, Hattingen E, Franz K, et al. **Cerebral gliomas: diffusional kurtosis imaging analysis of microstructural differences.** *Radiology* 2010;254:876–81 CrossRef Medline
 30. Van Cauter S, Veraart J, Sijbers J, et al. **Gliomas: diffusion kurtosis MR imaging in grading.** *Radiology* 2012;263:492–501 CrossRef Medline
 31. Rosenkrantz AB, Sigmund EE, Johnson G, et al. **Prostate cancer: feasibility and preliminary experience of a diffusional kurtosis model for detection and assessment of aggressiveness of peripheral zone cancer.** *Radiology* 2012;264:126–35 CrossRef Medline
 32. Steven AJ, Zhuo J, Melhem ER. **Diffusion kurtosis imaging: an emerging technique for evaluating the microstructural environment of the brain.** *AJR Am J Roentgenol* 2014;202:W26–33 CrossRef Medline
 33. Glenn GR, Helpert JA, Tabesh A, et al. **Optimization of white matter fiber tractography with diffusional kurtosis imaging.** *NMR Biomed* 2015;28:1245–56 CrossRef Medline
 34. Tabesh A, Jensen JH, Ardekani BA, et al. **Estimation of tensors and tensor-derived measures in diffusional kurtosis imaging.** *Magn Reson Med* 2011;65:823–36 CrossRef Medline
 35. Veraart J, Fieremans E, Jolescu IO, et al. **Gibbs ringing in diffusion MRI.** *Magn Reson Med* 2015 Aug 10. [Epub ahead of print] CrossRef Medline
 36. Perrone D, Aelterman J, Pižurica A, et al. **The effect of Gibbs ringing artifacts on measures derived from diffusion MRI.** *Neuroimage* 2015;120:441–55 CrossRef Medline
 37. Glenn GR, Tabesh A, Jensen JH. **A simple noise correction scheme for diffusional kurtosis imaging.** *Magn Reson Imaging* 2015;33:124–33 CrossRef Medline
 38. Kuo LW, Chen JH, Wedeen VJ, et al. **Optimization of diffusion spectrum imaging and q-ball imaging on clinical MRI system.** *Neuroimage* 2008;41:7–18 CrossRef Medline
 39. Tefera GB, Zhou Y, Juneja V, et al. **Evaluation of fiber tracking from subsampled q-space data in diffusion spectrum imaging.** *Magn Reson Imaging* 2013;31:820–26 CrossRef Medline
 40. Kuo LW, Chiang WY, Yeh FC, et al. **Diffusion spectrum MRI using body-centered-cubic and half-sphere sampling schemes.** *J Neurosci Methods* 2013;212:143–55 CrossRef Medline
 41. Yeh CH, Cho KH, Lin HC, et al. **Reduced encoding diffusion spectrum imaging implemented with a bi-Gaussian model.** *IEEE Trans Med Imaging* 2008;27:1415–24 CrossRef Medline
 42. Menzel MI, Tan ET, Khare K, et al. **Accelerated diffusion spectrum imaging in the human brain using compressed sensing.** *Magn Reson Med* 2011;66:1226–33 CrossRef Medline
 43. Feinberg DA, Setsompop K. **Ultra-fast MRI of the human brain with simultaneous multi-slice imaging.** *J Magn Reson* 2013;229:90–100 CrossRef Medline
 44. Larkman DJ, Hajnal JV, Herlihy AH, et al. **Use of multicoil arrays for separation of signal from multiple slices simultaneously excited.** *J Magn Reson Imaging* 2001;13:313–17 Medline
 45. Setsompop K, Cohen-Adad J, Gagoski BA, et al. **Improving diffusion MRI using simultaneous multi-slice echo planar imaging.** *Neuroimage* 2012;63:569–80 CrossRef Medline
 46. Reese TG, Benner T, Wang R, et al. **Halving imaging time of whole brain diffusion spectrum imaging and diffusion tractography using simultaneous image refocusing in EPI.** *J Magn Reson Imaging* 2009;29:517–22 CrossRef Medline
 47. Setsompop K, Kimmlingen R, Eberlein E, et al. **Pushing the limits of in vivo diffusion MRI for the Human Connectome Project.** *Neuroimage* 2013;80:220–33 CrossRef Medline
 48. Kiselev VG. **The cumulant expansion: an overarching mathematical framework for understanding diffusion NMR.** In: Jones DK, ed. *Diffusion MRI: Theory, Methods and Applications*. New York: Oxford University Press; 2011:152–68
 49. Jensen JH, Helpert JA. **Resolving power for the diffusion orientation distribution function.** *Magn Reson Med* 2015 Oct 7. [Epub ahead of print] CrossRef Medline
 50. Neto Henriques R, Correia MM, Nunes RG, et al. **Exploring the 3D geometry of the diffusion kurtosis tensor: impact on the development of robust tractography procedures and novel biomarkers.** *Neuroimage* 2015;111:85–99 CrossRef Medline
 51. Jensen JH, Russell Glenn G, Helpert JA. **Fiber ball imaging.** *Neuroimage* 2016;124:824–33 CrossRef Medline
 52. Tournier JD, Calamante F, Connelly A. **Robust determination of the fibre orientation distribution in diffusion MRI: non-negativity constrained super-resolved spherical deconvolution.** *Neuroimage* 2007;35:1459–72 CrossRef Medline
 53. Tournier JD, Yeh CH, Calamante F, et al. **Resolving crossing fibres using constrained spherical deconvolution: validation using diffusion-weighted imaging phantom data.** *Neuroimage* 2008;15:617–25 CrossRef Medline
 54. Wilkins B, Lee N, Gajawelli N, et al. **Fiber estimation and tractography in diffusion MRI: development of simulated brain images and comparison of multi-fiber analysis methods at clinical b-values.** *Neuroimage* 2015;109:341–56 CrossRef Medline

Iron and Non-Iron-Related Characteristics of Multiple Sclerosis and Neuromyelitis Optica Lesions at 7T MRI

S. Chawla, I. Kister, J. Wuerfel, J.-C. Brisset, S. Liu, T. Sinnecker, P. Dusek, E.M. Haacke, F. Paul, and Y. Ge



ABSTRACT

BACKGROUND AND PURPOSE: Characterization of iron deposition associated with demyelinating lesions of multiple sclerosis and neuromyelitis optica has not been well studied. Our aim was to investigate the potential of ultra-high-field MR imaging to distinguish MS from neuromyelitis optica and to characterize tissue injury associated with iron pathology within lesions.

MATERIALS AND METHODS: Twenty-one patients with MS and 21 patients with neuromyelitis optica underwent 7T high-resolution 2D-gradient-echo-T2* and 3D-susceptibility-weighted imaging. An in-house-developed algorithm was used to reconstruct quantitative susceptibility mapping from SWI. Lesions were classified as “iron-laden” if they demonstrated hypointensity on gradient-echo-T2*-weighted images and/or SWI and hyperintensity on quantitative susceptibility mapping. Lesions were considered “non-iron-laden” if they were hyperintense on gradient-echo-T2* and isointense or hyperintense on quantitative susceptibility mapping.

RESULTS: Of 21 patients with MS, 19 (90.5%) demonstrated at least 1 quantitative susceptibility mapping–hyperintense lesion, and 11/21 (52.4%) had iron-laden lesions. No quantitative susceptibility mapping–hyperintense or iron-laden lesions were observed in any patients with neuromyelitis optica. Iron-laden and non-iron-laden lesions could each be further characterized into 2 distinct patterns based on lesion signal and morphology on gradient-echo-T2*/SWI and quantitative susceptibility mapping. In MS, most lesions ($n = 262$, 75.9% of all lesions) were hyperintense on gradient-echo T2* and isointense on quantitative susceptibility mapping (pattern A), while a small minority ($n = 26$, 7.5% of all lesions) were hyperintense on both gradient-echo-T2* and quantitative susceptibility mapping (pattern B). Iron-laden lesions ($n = 57$, 16.5% of all lesions) were further classified as nodular ($n = 22$, 6.4%, pattern C) or ringlike ($n = 35$, 10.1%, pattern D).

CONCLUSIONS: Ultra-high-field MR imaging may be useful in distinguishing MS from neuromyelitis optica. Different patterns related to iron and noniron pathology may provide in vivo insight into the pathophysiology of lesions in MS.

ABBREVIATIONS: GRE = gradient-echo; NMO = neuromyelitis optica; ppb = parts per billion; QSM = quantitative susceptibility mapping; R2* = transverse relaxation rate

Multiple sclerosis and neuromyelitis optica (NMO) are distinct inflammatory disorders of the CNS with different pathophysiology and approaches to treatment.¹ It is imperative to

differentiate MS from NMO before the commencement of treatment, but this task can be challenging in view of the overlap in clinical manifestations and findings on conventional neuroimaging.² Ultra-high-field imaging, by virtue of increased SNR, increased spatial resolution, and markedly improved venous and iron contrast within lesions,³ has the potential to shed light on the underlying pathophysiology of MS and NMO and help distinguish these 2 conditions. 7T MR imaging studies^{4,5} have shown that 60%–80% of MS lesions are traversed by a central venule, while only a small minority of NMO lesions contain a central

Received September 14, 2015; accepted after revision January 1, 2016.

From the Department of Radiology (S.C., J.-C.B., Y.G.), Center for Advanced Imaging Innovation and Research and Bernard and Irene Schwartz Center for Biomedical Imaging, and Department of Neurology (I.K.), New York University School of Medicine, New York, New York; Department of Radiology (S.C.), Perelman School of Medicine at the University of Pennsylvania, Philadelphia, Pennsylvania; Neuro-Cure (J.W., T.S., F.P.), Charité University Medicine, Berlin, Germany; Institute of Neuroradiology (J.W., P.D.), Universitätsmedizin Göttingen, Göttingen, Germany; Medical Image Analysis Center (J.W.), Basel, Switzerland; Department of Radiology (S.L., E.M.H.), Wayne State University School of Medicine, Detroit, Michigan; and Department of Neurology and Center of Clinical Neuroscience (P.D.), Charles University in Prague, First Faculty of Medicine and General University Hospital in Prague, Prague, Czech Republic.

This work was supported by a Cure Grant of the Guthy-Jackson Charitable Foundation and a Research Grant (RG 5187-A-3) of the National Multiple Sclerosis Society. Additionally, this work was also partly supported by grant numbers 5R01 NS029029, 3NS-029029–2051, and 5NS-076588 of the National Institutes of Health and a Research Grant (RG4707A1) of the National Multiple Sclerosis Society.

Paper previously presented in part as an oral presentation at: Annual Meeting and Exhibition of the International Society for Magnetic Resonance in Medicine, May 30 to June 5, 2015; Toronto, Ontario, Canada.

Please address correspondence to Yulin Ge, MD, New York University School of Medicine, 660 First Ave, Fourth Floor, New York, NY 10016; e-mail: yulin.ge@nyumc.org

Indicates open access to non-subscribers at www.ajnr.org

<http://dx.doi.org/10.3174/ajnr.A4729>

venule.^{5,6} Iron pathology may also be different in these 2 diseases: substantially higher iron content has been observed in deep GM regions of patients with MS than in those with NMO.⁷ In MS, iron accumulation in both acute and chronic phases of lesion development has been reported,⁸⁻¹² but to our knowledge, no studies have investigated whether iron is present in brain lesions of NMO.

The underlying pathology of MS lesions can be a dynamic process involving both demyelination and iron-related pathophysiology during the course of the disease.¹³⁻¹⁶ Compared with conventional T2* imaging or SWI, the recent development of quantitative susceptibility mapping (QSM) offers a useful tool for iron quantification by deconvolving the phase images.¹⁷⁻¹⁹ Both paramagnetic (eg, iron) and diamagnetic materials (eg, myelin) present low signal on conventional T2* or SWI; however, their susceptibility sources can be well-differentiated on QSM, with paramagnetic materials being high signal and diamagnetic material being low signal.¹⁹ Consequently, demyelination (diamagnetic myelin loss) and accompanying tissue water changes result in increased signal on T2* or SWI, but relatively low QSM values compared with iron deposition. Therefore, it is possible to make inferences about underlying tissue pathology associated with iron deposition and demyelination by using QSM combined with other multicontrast sequences. Moreover, QSM improves the detection and spatial distribution of subtle iron deposition that is not seen on conventional T2* imaging.²⁰ This improvement makes it possible to describe patterns of iron deposition within lesions (eg, nodular versus ringlike) on the basis of their 7T MR imaging findings, which have been rarely described in the literature.

The purpose of the present study was to investigate the potential of multicontrast ultra-high-field MR imaging to distinguish patients with MS from those with NMO and to characterize 7T MR imaging lesion patterns that are associated with iron and noniron pathology in these diseases.

MATERIALS AND METHODS

Subjects

This study was conducted at 2 academic MS referral centers: New York University Medical Center, New York, and Charité University, Berlin. Both sites received approval from local institutional review boards. Written informed consent was obtained from all patients before study entry. Inclusion criteria were a diagnosis of NMO spectrum disorders (International Panel for NMO Diagnosis Criteria²¹) or definite MS (McDonald Criteria²²). Twenty-one patients with NMO (mean age, 47.6 ± 14.2 years; all women, mean disease duration, 8.4 ± 6.7 years; range, 1–26.6 years) were enrolled in this study. All patients were NMO Ab seropositive by immunohistochemical or by enzyme-linked immunosorbent assays.

Twenty-one patients with MS were enrolled (mean age, 47.1 ± 10.3 years; 6 men/15 women; disease duration, 11.5 ± 5.9 years; range, 4–25 years). This group included patients with relapsing-remitting (*n* = 19) and secondary-progressive (*n* = 2) MS. There was no significant difference in mean age and mean disease duration between MS and NMO groups (*P* > .05).

Ultra-High-Field MR Imaging

All patients underwent ultra-high-field MR imaging by using identical whole-body 7T human MR imaging systems (Magne-

tom; Siemens, Erlangen, Germany) equipped with a 24-channel phased array coil (Nova Medical, Wilmington, Massachusetts). The imaging protocol included high-resolution axial 2D-gradient-echo (GRE) T2*-weighted imaging, high-resolution axial 3D-SWI, FLAIR, and sagittal T1-weighted 3D-MPRAGE sequences. Only supratentorial brain regions were covered while acquiring 2D-GRE-T2* and 3D-SWI to avoid susceptibility artifacts from air-tissue interfaces. None of the patients received intravenous contrast agent. The acquisition parameters were the following: for GRE-T2*-weighted imaging: TR/TE = 580/25 ms, flip angle = 35°, section thickness = 2 mm, FOV = 240 × 240 mm², voxel size = 0.2 × 0.2 mm²; for sagittal 3D sampling perfection with application-optimized contrasts by using different flip angle evolution sequence (SPACE; Siemens) FLAIR: TR/TE/ TI = 8000/380/2100 ms, isotropic voxel size = 1.0 × 1.0 × 1.0 mm³; and for sagittal T1-weighted 3D-MPRAGE: TR/TE/TI = 2000/2.92/1100 ms, isotropic voxel size = 1.0 × 1.0 × 1.0 mm³.

High-resolution flow-compensated 3D-SWI was acquired with the following parameters: TR/TE = 27/18 ms, flip angle = 18°, section thickness = 2 mm, FOV = 240 × 240 mm², base resolution = 1024, voxel size = 0.2 × 0.2 × 2 mm³, bandwidth = 110 Hz/px, acquisition time = 7 minutes and 49 seconds, and integrated parallel imaging technique factor = 2. Equivalent imaging parameters were used at both sites for all the sequences; however, at the German site, a voxel size of 0.5 × 0.5 × 2 mm³ was used for the 3D-SWI sequence.

Data Postprocessing

The source magnitude and phase images from each SWI scan were obtained and used to generate SWI venography. All phase images were reconstructed and corrected for field inhomogeneities with a Hanning high-pass filter (96 × 96) by using Signal Processing In NMR software (SPIN; MR Imaging Institute for Biomedical Research, Detroit, Michigan). The original magnitude image was multiplied by the phase mask 4 times to enhance the visibility of lesion and venous structures. Finally, SWI venograms were created by performing minimum intensity projection over 2 contiguous sections.

Susceptibility-weighted imaging and the mapping algorithm developed by Haacke et al²³ were used to reconstruct QSM maps from high-resolution 3D-SWI data. The postprocessing involved skull stripping to remove the artifacts caused by skull and brain tissue interface by using the FSL Brain Extraction Tool (<http://fsl.fmrib.ox.ac.uk/fsl/fslwiki/BET>), followed by phase unwrapping by using a Laplacian operator. To remove background field inhomogeneity, we applied a variable high-pass filter of 32 pixels and, finally, performed inverse filtering to generate QSM maps.

Data Analysis

All MR images were analyzed by using ImageJ software (National Institutes of Health, Bethesda, Maryland). All MS and NMO lesions were analyzed side by side on axial GRE-T2*, 3D-SWI, and QSM images. The following morphologic imaging characteristics were recorded for each lesion: 1) the largest cross-sectional diameter, 2) the presence of 1 or multiple central intralesional venules, 3) differential signal intensity within the lesions, and 4) the presence of a peripheral rim.

The lesion signals on GRE-T2*, SWI, and QSM and their putative correlations with underlying pathology are summarized in

Table 1: Proposed histopathologic interpretation based on signal-intensity changes on MR images

Tissue Content	Susceptibility Effect	Signal Intensity on GRE-T2*	Signal Intensity on SWI	Signal Intensity on QSM
Calcium	Diamagnetism	Hypointense	Hypointense	Hypointense
Myelin	Diamagnetism	Isointense	Isointense	Isointense
Variable degree of micronecrosis, edema, gliosis, demyelination, and macromolecules	Diamagnetism	Hyperintense	Isointense or hyperintense	Isointense
Extensive degree of demyelination	Loss of diamagnetism (paramagnetism)	Hyperintense	Isointense or hyperintense	Hyperintense
Iron	Paramagnetism	Hypointense	Hypointense	Hyperintense

Table 1. On the basis of this table, we analyzed lesion signal intensity on GRE-T2*, SWI, and QSM images. Pattern A lesions were hyperintense on GRE-T2*-weighted images, hyperintense or isointense on SWI, and isointense (inconspicuous) on QSM. Pattern B lesions were hyperintense on GRE-T2* and hyperintense on QSM. Pattern A and B lesions were considered non-iron-enriched. On the other hand, lesions that demonstrated hypointensity on GRE-T2* and/or SWI and hyperintensity on QSM were considered “iron-laden.” These lesions were further classified as nodular (pattern C) or exhibiting a peripheral rim (pattern D). We computed QSM values from all lesions that demonstrated hyperintensity on QSM by manually drawing ROIs. Because the use of a high-pass filter while reconstructing QSM maps may reduce the effective iron content from different tissue compartments, we believe this process might have resulted in underestimation of the QSM values computed from iron- and non-iron-laden lesions. To correct for the QSM values, we used a simulation algorithm²⁴ to obtain a scaling factor based on the size of the lesions. This size-dependent scaling factor was multiplied by the original QSM values to obtain corrected QSM values for each lesion.

Statistical Analysis

A χ^2 test was performed to look for differences in proportions of lesions with central venules in patients with MS and NMO. Receiver operating characteristic analyses were performed to estimate the sensitivity and specificity of selected subject-level conditions (at least 1 lesion with a central venule, at least 1 iron-laden lesion, at least 1 QSM hyperintense lesion) as criteria for classifying patients as testing positive for MS. Clopper-Pearson confidence intervals were derived for the sensitivity and specificity associated with each condition.

All lesions providing a QSM value were classified as having a central venule. Mixed-model analysis of variance was used to compare iron-laden from non-iron-laden lesions in terms of QSM while accounting for the correlation among QSM values derived for lesions in the same patient. The covariance structure was modeled by assuming QSM values to be independent when acquired from different patients and symmetrically correlated when acquired from lesions within the same patient, with the strength of correlation dependent on whether lesions were of the same type (eg, lesions were both classified as iron-laden). A probability value $< .05$ was considered significant. All data analysis was performed by using SPSS for Windows, Version 15.0 (IBM, Armonk, New York).

RESULTS

Distinguishing Patients with MS from Those with NMO

A total of 345 MS and 132 NMO discrete lesions were observed in supratentorial brain regions of 21 patients with MS and 21 with NMO. The mean cross-sectional diameter for MS lesions (5.44 ± 2.66 mm) was significantly larger than that of NMO lesions (3.19 ± 1.12 mm, $P < .001$). While MS lesions had variable shapes, most of the NMO lesions were round. Of 345 MS lesions, 227 (65.8%) were traversed by intralesional central venules, while only 8/132 (6.1%) NMO lesions showed this feature. All patients with MS had ≥ 1 lesion traversed by a central venule. On the other hand, only 4 patients with NMO had ≥ 1 lesion traversed by a central venule. The presence of at least 1 lesion with a central venule distinguished MS from NMO with a sensitivity of 100% (95% CI, 83.9%–100%) and a specificity of 71.4% (95% CI, 47.8%–88.7%).

MS lesions varied in signal intensity on GRE-T2*, SWI, and QSM. In the MS cohort, 19/21 (90.5%) patients had at least 1 hyperintense lesion on QSM, and this feature distinguished patients with MS from those with NMO with a sensitivity of 90.5% (95% CI, 69.6%–98.8%) and a specificity of 100% (95% CI, 83.9%–100%). Moreover, 11/21 (52.4%) patients had iron-laden lesions (see the “Data Analysis” section for a definition). In contrast, all NMO lesions demonstrated hyperintense signal relative to surrounding brain parenchyma on GRE-T2* weighted images and were isointense (inconspicuous) on QSM. Thus, none of the patients with NMO had any iron-rich lesions (Fig 1). The presence of at least 1 iron-laden lesion characteristic distinguished MS from NMO with a sensitivity of 52.4% (95% CI, 29.8%–74.3%) and a specificity of 100% (95% CI, 83.9%–100%).

Characterization of Different Lesion Patterns in MS

Examples of 4 morphologically distinct lesion patterns seen in MS are shown in Figs 2 and 3. Signal intensity on GRE-T2*, SWI, and QSM for different lesion patterns in MS is presented in Table 2. Most of the MS lesions ($n = 262$, 75.9%) were pattern A (all were hyperintense on GRE-T2*-weighted images and inconspicuous on QSM). On SWI, only 53/262 of these lesions demonstrated hyperintensity. Of 262 pattern A lesions, 148 (56.4%) were traversed by a central venule. A small number of lesions ($n = 26$, 7.5%) were pattern B (hyperintensity on both GRE-T2*-weighted images and QSM). On SWI, only 11/26 of these lesions demonstrated hyperintensity. Of the 26 pattern B lesions, 22 (84%) were traversed by a central venule.

Some lesions ($n = 57$, 16.5% of all MS lesions) demonstrated

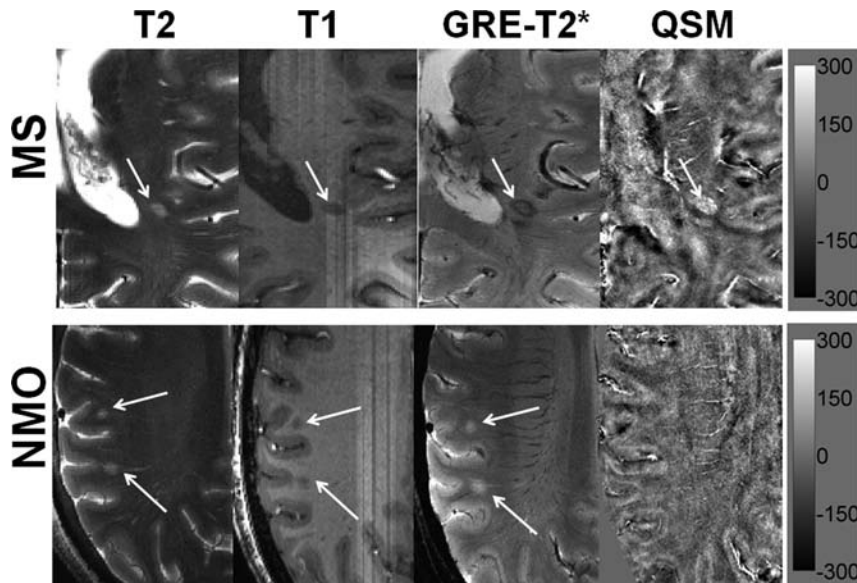


FIG 1. Distinguishing MS from NMO lesions. Axial T2-weighted image from a representative patient with MS demonstrating a hyperintense lesion (*black arrow*) traversed by an ill-defined central venule adjacent to the inferior horn of the lateral ventricles. The lesion appears hypointense on a corresponding T1-weighted MPRAGE image. The lesion shows a hypointense peripheral rim and an iso- to hypointense central core traversed by a well-defined venule on GRE-T2*-weighted image. This lesion is hyperintense on QSM. Hypointense signal intensity within the lesion on GRE-T2*-weighted image and hyperintensity on QSM suggest iron accumulation (*upper row*). An axial T2-weighted image from a representative NMO lesion reveals 2 round hyperintense lesions (*white arrows*) in the subcortical WM region. The lesions appear hypointense on T1-weighted and hyperintense on GRE-T2*-weighted images. However, these lesions are isointense and therefore inconspicuous on QSM (*lower row*). The scale bar is for the QSM image with units of parts per billion.

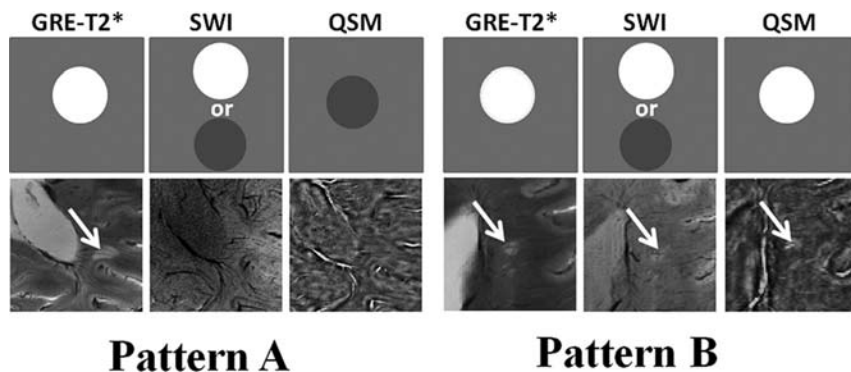


FIG 2. Non-iron-laden MS lesions (2 differential signal-intensity patterns). In the upper rows, schematic sketches are shown for pattern A and B lesions depicting ideal signal-intensity distribution on the GRE-T2*-weighted image, SWI, and QSM. In the lower rows, axial GRE-T2*-weighted image shows a hyperintense lesion traversed by a central intralesional venule. This lesion is located in close proximity to the posterior horn of the lateral ventricle. However, it appears isointense on SWI and QSM (pattern A) and hence inconspicuous on these images; this feature suggests a chronic inactive stage of lesion development comprising variable degrees of edema, demyelination, micronecrosis, and gliosis. Axial GRE-T2*-weighted image highlights a hyperintense lesion in the periventricular region traversed by a clearly distinguishable central venule. This lesion also appears hyperintense on corresponding SWI and QSM (pattern B), suggesting acute and extensive demyelinating (loss of diamagnetism) and inflammatory processes within the lesion.

hypointensity on GRE-T2*-weighted images and/or SWI, but hyperintensity on QSM; these lesions were presumed to be iron-laden. Seventeen of 57 iron-laden MS lesions demonstrated hyperintensity on GRE-T2*, and 40/57 were hypointense on GRE-T2* images. All except 1 (56/57) demonstrated hypointensity on SWI. All of these iron-laden QSM hyperintense lesions

were traversed by a central venule (57/57). Furthermore, of 288 non-iron-laden MS lesions, 240 (83.3%) had ill-defined and faint margins generally, while only 12 of 57 (21%) iron-laden MS lesions had ill-defined margins (Fig 4).

The iron-laden lesions had 2 geometrically distinct susceptibility patterns: nodular if they had solid signal intensity on QSM ($n = 22$, 6.4%; pattern C) or ringlike if they had a distinct peripheral rim on QSM ($n = 35$, 10.1%; pattern D). However, all of these iron-laden lesions demonstrated hypointensity on SWI. The mean QSM was significantly higher for iron-laden lesions than for non-iron-laden lesions ($P = .027$; Fig 5A). The least squares mean \pm standard error of the mean of QSM, adjusted for within-subject correlations, was 38.73 ± 4.81 parts per billion (ppb) for iron-laden lesions and 26.36 ± 2.2 ppb for lesions that were not iron-laden. Receiver operating characteristic analysis provided a threshold QSM value of 39.26 ppb to distinguish iron- from non-iron-laden lesions with a sensitivity of 70.2% and specificity of 57.7% (Fig 5B).

DISCUSSION

Early differentiation of NMO from MS is crucial for optimal management clinically.^{1,2} Although the recent availability of commercial testing for antibodies to Aquaporin-4 water has facilitated differentiation of NMO from MS, a correct diagnosis still remains challenging, particularly in those patients with NMO with multiple brain lesions on MR imaging. Many patients with NMO are still misdiagnosed with MS.²⁵ Hence, development of newer imaging biomarkers that can enable objective separation of these 2 diseases is warranted. Our analysis of the morphologic and structural features of MS and NMO supratentorial lesions by using multicontrast 7T MR imaging helps to further differentiate the 2 conditions and provides insight into lesional pathology in vivo. We found that iron deposition within a lesion (hyperintense signal on QSM) distinguished

patients with MS from those with NMO with a sensitivity of 90.5% (95% CI, 69.6%–98.8%) and a specificity of 100% (95% CI, 83.9%–100%). Analysis of the signal intensity of lesions on GRE, SWI, and QSM sequences allowed us to divide all lesions into 4 patterns, of which 2 were iron-enriched and 2 were non-iron-enriched (Table 2). A characteristic feature of MS was the

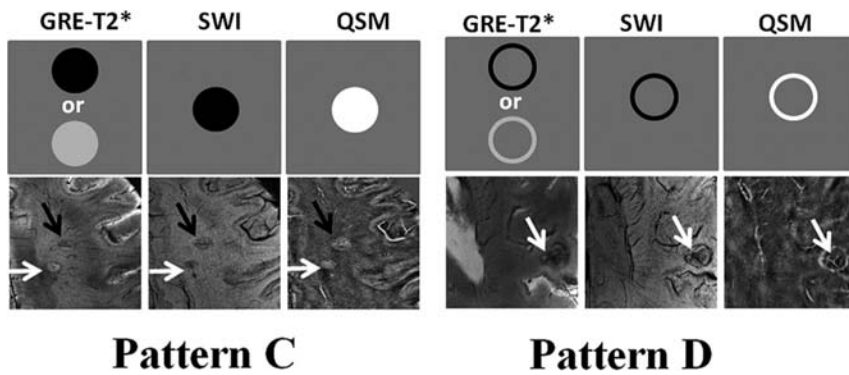


FIG 3. Iron-laden MS lesions (2 geometrically distinct susceptibility patterns). In the *upper rows*, schematic sketches are shown for pattern C and D lesions, depicting a characteristic signal-intensity distribution on GRE-T2*-weighted images, SWI, and QSM. In the *lower rows*, axial GRE-T2*-weighted image presents a pair of lesions in the subcortical WM region. While one lesion is nodular hyperintense (*white arrow*), another lesion is nodular hypointense (*black arrow*). Both lesions are crisscrossed by intralésional central venules and show hypointense signal on SWI but hyperintense signal on QSM, thus indicating iron deposition (pattern C). Axial GRE-T2*-weighted image reveals a lesion (*white arrow*) with a hypointense peripheral rim having a central venous structure in the subcortical WM region. The lesion also shows a hypointense rim on the corresponding SWI and a hyperintense rim on the corresponding QSM, suggesting a ringlike lesion with iron deposition only at the edges (pattern D).

Table 2: Signal intensity on GRE-T2*, SWI, and QSM for different lesion patterns in MS

Lesion Pattern	Signal Intensity on GRE-T2*	Signal Intensity on SWI	Signal Intensity on QSM
A (n = 262)	Hyperintense	Isointense or hyperintense	Isointense
B (n = 26)	Hyperintense	Isointense or hyperintense	Hyperintense
C (n = 22)	Hyperintense or hypointense	Hypointense	Hyperintense
D (n = 35)	Hyperintense or hypointense	Hypointense	Hyperintense

variety of lesion types observed: All patients with MS had lesions of >1 type, though most lesions were of pattern A, while all NMO lesions were of 1 type only (pattern A).

Using phase imaging and transverse relaxation rate (R2*) mapping on high-field MR imaging, prior studies have assessed the iron content of MS lesions qualitatively^{11,12,26} and quantitatively.²⁷ However, many confounding factors are associated with these imaging techniques, including dependence on orientation and distribution of susceptibility sources that may influence the heterogeneity of phase and R2* and thereby render these images less reliable and quantifiable. QSM, on the other hand, provides more robust and quantitative evaluation of magnetic susceptibility sources such as iron, myelin, and calcium that are present in normal and diseased brain tissues.²⁸ Moreover, susceptibility is a physical quantity that is independent of imaging parameters and has the potential to distinguish and quantify different susceptible tissues.²⁹ In the present study, a recently²³ described susceptibility-weighted imaging and mapping method was used to reconstruct QSM from 3D-SWI, providing susceptibility values from different tissue compartments with high accuracy.³⁰

Our findings on 7T MR imaging that not all MS lesions have iron deposition are consistent with the earlier, lower field studies.⁹ Iron deposition may vary among individual lesions on the basis of their age and inflammatory status. We observed 4 morphologically dis-

tinct patterns of MS lesions, 2 of which were considered iron-enriched. Most non-iron-enriched MS lesions were hyperintense on GRE-T2*-weighted images and isointense and thus inconspicuous on QSM (pattern A). This pattern could be plausibly attributed to varying degrees of demyelination, edema, micronecrosis, and gliosis in chronic inactive lesions. A minority of non-iron-containing lesions demonstrated hyperintensity on both GRE-T2* and QSM images (pattern B), suggesting more acute and extensive demyelination (loss of diamagnetism, but less magnetic susceptibility effect than iron deposition) and inflammation compared with pattern A lesions. Because no tissue specimens were available to perform histopathologic/histochemical analysis from our patients, our interpretation of the imaging features was based on the prior correlative imaging and histopathologic studies.^{11,12} More work is needed to ascertain the pathologic significance of susceptibility changes.

Iron-laden MS lesions with hyperintensities on QSM were of 2 patterns: iron either deposited in the center core (nodular iron-laden lesions, pattern C) or in a ringlike fashion at the lesion edge (pattern D). Previous histochemical studies showed that iron deposits were present in a subset of chronic, demyelinating active MS lesions.^{11,12} The molecular pathways for iron accumulation in MS lesions are still not fully understood; however, several possible biologic mechanisms, such as iron-rich oligodendrocyte debris, iron-sequestered microglia or macrophages, and products of local microhemorrhages following venule wall damage may contribute to iron deposition.^{14,15} On 3T MR imaging, Chen et al¹⁸ observed lower QSM values from acute enhancing lesions (small susceptibilities) and increased QSM values from nonenhancing lesions (high susceptibilities). This observation suggests that lesion susceptibility measured by QSM is a useful biomarker for monitoring MS disease activities. Perhaps, the preponderance of non-iron-containing lesions in MS in our study is because they were imaged long after their formative stage.

Most iron-laden lesions in our study were ringlike. Histopathologically, it has been observed that maximum accumulation of iron occurs at the edges of classic, reactive, slowly expanding chronically existing MS lesions.¹¹ In these reactive lesions, demyelination and oligodendrocyte destruction occur in a zone of variable size at the lesion border. Thus, iron-containing myelin and oligodendrocytes gradually decreased from the perilesional regions toward the lesion centers. Additionally, iron-containing microglia and macrophages that are mainly located at the edge of chronic reactive lesions undergo microglial dystrophy leading to a variable degree of iron deposition within the different compartments of the MS lesions.^{11,12} Moreover, iron-laden MS lesions were well-circumscribed with well-defined margins while non-iron-laden lesions had poorly defined margins and were generally larger. The reason for this observation is not clearly understood; however, it might be because of accumulation of

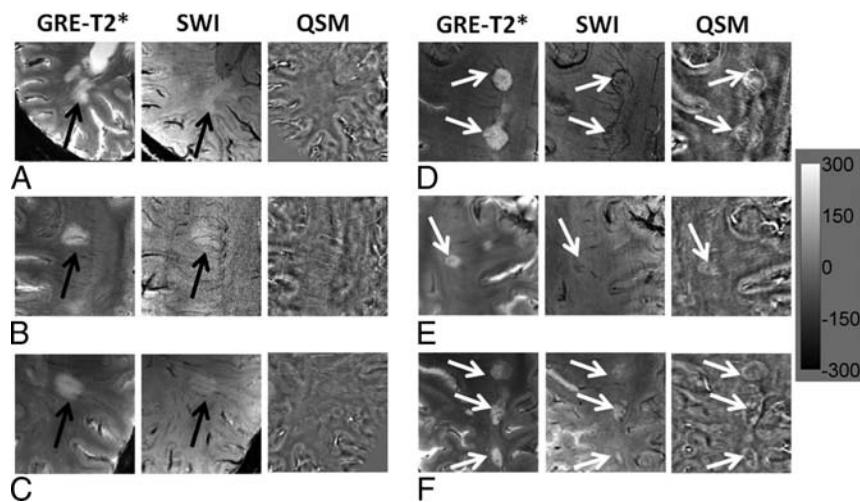


FIG 4. Large MS lesions with well-defined and ill-defined margins. Axial GRE-T2*-weighted images (A–C) demonstrate large but faint hyperintense lesions (*black arrow*) without any definite margins. These lesions appear hyperintense on SWI (*black arrows*) and isointense on QSM; this appearance indicates the absence of iron deposits (*left panel*). On the other hand, axial GRE-T2*-weighted images (D–F) also show large hyperintense lesions (*white arrows*) with well-defined margins. These lesions are visible as hypointense structures on SWI and hyperintense on QSM; this appearance is highly suggestive of intralésional iron deposits (*right panel*). The scale bar is for the QSM image with units of parts per billion.

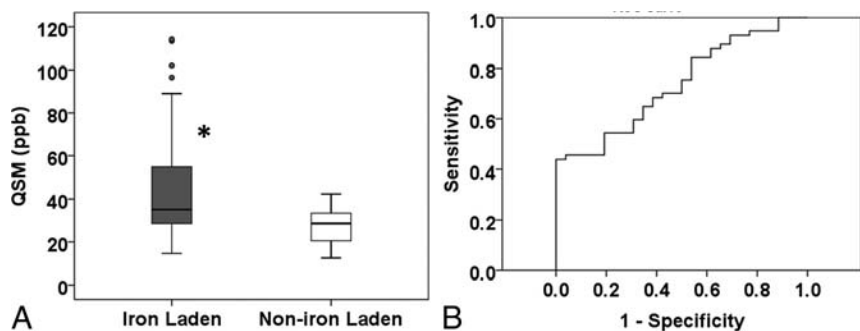


FIG 5. QSM values from iron-laden and non-iron-laden lesions. Box-and-whisker plots (A) show the distribution of mean QSM (parts per billion) from iron-laden and non-iron-laden lesions. Iron-laden lesions (patterns C and D) had significantly higher QSM than non-iron-laden QSM hyperintense lesions (pattern B). Boxes represent the median, 25th percentile, and 75th percentile. The *asterisk* indicates a significant difference ($P = .001$). *Solid circles* represent the outliers. The receiver operating characteristic curve shows an area under the curve of 0.74. The receiver operating characteristic analysis (B) provides a sensitivity of 70.2% and a specificity of 57.7% in distinguishing these 2 types of lesions at a threshold QSM value of 30.26 ppb.

iron-enriched microphages or microglia cells in the iron-laden lesions or more activity associated with these lesions.

An interesting observation to emerge from our study is that the probability of finding a small venule in the center of lesions depends on the lesion pattern. All of the iron-laden MS lesions, 100% (patterns C and D), and 84% of presumed extensive demyelinating lesions (pattern B) were traversed by central venule. However, only 56% of non-iron-containing pattern A lesions had a central venule. We hypothesize that iron-containing and extensively demyelinating lesions are chronologically “younger” than the non-iron-containing pattern A lesions and, therefore, are more likely to indicate the presence of central vein. The pattern A lesions are more chronic, and a central vein may become occluded at this stage.

Only a few studies have reported QSM values from MS lesions and even fewer used 7T MR imaging combining different signal patterns on various sequences. In a 3T MR imaging study, Chen et

al¹⁸ reported QSM values from MS lesions at various evolutionary stages. Investigators observed QSM values of ~38 ppb from early-to-intermediary-aged nonenhanced iron-laden MS lesions. Slightly lower QSM values (~30 ppb) were observed from iron-laden lesions in another study.¹⁹ In close agreement with these prior studies,^{18,19} the mean QSM value in iron-laden lesions in our study was ~44 ppb. QSM increases are seen in demyelination and iron deposition, but because iron is strongly paramagnetic, the QSM values due to iron deposition were higher than those due to loss of myelin. The susceptibility of myelin is only slightly more diamagnetic than that of CSF; therefore, a voxel completely packed with WM fibers would be expected to undergo a maximal susceptibility increase at complete demyelination (loss of diamagnetism). Therefore, susceptibility increases beyond those observed for CSF derive from sources other than demyelination.²⁸ Because ferritin, hemosiderin, and breakdown products of hemorrhage make up for a substantially high susceptibility effect, we hypothesize that higher QSM values from pattern C and D lesions further support the notion that the susceptibility of these lesions is caused predominantly by their iron content. On the other hand, pattern B lesions that also showed hyperintense signal on QSM were presumably associated with extensive demyelination, but not iron deposition, which explains why QSM values of pattern B lesions are lower than those of patterns C and D as indicated by the receiver operating characteristic analysis (Fig 5).

Another interesting observation was that only 70% of the iron-laden lesions demonstrated hypointense signal on GRE-T2*-weighted images, whereas 98% of the lesions showed hypointensity on SWI, despite similar section thickness and in-plane resolution for both of these images. In accordance with previous studies,^{31,32} our observation suggests that SWI is more sensitive to susceptibility effects than GRE-T2*-weighted images, probably because SWI combines information both from phase and magnitude images to ascertain the local susceptibility changes among neighboring tissues, whereas susceptibility contrast on GRE-T2* is mainly dependent on a combination of spin-spin relaxation (T2) and magnetic field inhomogeneity. We believe that inclusion of phase information renders SWI more sensitive to susceptibility effects than GRE-T2* images.

There were some limitations to the current study. Most of the patients with MS had a diagnosis of relapsing-remitting MS. To

obtain a more comprehensive understanding of the evolution of MS lesions by using multicontrast imaging, future studies would need to include patients with different types of MS (clinically isolated syndrome, secondary- and primary-progressive MS). Our patients with NMO had similar kinds of “nonspecific” subcortical lesions. A number of other kinds of NMO-specific lesions have been described³³ but were not seen in our series. Another limitation of the current study was that R2* or T2* mapping was not performed; these sequences may provide additional quantitative information for the characterization of NMO and MS lesions.

CONCLUSIONS

Four morphologically different patterns were observed for MS lesions, while NMO lesions exhibited only 1 pattern. Approximately half of patients with MS (52.4%) had at least 1 iron-laden lesion, but none of the patients with NMO had iron-enriched lesions. Our study suggests that QSM, combined with other imaging sequences at 7T, helps further differentiate MS from NMO and provides insight into lesional pathogenesis and iron metabolism in these 2 autoimmune disorders of the central nervous system.

ACKNOWLEDGMENTS

We thank Dr James Babb for his help with data analysis.

Disclosures: Ilya Kister—RELATED: Grant: Guthy-Jackson Charitable Foundation*; UNRELATED: Consultancy: Biogen-Idec; Grants/Grants Pending: National Multiple Sclerosis Society,* Biogen-Idec,* Serono,* Novartis.* Jens Wuerfel—UNRELATED: Board Membership: Novartis Advisory Board; Employment: CEO, MIAC AG; Payment for Lectures (including service on Speakers Bureaus): Novartis, Biogen-Idec, Bayer, Teva; Payment for Development of Educational Presentations: Novartis. Saifeng Liu—RELATED: Grant: Canadian Institutes of Health Research,* Heart and Stroke Foundation of Canada,* Synchrontron Medical Imaging Team grant CIF 99472.* Tim Sinnecker—RELATED: Grant: German Research Foundation,* German Competence Network Multiple Sclerosis,* Guthy-Jackson Charitable Foundation*; UNRELATED: Employment: Charité University Berlin; Asklepios Fachklinikum Teupitz; Travel/Accommodations/Meeting Expenses Unrelated to Activities Listed: Bayer, Novartis, Genzyme, Teva. E. Mark Haacke—UNRELATED: Patents (planned, pending or issued) and Royalties: MR Innovations, Comments: patents on SWI and susceptibility-weighted imaging and mapping. Friedemann Paul—RELATED: Grant: Guthy-Jackson Charitable Foundation*; UNRELATED: Board Membership: Novartis, Chugai Pharmaceutical, Genzyme, Alexion Pharmaceuticals, MedImmune, Comments: various steering committees and advisory boards; Consultancy: Novartis, Biogen-Idec, Roche, Teva, Alexion Pharmaceuticals, MedImmune; Grants/Grants Pending: Guthy-Jackson Charitable Foundation,* National Multiple Sclerosis Society*; Payment for Manuscript Preparation: Bayer, Genzyme. Yulin Ge—RELATED: Grant: National Institutes of Health,* National Multiple Sclerosis Society,* Comments: This work was also partly supported by grant numbers: 5R01 NS029029, 3NS-029029–20S1, and 5NS-076588 of the National Institutes of Health and a Research Grant (RG4707A1) of the National Multiple Sclerosis Society. *Money paid to the institution.

REFERENCES

- Lennon VA, Wingerchuk DM, Kryzer TJ, et al. A serum autoantibody marker of neuromyelitis optica: distinction from multiple sclerosis. *Lancet* 2004;364:2106–12 CrossRef Medline
- Cheng C, Jiang Y, Chen X, et al. Clinical, radiographic characteristics and immunomodulating changes in neuromyelitis optica with extensive brain lesions. *BMC Neurol* 2013;13:72 CrossRef Medline
- Sinnecker T, Mittelstaedt P, Dörr J, et al. Multiple sclerosis lesions and irreversible brain tissue damage: a comparative ultrahigh-field strength magnetic resonance imaging study. *Arch Neurol* 2012;69:739–45 CrossRef Medline
- Ge Y, Zohrabian VM, Grossman RI. Seven-Tesla magnetic resonance imaging: new vision of microvascular abnormalities in multiple sclerosis. *Arch Neurol* 2008;65:812–16 Medline
- Sinnecker T, Dörr J, Pfueller CF, et al. Distinct lesion morphology at 7-T MRI differentiates neuromyelitis optica from multiple sclerosis. *Neurology* 2012;79:708–14 CrossRef Medline
- Kister I, Herbert J, Zhou Y, et al. Ultrahigh-field MR (7 T) imaging of brain lesions in neuromyelitis optica. *Mult Scler Int* 2013;2013:398259 CrossRef Medline
- Chen X, Zeng C, Luo T, et al. Iron deposition of the deep grey matter in patients with multiple sclerosis and neuromyelitis optica: a control quantitative study by 3D-enhanced susceptibility-weighted angiography (ESWAN). *Eur J Radiol* 2012;81:e633–39 CrossRef Medline
- LeVine SM, Chakrabarty A. The role of iron in the pathogenesis of experimental allergic encephalomyelitis and multiple sclerosis. *Ann N Y Acad Sci* 2004;1012:252–66 CrossRef Medline
- Haacke EM, Makki M, Ge Y, et al. Characterizing iron deposition in multiple sclerosis lesions using susceptibility weighted imaging. *J Magn Reson Imaging* 2009;29:537–44 CrossRef Medline
- Wuerfel J, Sinnecker T, Ringelstein EB, et al. Lesion morphology at 7 Tesla MRI differentiates Susac syndrome from multiple sclerosis. *Mult Scler* 2012;18:1592–99 CrossRef Medline
- Bagnato F, Hametner S, Yao B, et al. Tracking iron in multiple sclerosis: a combined imaging and histopathological study at 7 Tesla. *Brain* 2011;134:3602–15 CrossRef Medline
- Mehta V, Pei W, Yang G, et al. Iron is a sensitive biomarker for inflammation in multiple sclerosis lesions. *PLoS One* 2013;8:e57573 CrossRef Medline
- Hogarth P. Neurodegeneration with brain iron accumulation: diagnosis and management. *J Mov Disord* 2015;8:1–13 CrossRef Medline
- Williams R, Buchheit CL, Berman NE, et al. Pathogenic implications of iron accumulation in multiple sclerosis. *J Neurochem* 2012;120:7–25 CrossRef Medline
- Adams CW. Perivascular iron deposition and other vascular damage in multiple sclerosis. *J Neurol Neurosurg Psychiatry* 1988;51(2):260–65 CrossRef Medline
- Stankiewicz JM. Iron and multiple sclerosis. *Neurobiol Aging* 2014;35(suppl 2):S51–58 CrossRef Medline
- Li X, Harrison DM, Liu H, et al. Magnetic susceptibility contrast variations in multiple sclerosis lesions. *J Magn Reson Imaging* 2016;43:463–73 CrossRef Medline
- Chen W, Gauthier SA, Gupta A, et al. Quantitative susceptibility mapping of multiple sclerosis lesions at various ages. *Radiology* 2014;271:183–92 CrossRef Medline
- Wisniewski C, Ramanan S, Olesik J, et al. Quantitative susceptibility mapping (QSM) of white matter multiple sclerosis lesions: interpreting positive susceptibility and the presence of iron. *Magn Reson Med* 2015;74:564–70 CrossRef Medline
- Eskreis-Winkler S, Deh K, Gupta A, et al. Multiple sclerosis lesion geometry in quantitative susceptibility mapping (QSM) and phase imaging. *J Magn Reson Imaging* 2015;42:224–29 CrossRef Medline
- Wingerchuk DM, Weinshenker BG. Neuromyelitis optica: clinical predictors of a relapsing course and survival. *Neurology* 2003;60:848–53 CrossRef Medline
- Polman CH, Reingold SC, Banwell B, et al. Diagnostic criteria for multiple sclerosis: 2010 revisions to the McDonald criteria. *Ann Neurol* 2011;69:292–302 CrossRef Medline
- Haacke EM, Tang J, Neelavalli J, et al. Susceptibility mapping as a means to visualize veins and quantify oxygen saturation. *J Magn Reson Imaging* 2010;32:663–76 CrossRef Medline
- Liu S, Neelavalli J, Cheng YC, et al. Quantitative susceptibility mapping of small objects using volume constraints. *Magn Reson Med* 2013;69:716–23 CrossRef Medline
- Mealy MA, Wingerchuk DM, Greenberg BM, et al. Epidemiology of neuromyelitis optica in the United States: a multicenter analysis. *Arch Neurol* 2012;69:1176–80 CrossRef Medline
- Pitt D, Boster A, Pei W, et al. Imaging cortical lesions in multiple sclerosis with ultra-high-field magnetic resonance imaging. *Arch Neurol* 2010;67:812–18 CrossRef Medline
- Walsh AJ, Lebel RM, Eissa A, et al. Multiple sclerosis: validation of

- MR imaging for quantification and detection of iron. *Radiology* 2013;267:531–42 CrossRef Medline
28. Stüber C, Morawski M, Schäfer A, et al. **Myelin and iron concentration in the human brain: a quantitative study of MRI contrast.** *Neuroimage* 2014;93(pt 1):95–106 CrossRef Medline
29. Liu T, Surapaneni K, Lou M, et al. **Cerebral microbleeds: burden assessment by using quantitative susceptibility mapping.** *Radiology* 2012;262:269–78 CrossRef Medline
30. Doshi H, Wiseman N, Liu J, et al. **Cerebral hemodynamic changes of mild traumatic brain injury at the acute stage.** *PLoS One* 2015;10:e0118061 CrossRef Medline
31. Löbel U, Sedlacik J, Sabin ND, et al. **Three-dimensional susceptibility-weighted imaging and two-dimensional T2*-weighted gradient-echo imaging of intratumoral hemorrhages in pediatric diffuse intrinsic pontine glioma.** *Neuroradiology* 2010;52:1167–77 CrossRef Medline
32. Soman S, Holdsworth SJ, Barnes PD, et al. **Improved T2* imaging without increase in scan time: SWI processing of 2D gradient echo.** *AJNR Am J Neuroradiol* 2013;34:2092–97 CrossRef Medline
33. Cabrera-Gomez JA, Kister I. **Conventional brain MRI in neuromyelitis optica.** *Eur J Neurol* 2012;19:812–19 CrossRef Medline

Assessment of Collateral Status by Dynamic CT Angiography in Acute MCA Stroke: Timing of Acquisition and Relationship with Final Infarct Volume

I.R. van den Wijngaard, G. Holswilder, M.J.H. Wermer, J. Boiten, A. Algra, D.W.J. Dippel, J.W. Dankbaar, B.K. Velthuis, A.M.M. Boers, C.B.L.M. Majoie, and M.A.A. van Walderveen



ABSTRACT

BACKGROUND AND PURPOSE: Dynamic CTA is a promising technique for visualization of collateral filling in patients with acute ischemic stroke. Our aim was to describe collateral filling with dynamic CTA and assess the relationship with infarct volume at follow-up.

MATERIALS AND METHODS: We selected patients with acute ischemic stroke due to proximal MCA occlusion. Patients underwent NCCT, single-phase CTA, and whole-brain CT perfusion/dynamic CTA within 9 hours after stroke onset. For each patient, a detailed assessment of the extent and velocity of arterial filling was obtained. Poor radiologic outcome was defined as an infarct volume of ≥ 70 mL. The association between collateral score and follow-up infarct volume was analyzed with Poisson regression.

RESULTS: Sixty-one patients with a mean age of 67 years were included. For all patients combined, the interval that contained the peak of arterial filling in both hemispheres was between 11 and 21 seconds after ICA contrast entry. Poor collateral status as assessed with dynamic CTA was more strongly associated with infarct volume of ≥ 70 mL (risk ratio, 1.9; 95% CI, 1.3–2.9) than with single-phase CTA (risk ratio, 1.4; 95% CI, 0.8–2.5). Four subgroups (good-versus-poor and fast-versus-slow collaterals) were analyzed separately; the results showed that compared with good and fast collaterals, a similar risk ratio was found for patients with good-but-slow collaterals (risk ratio, 1.3; 95% CI, 0.7–2.4).

CONCLUSIONS: Dynamic CTA provides a more detailed assessment of collaterals than single-phase CTA and has a stronger relationship with infarct volume at follow-up. The extent of collateral flow is more important in determining tissue fate than the velocity of collateral filling. The timing of dynamic CTA acquisition in relation to intravenous contrast administration is critical for the optimal assessment of the extent of collaterals.

ABBREVIATION: CS = collateral score

Collateral vessel status is an important predictor of final infarct size and clinical outcome in patients with a stroke due to acute proximal anterior circulation occlusions.^{1,2} Leptomenigeal collaterals can provide a detour for blood to reach the ischemic territory of an occluded artery, thereby sustaining tissue at

risk for a longer time.^{1,3,4} DSA is considered the criterion standard for visualization of the collateral circulation. However, DSA is currently reserved for part of the thrombectomy procedures and has no role in the diagnostic work-up of patients with acute ischemic stroke.

In clinical practice, imaging of collaterals is often performed with single-phase CTA. Single-phase CTA visualizes the cerebral circulation at only a single moment in time. The information captured in this snapshot depends on the timing of the CTA acquisition after contrast injection, which may lead to inaccurate estimation of the collateral circulation.^{1,5,6} Dynamic CTA is increasingly investigated for the visualization of collaterals in acute

Received September 17, 2015; accepted after revision January 4, 2016.

From the Departments of Radiology (I.R.v.d.W., G.H., M.A.A.v.W.), Neurology (M.J.H.W.), and Clinical Epidemiology (A.A.), Leiden University Medical Center, Leiden, the Netherlands; Department of Neurology (I.R.v.d.W., J.B.), Medical Center Haaglanden, the Hague, the Netherlands; Department of Neurology and Neurosurgery (A.A.), Brain Center Rudolf Magnus, and Department of Radiology (J.W.D., B.K.V.), University Medical Center Utrecht, Utrecht, the Netherlands; Department of Neurology (D.W.J.D.), Erasmus University Medical Center, Rotterdam, the Netherlands; and Departments of Radiology (A.M.M.B., C.B.L.M.M.) and Biomedical Engineering and Physics (A.M.M.B.), Academic Medical Center, Amsterdam, the Netherlands.

DUST was supported by the Dutch Heart Foundation (2008T034) and the NutsOhra Foundation (0903–012). The MR CLEAN trial was supported by the Dutch Heart Foundation and by unrestricted grants from AngioCare, Covidien/ev3, Medac/Lamepro, and Penumbra.

I.R. van den Wijngaard and G. Holswilder contributed equally to this work.

Please address correspondence to Ido van den Wijngaard, MD, Department of Radiology, Leiden University Medical Center, PO Box 9600, 2300 RC Leiden, the Netherlands; e-mail: wijngaardido@gmail.com

Indicates open access to non-subscribers at www.ajnr.org

Indicates article with supplemental on-line appendix and tables.

Indicates article with supplemental on-line photos.

<http://dx.doi.org/10.3174/ajnr.A4746>

ischemic stroke.⁷⁻⁹ Dynamic CTA can be derived from CT perfusion datasets and provides time-resolved images of the arterial, parenchymal, and venous phases. Not only the extent but also the velocity of collateral filling can be evaluated with dynamic CTA.

The aim of this study was to assess dynamic CTA as a method for imaging the collateral circulation in patients with acute ischemic stroke. We devised a grading system that gives information on the extent and velocity of pial arterial filling in a time-resolved manner. We compared this new method with collateral assessment on single-phase CTA in relation to infarct volume at follow-up.

MATERIALS AND METHODS

Study Population

Patients from the Leiden University Medical Center were selected from the Dutch Acute Stroke Study (DUST) and the Multicenter Randomized CLinical trial of Endovascular treatment for Acute ischemic stroke in the Netherlands (MR CLEAN). Protocol details of these clinical studies with inclusion and exclusion criteria have been published before.^{10,11} Patients with an acute ischemic stroke with a proximal MCA occlusion (M1 or M2 segments) were included, with or without occlusion of the ICA. All patients underwent multimodal CT imaging including NCCT, single-phase CTA, and whole-brain CT perfusion/dynamic CTA at presentation. Adult patients were included up to 9 hours after symptom onset in DUST. For the MR CLEAN trial, initiation of endovascular treatment had to be possible within 6 hours after symptom onset. Clinical data were retrieved from the study data bases. Informed consent was obtained from patients who participated in these clinical studies.

CT Image Acquisition

For CT image acquisition, a 320-section multidetector CT scanner, Aquilion ONE (Toshiba Medical Systems, Tokyo, Japan) was used, resulting in a whole-brain CTP coverage from 320-detector arrays of 0.5 mm. All patients underwent a standard scanning protocol at presentation, including NCCT, single-phase CTA from the aortic arch to the vertex, and whole-brain CT perfusion/dynamic CTA. For the whole-brain CT perfusion/dynamic CTA, 19 volumes were obtained during 1 minute. (See the On-line Appendix for more details about image acquisition.)

Image Analysis

Radiologic data were independently assessed by a trained neuro-radiologist and a trained neurologist, who were given information regarding the clinical symptoms only. At admission, early ischemic changes on NCCT were evaluated with the ASPECTS.¹² To evaluate the extent of arterial occlusion, we applied the clot burden score.¹³

NCCT was performed at 1- to 5-day follow-up for assessment of infarct volume (or earlier in case of severe clinical deterioration, ie, ≥ 4 -point increase in the NIHSS compared with baseline). Infarct volumes at follow-up were independently assessed and provided to us by the DUST and MR CLEAN investigators.¹⁴ Poor radiologic outcome was defined as an infarct volume of ≥ 70 mL.

Collateral Score

On single-phase CTA, the collaterals were graded with the collateral score (CS) proposed by Tan et al.¹⁵ This "Tan CS" uses a 4-point grading system, ranging from 0 to 3, with which it grades vessel filling in the territory of the occluded artery to assess collateral circulation. A Tan CS of zero indicates absent filling, in which no vessels are visible within the occluded MCA territory. A Tan CS of 1 indicates arterial contrast filling of $\leq 50\%$ of the occluded MCA territory. A score of 2 was given when contrast filling was present in $>50\%$ but $<100\%$ of the occluded MCA territory, and a score of 3, when contrast filling was present in 100% of the occluded MCA territory.

On dynamic CTA, a more extensive grading system was devised to assess the collateral circulation; this grading system used the same 4-point grading system of the CS of Tan et al,¹⁵ but now applied in 4 separate brain regions. Each of the 19 volumes of the dynamic CTA acquisitions was evaluated to obtain information about the velocity of contrast filling and the extent of the contrast-filled arteries with time. Vessel filling was graded in 4 separate brain regions, areas 1a, 1b, 2a, and 2b, with the objective of obtaining a detailed description of vessel filling with time as visualized by dynamic CTA. Area 1 indicated the ipsilateral (ie, affected) hemisphere, and area 2 indicated the contralateral (ie, unaffected) hemisphere. Both areas were divided into 2 separate areas, in which *a* indicated the part of area 1 or 2 below the body of the caudate nucleus and *b* indicated the part above the body of the caudate nucleus. All 4 areas were provided with a Tan CS from 0 to 3. To obtain information about the extent of vessel filling with time for the ipsilateral hemisphere, we added the Tan CS for area 1a to the Tan CS of area 1b, resulting in a total score ranging from 0 to 6. The same was performed for the contralateral hemisphere, by adding a Tan CS of area 2a to area 2b. A total extent of filling from 0 to 3 corresponded to arterial filling of $\leq 50\%$ of the hemisphere and a total extent of filling from 4 to 6 denoted filling of $>50\%$ (see On-line Fig 1 for examples).

The velocity of filling was evaluated by calculating the duration in seconds of contrast arrival at the ICA until maximal contrast enhancement for each hemisphere separately. Subsequently, the difference in the duration of filling between the ipsilateral and contralateral hemisphere was calculated. The median difference in optimal filling time for all patients was used as cutoff value to discern fast-from-slow ipsilateral filling. The combined data of the extent and velocity of filling enabled subgroup analysis (On-line Fig 2). For each subgroup, we defined the optimal assessment interval as the interval that contained the 3 highest average collateral scores in both the affected and unaffected hemispheres.

Statistical Analysis

Statistical analysis was performed with SPSS statistics (Version 22; IBM, Armonk, New York). The associations between clinical and radiologic characteristics and a poor radiologic outcome were analyzed with univariable Poisson regression and were expressed as risk ratios. Accompanying 95% confidence intervals were used to describe their precision. Interobserver agreement was assessed by using the Cohen κ statistic. The additional prognostic value of collaterals as assessed by using dynamic CTA over the assessment by using single-phase CTA on radiologic outcome was analyzed

by using logistic regression models. In the first model, the dichotomized collateral score assessed on single-phase CTA was used to predict radiologic outcome. In a second model, the dichotomized collateral score assessed on dynamic CTA was added to the first model. Subsequently, the potential improvement of the second model with respect to the first model was compared by using the likelihood ratio test. Graphs were computed by calculating the mean filling of all patients grouped according to extent of collateral filling and for different time points in seconds after contrast arrival at the ICA. Standard error of the mean was indicated by error bars representing ± 1 standard error.

RESULTS

Patients

From July 2010 until July 2014, 70 patients were eligible, of whom 61 had follow-up imaging available for measurement of the final infarct volume. The mean age of the study participants was 67, the median NIHSS score was 15, and 27 patients (44%) were women. The median time from symptom onset to multimodal CT imaging was 64 minutes. Most patients (61%, $n = 37$) received intravenous thrombolysis, only 5% ($n = 3$) underwent mechanical thrombectomy without intravenous thrombolysis and 23% ($n = 14$) received a combined treatment of intravenous thrombolysis and mechanical thrombectomy. The remaining 11% ($n = 7$) did not receive any treatment (On-line Table 1). At follow-up, 33 patients (54%) had a poor radiologic outcome (infarct volume, ≥ 70 mL).

Collateral Assessment

Interobserver agreement for assessment of collateral extent with dynamic CTA was excellent ($\kappa = 0.88$, $n = 61$). Collateral filling assessed with single-phase CTA showed grade 0 (absent) in 8% ($n = 5$), grade 1 (moderate) in 61% ($n = 37$), grade 2 (good) in 30% ($n = 18$), and grade 3 (excellent) in 2% ($n = 1$). Collateral filling scores were distributed differently when evaluated by dynamic CTA. Most patients had, for each region (ie, below and above the body of the caudate nucleus), either a collateral score of 2 indicating $>50\%$ vessel filling (level *a*: $n = 30$, 49%; level *b*: $n = 23$, 38%) or a collateral score of 3 indicating complete vessel filling (level *a*: $n = 21$, 34%; level *b*: $n = 23$, 38%). The remaining patients were graded with a collateral score of 1 indicating $<50\%$ vessel filling (level *a*: $n = 10$, 16%; level *b*: $n = 15$, 25%) (On-line Fig 2).

For the entire study population, dynamic CTA analysis showed that the median time difference between optimal filling of the healthy hemisphere compared with the affected hemisphere was 4.5 seconds. Fast filling was defined as optimal filling within 4.5 seconds after optimal filling in the unaffected hemisphere. Combining the extent and velocity of filling resulted in 4 different subgroups: good-and-fast collaterals, good-but-slow collaterals, poor-but-fast collaterals, and poor-and-slow collaterals (On-line Fig 3).

Patterns of vessel filling with dynamic CTA were described for the contralateral (ie, unaffected) and the ipsilateral (ie, affected) hemisphere as shown in Fig 1A. The unaffected hemisphere reached complete arterial filling (ie, score of 6) on average at 14 seconds after contrast entry at the ICA, while the ipsilateral hemi-

sphere showed average optimal collateral filling (ie, filling score of 4) 16 seconds after contrast entry at the ICA. For all patients combined, the interval that contained the 3 highest average collateral filling scores for both hemispheres was between 11 and 21 seconds after ICA contrast entry; the optimal assessment interval was 10 seconds.

Subgroups with fast filling showed a narrow optimal assessment interval of 8 seconds (ie, between 11 and 19 seconds after ICA contrast entry), while subgroups with slow attainment of optimal ipsilateral filling had a broader optimal assessment interval of 14 seconds (range, 11–25 seconds in case of poor extent) and 10 seconds (range, 11–21 seconds in case of good extent) (Fig 1B–E).

Dynamic versus Single-Phase CTA

In comparison with collateral status as evaluated on single-phase CTA, collateral status assessed with dynamic CTA had a stronger association with poor radiologic outcome, as shown in the Table. Poor collaterals (ie, filling in $\leq 50\%$ of the occluded MCA territory) as assessed with dynamic CTA showed an increased risk of poor radiologic outcome compared with good collaterals (ie, $>50\%$ filling), with a risk ratio of 1.9 (95% CI, 1.3–2.9).

The dichotomized collateral score assessed on single-phase CTA showed a less strong relationship; poor collaterals showed a risk ratio of 1.4 (95% CI, 0.8–2.5) on poor radiologic outcome. (Table; risk ratios of other clinical and radiologic variables are presented in On-line Table 2). With logistic regression, the prediction of radiologic outcome by using model 1, containing dichotomized collateral scores as assessed on single-phase CTA, was compared with the prediction of model 2 with the addition of dichotomized collateral scores as assessed on dynamic CTA. The likelihood ratio test showed a significant increase in predictive value between model 1 and model 2 ($P < .01$). Characterizing patients based on the extent and velocity of filling assessed with dynamic CTA indicated an increased risk of poor radiologic outcome with decreasing collateral status. Poor collaterals and slow filling showed an increased risk compared with good collaterals and fast filling, with a risk ratio of 2.0 (95% CI, 1.0–3.8). Poor collaterals and fast filling had an almost identical effect, with a risk ratio of 1.9 (95% CI, 1.1–3.2). Good collaterals and slow filling showed a risk for poor radiologic outcome identical to that of good collaterals and the fast-filling group, with a risk ratio of 1.3 (95% CI, 0.7–2.4) (Table). Patients who received different treatments or had different rates of reperfusion were equally represented in the groups with different collateral scores (On-line Tables 3 and 4).

DISCUSSION

This study showed that dynamic CTA enables detailed description of the collateral circulation by assessing contrast flow through the cerebral arteries during multiple time points in patients with acute ischemic stroke. Collateral assessment with dynamic CTA had a stronger relationship with infarct volume at follow-up than assessment with single-phase CTA. Although multiple studies have indicated that collateral status as evaluated on single-phase CTA can predict both clinical and radiologic outcomes,^{1,4,16} relatively few studies have been performed with dynamic CTA.^{5,17}

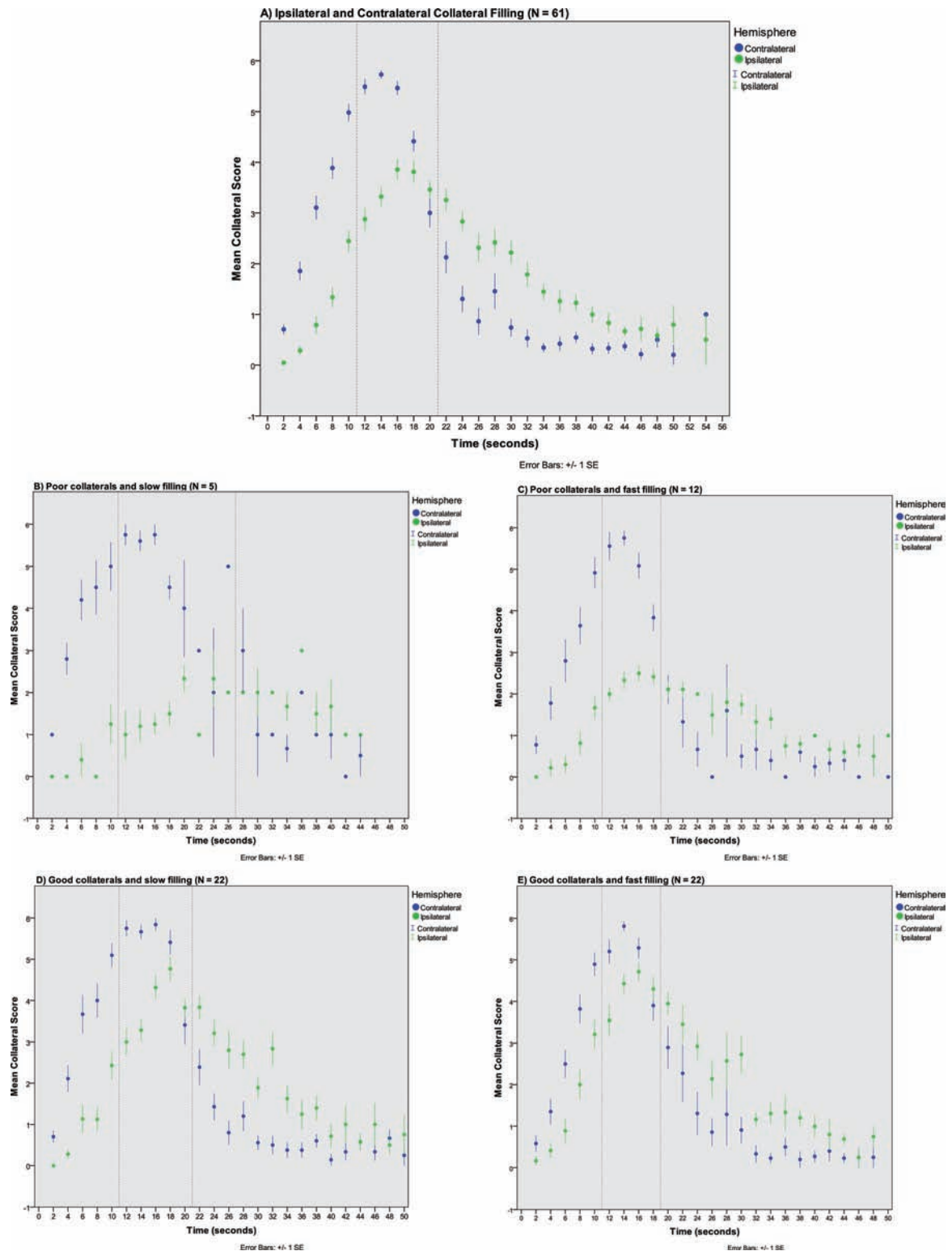


FIG 1. Patterns of contralateral and ipsilateral vessel filling for all patients and for 4 different subgroups. A, Ipsilateral and contralateral vessel filling of all patients ($n = 61$). Time in seconds after contrast arrival in the ICA was calculated for each volume and averaged for multiple patients for each different time point in seconds. *Green dots* represent mean filling with time after contrast arrival for the ipsilateral (ie, affected) hemisphere. *Blue dots* represent mean filling with time after contrast arrival in the ICA for the unaffected contralateral hemisphere. *Error bars* represent 1 standard error of the mean (1 standard error). *Dotted vertical lines* indicate the optimal assessment interval, which is defined by the presence of the 3 highest average collateral scores in both the affected and unaffected hemispheres. B, Patients with poor collateral filling of $<50\%$ of the ischemic territory and slow filling, defined as ipsilateral filling reaching optimal filling >4.5 seconds later than contralateral optimal vessel filling ($n = 5$). C, Patients with poor collateral filling of $<50\%$ of the ischemic territory but with fast filling within 4.5 seconds after contralateral optimal vessel filling ($n = 12$). D, Patients with good collateral filling of $>50\%$ and slow filling ($n = 22$). E, Patients with good collateral filling of $>50\%$ and fast filling ($n = 22$).

Poor radiologic outcome at follow-up (infarct volume ≥ 70 mL) in relation to CSs (N = 61)

	Poor Outcome/ Characteristic Present (n/N) (%)	Poor Outcome/ Characteristic Absent (n/N) (%)	Risk Ratio (95% CI)
Single-phase CTA			
Poor extent of collateral filling ^a	25/42 (60%)	8/19 (42%)	1.4 (0.8–2.5)
Dynamic CTA, extent of filling			
CS 0–1	–	–	–
CS 2	5/5 (100%)	7/19 (37%) ^b	2.7 (1.5–4.9)
CS 3	9/12 (75%)	7/19 (37%) ^b	2.0 (1.0–4.0)
CS 4	8/13 (62%)	7/19 (37%) ^b	1.7 (0.8–3.5)
CS 5	4/12 (33%)	7/19 (37%) ^b	0.9 (0.4–2.4)
Dynamic CTA			
Poor extent of collateral filling ^a	14/17 (82%)	19/44 (43%)	1.9 (1.3–2.9)
Dynamic CTA, extent and timing of filling			
Poor collaterals and slow filling	4/5 (80%)	9/22 (41%) ^c	2.0 (1.0–3.8)
Poor collaterals and fast filling	23/30 (77%)	9/22 (41%) ^c	1.9 (1.1–3.2)
Good collaterals and slow filling	14/26 (54%)	9/22 (41%)	1.3 (0.7–2.4)

^a Poor extent of collateral filling was defined as collateral filling in $\leq 50\%$ of the occluded MCA territory in the affected hemisphere.

^b CS 6 (maximum collateral score) was taken as a reference.

^c Group with good and fast collateral filling was taken as a reference.

Dynamic CTA resulted in higher collateral scores than collateral scores assessed with single-phase CTA, which indicates underestimation when depicting the collateral circulation at 1 time point only. This outcome is in accordance with that of a previous study in which patients with acute ischemic stroke were found to show higher filling scores when imaged with multiphase CTA than with single-phase CTA.^{17,18} Multiphase CTA is an alternative method for collateral assessment by using only a few strategic time points. Both multiphase and dynamic CTA have shown superior results of collateral assessment for predicting clinical outcome compared with conventional single-phase CTA.^{18,19} Because collateral assessment with multiphase CTA has already been used for patient selection in a large thrombectomy trial,²⁰ assessment with dynamic CTA also looks promising for implementation in future endovascular treatment trials and clinical practice. A potential advantage of dynamic CTA over multiphase CTA is that dynamic CTA is constructed from CT perfusion data, which have additional value for predicting clinical outcome.²¹

Furthermore, dynamic CTA provided us with contrast-filling data to compute an average contrast flow through the cerebral arteries of the affected and the unaffected hemispheres of patients with acute ischemic stroke. We found that collaterals become increasingly apparent from the early-to-late phases up to a point at which the affected hemisphere shows stronger opacification than the unaffected hemisphere due to more rapid contrast medium washout of the unaffected hemisphere. On average, the affected hemisphere reaches a lower extent of optimal filling at a later time point in comparison with the unaffected hemisphere. Recently, the arteriovenous phase of dynamic CTA was found to be optimal for collateral assessment to predict follow-up infarct volume.⁷ Although we did not assess the venous circulation for this study, our results also indicate that the timing of CTA acquisition for optimal collateral assessment of the affected hemisphere is always after the peak arterial phase of the unaffected hemisphere.

A limitation of our study is that our dynamic collateral scoring system is new and requires validation by future research. The grading system was a modification of the one used by Souza et al,²² whose scores were based on the division of M2 branching. Be-

cause the division of the MCA is variable and because we wanted to take the extent and velocity of all vessel filling into account, we chose a recognizable brain structure on axial images, namely the body of the caudate nucleus, which was not dependent on vessel filling. Although we acknowledge that this may be only an approximation of the true division of vascular territories, it resulted in a consistent distinction of upper and lower MCA territories over all dynamic CTA volumes. Moreover, we have demonstrated high interobserver agreement.

Another limitation of our study was the relatively low number of patients (ie, $< 25\%$) who underwent DSA, which prevented a direct comparison of dynamic CTA with DSA. Another limitation is the applicability of this grading

system in clinical practice, because assessment of dynamic CTA in all 19 volumes is time-consuming. However, for fast interpretation in clinical practice, maximum intensity projections of all 19 volumes can be created and displayed chronologically. This feature creates angiography-like movies of time-resolved MIPs. As discussed before, optimization of the conventional CTA scanning with ≥ 3 strategic time points (ie, multiphase CTA) is another alternative and could be sufficient for the assessment of the complete collateral circulation.¹⁶ Future prospective studies with larger sample sizes are needed to compare dynamic CTA with multiphase CTA.

Our results show that the velocity of collateral filling does not seem to determine radiologic outcome as much as the extent of filling; these findings are in line with a previous study.⁵ We demonstrated that optimal image acquisition is performed within the 11- to 21-second range after ICA contrast entry. We observed that the period containing the peak filling phases of both hemispheres (ie, the optimal assessment interval) differed depending on the collateral status based on extent and velocity of filling. For patients with a poor and slow collateral circulation, it seems less important to image at a later time point because vessel filling will remain suboptimal during the entire contrast bolus passage. However, in case of slow-but-good collateral filling, it is important to have an extra image acquisition moment at a later time point. Patients with slow-but-good collateral circulation might be incorrectly labeled as having a poor collateral circulation at the point of peak arterial filling in the unaffected hemisphere. Thus, additional image acquisitions at later time points are required.

CONCLUSIONS

Dynamic CTA is a useful method for the evaluation of the collateral circulation in patients with acute ischemic stroke. It has a strong association with radiologic outcome at follow-up and provides detailed information on the extent and velocity of contrast bolus filling through the cerebral vasculature. This study indicates that it might be important to extend the CTA acquisition for a longer time. Because collateral assessment on dynamic CTA is

time-consuming, this acquisition can possibly be reduced to only 3 or 4 strategic image-acquisition phases to simplify and speed up assessment of collaterals in patients with acute MCA stroke.

Disclosures: Marieke J.H. Wermer—*RELATED: Grant:* supported by a personal grant from the Netherlands Organisation for Scientific Research (NWO/ZonMw VENI grant) and the Netherlands Heart Foundation (2011T055).* Diederik W.J. Dippel—*UNRELATED: Consultancy:* Erasmus MC received funds from Stryker for consultations*; The MR CLEAN trial was partly funded by the Dutch Heart Foundation* and by unrestricted grants from AngioCare BV,* Medtronic/Covidien/ev3,* Medac/Lamepro,* Penumbra,* Stryker,* Top Medical/Concentric.* Jan W. Dankbaar—*RELATED: Grant:* supported by a personal grant from the Netherlands Heart Foundation (2012T061). Birgitta K. Velthuis—*RELATED: Grant:* Dutch Heart Foundation (grant No. 2008T034)*; *UNRELATED: Payment for Lectures (including service on Speakers Bureau):* Philips Healthcare.* Charles B.L.M. Majole—*RELATED: Grant:* Dutch Heart Foundation*; *UNRELATED: Payment for Lectures (including service on Speakers Bureau):* Stryker.* *Money paid to the institution.

REFERENCES

1. Menon BK, Smith EE, Modi J, et al. **Regional leptomeningeal score on CT angiography predicts clinical and imaging outcomes in patients with acute anterior circulation occlusions.** *AJNR Am J Neuroradiol* 2011;32:1640–45 CrossRef Medline
2. Singer OC, Berkefeld J, Nolte CH, et al. **Collateral vessels in proximal middle cerebral artery occlusion: the ENDOSTROKE study.** *Radiology* 2015;274:851–58 CrossRef Medline
3. Liebeskind DS, Tomsick TA, Foster LD, et al; IMS III Investigators. **Collaterals at angiography and outcomes in the Interventional Management of Stroke (IMS) III trial.** *Stroke* 2014;45:759–64 CrossRef Medline
4. Lima FO, Furie KL, Silva GS, et al. **Prognosis of untreated strokes due to anterior circulation proximal intracranial arterial occlusions detected by use of computed tomography angiography.** *JAMA Neurol* 2014;71:151–57 CrossRef Medline
5. Frölich AM, Wolff SL, Psychogios MN, et al. **Time-resolved assessment of collateral flow using 4D CT angiography in large-vessel occlusion stroke.** *Eur Radiol* 2014;24:390–96 CrossRef Medline
6. Higashida RT, Furlan AJ, Roberts H, et al; Technology Assessment Committee of the American Society of Interventional and Therapeutic Neuroradiology, Technology Assessment Committee of the Society of Interventional Radiology. **Trial design and reporting standards for intra-arterial cerebral thrombolysis for acute ischemic stroke.** *Stroke* 2003;34:e109–37 CrossRef Medline
7. Beyer SE, Thierfelder KM, von Baumgarten L, et al. **Strategies of collateral blood flow assessment in ischemic stroke: prediction of the follow-up infarct volume in conventional and dynamic CTA.** *AJNR Am J Neuroradiol* 2015;36:488–94 CrossRef Medline
8. Latchaw RE, Alberts MJ, Lev MH, et al; American Heart Association Council on Cardiovascular Radiology and Intervention, Stroke Council, and the Interdisciplinary Council on Peripheral Vascular Disease. **Recommendations for imaging of acute ischemic stroke: a scientific statement from the American Heart Association.** *Stroke* 2009;40:3646–78 CrossRef Medline
9. Menon BK, O'Brien B, Bivard A, et al. **Assessment of leptomeningeal collaterals using dynamic CT angiography in patients with acute ischemic stroke.** *J Cereb Blood Flow Metab* 2013;33:365–71 CrossRef Medline
10. van Seeters T, Biessels GJ, van der Schaaf IC, et al; DUST investigators. **Prediction of outcome in patients with suspected acute ischaemic stroke with CT perfusion and CT angiography: the Dutch acute stroke trial (DUST) study protocol.** *BMC Neurol* 2014;14:37 CrossRef Medline
11. Franssen PS, Beumer D, Berkhemer OA, et al; MR CLEAN Investigators. **MR CLEAN, a multicenter randomized clinical trial of endovascular treatment for acute ischemic stroke in the Netherlands: study protocol for a randomized controlled trial.** *Trials* 2014;15:343 CrossRef Medline
12. Barber PA, Demchuk AM, Zhang J, et al. **Validity and reliability of a quantitative computed tomography score in predicting outcome of hyperacute stroke before thrombolytic therapy: ASPECTS Study Group—Alberta Stroke Programme Early CT Score.** *Lancet* 2000; 13:1670–74 Medline
13. Puetz V, Dzialowski I, Hill MD, et al; Calgary CTA Study Group. **Intracranial thrombus extent predicts clinical outcome, final infarct size and hemorrhagic transformation in ischemic stroke: the clot burden score.** *Int J Stroke* 2008;3:230–36 CrossRef Medline
14. Boers AM, Marquering HA, Jochem JJ, et al; MR CLEAN investigators. **Automated cerebral infarct volume measurement in follow-up noncontrast CT scans of patients with acute ischemic stroke.** *AJNR Am J Neuroradiol* 2013;34:1522–27 CrossRef Medline
15. Tan JC, Dillon WP, Liu S, et al. **Systematic comparison of perfusion-CT and CT-angiography in acute stroke patients.** *Ann Neurol* 2007;61:533–43 CrossRef Medline
16. Maas MB, Lev MH, Ay H, et al. **Collateral vessels on CT angiography predict outcome in acute ischemic stroke.** *Stroke* 2009;40:3001–05 CrossRef Medline
17. Smit EJ, Vonken EJ, van Seeters T, et al. **Timing-invariant imaging of collateral vessels in acute ischemic stroke.** *Stroke* 2013;44:2194–99 CrossRef Medline
18. Menon BK, d'Esterre CD, Qazi EM, et al. **Multiphase CT angiography: a new tool for the imaging triage of patients with acute ischemic stroke.** *Radiology* 2015;275:510–20 CrossRef Medline
19. van den Wijngaard IR, Boiten J, Holswilder G, et al. **Impact of collateral status evaluated by dynamic computed tomographic angiography on clinical outcome in patients with ischemic stroke.** *Stroke* 2015;46:3398–404 CrossRef Medline
20. Goyal M, Demchuk AM, Menon BK, et al; ESCAPE Trial Investigators. **Randomized Assessment of Rapid Endovascular Treatment of Ischemic Stroke.** *N Engl J Med* 2015;372:1019–30 CrossRef Medline
21. Borst J, Berkhemer OA, Roos YB, et al; MR CLEAN Investigators and Affiliations. **Value of computed tomographic perfusion-based patient selection for intra-arterial acute ischemic stroke treatment.** *Stroke* 2015;46:3375–82 CrossRef Medline
22. Souza LC, Yoo AJ, Chaudhry ZA, et al. **Malignant CTA collateral profile is highly specific for large admission DWI infarct core and poor outcome in acute stroke.** *AJNR Am J Neuroradiol* 2012;33: 1331–36 CrossRef Medline

Improving Perfusion Measurement in DSC–MR Imaging with Multiecho Information for Arterial Input Function Determination

A.T. Newton, S. Pruthi, A.M. Stokes, J.T. Skinner, and C.C. Quarles



ABSTRACT

BACKGROUND AND PURPOSE: Clinical measurements of cerebral perfusion have been increasingly performed with multiecho dynamic susceptibility contrast–MR imaging techniques due to their ability to remove confounding T1 effects of contrast agent extravasation from perfusion quantification. However, to this point, the extra information provided by multiecho techniques has not been used to improve the process of estimating the arterial input function, which is critical to accurate perfusion quantification. The purpose of this study is to investigate methods by which multiecho DSC–MRI data can be used to automatically avoid voxels whose signal decreases to the level of noise when calculating the arterial input function.

MATERIALS AND METHODS: Here we compare postprocessing strategies for clinical multiecho DSC–MR imaging data to test whether arterial input function measures could be improved by automatically identifying and removing voxels exhibiting signal attenuation (truncation) artifacts.

RESULTS: In a clinical pediatric population, we found that the Pearson correlation coefficient between ΔR_2^* time-series calculated from each TE individually was a valuable criterion for automated estimation of the arterial input function, resulting in higher peak arterial input function values while maintaining smooth and reliable arterial input function shapes.

CONCLUSIONS: This work is the first to demonstrate that multiecho information may be useful in clinically important automatic arterial input function estimation because it can be used to improve automatic selection of voxels from which the arterial input function should be measured.

ABBREVIATIONS: AIF = arterial input function; ΔR_2^* = change in effective transverse relaxation rate; QM = quality of merit; R = Pearson correlation coefficient; RMS_{error} = root-mean-square error

Dynamic susceptibility contrast–MR imaging is an established clinical technique for imaging perfusion characteristics of the brain. Clinically, there has been interest in methods for accurate perfusion quantification across pathologies, which has moti-

vated the transition from single-echo to multiecho techniques.^{1,2} These techniques desensitize perfusion measurements from bias resulting from contrast agent extravasation as is common in clinical contexts such as high-grade brain tumors.³ Most interesting, along with the measurement of multiecho signals comes the possibility of using this additional information beyond leakage correction.

The problems associated with standard single-echo DSC–MR imaging techniques arise from the assumption that changes in the measured signal intensity solely reflect changes in T2* relaxation times associated with contrast agent passage through the vasculature. This assumption is not valid in pathologies characterized by a disruption of the blood-brain barrier, in which contrast agent will accumulate in the surrounding tissue affecting both T2* and T1 relaxation times significantly and simultaneously. Fundamentally, contrast agent leakage breaks down the assumed relationship between measured signal intensity and underlying contrast agent concentration because signal changes cannot be assumed to be dominated by changes in T2*. Clinically, this broken assump-

Received September 24, 2015; accepted after revision December 14.

From the Department of Radiology and Radiological Sciences (A.T.N., S.P.), Vanderbilt University Medical Center, Nashville, Tennessee; Institute of Imaging Science (A.T.N.), Vanderbilt University, Nashville, Tennessee; Monroe Carell Jr. Children's Hospital at Vanderbilt (S.P.), Nashville, Tennessee; Barrow Neurological Institute (A.M.S., C.C.Q.), Phoenix, Arizona; Saint Joseph's Hospital and Medical Center (A.M.S., C.C.Q.), Phoenix, Arizona; and National Comprehensive Cancer Network (J.T.S.), Fort Washington, Pennsylvania.

This work was partially supported by the National Institutes of Health grant R01-CA158079.

Paper previously presented in part at: Annual Meeting of the International Society of Magnetic Resonance in Medicine, April 20–26, 2013; Salt Lake City, Utah.

Please address correspondence to Allen T. Newton, PhD, Vanderbilt University Institute of Imaging Science, 1161 21st Ave South, Medical Center North, AA-1105, Nashville, TN 37232-2310; e-mail: allen.t.newton@vanderbilt.edu

Indicates open access to non-subscribers at www.ajnr.org

<http://dx.doi.org/10.3174/ajnr.A4700>

tion means that single-echo DSC–MR imaging techniques lacking leakage correction yield unreliable estimates of tissue perfusion.³ Therefore, there has been significant interest in implementation of multiecho techniques for perfusion measurement because they are insensitive to the T1 effects of contrast agent extravasation.^{4–8}

Multiecho DSC–MR imaging data also provide new information beyond leakage correction. For example, this new information could be used to improve the estimation of the arterial input function (AIF). AIF estimation is necessary for quantitative determination of cerebral blood volume, cerebral blood flow, and mean transit time from DSC–MR imaging data, and accurate estimation is highly dependent on the choice of locations for this estimation.^{9–12} Therefore, clinical applications place a priority on automated methods for AIF estimation due to their ease of use and consistency across users.¹³ However, to date, there is no consensus on how to reliably extract AIFs from multiecho data or to automate this process.

The goal of this study was to investigate methods by which multiecho DSC–MR imaging data can be used to automatically avoid voxels whose signal decreases to the level of noise when calculating the AIF. Such voxels are difficult to automatically identify with single-echo acquisitions. We expect that automatically avoiding such voxels would result in improved estimates of the AIF and would thereby provide more accurate measures of perfusion that are clinically feasible due to their automated nature.

MATERIALS AND METHODS

Data Acquisition

In the present study, 117 pediatric clinical dual-echo DSC–MR imaging perfusion datasets were acquired on a 3T clinical MR imaging scanner with a body transmit coil used for excitation and an 8-channel array coil used for signal reception. Data were retrospectively anonymized and analyzed in accordance with the study regulations specified by the local internal review board. In each patient, standard clinical doses of Gd-DTPA contrast agent (0.1 mmol/kg) were administered through manual bolus injection approximately 1 minute after the beginning of perfusion imaging, followed immediately by a saline injection. Images were continually acquired for 4 additional minutes following the injection, yielding 5 minutes of data per patient. All data were acquired with the following parameters: single-shot gradient-echo EPI, FOV = 224 × 224 mm, voxel dimensions = 2.94 × 3.02 × 4.5 mm, number of sections = 21, TE₁/TE₂/TR = 15.16 ± 0.28/45.4/1500 ms, sensitivity encoding factor = 2, flip angle = 90°.

Image Processing

For each patient, images from each TE were separately converted to maps of change in effective transverse relaxation rate (ΔR_{2^*}) according to Equation 1.¹⁴ Dual-echo-based ΔR_{2^*} maps were also estimated according to Equation 2.¹⁴

$$1) \quad \Delta R_{2^*} = -\frac{1}{TE} \times \log\left(\frac{S}{S_{pre}}\right)$$

$$2) \quad \Delta R_{2^*,DE} = \frac{1}{(TE_2 - TE_1)} \times \log\left[\frac{(S_{TE_1}/S_{TE_1,pre})}{(S_{TE_2}/S_{TE_2,pre})}\right]$$

where S_{pre} refers to signal measured before contrast injection, S_{TE_1} refers to the signal at the earlier TE, S_{TE_2} correspondingly

refers to signal measured at the later TE, and $\Delta R_{2^*,DE}$ refers to the dual-echo based estimate of ΔR_{2^*} .

Estimation of Bolus Arrival Time

To account for variable injection times among patients, we estimated the bolus arrival time for each patient. In general, our strategy was to identify the earliest time point whose signal demonstrated a significantly greater rate of change compared with the entire time course. Specifically, the temporal derivative of the mean whole-brain signal at TE₁ was estimated for each patient. The extreme studentized deviate¹⁵ was calculated for each time point to identify outliers ($P < .001$), with the expectation that the points along the drop in signal corresponding to bolus arrival would have significantly higher rates of change than other time points. Isolated outliers (ie, outliers lacking a corresponding outlier either preceding or following it in time) were disregarded due to the expectation that bolus passage would have a duration of >1.5 seconds, desensitizing this analysis to random noise. The earliest remaining time point identified was considered the point of bolus arrival.

Automated AIF Estimation

To identify the most suitable voxels for AIF determination, we implemented a system of ranking candidate voxels. All voxels within the brain were ranked according to various qualities of merit (QMs), with low ranks indicating that a particular voxel was more suitable for AIF use and high ranks indicating poorer suitability. A combined score for each voxel was then calculated as the sum of all QM ranks being considered, with low combined scores indicating better suitability for AIF determination. The 10 voxels with the lowest combined score were selected for each patient, and the AIF was calculated as the average dual-echo-based ΔR_{2^*} time course across all 10 voxels. Thus, the different QM combinations could be assessed because any combination of QMs could be used in calculating the combined score.

Five QMs were measured in total and were available for use in identifying voxels for AIF estimation. The first 2 represented well-established AIF characteristics, and the final 3 represented potential new methods of comparing TE₁ with TE₂ to improve the AIF estimation. The first 2 QMs considered across all cases were the slope of the rise (ie, the rate of increase) in $\Delta R_{2^*,DE}$ across 4.5 seconds following bolus onset (ie, “slope”), and peak height of the $\Delta R_{2^*,DE}$ time courses in units of milliseconds⁻¹ (ie, “height”). These QM metrics are routinely used for automated AIF detection with single-echo DSC–MR imaging data.¹⁰ The 3 additional QMs considered alongside the first 2 were the following: 1) the linear Pearson correlation coefficient between ΔR_{2^*} calculated from TE₁ and TE₂ across 70 seconds spanning 10 seconds before bolus onset to 60 seconds following bolus onset (R); 2) the difference in the peak height of ΔR_{2^*} calculated from TE₁ and TE₂ (peak height difference); and 3) the root-mean-square difference (RMS_{error}) between the ΔR_{2^*} curves calculated from TE₁ and TE₂ according to Equation 3, where n represents the number of imaging volumes acquired.

$$3) \quad RMS_{error} = \sqrt{\frac{\sum_{t=0}^{\infty} (\Delta R_{2^*,TE_1} - \Delta R_{2^*,TE_2})^2}{n}}$$

We considered 4 possible QM combinations for identification of voxels for AIF calculation. These combinations were the follow-

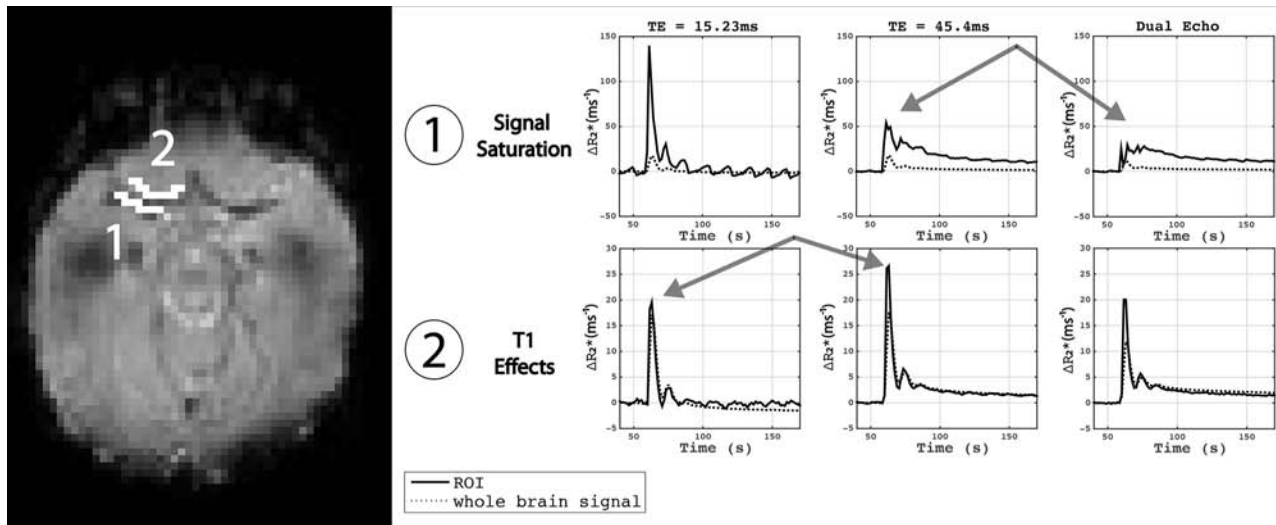


FIG 1. Examples of potential pitfalls when selecting voxels from which to measure the arterial input function. Region 1: region including voxels within the major arterial branches. Note the decreased estimates at TE₂, resulting in a distorted dual-echo estimate of ΔR_2^* . Region 2: voxels immediately outside the major arterial branch showing enhancement, resulting in artifactually low estimates of ΔR_2^* at TE₁. Taken together, these regions illustrate the need for dual-echo estimates to avoid T1 effects and the need to avoid voxels that saturate into the noise floor to ensure accurate estimation of ΔR_2^* from the dual-echo data.

ing: 1) slope and height; 2) slope, height, and correlation; 3) slope, height, and peak height difference; and 4) slope, height, and RMS_{error}. These combinations represented standard parameters commonly used in the automated analysis of single-echo data (ie, combination 1) and 3 different combinations that leveraged the new multiecho information.

Perfusion Estimation

With each AIF selection method described above, perfusion maps were calculated for each patient on the basis of the dual-echo-based ΔR_2^* time courses. The AIF was converted to units of contrast agent concentration, assuming a quadratic relationship for contrast agent inside a blood vessel¹⁶ and a transverse relaxivity of Gd-DTPA (r_2^*) at 3T of 87 mmol⁻¹ ms⁻¹.¹⁷ Standard estimation by using circular singular-value decomposition was used to calculate CBV, CBF (milliliters/100 grams/minute), and MTT for the entire brain.^{18,19}

RESULTS

All data were manually inspected for evidence of artifacts associated with manual contrast agent injections. Features used for exclusion were evidence of double bolus peaks (indicating delay between contrast and saline injections) and insufficient baseline periods (inaccurate bolus timing and thus insufficient baseline periods). Of 117 datasets collected clinically during the study period (2 years and 162 days), 93 were considered acceptable quality for inclusion in the study. Qualitative inspection of the remaining voxel time courses in and around the branches of the middle cerebral artery in these data showed evidence of signal saturation at later TEs and potential T1 contamination at earlier TEs. An example can be seen in Fig 1.

In all patients, voxels across the brain were ranked with respect to each QM. To evaluate how each of the 3 new metrics (R , peak height difference, RMS_{error}) for AIF voxel selection varied, along with more well-characterized metrics (ΔR_2^* on-

set slope and peak height), we calculated the mean values for R , peak height difference, and RMS_{error} across voxels and subjects and plotted them as a function of ΔR_2^* slope and peak height rank (Fig 2). In voxels with the shallowest bolus onset slope and shortest ΔR_2^* peak height, we observed low correlation between the ΔR_2^* _{TE1} and ΔR_2^* _{TE2}. This may be consistent with voxels more distant from major arteries that have a lower contrast-to-noise ratio.

Moving along the diagonal from shallow slopes and low peak heights toward steeper slopes and higher peak heights in ΔR_2^* , we observed that the correlation between ΔR_2^* _{TE1} and ΔR_2^* _{TE2} increased, reaching a maximum, and then decreased (Fig 2, upper right). This finding indicates that in the voxels with the highest ΔR_2^* peak height and steepest ΔR_2^* bolus onset slope, there is a discrepancy between the ΔR_2^* estimates measured from TE₁ and TE₂ independently. This is consistent with voxels experiencing signal saturation to the level of noise at later TEs. Likewise, the difference between ΔR_2^* peak heights measured from TE₁ and TE₂ was low for voxels with the shallowest onset slope and shortest peaks and then increased as the onset slope and peak heights increased (Fig 2, center right). The root-mean-square error between ΔR_2^* _{TE1} and ΔR_2^* _{TE2} followed a pattern similar to that of the peak height difference, though values of RMS_{error} varied little across voxels with shallow onset slope and short peak height (Fig 2, lower right).

Figure 3 shows an example of the effect of AIF selection strategy on the resulting global AIF shapes. When we considered only traditional AIF characteristics like bolus peak height and rate of ΔR_2^* increase, ΔR_2^* peaks were notably heightened initially, followed by broadened and truncated peaks, suggesting inclusion of voxels whose signal decreases to the level of noise during bolus passage. When using multiecho information to avoid voxels potentially with truncation artifacts, we saw the highest AIF peaks when using the correlation between ΔR_2^* _{TE1} and ΔR_2^* _{TE2} as the additional criterion for ranking voxels. This result corresponds to

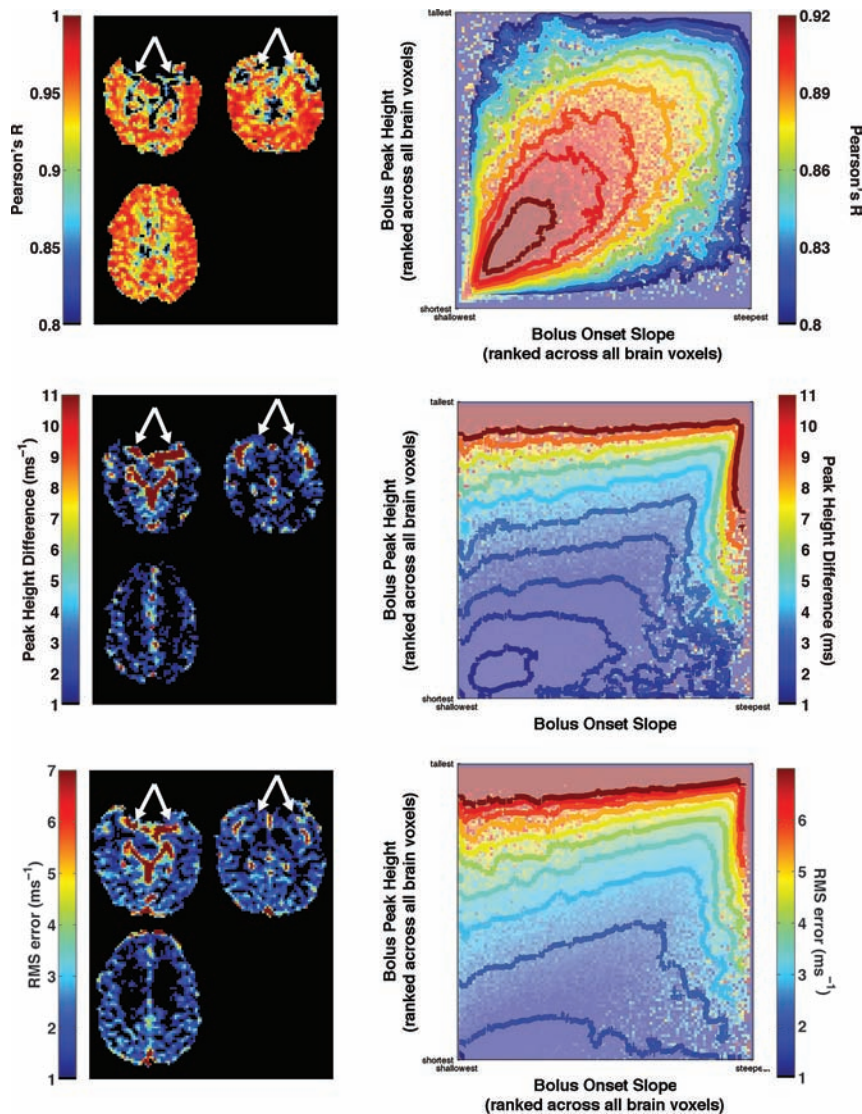


FIG 2. Illustration of potential markers of signal saturation by using multiecho data. Each potential marker (R , peak height difference, RMS_{error}) is shown across 3 sample sections in a representative subject (*left column*). Note markers identifying major arterial branches that are known to have signal saturation effects. In addition, each saturation metric is shown as a function of both ΔR_2^* peak height and bolus onset slope (*right column*). Contours are drawn on smoothed versions of the underlying images. Note that each marker varies nonmonotonically along the diagonal, indicating that simply maximizing the ΔR_2^* peak height and rise slope leads to suboptimal voxel identification for use in AIF determination.

values for CBF that are slightly lower than reported values in adults.^{20,21} AIF peak heights were shorter when using peak height difference between $\Delta R_{2^*,TE1}$ and $\Delta R_{2^*,TE2}$ as the metric for avoiding voxels whose signal saturates to the level of noise and were shorter still when using the mean square error between the estimates of ΔR_{2^*} .

Comparing AIF estimates across patients, we saw similar results with reduced peak heights when using peak height difference or RMS_{error} as opposed to the Pearson R as the method for quantifying truncation artifacts. Looking at the distribution of mean whole-brain CBF estimates across subjects, we saw lower CBF when using peak height difference quantifications compared with RMS_{error} and Pearson R . Likewise, we saw the lowest CBV estimates under that condition as well, likely reflecting the larger area under the curve of the estimated AIF, due to its elevated tail fol-

lowing bolus passage (Fig 4). This finding is consistent with the sample perfusion maps shown in Fig 3.

DISCUSSION

Here we present a new approach to automate AIF determination for multiecho DSC-MR imaging-based perfusion studies. The information contained in multiecho data enables improved estimation of the arterial input function through removal of T1 effects and identification and avoidance of voxels that are likely to be dominated by noise at later TEs. Data recorded from separate TEs can be independently quantified and compared against each other to identify voxels whose data are corrupted at either TE by artifacts. The multiecho-based AIFs exhibit features that are more consistent with the expected AIF shape and temporal characteristics and yield perfusion estimates in agreement with those in prior studies.

The advantages of the methods described here are not tied solely to the specifics of the automated AIF selection method. The “conventional” method for identifying AIF voxels, which is based on prior automated techniques,¹³ focuses on prioritizing the steepness of onset slope and ΔR_{2^*} peak height, though additional features could also have been included. For example, metrics like the bolus peak width and first moment of the concentration time curve may also be useful as AIF voxel-selection criteria, though all these criteria have important caveats that must be considered.²² In fact, the comparative benefits of incorporating multiecho information into the process of AIF voxel selection may decrease relative to con-

ventional methods as more selection criteria are incorporated. Nevertheless, the specific choice of conventional AIF criteria is partially independent of the broader concept that multiecho information can be leveraged to provide information about physiologic signals that are not available when analyzing single-echo signals alone. For example, identifying slightly truncated ΔR_{2^*} peaks in single-echo data is difficult and, in some cases, may not be possible. The method of using multiecho information to avoid truncation artifacts can be implemented across a wide variety of AIF calculation strategies.

An interesting trend in multiecho DSC-MR imaging studies has been to estimate the AIF by using $\Delta R_{2^*,TE1}$ alone, attempting to avoid the complication of identifying and avoiding voxels with truncation artifacts at the later TE. However, several disadvan-

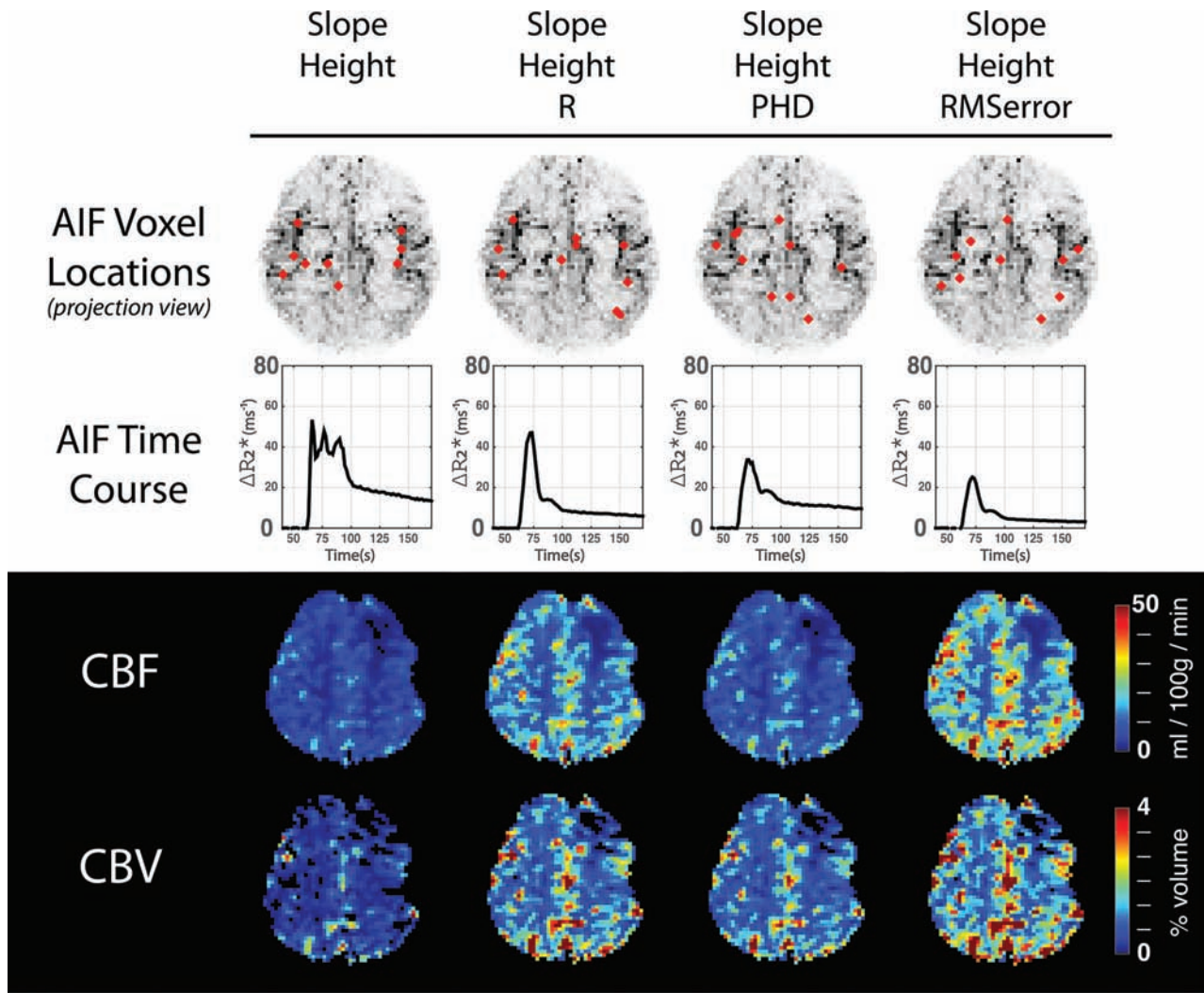


FIG 3. A demonstration of the difference between methods for selecting arterial input function voxels in a patient demonstrating abnormal left frontal perfusion. The *upper row* shows the location of the 10 voxels selected for AIF estimation in red, according to the indicated temporal properties. A projection map of major vessel locations, generated from maps of ΔR_2^* peak slope, is underlaid for spatial reference. The *second row* shows AIF time courses. Note that in all cases, comparing TE₁ with TE₂ results in avoidance of voxels whose signals are truncated by the noise floor, though there are differences in actual AIF according to which comparison method is chosen. The *third and fourth rows* show perfusion maps resulting from the above AIF estimates.

tages to this approach may be underappreciated. While it is less common for signals at early TEs to decrease to the level of noise, they may still be attenuated, resulting in noisier and more error-prone measures of ΔR_2^* during bolus passage. Furthermore, signals at early TEs are potentially confounded by T1 effects as illustrated in Fig 1. These effects theoretically underlie signals at later TEs as well, though they are more likely to be overlooked due to signals being dominated by T2* effects that result in a more characteristic signal decrease following bolus passage. These effects only become realized after the T1 effects of contrast agent passage are removed.

Advances in acquisition strategy such as multiband excitations²³ and improved non-Cartesian *k*-space imaging have resulted in acquisitions with shorter TRs and TEs than have typically been available. Reductions in the TR may increase T1-weighting in the data similar to, though not as extreme as, the effect studied in the context of 3D PRESTO (Principles of Echo-Shifting with a Train of Observations) acquisitions.²⁴ In the case

in which section-wise acceleration results in reduced TR, multiecho techniques for AIF determination and tissue perfusion estimation gain increased importance. Likewise, as alternate acquisition strategies are used, in particular alternate *k*-space trajectories, very short TEs may become possible for the initial echo of multiecho acquisitions. This possibility too will alter the relative T1- and T2*-weighting of the resulting images, lending increased importance to multiecho approaches. In the extreme case in which the weightings of echoes in multiecho acquisitions become significantly different from each other, the approach of measuring the temporal similarity of one echo with the other may need to be reconsidered.

Because multiecho information is used to better select AIF voxels through avoiding truncation artifacts, the overall location of AIF voxels changes. This change may have implications for inclusion of partial-volume averaging artifacts. As Fig 3 illustrates, when one uses only bolus onset slope and peak height as the criteria for identifying AIF voxels, voxels are mainly identified along the M1 and M2 segments of the MCA. However, when one

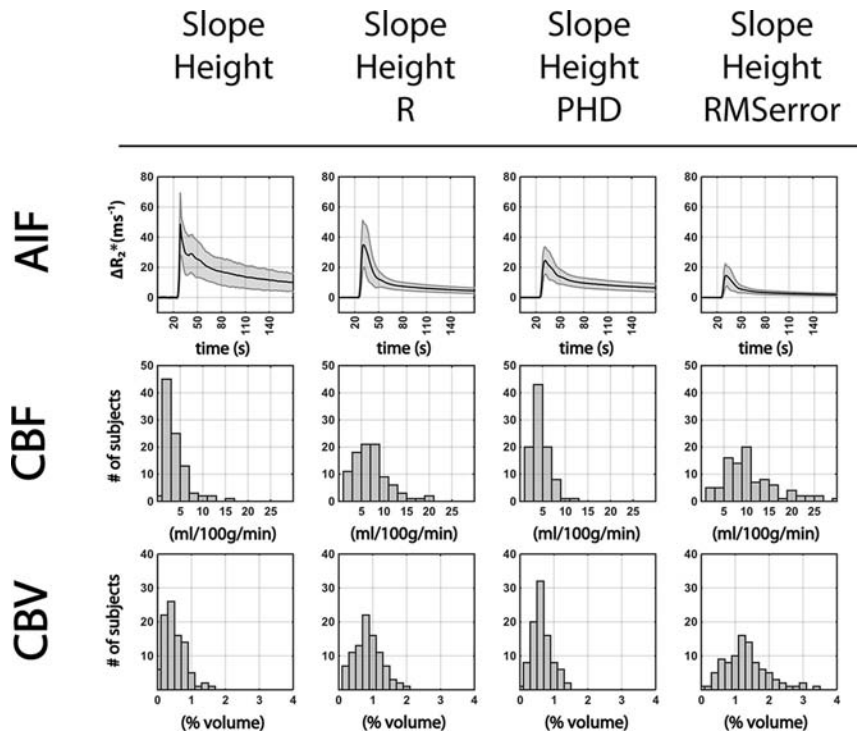


FIG 4. The upper row shows AIF curves across subjects (mean \pm SD). The middle row shows normal-appearing white matter mean CBF histograms across subjects. The lower row shows normal-appearing white matter mean CBV histograms across subjects. White matter measurements are made in individually drawn, normal-appearing white matter ROIs. PHD indicates peak height difference.

uses any of the methods for avoiding truncation artifacts, selected voxels increasingly lie along the posterior arteries, more distal points along the M2 MCA segments, and along smaller arterioles. While this outcome is the result of the advantageous avoidance of truncation artifacts, there is the potential of introducing partial volume artifacts. The chosen voxels may have reduced ΔR_2^* peaks due to voxels containing a mixture of signal from supplying arteries and local microcirculation. While other methods exist for addressing the issues of partial volume averaging,²⁵ here our use of the peak height and bolus onset slope of ΔR_2^* as additional selection criteria rank arterial voxels more favorably. If one looked simply at ΔR_2^* peak height, Figs 3 and 4 suggest that using the Pearson correlation coefficient between $\Delta R_2^*_{TE1}$ and $\Delta R_2^*_{TE2}$ is the best choice as the metric for quantifying (and avoiding) truncation artifacts while minimizing partial volume artifacts.

CONCLUSIONS

The results shown herein indicate that multiecho information can be used to improve AIF estimation in DSC-MR imaging data through avoidance of truncation artifacts and removal of T1 effects. These represent another example of the larger concept that multiecho data can be used to provide a more robust measure of perfusion in clinical settings.

Disclosures: Ashley M. Stokes—RELATED: Grant: National Institutes of Health National Cancer Institute (1R01CA158079).* Christopher C. Quarles—RELATED: Grant: National Institutes of Health National Cancer Institute (1R01CA158079).**Money paid to the institution.

REFERENCES

1. Uematsu H, Maeda M, Sadato N, et al. Blood volume of gliomas determined by double-echo dynamic perfusion-weighted MR imaging: a preliminary study. *AJNR Am J Neuroradiol* 2001;22:1915–19 Medline
2. Uematsu H, Maeda M. Double-echo perfusion-weighted MR imaging: basic concepts and application in brain tumors for the assessment of tumor blood volume and vascular permeability. *Eur Radiol* 2006;16:180–86 CrossRef Medline
3. Boxerman JL, Schmainda KM, Weisskoff RM. Relative cerebral blood volume maps corrected for contrast agent extravasation significantly correlate with glioma tumor grade, whereas uncorrected maps do not. *AJNR Am J Neuroradiol* 2006;27:859–67 Medline
4. Skinner JT, Robison RK, Elder CP, et al. Evaluation of a multiple spin- and gradient-echo (SAGE) EPI acquisition with SENSE acceleration: applications for perfusion imaging in and outside the brain. *Magn Reson Imaging* 2014;32:1171–80 CrossRef Medline
5. Stokes AM, Skinner JT, Quarles CC. Assessment of a combined spin- and gradient-echo (SAGE) DSC-MRI method for preclinical neuroimaging. *Magn Reson Imaging* 2014;32:1181–90 CrossRef Medline
6. Schmiedeskamp H, Andre JB, Straka M, et al. Simultaneous perfusion and permeability measurements using combined spin- and gradient-echo MRI. *J Cereb Blood Flow Metab* 2013;33:732–43 CrossRef Medline
7. Schmiedeskamp H, Straka M, Newbould RD, et al. Combined spin- and gradient-echo perfusion-weighted imaging. *Magn Reson Med* 2012;68:30–40 CrossRef Medline
8. Gore JC, Manning HC, Quarles CC, et al. Magnetic resonance in the era of molecular imaging of cancer. *Magn Reson Imaging* 2011;29:587–600 CrossRef Medline
9. Kellner E, Mader I, Mix M, et al. Arterial input function measurements for bolus tracking perfusion imaging in the brain. *Magn Reson Med* 2013;69:771–80 CrossRef Medline
10. Calamante F. Arterial input function in perfusion MRI: a comprehensive review. *Prog Nucl Magn Reson Spectrosc* 2013;74:1–32 CrossRef Medline
11. Bleeker EJ, Webb AG, van Walderveen MA, et al. Evaluation of signal formation in local arterial input function measurements of dynamic susceptibility contrast MRI. *Magn Reson Med* 2012;67:1324–31 CrossRef Medline
12. Enmi J, Kudomi N, Hayashi T, et al. Quantitative assessment of regional cerebral blood flow by dynamic susceptibility contrast-enhanced MRI, without the need for arterial blood signals. *Phys Med Biol* 2012;57:7873–92 CrossRef Medline
13. Carroll TJ, Rowley HA, Haughton VM. Automatic calculation of the arterial input function for cerebral perfusion imaging with MR imaging. *Radiology* 2003;227:593–600 CrossRef Medline
14. Willatts L, Calamante F. The 39 steps: evading error and deciphering the secrets for accurate dynamic susceptibility contrast MRI. *NMR Biomed* 2013;26:913–31 CrossRef Medline
15. Grubbs FE. Sample criteria for testing outlying observations. *The Annals of Mathematical Statistics* 1950;21:27–58 CrossRef
16. Calamante F, Connelly A, van Osch MJ. Nonlinear DeltaR*2 effects

- in perfusion quantification using bolus-tracking MRI. *Magn Reson Med* 2009;61:486–92 CrossRef Medline
17. Kjolby BF, Østergaard L, Kiselevy VG. **Theoretical model of intravascular paramagnetic tracers effect on tissue relaxation.** *Magn Reson Med* 2006;56:187–97 CrossRef Medline
 18. Østergaard L. **Principles of cerebral perfusion imaging by bolus tracking.** *J Magn Reson Imaging* 2005;22:710–17 CrossRef Medline
 19. Wu O, Østergaard L, Weisskoff RM, et al. **Tracer arrival timing-insensitive technique for estimating flow in MR perfusion-weighted imaging using singular value decomposition with a block-circulant deconvolution matrix.** *Magn Reson Med* 2003;50:164–74 CrossRef Medline
 20. Mutsaerts HJ, Steketee RM, Heijtel DF, et al. **Inter-vendor reproducibility of pseudo-continuous arterial spin labeling at 3 Tesla.** *PLoS One* 2014;9:e104108 CrossRef Medline
 21. Vonken EJ1, van Osch MJ, Bakker CJ, et al. **Measurement of cerebral perfusion with dual-echo multi-slice quantitative dynamic susceptibility contrast MRI.** *J Magn Reson Imaging* 1999;10:109–17 Medline
 22. Weisskoff RM, Chesler D, Boxerman JL, et al. **Pitfalls in MR measurement of tissue blood flow with intravascular tracers: which mean transit time?** *Magn Reson Med* 1993;29:553–58 CrossRef Medline
 23. Larkman DJ, Hajnal JV, Herlihy AH, et al. **Use of multicoil arrays for separation of signal from multiple slices simultaneously excited.** *J Magn Reson Imaging* 2001;13:313–17 Medline
 24. Calamante F, Vonken EJ, van Osch MJ. **Contrast agent concentration measurements affecting quantification of bolus-tracking perfusion MRI.** *Magn Reson Med* 2007;58:544–53 CrossRef Medline
 25. Bleeker EJ, van Osch MJ, Connelly A, et al. **New criterion to aid manual and automatic selection of the arterial input function in dynamic susceptibility contrast MRI.** *Magn Reson Med* 2011;65:448–56 CrossRef Medline

Time-of-Flight MR Angiography for Detection of Cerebral Hyperperfusion Syndrome after Superficial Temporal Artery–Middle Cerebral Artery Anastomosis in Moyamoya Disease

K. Sato, M. Yamada, H. Kuroda, D. Yamamoto, Y. Asano, Y. Inoue, K. Fujii, and T. Kumabe

ABSTRACT

BACKGROUND AND PURPOSE: Cerebral hyperperfusion syndrome is a potential complication of superficial temporal artery–MCA anastomosis for Moyamoya disease. In this study, we evaluated whether TOF-MRA could assess cerebral hyperperfusion syndrome after superficial temporal artery–MCA anastomosis for this disease.

MATERIALS AND METHODS: This retrospective study included patients with Moyamoya disease who underwent superficial temporal artery–MCA single anastomosis. TOF-MRA and SPECT were performed before and 1–6 days after anastomosis. Bilateral ROIs on the source image of TOF-MRA were manually placed directly on the parietal branch of the superficial temporal artery just after branching the frontal branch of the superficial temporal artery and on the contralateral superficial temporal artery on the same axial image, respectively. The change ratio of the maximum signal intensity of the superficial temporal artery on TOF-MRA was calculated by using the following formula: (Postoperative Ipsilateral/Postoperative Contralateral)/(Preoperative Ipsilateral/Preoperative Contralateral).

RESULTS: Of 23 patients (26 sides) who underwent the operation, 5 sides showed cerebral hyperperfusion syndrome postoperatively. There was a significant difference in the change ratio of signal intensity on TOF-MRA observed between the cerebral hyperperfusion syndrome and non-cerebral hyperperfusion syndrome groups (cerebral hyperperfusion syndrome group: 1.88 ± 0.32 ; non-cerebral hyperperfusion syndrome group: 1.03 ± 0.20 ; $P = .0009$). The minimum ratio value for the cerebral hyperperfusion syndrome group was 1.63, and the maximum ratio value for the non-cerebral hyperperfusion syndrome group was 1.30. Thus, no overlap was observed between the 2 groups for the change ratio of signal intensity on TOF-MRA.

CONCLUSIONS: Diagnosis of cerebral hyperperfusion syndrome is indicated by an increase in the change ratio of signal intensity on TOF-MRA by more than approximately 1.5 times the preoperative levels.

ABBREVIATIONS: CHPS = cerebral hyperperfusion syndrome; MMD = Moyamoya disease; Obs = observer; SI = signal intensity; STA = superficial temporal artery

Moyamoya disease (MMD) is a chronic occlusive cerebrovascular disease characterized by bilateral steno-occlusive changes at the terminal portion of the internal carotid artery and an abnormal vascular network at the base of the brain.¹ Superficial temporal artery (STA)-MCA anastomosis is the standard surgical treatment for MMD. The incidence of cerebral hyperperfu-

sion syndrome (CHPS) after STA-MCA anastomosis for MMD was reported to range from 15.0% to 38.2%.^{2–5} With CHPS, transient focal neurologic deterioration is often exhibited, and if intracerebral hemorrhage occurs, it may lead to permanent neurologic deficits.⁶ Therefore, it is important to evaluate the regional cerebral blood flow after STA-MCA anastomosis for MMD.

Positron-emission tomography and single-photon emission CT are criterion standard tools for the evaluation of regional CBF in patients with MMD^{4,7–9}; however, they are time-consuming modalities and require the injection of a radiotracer. MR imaging is a powerful method for comprehensive assessment of the brain without radiation exposure, and time-of-flight MR angiography is widely available. An increase in the signal intensity (SI) of the donor from the STA on TOF-MRA after STA-MCA anastomosis is observed in some patients with MMD.^{2,3,6} Furthermore, we have previously reported that TOF-MRA revealed an increase in SI at the middle cerebral artery after carotid endarterectomy and

Received September 24, 2015; accepted after revision January 4, 2016.

From the Departments of Neurosurgery (K.S., M.Y., H.K., D.Y., K.F., T.K.) and Diagnostic Radiology (Y.A., Y.I.), Kitasato University School of Medicine, Sagami-hara, Kanagawa, Japan.

Dr. Sato conceived the study; Drs Sato, Kuroda, Yamamoto, Inoue, and Asano collected and assembled the data; and Drs Sato, Yamada, and Fujii drafted and Drs Sato, Inoue, and Kumabe co-wrote the manuscript. All authors discussed the manuscript and approved its final form.

Please address correspondence to: Kimitoshi Sato, MD, Department of Neurosurgery, Kitasato University School of Medicine, 1-15-1 Kitasato, Minami-ku, Sagami-hara, Kanagawa, 252-0374 Japan; e-mail: kimitoshi@k8.dion.ne.jp

<http://dx.doi.org/10.3174/ajnr.A4715>

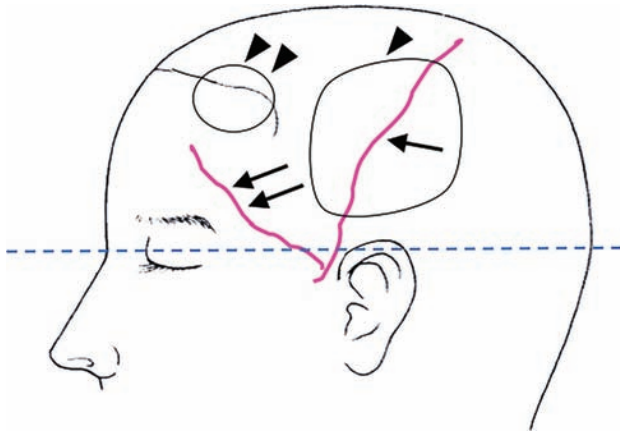


FIG 1. The schema shows the procedure for encephalo-myo-synangiosis (arrowhead) and encephalo-galeo-synangiosis (double arrowheads). The dashed line indicates the estimated axial section of time-of-flight MR angiography on the parietal branch (arrow) of the superficial temporal artery immediately after branching the frontal branch (double arrows) of the STA.

that the SI changes corresponded to acute hemodynamic changes.¹⁰ In the present study, we used similar methods to retrospectively investigate whether CHPS diagnosis could be performed on the basis of the degree of increased SI in the donor from the parietal branch of the STA on TOF-MRA after STA-MCA anastomosis for MMD.

MATERIALS AND METHODS

The ethics committee of our hospital approved this study, and the requirement for informed consent was waived (B14–229).

Subjects and Surgery

All patients were diagnosed with MMD according to the criteria issued by the Japanese Ministry of Health, Labor, and Welfare.¹² The indications for surgical revascularization were patients with ischemic symptoms or hemodynamic compromise as detected by SPECT. The same surgeon (K.S.) performed STA-MCA anastomosis by using a parietal branch of the STA + encephalo-myo-synangiosis and encephalo-galeo-synangiosis procedures with the patient under general anesthesia between October 2009 and August 2013 at the Kitasato University Hospital (Fig 1). Of the 35 patients undergoing the MMD operation (41 sides), 12 patients (15 sides) were excluded due to a lack of MRA or SPECT data. The remaining 23 consecutive patients (26 sides, 11 patients younger than 16 years of age; 7 male patients, 16 female patients; age range, 6–67 years; mean age, 25 years) were subject to analysis. MR imaging/TOF-MRA and iodine 123 *N*-isopropyl-*p*-iodoamphetamine (¹²³I-IMP)–SPECT evaluation were performed before the operation and within 1–6 days after the operation in all 23 patients.

Assessment of STA Signal Intensity on MRA Images

A 1.5T scanner (Signa Excite HD or HDxt or CV/i; GE Healthcare, Milwaukee, Wisconsin) was used to perform MRA. Axial TOF-MRA images of the intracranial arteries, parallel to the anterior/posterior commissure line and covering the top of the head, were acquired by using an 8- or 12-channel head coil or a single-channel quadrature head coil (HD or HDxt [TR, 25 ms; TE, 2.7 ms; flip

angle, 18°; FOV, 22 cm; matrix, 320 × 192; section thickness, 1.6 mm; NEX, 1 acquisition; time, 5 minutes 19 seconds]; CV/i [TR, 25 ms; TE, 6.9 ms; flip angle, 18°; FOV, 22 cm; matrix, 288 × 160; section thickness, 1.6 mm; NEX, 1 acquisition; time, 6 minutes 11 seconds]). Bilateral ROIs on the source image of TOF-MRA were manually placed on the parietal branch of the STA just after branching the frontal branch of the STA and on the contralateral STA on the same axial image. The maximum SI was determined for each ROI. Three neurosurgeons (observer [Obs] 1, K.S.; Obs 2, H.K.; and Obs 3, D.Y., with >10 years of experience) placed the ROIs independently, and Obs 1 placed the ROI twice at an interval of >3 months without knowledge of the clinical information or SPECT findings.

Change Ratio of SI of the STA on MRA

The ipsilateral and contralateral SI values were used to create postoperative and preoperative ratios.

The ipsilateral-to-contralateral ratio was determined as the ratio of the maximum SI for the ipsilateral ROI and the contralateral ROI. The change ratio of SI was calculated by dividing the postoperative ipsilateral-to-contralateral ratio by the preoperative ipsilateral-to-contralateral ratio.¹⁰

Definition of CHPS

The diagnosis of CHPS satisfied all criteria as follows: 1) the presence of focal neurologic signs; 2) confirmed patency of the bypass by MRA and the absence of any ischemic changes by diffusion-weighted imaging; 3) marked postoperative increase in regional CBF on SPECT in the ipsilateral hemisphere and exceeding that in the contralateral hemisphere; and 4) the absence of other pathologies such as compression of the brain surface by swelling of the temporal muscle graft or ischemic attack. All patients were evaluated by the same clinician for the presence of CHPS.

Statistical Analysis

Differences between the 2 groups (with or without CHPS) were evaluated by the Mann-Whitney *U* test for continuous variables (age) and the Fisher exact test (sex, initial symptom at disease onset, and operation side) for absolute categorical variables. We assessed the measures of the reliability of the change ratio of SI of the STA on MRA for continuous measures by using intraclass correlation coefficients. The Mann-Whitney *U* test was used for comparison in the change ratio of SI between the CHPS and non-CHPS groups. The larger change ratio of SI was analyzed for the 3 patients with bilateral operations, and we used 1 side per patient in the analysis. A *P* value <.05 was statistically significant. All statistical analyses were conducted by using JMP 10 software (SAS Institute, Cary, North Carolina).

RESULTS

Of 23 patients (26 sides) who underwent the operation, 5 patients (5 sides) showed CHPS postoperatively. The baseline characteristics of the patients are shown in Table 1. There were no statistically significant differences in age, sex, initial symptom at disease onset (TIA or infarction), and operation side between groups.

The change ratio of SI regarding TOF-MRA was significantly larger in the CHPS group than in the non-CHPS group (CHPS

Table 1: Clinical baseline characteristics of the patients

	CHPS+ (n = 5)	CHPS- (n = 18)	P Value
Median age (25%, 75%) (yr)	32.0 (16.5, 60.0)	15.5 (11.8, 39.2)	.28 ^a
Sex (male/female)	1:4	6:12	1.0 ^b
Presentation at onset (TIA/infarction)	3/2	15/3	.29 ^b
Operation side (right/left)	3/2	9/9	1.0 ^b

Note:—CHPS+ indicates patients with cerebral hyperperfusion syndrome; CHPS-, patients without cerebral hyperperfusion syndrome.

^aMann-Whitney *U* test.

^bFisher exact test.

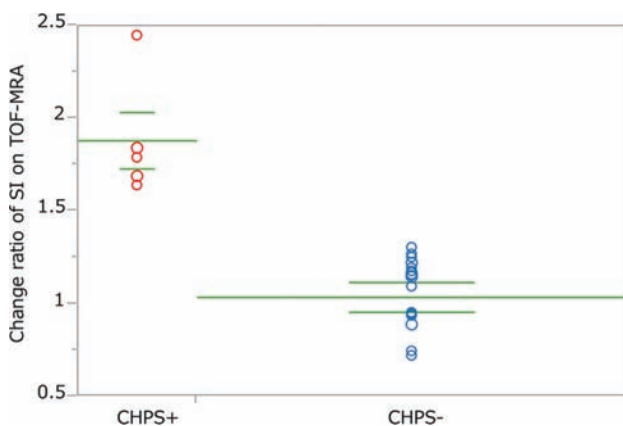


FIG 2. The change ratio of signal intensity on time-of-flight MR angiography observed for the cerebral hyperperfusion syndrome group and the non-CHPS group. The horizontal lines represent the median, first quartile, and third quartile. CHPS+ indicates patients with cerebral hyperperfusion syndrome; CHPS-, patients without cerebral hyperperfusion syndrome.

group: 1.88 ± 0.32 ; range, 1.63–2.44; non-CHPS group: 1.03 ± 0.20 ; range, 0.71–1.30; $P = .0009$ (Fig 2). The minimum ratio value for the CHPS group was 1.63, and the maximum ratio value for the non-CHPS group was 1.32. Thus, no overlap was observed between the 2 groups for the change ratio of SI on TOF-MRA (Table 2).

A summary of the 5 patients with postoperative CHPS is shown in Table 2. All patients immediately recovered after surgery without developing new neurologic deficits. Furthermore, patients did not exhibit additional ischemic lesions on postoperative MR images, including T1-, T2-, and diffusion-weighted images. Postoperative bypass patency was confirmed in all cases.

The reliability of the calculation of the change ratio of SI was assessed by using intraclass correlation coefficients. Strong intraobserver agreement was demonstrated for Obs 1 (intraclass correlation coefficient, $r = 0.9830$). When the first estimates obtained by Obs 1 were compared with the estimates obtained by Obs 2 and Obs 3, interobserver agreement was also excellent (versus Obs 2: intraclass correlation coefficient, $r = 0.9572$; versus Obs 3: intraclass correlation coefficient, $r = 0.9641$). On the basis of these findings, the first estimates obtained by Obs 1 were used for analysis.

Representative Cases

Case 1. A 53-year-old woman who had a visual disturbance caused by a right occipital infarction and sensory disturbance in the left hemisphere was diagnosed with MMD (Fig 3). She underwent a bypass operation consisting of right STA-MCA + encephalo-myo-synangiosis and encephalo-galeo-synangiosis. Sub-

arachnoid hemorrhage occurred 4 days after the operation, and CHPS was diagnosed. Her change ratio of SI was 2.44. Subsequently, CHPS disappeared, and the patient was discharged from the hospital without any new neurologic deficit.

Case 2. A 13-year-old boy had experienced TIAs and was diagnosed with MMD (Fig 4). He underwent a bypass

operation consisting of left STA-MCA + encephalo-myo-synangiosis and encephalo-galeo-synangiosis. No postoperative CHPS was observed (change ratio of SI = 0.93), and the patient was discharged without a neurologic deficit.

DISCUSSION

In the present study, we evaluated TOF-MRA findings and postoperative CHPS after STA-MCA anastomosis for MMD. The change ratio of SI in the donor vessel was significantly larger in the CHPS group than in the non-CHPS group, and a cutoff of 1.5 completely discriminated patients with CHPS from those without CHPS. We suggest that MRA can be used to screen patients with CHPS after STA-MCA anastomosis.

CHPS after STA-MCA Anastomosis for Moyamoya Disease

CHPS following cerebral revascularization is well-recognized, particularly in the context of carotid endarterectomy. In previous reports on carotid endarterectomy, postoperative CHPS was most commonly defined as an increase of >100% over baseline (preoperative values).¹² However, there is no reported definition of CHPS after STA-MCA anastomosis for MMD, to our knowledge.

Increasing evidence suggests that CHPS may occur after a revascularization operation in 15.0%–38.2% of patients with MMD, more frequently than after a revascularization operation for atherosclerotic disease, despite the same STA-MCA bypass operation.²⁻⁵ In addition, CHPS occurs more frequently in adult MMD than in pediatric MMD^{3-5,13} and leads to transient neurologic deterioration, seizures, or delayed intracerebral hemorrhage.⁶ Therefore, careful management of CHPS is mandatory after anastomosis for MMD.¹⁴

Hemodynamic Study in Moyamoya Disease

Although SPECT, positron-emission tomography, xenon-enhanced CT, dynamic perfusion CT, and MR imaging with dynamic susceptibility contrast and arterial spin-labeling have been reported useful for evaluating cerebral hemodynamics in MMD,^{4,8,9} they involve radiation exposure or have limitations in availability. In contrast, TOF-MRA does not require the administration of radioisotopes and contrast agents, can be undertaken quickly, and is widely available.

Underlying Mechanisms of Change of Signal Intensity on TOF-MRA

TOF-MRA is a widely used noninvasive technique for evaluating intracranial arteries. The SI loss attributable to the saturation effect is flow-velocity-dependent and more pronounced at lower

Table 2: Summary of 5 patients with CHPS

Age (yr)	Sex	Initial Presentation at Disease Onset	CHPS Symptom	Duration from Operation to CHPS (days)	Duration from Operation to TOF-MRA (days)	Change Ratio of SI on TOF-MRA
26	Female	TIA	Numbness of upper limb	2	1	1.63
32	Female	Infarction	Partial seizure	3	4	1.68
67	Female	TIA	Palsy of upper limb	1	5	1.79
7	Male	TIA	Numbness of upper limb and dysarthria	5	3	1.84
53	Female	Infarction	Subarachnoid hemorrhage	4	4	2.44

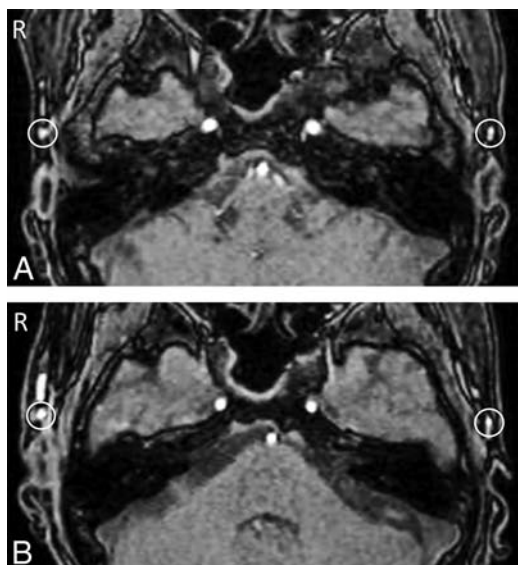


FIG 3. Preoperative (A) and postoperative (B) time-of-flight MR angiography in a case in which cerebral hyperperfusion syndrome was observed after left superficial temporal artery–middle cerebral artery anastomosis. Bilateral regions of interest were manually placed on the parietal branch of the STA immediately after branching the frontal branch of the STA on the same axial image at the axial sections of TOF-MRA; the signal intensity of the graft from the parietal branch of the STA increased postoperatively (B) compared with preoperatively (A).

flow velocities,¹⁵ particularly on single-slab 3D TOF-MRA.¹⁶ On the basis of the contrast mechanism of TOF-MRA, which reflects flow-related enhancement, a change in SI on TOF-MRA can partly reflect the hemodynamics of flowing blood. The degree of enhancement in flowing blood on MRA images, referred to as SI within the vessel lumen, increases nonlinearly with increasing absolute flow velocity.^{17,18} MIP images are frequently used for TOF-MRA. However, because the target blood vessels in the present study were thin and were depicted as having a low SI, they were difficult to assess on MIP images. Thus, source images were used for assessment. Furthermore, we consider that the use of maximum SI improves reproducibility.

Kohama et al¹⁹ reported a case with intense high signal of the donor STA and dilated branches of the MCA around the site of anastomosis on 3T MRA, but not 1.5T MRA. However, the results of the present study were acquired by using 1.5T, proving that these findings were not 3T-specific. Moreover, strong intra- and interobserver agreement was obtained by using our method.

Study Limitations

We used 3 types of 1.5T MR imaging scanners in this series. Although further studies are required to assess possible scan-

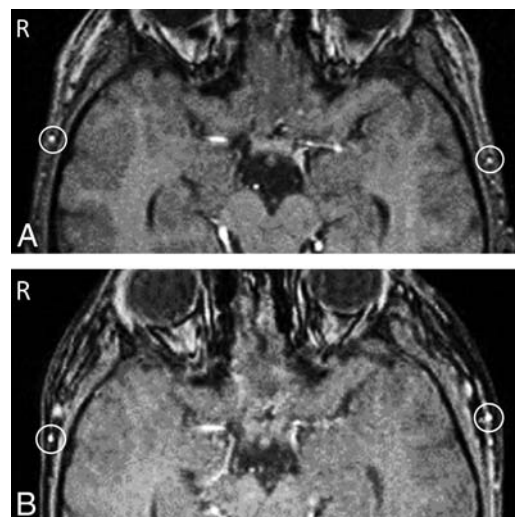


FIG 4. Preoperative (A) and postoperative (B) time-of-flight MR angiography in a case in which cerebral hyperperfusion syndrome was not observed after left superficial temporal artery–middle cerebral artery anastomosis. Bilateral ROIs were manually placed on the parietal branch of the STA immediately after branching the frontal branch of the STA on the same axial image at the axial sections of TOF-MRA; the signal intensity of the graft from the parietal branch of the STA did not increase postoperatively (B) compared with preoperatively (A).

ner-related differences by comparing the increase in the change ratio on both ipsilateral and contralateral sides, our method can help reduce the effects of scanner-related differences and physiologic fluctuations such as blood pressure and partial pressure of carbon dioxide in arterial blood.^{20,21} Because our study included both adults and children, ¹²³I-IMP-SPECT was used in both a quantitative and qualitative manner. However, because the TOF-MRA method does not require administration of radiotracers or the securing of an intravenous line, this method may be effectively applied to pediatric cases with ease. Uchino et al⁵ reported that the onset of CHPS varied from 0 to 9 days after the operation (mean, 3.5 ± 3.5 days). In the present study, TOF-MRA and ¹²³I-IMP-SPECT were not always performed on the same day within 1–6 days after surgery. Because this was a single-institution study with a small sample size, future comprehensive studies with more cases are required.

CONCLUSIONS

Our results suggest that an increase of the change ratio of SI on TOF-MRA of more than approximately 1.5 times the preoperative levels is useful for screening CHPS.

ACKNOWLEDGMENTS

We thank Dr Keika Hoshi, Department of Preventive Medicine, Kitasato University School of Medicine, for data analysis.

Disclosures: Toshihiro Kumabe—UNRELATED: Payment for Lectures (including service on Speakers Bureaus): Eisai.

REFERENCES

1. Suzuki J, Takaku A. Cerebrovascular “moyamoya” disease: disease showing abnormal net-like vessels in base of brain. *Arch Neurol* 1969;20:288–99 CrossRef Medline
2. Fujimura M, Niizuma K, Inoue T, et al. Minocycline prevents focal neurological deterioration due to cerebral hyperperfusion after extracranial-intracranial bypass for moyamoya disease. *Neurosurgery* 2014;74:163–70; discussion 170 CrossRef Medline
3. Fujimura M, Shimizu H, Inoue T, et al. Significance of focal cerebral hyperperfusion as a cause of transient neurologic deterioration after extracranial-intracranial bypass for moyamoya disease: comparative study with non-moyamoya patients using N-isopropyl-p-[(123)I]iodoamphetamine single-photon emission computed tomography. *Neurosurgery* 2011;68:957–64; discussion 964–65 CrossRef Medline
4. Kaku Y, Iihara K, Nakajima N, et al. Cerebral blood flow and metabolism of hyperperfusion after cerebral revascularization in patients with moyamoya disease. *J Cereb Blood Flow Metab* 2012;32:2066–75 CrossRef Medline
5. Uchino H, Kuroda S, Hirata K, et al. Predictors and clinical features of postoperative hyperperfusion after surgical revascularization for moyamoya disease: a serial single photon emission CT/positron emission tomography study. *Stroke* 2012;43:2610–16 CrossRef Medline
6. Fujimura M, Shimizu H, Mugikura S, et al. Delayed intracerebral hemorrhage after superficial temporal artery-middle cerebral artery anastomosis in a patient with moyamoya disease: possible involvement of cerebral hyperperfusion and increased vascular permeability. *Surg Neurol* 2009;71:223–27; discussion 227 CrossRef Medline
7. Horie N, Morikawa M, Morofuji Y, et al. De novo ivy sign indicates postoperative hyperperfusion in moyamoya disease. *Stroke* 2014; 45:1488–91 CrossRef Medline
8. Lee M, Zaharchuk G, Guzman R, et al. Quantitative hemodynamic studies in moyamoya disease: a review. *Neurosurg Focus* 2009;26:E5 CrossRef Medline
9. Sugino T, Mikami T, Miyata K, et al. Arterial spin-labeling magnetic resonance imaging after revascularization of moyamoya disease. *J Stroke Cerebrovasc Dis* 2013;22:811–16 CrossRef Medline
10. Sato K, Kurata A, Oka H, et al. Signal intensity changes for the middle cerebral artery on 3-dimensional time-of-flight magnetic resonance angiography indicate acute hemodynamic changes after carotid endarterectomy. *J Stroke Cerebrovasc Dis* 2013;22:e511–15 CrossRef Medline
11. Research Committee on the Pathology and Treatment of Spontaneous Occlusion of the Circle of Willis; Health Labour Sciences Research Grant for Research on Measures for Intractable Diseases. Guidelines for diagnosis and treatment of moyamoya disease (spontaneous occlusion of the circle of Willis). *Neurol Med Chir (Tokyo)* 2012;52:245–66 CrossRef Medline
12. Piepgras DG, Morgan MK, Sundt TM Jr, et al. Intracerebral hemorrhage after carotid endarterectomy. *J Neurosurg* 1988;68:532–36 Medline
13. Fujimura M, Mugikura S, Kaneta T, et al. Incidence and risk factors for symptomatic cerebral hyperperfusion after superficial temporal artery-middle cerebral artery anastomosis in patients with moyamoya disease. *Surg Neurol* 2009;71:442–47 CrossRef Medline
14. Fujimura M, Inoue T, Shimizu H, et al. Efficacy of prophylactic blood pressure lowering according to a standardized postoperative management protocol to prevent symptomatic cerebral hyperperfusion after direct revascularization surgery for moyamoya disease. *Cerebrovasc Dis* 2012;33:436–45 CrossRef Medline
15. Kodama T, Watanabe K. Influence of imaging parameters, flow velocity, and pulsatile flow on three-dimensional time-of-flight MR angiography: experimental studies. *Eur J Radiol* 1997;26:83–91 CrossRef Medline
16. Davis WL, Blatter DD, Harnsberger HR, et al. Intracranial MR angiography: comparison of single-volume three-dimensional time-of-flight and multiple overlapping thin slab acquisition techniques. *AJR Am J Roentgenol* 1994;163:915–20 CrossRef Medline
17. Leng X, Ip HL, Soo Y, et al. Interobserver reproducibility of signal intensity ratio on magnetic resonance angiography for hemodynamic impact of intracranial atherosclerosis. *J Stroke Cerebrovasc Dis* 2013;22:e615–19 CrossRef Medline
18. Leng X, Wong KS, Soo Y, et al. Magnetic resonance angiography signal intensity as a marker of hemodynamic impairment in intracranial arterial stenosis. *PLoS One* 2013;8:e80124 CrossRef Medline
19. Kohama M, Fujimura M, Mugikura S, et al. Temporal change of 3-T magnetic resonance imaging/angiography during symptomatic cerebral hyperperfusion following superficial temporal artery-middle cerebral artery anastomosis in a patient with adult-onset moyamoya disease. *Neurosurg Rev* 2008;31:451–55; discussion 455 CrossRef Medline
20. Greenberg JH, Kushner M, Rango M, et al. Validation studies of iodine-123-iodoamphetamine as a cerebral blood flow tracer using emission tomography. *J Nucl Med* 1990;31:1364–69 Medline
21. Naylor AR, Merrick MV, Slattery JM, et al. Parametric imaging of cerebral vascular reserve, 2: reproducibility, response to CO₂ and correlation with middle cerebral artery velocities. *Eur J Nucl Med* 1991;18:259–64 Medline

Comparison of CSF Distribution between Idiopathic Normal Pressure Hydrocephalus and Alzheimer Disease

S. Yamada, M. Ishikawa, and K. Yamamoto



ABSTRACT

BACKGROUND AND PURPOSE: CSF volumes in the basal cistern and Sylvian fissure are increased in both idiopathic normal pressure hydrocephalus and Alzheimer disease, though the differences in these volumes in idiopathic normal pressure hydrocephalus and Alzheimer disease have not been well-described. Using CSF segmentation and volume quantification, we compared the distribution of CSF in idiopathic normal pressure hydrocephalus and Alzheimer disease.

MATERIALS AND METHODS: CSF volumes were extracted from T2-weighted 3D spin-echo sequences on 3T MR imaging and quantified semi-automatically. We compared the volumes and ratios of the ventricles and subarachnoid spaces after classification in 30 patients diagnosed with idiopathic normal pressure hydrocephalus, 10 with concurrent idiopathic normal pressure hydrocephalus and Alzheimer disease, 18 with Alzheimer disease, and 26 control subjects 60 years of age or older.

RESULTS: Brain to ventricle ratios at the anterior and posterior commissure levels and 3D volumetric convexity cistern to ventricle ratios were useful indices for the differential diagnosis of idiopathic normal pressure hydrocephalus or idiopathic normal pressure hydrocephalus with Alzheimer disease from Alzheimer disease, similar to the z-Evans index and callosal angle. The most distinctive characteristics of the CSF distribution in idiopathic normal pressure hydrocephalus were small convexity subarachnoid spaces and the large volume of the basal cistern and Sylvian fissure. The distribution of the subarachnoid spaces in the idiopathic normal pressure hydrocephalus with Alzheimer disease group was the most deformed among these 3 groups, though the mean ventricular volume of the idiopathic normal pressure hydrocephalus with Alzheimer disease group was intermediate between that of the idiopathic normal pressure hydrocephalus and Alzheimer disease groups.

CONCLUSIONS: The z-axial expansion of the lateral ventricle and compression of the brain just above the ventricle were the common findings in the parameters for differentiating idiopathic normal pressure hydrocephalus from Alzheimer disease.

ABBREVIATIONS: AC = anterior commissure; AD = Alzheimer disease; BVR = brain to ventricle ratios; CVR = convexity cistern to ventricle ratio; iNPH = idiopathic normal pressure hydrocephalus; PC = posterior commissure; SPACE = sampling perfection with application-optimized contrasts by using different flip angle evolution

Idiopathic normal pressure hydrocephalus (iNPH) has been diagnosed with several highly sensitive radiologic findings since the evidence-based guidelines for the diagnosis and management

of iNPH were announced.¹⁻¹¹ Due to the expansion of the lateral ventricles toward the vertex, upward displacement of the superior parietal lobule and decrease of the subarachnoid space at part of the high parietal convexity area are specific morphologic features for iNPH, called “disproportionately enlarged subarachnoid-space hydrocephalus (DESH).”¹ As an alternative to the Evans index, we recently proposed that the “z-Evans index,” which was defined as the maximum z-axial length of the frontal horns of the lateral ventricles to the maximum cranial z-axial length, was useful for iNPH diagnosis.¹² iNPH occurs in the elderly population prone to many types of comorbidities including Alzheimer disease (AD).¹³⁻²¹ Therefore, differential diagnosis between iNPH and AD with brain atrophy is important, though the quantitative

Received November 9, 2015; accepted after revision December 7.

From the Normal Pressure Hydrocephalus Center (S.Y., M.I.) and Department of Neurosurgery and Stroke Center (S.Y., M.I., K.Y.), Rakuwakai Otowa Hospital, Kyoto, Japan.

Drs Yamada and Ishikawa have made substantial contributions to the intellectual content of the article, have approved the final manuscript, and agree with submission to this journal. Dr Yamada is the corresponding author for this study and the principal investigator. He is responsible for data management, accuracy of statistical analysis, conduct of the research, and drafting of the manuscript.

Please address correspondence to Shigeki Yamada, MD, PhD, Normal Pressure Hydrocephalus Center, Department of Neurosurgery and Stroke Center, Rakuwakai Otowa Hospital, Otowachinji-cho 2, Yamashina-ku, Kyoto 607-8602, Japan; e-mail: shigekiyamada39@gmail.com

Indicates article with supplemental on-line photo.

<http://dx.doi.org/10.3174/ajnr.A4695>

rating system on MR imaging to distinguish iNPH from AD with brain atrophy has not yet been established, to our knowledge.

A new automated segmentation technique by using a simple threshold algorithm has been developed, taking advantage of the high sensitivity to detect CSF on the T2-weighted 3D spin-echo sampling perfection with application-optimized contrasts by using different flip angle evolution (SPACE) sequence.^{12,22-24} The aim of the present study was to establish a novel representative characteristic of CSF volume and distribution, which can differentiate iNPH from AD.

MATERIALS AND METHODS

Study Population

The study design and protocol were approved by the ethics committee for human research at our hospital. We have prospectively collected intracranial CSF volume data by using a T2-weighted 3D-SPACE sequence on 3T MR imaging since November 2013. Details of the clinical data collections, image acquisition, and segmentation and quantification of the ventricular and subarachnoid space were described in our prior publication.¹² In brief, 112 participants underwent an MR imaging examination for CSF volume analysis after written informed consent. Of them, 82 patients underwent a CSF tap test, which consisted of removing ≥ 30 mL of CSF via a lumbar tap for evaluating the improvement in their symptoms. On the basis of the response to the CSF tap test, 40 patients were diagnosed with iNPH, 14 were diagnosed with secondary NPH that developed after subarachnoid hemorrhage or trauma, 3 were diagnosed with congenital/developmental etiology, and the responses of the other 25 patients were judged as negative to the CSF tap test. Patients diagnosed with secondary NPH or congenital/developmental etiology NPH were excluded from this study.

All patients were diagnosed with or without AD by neurologists on the basis of their symptoms, MR imaging, and SPECT, according to the updated recommendations from the National Institute on Aging–Alzheimer’s Association workgroups.²⁵ Ten of 40 patients diagnosed with iNPH had a comorbidity of AD, whereas 11 of 18 patients who had a history of AD underwent the CSF tap test and were judged as nonresponders and were not diagnosed with iNPH. Additionally, 26 participants 60 years of age or older were recruited as control subjects because they did not have any symptoms of short-stepped gait and/or cognitive impairment and were confirmed as not having ventriculomegaly, disproportionately enlarged subarachnoid space hydrocephalus, or fluid collection such as subdural hematoma on MR imaging. Some of them had small vascular lesions such as small unruptured intracranial aneurysms.

Measurement of CSF Volume and Linear Indices

All MR imaging examinations were performed with a 64-channel 3T MR imaging system (Magnetom Skyra; Siemens, Erlangen, Germany). The sagittal source images of T2-weighted 3D-SPACE were automatically processed to create 3D volume-rendering reconstruction and multiplanar reconstruction images by using an independent 3D volume analyzer workstation (SYNAPSE 3D; Fujifilm Medical Systems, Tokyo, Japan). Next, the ventricles and subarachnoid spaces were semi-automatically segmented. The

subarachnoid spaces were divided into the upper and lower parts in a horizontal section on the anterior/posterior commissure plane at the level of the junction point of the vein of Galen and the straight sinus. In addition, the subarachnoid spaces were segmented in 3D into the following 4 parts: frontal convexity, parietal convexity, Sylvian fissure and basal cistern, and posterior fossa. The borderline between the frontal and parietal convexity–subarachnoid spaces was defined as the central sulcus.

Maximum widths of the lateral ventricles and brain substances just above the lateral ventricles were measured on the reference coronal planes at the anterior commissure (AC) and posterior commissure (PC), perpendicular to the anterior/posterior commissure plane (Fig 1). Brain to ventricle ratios (BVR) were calculated as the maximum width of the brain divided by the maximum width of the lateral ventricles at the anterior and posterior commissure levels, respectively. In addition, 3D volumetric convexity subarachnoid space to ventricle ratio-1 (CVR-1) was defined as the volume of the upper part of the subarachnoid space divided by the total ventricular volume, and CVR-2 was defined as the volume of the frontal and parietal convexity subarachnoid space divided by the total ventricular volume.

Statistical Analysis

Mean values and SDs for age and several parameters were calculated and compared among the 4 groups by the Mann-Whitney–Wilcoxon test. Sex difference was compared by the χ^2 test. Statistical significance was assumed at $P < .05$. These parameters were calculated as the area under the receiver operating characteristic curves to evaluate the optimal thresholds to maximize the sum of sensitivities and specificities for differentiating iNPH or iNPH with AD from AD or control groups. All missing data were treated as deficit data that did not affect other variables. Statistical analysis was performed by using R software (Version 3.0.1; <http://www.R-project.org>).

RESULTS

Clinical Characteristics

Eighty-four patients (mean age, 77.2 ± 6.8 years; range, 62–89 years; 49 men, 35 women) met our inclusion criteria. Among them, 30 patients were categorized into the iNPH group; 10, into the iNPH with AD group; 18, into the AD group; and 26, into the control group. The mean ages were not statistically different among the 4 groups (Table 1). The mean values of the z-Evans index and callosal angle in the iNPH or iNPH with AD group were significantly different from those in the AD group, whereas those of the Evans index were not significantly different (Table 2). The area under the receiver operating characteristic curves of the z-Evans index, callosal angle, and Evans index for distinguishing iNPH from AD were 0.769, 0.753, and 0.647, respectively. The mean widths of the ventricles at the AC and PC levels in the iNPH or iNPH with AD group were significantly enlarged concurrent with the thinning of the brain parenchyma, compared with those in the AD or control group. However, the widths of the ventricles and the brain substances just above the ventricles at the anterior and posterior commissure levels in the iNPH with AD and AD groups ranged between those in the iNPH and control groups (On-line Figure). The widths of the ventricles were significantly associated with the widths of the brain substances

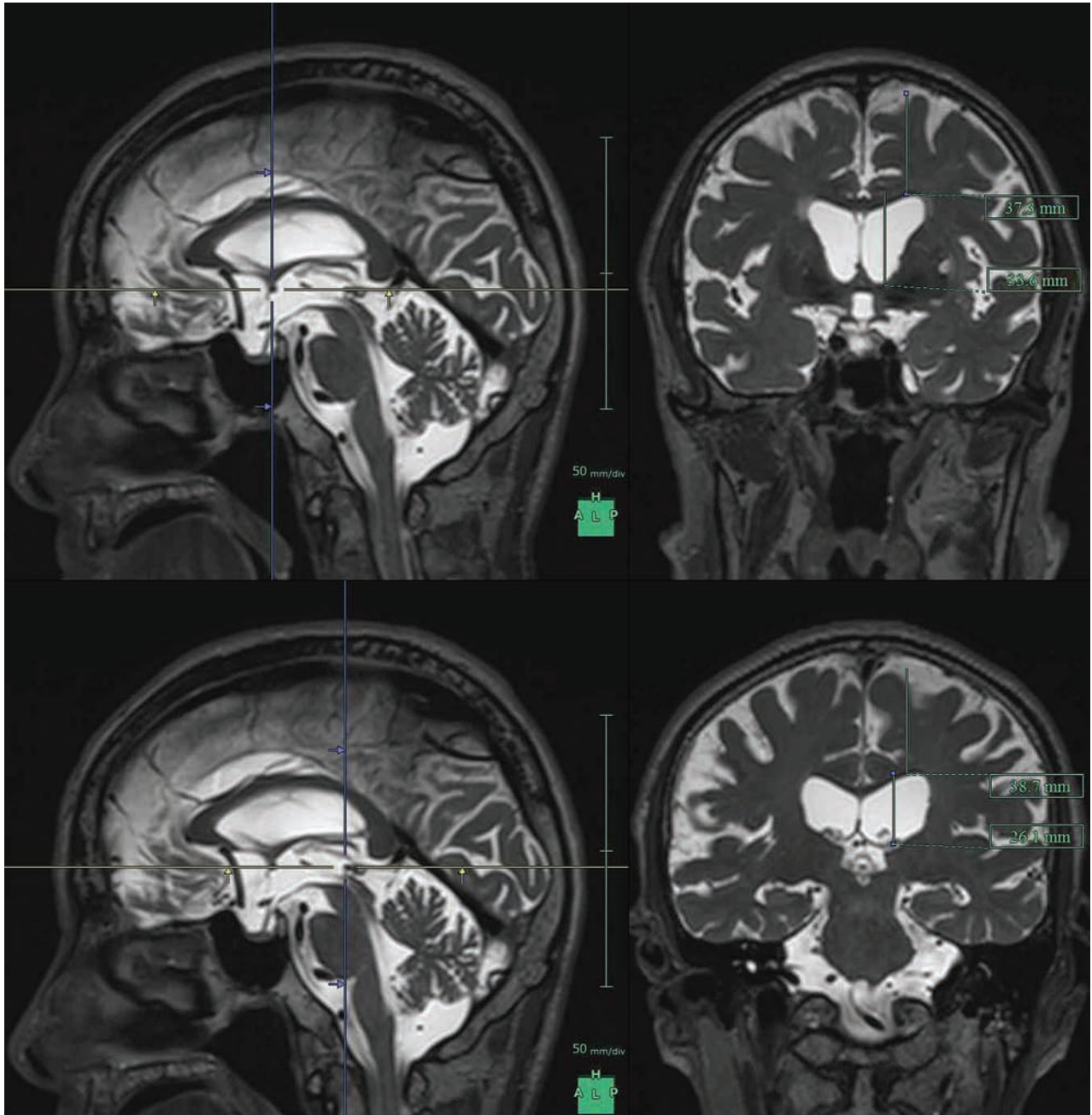


FIG 1. Maximum widths of the lateral ventricles and brain substances just above the lateral ventricles. The figures show the multiplanar reconstruction images on the T2-weighted 3D SPACE sequence. The crosses of the blue and yellow lines on the left figures indicate the points of the anterior commissure (*upper*) and posterior commissure (*lower*), and the right figures show the coronal planes at the blue lines of the left figures.

Table 1: Clinical characteristics of the study population

	iNPH	iNPH + AD	AD	Control	P1 ^a	P2 ^b	P3 ^c
Total No.	30	10	18	26			
Male	22	2	10	15	.343	.155	.342
Mean age (yr)	77.0 ± 6.6	79.7 ± 7.7	79.1 ± 5.0	75.2 ± 7.2	.281	.485	.292

^a P1 indicates the probability value of iNPH vs AD.

^b P2 indicates the probability value of iNPH + AD vs AD.

^c P3 indicates the probability value of iNPH vs controls.

just above the ventricles at the anterior and posterior commissure levels, respectively. Therefore, we checked the distribution of BVR at the anterior and posterior commissure levels. The scatter diagrams in Fig 2 reveal that the BVR at the AC level had a complete linear asso-

ciation with the BVR at the PC level. Furthermore, the receiver operating characteristic curves revealed that both BVR at the AC and PC levels were useful indices for the differential diagnosis of iNPH or iNPH with AD from AD (Fig 2).

Volumetric Comparison

The total ventricle size in the iNPH group was the largest among the 4 groups, whereas the mean volume of the upper part of the total subarachnoid spaces was the smallest (Fig 3). The mean volumes of the total intracranial

Table 2: Mean values and SDs for measurements

	iNPH (n = 30)	iNPH + AD (n = 10)	AD (n = 18)	Controls (n = 26)	P1 ^a	P2 ^b
Width of the ventricle at AC level (mm)	41.2 ± 5.0	41.0 ± 5.9	35.6 ± 5.8	27.2 ± 6.2	.002	.014
Width of the brain at AC level (mm)	29.7 ± 3.5	29.3 ± 3.6	33.2 ± 4.6	40.7 ± 4.2	.006	.029
Width of the ventricle at PC level (mm)	35.3 ± 6.1	32.9 ± 4.7	28.7 ± 6.9	18.8 ± 6.2	.002	.027
Width of the brain at PC level (mm)	29.6 ± 3.9	31.0 ± 3.0	34.0 ± 5.3	41.9 ± 4.7	.010	.150
BVR at AC level	0.74 ± 0.16	0.75 ± 0.26	0.98 ± 0.31	1.59 ± 0.45	<.001	<.001
BVR at PC level	0.88 ± 0.25	0.97 ± 0.25	1.34 ± 0.76	2.54 ± 1.08	<.001	<.001
Evans index	0.34 ± 0.04	0.34 ± 0.37	0.32 ± 0.40	0.28 ± 3.8	.079	.286
z-Evans index	0.43 ± 0.04	0.43 ± 0.61	0.38 ± 0.61	0.29 ± 6.3	.001	.016
Callosal angle (degree)	65.0 ± 20.2	61.0 ± 15.5	86.1 ± 24.0	103.7 ± 15.9	.005	.010
Total intracranial volume (mL)	1519 ± 127	1457 ± 139	1513 ± 200	1484 ± 146	.741	.443
Total CSF volume (mL)	433.2 ± 82.0	408.7 ± 105	406.6 ± 97.1	332.2 ± 112	.428	.654
Brain parenchyma volume (mL)	1086 ± 85.4	1048 ± 120	1106 ± 145	1152 ± 157	.358	.175

^a P1 indicates a probability value of iNPH vs AD based on the Mann-Whitney–Wilcoxon test.

^b P2 indicates the probability value of iNPH + AD vs AD based on the Mann-Whitney–Wilcoxon test.

CSF spaces in the iNPH with AD and AD groups were almost the same (408.7 and 406.6 mL), but the CSF distribution was quite different between these 2 groups. Although the mean volumes of the total subarachnoid spaces were not significantly different among the 4 groups, the distribution of the 4 segmented subarachnoid spaces was notably different, as shown in Fig 4. The most distinct characteristics of the CSF distribution in the iNPH and iNPH with AD groups were the significant small volumes of the frontal and parietal convexity subarachnoid spaces and the upper part of the subarachnoid spaces, compared with the AD group. Conversely, the basal cistern and Sylvian fissure in the iNPH, iNPH with AD, and AD groups had similar mean volumes that were significantly larger (>30 mL) than those in the control group. Therefore, we evaluated the distribution of the CVR-1 and CVR-2 as combined 3D volumetric parameters (Fig 2). The areas under the receiver operating characteristic curve and the sensitivities and specificities of the CVR-1 and CVR-2 for the differential diagnosis of iNPH or iNPH with AD from AD or controls were similar to those of the BVR at the AC and PC levels.

DISCUSSION

This study has shown that there is a significant difference in the ventricular size and distribution patterns of the subarachnoid spaces in iNPH versus AD. Patients with iNPH had enlarged ventricles and decreased convexity subarachnoid spaces compared with those with AD. Previous volumetric analyses had reported that the combined parameters of ventricular size and cortical thickness or high parietal CSF spaces more clearly distinguished iNPH from AD rather than a single parameter.^{5,7,10,11} Therefore, we checked the CVR-1 and CVR-2, as combined 3D volumetric parameters, which were similar to the area under the receiver operating characteristic curves for distinguishing iNPH from AD as previously reported.^{7,10} However, the volumetric analysis is difficult to perform in routine clinical use because it is time-consuming and involves complex 3D imaging techniques. Therefore, we have provided the BVR at the anterior and posterior commissure levels as novel combined 2D parameters. We checked these at the 2 points because there was no previous study to evaluate whether the anterior or the posterior brain was strongly compressed by the lateral ventricles in patients with iNPH.

This study revealed that the areas under the receiver operating characteristic curve and the threshold of the BVR at the

AC level for distinguishing iNPH from AD were equal to those at the PC level. Therefore, we concluded that the brain compression due to enlarged ventricles in patients with iNPH was similar at the anterior and posterior parts of the brain. However, the volumes in the parietal convexity subarachnoid spaces were smaller than those of the frontal convexity subarachnoid spaces in iNPH or iNPH concurrent with AD. We confirmed that the z-Evans index and callosal angle were also useful single parameters, which had an accuracy equal to that of the combined parameters such as the CVRs and BVR, for the differential diagnosis of iNPH or iNPH concurrent with AD from AD.

AD is known to be the most common comorbidity in patients with iNPH in the pathogenesis of CSF stagnation^{13,14,17-21} that might cause an obstacle to clearance of neurotoxic molecules such as amyloid- β peptide or tau.²⁶⁻²⁹ Nevertheless, previous studies of quantitative CSF measurements for the differential diagnosis of NPH excluded the patients diagnosed with concurrent NPH and AD from volumetric analysis. Therefore, a question could be raised about how the ventricular size or distribution of the subarachnoid spaces in concurrent cases with iNPH and AD was comparable with that in a pure iNPH or AD case. Thus, the cases with concurrent iNPH and AD had the largest volume of the basal cistern and Sylvian fissure and the smallest volume of the frontal and parietal convexity subarachnoid spaces among the 3 groups, though their ventricular volume was intermediate between that in iNPH and AD groups. These findings help in understanding the cause and process of concurrent expansion of the ventricles and basal cistern and Sylvian fissure in iNPH. Our results support the view that CSF moves freely and rapidly between ventricles and cisterns. One animal model provided evidence concerning a novel CSF pathway via the choroidal fissure between the ambient cistern and the temporal horn of the lateral ventricles, besides the direct traditional CSF pathway via the foramina of the fourth ventricle.³⁰

Our study had some limitations. First, we used semi-automatic threshold-based segmentation methods by using a T2-weighted sequence. The T2-weighted sequence has an advantage of high-signal intensity for CSF analysis, instead of relatively poor contrast between gray matter and white matter. Conversely, voxel-based morphometry by using a T1-weighted sequence and statistical parametric mapping technique is

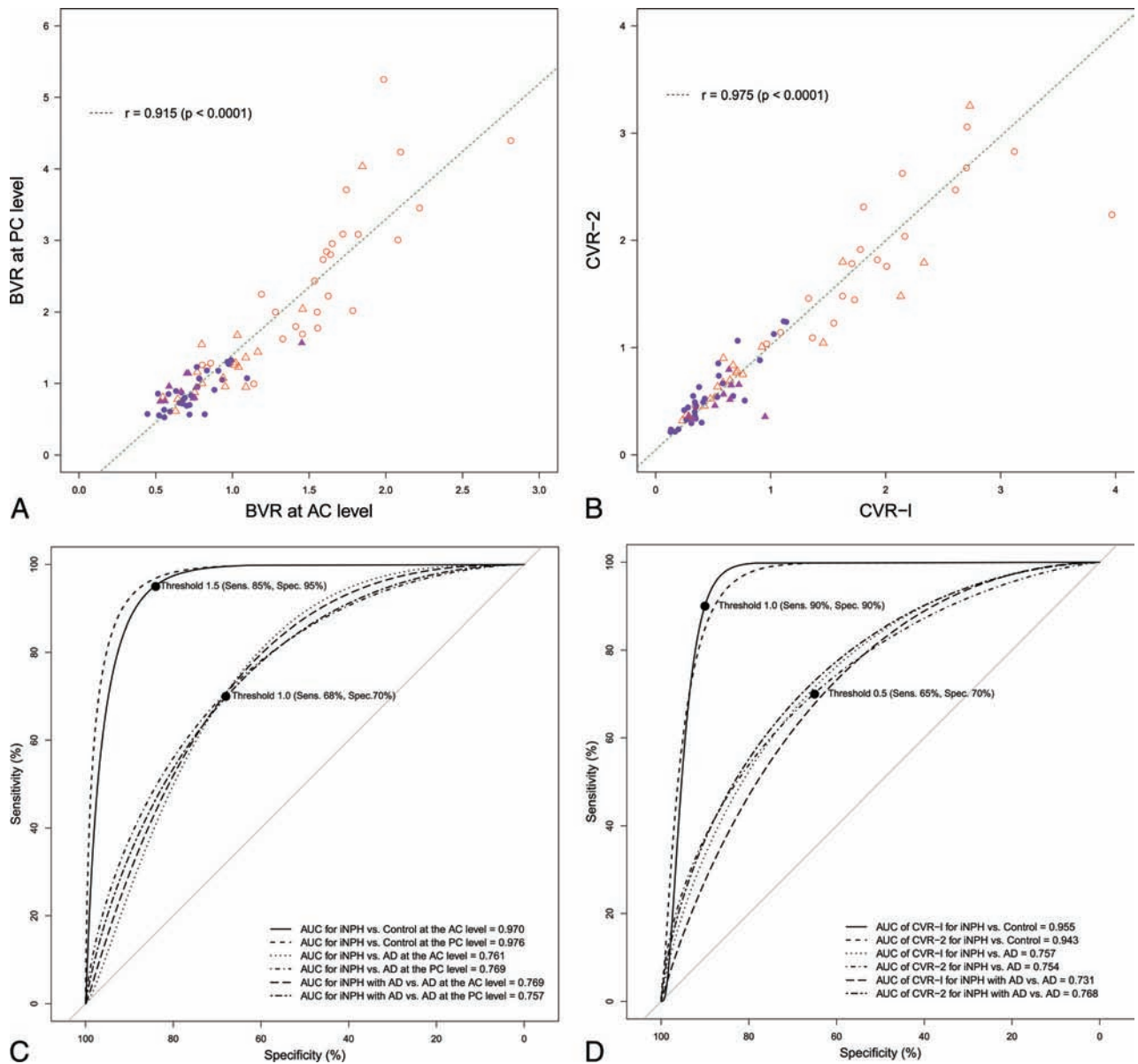


FIG 2. Scatterplots and receiver operating characteristic curves for the differential diagnosis of idiopathic normal pressure hydrocephalus and Alzheimer disease. The *left upper diagram* (A) shows the scatterplot and linear regression for the correlation between the BVR at the anterior level (x-axis) and those at the posterior commissure level (y-axis). The *right upper diagram* (B) shows the scatterplot of the 3D volumetric convexity subarachnoid space to ventricle ratio-1 (CVR-1) and CVR-2. The *purple circle* indicates iNPH, the *purple triangle* indicates iNPH concurrent with Alzheimer disease, the *open red triangle* indicates AD, and the *open red circle* indicates control. The *lower diagram* shows the receiver operating characteristic graph curves of BVR (*left, C*), CVR-1, and CVR-2 (*right, D*) for the differential diagnosis of iNPH or iNPH with AD from AD or controls. The x-axis shows specificity, and the y-axis shows sensitivity. The *black marks* indicate the point of the maximum area under the receiver operating characteristic curve and optimal thresholds (sensitivity and specificity). The maximum areas under the receiver operating characteristic curves for each comparison are displayed in the *lower graph*.

needed for spatial normalization as a first step. However, ventricular size in iNPH would be too large and the distribution of the subarachnoid spaces would be too different for normalization by using templates of the standard brain atlas. Second, AD diagnosis was not confirmed pathologically by brain biopsy in this study. The prevalence of Alzheimer pathology at biopsy in patients with iNPH was reported higher than the prevalence in patients clinically diagnosed with AD.^{13,14,18-20} Additional information about CSF biomarkers or amyloid imaging could increase the diagnostic accuracy of AD.^{15,27,28} In addition, the present results might pave the way for the investigation of the

pathophysiologic mechanisms of the development of iNPH frequently concurrent with AD.

CONCLUSIONS

This study revealed that CVR-1, CVR-2, and BVR at the AC and PC levels were useful indices for the differential diagnosis of iNPH from AD, similar to z-Evans index and callosal angle. The common finding in these parameters was the z-axial expansion of the bilateral ventricles. Furthermore, the distribution of the subarachnoid spaces in the iNPH concurrent with AD group was the most different from that in controls, compared with iNPH or AD.

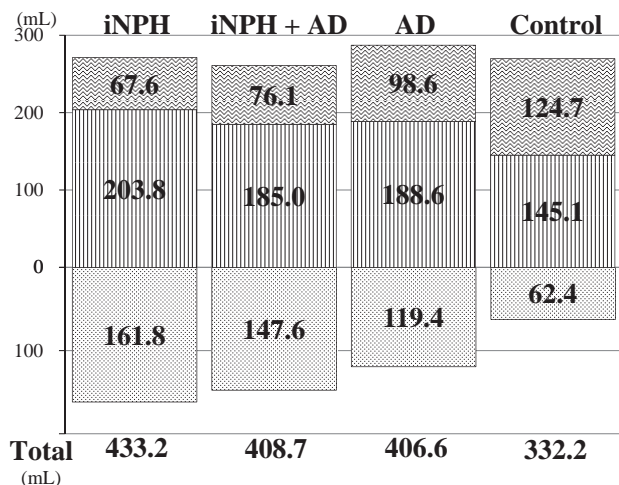


FIG 3. Mean volumes of the total ventricle and total subarachnoid space. The mean volumes of the total ventricle are displayed in a downward direction (*dotted pattern*). The mean volumes of the total subarachnoid spaces are displayed after division of the upper (*vertical striped pattern*) and lower parts (*wave pattern*) in a horizontal section on the anterior/posterior commissure plane at the level of the junction point of the vein of Galen and straight sinus.

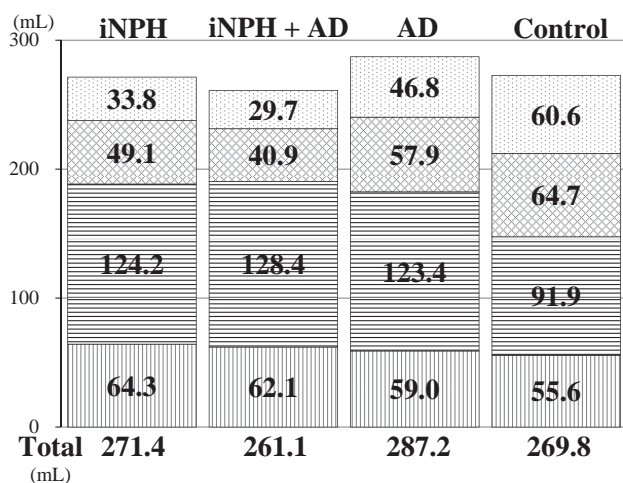


FIG 4. The mean volumes of the segmented parts of the subarachnoid spaces. The *vertical-striped pattern* indicates the subarachnoid space in the posterior fossa. The *horizontal-striped pattern* indicates the subarachnoid space in the basal cistern and Sylvian fissure, the *checked pattern* indicates the subarachnoid space in the frontal convexity subarachnoid space, and the *dotted pattern* indicates the subarachnoid space in the parietal convexity subarachnoid space.

These novel findings may contribute to future studies on the mechanisms underlying the concurrent progression of iNPH and AD.

ACKNOWLEDGMENTS

We thank the radiology staff of the Rakuwakai Otowa Hospital.

Disclosures: Masatsune Ishikawa—*UNRELATED: Grants/Grants Pending:* Japan's Ministry of Health, Labour and Welfare, *Comments:* Normal Pressure Hydrocephalus Center; *Consulting Fee or Honorarium:* Johnson and Johnson, Medtronic, Nihon-Medi-Physics, *Comments:* Honoraria as a speaker at seminars.

REFERENCES

1. Hashimoto M, Ishikawa M, Mori E, et al; Study of INPH on neurological improvement (SINPHONI). **Diagnosis of idiopathic normal pressure hydrocephalus is supported by MRI-based scheme: a prospective cohort study.** *Cerebrospinal Fluid Res* 2010;7:18 CrossRef Medline
2. Ishii K, Kanda T, Harada A, et al. **Clinical impact of the callosal angle in the diagnosis of idiopathic normal pressure hydrocephalus.** *Eur Radiol* 2008;18:2678–83 CrossRef Medline
3. Ishikawa M. Guideline Committee for Idiopathic Normal Pressure Hydrocephalus, Japanese Society of Normal Pressure Hydrocephalus. **Clinical guidelines for idiopathic normal pressure hydrocephalus.** *Neurol Med Chir (Tokyo)* 2004;44:222–23 CrossRef Medline
4. Ishikawa M, Hashimoto M, Kuwana N, et al. **Guidelines for management of idiopathic normal pressure hydrocephalus.** *Neurol Med Chir (Tokyo)* 2008;48(suppl):S1–23 CrossRef Medline
5. Kang K, Yoon U, Lee JM, et al. **Idiopathic normal-pressure hydrocephalus, cortical thinning, and the cerebrospinal fluid tap test.** *J Neurol Sci* 2013;334:55–62 CrossRef Medline
6. Marmarou A, Bergsneider M, Relkin N, et al. **Development of guidelines for idiopathic normal-pressure hydrocephalus: introduction.** *Neurosurgery* 2005;57:S1–3; discussion ii–v Medline
7. Moore DW, Kovanlikaya I, Heier LA, et al. **A pilot study of quantitative MRI measurements of ventricular volume and cortical atrophy for the differential diagnosis of normal pressure hydrocephalus.** *Neurol Res Int* 2012;2012:718150 CrossRef Medline
8. Mori E, Ishikawa M, Kato T, et al; Japanese Society of Normal Pressure Hydrocephalus. **Guidelines for management of idiopathic normal pressure hydrocephalus: second edition.** *Neurol Med Chir (Tokyo)* 2012;52:775–809 CrossRef Medline
9. Relkin N, Marmarou A, Klinge P, et al. **Diagnosing idiopathic normal-pressure hydrocephalus.** *Neurosurgery* 2005;57(3 suppl):S4–16; discussion ii–v Medline
10. Serulle Y, Rusinek H, Kirov II, et al. **Differentiating shunt-responsive normal pressure hydrocephalus from Alzheimer disease and normal aging: pilot study using automated MRI brain tissue segmentation.** *J Neurol* 2014;261:1994–2002 CrossRef Medline
11. Yamashita F, Sasaki M, Takahashi S, et al. **Detection of changes in cerebrospinal fluid space in idiopathic normal pressure hydrocephalus using voxel-based morphometry.** *Neuroradiology* 2010;52:381–86 CrossRef Medline
12. Yamada S, Ishikawa M, Yamamoto K. **Optimal diagnostic indices for idiopathic normal pressure hydrocephalus based on the 3D quantitative volumetric analysis for the cerebral ventricle and subarachnoid space.** *AJNR Am J Neuroradiol* 2015;36:2262–69 CrossRef Medline
13. Cabral D, Beach TG, Vedders L, et al. **Frequency of Alzheimer's disease pathology at autopsy in patients with clinical normal pressure hydrocephalus.** *Alzheimers Dement* 2011;7:509–13 CrossRef Medline
14. Golomb J, Wisoff J, Miller DC, et al. **Alzheimer's disease comorbidity in normal pressure hydrocephalus: prevalence and shunt response.** *J Neurol Neurosurg Psychiatry* 2000;68:778–81 CrossRef Medline
15. Hiraoka K, Narita W, Kikuchi H, et al. **Amyloid deposits and response to shunt surgery in idiopathic normal-pressure hydrocephalus.** *J Neurol Sci* 2015;356:124–28 CrossRef Medline
16. Leinonen V, Alafuzoff I, Aalto S, et al. **Assessment of beta-amyloid in a frontal cortical brain biopsy specimen and by positron emission tomography with carbon 11-labeled Pittsburgh Compound B.** *Arch Neurol* 2008;65:1304–09 CrossRef Medline
17. Malm J, Graff-Radford NR, Ishikawa M, et al. **Influence of comorbidities in idiopathic normal pressure hydrocephalus: research and clinical care: a report of the ISHCSF task force on comorbidities in INPH.** *Fluids Barriers CNS* 2013;10:22 CrossRef Medline
18. Pomeranic IJ, Bond AE, Lopes MB, et al. **Concurrent Alzheimer's pathology in patients with clinical normal pressure hydrocephalus: correlation of high-volume lumbar puncture results, cortical brain biopsies, and outcomes.** *J Neurosurg* 2015 Sep 4. [Epub ahead of print] CrossRef Medline
19. Savolainen S, Paljärvi L, Vapalahti M. **Prevalence of Alzheimer's disease in patients investigated for presumed normal pressure**

- hydrocephalus: a clinical and neuropathological study.** *Acta Neurochir (Wien)* 1999;141:849–53 CrossRef Medline
20. Silverberg GD, Mayo M, Saul T, et al. **Alzheimer's disease, normal-pressure hydrocephalus, and senescent changes in CSF circulatory physiology: a hypothesis.** *Lancet Neurol* 2003;2:506–11 CrossRef Medline
 21. Williams MA, Relkin NR. **Diagnosis and management of idiopathic normal-pressure hydrocephalus.** *Neurol Clin Pract* 2013;3:375–85 CrossRef Medline
 22. Gao KC, Nair G, Cortese IC, et al. **Sub-millimeter imaging of brain-free water for rapid volume assessment in atrophic brains.** *Neuroimage* 2014;100:370–78 CrossRef Medline
 23. Hodel J, Lebret A, Petit E, et al. **Imaging of the entire cerebrospinal fluid volume with a multistation 3D SPACE MR sequence: feasibility study in patients with hydrocephalus.** *Eur Radiol* 2013;23:1450–58 CrossRef Medline
 24. Lebret A, Hodel J, Rahmouni A, et al. **Cerebrospinal fluid volume analysis for hydrocephalus diagnosis and clinical research.** *Comput Med Imaging Graph* 2013;37:224–33 CrossRef Medline
 25. McKhann GM, Knopman DS, Chertkow H, et al. **The diagnosis of dementia due to Alzheimer's disease: recommendations from the National Institute on Aging-Alzheimer's Association workgroups on diagnostic guidelines for Alzheimer's disease.** *Alzheimers Dement* 2011;7:263–69 CrossRef Medline
 26. Miyajima M, Nakajima M, Ogino I, et al. **Soluble amyloid precursor protein α in the cerebrospinal fluid as a diagnostic and prognostic biomarker for idiopathic normal pressure hydrocephalus.** *Eur J Neurol* 2013;20:236–42 CrossRef Medline
 27. Moriya M, Miyajima M, Nakajima M, et al. **Impact of cerebrospinal fluid shunting for idiopathic normal pressure hydrocephalus on the amyloid cascade.** *PLoS One* 2015;10:e0119973 CrossRef Medline
 28. Jingami N, Asada-Utsugi M, Uemura K, et al. **Idiopathic normal pressure hydrocephalus has a different cerebrospinal fluid biomarker profile from Alzheimer's disease.** *J Alzheimers Dis* 2015;45:109–15 CrossRef Medline
 29. Pyykkö OT, Lumela M, Rummukainen J, et al. **Cerebrospinal fluid biomarker and brain biopsy findings in idiopathic normal pressure hydrocephalus.** *PLoS One* 2014;9:e91974 CrossRef Medline
 30. Park JH, Park YS, Suk JS, et al. **Cerebrospinal fluid pathways from cisterns to ventricles in N-butyl cyanoacrylate-induced hydrocephalic rats.** *J Neurosurg Pediatr* 2011;8:640–46 CrossRef Medline

Atypical Presentations of Intracranial Hypotension: Comparison with Classic Spontaneous Intracranial Hypotension

A.A. Capizzano, L. Lai, J. Kim, M. Rizzo, L. Gray, M.K. Smoot, and T. Moritani



ABSTRACT

BACKGROUND AND PURPOSE: Atypical clinical presentations of spontaneous intracranial hypotension include obtundation, memory deficits, dementia with frontotemporal features, parkinsonism, and ataxia. The purpose of this study was to compare clinical and imaging features of spontaneous intracranial hypotension with typical-versus-atypical presentations.

MATERIALS AND METHODS: Clinical records and neuroimaging of patients with spontaneous intracranial hypotension from September 2005 to August 2014 were retrospectively evaluated. Patients with classic spontaneous intracranial hypotension ($n = 33$; mean age, 41.7 ± 14.3 years) were compared with those with intracranial hypotension with atypical clinical presentation ($n = 8$; mean age, 55.9 ± 14.1 years) and 36 controls (mean age, 41.4 ± 11.2 years).

RESULTS: Patients with atypical spontaneous intracranial hypotension were older than those with classic spontaneous intracranial hypotension (55.9 ± 14.1 years versus 41.7 ± 14.3 years; $P = .018$). Symptom duration was shorter in classic compared with atypical spontaneous intracranial hypotension (3.78 ± 7.18 months versus 21.93 ± 18.43 months; $P = .015$). There was no significant difference in dural enhancement, subdural hematomas, or cerebellar tonsil herniation. Patients with atypical spontaneous intracranial hypotension had significantly more elongated anteroposterior midbrain diameter compared with those with classic spontaneous intracranial hypotension (33.6 ± 2.9 mm versus 27.3 ± 2.9 mm; $P < .001$) and shortened pontomammillary distance (2.8 ± 1 mm versus 5.15 ± 1.5 mm; $P < .001$). Patients with atypical spontaneous intracranial hypotension were less likely to become symptom-free, regardless of treatment, compared with those with classic spontaneous intracranial hypotension ($\chi^2 = 13.99$, $P < .001$).

CONCLUSIONS: In this sample of 8 patients, atypical spontaneous intracranial hypotension was a more chronic syndrome compared with classic spontaneous intracranial hypotension, with more severe brain sagging, lower rates of clinical response, and frequent relapses. Awareness of atypical presentations of spontaneous intracranial hypotension is paramount.

ABBREVIATIONS: AP = average anteroposterior midbrain diameter; FBSS = frontotemporal brain sagging syndrome; PM = pontomammillary distance; SIH = spontaneous intracranial hypotension

Spontaneous intracranial hypotension (SIH) results from CSF hypovolemia, most commonly from a CSF spinal leak, and typically presents with orthostatic headache.¹ On brain MR imaging, classic features of SIH are the following: downward brain

sagging with effacement of perimesencephalic cisterns and pituitary and dural engorgement, which are sometimes associated with subdural hematoma.^{1,2} Recognition of SIH is very important for adequate management, which may include epidural blood patch when appropriate. Atypical clinical presentations of SIH have been sparsely reported in the literature, mostly in case report format, and include the following: obtundation,³ stupor,⁴ sensorineural deafness,⁵ short-term memory deficit,⁵ dementia with frontotemporal features,⁶⁻⁸ and parkinsonism and ataxia.⁹ An intriguing association of behavioral variant frontotemporal dementia-like symptoms with SIH has recently been reported as “frontotemporal brain sagging syndrome” (FBSS) on the basis of clinical-radiologic correlation.¹⁰

The prevalence of FBSS is thought to be very low, with the retrospective series from the Mayo Clinic consisting of 8 patients identified between January 1996 and July 2010.¹⁰ However, the

Received October 29, 2015; accepted after revision December 21.

From the Department of Radiology (A.A.C., T.M.), University of Iowa Carver College of Medicine, Iowa City, Iowa; Department of Radiology (L.L.), Stanford University School of Medicine, Stanford, California; Department of Radiology (J.K.), University of Illinois at Chicago, Chicago, Illinois; Department of Neurological Sciences (M.R.), University of Nebraska Medical Center, Omaha, Nebraska; Department of Radiology (L.G.), Duke University Medical Center, Durham, North Carolina; and Department of Orthopaedic Surgery and Sports Medicine (K.S.), University of Kentucky, Lexington, Kentucky.

Please address correspondence to Aristides A. Capizzano, MD, Department of Radiology, Division of Neuroradiology, University of Iowa Carver College of Medicine, 200 Hawkins Dr, IA 52242; e-mail: aristides-capizzano@uiowa.edu

 Indicates article with supplemental on-line table.

<http://dx.doi.org/10.3174/ajnr.A4706>

true incidence of intracranial hypotension is most likely underestimated, particularly with atypical clinical presentations. Furthermore, an incorrect diagnosis of SIH is very common, such as misdiagnosis of SIH as Chiari I malformation, leading to improper patient management.¹¹ Neuroradiologists play a key role in diagnosing classic and particularly atypical intracranial hypotension by recognizing the specific findings of brain sagging on MR imaging, detecting the level of CSF leak on spinal imaging, and guiding therapy accordingly. Therefore, the aim of this study was to illustrate different clinical presentations of intracranial hypotension that differ from the classic SIH syndrome and to assess their neuroimaging correlates and outcome. Specifically, the purpose of this study was to compare demographic, clinical, and brain imaging features of patients with classic SIH versus intracranial hypotension with atypical clinical presentations, including FBSS.

MATERIALS AND METHODS

An institutional review board–approved, retrospective review was performed of clinical records and brain MRI of patients evaluated for intracranial hypotension from September 2005 to August 2014 at the University of Iowa Carver College of Medicine. A waiver of consent was obtained from the local institutional review board. Only patients with brain MRI available for review were included. Patients were divided into 2 groups: classic spontaneous intracranial hypotension (SIH, $n = 33$; mean age, 41.7 ± 14.3 years; 10 men, 23 women) and intracranial hypotension with atypical clinical presentation (atypical, $n = 8$; mean age, 55.9 ± 14.1 years; 5 men, 3 women). The control group consisted of 36 subjects with normal brain MRI findings, age- and sex-matched to patients with SIH (mean age, 41.4 ± 11.2 years; 12 men, 24 women). Patients with SIH presented with orthostatic headaches and brain MR imaging findings of brain sagging and dural enhancement with or without subdural fluid collections. Patients with atypical SIH were selected on the basis of clinical and imaging features of intracranial hypotension with atypical brain stem, cognitive, and/or behavioral symptoms previously referred to as FBSS,¹⁰ for which no other explanation for brain sagging could be obtained after extensive clinical, laboratory, and imaging assessment. The average clinical follow-up was 42.5 ± 37.2 months for atypical SIH and 18.2 ± 23.7 months for classic SIH.

All subjects were scanned with clinical 1.5T or 3T MR imaging scanners with clinical brain MR imaging protocols, including conventional pre- and postgadolinium T1-, T2-, and T2*-weighted sequences and an axial DTI sequence with 12 diffusion directions. The axial level of the midbrain was selected on 5-mm-thick axial T2 images oriented parallel to the line connecting the inferiormost points of the genu and splenium of the corpus callosum at the level showing the red nuclei. The average anteroposterior midbrain diameter (AP) and pontomammillary distance (PM) were combined in the Sagging Index = AP/PM (Fig 1), which was used as an imaging biomarker of the severity of brain sagging and not to diagnose SIH. The intraclass correlation coefficients for the 36 controls between 2 independent image readers were 0.86, 0.81, and 0.8 for the AP midbrain diameter, the PM distance, and the Sagging Index, respectively, indicating very good

reproducibility. When available, spinal imaging (nuclear medicine cisternography, CT myelography, and/or whole-spine MR imaging) was assessed for determination of the site of CSF leak. Statistical analyses were performed with SPSS 21 (IBM, Armonk, New York). Nonparametric statistical analyses by using the Kruskal-Wallis or Mann-Whitney U test as appropriate were performed. Distribution of discrete variables between groups was assessed with the χ^2 test. A 2-tailed P value $<.05$ was used as a statistical significance threshold.

RESULTS

Demographics and Clinical Data

There were no significant differences in age or sex distribution between patients with classic SIH and controls (SIH: 41.7 ± 14.3 years, 70% women versus controls: 41.4 ± 11.2 years, 67% women). Patients with atypical SIH were older than those with classic SIH (55.9 ± 14.1 years versus 41.7 ± 14.3 years, $P = .018$). Among those with atypical SIH, there was a higher percentage of men (63%) compared with classic SIH (30%), but this trend in sex distribution did not reach statistical significance ($\chi^2 = 2.87$, $P = .09$). No differences among the 3 groups were detected for body mass index ($P = .86$). No neuropsychological assessment was performed for patients with classic SIH. A formal neurologic examination at the time of SIH symptoms was performed in 94% (31/33) of patients with classic SIH. Classic SIH invariably presented with orthostatic headaches (ie, with worsening pain while standing up and improving on lying down), and 6 of these patients (18%) had uni- or bilateral sixth nerve palsy, which resolved along with the headache. Symptom duration was <1 year for all classic SIH cases except for 1 woman with 10 years of positional headaches after delivery. When this latter patient was excluded, symptom duration was significantly shorter in classic SIH compared with atypical SIH (3.78 ± 7.18 months versus 21.93 ± 18.43 months, $P = .015$).

The On-line Table summarizes the clinical features of 8 patients with atypical intracranial hypotension. Seven of 8 patients with atypical SIH had headache, which was mild in 2 of them. None of these patients had oculomotor abnormalities. Neuropsychological assessment of patients with atypical SIH yielded an atypical, not-otherwise-specified neuropsychological profile. Seven of 8 patients had anterograde memory impairment, which, in 4 cases, was associated with disinhibition, with 2 of these patients (cases 2 and 3 in the On-line Table) fulfilling the clinical diagnostic criteria for behavioral variant frontotemporal dementia.¹² However, follow-up did not confirm this diagnosis: Neuropathologic assessment of patient 2 at postmortem examination did not show changes of frontotemporal dementia or any other neurodegenerative disease, while patient 3 showed clinical improvement after patching of spinal leaks, intraspinal fluid infusions, and ultimately a spinal operation. Notably, 7 of 8 patients with atypical SIH had daytime hypersomnia. Five of 8 had gait anomalies with ataxic gait and imbalance resulting in frequent falls. Four of 8 had movement disorders: Two had facial grimacing, 1 had upper limb chorea, and 1 had resting tremor. Finally, 3 of 8 patients with atypical SIH had dysarthria and dysphagia, and 2 of 8 had stereotyped vocal tics.

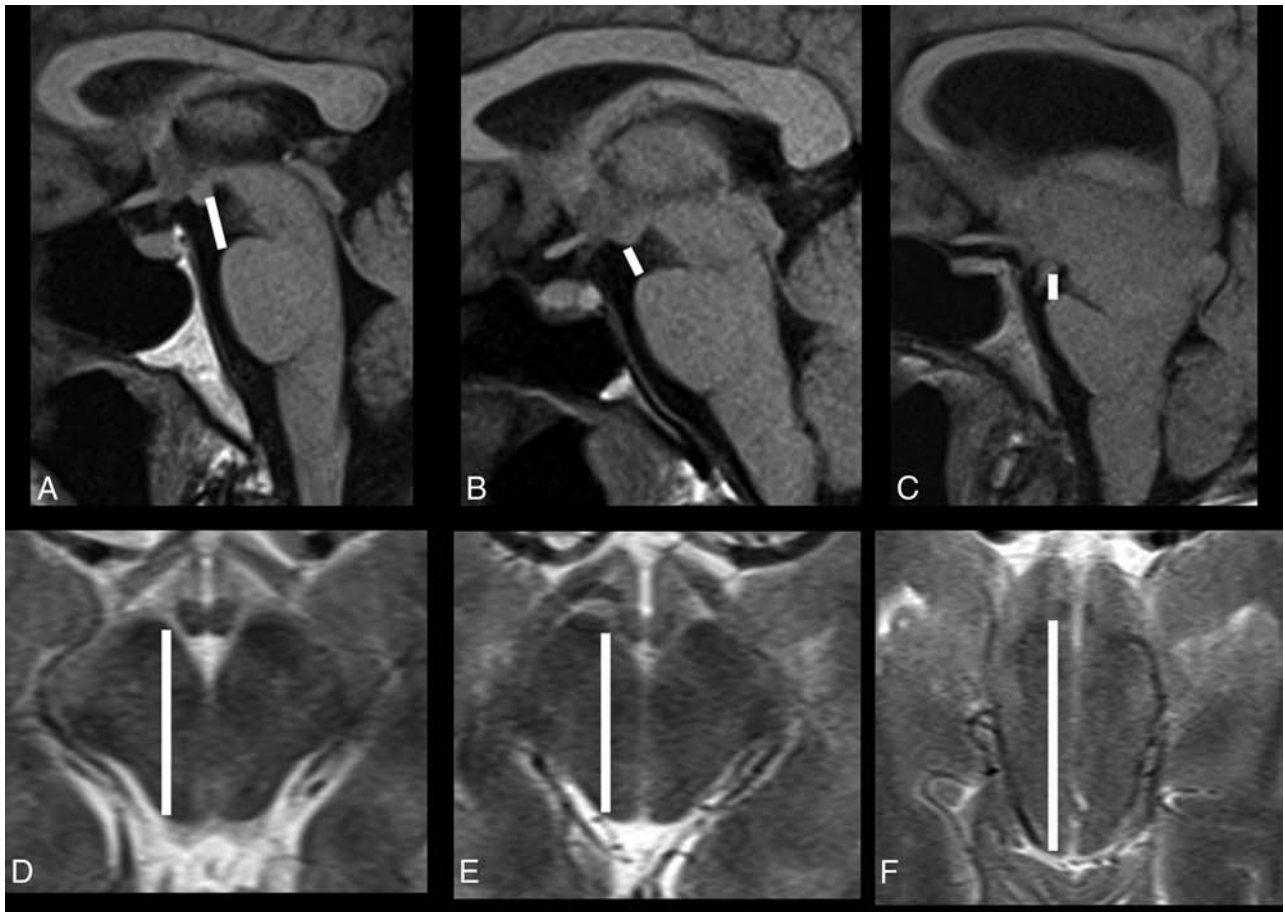


FIG 1. Pontomammillary distance on sagittal T1 (A–C) and anteroposterior midbrain diameter on axial T2-weighted MRI (D–F) in a healthy control (A and D), and patients with classic SIH (B and E) and atypical SIH (C and F).

Imaging Findings: Classic SIH versus Atypical SIH

Twenty-seven (82%) patients with classic SIH had dural enhancement, and 14 (42%) had subdural fluid collections. Patients with atypical SIH had a lower prevalence of dural enhancement (62%) and subdural hematomas (25%) compared with those with classic SIH, but this was not statistically significant. Furthermore, no significant difference in the extent of herniation of the cerebellar tonsils below the plane of the foramen magnum was detected (SIH: 2.25 ± 2.96 mm versus atypical: 5.96 ± 6.44 mm; $P = .2$). Patients with atypical SIH had more distorted midbrain anatomy at the level of the tentorial incisura compared with those with classic SIH, with significantly elongated anteroposterior midbrain diameter (atypical: 33.6 ± 2.9 mm versus SIH: 27.3 ± 2.9 mm, $P < .001$) and shortened pontomammillary distance (atypical: 2.8 ± 1 mm versus SIH: 5.15 ± 1.5 mm; $P < .001$). The combination of the latter 2 measurements in the Sagging Index (AP/PM) showed highly significant differences between the 2 groups (atypical: 14.98 ± 8.6 versus SIH: 6.02 ± 2.25 , $P < .001$) (Fig 2). When we used a cutoff value of 10 in the Sagging Index, only 3 patients were misclassified, with a correct classification of 93%. Finally, 4 of 8 (50%) patients with atypical SIH had CSF leaks on spinal imaging (spine MR imaging, CT myelography, and/or radioisotope cisternography), while 19 of 33 (57%) patients with classic SIH had CSF leaks on spinal imaging, with no significant statistical difference between the groups.

Treatment and Follow-Up

All 30 patients with classic SIH with follow-up clinical data available found their symptoms resolved following blood patch (13/30), burr-hole for subdural drainage (2/30), spinal dural surgical repair (1/30), or medical treatment alone (14/30). There was a significantly lower chance of symptom resolution for patients with atypical compared with classic SIH ($\chi^2 = 13.99$, $P < .001$). Four of 7 patients with atypical SIH with available follow-up showed continued clinical improvement; these were treated with epidural blood patch (case 6 in the On-line Table), multiple epidural blood and glue patches and CSF infusions followed by surgery (case 3), thoracic dural cyst ligation (case 4), and burr-hole drainage of a subdural hematoma (case 8). The remaining 3 patients with atypical SIH did not show clinical improvement: One was treated with Chiari decompression and had stable symptoms of ataxia and resting tremor (case 5), and 2 patients died from unrelated conditions (cases 2 and 7). One patient with atypical SIH was lost on follow-up due to relocation before receiving specific treatment (case 1). Three patients with atypical SIH died of unrelated conditions (case 2, from myocardial infarction; case 4 died at another institution; and case 7, from complications of trauma and anticoagulation). Postmortem examination with neuropathologic assessment of the brain for neurodegenerative disease was performed in case 2 and did not show evidence of frontotemporal dementia pathology or any other neurodegenerative disease.

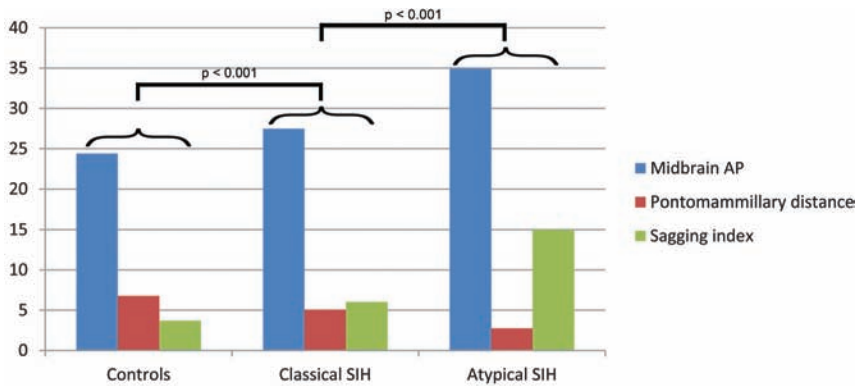


FIG 2. Pontomammillary distance, anteroposterior midbrain diameter, and Sagging Index in patients with atypical and classic SIH and controls.

DISCUSSION

Patients with atypical SIH were older than those with classic SIH and had a trend toward higher representation of men, while women are more commonly affected than men in classic SIH.² Patients with atypical SIH had a longer clinical history and lower odds of becoming symptom-free compared with those with classic SIH. The degree of brain sagging at the tentorial incisura was more severe in patients with atypical-versus-classic SIH without significant differences in other radiographic signs of intracranial hypotension, such as dural enhancement, fluid collections, or cerebellar tonsillar herniation. A Sagging Index higher than 10 should prompt consideration of intracranial hypotension in subjects with atypical clinical presentations.

Case 3 (On-line Table) exemplifies the challenges associated with atypical SIH. A 57-year-old man presented with behavioral changes, anterograde amnesia, headache, hypersomnia, dysphagia, ataxia, dysarthria, and gait instability and was diagnosed with behavioral variant frontotemporal dementia. He had a history of mitral valve prolapse, suggesting connective tissue laxity. Brain MR imaging showed severe brain sagging but no cortical atrophy. On CT myelography, 2 small CSF leaks at T10–T11 and T11–T12 were seen and treated with fluoroscopically guided autologous blood patches (3 times), followed by transient clinical improvement. Neuropsychological evaluation showed mild deficits in processing speed, attention, and concentration, with improvement after blood patches. His symptoms relapsed. Therefore, he was referred to another institution, where on dynamic CT myelogram, multiple CSF leaks at the cervicothoracic neuroforamina were detected and patched under CT guidance first with blood and later with glue; and he also received artificial CSF infusions. The patient's gait and speech improved after the spinal procedures, but symptoms eventually relapsed.

Three years after presentation, he underwent endoscopic third ventriculostomy. Although intracranial hypotension is not an indication for endoscopic third ventriculostomy, the rationale was the presence of a gradient between low intracranial pressure (as measured in an outside ventriculostomy) and normal spinal pressure measured at spinal procedures. Because there was no evidence of a blockade at the foramen magnum, the neurosurgeons hypothesized that the endoscopic third ventriculostomy would equalize pressures between the ventricular system and the subarachnoid spaces of the basal cisterns and spine. His gait and

speech improved for 2 weeks, but full relapse followed. Brain MR imaging showed stable sagging and undetectable CSF flow in the aqueduct (Fig 3A–C). Technetium Tc99m SPECT spinal CSF leak study findings were negative. Four months after ventriculostomy, he underwent T9 through T12 laminoplasties, levels where small CSF leaks had been seen on myelography, but these were not found at the operation. Exposure of the arachnoid revealed adhesions, which were partially released, and arachnoid biopsy reported fibrosis without inflammation or granulomas. Fibrin sealant (TISSEEL; Baxter Healthcare, Deerfield,

Illinois) was applied to seal the dura. Six months after the operation, he had continued clinical improvement with normalization of gait and speech, recovery of the gag reflex, and behavioral and cognitive recovery to baseline. Brain MR imaging showed resolution of brain sagging and recovery of aqueductal CSF flow for the first time at the 4-year follow-up (Fig 3D–F).

The etiology of SIH has been linked to weakness of the spinal dura, resulting in spinal CSF leak, in some cases associated with hereditary connective tissue disorders.¹³ CSF venous fistulas have also recently been implicated in a few cases.¹⁴ Management includes medical treatment (rest, hydration, caffeine) with escalation to spinal epidural patching when symptoms persist. The success rate of the epidural blood patch for SIH, however, is about 30%, far lower than that for post-lumbar puncture headache,¹⁵ and patients with SIH may require repeat spinal procedures. Surgical repair of the spinal dural defect by using different techniques¹⁶ is reserved for cases that fail to respond to conservative measures. As in case 3, a CSF leak was not seen on surgery in 6 of 10 patients with SIH in whom epidural patching with muscle and Gelfoam (Pfizer, New York, New York) was, nevertheless, 100% successful in treating headache.¹⁶ Neuroradiologists make key contributions in the diagnosis and management of classic and particularly atypical SIH. The latter has a longer clinical history probably because the atypical clinical features distract clinicians from the consideration of intracranial hypotension. Furthermore, clinical response is less favorable in patients with atypical compared with those with classic SIH. This could result from structural weakness of the dura or insufficient physiologic adaptation to chronic CSF hypovolemia.¹

Atypical clinical presentations of SIH can be grouped into 4 domains: cognitive-behavioral, lower cranial nerve, imbalance-gait, and arousal deficits. Typically patients present with a combination of these symptom complexes. Neuropsychologically, patients with atypical SIH present with a not-otherwise-specified profile suggestive of a subcortical type of cognitive impairment¹⁷ with slowed information processing, preserved language, and anterograde amnesia. FBSS is a rare, recently recognized syndrome in which behavioral variant frontotemporal dementia-like symptoms present in the context of intracranial hypotension, though an unidentified etiology can not be ruled out,¹⁰ and therefore should be included among the causes of potentially reversible cog-

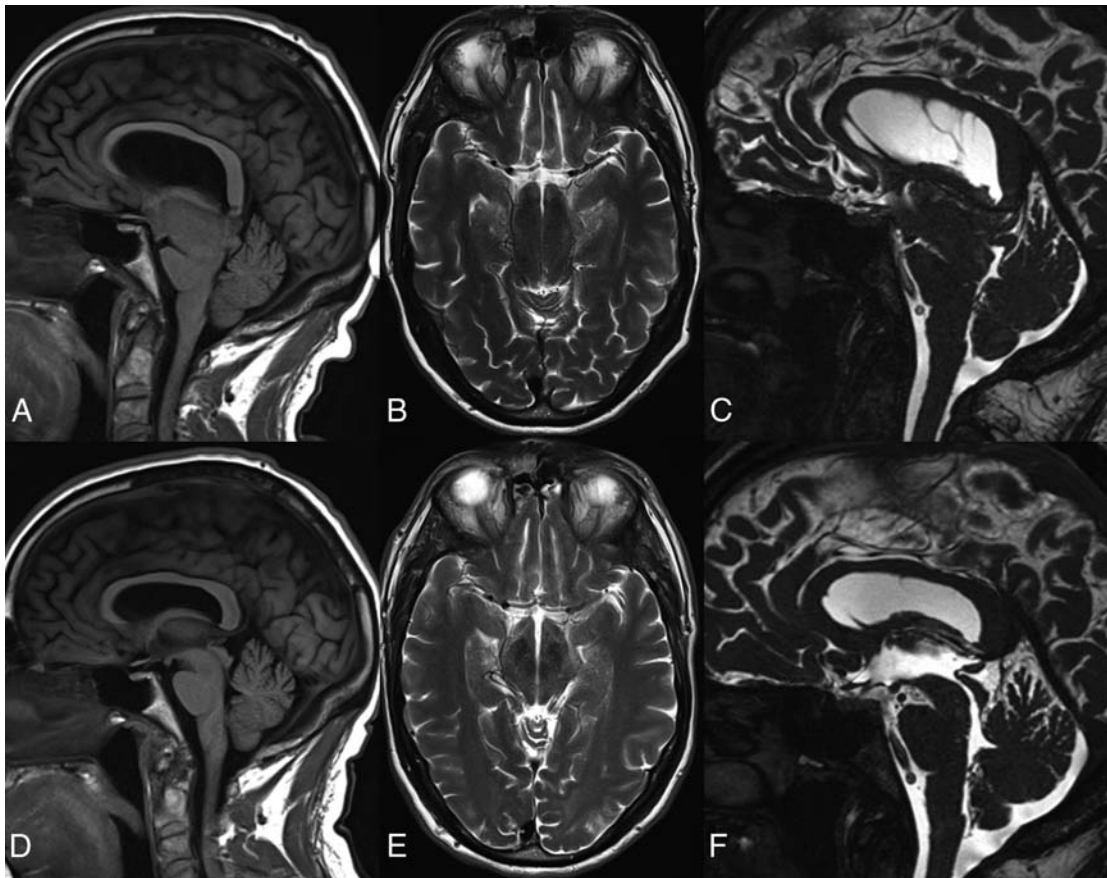


FIG 3. Preoperative (A–C) and postoperative (D–F) sagittal T1 (A and D), axial T2 (B and E), and sagittal CISS (C and F) brain MRI in case 3. Note postoperative resolution of brain sagging and recovery of aqueductal CSF lumen.

nitive impairment. Age of onset and male predominance in FBSS coincide with those in behavioral variant frontotemporal dementia. On imaging, FBSS lacks the typical cortical atrophy seen in frontotemporal dementia, presenting with brain sagging instead.¹⁰ In the few reported cases of neuropathologic examination,¹⁰ including our case 2, no specific neurodegenerative disease was found. We propose that FBSS, with its predominant neurocognitive presentation, should be included in the more inclusive category of atypical SIH.

Apart from cognitive and behavioral deficits, patients with atypical SIH frequently present with gait disturbance, imbalance, dysarthria, dysphagia, daytime somnolence, and movement disorders, which are not typical features of behavioral variant frontotemporal dementia. These clinical manifestations suggest midbrain and/or brain stem involvement, corresponding to the level of brain sagging and anatomic distortion. The frequent association of daytime somnolence in our sample of patients with atypical SIH and in the published series of FBSS¹⁰ points to involvement of the brain stem reticular activation system. In agreement with this notion, reversibility of obtundation from SIH has been highly time-correlated to recovery of a normal intracranial pressure waveform with reactive pupils after intrathecal saline infusion, supporting a mesencephalic level.³ Ataxia and dysarthria likely result from stretching of the superior cerebellar peduncles. Some of the symptoms associated with atypical SIH respond promptly to intrathecal saline infusion, such as the transient gait

improvements noted in our case 3. Half of our patients with atypical SIH presented with involuntary movement disorders including a case of upper limb chorea with negative neuropathologic findings for Huntington disease or other neurodegenerative diseases. Parkinsonism and ataxia with recovery after blood patch were reported in a case of SIH.⁹ Finally, oculomotor abnormalities were also reported in FBSS,¹⁰ though these were not observed in our sample.

The cardinal radiologic feature of SIH is brain sagging at the tentorial incisura, resulting in the following morphologic distortions: approximation of both thalami, caudal displacement of the mammillary bodies with shortened pontomammillary distance, and anteroposterior elongation from lateral compression of the midbrain at the tentorial incisura. The Monro-Kellie doctrine¹⁸ explains the imaging findings of pachymeningeal enhancement (from venous engorgement) and subdural fluid collections as compensatory mechanisms to preserve the homeostasis of intracranial volume in the setting of a CSF volume deficit.¹⁹ Atypical SIH is a more chronic and severe brain sagging syndrome compared with classic SIH, as evidenced by the significantly higher Sagging Index (Fig 2) in the absence of other neuroradiologic differences. Compensatory mechanisms to CSF hypovolemia might become insufficient in such chronic conditions to prevent the observed parenchymal stretching across the tentorial incisura. On the basis of imaging and clinical features, we propose that the anatomic site of involvement in atypical SIH corresponds to the

structures adjacent to the tentorial incisura: the medial thalamus, hypothalamus, midbrain tectum, and upper brain stem.

The main limitation of this study is the low number of patients with atypical SIH, inherent in the rarity of this syndrome and/or its underdiagnosis. Another limitation is the incomplete clinical and imaging follow-up related to the retrospective nature of this study. One patient with atypical SIH was treated with Chiari decompression based on neurosurgical indications, with no clinical improvement. Finally, no systematic information was available on connective tissue anomalies, which could underlie the chronicity and frequent relapses of patients with atypical SIH.

CONCLUSIONS

Atypical SIH, including FBSS, is a complex syndrome that should be included in the category of potentially reversible, treatable causes of dementia. It is therefore paramount to suspect it clinically and to confirm it on brain MR imaging, for which a Sagging Index of ≥ 10 is highly suggestive. Older age and male sex are more common in atypical compared with classic SIH. The longer clinical duration and less favorable outcome of atypical SIH may relate to a weaker dura from an underlying connective tissue anomaly and/or insufficient physiologic adaptation to CSF hypovolemia, leading to parenchymal stretching with brain sagging. The potential for reversibility of symptoms and signs, even in chronic cases with atypical presentation after tamponade of the CSF leak, underscores the relevant role of neuroradiologists in diagnosing and managing SIH.

REFERENCES

1. Schievink WI, Deline CR. **Headache secondary to intracranial hypotension.** *Curr Pain Headache Rep* 2014;18:457 CrossRef Medline
2. Urbach H. **Intracranial hypotension: clinical presentation, imaging findings, and imaging-guided therapy.** *Curr Opin Neurol* 2014;27:414–24 CrossRef Medline
3. Binder DK, Dillon WP, Fishman RA, et al. **Intrathecal saline infusion in the treatment of obtundation associated with spontaneous intracranial hypotension: technical case report.** *Neurosurgery* 2002;51:830–36; discussion 836–37 Medline
4. Pleasure SJ, Abosch A, Friedman J, et al. **Spontaneous intracranial hypotension resulting in stupor caused by diencephalic compression.** *Neurology* 1998;50:1854–57 CrossRef Medline
5. Peng PW. **Intracranial hypotension with severe neurological symptoms resolved by epidural blood patch.** *Can J Neurol Sci* 2004;31:569–71 CrossRef Medline
6. Sayao AL, Heran MK, Chapman K, et al. **Intracranial hypotension causing reversible frontotemporal dementia and coma.** *Can J Neurol Sci* 2009;36:252–56 CrossRef Medline
7. Hong M, Shah GV, Adams KM, et al. **Spontaneous intracranial hypotension causing reversible frontotemporal dementia.** *Neurology* 2002;58:1285–87 CrossRef Medline
8. Walker L, DeMeulemeester C. **Spontaneous intracranial hypotension masquerading as frontotemporal dementia.** *Clin Neuropsychol* 2008;22:1035–53 CrossRef Medline
9. Pakiam AS, Lee C, Lang AE. **Intracranial hypotension with parkinsonism, ataxia, and bulbar weakness.** *Arch Neurol* 1999;56:869–72 CrossRef Medline
10. Wicklund MR, Mokri B, Drubach DA, et al. **Frontotemporal brain sagging syndrome: an SIH-like presentation mimicking FTD.** *Neurology* 2011;76:1377–82 CrossRef Medline
11. Schievink WI. **Misdiagnosis of spontaneous intracranial hypotension.** *Arch Neurol* 2003;60:1713–18 CrossRef Medline
12. Neary D, Snowden JS, Gustafson L, et al. **Frontotemporal lobar degeneration: a consensus on clinical diagnostic criteria.** *Neurology* 1998;51:1546–54 CrossRef Medline
13. Schievink WI, Gordon OK, Tourje J. **Connective tissue disorders with spontaneous spinal cerebrospinal fluid leaks and intracranial hypotension: a prospective study.** *Neurosurgery* 2004;54:65–70; discussion 70–71 CrossRef Medline
14. Schievink WI, Moser FG, Maya MM. **CSF-venous fistula in spontaneous intracranial hypotension.** *Neurology* 2014;83:472–73 CrossRef Medline
15. Mokri B. **Spontaneous CSF leaks: low CSF volume syndromes.** *Neurol Clin* 2014;32:397–422 CrossRef Medline
16. Schievink WI, Morreale VM, Atkinson JL, et al. **Surgical treatment of spontaneous spinal cerebrospinal fluid leaks.** *J Neurosurg* 1998;88:243–46 CrossRef Medline
17. Cummings JL. **Subcortical dementia: neuropsychology, neuropsychiatry, and pathophysiology.** *Br J Psychiatry* 1986;149:682–97 Medline
18. Mokri B. **The Monro-Kellie hypothesis: applications in CSF volume depletion.** *Neurology* 2001;56:1746–48 CrossRef Medline
19. Fishman RA, Dillon WP. **Dural enhancement and cerebral displacement secondary to intracranial hypotension.** *Neurology* 1993;43:609–11 CrossRef Medline

Quantitative Assessment of Circumferential Enhancement along the Wall of Cerebral Aneurysms Using MR Imaging

 S. Omodaka,  H. Endo,  K. Niizuma,  M. Fujimura,  T. Inoue,  K. Sato,  S.-i. Sugiyama, and  T. Tominaga



ABSTRACT

BACKGROUND AND PURPOSE: The incidence of wall enhancement of cerebral aneurysms on vessel wall MR imaging has been described as higher in ruptured intracranial aneurysms than in unruptured intracranial aneurysms, but the difference in the degree of enhancement between ruptured and unruptured aneurysms is unknown. We compared the degree of enhancement between ruptured and unruptured intracranial aneurysms by using quantitative MR imaging measures.

MATERIALS AND METHODS: We performed quantitative analyses of circumferential enhancement along the wall of cerebral aneurysms in 28 ruptured and 76 unruptured consecutive cases by using vessel wall MR imaging. A 3D-T1-weighted fast spin-echo sequence was obtained before and after contrast media injection, and the wall enhancement index was calculated. We then compared characteristics between ruptured and unruptured aneurysms.

RESULTS: The wall enhancement index was significantly higher in ruptured than in unruptured aneurysms (1.70 ± 1.06 versus 0.89 ± 0.88 , respectively; $P = .0001$). The receiver operating characteristic curve analysis found that the most reliable cutoff value of the wall enhancement index to differentiate ruptured from unruptured aneurysms was 0.53 (sensitivity, 0.96; specificity, 0.47). The wall enhancement index remained significant in the multivariate logistic regression analysis ($P < .0001$).

CONCLUSIONS: Greater circumferential enhancement along the wall of cerebral aneurysms correlates with the ruptured state. A quantitative evaluation of circumferential enhancement by using vessel wall MR imaging could be useful in differentiating ruptured from unruptured intracranial aneurysms.

ABBREVIATIONS: CR = contrast ratio; SI = signal intensity; WEI = wall enhancement index

Vessel wall MR imaging with a 3D-T1-weighted FSE sequence has been increasingly used to study intracranial vascular lesions such as atherosclerosis, vasculitis, and aneurysms.¹⁻⁴ Previous reports established a link between ruptured aneurysms and wall enhancement by using qualitative vessel wall MR imaging assessments.^{1,5,6} However wall enhancement was also observed in unruptured aneurysms^{1,6}; thus, we hypothesized that the degree of enhancement is higher in ruptured than in unruptured aneurysms. In this study, we used a quantitative method to compare

the degree of enhancement between ruptured and unruptured intracranial aneurysms by using a 3D-T1WI FSE sequence.

MATERIALS AND METHODS

Study Population and Data Extraction

This study was approved by an institutional review board (Kohnan Hospital). Patient data were extracted from an institutional data base, which includes consecutive patients with surgically treated intracranial aneurysms. We included all patients with intracranial aneurysms surgically treated between December 2013 and May 2015. The exclusion criteria were the following: 1) the absence of preoperative MR imaging or 3D angiography data, 2) an aneurysm of <2 mm or >12 mm, 3) a previously treated aneurysm, 4) insufficient MR imaging quality to evaluate circumferential enhancement along the wall of the aneurysm, 5) a fusiform or partially thrombosed aneurysm, and 6) an unruptured aneurysm complicated by a ruptured aneurysm.

Imaging Protocol

A 3T or 1.5T MR imaging scanner (Signa HDxt; GE Healthcare, Milwaukee, Wisconsin) was used in this study. The vessel wall MR

Received September 29, 2015; accepted after revision January 3, 2016.

From the Departments of Neurosurgery (S.O., H.E.), Neuroendovascular Therapy (K.S.), and Neuroanesthesia (S.-i.S.), Kohnan Hospital, Sendai, Japan; Department of Neurosurgery (K.N., M.F., T.T.), Tohoku University Graduate School of Medicine, Sendai, Japan; and Department of Neurosurgery (T.I.), Sendai Medical Center, Sendai, Japan.

Please address correspondence to Hidenori Endo, MD, PhD, Department of Neurosurgery, Kohnan Hospital, 4-20-1 Nagamachiminami, Taihaku-ku, Sendai, 982-8523, Japan; e-mail: hideendo@gmail.com

 Indicates article with supplemental on-line tables.

<http://dx.doi.org/10.3174/ajnr.A4722>

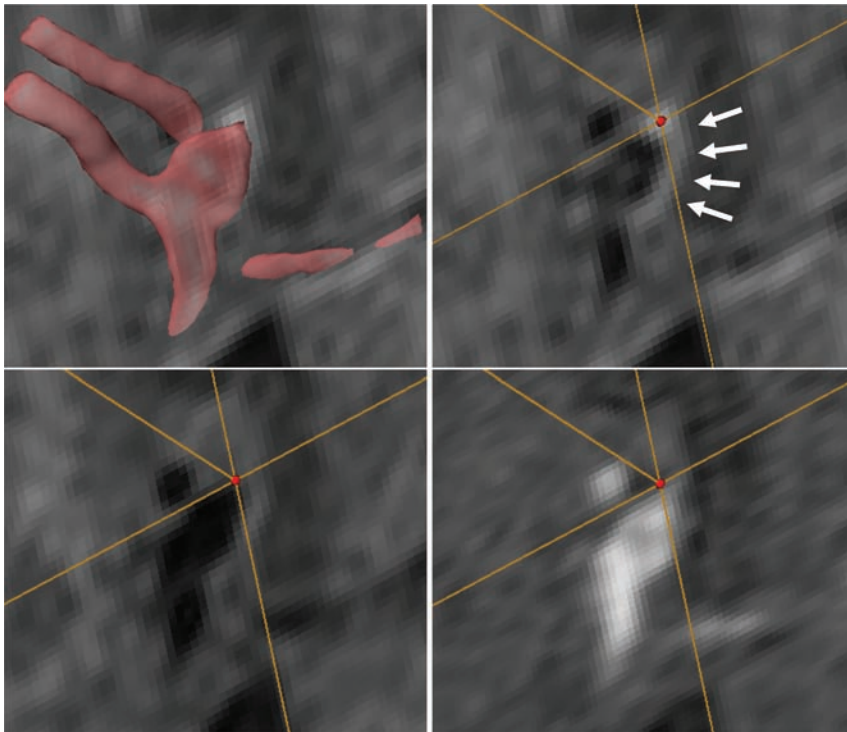


FIG 1. Images from a 40-year-old man with a ruptured anterior communicating artery aneurysm. Transparent volume-rendering of a 3D-TOF imaging is superimposed on an axial section of post-contrast T1WI (upper left). A VOI (red dot) is set on the enhanced aneurysmal wall on matched post- (upper right) and precontrast T1WI (lower left) and TOF (lower right) image. Arrows indicate the circumferential enhancement along the wall of the ruptured aneurysm (upper right).

imaging consisted of the single-slab 3D-T1WI FSE pulse sequence.⁷ We also performed 3D-TOF MR imaging. The acquisition parameters are summarized in On-line Tables 1 and 2. Gadodiamide (Omniscan; GE Healthcare, Piscataway, New Jersey) or gadopentetate dimeglumine (Magnevist; Bayer HealthCare Pharmaceuticals, Wayne, New Jersey) was administered intravenously (0.1 mmol/kg), and the 3D-T1WI FSE sequence was repeated 5 minutes after the contrast material was administered. The voxel data were exported into a personal computer for intensity analysis.

3D rotational angiography was performed by using an Innova 3131 IQ or IGS 630 scanner (GE Healthcare). Rotational angiographic images were obtained during a 200° rotation with imaging at 30 frames/s for 5 seconds. The corresponding 150 projection images were reconstructed into a 3D dataset of 512 × 512 × 512 voxels covering an FOV of 116 mm on a dedicated GE Healthcare Z800 workstation. The aneurysm location was classified as the anterior cerebral arteries, the posterior communicating artery, an internal carotid artery other than posterior communicating artery, a middle cerebral artery, and the posterior circulation, as described previously.⁸ The maximum measurement of aneurysm diameter was used as the aneurysm size.

Measurement of the Aneurysmal Wall Enhancement

Multiplanar oblique reconstructions obtained from pre- and postcontrast 3D-T1WI FSE and 3D-TOF were analyzed after coregistration with Amira 5.3 (www.amira.com). The reviewer was blinded to the clinical data but was aware of the aneurysm location. The circumferential enhancement along the wall of the aneurysm (wall enhancement index [WEI]) was used to charac-

terize the extent of the enhancement. We defined the VOI with the highest signal intensity (SI) as follows: First, we set a cubic VOI (volume of 0.125 mm³) on a visible enhanced region along the aneurysm wall on the 3D-T1WI FSE sequence while we checked the aneurysm configuration referencing the volume-rendering of 3D-TOF imaging. Next, we manually traced the enhanced region by moving the VOI, avoiding surrounding structures, while we checked the SI of the VOI, which was automatically calculated and displayed in real-time. We recorded several values of VOI with high average SI and finally defined the highest average SI from these candidate values. The highest SI within the VOI on the matched pre- and postcontrast images was measured (SI_{wall} ; Figs 1–3). The SI of normal brain parenchyma (SI_{brain}) averaged in a volume of 8.0 mm³ on matched pre- and postcontrast imaging was measured in the right frontal lobe as a reference. The SI of the stalk (SI_{stalk}) averaged in a volume of 1.0 mm³ on matched pre- and postcontrast images was also measured. Then, the WEI was calculated as follows: ($[SI_{wall}/SI_{brain}$ on postcontrast

imaging] – $[SI_{wall}/SI_{brain}$ on matched precontrast imaging]) / (SI_{wall}/SI_{brain} on matched precontrast imaging). The stalk enhancement index was calculated in a similar way. The contrast ratio of the circumference of the aneurysm against the stalk (CR_{stalk}) was calculated as follows: SI_{wall}/SI_{stalk} on postcontrast imaging. In the initial 20 patients, the SI_{wall} , SI_{brain} , and SI_{stalk} on matched pre- and postcontrast imaging were measured by the reviewer again and then by a different reviewer who was also blinded to the clinical data but aware of the aneurysm location for an estimation of intra- and interobserver variability.

Data Analysis

Continuous variables are presented as the mean ± SD, and categorical variables are presented as a number and corresponding percentage. The characteristics of ruptured and unruptured aneurysms were compared with the Student *t* test for continuous variables and the χ^2 or Fisher exact test for categorical variables. A 2-sided *P* value < .05 was considered significant. The cutoff values of variables with the best sensitivity and specificity for differentiating ruptured from unruptured aneurysms were identified by analyzing the receiver operating characteristic curve, and they were used in further analysis. Multivariate logistic regression analysis was performed to determine factors independently associated with ruptured aneurysms, including variables that reached *P* values < .2 in the univariate analysis. To determine the intra- and interobserver variability, we used the intraclass correlation coefficient with a 95% CI to assess the intra- and interobserver variability of the WEI and CR_{stalk} calculations. All statistical analyses were performed

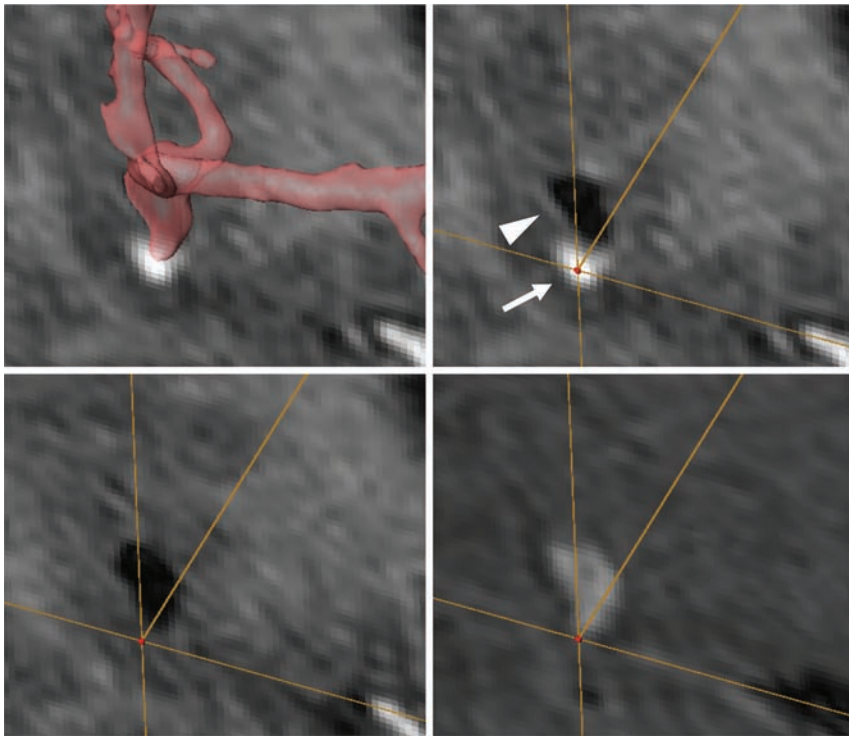


FIG 2. Images from a 52-year-old man with a ruptured left middle cerebral artery aneurysm. Transparent volume-rendering of a 3D-TOF imaging is superimposed on a coronal section of postcontrast TIWI (*upper left*). A VOI (*red dot*) is set on the enhanced aneurysmal wall on matched post- (*upper right*) and precontrast TIWI (*lower left*) and TOF (*lower right*) image. Circumferential enhancement along the wall of the aneurysm (*arrowhead*) was heterogeneous and locally enhanced (*arrow*) around the bleb in this case (*upper right*).

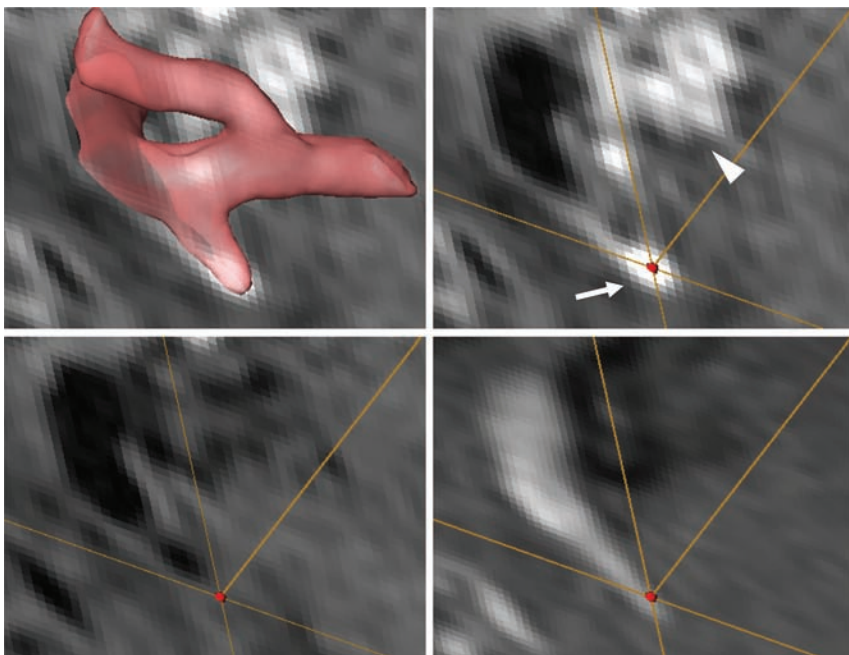


FIG 3. Images from a 55-year-old woman with a ruptured right anterior choroidal artery aneurysm. Transparent volume-rendering of a 3D-TOF imaging is superimposed on an axial section of postcontrast TIWI (*upper left*). A VOI (*red dot*) is set on the enhanced aneurysmal wall on matched post- (*upper right*) and precontrast TIWI (*lower left*) and TOF (*lower right*) image. In addition to the circumferential enhancement along the wall of the aneurysm (*arrow*, *upper right*), the cavernous sinus surrounding the proximal internal carotid artery was also enhanced (*arrowhead*, *upper right*); enhancement of the cavernous sinus is one of the confounding factors in the interpretation of circumferential enhancement along the wall of the aneurysm.

with JMP Pro 10.2 (SAS Institute, Cary, North Carolina) or SPSS Statistics 19.0 (IBM, Armonk, New York).

RESULTS

Of the 171 included patients, 89 were excluded because of the absence of MR imaging or 3D angiographic data ($n = 62$), for having an aneurysm size <2 mm or >12 mm ($n = 12$), for having a previously treated aneurysm ($n = 7$), for insufficient MR imaging quality ($n = 4$), or for the presence of a fusiform aneurysm ($n = 4$). The final study sample included 82 patients with 104 aneurysms (28 ruptured and 76 unruptured). In the ruptured aneurysms, MR imaging was performed on day 0 or 1 from the onset of the rupture in 24 (85.7%), on day 3 or 4 in 3 (10.7%), and on day 13 in 1 (3.6%) patient. All unruptured aneurysms were asymptomatic.

The results of the univariate analysis are summarized in Table 1. The WEI was significantly higher in ruptured than in unruptured aneurysms (1.70 ± 1.06 versus 0.89 ± 0.88 , respectively; $P = .0001$). Among the other clinical variables, age and CR_{stalk} were significantly related to having a ruptured aneurysm. The receiver operating characteristic curves (Fig 4) indicated that the most reliable cutoff values of the WEI and CR_{stalk} to differentiate ruptured and unruptured aneurysms were 0.53 and 0.64, respectively (the areas under the curve were 0.75 and 0.84, respectively). When the cutoff value of the WEI was 0.53, the sensitivity and specificity were 0.96 and 0.47, respectively. When the cutoff value of the CR_{stalk} was 0.64, the sensitivity and specificity were 0.75 and 0.83, respectively. The results of the multivariate analysis are summarized in Table 2. The WEI remained significant in the multivariate analysis (OR, 22.91; 95% CI, 4.59–142.08; $P < .0001$). The intraobserver variability was excellent for the WEI (intraclass correlation coefficient, 0.94; 95% CI, 0.86–0.98) and CR_{stalk} (intraclass correlation coefficient, 0.98; 95% CI, 0.94–0.99). The interobserver variability was also excellent for the WEI (intraclass correlation coefficient, 0.92; 95% CI, 0.81–0.97) and CR_{stalk} (intraclass correlation coefficient, 0.98; 95% CI, 0.95–0.99).

Table 1: Characteristics of ruptured and unruptured intracranial aneurysms^a

Characteristics	Ruptured (n = 28)	Unruptured (n = 76)	P Value
Age (yr)	58.5 ± 11.6	63.8 ± 9.4	.019
Women (No.) (%)	20 (71.4)	60 (79.0)	.439
Aneurysm location (No.) (%)			.087
Anterior cerebral arteries	6 (21.4)	12 (15.8)	
Posterior communicating artery	7 (25.0)	9 (11.8)	
Internal carotid artery other than posterior communicating artery	3 (10.7)	12 (15.8)	
Middle cerebral artery	9 (32.1)	41 (54.0)	
Posterior circulation	3 (10.7)	2 (2.6)	
Aneurysm size (mm)	5.4 ± 2.2	5.4 ± 2.1	.932
MR imaging quantitative measures			
Wall enhancement index	1.70 ± 1.06	0.89 ± 0.88	.0001
Stalk enhancement index	1.61 ± 0.42	1.71 ± 0.36	.214
Contrast ratio against the stalk	0.88 ± 0.40	0.45 ± 0.23	<.0001

^aThe data of continuous variables are mean ± SD.

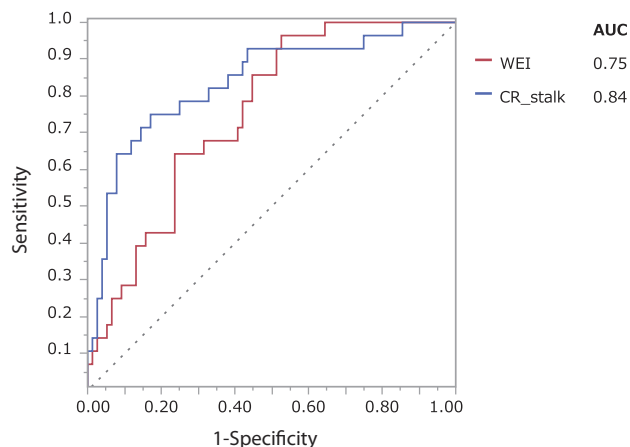


FIG 4. Receiver operating characteristic curves of the wall enhancement index (red) and the contrast ratio against the stalk (blue) in differentiating ruptured from unruptured aneurysms. The areas under the curve for the WEI and CR_{stalk} are 0.75 and 0.84, respectively.

Table 2: Multivariate logistic regression analysis for factors associated with ruptured aneurysms

	P Value	OR (95% CI)
Age < cutoff	.0042	4.94 (1.62–17.85)
Aneurysm location ^a	.0014	6.77 (1.92–19.90)
Wall enhancement index > cutoff	<.0001	22.91 (4.59–142.08)

^aIncluding anterior cerebral arteries, the internal carotid artery other than the posterior communicating artery, and the posterior circulation.

DISCUSSION

Our study used quantitative measures to demonstrate that the degree of circumferential enhancement along the wall of a cerebral aneurysm is significantly higher in ruptured than unruptured aneurysms. To our knowledge, this is the first report that quantitatively analyzes the degree of wall enhancement of cerebral aneurysms by using MR imaging.

Recently, wall enhancement of a cerebral aneurysm has been revealed as a characteristic of ruptured aneurysms by using vessel wall MR imaging. Matouk et al⁵ investigated 5 patients with aneurysmal subarachnoid hemorrhage, including 3 patients with multiple aneurysms. All ruptured aneurysms had wall enhancement, and none of the associated unruptured aneurysms demonstrated this trait. Nagahata et al⁶ investigated the frequency of wall enhancement in 61 ruptured and 83 unruptured aneurysms by

using a 3D-T1WI turbo spin-echo sequence. They classified the wall enhancement into 3 groups: strong, faint, and no enhancement. Strong enhancement of the aneurysm wall, which was defined as equal to that of the choroid plexus or venous plexus, was observed in 73.8% of ruptured aneurysms and in 4.8% of unruptured aneurysms. They found a higher degree of enhancement in ruptured aneurysms compared with unruptured aneurysms. Edjlali et al¹ investigated wall enhancement in 108 aneurysms by using a 3D-T1WI FSE sequence and found that wall enhancement was significantly more frequently observed in unstable (ruptured, symptomatic, or undergoing morphologic modification) than stable (incidental and nonevolving) intracranial aneurysms (87% versus 28.5%, respectively). These reports used qualitative assessments to demonstrate that the wall is frequently enhanced in ruptured aneurysms and infrequently enhanced in unruptured aneurysms.

In the present study, we show that the degree of circumferential enhancement along the wall of the aneurysm is significantly higher in ruptured than unruptured aneurysms by using a 3D-T1WI FSE sequence. In unruptured aneurysms, atherosclerosis, inflammation, and the development of vasa vasorum were thought to be possible mechanisms of this enhancement effect.^{1,9} In ruptured aneurysms, physical disruption and endothelial damage or an inflammatory healing process could explain this enhancement effect.^{5,10} Our results indicated that such mechanisms of enhancement in ruptured aneurysms could be associated with a higher degree of enhancement compared with unruptured aneurysms. Wall enhancement may be an indicator of a ruptured aneurysm, which is useful information for managing patients with subarachnoid hemorrhage, especially those with multiple aneurysms or microaneurysms.^{4,5} In ruptured aneurysms, this enhancement would correspond not to the wall enhancement itself but to enhancement of the interface between aneurysm wall and the surrounding brain tissue. The bleb of the aneurysm, which was likely to be the ruptured site, was locally enhanced in some cases (Fig 2). Thrombus or the platelet plug within or around the ruptured site might be enhanced in these cases. Visualization of the aneurysm wall itself has been attempted by using various magnetic fields from 1.5T to 7T.^{11–13} In these studies, the aneurysm wall thickness showed spatial variation within the aneurysm compared with the wall of the parent artery. The intensity of the wall is equal to the intensity of brain tissue; therefore, it is difficult to achieve complete visualization of the entire wall of the cerebral aneurysm, even by high-resolution MR imaging.¹² These studies would indicate the difficulty of visualizing the aneurysm wall itself. Thus, we describe the enhancement effect of cerebral aneurysms as “circumferential enhancement along the wall.” Further study is needed to prove the exact mechanisms of this enhancement effect.

The quantitative assessment of wall enhancement has been reported for intracranial atherosclerotic lesions by using vessel wall MR imaging.^{14,15} Similarly, we calculated the WEI and applied it to the quantitative assessment of the enhancement effect. Our re-

sults demonstrate that the quantitative assessment of circumferential enhancement along the wall by using a 3D-T1WI FSE sequence could be useful in diagnosing the ruptured aneurysmal state, and the most reliable cutoff value of the WEI for the differentiation of ruptured and unruptured aneurysms was 0.53. Because the SI on MR imaging varies considerably with different parameter settings, this cutoff value itself cannot be generalized. However, this study certainly shows that higher WEIs are closely related to a ruptured state.

Furthermore, the CR_{stalk} was also significantly higher in ruptured than in unruptured aneurysms. The CR_{stalk} was also a reliable measure for the differentiation of ruptured and unruptured aneurysms in the receiver operating characteristic analysis. CR_{stalk} can be obtained only from the postcontrast imaging, while both pre- and postcontrast MR imaging is necessary to calculate WEI. CR_{stalk} can reduce imaging time and would be convenient to use in daily practice. However, attention should be paid to the interpretation of circumferential enhancement along the wall of the aneurysm because of the presence of confounding factors. Vasculature with low blood flow velocity, such as aneurysms with intra-aneurysmal flow stagnation and surrounding veins, could be enhanced and potentially confusing. We excluded aneurysms of >12 mm because this intra-aneurysmal flow stagnation effect would occur in larger aneurysms. In addition, structures adjacent to the aneurysms with strong enhancements, such as the dura and venous sinus, or with high intensity on T1-weighted imaging, such as skull and hematomas, may obscure subtle wall enhancement (Fig 3). Thus, it would be difficult to assess the WEI of paracalcinoid aneurysms, which are located adjacent to the cavernous sinus and skull base dura. Both pre- and postcontrast imaging should be compared to accurately assess wall enhancement of cerebral aneurysms in these confusing situations.

In addition to the above-mentioned tips for the interpretation of a 3D-T1WI FSE sequence, our study has several limitations. First, the sample size was small because this was a single-center study. Second, the findings obtained by MR imaging are without histologic verification because of the difficulty of obtaining specimens from aneurysms. Third, this study focused only on surgically treated patients. This selection bias could explain why the patients with unruptured aneurysms were significantly older and why many more aneurysms were located in the middle cerebral artery. Fourth, we analyzed the data obtained at both 1.5T and 3 T. The signal-to-noise ratio and spatial resolution at 1.5T appeared to be somewhat insufficient for the precise evaluation of minute intramural lesions in the intracranial artery, which was the reason we excluded small aneurysms of <2 mm. The aneurysm wall and its variation in thickness can be more clearly visualized with higher magnetic fields.¹² Finally, we could not assess the causal relationship between circumferential enhancement and aneurysm rupture because of the retrospective design of this study. A prospective study with a larger number of patients using high-resolution MR imaging would provide more evidence for the association we indicated in the present study.

CONCLUSIONS

Our study quantitatively compared the degree of circumferential enhancement along the wall of ruptured and unruptured cerebral aneurysms by using a 3D-T1WI FSE sequence. Patients with

greater enhancement are more likely to have ruptured aneurysms, which is useful information for managing patients with subarachnoid hemorrhage.

Disclosures: Hidenori Endo—UNRELATED: Grants/Grants Pending: KAKENHI (Japan),* Comments: for developing a new intracranial stent (¥4,000,000 [US \$33,784.81]). Kuniyasu Niizuma—UNRELATED: Grants/Grants Pending: Translational Research Network Program from the Japan Agency for Medical Research and Development,* grant-in-aid from the New Energy and Industrial Technology Development Organization,* KAKENHI grants from the Japan Agency for Medical Research and Development,* and an A-STEP grant from the Japan Science and Technology Agency.* *Money paid to the institution.

REFERENCES

1. Edjlali M, Gentric JC, Régent-Rodriguez C, et al. Does aneurysmal wall enhancement on vessel wall MRI help to distinguish stable from unstable intracranial aneurysms? *Stroke* 2014;45:3704–06 CrossRef Medline
2. Natori T, Sasaki M, Miyoshi M, et al. Evaluating middle cerebral artery atherosclerotic lesions in acute ischemic stroke using magnetic resonance T1-weighted 3-dimensional vessel wall imaging. *J Stroke Cerebrovasc Dis* 2014;23:706–11 CrossRef Medline
3. Dieleman N, van der Kolk AG, Zwanenburg JJ, et al. Imaging intracranial vessel wall pathology with magnetic resonance imaging: current prospects and future directions. *Circulation* 2014;130:192–201 CrossRef Medline
4. Endo H, Niizuma K, Fujimura M, et al. Ruptured cerebral microaneurysm diagnosed by 3-dimensional fast spin-echo T1 imaging with variable flip angles. *J Stroke Cerebrovasc Dis* 2015;24:e231–35 CrossRef Medline
5. Matouk CC, Mandell DM, Günel M, et al. Vessel wall magnetic resonance imaging identifies the site of rupture in patients with multiple intracranial aneurysms: proof of principle. *Neurosurgery* 2013; 72:492–96; discussion 496 CrossRef Medline
6. Nagahata S, Nagahata M, Obara M, et al. Wall enhancement of the intracranial aneurysms revealed by magnetic resonance vessel wall imaging using three-dimensional turbo spin-echo sequence with motion-sensitized driven-equilibrium: a sign of ruptured aneurysm? *Clin Neuroradiol* 2014 Oct 21. [Epub ahead of print] Medline
7. Mugler JP 3rd. Optimized three-dimensional fast-spin-echo MRI. *J Magn Reson Imaging* 2014;39:745–67 CrossRef Medline
8. Greving JP, Wermer MJ, Brown RD Jr, et al. Development of the PHASES score for prediction of risk of rupture of intracranial aneurysms: a pooled analysis of six prospective cohort studies. *Lancet Neurol* 2014;13:59–66 CrossRef Medline
9. Portanova A, Hakakian N, Mikulis DJ, et al. Intracranial vasa vasorum: insights and implications for imaging. *Radiology* 2013; 267:667–79 CrossRef Medline
10. Krings T, Mandell DM, Kiehl TR, et al. Intracranial aneurysms: from vessel wall pathology to therapeutic approach. *Nat Rev Neurol* 2011; 7:547–59 CrossRef Medline
11. Matsushige T, Akiyama Y, Okazaki T, et al. Vascular wall imaging of unruptured cerebral aneurysms with a hybrid of opposite-contrast MR angiography. *AJNR Am J Neuroradiol* 2015;36:1507–11 CrossRef Medline
12. Kleinloog R, Korkmaz E, Zwanenburg JJ, et al. Visualization of the aneurysm wall: a 7.0-Tesla magnetic resonance imaging study. *Neurosurgery* 2014;75:614–22; discussion 622 CrossRef Medline
13. Park JK, Lee CS, Sim KB, et al. Imaging of the walls of saccular cerebral aneurysms with double inversion recovery black-blood sequence. *J Magn Reson Imaging* 2009;30:1179–83 CrossRef Medline
14. Qiao Y, Zeiler SR, Mirbagheri S, et al. Intracranial plaque enhancement in patients with cerebrovascular events on high-spatial-resolution MR images. *Radiology* 2014;271:534–42 CrossRef Medline
15. Lou X, Ma N, Ma L, et al. Contrast-enhanced 3T high-resolution MR imaging in symptomatic atherosclerotic basilar artery stenosis. *AJNR Am J Neuroradiol* 2013;34:513–17 CrossRef Medline

Evaluating Permeability Surface-Area Product as a Measure of Blood-Brain Barrier Permeability in a Murine Model

 E.K. Weidman,  C.P. Foley,  O. Kallas,  J.P. Dyke,  A. Gupta,  A.E. Giambone,  J. Ivanidze,  H. Baradaran,  D.J. Ballon, and  P.C. Sanelli



ABSTRACT

BACKGROUND AND PURPOSE: Permeability surface-area product has been suggested as a marker for BBB permeability with potential applications in clinical care and research. However, few studies have demonstrated its correlation with actual quantitative measurements of BBB permeability. Our aim was to demonstrate the correlation of quantitative permeability surface-area product and BBB permeability in a murine model by histologic confirmation.

MATERIALS AND METHODS: Coronal MR imaging was performed on mice treated with mannitol ($n = 6$) for disruption of the BBB and controls treated with saline ($n = 5$). Permeability surface-area product was determined by ROI placement and was compared between saline- and mannitol-treated mice. Correlation was made with contrast-enhancement measurements and immunohistologic-stained sections of tripeptidyl peptidase-1 distribution in mice treated with mannitol and saline followed by injection of a viral vector containing the *CLN2* gene, which directs production of tripeptidyl peptidase-1.

RESULTS: Significantly increased permeability surface-area product was seen in mannitol- compared with saline-treated mice in the whole brain ($P = .008$), MCA territory ($P = .014$), and mixed vascular territories ($P = .008$). These findings were compared with contrast-enhancement measurements of BBB permeability and were correlated with immunohistologic-stained sections demonstrating BBB permeability to a large vector.

CONCLUSIONS: Permeability surface-area product is increased in situations with known disruptions of the BBB, as evidenced by immunologic staining of large-vector passage through the BBB and concordance with contrast-enhancement measurements in a murine model. Quantitative permeability surface-area product has potential as an imaging marker of BBB permeability.

ABBREVIATIONS: ACA = anterior cerebral artery; BBBP = blood-brain barrier permeability; PCA = posterior cerebral artery; PS = permeability surface-area product

Developing a method of measuring BBB permeability is important for investigating the role of BBB disruption in the pathogenesis of many neurovascular diseases. The BBB is a highly regulated interface between the cerebral intravascular space and the brain parenchyma and comprises endothelial cells, astrocyte end-feet, the capillary basement membrane, and pericytes. In

normal conditions, tight junctions between cerebral endothelial cells form a highly selective diffusion barrier that prevents most intravascular solutes from entering the brain.¹ In some neurovascular diseases, these tight junctions are compromised; this compromise leads to increased BBB permeability and a cascade of pathologic events. For example, in stroke, there is increased BBB permeability that contributes to the development of cerebral edema and hemorrhagic transformation following ischemia.^{2,3} Following hemorrhagic stroke, increased BBB permeability due to thrombin activation⁴ and endothelial cell retraction⁵ results in vasogenic edema. In ischemic stroke, lack of adenosine triphosphate and instigation of a neuroinflammatory response with activation of matrix metalloproteinase-9^{6,7} and changes

Received August 19, 2015; accepted after revision December 7.

From the Department of Radiology (E.K.W., C.P.F., O.K., J.P.D., A.G., J.I., H.B., D.J.B., P.C.S.), New York-Presbyterian Hospital, Weill Cornell Medical College, New York, New York; Division of Biostatistics and Epidemiology Department of Healthcare Policy and Research (A.E.G.), Weill Cornell Medical College, New York, New York; and Department of Radiology (P.C.S.), Northwell Health, Manhasset, New York.

D.J. Ballon and P.C. Sanelli are senior authors who contributed equally to this work.

This work was supported by grant 5K23NS058387-02 from the National Institute of Neurological Disorders and Stroke, a component of the National Institutes of Health, to Pina C. Sanelli.

Paper previously presented in its preliminary form at: Eastern Neurological Society Annual Meeting, July 31 to August 3, 2014; Manchester Village, Vermont, and at American Society of Neuroradiology Annual Meeting, April 27, 2015; Chicago, Illinois.

Please address correspondence to Pina C. Sanelli, MD, MPH, FACR, Department of Radiology, Northwell Health, 300 Community Dr, Manhasset, NY 11030; e-mail: psanelli@nshs.edu

 Indicates open access to non-subscribers at www.ajnr.org

<http://dx.doi.org/10.3174/ajnr.A4712>

in aquaporin-4 expression⁸ contribute to a breakdown of homeostatic BBB functions. Increased pressure along the impaired BBB following reperfusion contributes to vasogenic edema and hemorrhage.^{2,3,9,10} Similarly, increased BBB permeability following subarachnoid hemorrhage has also been associated with cerebral edema, delayed cerebral ischemia, and poor clinical outcomes.¹¹⁻¹³

Recently, there have been new advances in imaging BBB permeability. CT perfusion and dynamic contrast-enhanced MR perfusion imaging have been used to evaluate the integrity of the BBB and have been proposed as guides for clinical decision-making in patients with stroke and subarachnoid hemorrhage. Mathematic algorithms based on dynamic contrast enhancement of the brain have been developed to noninvasively quantify BBB permeability. Permeability surface-area product (PS) has been suggested as a promising imaging marker for BBB permeability and measures contrast agent flow through blood vessel walls per unit volume of brain while accounting for the blood flow rate in the vessel and the hematocrit level. PS measurements may better reflect physiologic changes in the BBB compared with traditional contrast-enhancement measurements in the tissue, which measure volume of extracted contrast in the extravascular extracellular space instead of the flow rate across the vessel wall, and thus PS may represent a more accurate assessment of permeability. In the evaluation of the reliability of PS, animal models can provide *in vivo* imaging and histologic correlates of permeability. While several animal models have been developed to measure BBB permeability, many of these models use extravasation of Evans blue dye, radiolabeled markers, or quantitative fluorescence as permeability measures.¹⁴⁻¹⁹ Few models have been developed to test noninvasive quantitative imaging of BBB permeability, such as PS, that can be used in human clinical research and clinical practice.

Here, we propose an experimental murine model for quantitative BBB permeability imaging. The purpose of this study was to correlate quantitative PS with gadolinium-enhancement measurements and histologic confirmation of large-vector passage through the BBB in a murine model with known increase in BBB permeability.

MATERIALS AND METHODS

Animal Preparation and Immunohistologic Staining

Experiments were performed on adult male CD-1 mice (Charles River Laboratories, Wilmington, Massachusetts) weighing 22–24 g as previously published.^{20,21} All animal experiments were approved by our Institutional Animal Care and Use Committee. Mice were divided into 2 groups: mice used for immunohistologic staining and mice used for MR imaging gadolinium-enhancement measurements. Both groups underwent identical preparation with mannitol or saline injection in the same murine model. In brief, both groups underwent a standard procedure for anesthesia induced via isoflurane inhalation. The right external carotid artery was dissected and ligated, and a polyimide endovascular microcatheter was introduced into the lumen of the external carotid artery via small arteriotomy. The catheter was rotated so

that the tip was oriented in the right ICA distal to the carotid bifurcation. Mice studied for immunohistochemical analysis of BBB permeability received, intra-arterially, 750 μL of 25% weight/volume mannitol solution, a hyperosmolar agent known to disrupt the BBB,²² followed after 1 minute by administration of an adeno-associated viral vector containing the *CLN2* gene, known to direct the production of the lysosomal enzyme tripeptidyl peptidase-1, produced as previously published.²³ Tripeptidyl peptidase-1 distribution in the mouse brain, which has been used as a surrogate marker of BBB permeability, was assessed 5 weeks after gene transfer by immunoperoxidase staining of sagittal sections of the brain. Mice studied for MR perfusion analysis had right ICA catheters attached to a syringe mounted on an MR imaging-compatible programmable syringe pump.

MR Imaging Protocol, Postprocessing, and Data Collection

Mice were imaged on a 7T small-animal MR imaging system (BioSpec 70/30 USR; Bruker BioSpin, Billerica, Massachusetts). We examined treatment groups with mannitol injection (750 μL of 25% weight/volume mannitol, $n = 6$) and the control group with saline injection (750 μL , $n = 5$) at a constant flow rate of 1000 $\mu\text{L}/\text{min}$. Two minutes after either mannitol or saline injection, the mice were injected intra-arterially with 750 μL of Gd-DTPA (1:19 dilution in saline of Magnevist; Bayer HealthCare Pharmaceuticals, Wayne, New Jersey) at a rate of 800 $\mu\text{L}/\text{min}$ while we monitored the distributed volume and tissue uptake/washout of the injected agent in real-time by using a FLASH gradient-echo pulse sequence with TR = 25 ms, TE = 3.8 ms, FOV = 25 \times 25 mm, and matrix size = 192 \times 256. One midbrain coronal imaging frame was captured every 3.6 seconds before, during, and after the Gd-DTPA injection.

Postprocessing of the acquired images into permeability surface-area product (milliliter milliliter⁻¹ minute⁻¹, volume of liquid per volume brain per minute) and contrast enhancement were performed by using Olea Sphere 2.2 and 2.3 (Olea Medical, La Ciotat, France). PS is described by the permeability model of St. Lawrence and Lee²⁴ and characterizes contrast agent flow through blood vessel walls per unit volume of brain, providing a quantitative measure of BBB permeability. PS is described by the relationship^{24,25} accounting for the blood flow rate in the vessel (F) and hematocrit level (Hct):

$$PS = -F(1 - Hct) \times \log(1 - E),$$

where F represents cerebral blood flow per unit volume of tissue, corrected for the presence of blood cells with hematocrit (Hct), estimated at 0.45 with average mouse hematocrit reported at 39%–49%,²⁶ and E represents the extraction constant, the fraction of contrast that leaves the intravascular space on the first pass of bolus through the vasculature. PS increases with elevated BBB permeability, representing increased flow of contrast through the leaky BBB. The postprocessing technique was standardized for all subjects with the arterial input function placed at the center of the right ICA in a similar fashion for all mice, with representative arterial enhancement time curves shown in Fig 1.

Contrast enhancement was measured as the area under the tissue density curve and peak enhancement over baseline (peak

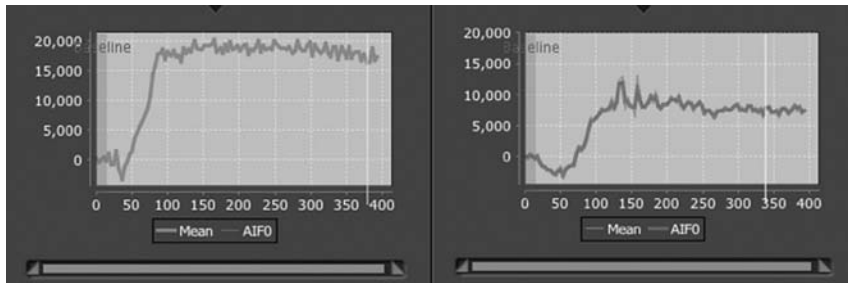


FIG 1. Arterial enhancement time curves in mannitol-treated (*left*) and saline control (*right*) mice.

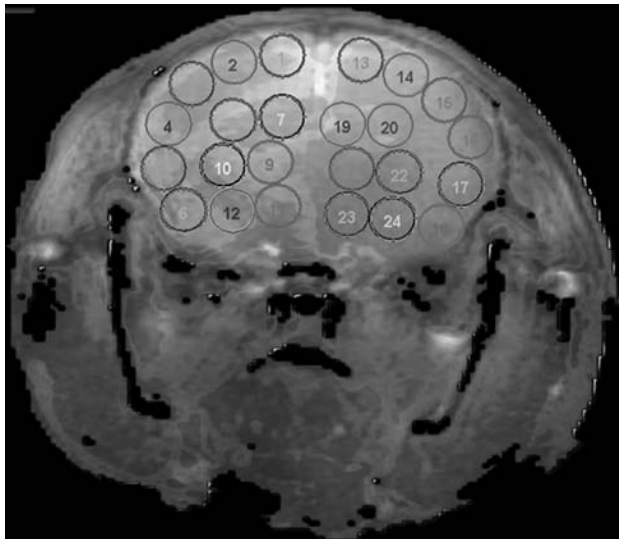


FIG 2. ROI placement on a coronal section of the mouse. ROIs 1–12 are in the injected hemisphere with mirror ROIs 13–24 in the contralateral noninjected hemisphere. ACA (1–2, 13–14), MCA (3–6, 15–18), PCA (7–8, 19–20), and mixed vascular territories (9–12, 21–24) are represented in the image.

enhancement), defined as $(S_1 - S_0)/S_0$, where S_1 is the signal intensity at the time of maximum enhancement and S_0 is the signal intensity at baseline. Contrast-enhancement curves for each vascular territory were generated from representative ROI placement.

Quantitative analysis was conducted by using a standardized method with contiguous ROI placement, measuring 1.0 mm², sampling the cerebral cortex, thalamus, and hypothalamus. Each injected hemisphere had 12 ROIs distributed in the following regions: 2 ROIs in the medial cortex (corresponding to anterior cerebral artery [ACA] territory), 4 ROIs in the lateral cortex (MCA territory), 2 in the hippocampus (posterior cerebral artery [PCA]), and 4 in the thalamic/hypothalamic territory (mixed vascular supply),^{27–29} with mirror ROIs placed in the contralateral control hemisphere (Fig 2).

Statistical Analysis

Quantitative imaging data were analyzed by calculating the mean PS for each ROI for each mouse. Parameter values of zero were excluded from analysis because this exclusion was consistent with noise artifacts. The ratio of the mean PS value of each ROI in the injected hemisphere to the mean PS value of the corresponding ROI in the contralateral-mirrored (noninjected) hemisphere was calculated to further control for noise variance in each ROI value.

The 2 ROIs in the ACA territory were excluded from ratio-based statistical analysis due to the azygous supply of the ACA territory, with expected resultant contamination of mannitol to the contralateral ACA territory.²⁷ Mean ROI ratios for each vascular territory (MCA, PCA, and mixed thalamic/hypothalamic supply) were calculated as well as the mean ROI ratio across all territories for each mouse, generating 1 parameter value per mouse, and were compared

between high-dose mannitol and saline-treated groups by using the nonparametric Wilcoxon rank sum test.

Quantitative gadolinium-enhancement data were analyzed by calculating area under the tissue density curve and peak enhancement over baseline for each ROI. Area under the tissue density curve and peak enhancement were compared with mean PS values for each ROI and PS ratio values (excluding the ACA territory) by using the Spearman rank correlation. Immunohistologic staining was quantified as previously described.²¹ Briefly, color images were converted to gray-scale binary images, and an ROI was drawn around the cerebrum. The relative staining efficiency was determined by calculating the number of stained voxels relative to total number of voxels within the ROI. Staining efficiency for mice treated with mannitol and those treated with saline was compared by using the nonparametric Wilcoxon test. All statistical analyses were performed by a biostatistician by using SAS, Version 9.3 (SAS Institute, Cary, North Carolina).

RESULTS

Twenty-four ROIs were placed on the coronal images of 6 mannitol-treated mice and 5 saline control mice. Only 2 ROIs (ROI 6, MCA territory; and ROI 10, mixed vascular territory) generated PS values of zero in a saline-treated mouse, consistent with generated noise in the image, and were not included in the analysis. No ROIs were excluded in the mannitol-treated mice. When we analyzed the noninjected-hemisphere ROIs (ROIs 13–24), there was no statistically significant difference between mannitol-treated and saline-treated mice in the mean PS ($P = .89$) or PS by vascular territory (ACA, $P = .32$; MCA, $P = .54$; PCA, $P = .38$; mixed vascular territory, $P = .18$) in these hemispheres, confirming that the noninjected sides for both comparison groups were quantitatively similar as would be expected because no intervention occurred in these hemispheres.

Analysis of the injection-side ROIs showed that PS was higher in mannitol-treated mice than in saline-treated mice in all comparisons (Table).

When we compared mean ratios across all ROIs, PS was significantly increased in the mannitol-treated mice ($n = 6$) versus saline control mice ($n = 5$) ($P = .008$). Relative staining efficiency was calculated from immunohistologic-stained slides of mannitol-treated ($n = 3$) and saline-treated ($n = 3$) mice. Statistically significant increased relative staining efficiency was seen in mannitol-treated mice (median, 3.73; interquartile range, 2.15–7.53) versus saline-treated mice (median, 1.13; interquartile range, 0.53–2.73) ($P = .030$).

Comparison of mean ROI ratio (treated hemisphere/contralateral noninjected hemisphere) by hemisphere and vascular territory between mannitol- and saline-treated mice^a

Comparison	Mannitol (n = 6)	Saline (n = 5)	P Value
PS ratio			
Total	6.35 (3.67)	1.32 (0.59)	.008
MCA	3.50 (1.75)	0.99 (0.60)	.014
PCA	8.39 (9.23)	3.42 (1.91)	.315
Mixed	8.18 (6.05)	0.53 (0.30)	.008

^aData are presented as mean (SD).

When we compared vascular territories, a statistically significant increased PS was seen in mannitol-treated versus saline-treated mice in the MCA ($P = .014$) and mixed vascular territories ($P = .008$). We observed a trend toward increased PS in mannitol-treated mice in the PCA territory ($P = .315$) (Fig 3). Due to differences in sectioning, qualitative comparison with the histologic correlate by vascular territories was performed, demonstrating increased vector staining in high-dose mannitol-treated mice in similar vascular territories (Fig 3). Particularly high areas of vector passage and staining were seen in the mixed vascular territory (hypothalamus), MCA territory (striatum and medial cerebral cortex), and PCA territory (superior colliculus).

Contrast-enhancement data and curves were generated for comparison with PS findings (Fig 4). Contrast-enhancement curves and quantitative data represent the contrast extravasation into the extravascular extracellular tissue of the brain. The highest peaks of contrast-enhancement curves were seen in the PCA territory in both mannitol-treated and saline control mice and corresponded to the high absolute PS values measured in these regions. A statistically significant moderate correlation was found between absolute PS with area under the tissue density curve and peak enhancement over baseline separately ($R = 0.61$, $R = 0.58$, $P < .0001$) (Fig 5), as well as between the PS ratio with area under the tissue density curve and peak enhancement over baseline ($R = 0.50$, $R = 0.59$, $P < .0001$).

DISCUSSION

In this study, we have described an experimental mouse model for measuring BBB permeability by using PS derived from MR imaging data. We demonstrated increased PS, a quantitative surrogate imaging measure of BBB permeability that could easily be adapted in clinical care, in the mouse brain with known disruption of the BBB. When we used imaging acquired after the same method of BBB disruption (route, dose, and rate of mannitol delivery) described for large-vector BBB passage, PS was statistically increased in the whole injected hemisphere and particularly in the MCA and mixed vascular territories compared with the control group. These findings correlated with contrast-enhancement measurements and corresponded to the increased transgene expression secondary to large-vector passage in the whole brain as measured by relative staining efficiency. Quantitative measures of blood-brain barrier permeability (BBBP) by using PS offer less inter-reader variability than qualitative assessment alone and have the potential for use in both clinical care and research to evaluate regional and global changes in BBBP with time.

This is the first study, to our knowledge, to evaluate the use of quantitative PS derived from MR imaging data in a murine model with histologically demonstrated increased BBB permeability. Previous studies have reported correlations between other dy-

namic contrast-enhanced MR imaging permeability parameters and histologic or auto-radiographic measures of permeability in animal models. For example, Hoffmann et al¹⁷ demonstrated a correlation between increased permeability measures by using the Patlak model and areas of histologically identified Evans blue extravasation and hem-

orrhage in a rat ischemic stroke model following MCA occlusion. The contrast transfer coefficient has been reported to correlate with increased BBB permeability as measured by auto-radiography in a rat brain tumor model.³⁰ Similarly, our study found increased PS with known BBB disruption, as confirmed by immunohistologic staining. In contrast to models using Evans blue, which measures the volume of dye in the extracellular space, our study parameter PS measured the flow and the leakage (volume) across the BBB. Most important, our study evaluated an imaging marker of BBBP with the potential for use in clinical care and research in humans because it does not require tissue staining and postmortem analyses.

Our sample size allowed us to detect statistically significant differences in quantitative PS between mannitol- and saline-treated mice in the whole injected hemisphere and in the MCA and mixed vascular territories. In addition, our data showed a trend toward increased PS in the PCA territory of mannitol- versus saline-treated mice. With increased sample size, we may also be able to detect a statistically significant difference between the mannitol and saline groups in the PCA territory, which represented the smallest vascular territory included in the analysis, comprising only 2 ROIs per hemisphere. The PCA territory demonstrated the highest PS values in both saline- and mannitol-treated mice, thus requiring a larger sample size to adequately power this subanalysis in our study. Increased enhancement and increased transgene expression were seen in the PCA-supplied superior colliculus and hippocampus on the histologic sections in mannitol-treated mice, corresponding to the high PS values seen in the PCA territory. The finding of increased PS in the PCA territory relative to other territories in both the mannitol- and saline-treated mice may reflect increased vulnerability of the BBB in the PCA territory due to high-pressure injection of saline. This explanation is in keeping with the concept that there is increased susceptibility of cerebrovascular auto-regulatory dysfunction in the PCA territory, as seen in hypertensive encephalopathy with development of interstitial edema.^{31,32}

For this initial study, we analyzed single coronal images that were obtained following BBB disruption in mannitol- or saline-treated mice. Histologic sections of a separate group of mice treated with mannitol or saline were made in the sagittal plane, and we compared coronal imaging findings with sagittal histologic samples. Both groups of mice (mice analyzed by MR imaging and mice analyzed by histologic analysis) were the same murine model comprising 22- to 24-g genetically engineered male CD-1 adult mice from the same laboratory receiving equal amounts of mannitol or saline via an identical intra-arterial injection method, representing replicate mice, so we believe that the comparison between groups is valid. To account for the differences in ana-

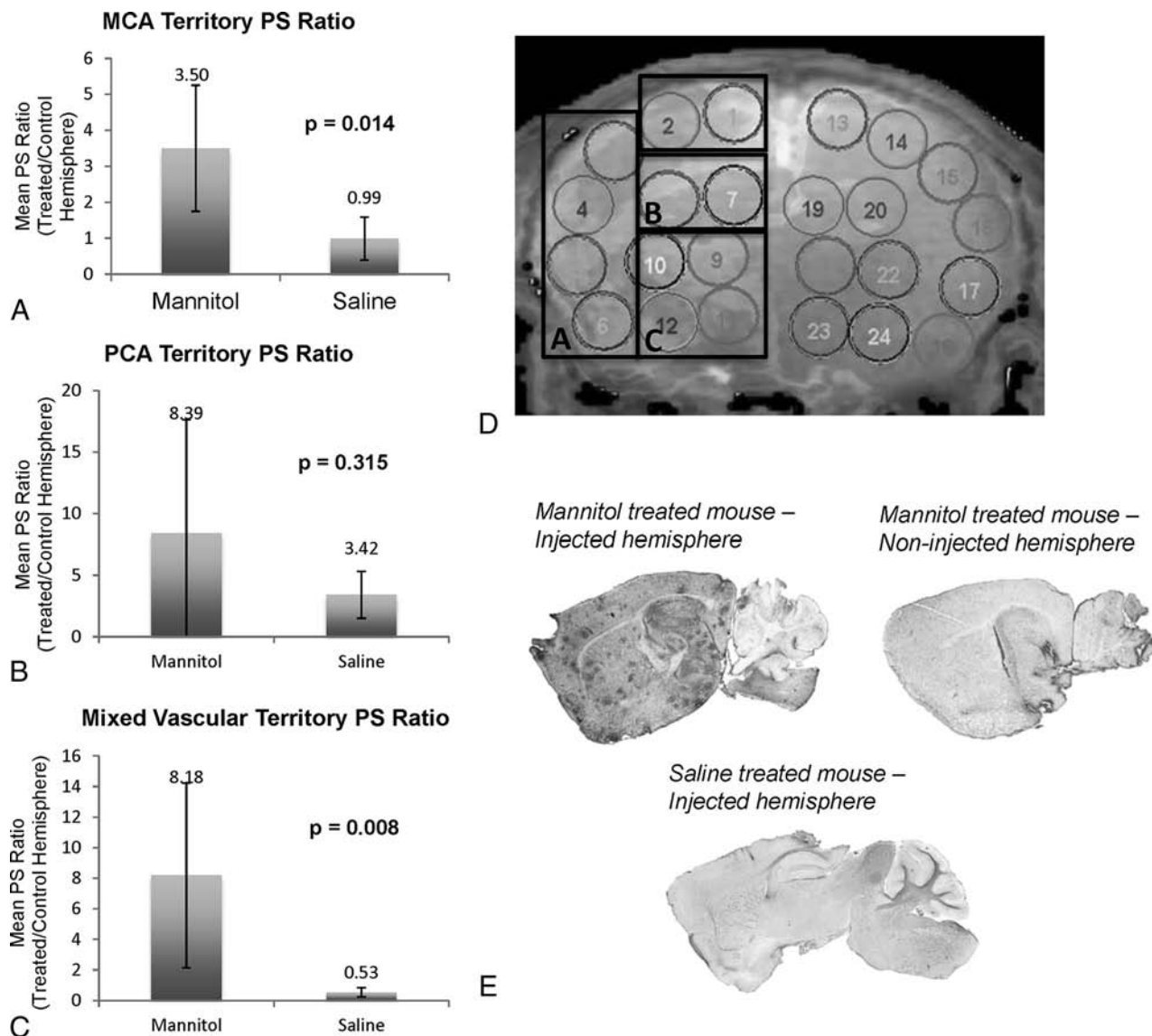


FIG 3. A–C, Mean PS ratio (injected hemisphere/contralateral noninjected hemisphere) per vascular territory in mannitol-treated mice versus saline controls. *Top of the column* represents the mean value, and *error bars* represent the SD. *D*, ROI placement on a representative coronal image. *Boxed areas (A–C)* correspond to vascular territory ROIs for MCA, PCA, and mixed territories, respectively. *E*, Immunoperoxidase staining on a sagittal section of a mannitol-treated mouse in the injected hemisphere, its contralateral noninjected hemisphere, and a saline-injected hemisphere demonstrate the effect of mannitol-mediated BBB disruption on transgene expression. *Darker regions* correspond to increased tripeptidyl peptidase-1 expression.

tomically, we qualitatively compared individual vascular territory and whole-hemispheric brain. We quantitatively measured increased staining efficiency in mice treated with mannitol compared with saline-treated mice, confirming that mannitol opened the blood-brain barrier. We expect that BBB permeability after ICA mannitol injection may vary by vascular territory due to collateral circulation; thus, we believe that this is a valid correlation. However, we acknowledge that the study is somewhat limited by the inability to directly quantitatively compare PS and staining efficiency in the same mouse. It may be further valuable for future studies to compare exact planes and both PS and histologic findings in the same subject in correlating imaging with histologic findings.

In this experimental model, direct intra-arterial injection of mannitol and vector into the right ICA has the potential compli-

cation of focal or global cerebral ischemia. To control for the possible effect of ischemia/infarction on vector passage and tripeptidyl peptidase-1 expression, we compared mannitol-treated mice with mice that were injected in an identical fashion (same rate and total volume) with saline followed by a vector. While the ICA injection pressure that could potentially lead to ischemia/infarction or BBB alterations in these mice is unknown, we believe the saline-treated mice were a valid control for this injection technique. Additionally, no evidence of ischemia or infarction was seen on MR images of the injected mice.

Our model of hyperosmotic mannitol disruption of the BBB resulted in global BBB alteration in this study. Mannitol-induced disruption of the BBB has been reported in other animal models, which demonstrate increased permeability to Evans blue, methotrexate, and the radiolabeled markers carbon 14 sucrose

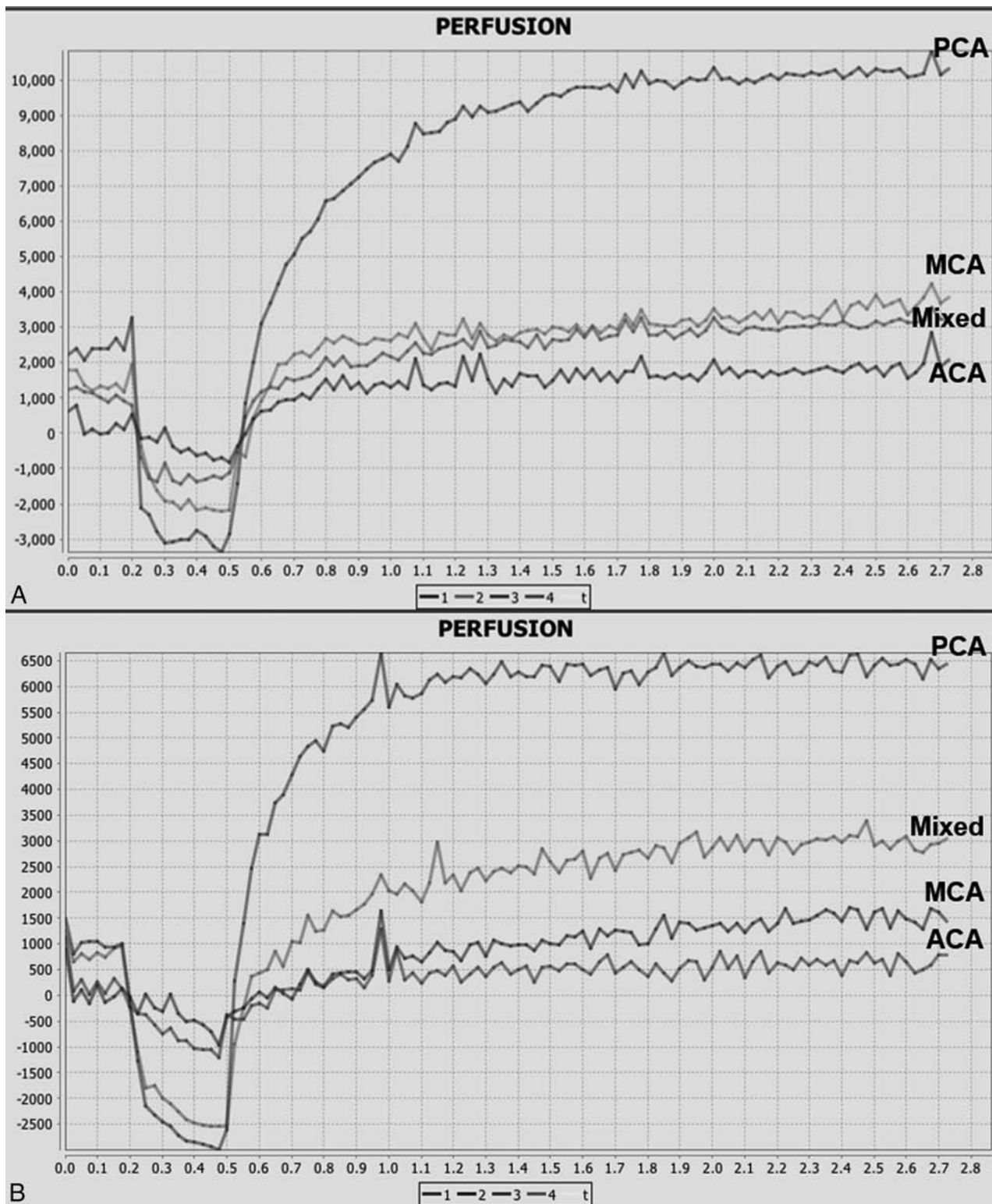


FIG 4. A, Representative contrast-enhancement curves in ROIs corresponding to ACA, MCA, PCA, and mixed vascular territories in a mannitol-treated mouse. B, Representative contrast-enhancement curves in ROIs corresponding to ACA, MCA, PCA, and mixed vascular territories in a saline-treated control mouse.

and rubidium $86^{+19,33}$ and in clinical use for therapeutic delivery in humans.^{34,35} One study by Cosolo et al³³ described methotrexate levels 4–5 times higher following intra-arterial mannitol injection compared with the noninjected hemisphere in rats, in keeping with our total-brain PS comparison between mannitol-

and saline-treated mice. Even though this murine model of global mannitol-induced disruption of the BBB does not directly study specific neurovascular diseases with regional alterations of permeability as seen in stroke and cerebral ischemia, we believe that these findings would be applicable in situations with both

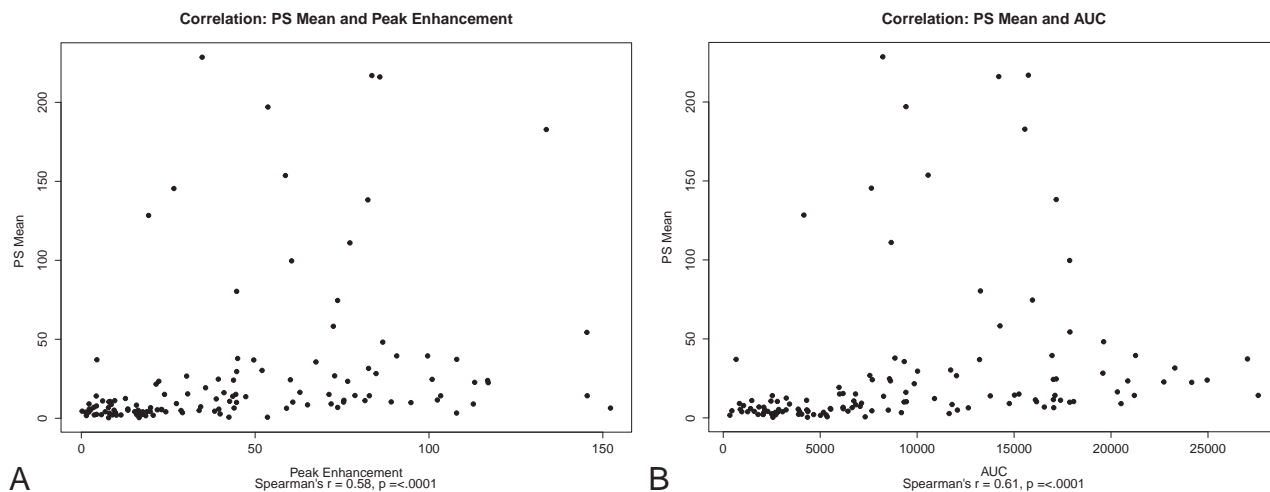


FIG 5. Scatterplots of PS versus contrast-enhancement parameters *A*, PS mean versus peak enhancement. *B*, PS mean versus area under the tissue density curve.

global and regional increased BBBP because we are studying the correlation of increased PS with increased barrier permeability as measured by contrast enhancement and histologic staining, rather than studying the specific underlying pathophysiologic mechanisms leading to the BBB disruption. Additionally, global changes in BBBP have been reported following subarachnoid hemorrhage^{11,12} with global cerebral edema and posttraumatic brain injury. While the aim of this initial proof-of-concept study has been to evaluate PS as a measure of BBBP, our study additionally adds to the literature further evidence of the use of mannitol for global BBBP disruption, which may be helpful in assessing pathologic conditions resulting in global cerebral edema.

We have demonstrated that PS correlates with disruption of the BBB by using Gd-DTPA and histologic staining. These results are accurate for the molecular weight of Gd-DTPA used in this study. We have not assessed other contrast agents of different molecular weights (eg, gadolinium-labeled albumin) in our analyses. Further evaluation of PS, which depends on the extraction constant and cerebral blood flow and hematocrit, with different molecular weights of gadolinium is warranted.

CONCLUSIONS

We have demonstrated the use of quantitative PS derived from MR imaging data as a surrogate imaging measure of BBB permeability in a murine model with gadolinium enhancement and histologic confirmation of increased barrier permeability. This study demonstrates the use of perfusion imaging to produce a quantitative measure of BBB permeability confirmed by histologic analysis, which could be translatable to other animal models of disease. Most important, these findings support the implementation of quantitative PS as a surrogate imaging marker of BBB permeability in future clinical research and, potentially, decision-making in clinical care.

ACKNOWLEDGMENTS

The authors thank Gulce Askin for assistance with this study.

Disclosures: Pina C. Sanelli—RELATED: Grant: National Institute of Neurological Disorders and Stroke (5K23NS058387-02). Conor P. Foley—RELATED: Grant: National Institutes of Health—National Institute of Neurological Disorders and Stroke, Comments: Ruth L. Kirchstein F32 postdoctoral fellowship, F32 NS073397/NS/NINDS NIH HHS/United States; UNRELATED: Patents (planned, pending or issued): Cornell University, Comments: patent for neural drug-delivery technology; Royalties: Cornell University, Comments: royalties on a patent for neural drug-delivery technology. Jana Ivanidze—UNRELATED: Grants/Grants Pending: Radiological Society of North American Resident Research Grant 2014–2015.

REFERENCES

- Ballabh P, Braun A, Nedergaard M. **The blood-brain barrier: an overview: structure, regulation, and clinical implications.** *Neurobiol Dis* 2004;16:1–13 CrossRef Medline
- Lin K, Kazmi KS, Law M, et al. **Measuring elevated microvascular permeability and predicting hemorrhagic transformation in acute ischemic stroke using first-pass dynamic perfusion CT imaging.** *AJNR Am J Neuroradiol* 2007;28:1292–98 CrossRef Medline
- Hom J, Dankbaar JW, Soares BP, et al. **Blood-brain barrier permeability assessed by perfusion CT predicts symptomatic hemorrhagic transformation and malignant edema in acute ischemic stroke.** *AJNR Am J Neuroradiol* 2011;32:41–48 CrossRef Medline
- Xi G, Hua Y, Bhasin RR, et al. **Mechanisms of edema formation after intracerebral hemorrhage: effects of extravasated red blood cells on blood flow and blood-brain barrier integrity.** *Stroke* 2001;32:2932–38 CrossRef Medline
- Satpathy M, Gallagher P, Lizotte-Waniewski M, et al. **Thrombin-induced phosphorylation of the regulatory light chain of myosin II in cultured bovine corneal endothelial cells.** *Exp Eye Res* 2004;79:477–86 CrossRef Medline
- Rosenberg GA, Estrada EY, Dencoff JE. **Matrix metalloproteinases and TIMPs are associated with blood-brain barrier opening after reperfusion in rat brain.** *Stroke* 1998;29:2189–95 CrossRef Medline
- Asahi M, Wang X, Mori T, et al. **Effects of matrix metalloproteinase-9 gene knock-out on the proteolysis of blood-brain barrier and white matter components after cerebral ischemia.** *J Neurosci* 2001;21:7724–32 Medline
- Ribeiro Mde C, Hirt L, Bogousslavsky J, et al. **Time course of aquaporin expression after transient focal cerebral ischemia in mice.** *J Neurosci Res* 2006;83:1231–40 CrossRef Medline
- Unterberg AW, Stover J, Kress B, et al. **Edema and brain trauma.** *Neuroscience* 2004;129:1021–29 Medline
- Strbian D, Durukan A, Pitkonen M, et al. **The blood-brain barrier is**

- continuously open for several weeks following transient focal cerebral ischemia. *Neuroscience* 2008;153:175–81 CrossRef Medline
11. Doczi T. **The pathogenetic and prognostic significance of blood-brain barrier damage at the acute stage of aneurysmal subarachnoid haemorrhage: clinical and experimental studies.** *Acta Neurochir (Wien)* 1985;77:110–32 CrossRef Medline
 12. Germanò A, d'Avella D, Imperatore C, et al. **Time-course of blood-brain barrier permeability changes after experimental subarachnoid haemorrhage.** *Acta Neurochir (Wien)* 2000;142:575–80; discussion 580–81 CrossRef Medline
 13. Sercombe R, Dinh YR, Gomis P. **Cerebrovascular inflammation following subarachnoid hemorrhage.** *Jpn J Pharmacol* 2002;88:227–49 CrossRef Medline
 14. Gotoh O, Asano T, Koide T, et al. **Ischemic brain edema following occlusion of the middle cerebral artery in the rat, I: the time courses of the brain water, sodium and potassium contents and blood-brain barrier permeability to 125I-albumin.** *Stroke* 1985;16:101–09 CrossRef Medline
 15. Belayev L, Busto R, Zhao W, et al. **Quantitative evaluation of blood-brain barrier permeability following middle cerebral artery occlusion in rats.** *Brain Res* 1996;739:88–96 CrossRef Medline
 16. Uyama O, Okamura N, Yanase M, et al. **Quantitative evaluation of vascular permeability in the gerbil brain after transient ischemia using Evans blue fluorescence.** *J Cereb Blood Flow Metab* 1988;8:282–84 CrossRef Medline
 17. Hoffmann A, Bredno J, Wendland MF, et al. **Validation of in vivo magnetic resonance imaging blood-brain barrier permeability measurements by comparison with gold standard histology.** *Stroke* 2011;42:2054–60 CrossRef Medline
 18. Hatashita S, Hoff JT. **Brain edema and cerebrovascular permeability during cerebral ischemia in rats.** *Stroke* 1990;21:582–88 CrossRef Medline
 19. Brown RC, Egleton RD, Davis TP. **Mannitol opening of the blood-brain barrier: regional variation in the permeability of sucrose, but not 86Rb+ or albumin.** *Brain Res* 2004;1014:221–27 CrossRef Medline
 20. Santillan A, Rubin DG, Foley CP, et al. **Cannulation of the internal carotid artery in mice: a novel technique for intra-arterial delivery of therapeutics.** *J Neurosci Methods* 2014;222:106–10 CrossRef Medline
 21. Foley CP, Rubin DG, Santillan A, et al. **Intra-arterial delivery of AAV vectors to the mouse brain after mannitol mediated blood brain barrier disruption.** *J Control Release* 2014;196:71–78 CrossRef Medline
 22. Zünkler B, Carson RE, Olson J, et al. **Quantification and pharmacokinetics of blood-brain barrier disruption in humans.** *J Neurosurg* 1996;85:1056–65 CrossRef Medline
 23. Sondhi D, Hackett NR, Peterson DA, et al. **Enhanced survival of the LINCL mouse following CLN2 gene transfer using the rh.10 rhesus macaque-derived adeno-associated virus vector.** *Mol Ther* 2007;15:481–91 CrossRef Medline
 24. St Lawrence KS, Lee TY. **An adiabatic approximation to the tissue homogeneity model for water exchange in the brain, I: theoretical derivation.** *J Cereb Blood Flow Metab* 1998;18:1365–77 Medline
 25. *Permeability Models: A Review [manual].* La Ciotat, France: Olea Medical
 26. *Reference Values for Laboratory Animals: Normal Hematologic Values.* Research Animal Resources, University of Minnesota. <http://www.ahc.umn.edu/rar/refvalues.html>. Accessed February 25, 2015
 27. Dorr A, Sled JG, Kabani N. **Three-dimensional cerebral vasculature of the CBA mouse brain: a magnetic resonance imaging and micro computed tomography study.** *Neuroimage* 2007;35:1409–23 CrossRef Medline
 28. Watson C, Paxinos G, Puelles L, eds. *The Mouse Nervous System.* Amsterdam: Elsevier Academic Press; 2012:xvii
 29. Lein ES, Hawrylycz MJ, Ao N, et al. **Genome-wide atlas of gene expression in the adult mouse brain.** *Nature* 2007;445:168–76 CrossRef Medline
 30. Ferrier MC, Sarin H, Fung SH, et al. **Validation of dynamic contrast-enhanced magnetic resonance imaging-derived vascular permeability measurements using quantitative autoradiography in the RG2 rat brain tumor model.** *Neoplasia* 2007;9:546–55 CrossRef Medline
 31. Sadoshima S, Fujii K, Yao H, et al. **Regional cerebral blood flow autoregulation in normotensive and spontaneously hypertensive rats: effects of sympathetic denervation.** *Stroke* 1986;17:981–84 CrossRef Medline
 32. Engelter ST, Provenzale JM, Petrella JR. **Assessment of vasogenic edema in eclampsia using diffusion imaging.** *Neuroradiology* 2000;42:818–20 CrossRef Medline
 33. Cosolo WC, Martinello P, Louis WJ, et al. **Blood-brain barrier disruption using mannitol: time course and electron microscopy studies.** *Am J Physiol* 1989;256:R443–47 Medline
 34. Rapoport SI. **Osmotic opening of the blood-brain barrier: principles, mechanism, and therapeutic applications.** *Cell Mol Neurobiol* 2000;20:217–30 CrossRef Medline
 35. Rodriguez A, Tatter SB, Debinski W. **Neurosurgical techniques for disruption of the blood-brain barrier for glioblastoma treatment.** *Pharmaceutics* 2015;7:175–87 CrossRef Medline

Multicenter Prospective Trial of Stent Placement in Patients with Symptomatic High-Grade Intracranial Stenosis

P. Gao, D. Wang, Z. Zhao, Y. Cai, T. Li, H. Shi, W. Wu, W. He, L. Yin, S. Huang, F. Zhu, L. Jiao, X. Ji, A.I. Qureshi, and F. Ling



ABSTRACT

BACKGROUND AND PURPOSE: On the basis of the high 1-month stroke and/or death (14.7%) rates associated with stent placement in the Stenting versus Aggressive Medical Management for Preventing Recurrent Stroke in Intracranial Stenosis trial, modifications in patient selection and procedural aspects for intracranial stent placement have been recommended. We performed a multicenter prospective single-arm trial to determine whether such modifications would result in lower rates of periprocedural stroke and/or death.

MATERIALS AND METHODS: The study enrolled patients with recent transient ischemic attack or ischemic stroke (excluding perforator ischemic events) related to high-grade (70%–99% in severity) stenosis of a major intracranial artery. Patients were treated by using angioplasty and self-expanding stents 3 weeks after the index ischemic event at 1 of the 10 high-volume centers in China. An independent neurologist ascertained the occurrence of any stroke and/or death within 1 month after the procedure.

RESULTS: A total of 100 consecutive patients were recruited. The target lesions were located in the middle cerebral artery (M1) ($n = 38$, 38%), intracranial internal carotid artery ($n = 17$, 17%), intradural vertebral artery ($n = 18$, 18%), and basilar artery ($n = 27$, 27%). The technical success rate of stent deployment with residual stenosis of $<50\%$ was 100%. The overall 1-month stroke and/or death rate was 2% (95% confidence interval, 0.2%–7.0%). Two ischemic strokes occurred in the pontine region (perforator distribution) in patients following angioplasty and stent placement for basilar artery stenosis.

CONCLUSIONS: The results of this prospective multicenter study demonstrated that modifications in patient selection and procedural aspects can substantially reduce the 1-month stroke and/or death rate following intracranial stent placement.

ABBREVIATION: SAMMPRIS = Stenting versus Aggressive Medical Management for Preventing Recurrent Stroke in Intracranial Stenosis

Intracranial atherosclerosis is an important cause of cerebral ischemia with a relatively high prevalence in Chinese patients.¹ The Chinese Intracranial Atherosclerosis study reported a prevalence of intracranial stenosis of 46.6% among 2864 consecutive

Chinese patients with cerebral ischemia.² Patients with ischemic symptoms related to high-grade intracranial stenosis (70%–99%) have an almost 20% risk of recurrent stroke within 1 year despite antithrombotic treatment.³ Therefore, intracranial angioplasty and stent placement have been recommended to reduce the rate of recurrent ischemic events.^{4–7} However, the Stenting versus Aggressive Medical Management for Preventing Recurrent Stroke in Intracranial Stenosis (SAMMPRIS) trial⁸ was prematurely terminated due to excessively high 1-month stroke and/or death rates in patients randomized to intracranial stent placement. At the time of the Data Safety Monitoring review, 14.7% of patients treated with angioplasty combined with stent placement experienced a stroke or died within 1 month after enrollment compared with 5.8% of patients treated with medical therapy alone, a highly

Received August 18, 2015; accepted after revision December 16.

From the Department of Neurosurgery (P.G., F.Z., L.J., X.J., F.L.), Xuanwu Hospital, Capital Medical University, Beijing, China; Department of Neurosurgery (D.W.), Beijing Hospital of the Ministry of Health, Beijing, China; Department of Neurosurgery (Z.Z.), Tangdu Hospital, the Fourth Military Medical University, Xi'an, Shaanxi Province, China; Department of Neurology (Y.C.), the 306 Hospital of the People's Liberation Army, Beijing, China; Department of Intervention (T.L.), Henan Provincial People's Hospital, Zhengzhou, Henan Province, China; Department of Neurosurgery (H.S.), the 1st Affiliated Hospital of Harbin Medical University, Harbin, Heilongjiang Province, China; Department of Neurology (W.W.), Qilu Hospital of Shandong University, Ji'nan, Shandong Province, China; Department of Neurosurgery (W.H.), the 2nd Affiliated Hospital of Guangzhou Medical College, Guangzhou, Guangdong Province, China; Department of Neurosurgery (L.Y.), Tianjin Huanhu Hospital, Tianjin, China; Department of Neurosurgery (S.H.), Guangdong Province Hospital of Traditional Chinese Medicine, Guangzhou, Guangdong Province, China; and Zeenat Qureshi Stroke Institute (A.I.Q.), St. Cloud, Minnesota.

This study was supported by National Health and Family Planning Commission of the People's Republic of China (2011BAI08B04) and the National Natural Science Foundation of China (81200910). This trial been registered and released in ClinicalTrials.gov with the ID NCT01763320.

Please address correspondence to Liqun Jiao, MD, PhD, Department of Neurosurgery, Xuanwu Hospital, Capital Medical University, 45 Changchun St, Beijing 100053, China; e-mail: liqunjiao@sina.cn

Indicates open access to non-subscribers at www.ajnr.org

Indicates article with supplemental on-line tables.

<http://dx.doi.org/10.3174/ajnr.A4698>

Table 1: Inclusion criteria

Criteria
1) Eligible patients between 30 and 80 years of age; intracranial arterial stenosis will not be considered if related to the following: nonatherosclerotic factors: arterial dissection, Moyamoya disease; vasculitic disease; herpes zoster, varicella zoster, or other viral vasculopathies; neurosyphilis; any other intracranial infection; any intracranial stenosis associated with CSF pleocytosis; radiation-induced vasculopathy; fibromuscular dysplasia; sickle cell disease; neurofibromatosis; benign angiopathy of the central nervous system; postpartum angiopathy; suspected vasospastic process; and suspected recanalized embolus
2) Symptomatic intracranial stenosis: presenting with TIA or stroke within the past 12 months attributed to 70%–99% stenosis of a major intracranial artery (internal carotid artery, MCA [M1], vertebral artery, or basilar artery)
3) Degree of stenosis: 70%–99% severity confirmed by catheter angiography for enrollment in the trial
4) Remote infarctions on MRI were acceptable, which could be accounted for by the occlusion of the terminal cortical branches or hemodynamic compromise (perforator strokes excluded); perforator strokes due to perforator occlusion are defined as basal ganglia or brain stem/thalamus infarction related with middle cerebral artery or basilar artery stenosis
5) Expected ability to deliver the stent to the lesion
6) All patients should be treated beyond a duration of 3 weeks from the latest ischemic symptom onset
7) No recent infarctions identified on MRI (indicated as high signals on DWI series) at enrollment
8) No massive cerebral infarction (more than one-half of the MCA territory), intracranial hemorrhage, epidural or subdural hemorrhage, and intracranial brain tumor on CT or MRI
9) mRS score of ≤ 2
10) Target vessel reference diameter must be measured at 2.00–4.50 mm; target area of stenosis is ≤ 14 mm in length
11) No childbearing potential or has a test negative for pregnancy within the week prior to study procedure; female patients had normal menses in the past 18 months
12) Patient is willing and able to return for all follow-up visits required by the protocol
13) Patients understand the purpose and requirements of the study and have signed an informed consent form

significant difference.^{1,9} The 1-month stroke and/or death rate was much higher than the 6.6%, 4.5%, and 6.5% rates in the prospective Stenting of Symptomatic Atherosclerotic Lesions in the Vertebral or Intracranial Arteries (SSYLVA) study,¹⁰ Wingspan study,¹¹ and Apollo Stent for Symptomatic Atherosclerotic Intracranial Stenosis (ASSIST) study,¹² respectively. Possible reasons for the disproportionately high rates of 1-month stroke and/or death included a very short time interval between the index ischemic event and the procedure, lack of stratification by ischemic event type, and less rigorous operator-experience requirements.¹³

The Food and Drug Administration in March 2012 announced that the Wingspan stent system (Stryker Neurovascular, Kalamazoo, Michigan) continues to remain an option for patients with recurrent stroke despite medical management who have not had any new stroke symptoms within 7 days before treatment with the Wingspan. The decision was based on review of the SAMMPRIS trial and the clinical study data supporting humanitarian device exemption approval data, supplemented by the opinions of an advisory panel of experts. The manufacturer, Stryker Neurovascular, was also required to enhance its physician training program for the Wingspan stent. Another expert panel concluded that the SAMMPRIS trial data support modification but not discontinuation of the use of intracranial angioplasty and/or stent placement for intracranial stenosis.¹³ The panel further recommended proceeding with another clinical trial with appropriate modifications in design based on lessons learned from the SAMMPRIS trial to avoid unnecessary elimination of a potentially beneficial treatment in appropriately selected patients.

On the basis of the above-mentioned considerations, a multicenter prospective single-arm trial with independent outcome ascertainment was undertaken to determine whether such modifications will result in lower rates of periprocedural 1-month stroke and/or death in patients treated with intracranial stent placement.

MATERIALS AND METHODS

Patient and Site Selection

The study was an investigator-initiated, government-funded, prospective, multicenter registration trial that was conducted at 10 clinical sites in China. Patients who had experienced a recent TIA or nondisabling ischemic stroke (modified Rankin Scale score, ≤ 2) caused by high-grade stenosis (70%–99% in severity) of a major intracranial artery (middle cerebral artery [M1], intracranial internal carotid artery, intradural vertebral artery, and basilar artery) were eligible. Conventional angiography was used to quantitate the severity of stenosis by using the Warfarin-Aspirin Symptomatic Intracranial Disease Study criterion.³ Patients who had ischemic symptoms within the most recent 3 weeks were excluded. Patients with perforator strokes only were not considered candidates for stent placement. Here, perforator strokes due to perforator occlusion are defined as basal ganglia or brain stem/thalamus infarction related to middle cerebral artery or basilar artery stenosis. The inclusion and exclusion criteria for the trial are provided in Table 1 and On-line Table 1. This study is registered in the ClinicalTrials.gov with ID NCT01763320 (China Angioplasty and Stenting for Symptomatic Intracranial Severe Stenosis).

The 10 participating sites were selected on the basis of the volume of procedures performed. At each site, the annual volume of intracranial angioplasty and stent placement procedures performed was >30 procedures for the past 3 years. At each site, the study team consisted of a neurologist, a neurosurgeon, a neuroradiologist, and a research coordinator. The study protocol was reviewed and approved by a central Data Safety Monitoring Board and subsequently by the local institutional review board. Each patient signed a written informed consent before the procedure. Relevant data were recorded on a standard case reporting form.

Treatment Protocol

The patients were placed on aspirin, 100 mg daily, and clopidogrel, 75 mg daily, for 3–5 consecutive days before the proce-

cedure. The procedure was performed with the patient under general anesthesia in all except 1 case. The case was typically performed via a transfemorally placed 6F-long sheath or guiding catheter. The intracranial stenotic lesion was traversed by using a standard 0.014-inch microcatheter-microguidewire system by using high-magnification fluoroscopic road-mapping techniques. The microcatheter was exchanged over a 300-cm-long 0.014-inch microguidewire for a Gateway angioplasty balloon (Stryker Neurovascular). After angioplasty, the Gateway angioplasty balloon catheter was exchanged over the existing 0.014-inch microguidewire for a self-expanding nitinol Wingspan stent delivery system. In general, the Wingspan stent diameter was 0.5–1.0 mm greater than the target artery and was deployed to extend at least 3 mm on either side of the lesion.¹¹ The Wingspan was deployed across the lesion by using the standard technique of outer containing catheter withdrawal. If the residual stenosis after Wingspan stent deployment was >50% in severity, the study protocol allowed postdilation with a new angioplasty balloon catheter. Technical success was determined by successful placement of the stent across the lesion and residual stenosis of <50% on postprocedural angiography. Throughout the procedure, intravenous heparin boluses were given to maintain the activated clotting time between 250 and 300 seconds.

The protocol required frequent measurements of blood pressure during the procedure and at least 1 measurement every half an hour during the next 24 hours while the patient was monitored in an intensive care unit. The systolic blood pressure was maintained between 100 and 120 mm Hg for 24 hours after the procedure. The patient was continued on aspirin, 100 mg daily, and clopidogrel, 75 mg daily, for the next 90 days and subsequently on aspirin alone. Concurrent risk-factor modification was undertaken, consisting of normalizing low-density lipoprotein (statins, target low-density lipoprotein of <2.58 mmol/L [100 mg/dL]), hypertension (systolic pressure of <140 mm Hg and diastolic pressure of <90 mm Hg), and glycemic status (in patients with diabetes, the hemoglobin A1c level was checked with a target level of <6.5%), and lifestyle modification.¹⁴

End Point Definition and Ascertainment

Primary end points included any stroke and/or death within 1 month. A stroke was defined as a sudden-onset neurologic deficit that persisted for at least 24 hours and could be ischemic or hemorrhagic in nature. Ischemic stroke was further defined as a new focal neurologic deficit that was not associated with an intracranial hemorrhage on brain CT or MR imaging. Hemorrhagic stroke was defined as parenchymal, subarachnoid, or intraventricular hemorrhage detected by CT or MR imaging that resulted in a stroke (as defined above) or seizure. The hemorrhage was classified as asymptomatic if symptoms or signs were temporary (lasted <24 hours) without any seizures.¹⁵ Asymptomatic strokes were considered adverse events but were not included as primary end points.

At each site, the site-designated neurologist who was not part of the treating team ascertained the clinical outcomes within the 1-month follow-up. The neurologist along with the study coordinator performed each follow-up visit and collected the data regarding study end points.

Table 2: Demographic and clinical characteristics of the patients treated in the single-arm trial

Baseline Demographics	
Age (median) (IQR)	56.0 (49–63)
Men (No.) (%)	73 (73%)
Risk factors	
Hypertension (No.) (%)	61 (61%)
Hyperlipidemia (No.) (%)	15 (16%)
Diabetes mellitus (No.) (%)	25 (28%)
History of cigarette smoking (No.) (%)	44 (44%)
History of alcoholism (No.) (%)	28 (28%)
Ischemic stroke as qualifying event (No.) (%)	50 (50%)
NIHSS scores at admission (median) (IQR)	0 (0–1)
mRS scores at admission (median) (IQR)	0 (0–1)
Barthel Index at admission (median) (IQR)	100 (100–100)
Angiographic characteristics	
Preprocedure: average degree of stenosis (%)	82.7 ± 8.9
Location	
Basilar artery	27 (27%)
Intracranial internal carotid artery	17 (17%)
Middle cerebral artery	38 (38%)
Intradural vertebral artery	18 (18%)
Postprocedure: average stenosis (%)	13.5 ± 10.2

Note:—IQR indicates interquartile range.

Statistical Analysis

The statistical methods used were predominantly descriptive. Continuous data were presented as means (with SDs), and categorical data were presented as percentages. For selected percentages, 95% confidence intervals were calculated by using the binomial (Clopper-Pearson) “exact” method.¹⁶

RESULTS

From July 2013 to March 2014, 10 participating sites evaluated 235 consecutive patients with symptomatic high-grade intracranial stenosis or occlusion (70%–100% in severity by angiography). Among them, 135 patients were finally excluded from the study because of the following aspects: 1) Patients did not meet the inclusion criteria; 2) refused to accept endovascular stent placement; and 3) had chronic occlusion of target major intracranial artery. A total of 100 intracranial lesions were treated in 100 enrolled patients (median age, 56 years; 73% were men) (Table 2). All procedures were a combination of angioplasty followed by stent placement performed with the patient under general anesthesia (except 1 case) via the femoral approach. None of the patients required additional postdilation or >1 stent placement. Angioplasty and stent placement were performed in the following locations: 27 (27%) in the basilar artery, 17 (17%) in the intracranial internal carotid artery, 38 (38%) in the middle cerebral artery, and 18 (18%) in the intradural vertebral artery. The technical success rate was 100%. The mean severity of preprocedural stenosis was 82.7% ± 8.9% and postprocedure stenosis was 13.5% ± 10.2% (Table 2).

The overall 1-month stroke and/or death rate was 2% (95% confidence interval, 0.2%–7.0%). Ischemic stroke occurred in the distribution of the perforating arteries (pontine) in 2 patients (On-line Table 2), both of whom had undergone the procedure for high-grade basilar artery stenosis. Both of them had midpontine infarctions on the postprocedure MR imaging. One patient developed hemiparesis and ataxia within 24 hours after the procedure. The other patient developed hemiplegia and facial paral-

ysis (central) 72 hours after the procedure. The patients were treated with anticoagulation and intravenous hypervolemic hemodilution. Both patients had good recovery (mRS of 0 and 1 at 30-day follow-up, respectively). None of the remaining 98 patients had any new neurologic deficits or died within the 30-day visit. No hemorrhagic stroke, myocardial infarction, or severe adverse events were observed in this study.

DISCUSSION

We observed a high technical success rate and low rate of 1-month stroke and/or death in patients with high-grade intracranial stenosis treated with intracranial stent placement within this prospective multicenter study. The study was designed after the completion of the SAMMPRIS trial and incorporated modifications in protocol from observations derived from trial results and subsequent expert recommendations.⁸ Several factors may have contributed to the more favorable short-term results observed within the current study. Restriction of patient recruitment to high-volume centers and modifications in patient selection were probably important factors.

In the SAMMPRIS trial, 220 procedures were performed in 50 sites in the United States during 29 months with an average of <2 procedures at each site per year.⁸ Such recruitment patterns suggest that either familiarity with the protocol or even operator experience differed from that in our study, which treated 30 patients per year at each site on an average. To participate as an interventionalist in the SAMMPRIS trial, the operator was required to demonstrate previous experience with 20 intracranial angioplasty/stent procedures, of which at least 3 procedures were performed with the Wingspan or Neuroform stent system (Stryker Neurovascular).⁸ In the current study, an annual volume of >30 intracranial stent procedures sustained during the past 3 years was required. Our results are comparable with the recent data (1-month stroke and/or death rate of 4.4%–6.2%) derived from some high-volume centers (>100 cases per year).^{17–19} A retrospective analysis of 96 patients treated with intracranial angioplasty and stent placement at 3 university-affiliated institutions in the United States reported that the overall 1-month stroke and/or death rate was 7.2% in the 69 SAMMPRIS-eligible group and 7.4% in the 27 SAMMPRIS-ineligible group.²⁰ The 30-day stroke and/or death rate was 3.3% and 10.2% in the SAMMPRIS-eligible, angioplasty-treated subgroup and the stent-treated subgroup, respectively.

Patient selection, particularly exclusion of patients with recent ischemic events and those with perforating artery ischemic stroke (in specific contrast to SAMMPRIS) may have contributed to the favorable short-term results in our trial. Our trial recruited patients who had experienced an index ischemic event at least 3 weeks before recruitment, which is longer than the recommended 7-day interval (range, 7–19 days) in the SAMMPRIS trial. The longer time interval may have allowed plaque stabilization and spontaneous lysis of overlying thrombus and probably also reduced the risk of hemorrhagic transformation for patients with recent ischemic stroke (<3 weeks).^{17,21–23} An analysis of the National Institutes of Health Multicenter Wingspan Intracranial Stent Registry Study found that stent placement performed within 10 days of a qualifying ischemic event was associated with a higher

rate of 30-day stroke and/or death compared with procedures performed after 10 days (8% versus 17%, $P = .06$).^{21,24} In the SAMMPRIS trial, the rates of ischemic stroke, symptomatic hemorrhagic stroke, or any death within 1 month were 15.7% and 13.8% in the patients enrolled within 7 days or after 7 days of their qualifying event, respectively.¹⁵ Exclusion of patients with recent ischemic stroke may also exclude those with the highest risk of an ischemic event recurrence; therefore, the benefit of stent placement in the reduction of stroke recurrence may also be diminished.

We included patients with distal hypoperfusion and/or cortical involvement. The exclusion of patients with perforating artery ischemic stroke may have reduced the occurrence of this type of stroke postprocedurally.²⁵ However, in a post hoc analysis of the SAMMPRIS trial, the rate of postprocedural ischemic events was not higher among those recruited due to perforating artery ischemic stroke (0%) compared with those with TIAs (8.9%) or nonperforating artery ischemic strokes (14.3%).¹⁵ Certain procedure-related factors such as clopidogrel load ($\approx 10\%$) and poststent angioplasty ($\approx 10\%$) performed in the SAMMPRIS trial were avoided in the current study and may have made some contribution to the differences in adverse event rates.

Two additional aspects that could improve the results of the intracranial angioplasty and stent placement are improvement in device design and point-of-care testing for assessing the magnitude of platelet inhibition with antiplatelet medication. Although the self-expandable Wingspan stent with the over-the-wire technique was widely adapted because of the relative ease of delivery over balloon-expandable stents with the rapid-exchange technique; however, the effectiveness of the self-expanding stent in restoring lumen diameter and preventing restenosis has been questioned. Although the radial force exerted by the Wingspan is superior to that of other self-expandable stents such as the Enterprise (Codman & Shurtleff, Raynham, Massachusetts) and Neuroform stents, it is not comparable with that of balloon-expanding stents. A new generation of balloon-expanding stents with a rapid-exchange platform may result in superior technical results. We did not perform point-of-care testing to guide antiplatelet treatment in our cohort of patients. Point-of-care testing was introduced because considerable differences can be observed within individuals in regard to platelet inhibition with the same doses of aspirin and clopidogrel.²⁶ Such assessment may allow the use of higher doses of clopidogrel and intravenous glycoprotein IIb/IIIa inhibitors among those with inadequate response (resistance) to standard doses of antiplatelet medication.

The low rate of adverse events following intracranial angioplasty and stent placement in our trial raises the question of the superiority of such a procedure over intense medical treatment for high-grade symptomatic intracranial stenosis. Intensive medical therapy in the SAMMPRIS trial consisting of aspirin, 325 mg/day, for entire follow-up; clopidogrel, 75 mg per day for 90 days after enrollment; and aggressive risk-factor management (targeting blood pressure <130/80 mm Hg and low-density lipoprotein concentration of <70 mg/dL) had reduced the 30-day stroke and/or death rate to 5.8%, which was substantially lower than the estimated rate of 10.7% based on historical controls.⁸

Chaudhry et al²⁷ reported that a $\leq 3.8\%$ 1-month rate of stroke and/or death was required to achieve a 35% relative risk reduction of the primary end point (composite of 1-month stroke and/or death and ipsilateral stroke beyond 1 month) among the intracranial stent-treated group compared with the medically treated group at 1-year follow-up, as specified by the superiority threshold within the SAMMPRIS hypothesis.

One of the limitations in our study was the restrictions posed by sample size. We provided the 95% confidence interval values to provide quantitative assessment of the precision of the estimate. Although the current 1-month stroke and/or death rates seen following intracranial stent placement are encouraging, our study does not provide any information regarding the long-term results in regard to both clinical events and restenosis. Based on the results of the current study, the China Angioplasty and Stenting for Symptomatic Intracranial Severe Stenosis trial has been initiated and is an ongoing, prospective, multicenter randomized trial, which is being conducted in 8 sites intending to recruit 380 subjects (stent placement, 190; medical treatment alone, 190).²⁸ The study aims to demonstrate a 10.7% absolute reduction in ipsilateral stroke and/or death during 12 months (assuming an event rate of 18% for medically treated patients³ and 7.3% for stent-treated patients¹⁹). The sample size provides 80% power with a 2-sided test at the 5% level of significance and provides a 20% rate of lost follow-up.

CONCLUSIONS

The results of this prospective multicenter study demonstrated the outcome with safety in patients treated with Wingspan stent within 30 days, which suggested operators' experience at high-volume sites and strict patient selection are critical in reducing periprocedural complications and events.

APPENDIX

Principal investigators: L. Jiao, F. Ling, D. Wang

Participating clinical centers:

- 1) Xuanwu Hospital, Capital Medical University, Beijing: F. Ling, L. Jiao, P. Gao, F. Zhu, Y. Wang, Z. Wang, Y. Lu
- 2) Tangdu Hospital, Fourth Military Medical University, Xi'an: Z. Zhao, J. Yu
- 3) The 306 Hospital of the People's Liberation Army, Beijing: Y. Cai, Y. Cui
- 4) Henan Provincial People's Hospital, Zhengzhou: T. Li, L. Zhu, Z. Feng, Y. He
- 5) The 1st Affiliated Hospital of Harbin Medical University, Harbin: H. Shi, S. Xu, B. Zheng
- 6) Qilu Hospital of Shandong University, Ji'nan: W. Wu, S. Yin
- 7) The 2nd Affiliated Hospital of Guangzhou Medical College, Guangzhou: W. He, Y. He, S. Pu, B. Long
- 8) Tianjin Huanhu Hospital, Tianjin: L. Yin
- 9) Guangdong Province Hospital of Traditional Chinese Medicine, Guangzhou: S. Huang
- 10) Beijing Hospital of the Ministry of Health of China, Beijing: D. Wang, J. Liu.

REFERENCES

1. Wong KS, Li H. **Long-term mortality and recurrent stroke risk among Chinese stroke patients with predominant intracranial atherosclerosis.** *Stroke* 2003;34:2361–66 CrossRef Medline
2. Wang Y, Zhao X, Liu L, et al; CICAS Study Group. **Prevalence and outcomes of symptomatic intracranial large artery stenoses and occlusions in China: the Chinese Intracranial Atherosclerosis (CICAS) study.** *Stroke* 2014;45:663–69 CrossRef Medline
3. Chimowitz MI, Lynn MJ, Howlett-Smith H, et al; Warfarin-Aspirin Symptomatic Intracranial Disease Trial Investigators. **Comparison of warfarin and aspirin for symptomatic intracranial arterial stenosis.** *N Engl J Med* 2005;352:1305–16 CrossRef Medline
4. Fiorella D, Levy EI, Turk AS, et al. **US multicenter experience with the Wingspan stent system for the treatment of intracranial atherosclerotic disease: periprocedural results.** *Stroke* 2007;38:881–87 CrossRef Medline
5. Cruz-Flores S, Diamond AL. **Angioplasty for intracranial artery stenosis.** *Cochrane Database Syst Rev* 2006;CD004133 Medline
6. Ma N, Mo DP, Gao F, et al. **Endovascular recanalization for chronic symptomatic middle cerebral artery total occlusion.** *J Neurointerv Surg* 2013;5:e15 CrossRef Medline
7. Aghaebrahim A, Jovin T, Jadhav AP, et al. **Endovascular recanalization of complete subacute to chronic atherosclerotic occlusions of intracranial arteries.** *J Neurointerv Surg* 2014;6:645–48 CrossRef Medline
8. Chimowitz MI, Lynn MJ, Derdeyn CP, et al; SAMMPRIS Trial Investigators. **Stenting versus aggressive medical therapy for intracranial arterial stenosis.** *N Engl J Med* 2011;365:993–1003 CrossRef Medline
9. Derdeyn CP, Chimowitz MI, Lynn MJ, et al; Stenting and Aggressive Medical Management for Preventing Recurrent Stroke in Intracranial Stenosis Trial Investigators. **Aggressive medical treatment with or without stenting in high-risk patients with intracranial artery stenosis (SAMMPRIS): the final results of a randomised trial.** *Lancet* 2014;383:333–41 CrossRef Medline
10. SSYL VIA Study Investigators. **Stenting of Symptomatic Atherosclerotic Lesions in the Vertebral or Intracranial Arteries (SSYL VIA): study results.** *Stroke* 2004;35:1388–92 CrossRef Medline
11. Bose A, Hartmann M, Henkes H, et al. **A novel, self-expanding, nitinol stent in medically refractory intracranial atherosclerotic stenoses: the Wingspan study.** *Stroke* 2007;38:1531–37 CrossRef Medline
12. Jiang WJ, Xu XT, Jin M, et al. **Apollo stent for symptomatic atherosclerotic intracranial stenosis: study results.** *AJNR Am J Neuroradiol* 2007;28:830–34 Medline
13. Qureshi AI, Al-Senani FM, Husain S, et al. **Intracranial angioplasty and stent placement after stenting and aggressive medical management for preventing recurrent stroke in intracranial stenosis (SAMMPRIS) trial: present state and future considerations.** *J Neuroimaging* 2012;22:1–13 CrossRef Medline
14. Kernan WN, Ovbiagele B, Black HR, et al; American Heart Association Stroke Council, Council on Cardiovascular and Stroke Nursing, Council on Clinical Cardiology, and Council on Peripheral Vascular Disease. **Guidelines for the prevention of stroke in patients with stroke and transient ischemic attack: a guideline for healthcare professionals from the American Heart Association/American Stroke Association.** *Stroke* 2014;45:2160–236 CrossRef Medline
15. Fiorella D, Derdeyn CP, Lynn MJ, et al; SAMMPRIS Trial Investigators. **Detailed analysis of periprocedural strokes in patients undergoing intracranial stenting in Stenting and Aggressive Medical Management for Preventing Recurrent Stroke in Intracranial Stenosis (SAMMPRIS).** *Stroke* 2012;43:2682–88 CrossRef Medline
16. DasGupta A, Cai TT, Brown LD. **Interval estimation for a binomial proportion.** *Statist Sci* 2001;16:101–33 CrossRef
17. Miao Z, Song L, Liebeskind DS, et al. **Outcomes of tailored angioplasty and/or stenting for symptomatic intracranial atherosclerosis: a prospective cohort study after SAMMPRIS.** *J Neurointerv Surg* 2015;7:331–35 CrossRef Medline
18. Jiang WJ, Cheng-Ching E, Abou-Chebl A, et al. **Multicenter analysis**

- of stenting in symptomatic intracranial atherosclerosis. *Neurosurgery* 2012;70:25–30; discussion 31 CrossRef Medline
19. Jiang WJ, Yu W, Du B, et al. **Outcome of patients with $\geq 70\%$ symptomatic intracranial stenosis after Wingspan stenting.** *Stroke* 2011; 42:1971–75 CrossRef Medline
 20. Siddiq F, Chaudhry SA, Khatri R, et al. **Rate of postprocedural stroke and death in SAMMPRIS trial-eligible patients treated with intracranial angioplasty and/or stent placement in practice.** *Neurosurgery* 2012;71:68–73 CrossRef Medline
 21. Nahab F, Lynn MJ, Kasner SE, et al; NIH Multicenter Wingspan Intracranial Stent Registry Study Group. **Risk factors associated with major cerebrovascular complications after intracranial stenting.** *Neurology* 2009;72:2014–19 CrossRef Medline
 22. Chaturvedi S, Dumont AS. **The learning curve for neuroendovascular procedures: how important is it?** *Neurology* 2009;72:1974–75 CrossRef Medline
 23. Derdeyn CP, Fiorella D, Lynn MJ, et al; Stenting and Aggressive Medical Management for Preventing Recurrent Stroke in Intracranial Stenosis Trial Investigators. **Mechanisms of stroke after intracranial angioplasty and stenting in the SAMMPRIS trial.** *Neurosurgery* 2013;72:777–95; discussion 795 CrossRef Medline
 24. Zaidat OO, Klucznik R, Alexander MJ, et al; NIH Multi-center Wingspan Intracranial Stent Registry Study Group. **The NIH registry on use of the Wingspan stent for symptomatic 70–99% intracranial arterial stenosis.** *Neurology* 2008;70:1518–24 CrossRef Medline
 25. Abou-Chebl A, Steinmetz H. **Critique of “Stenting versus aggressive medical therapy for intracranial arterial stenosis” by Chimowitz et al in the New England Journal of Medicine.** *Stroke* 2012;43:616–20 CrossRef Medline
 26. Hussein HM, Emiru T, Georgiadis AL, et al. **Assessment of platelet inhibition by point-of-care testing in neuroendovascular procedures.** *AJNR Am J Neuroradiol* 2013;34:700–06 CrossRef Medline
 27. Chaudhry SA, Watanabe M, Qureshi AI. **The new standard for performance of intracranial angioplasty and stent placement after Stenting versus Aggressive Medical Therapy for Intracranial Arterial Stenosis (SAMMPRIS) trial.** *AJNR Am J Neuroradiol* 2011;32: E214 CrossRef Medline
 28. Gao P, Zhao Z, Wang D, et al. **China Angioplasty and Stenting for Symptomatic Intracranial Severe Stenosis (CASSISS): a new, prospective, multicenter, randomized controlled trial in China.** *Interv Neuroradiol* 2015;21:196–204 CrossRef Medline

Endovascular Management of Tandem Occlusion Stroke Related to Internal Carotid Artery Dissection Using a Distal to Proximal Approach: Insight from the RECOST Study

G. Marnat, I. Mourand, O. Eker, P. Machi, C. Arquizan, C. Riquelme, X. Ayrygnac, A. Bonafé, and V. Costalat



ABSTRACT

BACKGROUND AND PURPOSE: Internal carotid artery dissection is a common cause of stroke in young adults. It may be responsible for tandem occlusion defined by a cervical steno-occlusive carotid wall hematoma associated with an intracranial large-vessel stroke. Intravenous thrombolysis is associated with a poor clinical outcome in these cases, and endovascular treatment has not been specifically evaluated to date. Our aim was to evaluate endovascular treatment technical and clinical efficiency in this specific occlusion topography, in comparison with treatment of isolated anterior circulation stroke.

MATERIALS AND METHODS: As part of our ongoing prospective stroke data base started in August 2009 (Prognostic Factors Related to Clinical Outcome Following Thrombectomy in Ischemic Stroke [RECOST] Study), we analyzed all carotid artery dissection tandem occlusion strokes and isolated anterior circulation occlusions. All patients were selected for endovascular treatment according to clinical-radiologic mismatch, NIHSS ≥ 7 and DWI-ASPECTS ≥ 5 , within 6 hours after onset. For carotid artery dissection, the revascularization procedure consisted first of distal recanalization by a stent retriever in the intracranial vessel. Following assessment of the circle of Willis, internal carotid artery stent placement was only performed in case of insufficiency. Carotid artery dissection treatment efficacy, safety, and clinical outcome were compared with the results of the isolated anterior circulation occlusion cohort.

RESULTS: Two hundred fifty-eight patients with an anterior circulation stroke were analyzed, including 57 with tandem occlusions (22%); among them, 20 were carotid artery dissection–related occlusions (7.6%). The median age of patients with tandem occlusions with internal carotid dissection was 52.45 versus 66.85 years for isolated anterior circulation occlusion ($P < .05$); the mean initial NIHSS score was 17.53 ± 4.11 versus 17.55 ± 4.8 ($P = .983$). The median DWI-ASPECTS was 6.05 versus 6.64 ($P = .098$), and the average time from onset to puncture was 4.38 for tandem occlusions versus 4.53 hours in isolated anterior circulation occlusion ($P = .704$). Complication rates and symptomatic intracranial hemorrhage were comparable in both groups (5% versus 3%, $P = .49$). The duration of the procedure was significantly prolonged in case of tandem occlusion (80.69 versus 65.45 minutes, $P = .030$). Fourteen patients with carotid artery dissection (70%) had a 3-month mRS of ≤ 2 , without a significant difference from patients with an isolated anterior circulation occlusion (44%, $P = .2$). Only 5 carotid artery dissections (25%) necessitated cervical stent placement. No early ipsilateral stroke recurrence was recorded, despite the absence of stent placement in 15 patients (75%) with carotid artery dissection.

CONCLUSIONS: Mechanical endovascular treatment of carotid artery dissection tandem occlusions is safe and effective compared with isolated anterior circulation occlusion stroke therapy. Hence, a more conservative approach with stent placement only in cases of circle of Willis insufficiency may be a reliable and safe strategy.

ABBREVIATIONS: ICD = internal carotid artery dissection; IOAC = isolated occlusion of the anterior circulation; IVT = intravenous thrombolysis

Internal carotid artery dissection (ICD) appears to be a common and increasingly diagnosed cause of ischemic stroke. It represents up to 20%–25% of stroke etiology in young adults¹ and is the most common cause in patients younger than 55 years of age. ICD

is the consequence of a mural hematoma in the arterial wall, with separation of the intima from the media. The ischemic mechanism consists mainly of an internal carotid obstacle associated with intracranial clot migration, resulting in a so-called tandem occlusion.² Rarely, ICD may also be responsible for a hemody-

Received August 13, 2015; accepted after revision January 3, 2016.

From the Department of Interventional and Diagnostic Neuroradiology (G.M.), Bordeaux University Hospital, Bordeaux, France; and Departments of Neurology (I.M., C.A., X.A.) and Interventional and Diagnostic Neuroradiology (O.E., P.M., C.R., A.B., V.C.), Montpellier University Hospital, Montpellier, France.

Please address correspondence to Gaultier Marnat, MD, Service de Neuroradiologie Diagnostique et Interventionnelle, Hopital Pellegrin, CHU de Bordeaux, Place Amélie Raba-Léon, 33000 Bordeaux, France; e-mail: gaultier.marnat@chu-bordeaux.fr

<http://dx.doi.org/10.3174/ajnr.A4752>

namic stroke due to ICA lumen narrowing without intracranial occlusion in case of circle of Willis insufficiency. This last rare presentation was not addressed in the present study.

ICD with tandem occlusion represents a stroke subtype associated with a poor prognosis.^{3,4} Intravenous thrombolysis (IVT)⁵ is associated with poor recanalization rates and poor clinical outcomes.^{1,3} Several published series have reported very low recanalization rates in tandem occlusions, from 8% to 9% during the first 2 hours^{6,7} after thrombolytic drug infusion to 31% in the next 24–72 hours.⁴

Endovascular treatment is now increasingly considered and performed, especially following the results from randomized controlled trials (Multicenter Randomized Clinical trial of Endovascular Treatment for Acute Ischemic Stroke in the Netherlands [MR CLEAN], Endovascular Treatment for Small Core and Proximal Occlusion Ischemic Stroke [ESCAPE], Extending the Time for Thrombolysis in Emergency Neurological Deficits–Intra-Arterial [EXTEND-IA], Endovascular Revascularization With Solitaire Device Versus Best Medical Therapy in Anterior Circulation Stroke Within 8 Hours [REVASCAT], and Solitaire With the Intention for Thrombectomy as Primary Endovascular Treatment [SWIFT PRIME]),^{8–12} which demonstrated the superiority of combined strategies versus stand-alone intravenous treatments in large-vessel occlusion stroke. The particular, but not rare, tandem occlusion stroke subtype is still poorly explored. Despite promising results reported in the literature,^{13–22} most of the larger trials available on thrombectomy previously cited^{23–25} excluded ICD. As a result, to date there has been only limited evidence predominantly using a first-generation device for mechanical thrombectomy^{26,27} and mixing tandem occlusion associated with ICD and ICA atheromatous stenosis. The aim of this study was to report the experience of our center in ICD tandem occlusion stroke and to compare the technical safety, efficacy, and 3-month clinical outcome in this subgroup with the results of our large-vessel anterior circulation stroke study (Prognostic Factors Related to Clinical Outcome Following Thrombectomy in Ischemic Stroke [RECAST])^{28,29}.

MATERIALS AND METHODS

Sample

All patients presenting with an anterior circulation ischemic stroke treated with an endovascular approach in our institution between August 2009 and April 2013 were retrospectively retrieved from our prospectively maintained stroke data base.

Patient Selection

The inclusion criteria were as follows: 1) patients with acute ischemic stroke presenting within 6 hours from symptom onset; 2) anterior circulation acute ischemic stroke; 3) DWI-ASPECTS ≥ 5 ; 4) severe clinical deficits following physician evaluation, NIHSS ≥ 7 ; 5) large-vessel occlusion (M1, M1–M2 junction, carotid terminus); and 6) pre-morbid modified Rankin Scale score of ≤ 2 .

Decision-Making and Imaging

The initial NIHSS and the Glasgow Coma Scale scores were assessed by a neurologist. MR imaging protocol consisted of diffu-

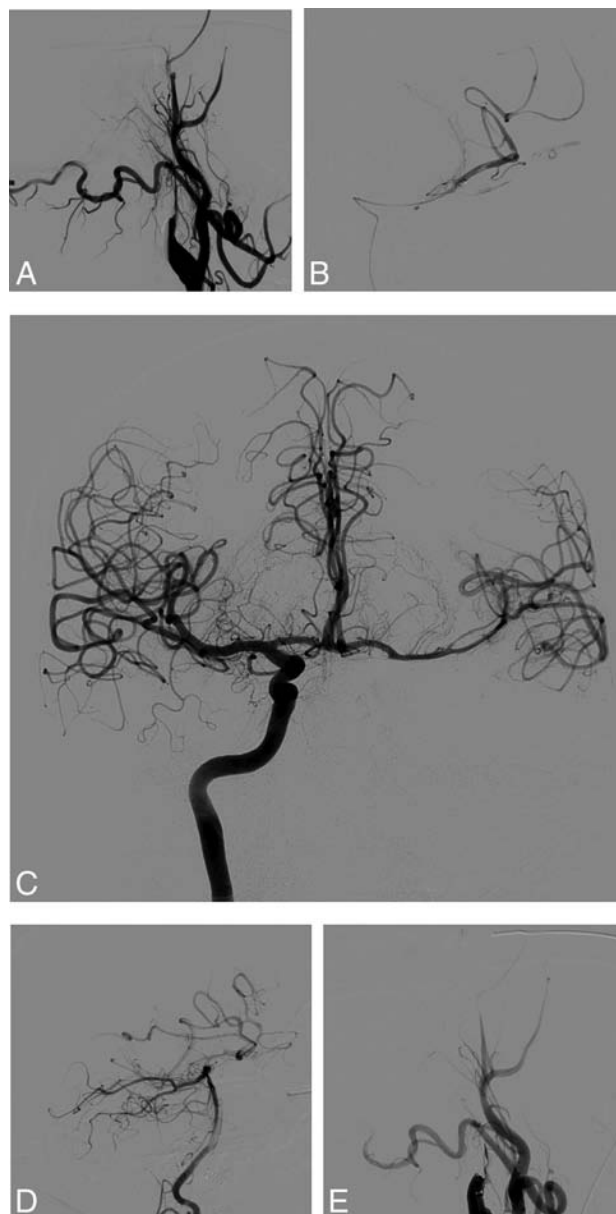


FIG 1. This patient presented with severe right hemiplegia and aphasia (NIHSS score = 20). Initial MR imaging revealed a DWI-ASPECTS = 6 after 4.5 hours since symptom onset, associated with left tandem ICA and middle cerebral artery occlusions. The initial angiogram (A) demonstrates left internal carotid occlusion related to cervical dissection. We then carefully navigated the microcatheter through the dissected ICA to the intracranial occlusion (B). Thrombectomy performed after contralateral femoral puncture and right ICA run shows a functional circle of Willis and no residual left M1 occlusion (C). The posterior communicating artery is also permeable as seen on the left vertebral artery run (D). Consequently, we decided not to treat the cervical ICA dissection, and the artery was left in its initial condition (E).

sion-weighted imaging, FLAIR, T2*, and MR angiography of the supra-aortic trunks. Tandem occlusion was suspected on initial imaging explorations and was confirmed on angiography with the morphologic aspect of the cervical segment of the internal carotid artery (Fig 1) associated with a proximal intracranial occlusion (carotid termination, M1 segment, and/or M1–M2 junction of the middle cerebral artery).

Intravenous Thrombolysis

IVT (0.9 mg/kg, 10% of the dose as a bolus and the remainder during 60 minutes) was administered to patients within a maximum of 4.5 hours after stroke onset. Conventional clinical and laboratory inclusion and exclusion criteria for IVT were applied.

Endovascular Procedure

We defined 2 types of treatment depending on the association with IVT: combined procedures and stand-alone thrombectomy. Combined procedures corresponded to endovascular treatment and IVT administered in the same time. Stand-alone thrombectomy was performed in case of contraindications for IVT.

Treatments were performed with the patient under general anesthesia. A 9F balloon-guiding catheter (Merci retriever; Concentric Medical, Mountain View, California) was introduced through a femoral sheath into the common carotid artery, and an initial angiographic run was performed to evaluate the occlusion. Isolated intracranial occlusions were treated with a triple coaxial approach: We placed an intermediate 5F guiding catheter (5MAX and 5MAX ACE; Penumbra, Alameda, California) into the distal internal carotid artery upward; a 0.021-inch microcatheter (Headway; MicroVention, Tustin, California) was used to cross the thrombus over a 0.014-inch microwire (Transend 014; Stryker, Kalamazoo, Michigan; or Traxcess; MicroVention). Mechanical thrombectomy was performed with a Solitaire FR (Covidien, Irvine, California) or Trevo (Stryker) system after inflation of the balloon-guiding catheter, under manual aspiration through the intermediate catheter to prevent clot fragmentation and embolism.

In cases of tandem occlusion, we performed an angiographic evaluation to determine the cause (atheromatous disease or dissection). In cases of obstruction related to cervical ICD, a 0.021-inch microcatheter was navigated through the true lumen of the dissection over a microwire. The intermediate 5F guiding catheter was then advanced over the microcatheter into the distal internal carotid artery. Intracranial thrombus retrieval was performed in the same manner as that for isolated occlusion by using a Solitaire FR (Covidien) or Trevo (Stryker) system, which was fully deployed and gently withdrawn with synchronous manual aspiration through the 5F intermediate guiding catheter.

The result of intracranial recanalization was evaluated by using the Thrombolysis in Cerebral Infarction score. Successful recanalization was defined as TICI 2b or 3.

If intracranial recanalization was achieved, the next step consisted of a contralateral femoral puncture and an angiographic run through the contralateral common carotid artery and eventually through the vertebral arteries to assess the circle of Willis functionality. In particular, the efficiency of anterior and posterior communicating arteries was assessed. While endovascular treatments were performed with the patient under general anesthesia, our only criterion to evaluate circle of Willis efficiency was angiographic. As previously demonstrated,³⁰ we focused on the anterior and posterior communicating artery permeability and bilateral venous phase comparison. If venous drainage was symmetric or delayed <2 seconds, the circle of Willis was efficient. If there was no supply from the communicating artery or if venous

drainage was significantly delayed (>2 seconds), we considered stent placement in the dissected internal carotid artery.

In case of cervical stent placement, the 0.014-inch microwire was placed into the petrous segment of the carotid artery to preserve distal access in the true arterial lumen. The balloon-guiding catheter and the 5F intermediate catheter were re-placed into the common carotid artery, just before carotid bifurcation. In case of persisting occlusive dissection, ICA stent placement was performed.

A 500-mg bolus of aspirin was administered intravenously. A carotid stent (Wallstent; Boston Scientific, Natick, Massachusetts) or LEO stent (Balt Extrusion, Montmorency, France) was navigated and deployed in the dissected segment. No additional angioplasty was required. Adequate position and opening of the stent were immediately assessed angiographically. Several stents might be needed if dissection was extensive and occlusive on the upper cervical and prepetrous segments.

Continuation of antiplatelet therapy was discussed, depending on hemorrhagic transformation detected by 24-hour imaging. If no significant intraparenchymal hemorrhage appeared, dual antiplatelet therapy was performed for 3 months. One single antiplatelet treatment was then maintained during 1 year.

In case of major hemorrhagic transformation (parenchymal hematoma-1, parenchymal hematoma-2), antiplatelet therapy was stopped at the acute phase. Depending on the follow-up CT or MR imaging during the postoperative period, the antiplatelet therapy restart was discussed by the medical team.

Figure 1 illustrates a typical procedure according to our protocol.

Follow-Up

CT was performed immediately after each procedure to detect any hemorrhagic intracranial complication. A follow-up control CT or MR imaging was performed 24 hours after the acute therapy to assess infarction volume and hemorrhagic status. Hemorrhagic transformation was defined according to European Cooperative Acute Stroke Study (ECASS) classification among none, hemorrhagic infarction-1, hemorrhagic infarction-2, parenchymal hematoma-1, or parenchymal hematoma-2. Symptomatic intracranial hemorrhage was defined as a documented hemorrhage associated with a decline of ≥ 4 points in the NIHSS. If no hemorrhage was present, antiplatelet drugs were prescribed.

Device-related complications were also reported. Embolic complications were defined as an angiographic occlusion in a previously unaffected vascular territory observed on the angiography after clot removal and associated with new ischemic changes on 24-hour CT or MR imaging.

NIHSS was measured following recovery from anesthesia, at 24 hours, and at discharge. Patients were followed up after 3 months to evaluate their disability by using the mRS. Clinical outcome was quantified by 3-month mRS and mortality. Favorable outcome was defined as an mRS of ≤ 2 .

Statistical Analyses

We performed a global description of all the samples, giving the frequencies of each category for quantitative data. The distribution of those quantitative variables was not always Gaussian, so

their description was realized with average, SD, median, and interquartile range. Comparison between groups was realized with average comparison tests (Student or Wilcoxon) for quantitative data and the χ^2 or Fisher test for qualitative data. The significance threshold was 5% for all tests.

RESULTS

Sample

Between August 2009 and April 2013, 258 patients with an anterior circulation ischemic stroke were identified. Mean age was 66.2 ± 14.14 years, and median NIHSS score was 18 (range, 4–29). The baseline characteristics of the population are given in Table 1. Of 258, 179 procedures were combined (69.4%) and 79 consisted of stand-alone mechanical treatments (30.6%). Fifty-seven patients had tandem occlusion, and 201 had simple intracranial occlusion (M1 or M1–M2 junction or terminal internal carotid artery). Among patients with tandem occlusion, 37 occlusions were due to carotid atheromatous disease and 20 to ICD. Except for undetermined timing such as wake-up strokes, the average time from symptom onset to arterial puncture was 4.5 ± 1.35 hours; range, 1.75–8.35 hours).

Patients with atheromatous tandem occlusion were excluded from the study.

In the ICD group, patients were significantly younger than those belonging to the isolated occlusion of the anterior circulation (IOAC) group, 52.45 versus 66.85 years ($P < .05$). There was a masculine predominance: 70% in the ICD group versus

47% in the IOAC group ($P < .05$). In contrast, stroke characteristics did not differ significantly: NIHSS score, ASPECTS, time from onset to puncture, and IVT association. Characteristics and comparability of the 2 studied groups are summarized in Table 2.

Procedural Results and Early Evolution

Intracranial recanalization (TICI 2b or 3) was achieved for 14 patients (70%) in the ICD group and 164 patients (82%) in the IOAC group. This was not significantly different ($P = .23$). Two stent retriever passes were needed, on average, for both groups, without any significant difference ($P = .112$). However, the total duration of the revascularization procedure was significantly prolonged in case of tandem occlusion (80.69 versus 65.45 minutes, $P = .030$).

Among the ICD population, 5 (25%) patients finally required cervical internal carotid stent deployment. Stent placement was feasible in all cases when chosen without catheterization issues. There was no thromboembolic event related to stent placement. Figures 1 and 2 represent the 2 different types of procedures, depending on circle of Willis functionality.

Symptomatic intracranial hemorrhage affected 1 patient (5%) in the ICD group, whereas it concerned 9 (4.5%) of those with IOAC, without a significant difference ($P = .49$). In the case of the patient with ICD, significant intracranial bleeding occurred early in the intensive care unit after an unfavorable mechanical revascularization (TICI score = 1) and cervical carotid stent placement. This patient was mRS = 4 at the end of follow-up. The stent was still patent on the 3-month follow-up CTA.

Periprocedural complications consisted of 2 embolic migrations in the ICD group (10%). In the IOAC group, 22 complications were reported (11%, $P = .10$): 16 embolic migrations, 2 proximal arterial perforations, 2 distal per procedural bleedings, 1 severe groin puncture complication requiring an operation, and 1 device breakage.

Three-Month Clinical Assessment

In the ICD group, no patient was lost to follow-up, whereas 7 were in the IOAC group. After 3 months, 14 (70%) of the 20 patients from the ICD group had a favorable outcome. On the other hand, 92 among 183 (50.3%) available patients treated for IOAC had an mRS ≤ 2 . This was not significantly different ($P = .093$). Mortality rates were 10% in the ICD group (2 patients) and 15.4% in the IOAC group (31 patients), without a significant difference.

In the subgroup of patients who benefited from ICA stent placement, 2 of them (40%) had a 3-month mRS ≤ 2 (1 mRS = 0 and 1 mRS = 1). Two patients had a poor neurologic outcome (mRS = 4 and 5), and 1 died.

In the unstented subgroup, 11 patients (73%) had a satisfactory clinical outcome (4 patients were mRS = 0; 3 patients, mRS = 1; and 4 patients, mRS = 2). The remaining 4 had poor neurologic outcome ($n = 3$) or died ($n = 1$).

Table 1: Population and stroke characteristics

	Values (%)	Average		
		Values	Median	Range
Age (yr)		66.02	69	22–90
Sex				
Male	135 (52.33)			
Female	123 (47.67)			
Hypertension	140 (54.26)			
Smoking	73 (28.29)			
NIHSS score		17.46	18	3–29
ASPECTS		6.51	7	2–10
Time between onset and arterial puncture (hr)		4.5	4.42	1.75–8.35
Intravenous thrombolysis association	179 (69.38)			

Table 2: Baseline characteristics and comparability of the 2 stroke subgroups

	Tandem Occlusion Related to Internal Carotid Dissection Group ($n = 20$)	Isolated Intracranial Occlusion Group ($n = 201$)	P Value
Age (yr)	52.5	66.9	$<.001^a$
Sex			$<.05^a$
Female	30%	53%	
Male	70%	47%	
Hypertension	30%	59%	$<.01^a$
Smoking	29%	26%	.78
Initial NIHSS score	17.53	17.55	.983
Initial DWI-ASPECTS	6.05	6.64	.098
Delay between stroke onset and arterial puncture (hr)	4.38	4.53	.704
Intravenous thrombolysis association	75%	68%	.7

^a Significant differences.

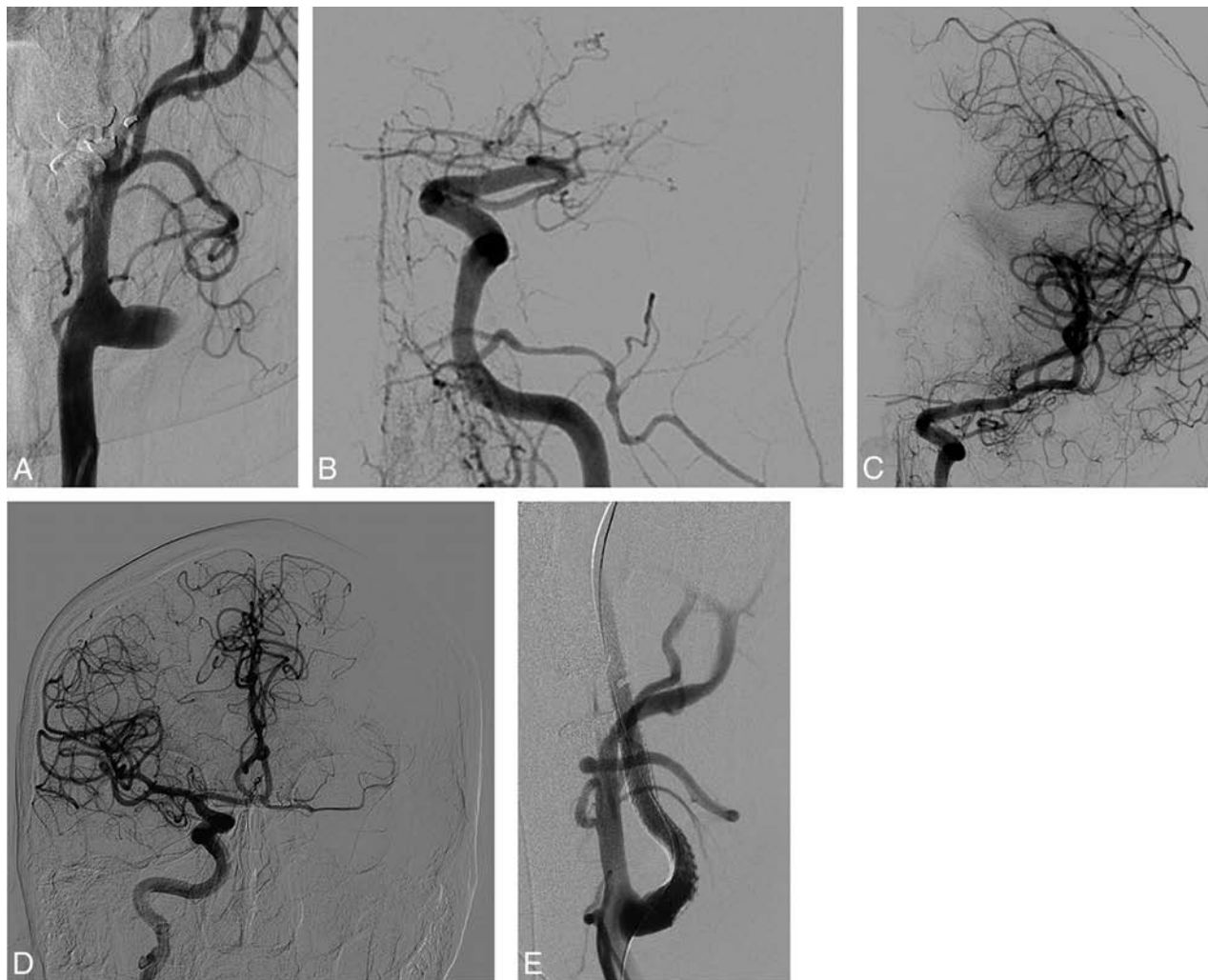


FIG 2. This acute tandem occlusion related to left cervical internal carotid dissection with a downstream intracranial M1 embolus was responsible for right hemiplegia and aphasia (NIHSS score = 22). The first angiographic (A) run demonstrated postbulbar internal carotid occlusion. After we navigated through the dissected segment, an intracranial initial angiogram confirmed the M1 thrombus (B). Complete intracranial recanalization was performed with 1 stent retriever pass (C). Thus, a contralateral internal carotid run revealed insufficient filling of the left MCA territory through the anterior communicating artery (D). In this case, cervical internal carotid stent placement of the dissected occlusive segment was mandatory (E). Clinical evolution was favorable (mRS = 1 after 3 months).

Table 3: Angiographic results, complication rates, and clinical follow-up

	Tandem Occlusion Related to Internal Carotid Dissection Group (n = 20)	Isolated Intracranial Occlusion Group (n = 201)	P Value
Favorable recanalization, TIC1 2b and 3	70%	82%	.23
Procedure duration (median) (min)	74	47	.030
Median No. of intracranial device passes	2	2	.112
Internal carotid stenting	5/20 (25%)		
Significant hemorrhagic rate	5%	3%	.49
Clinical favorable outcome after 3 months (mRS ≤ 2)	70%	50%	.093

No stroke recurrence was observed in the unstented ICD group. The results are summarized in Table 3.

DISCUSSION

Tandem occlusion stroke is an important therapeutic issue with poor prognosis, accounting for roughly 20% of large-vessel occlusion strokes.^{1,3,4} Since the early 1990s, IVT has been the first-line medical treatment widely prescribed.³¹⁻³⁴ However, in cervical

vessel occlusion, its efficiency is limited. Kim et al⁷ reported an early arterial recanalization after IVT in 9.4% of cervical vessel occlusions after 2 hours. Engelter et al¹ obtained a significant clinical improvement in only 36% of patients with stroke due to acute internal carotid dissection, despite the young age of the subgroup.

The endovascular approach remains poorly studied. Indeed, prospective data are scarce because tandem occlusion is

considered an exclusion criterion in many cohorts such as Solitaire FR With the Intention For Thrombectomy (SWIFT), SWIFT PRIME, Solitaire FR Thrombectomy for Acute Revascularization (STAR), and Thrombectomy REvascularization of Large Vessel Occlusions in Acute Ischemic Stroke (TREVO 2).^{23-25,35} Recently, MR-CLEAN, ESCAPE, and EXTEND-IA^{9,11,12} demonstrated the efficiency and safety of combined strategies in anterior

circulation single proximal occlusion. Nevertheless, there was no subgroup analysis for patients with cervical dissection. Most of the recent literature data reported a mix of atheromatous and dissection, pooled as a single anatomic description so-called “tandem occlusion.” From a nosologic point of view, it looks confusing to associate 2 different diseases in different populations of patients with a different physiopathologic origin in a unique strategic approach. We consider these 2 entities completely different. Patients with ICD are younger and more prone to present with a very good circle of Willis to justify a simple intracranial treatment. Moreover, if the recurrence rate of stroke is proved in ICA atheromatous stenosis,^{36,37} the stroke recurrence from ICD after efficient medical therapy is very low.³⁸ In this spirit, we usually tend to be conservative for ICD lesions but more aggressive with atheromatous stenosis, which is more prone to induce an ipsilateral stroke recurrence.

Our results by using this simple strategy allowed a satisfying intracranial revascularization in 70% of cases but also a substantial clinical recovery. Of course, the age of the subgroup positively influences the results in favor of the ICD subgroup, with a 70% rate of good outcome. Nevertheless, this study supports the hypothesis that ICD tandem occlusion stroke may be a very good indication for mechanical therapy and needs to be included in standard guidelines.

Thus, many approaches have been described to date, in particular antegrade revascularization.³⁹⁻⁴¹ In this case, recanalization is performed first in the cervical internal carotid artery, most often by stent placement, and second in the intracranial vessel. Even if good results had been demonstrated with satisfying revascularization rates and acceptable clinical outcomes (range, 41%–54%), in our opinion, this method is not optimal. First, the procedural time used for carotid stent placement increases the time from symptom onset to intracranial revascularization, resulting in increased final necrotic core volume, when a direct intracranial revascularization will offer immediate brain flow through the circle of Willis in many cases. Second, complex stent placement may be needed in case of extensive dissection with a systematic need for antiplatelet therapy to ensure stent patency during the postoperative period, increasing the risk of hemorrhagic transformation.

Our approach is based on an understanding of the anatomic parameters. We believe it is necessary to evaluate the completeness of the circle of Willis, which requires a contralateral femoral puncture, allowing selective contralateral common carotid and eventually vertebrobasilar catheterizations. In this young stroke subpopulation, contralateral exploration is simple. It does not prolong the revascularization procedure because the circle of Willis assessment is performed after intracranial revascularization, when cerebral blood flow has already been restored.

First focused on internal carotid artery treatment, the antegrade approach would slow down intracranial recanalization, which is an essential end point and the main target of the treatment. Indeed cervical stent placement may take time, especially in the dissection situation, in which navigation takes place in an already-injured artery that could also be tortuous. In addition, worsening of the mobilization of in situ thrombus during stent

deployment against the wall hematoma has already been observed in previous experience.⁴²

Navigation inside the dissected artery is the main technical difficulty. The classic pitfall is catheterizing the false lumen, with the potential risk of dissection extension. Indeed, the stenosed or occluded cervical segment of the internal carotid artery relegates the operator to a blind navigation, only guided by the smooth progression of the microwire. In our experience, there has not been any iatrogenic complication during this specific stage. Nevertheless, we still believe that this maneuver remains a potential risk.

One of the major points of our rationale is anticoagulation and antiplatelet management. In the acute phase, patients with stroke carry an increased risk of hemorrhagic transformation of the infarction territory, depending especially on its size and the hemostasis status. The difficulty is because acute carotid stent placement necessitates antiplatelet drugs. These necessarily increase the risk of a hemorrhagic event, but in-stent thrombosis could potentially lead to new embolic events. In the context of acute stroke, dual antiplatelet drug introduction is not an established practice and relies more on empiric assessment based on stroke extent, postprocedure blood-brain barrier disruption, and so forth—all this with a potentially negative impact on clinical recovery.

This antiplatelet-related hemorrhagic risk is illustrated by our patient who presented with a symptomatic intracranial hemorrhage after 24 hours, while she previously benefited from ICA stent placement during a revascularization procedure. Comparing our stented and unstented subgroups was not easy, given the small number of patients in each group.

Still we think that limiting stent implantation should permit a reduction in the postprocedural complication risk.

Hence, distal to proximal revascularization appears to be a truly appealing alternative. In our experience, most of cases did not require any cervical carotid treatment because only 5 patients (corresponding to 25% of our population) required stent placement. This approach allows a quicker procedure to reach intracranial recanalization. In addition, no stroke recurrence was observed in the unstented ICD group, making this strategy a reliable option in the management of ICD with intracranial occlusion.

In our daily practice, triaxial access is a common endovascular approach. Our aim is to reach, as quickly as possible, the intracranial occlusion and to minimize intra-arterial maneuvers and complications. Positioning a 5F intermediate guiding catheter into the distal ICA facilitates thrombectomy maneuvers, first by providing more support and stability to the system and second by allowing a rapid recatheterization in case of failed thrombectomy, avoiding the need for crossing the injured cervical ICA again.

Following intracranial reopening, the intermediate guiding catheter is withdrawn, leaving only a microwire inside the ICA to preserve access for potential cervical stent placement.

The postoperative hemorrhagic risk was tolerable. We reported 5% symptomatic intracranial hemorrhage, which is a comparable rate in the IOAC population. Besides, intracranial hemorrhages of the infarcted territories were mostly asymptomatic and limited and did not influence the clinical evolution ob-

served in cases of IOAC. We did not encounter any complications related to arterial catheterization.

Our study has several limitations. Its monocentric retrospective nature, the restricted population, and the absence of a real control group did not allow a strict comparison. The results are limited to a specific strategy of distal to proximal revascularization and may not be reproducible in other conditions.

CONCLUSIONS

Mechanical treatment of internal carotid dissection tandem occlusion by using a distal to proximal triaxial strategy looks safe and effective compared with isolated intracranial occlusion stroke. The conservative approach of ICD, considering stent placement only after intracranial revascularization, in case of circle of Willis insufficiency, may be a reliable and safe strategy, reducing the need for systematic double antiplatelet therapy in the postoperative period. Randomized, multicenter trials are required to potentially confirm these results and to identify further clinical and radiologic factors contributing to a good outcome.

Disclosures: Alain Bonafé—UNRELATED: Consultancy: Covidien; ev3; Grants/Grants Pending: Covidien*; Vincent Costalat—UNRELATED: Consultancy: Sequent Medical, Balt, Codman, Stryker; Payment for Lectures (including service on Speakers Bureaus): Stryker, Balt, Payment for Development of Educational Presentations: Covidien; Payment for Development of Educational Presentations: Medtronic, Stryker. *Money paid to the institution.

REFERENCES

- Engelter ST, Rutgers MP, Hatz F, et al. **Intravenous thrombolysis in stroke attributable to cervical artery dissection.** *Stroke* 2009;40:3772–76 CrossRef Medline
- Benninger DH, Georgiadis D, Kremer C, et al. **Mechanism of ischemic infarct in spontaneous carotid dissection.** *Stroke* 2004;35:482–85 CrossRef Medline
- Rubiera M, Ribo M, Delgado-Mederos R, et al. **Tandem internal carotid artery/middle cerebral artery occlusion: an independent predictor of poor outcome after systemic thrombolysis.** *Stroke* 2006;37:2301–05 CrossRef Medline
- Linfante I, Llinas RH, Selim M, et al. **Clinical and vascular outcome in internal carotid artery versus middle cerebral artery occlusions after intravenous tissue plasminogen activator.** *Stroke* 2002;33:2066–71 CrossRef Medline
- Hacke W, Kaste M, Bluhmki E, et al; ECASS Investigators. **Thrombolysis with alteplase 3 to 4.5 hours after acute ischemic stroke.** *N Engl J Med* 2008;359:1317–29 CrossRef Medline
- del Zoppo GJ, Poeck K, Pessin MS, et al. **Recombinant tissue plasminogen activator in acute thrombotic and embolic stroke.** *Ann Neurol* 1992;32:78–86 CrossRef Medline
- Kim YS, Garami Z, Mikulik R, et al; CLOTBUST Collaborators. **Early recanalization rates and clinical outcomes in patients with tandem internal carotid artery/middle cerebral artery occlusion and isolated middle cerebral artery occlusion.** *Stroke* 2005;36:869–71 CrossRef Medline
- Saver JL, Goyal M, Bonafe A, et al; SWIFT PRIME Investigators. **Stent-retriever thrombectomy after intravenous t-PA vs. t-PA alone in stroke.** *N Engl J Med* 2015;372:2285–95 CrossRef Medline
- Goyal M, Demchuk AM, Menon BK, et al; ESCAPE Trial Investigators. **Randomized assessment of rapid endovascular treatment of ischemic stroke.** *N Engl J Med* 2015;372:1019–30 CrossRef Medline
- Jovin T, Chamorro A, Cobo E, et al; REVASCAT Investigators. **Thrombectomy within 8 hours after symptom onset in ischemic stroke.** *N Engl J Med* 2015;372:2296–306 CrossRef Medline
- Campbell BCV, Mitchell PJ, Kleinig TJ, et al; EXTEND-IA Investigators. **Endovascular therapy for ischemic stroke with perfusion-imaging selection.** *N Engl J Med* 2015;372:1009–18 CrossRef Medline
- Berkhemer O, Fransen P, Beumer D, et al. **A randomized trial of intraarterial treatment for acute ischemic stroke.** *N Engl J Med* 2015;372:11–20 CrossRef Medline
- Fischer U, Mono M-L, Schroth G, et al. **Endovascular therapy in 201 patients with acute symptomatic occlusion of the internal carotid artery.** *Eur J Neurol* 2013;20:1017–24, e87 CrossRef Medline
- Kappelhof M, Marquering HA, Berkhemer OA, et al. **Intra-arterial treatment of patients with acute ischemic stroke and internal carotid artery occlusion: a literature review.** *J Neurointerv Surg* 2015;7:8–15 CrossRef Medline
- Kwak HS, Hwang SB, Jin GY, et al. **Predictors of functional outcome after emergency carotid artery stenting and intra-arterial thrombolysis for treatment of acute stroke associated with obstruction of the proximal internal carotid artery and tandem downstream occlusion.** *AJNR Am J Neuroradiol* 2013;34:841–46 CrossRef Medline
- Lavallée PC, Mazighi M, Saint-Maurice JP, et al. **Stent-assisted endovascular thrombolysis versus intravenous thrombolysis in internal carotid artery dissection with tandem internal carotid and middle cerebral artery occlusion.** *Stroke* 2007;38:2270–74 CrossRef Medline
- Baumgartner RW, Georgiadis D, Nedelchev K, et al. **Stent-assisted endovascular thrombolysis versus intravenous thrombolysis in internal carotid artery dissection with tandem internal carotid and middle cerebral artery occlusion.** *Stroke* 2008;39:e27–28 CrossRef Medline
- Machi P, Lobotesis K, Maldonado IL, et al. **Endovascular treatment of tandem occlusions of the anterior cerebral circulation with Solitaire FR thrombectomy system: initial experience.** *Eur J Radiol* 2012;81:3479–84 CrossRef Medline
- Malik AM, Vora NA, Lin R, et al. **Endovascular treatment of tandem extracranial/intracranial anterior circulation occlusions: preliminary single-center experience.** *Stroke* 2011;42:1653–57 CrossRef Medline
- Matsubara N, Miyachi S, Tsukamoto N, et al. **Endovascular intervention for acute cervical carotid artery occlusion.** *Acta Neurochir (Wien)* 2013;155:1115–23 CrossRef Medline
- Mourand I, Brunel H, Vendrell JF, et al. **Endovascular stent-assisted thrombolysis in acute occlusive carotid artery dissection.** *Neuroradiology* 2010;52:135–40 CrossRef Medline
- Suh DC, Kim JK, Choi CG, et al. **Prognostic factors for neurologic outcome after endovascular revascularization of acute symptomatic occlusion of the internal carotid artery.** *AJNR Am J Neuroradiol* 2007;28:1167–71 CrossRef Medline
- Pereira V, Gralla J, Davalos A, et al. **Prospective, multicentre, single-arm study of mechanical thrombectomy using Solitaire flow restoration in acute ischemic stroke: STAR.** *Stroke* 2014;44:2802–07 CrossRef Medline
- Saver JL, Jahan R, Levy EI, et al. **Solitaire flow restoration device versus the Merci retriever in patients with acute ischaemic stroke (SWIFT): a randomised, parallel-group, non-inferiority trial.** *Lancet* 2012;380:1241–49 CrossRef Medline
- Nogueira RG, Lutsep HL, Gupta R, et al; TREVO 2 Trialists. **Trevo versus Merci retrievers for thrombectomy revascularisation of large vessel occlusions in acute ischaemic stroke (TREVO 2): a randomised trial.** *Lancet* 2012;380:1231–40 CrossRef Medline
- Ciccone A, Valvassori L, Nichelatti M, et al; SYNTHESIS Expansion Investigators. **Endovascular treatment for acute ischemic stroke.** *N Engl J Med* 2013;368:904–13 CrossRef Medline
- Broderick JP, Palesch YY, Demchuk AM, et al; Interventional Management of Stroke (IMS) III Investigators. **Endovascular therapy after intravenous t-PA versus t-PA alone for stroke.** *N Engl J Med* 2013;368:893–903 CrossRef Medline
- Danière F, Lobotesis K, Machi P, et al. **Patient selection for stroke endovascular therapy: DWI-ASPECTS thresholds should vary among age groups—insights from the RECAST study.** *AJNR Am J Neuroradiol* 2015;36:32–39 CrossRef Medline
- Costalat V, Machi P, Lobotesis K, et al. **Rescue, combined, and stand-**

- alone thrombectomy in the management of large vessel occlusion stroke using the Solitaire device: a prospective 50-patient single-center study—timing, safety, and efficacy. *Stroke* 2011;42:1929–35 CrossRef Medline
30. Abud DG, Spelle L, Piotin M, et al. **Venous phase timing during balloon test occlusion as a criterion for permanent internal carotid artery sacrifice.** *AJNR Am J Neuroradiol* 2005;26:2602–09 Medline
 31. Hacke W, Kaste M, Fieschi C, et al. **Randomised double-blind placebo-controlled trial of thrombolytic therapy with intravenous alteplase in acute ischaemic stroke (ECASS II): Second European-Australasian Acute Stroke Study Investigators.** *Lancet* 1998;352:1245–51 Medline
 32. Bluhmki E, Chamorro A, Dávalos A, et al. **Stroke treatment with alteplase given 3.0–4.5 h after onset of acute ischaemic stroke (ECASS III): additional outcomes and subgroup analysis of a randomised controlled trial.** *Lancet Neurol* 2009;8:1095–102 CrossRef Medline
 33. The National Institute of Neurological Disorders and Stroke (NINDS) rt-PA Stroke Trial Study Group. **Tissue plasminogen activator for acute ischemic stroke.** *N Engl J Med* 1995;333:1581–87 CrossRef Medline
 34. Clark WM, Wissman S, Albers GW et al. **Recombinant tissue-type plasminogen activator (Alteplase) for ischemic stroke 3 to 5 hours after symptom onset: The ATLANTIS Study—a randomized controlled trial.** *JAMA* 1999;282:2019–26 CrossRef Medline
 35. Saver JL, Goyal M, Bonafe A, et al; SWIFT PRIME Investigators. **Solitaire™ with the Intention for Thrombectomy as Primary Endovascular Treatment for Acute Ischemic Stroke (SWIFT PRIME) trial: protocol for a randomized, controlled, multicenter study comparing the Solitaire revascularization device with IV tPA with IV tPA alone in acute ischemic stroke.** *Int J Stroke* 2015;10:439–48 CrossRef Medline
 36. Lovett JK, Coull AJ, Rothwell PM. **Early risk of recurrence by subtype of ischemic stroke in population-based incidence studies.** *Neurology* 2004;62:569–73 CrossRef Medline
 37. Marnane M, Ni Chroinin DN, Callaly E, et al. **Stroke recurrence within the time window recommended for carotid endarterectomy.** *Neurology* 2011;77:738–43 CrossRef Medline
 38. Arauz A, Hoyos L, Espinoza C, et al. **Dissection of cervical arteries: long-term follow-up study of 130 consecutive cases.** *Cerebrovasc Dis* 2006;22:150–54 CrossRef Medline
 39. Mpotsaris A, Bussmeyer M, Buchner H, et al. **Clinical outcome of neurointerventional emergency treatment of extra- or intracranial tandem occlusions in acute major stroke: antegrade approach with Wallstent and Solitaire stent retriever.** *Clin Neuroradiol* 2013;23:207–15 CrossRef Medline
 40. Spiotta AM, Lena J, Vargas J, et al. **Proximal to distal approach in the treatment of tandem occlusions causing an acute stroke.** *J Neurointerv Surg* 2015;7:164–69 CrossRef Medline
 41. Papanagiotou P, Roth C, Walter S, et al. **Carotid artery stenting in acute stroke.** *J Am Coll Cardiol* 2011;58:2363–69 CrossRef Medline
 42. Xianjun H, Zhiming Z. **A systematic review of endovascular management of internal carotid artery dissections.** *Interv Neurol* 2013;1:164–70 CrossRef Medline

Hemodynamic and Anatomic Variations Require an Adaptable Approach during Intra-Arterial Chemotherapy for Intraocular Retinoblastoma: Alternative Routes, Strategies, and Follow-Up

 E. Bertelli,  S. Leonini,  D. Galimberti,  S. Moretti,  R. Tinturini,  T. Hadjistilianou,  S. De Francesco,  D.G. Romano,  I.M. Vallone,  S. Cioni,  P. Gennari,  P. Galluzzi,  I. Grazzini,  S. Rossi, and  S. Bracco



ABSTRACT

BACKGROUND AND PURPOSE: Intra-arterial chemotherapy for retinoblastoma is not always a straightforward procedure, and it may require an adaptable approach. This study illustrates strategies used when the ophthalmic artery is difficult to catheterize or not visible, and it ascertains the effectiveness and safety of these strategies.

MATERIALS AND METHODS: A retrospective study was performed on a series of 108 eyes affected by intraocular retinoblastoma and selected for intra-arterial chemotherapy (follow-up range, 6–82 months). We recognized 3 different patterns of drug delivery: a fixed pattern through the ophthalmic artery, a fixed pattern through branches of the external carotid artery, and a variable pattern through either the ophthalmic or the external carotid artery.

RESULTS: We performed 448 sessions of intra-arterial chemotherapy, 83.70% of them through the ophthalmic artery and 16.29% via the external carotid artery. In 24.52% of eyes, the procedure was performed at least once through branches of the external carotid artery. In 73 eyes, the pattern of drug delivery was fixed through the ophthalmic artery; for 9 eyes, it was fixed through branches of the external carotid artery; and for 17 eyes, the pattern was variable. Statistical analysis did not show any significant difference in the clinical outcome of the eyes (remission versus enucleation) treated with different patterns of drug delivery. Adverse events could not be correlated with any particular pattern.

CONCLUSIONS: Alternative routes of intra-arterial chemotherapy for intraocular retinoblastoma appear in the short term as effective and safe as the traditional drug infusion through the ophthalmic artery.

ABBREVIATIONS: ECA = external carotid artery; FPEC = fixed pattern through the ECA; FPO = fixed pattern through the OA; IAC = intra-arterial chemotherapy; MMA = middle meningeal artery; OA = ophthalmic artery; VP = variable pattern

Intra-arterial chemotherapy (IAC) is a therapeutic strategy devised for the local treatment of primary and metastatic tumors.¹ At first, its application was mainly for treatment of hepatocellular carcinoma or hepatic metastasis of tumors of the digestive tract. However, this approach rapidly spread from the liver to several extrahepatic sites.¹ In the orbit, one of the most striking applica-

tions, in terms of success rate, was certainly the infusion of anti-tumoral drugs through the ophthalmic artery (OA) to treat intra-ocular retinoblastoma.^{2–8} Across time, the technique of delivering drugs intra-arterially to the eye has been refined. Balloon occlusion of the internal carotid artery just distal to the OA origin⁴ has been rapidly replaced by the direct catheterization of the OA.^{3,5,8}

However, in some cases, the procedure is not as straightforward as expected because of difficulties in catheterizing the OA or because angiographic visualization of the OA fails altogether.^{5,7–9} Two alternative techniques have been previously proposed in such cases: The first one involves the superselective catheterization of the middle meningeal artery (MMA), provided that an anastomosis between this vessel and the OA allows an acceptable choroidal blush; the second one is to just reapply the balloon technique to the ICA.^{5,9} Failure to catheterize or infuse the OA can be a temporary occurrence, and the procedure can be successfully performed sometime later⁸; on the other hand, a successful procedure through the OA on 1 or >1 occasion does not guarantee the same achievement in the following scheduled sessions of IAC.⁹

Received September 23, 2015; accepted after revision December 9.

From the Department of Molecular and Developmental Medicine (E.B., S.R.), University of Siena, Siena, Italy; Units of Neuroimaging and Neurointervention (S.L., D.G.R., I.M.V., S.C., P. Gennari, P. Galluzzi, I.G., S.B.), Pediatrics (D.G., S.M.), and Neurosurgical Intensive Care (R.T.), Azienda Ospedaliera Universitaria Senese, University of Siena, Policlinico “Santa Maria alle Scotte,” Siena, Italy; and Department of Medicine, Surgery and Neuroscience (T.H., S.D.F.), Unit of Ophthalmology, University of Siena, Policlinico “Santa Maria alle Scotte,” Siena, Italy.

E. Bertelli and S. Leonini contributed equally to this study.

Please address correspondence to Sandra Bracco, MD, Unit of Neuroimaging and Neurointervention, AOUS, Policlinico “Santa Maria alle Scotte,” Viale Mario Bracci, 16, 53100 Siena, Italy; e-mail: sandrabracco64@gmail.com



Indicates article with supplemental on-line video.

<http://dx.doi.org/10.3174/ajnr.A4741>

We observed that in a remarkable percentage of children, the technical success of the treatment required different routes of drug infusion, depending on anatomic variants or on temporary hemodynamic variations. In some cases, the route of administration of the drugs had to be changed even within the same procedure so that the antitumoral agents were delivered in part through 1 artery and in part via another one. In our experience, in children, hemodynamics are not as stable as in adults, so the blood flow in the OA is the result of a balance between the external and the internal carotid systems, which is susceptible to temporary changes. Accordingly, an adaptable approach may be required to successfully deliver antitumoral drugs to the affected eye. Here, we report our experience based on a retrospective review of 108 eyes affected by retinoblastoma and selected for intra-arterial infusion of melphalan or melphalan plus topotecan. We report the alternative strategies and routes of administration used along with an evaluation of the clinical outcome of eyes treated via the external carotid artery (ECA) versus eyes treated through the ICA.

MATERIALS AND METHODS

From June 2008 to November 2014, a series of 99 patients with retinoblastoma (44 females, 55 males; age range at first treatment, 5–108 months) in 108 eyes were scheduled for superselective ophthalmic artery infusion of melphalan alone or in association with topotecan. The minimum follow-up was 6 months (up to 82 months). A multidisciplinary group jointly discussed the opportunity for treatment and obtained informed consent. Inclusion criteria were newly diagnosed unilateral or bilateral groups C–D retinoblastomas; unilateral groups A–B with macular involvement; and unilateral or bilateral groups A–D retinoblastomas with partial remission and/or relapse after systemic chemotherapy and/or focal therapies including cryotherapy, laser ablation, brachytherapy and external beam radiation therapy, intravitreal melphalan, or a combination of these. Exclusion criteria were diffuse infiltrating retinoblastoma, anterior chamber invasion, secondary glaucoma, vitreous hemorrhage, optic nerve infiltration, diffuse choroidal infiltration, scleral infiltration, extraocular disease extent, and intracranial metastatic disease at gadolinium-enhanced MR imaging of the head and orbits. Ophthalmic evaluations were performed 1–7 days before and 3 weeks after each treatment and included external examination; visual acuity testing when possible, depending on the patient's age and cooperation; pupil and eye motility evaluation; and complete fundus examination. All ophthalmic evaluations were performed with the patient under anesthesia, and included RetCam digital photography (Clarity Medical Systems, Pleasanton, California) and B-scan sonography at 12 MHz. Grading was based on the tumor volume at RetCam digital photography at the beginning of chemosurgery and after each treatment follow-up examination as previously reported.¹⁰

After the final session, we evaluated the effectiveness of the treatment, measuring the ophthalmologic response (ie, the rate of reduction of the tumor volume). A decrease of <50% of the volume (0%–49%) was considered a low response; a medium response was achieved when the decrease was between 50% and 79% of the volume; and a decrease between 80% and 100% of the volume was considered a high response. The follow-up schedule

consisted of clinical, ophthalmic, and eventually MR imaging evaluation, every 4–6 weeks for 6 months, every 6–8 weeks for the following 6 months, and every 8–10 weeks starting from the second year.

Angiographic Procedure

All patients underwent general anesthesia with intubation. A 4F micropuncture set was used to access the common femoral artery with subsequent placement of an arterial sheath. The patient was then anticoagulated with intravenous heparin (70 IU/kg, followed by a continuous infusion of 10–15 IU/kg/h). A selective angiography of the ICA was always performed at the beginning of each session of treatment. The micronavigation of the ICA and direct catheterization of the OA ostium by using a flow-directed straight microcatheter (Magic 1.5 or Baltacci 1.2; Balt, Montmorency, France; or UltraFlow 1.5, Covidien, Irvine, California) were always attempted before considering alternative routes of IAC. When required, vasospasm reactions were solved with the infusion of nimodipine. If an adequate choroidal blush was unattainable via the direct catheterization of the OA (On-line Video), alternative routes of IAC delivery through the anastomoses with the ECA were sought. A detailed description of our procedure has been previously reported.⁸ When the OA was visible but its entrance was too angulated for regular catheterization, we customized the tip of the microcatheter, shaping it to properly fit the anatomy of the patient.⁸ In a few selected cases, embolization of some branches of the ECA with a mixture of a cyanoacrylate-based synthetic and Lipiodol (Guerbet, Roissy, France), administered through a flow-directed microcatheter (Magic 1.2, Balt), was performed. The balloon technique was never applied in our patients.

The dose of melphalan was chosen according to the patient's age and the size of the globe at sonography,^{5,8,11} ranging from 3 to 6 mg/mL and possibly associated with 0.3 or 0.4 mg of topotecan (based on the patient's age). Drugs were injected by a 30-minute pulsatile infusion to avoid streaming and nonhomogeneous drug delivery.⁸ After delivering a half dose and at the end of the procedure, we checked blood flow efficiency by the microcatheter under fluoroscopy to confirm hemodynamic stability.

A final lateral arteriogram of the ICA or common carotid artery (depending on the pathway of drug delivery) was performed to rule out any procedure-related complications such as vasospasm, embolism, or arterial dissection.

Once the session was completed, the catheters were removed, the femoral sheath was pulled, and hemostasis of the groin puncture was achieved by manual pressure. Anesthesia was discontinued, and the child was kept under observation for 24 hours before discharging.

Any angiographic procedural complications, as well as systemic and local adverse events, were noted on the patient's medical record after each treatment session and during follow-up.

Retrospective and Statistical Analysis

To compare the clinical outcome and the safety of the IAC conveyed via branches of the ECA, we retrospectively divided the treated eyes into 3 groups according to the technique of drug delivery during the entire treatment: Group 1 consisted of eyes

that received IAC with a fixed pattern of drug delivery through the OA (FPO) (ie, they were always treated through the OA); group 2 included eyes with a fixed pattern through the ECA (FPEC) (ie, they were treated consistently through branches of the ECA); and group 3 referred to eyes that received IAC at times via the OA and at times via branches of the ECA, describing a variable pattern (VP) of drug delivery (interprocedural variability). A χ^2 test was used to verify whether the proportion of eyes that received pretreatment of any sort before undergoing IAC or that were treated with just melphalan (monotherapy) were the same in the 3 groups. Data on the ophthalmologic response of the eyes treated in the 3 groups and data on the adverse events were compared by means of the χ^2 test. Significant age differences in patients in the 3 groups and differences in radiation exposures were verified with ANOVA tests. A $P < .05$ was considered statistically significant for all tests.

RESULTS

From June 2008 to November 2014, 99 patients were selected for IAC. Because 9 patients were affected bilaterally, the total number of treatable eyes was 108. Two patients among the first 10 treated did not receive IAC due to technical failure. Overall, 106 eyes were treated, and we performed 448 sessions of IAC, 375 of them (83.70%) through the OA and 73 (16.29%) via branches of the ECA. In 26 eyes (24.52% of cases), IAC was performed at least once through branches of the ECA by using 1 of the many anastomoses that connect this artery with the OA.¹²

When the IAC was performed through the ECA, the branch most frequently used to deliver the antitumoral drugs was the MMA. This artery was used, often more than once, in 24 orbits for 64 sessions of IAC. Overall, the MMA was catheterized in 87.67% of the sessions in which IAC was performed through the ECA. However, several anastomoses connecting the MMA with the OA were used for drug delivery: the direct anastomosis between the 2 vessels (meningo-ophthalmic artery) was used in 14 eyes (38 sessions); the anastomosis between the MMA and the lacrimal artery was used in 9 orbits (24 sessions); and finally, in 1 orbit (2 sessions), we used an unusual anastomosis between the MMA and the supraorbital artery.¹²

Less frequently, the arteries used for delivering the antitumoral drugs were periorbital vessels that anastomosed with arteries running in the anterior orbit and were identified following previously published criteria,¹³ such as the dorsal nasal artery anastomosed with the angular artery (1 eye, 1 session),¹² the frontal branch of the superficial temporal artery that anastomosed with the supratrochlear artery (1 eye, 1 session),¹² the zygomatico-orbital artery anastomosed with the lacrimal artery (1 eye, 2 sessions),¹² and the anterior deep temporal artery connected to the lacrimal artery (3 eyes, 5 sessions).¹²

Seven patients (7 eyes affected by grade D tumors) abandoned the treatment after just 1 session (1 patient treated via a branch of the ECA and 6 via the OA). In 4 of these 7 patients, the ophthalmologic evaluation showed a poor response or the progression of the disease; in the remaining patients, a massive tumor necrotic fragmentation involving the whole vitreous cavity occurred. The remaining 90 patients (99 eyes) underwent from 3 to 6 sessions of

IAC. For some eyes, the technique of drug delivery was consistent throughout all cycles of treatment (FPO or FPEC); for others, it could vary from session to session or even within the same session (VP) (Fig 1). As expected, the most frequent pattern of drug delivery was the FPO, observed for 73 eyes (73.74%). For 9 eyes (9.1%), the pattern of drug delivery was the FPEC. The VP was used in 17 eyes (17.2%). Eyes that were pretreated before undergoing IAC were 52%, 33%, and 41%, respectively, in groups 1, 2, and 3. On the other hand, the proportion of eyes treated in monotherapy with melphalan in groups 1, 2, and 3 were respectively 45%, 55.5%, and 76.5%. The χ^2 test did not show any statistically significant association between pretreatments or monotherapy and the pattern of drug delivery ($P > .05$). The mean age distribution of the patients in the 3 groups was 33.84 ± 42.47 months in group 1, 21.55 ± 10.26 months in group 2, and 33.11 ± 10.26 months in group 3. Statistical analysis did not show any significant age difference among groups ($P > .05$).

Within group 3 (VP), in 2 different patients, chemotherapeutic agents were delivered through 2 different pathways within the same session (intraprocedural variability). However, even within group 2 (FPEC), the pattern could be somewhat variable, meaning that in some patients, we had to perform IAC through different branches of the ECA. For instance, in 1 case, we used 3 different anastomotic pathways (2 sessions through MMA, 1 session via the facial artery, and 3 sessions through the anterior deep temporal artery).

Particular Angiographic Procedures

In 14 patients, the angiographic procedure required a more creative approach. For instance, sometimes the stemming of the OA from the ICA was unfavorable (too angulated) and its direct catheterization was not possible. Thus, in 16 patients (16.2%), we had to customize the tip of the microcatheter, as previously reported,⁸ shaping it like an S to properly fit the anatomy of the patient (Fig 2A).

In other cases, 2 different hemodynamic conditions prompted us to embolize selected branches of the ECA: In 2 patients, we observed a too large amount of chemotherapy dispersion into branches of the MMA. To maximize drug availability to the target, we embolized a major branch of the MMA (Fig 1) as previously reported in other vascular areas.¹⁴ In the remaining patient (Fig 2B–D), the orbit not supplied through a single anastomosis that could be exploited for drug delivery and received blood mainly through an extensive network of several small branches connecting the superficial temporal artery with the supratrochlear artery. In this case, we navigated the superficial temporal artery and embolized the anastomotic network to induce the anterograde redirection of the blood flow within the ophthalmic artery (Fig 2D).

Outcome

The outcome of the eyes treated via the different patterns of drug delivery after a follow-up of at least 6 months is summarized in Table 1. The rate of success (tumor remission versus recurrence/enucleation) of the IAC was 63% for the eyes treated with an FPO, 77.7% for the eyes treated with an FPEC, and 47% for the eyes treated with a VP. No significant association was found between

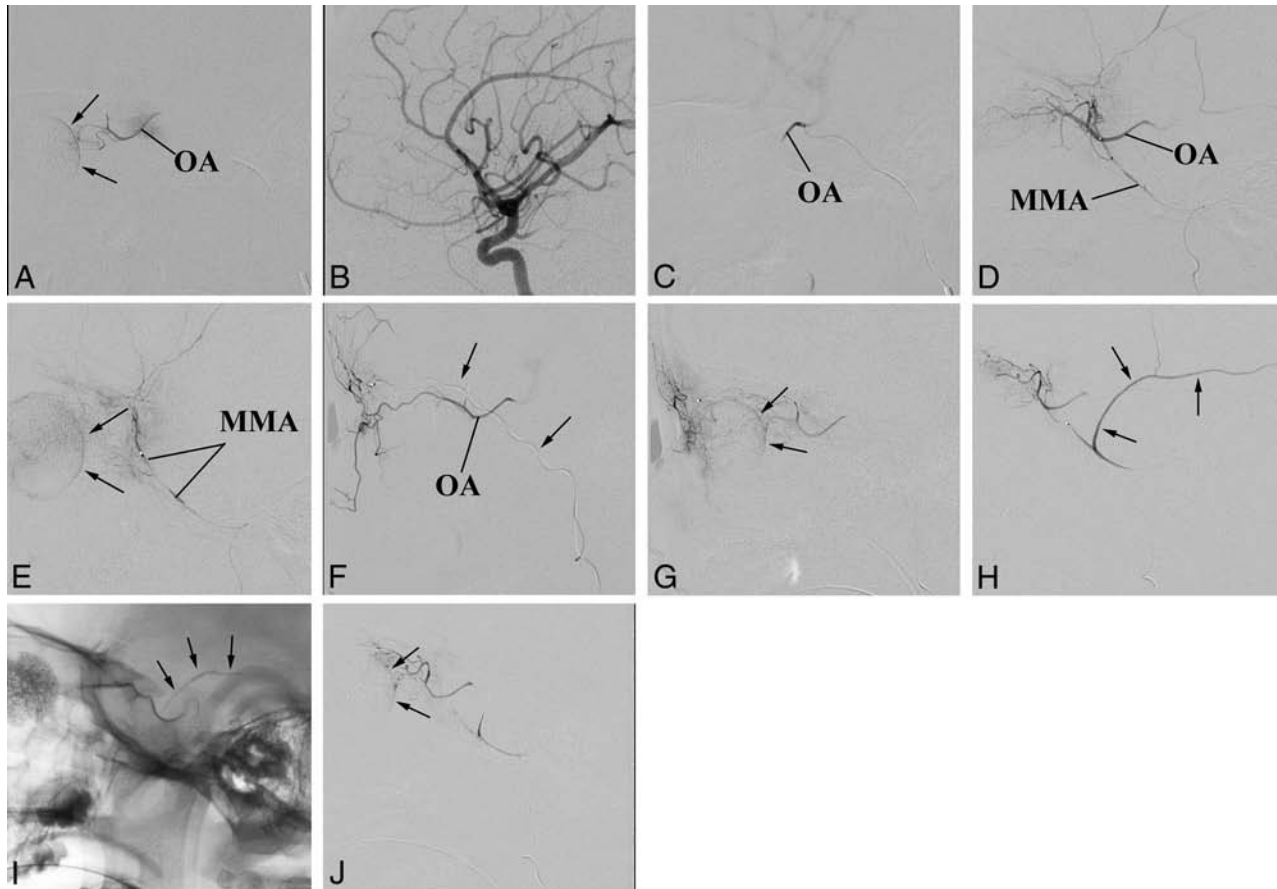


FIG 1. An exemplary case of adaptable approaches to the IAC. The patient has bilateral retinoblastoma previously enucleated on 1 side (the prosthesis is visible). The remaining eye is a case of VP of drug delivery. A, The OA is successfully catheterized and used in 2 sessions of IAC because the choroidal blush (arrows) is regularly achieved. B–E, Third session of IAC. Selective angiography of the ICA does not show any visible OA (B). Nevertheless catheterization of the OA is successful (C), though the contrast flows back into the ICA (On-line Video). Superselective angiography of the MMA shows a good anastomotic pathway to the OA (D), which allows achieving the choroidal blush (arrows in E). F and G, Fourth session of IAC. This time the anastomosis between the MMA and the OA does not guarantee the choroidal blush. An alternative route for drug delivery through the ECA is sought and found between the frontal branch of the superficial temporal artery (arrows point to the microcatheter within the artery) and the supratrochlear artery (F). A later angiographic phase shows that this pathway guarantees the choroidal blush (arrows) (G). H–J, Fifth session of IAC. The anastomosis between the MMA and the OA is working again. However, the contrast medium flows back even into a large branch of the MMA (arrows in H). To reduce the volume of distribution, we glued the meningeal branch (arrows point to the cast in I), and the following injection of contrast medium achieves the choroidal blush (arrows in J).

the pathway of drug delivery and the outcome of the treatment ($P = .276$).

Data on the ophthalmologic response arranged according to the pattern of drug delivery are summarized in Table 2. A high response was achieved in 90.4%, 77.8%, and 88.2% of the treatments delivered, respectively, through an FPO, FPEC, and VP. A medium response was obtained in 4.1%, 0%, and 5.9% of the treatments delivered, respectively, through an FPO, FPEC, and VP; and a low response was achieved in 5.5%, 22.2%, and 5.9% of the treatments via an FPO, FPEC, and VP. Statistical analysis suggested that different patterns of drug delivery do not result in a significant change in the ophthalmologic response ($P = .424$).

Adverse Events

A list of local adverse events observed in our survey is reported in Table 3. We compared the frequency of the more common transient local adverse events (palpebral edema/hyperemia, frontal edema/hyperemia, and retinal bleeding) to see if they could be

preferentially associated with a particular pattern of IAC drug delivery (Table 3). We did not find any significant association between transient local adverse events and patterns of administration ($P = .784$). The number of events observed for all other temporary local adverse events was too low to attempt any statistical evaluation.

The same type of analysis was performed to compare the most frequent permanent local adverse events (chorioretinal atrophy, exotropia). Even in this case, permanent ocular complications could not be associated with any particular pattern of drug delivery ($P = .233$).

Permanent systemic adverse events have not been observed. In contrast, transient systemic adverse events, though rare, were found in 3 patients. They included blood disorders like febrile neutropenia (1 patient), treated with granulocyte colony stimulating factor; and bone marrow hypocellularity (2 patients). One of these patients presented with anemia that required blood transfusion. Two cases belonged to the group of patients characterized

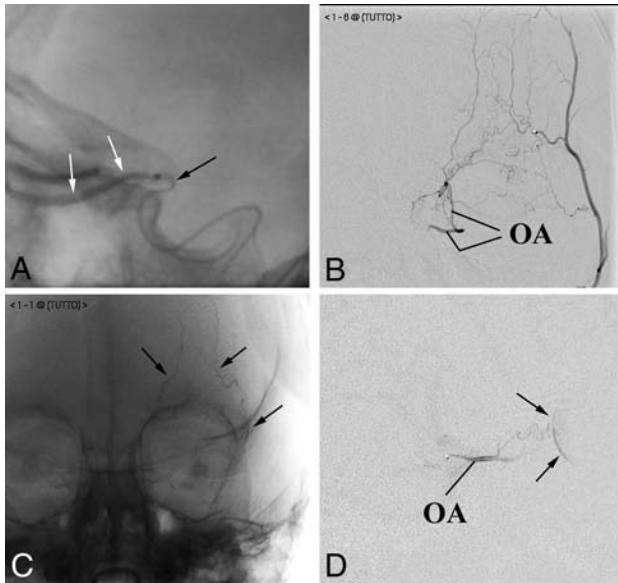


FIG 2. Particular angiographic procedures. *A*, Customization of the microcatheter. The tip of the microcatheter (*black arrow*), manually bent to fit the angioanatomy of the patient, has been firmly placed at the entrance of the OA to release the contrast medium (*white arrows*). *B–D*, Flow anterograde redirection within the OA. Anteroposterior projections. Contrast medium injection into the superficial temporal artery shows a rich network of small vessels connecting the superficial temporal artery with the OA (*B*). Embolization of the arterial network. The cast of glue outlines the embolized frontal vessels (*arrows* in *C*). The flow in the OA, redirected anterogradely (*D*), allows achieving the choroidal blush (*arrows* in *D*).

Table 1: Outcome of the eyes according to the pattern of IAC drug delivery

	Tumor Remission	Recurrence/Enucleation
FPO	46	27 ^a
FPEC	7	2
VP	8	9

^aOne patient died. After all conservative treatments were tried, the disease still progressed. Nevertheless, the parents refused enucleation of the eye.

Table 2: Ophthalmologic response according to the pattern of IAC drug delivery

	Low Response	Medium Response	High Response
FPO	4	3	66
FPEC	2	0	7
VP	1	1	15

by an FPO of drug delivery, and 1 case, to the group of patients treated through an FPEC of drug delivery.

Intraprocedural Complications

A transient increase of airway resistance followed by blood oxygen desaturation of variable degrees from moderate to severe was observed in 200/448 procedures, resulting in a saturation of peripheral oxygen lower than 90% in 145 patients (32.3% of sessions) and lower than 60% in 5 patients. The latter 5 cases were accompanied by bradycardia and hypotension, leading to treatment interruption in 1 occasion. The above-mentioned cardiac and respiratory complications occurred following the insertion of the microcatheter into the cavernous segment of the ICA or during cannulation of the OA. A distal small embolism of the middle cerebral artery occurred in 2 patients, both treated via the ICA.

Table 3: Local adverse events according to the pattern of IAC drug delivery

Adverse Events (No.) (%)	FPO	FPEC	VP
Transient			
Palpebral edema/hyperemia, 55 (55.6%)	40	6	9
Frontal edema/hyperemia, 14 (14.1%)	10	1	3
Retinal bleeding, 12 (12.1%)	10	0	2
Anterior ischemia of the optic nerve, 2 (2%)	1	0	1
Madarosis, 2 (2%)	2	0	0
Frontal alopecia, 2 (2%)	1	0	1
Orbital cellulitis, 1 (1%)	1	0	0
Glaucoma, 1 (1%)	0	0	1
Roth spots, 1 (1%)	1	0	0
Iridocyclitis, 1 (1%)	1	0	0
Permanent			
Chorioretinic atrophy, 16 (16.2%)	13	2	1
Exotropia, 4 (4%)	2	2	0
Ptosis, 1 (1%)	1	0	0
Anisocoria, 1 (1%)	0	0	1
Cutaneous scar necrosis, 1 (1%)	0	1	0
Iris heterochromia, 1 (1%)	0	0	1

One of them required 1-day monitoring in a neurointensive care unit under IV heparin infusion. All previously reported complications were transitory, and no child presented with clinical disabilities on reawakening.

Radiation Exposure

The radiation exposure was measured in a sample of 5 patients randomly selected for each group. For the FPO group, the dose-area product was $4.15 \pm 0.83 \text{ Gy/cm}^2$; it was $12.74 \pm 2.34 \text{ Gy/cm}^2$ for the FPEC group and $17.35 \pm 3.47 \text{ Gy/cm}^2$ for the VP group. Radiation exposure comparison among the groups was significantly different ($P < .001$).

DISCUSSION

IAC in the treatment of intraocular retinoblastoma is currently a widely accepted therapeutic strategy used in specialized centers. Theoretically, the technique of drug delivery into the OA to target the tumor is not difficult if the neurovascular interventionalist has been properly trained. Indeed, navigation of the ICA and catheterization of the OA are facilitated by the very small size of the currently available microcatheters. However, in a remarkable number of cases, the procedure is more difficult and laborious than expected and cannot proceed conventionally. In such cases, the neurovascular interventionalist is required to use a more adaptable approach to minimize technical failures and to maximize IAC efficacy.

Two technically challenging scenarios potentially undermining IAC success can be found with a certain frequency in the angiographic room. The first scenario is a troublesome and unstable catheterization of the OA ostium despite its visualization by selective angiography of the ICA. As previously reported,⁹ this situation is usually secondary to a too angulated origin of the OA from the ICA, which makes the catheterization unsteady. In such cases, resuming the balloon technique applied to the ICA has been suggested⁹ despite all its drawbacks (ie, the risk of evoking ischemic complications, dilution of the drugs in a volume of blood that is too large, the reduced time of drug perfusion). We have found that this technical problem can be overcome by just cus-

tomizing the tip of the catheter; in particular, it is possible to bend it to the desired angulation to fit the anatomy of the patient. Thus, >16% of our patients have been regularly treated as scheduled without the necessity of performing the balloon-assisted occlusion of the ICA.

The second unfavorable scenario is when an adequate choroidal blush is unattainable even when OA catheterization is achieved. In this situation, the contrast medium flows back into the ICA instead of diffusing along the OA without any visible vasospasm. Indeed, the reflux of contrast medium into the ICA is likely secondary to an inversion of the blood flow within the OA due to several possible anastomoses with the ECA, which may provide alternative pathways for the orbital blood supply.^{12,15} In such cases, balloon occlusion of the ICA with drug infusion just below the block may not be as effective as the use of alternative routes through the ECA because the blood supply to the orbit comes just from the latter source. In children, the hemodynamic balance between the OA and the ECA may be subtle. This balance is verified by the number of eyes treated with a VP (17.2% of cases) and, when the pattern was FPFC, by the various anastomoses that, in some cases, have been used for drug delivery in the same children.

Actually, even when previous visualization of the OA has been successful, subsequent attempts to achieve an acceptable choroidal blush through the OA in the same child may fail due to momentary imbalances of the local hemodynamics in favor of the ECA, leading to an inversion of the flow. A series of unpredictable and possibly unknown factors, including vasospasm, are possibly at the basis of such phenomena. The presence of the catheter itself into the OA origin has been suggested as a possible cause of hemodynamic disturbance leading to the activation of collateral circulations.¹⁰ Previous chemotherapy may even reduce the caliber of the OA,⁴ inducing the recruitment of blood via anastomoses with the ECA. At any rate, the presence of anastomoses between the OA and the ECA has been suspected as a variable that could negatively impact the effectiveness of the IAC.¹⁰ Far from it, we believe that the ECA and some of its branches represent potential alternative routes for IAC. In our and in others' experience,^{9,16,17} some of these routes have already been used to deliver antitumoral drugs. Our study shows that 16.29% of procedures occurred via 1 of the many alternative pathways previously described and involving branches of the ECA.¹² This adaptable approach allowed us to increase the number of successful sessions of IAC. In particular, we calculated that 24.52% of eyes could have skipped at least 1 session of IAC if we had not looked for anastomotic pathways. In a retrospective review of 351 procedures of IAC, Klufas et al⁹ reported that 7.8% of IAC infusions occurred through the MMA and that in 4.7% of cases, they resumed the balloon-assisted occlusion of the ICA because a suitable anastomosis between the OA and MMA was not found.

By using other anastomotic pathways, we show that IAC can be successfully performed in a larger number of patients. Thus, a promising technique has been recently proposed to manage competitive backflow from ECA collaterals. Instead of searching and catheterizing the anastomoses between the ECA and the OA, anterograde redirection of the blood flow was achieved by balloon occlusion of the ECA.¹⁸ However, even this approach has draw-

backs (puncture of both femoral arteries, 2 catheter-microcatheter systems within the same artery), and its efficacy/safety versus catheterization of the ECA branches still requires validation.

Although the use of the ECA and its branches for IAC has been previously reported,^{9,16,17} its effectiveness and safety have never been demonstrated in comparison with regular IAC via the OA. Our retrospective study suggests that the use of branches of the ECA in selected cases is as effective as the direct injection into the OA in terms of ophthalmologic response (90.4% for PFO, 88.2% for VP, 77.8% for PFEC). Concerning the outcome, our results show that no statistically significant difference can be found when comparing the 3 groups. However, in light of the limited number of drug deliveries through branches of the ECA and the short follow-up, results have to be interpreted with caution and conclusions should be validated in a larger population and in a longer time perspective.

An even more adaptable approach for IAC can be applied in extremely selected cases. For instance, we artificially altered the orbital circulation, gluing some extraorbital vessels to reduce the volume of drug distribution or to create a more favorable intraorbital circulation to target the tumor. Although the desired goal was achieved and the choroidal blush was obtained, the number of cases was too low to allow a valid statistical evaluation on the efficacy of such procedures. We are aware that embolization of ECA branches is potentially dangerous even in very experienced hands because it can induce retinal or cranial nerve ischemia or stroke due to ICA reflux. However, in our case, embolizations have been performed by a skilled interventional neuroradiologist (S.B.) with experience in managing glue for arteriovenous malformations or fistulas even in the pediatric age group. In addition, this type of embolization is performed with a very small amount of glue for a proximal deafferentation.

Data concerning transient adverse events are in line with those described in other studies.^{6,19-21} Procedural complications, including embolic events, are rarely described in the literature,²¹ and this finding is consistent with our experience (0.4% of sessions). On the other hand, cardiac and respiratory reactions are commonly observed during this procedure. The pathophysiologic mechanism of these complications is currently unknown, likely involving an autonomic reflex.²² Most interesting, neither the cardiac and respiratory complications nor the embolic events ever occurred when patients were treated through the ECA; this finding suggests that this route of drug delivery, though more troublesome, should be considered safer than the OA cannulation.

Systemic adverse events, mainly pancytopenia, are also rare, probably due to the cumulative result from previous administration of systemic chemotherapy. Most local adverse events were transient and minor. Permanent local adverse events (chorioretinal atrophy and exotropia) were observed in 18.9% of eyes, a lower incidence compared with other reports.^{3,23} Statistical analysis did not allow us to associate any adverse event with particular patterns of drug delivery. Concerns remain regarding the toxic effects of irradiation from repeat fluoroscopy in children with retinoblastoma. However, although the VP and PFEC showed higher exposure levels compared with the FPO, the overall irradiation was far lower than the toxic levels previously reported.⁸

CONCLUSIONS

IAC is a valuable therapeutic strategy to treat intraocular retinoblastoma. However, in some cases, it may present technical challenges requiring an unconventional approach, in particular concerning the search for alternative routes of drug delivery through branches of the ECA. The use of these pathways is as effective as the traditional drug infusion through the OA in terms of ophthalmologic response without increasing adverse events and complications.

REFERENCES

1. Lewandowski RJ, Geschwind JF, Liapi E, et al. **Transcatheter intra-arterial therapies: rationale and overview.** *Radiology* 2011;259:641–57 CrossRef Medline
2. Abramson DH, Dunkel IJ, Brodie SE, et al. **A phase I/II study of direct intraarterial (ophthalmic artery) chemotherapy with melphalan for intraocular retinoblastoma initial results.** *Ophthalmology* 2008;115:1398–404, 1404.e1 CrossRef Medline
3. Shields CL, Bianciotto CS, Jabbour P, et al. **Intra-arterial chemotherapy for retinoblastoma: report No. 1, control of retinal tumors, subretinal seeds, and vitreous seeds.** *Arch Ophthalmol* 2011;129:1399–406 CrossRef Medline
4. Suzuki S, Yamane T, Mohri M, et al. **Selective ophthalmic arterial injection therapy for intraocular retinoblastoma: the long-term prognosis.** *Ophthalmology* 2011;118:2081–87 CrossRef Medline
5. Gobin YP, Dunkel IJ, Marr BP, et al. **Intraarterial chemotherapy for the management of retinoblastoma: four-year experience.** *Arch Ophthalmol* 2011;129:732–37 CrossRef Medline
6. Jabbour P, Chalouhi N, Tjoumakaris S, et al. **Pearls and pitfalls of intraarterial chemotherapy for retinoblastoma.** *J Neurosurg Pediatr* 2012;10:175–81 CrossRef Medline
7. Abramson DH, Marr BP, Brodie SE, et al. **Ophthalmic artery chemosurgery for less advanced intraocular retinoblastoma: five year review.** *PLoS One* 2012;7:e34120 CrossRef Medline
8. Venturi C, Bracco S, Cerase A, et al. **Superselective ophthalmic artery infusion of melphalan for intraocular retinoblastoma: preliminary results from 140 treatments.** *Acta Ophthalmol* 2013;91:335–42 CrossRef Medline
9. Klufas MA, Gobin YP, Marr B, et al. **Intra-arterial chemotherapy as a treatment for intraocular retinoblastoma: alternatives to direct ophthalmic artery catheterization.** *AJNR Am J Neuroradiol* 2012;33:1608–14 CrossRef Medline
10. Marr BP, Hung C, Gobin YP, et al. **Success of intra-arterial chemotherapy (chemosurgery) for retinoblastoma: effect of orbitovascular anatomy.** *Arch Ophthalmol* 2012;130:180–85 CrossRef Medline
11. Bracco S, Leonini S, De Francesco S, et al. **Intra-arterial chemotherapy with melphalan for intraocular retinoblastoma.** *Br J Ophthalmol* 2013;97:1219–21 CrossRef Medline
12. Bracco S, Venturi C, Leonini S, et al. **Transorbital anastomotic pathways between the external and internal carotid systems in children affected by intraocular retinoblastoma.** *Surg Radiol Anat* 2016;38:79–87 CrossRef Medline
13. Bracco S, Venturi C, Leonini S, et al. **Identification of intraorbital arteries in pediatric age by high resolution superselective angiography.** *Orbit* 2015;34:237–47 CrossRef Medline
14. Tanaka T, Sho M, Nishiofuku H, et al. **Unresectable pancreatic cancer: arterial embolization to achieve a single blood supply for intraarterial infusion of 5-fluorouracil and full-dose IV gemcitabine.** *AJR Am J Roentgenol* 2012;198:1445–52 CrossRef Medline
15. Macchi V, Regoli M, Bracco S, et al. **Clinical anatomy of the orbito-meningeal foramen: variational anatomy of the canals connecting the orbit with the cranial cavity.** *Surg Radiol Anat* 2016;38:165–77 CrossRef Medline
16. Amans MR, Narvid J, Halbach VV. **Intra-arterial chemotherapy for bilateral retinoblastoma via left ophthalmic artery and right anterior deep temporal artery.** *BMJ Case Rep* 2014;2014. pii: bcr2014204549 CrossRef Medline
17. Cooke D, Farid H, Kim W, et al. **Zygomatico-orbital intra-arterial melphalan infusion for intraocular retinoblastoma.** *J Neurointerv Surg* 2012;4:e16 CrossRef Medline
18. Abruzzo TA, Geller JI, Kimbrough DA, et al. **Adjunctive techniques for optimization of ocular hemodynamics in children undergoing ophthalmic artery infusion chemotherapy.** *J Neurointerv Surg* 2015;7:770–76 CrossRef Medline
19. Shields CL, Fulco EM, Arias JD, et al. **Retinoblastoma frontiers with intravenous, intra-arterial, periocular, and intravitreal chemotherapy.** *Eye* 2013;27:253–64 CrossRef Medline
20. Marr B, Gobin PY, Dunkel IJ, et al. **Spontaneously resolving periocular erythema and ciliary madarosis following intra-arterial chemotherapy for retinoblastoma.** *Middle East Afr J Ophthalmol* 2010;17:207–09 CrossRef Medline
21. Peterson EC, Elharmady MS, Quintero-Wolfe S, et al. **Selective ophthalmic artery infusion of chemotherapy for advanced intraocular retinoblastoma: initial experience with 17 tumors.** *J Neurosurg* 2011;114:1603–08 CrossRef Medline
22. Kato MA, Green N, O'Connell K, et al. **A retrospective analysis of severe intraoperative respiratory compliance changes during ophthalmic arterial chemosurgery for retinoblastoma.** *Paediatr Anaesth* 2015;25:595–602 CrossRef Medline
23. Munier FL, Beck-Popovic M, Balmer A, et al. **Occurrence of sectoral choroidal occlusive vasculopathy and retinal arteriolar embolization after superselective ophthalmic artery chemotherapy for advanced intraocular retinoblastoma.** *Retina* 2011;31:566–73 CrossRef Medline

Prediction of Stent-Retriever Thrombectomy Outcomes by Dynamic Multidetector CT Angiography in Patients with Acute Carotid T or MCA Occlusions

K.M. Thierfelder, W.H. Sommer, B. Ertl-Wagner, S.E. Beyer, F.G. Meinel, W.G. Kunz, G. Buchholz, M.F. Reiser, and H. Janssen

ABSTRACT

BACKGROUND AND PURPOSE: The selection of patients for endovascular therapy is an important issue in stroke imaging. The aim of this study was to determine the predictive value of 3 different dynamic CT angiography parameters, occlusion length, collateralization extent, and time delay to maximum enhancement, for latest generation of stent retriever thrombectomy recanalization outcomes in patients with acute ischemic stroke.

MATERIALS AND METHODS: In this study, subjects were selected from an initial cohort of 2059 consecutive patients who had undergone multiparametric CT, including whole-brain CT perfusion. We included all patients with a complete occlusion of the M1 segment of the MCA or the carotid T and subsequent intra-arterial stent retriever thrombectomy. Dynamic CT angiography was reconstructed from whole-brain CT perfusion raw datasets. Angiographic outcome was scored by using the modified TIC1 scale; and clinical outcome, by using the modified Rankin Scale. Logistic regression analyses were performed to determine independent predictors of a favorable angiographic (mTIC1 = 3) and clinical outcome (mRS ≤2).

RESULTS: Sixty-nine patients (mean age, 68 ± 14 years; 46% men) were included for statistical analysis. In the regression analysis, a short occlusion length was an independent predictor of favorable angiographic outcome (OR, 0.41; $P < .05$). Both collateralization grade (OR, 1.00; $P > .05$) and time delay to peak enhancement (OR, 0.90; $P > .05$) failed to predict a favorable angiographic outcome. None of the dynamic CT angiography predictors were significantly associated with clinical outcome on discharge (OR, 0.664–1.011; $P = .330$ –.953) or at 90 days (OR, 0.779–1.016; $P = .130$ –.845).

CONCLUSIONS: A short occlusion length as determined by dynamic CT angiography is an independent predictor of a favorable angiographic outcome of stent retriever thrombectomy in patients with ischemic stroke.

ABBREVIATIONS: IVT = intravenous thrombolysis; mTIC1 = modified Thrombolysis in Cerebral Infarction scale; spCTA = single-phase CT angiography; WB-CTP = whole-brain CT perfusion

Endovascular treatment in patients with acute stroke is known to be effective for emergency vascularization. Recently published data of randomized clinical trials focusing on the latest generation stent retriever devices (Multicenter Randomized Clinical Trial of Endovascular Treatment for Acute Ischemic Stroke in the Netherlands [MR CLEAN],¹ Endovascular Treatment for Small Core and Proximal Occlusion Ischemic Stroke [ESCAPE],² Solitaire With the Intention for Thrombectomy as Primary Endovascular Treatment [SWIFT-PRIME],³ and Extending the Time

for Thrombolysis in Emergency Neurological Deficits–Intra-Arterial [EXTEND-IA]⁴) have demonstrated a benefit of intra-arterial treatment over intravenous thrombolysis with respect to reperfusion, functional outcome, and mortality.

While the stent retriever trial results are an important milestone in the therapy of ischemic stroke, patient selection for this treatment option should be an important focus for future studies. To date, the decision to perform endovascular treatment is primarily based on the presence or absence of the demarcation of infarction on nonenhanced CT and the site of the vessel occlusion. In addition, a recent study suggests that more robust leptomeningeal collaterals as assessed by conventional angiography are associated with better recanalization results.⁵ However, invasive catheter-based angiography is not available as a screening technique for all patients with stroke.

Occlusion length is another potential predictor of endovascular therapy success because it has been shown to predict intrave-

Received April 21, 2015; accepted after revision December 7.

From the Institute for Clinical Radiology (K.M.T., W.H.S., B.E.-W., S.E.B., F.G.M., W.G.K., M.F.R.), Department of Neurology (G.B.), and Department of Neuroradiology (H.J.), Ludwig-Maximilians-University Hospital, Munich, Germany.

Please address correspondence to Kolja M. Thierfelder, MD, MSc, Institute for Clinical Radiology, Ludwig-Maximilians-University Hospital Munich, Marchioninistr 15, 81377 Munich, Germany; e-mail: kolja.thierfelder@med.uni-muenchen.de

<http://dx.doi.org/10.3174/ajnr.A4694>

nous thrombolysis (IVT) outcome.^{6,7} Animal model studies have shown that clots with a length of >10 mm are associated with decreased success of endovascular procedures and increased rates of complications such as distal embolization during mechanical thrombectomy.⁸ In contrast, previous studies using nonenhanced CT and single-phase CTA have failed to find an association between occlusion length and the success of mechanical recanalization.⁹⁻¹¹ Clarification of these conflicting results is important because endovascular recanalization procedures are especially considered as a treatment option in patients with large-vessel occlusions in whom IVT would be expected to have a low success rate.

Dynamic CTA is a promising new technique that has been shown to noninvasively predict the success of IVT.¹² Dynamic CTA images can be reconstructed from time-resolved CT perfusion data and provide a broad temporal coverage from nonenhanced through arterial-to-venous phases,¹³ thus allowing a noninvasive assessment of the extent of leptomeningeal collateralization.^{12,14,15} Moreover, dynamic CTA is more sensitive to delayed contrast arrival and therefore more closely defines thrombus burden than single-phase CTA.¹⁶ It has been shown that the time delay of maximum enhancement predicts the final infarction size.¹⁷ These advantages of dynamic CTA qualify the technique as a candidate for the prediction of vascular recanalization, which is a major prerequisite for a favorable clinical outcome and reduced mortality in acute ischemic stroke.¹⁸

The aim of this study was to determine the predictive value of 3 different dynamic CTA parameters, occlusion length, collateralization extent, and time delay to maximum enhancement, for the latest generation stent retriever thrombectomy success in patients with acute ischemic stroke.

MATERIALS AND METHODS

Study Design and Population

Institutional review board approval was obtained for this retrospective study, and the requirement for informed consent was waived. Our initial cohort consisted of 2059 consecutive patients who had undergone whole-brain CT perfusion (WB-CTP) for suspected stroke between April 2009 and June 2014.

Of this cohort, we included all subjects with the following:

- 1) Complete occlusion of the middle cerebral artery in the M1 segment or carotid T occlusion as demonstrated by single-phase CT angiography (spCTA)

- 2) Subsequent intra-arterial stent retriever recanalization therapy.

We excluded patients with the following:

- 1) Incomplete WB-CTP raw datasets
- 2) Nondiagnostic quality of dynamic CTA
- 3) Failure of visualization of thrombus length in dynamic CTA
- 4) Cancelled stent retriever thrombectomy.

CT Examination Protocol and Image Processing

All patients underwent a standardized multiparametric CT protocol. It consisted of nonenhanced CT, spCTA, and WB-CTP. All CT examinations were performed by using 1 of the following 3 CT scanners: Somatom Definition Flash, a 128-section dual-source CT scanner, and Somatom Definition Edge and Somatom Defi-

nition AS+, both 128-section CT scanners (all by Siemens, Erlangen, Germany).

WB-CTP was performed with 0.6-mm collimation and 100-mm scan coverage in the z-axis by using an adaptive spiral scanning technique. The datasets were acquired continuously for 48 seconds (32 cycles, 1 sweep every 1.5 seconds). Tube voltage and current were 80 kV and 200 mAs, respectively. The CT dose index was 276 mGy. A total of 35 mL of iodinated contrast agent (400 mg/mL) was administered at a flow rate of 5 mL/s, followed by a saline flush of 40 mL at 5 mL/s.

CT perfusion raw datasets were reconstructed as dynamic angiographies by using the syngo.CT Dynamic angio module (Syngo, via VA 20; Siemens). The image processing included motion correction and automated bone removal. Computation of temporal MIPs included a 4D noise reduction.¹⁹

Defining the Predictors: Dynamic CTA Image Analysis

Dynamic CTA information was used to define 3 predictors: length of occlusion, collateralization grade, and collateral blood flow time delay. All measurements were performed by a reader (S.E.B.) with >2 years of experience in stroke imaging. For quantitative assessment of the collateralization status and in unclear cases, a board-certified neuroradiologist (H.J.) with >12 years of experience in neuroimaging was consulted. Both readers were blinded to clinical data and spCTA.

Length of Occlusion

The length of the filling defect (length of occlusion) was measured on temporal maximum intensity projections that combined all scans of the WB-CTP examination through temporal fusion (temporal MIP).¹⁹ Temporal MIP images depict the maximum enhancement during the entire scan time for every voxel, thereby fusing contrast opacification from early arterial-to-late venous phases of the WB-CTP examination into 1 CT dataset. The length of the filling defect within the occluded artery was measured by connecting straight lines in axial, sagittal, or coronal planes in all cases in which the reader could define a proximal and distal end of the filling defect (Fig 1).¹⁶ We then approximated the occlusion length, taking into account the vessel course over >1 section by using the Pythagorean theorem. If the distal end of the filling defect extended to >1 M2 segment, the average of the filling defects of the single M2 branches was calculated and used as a predictor.

Collateralization Grade

Leptomeningeal collateral vessels of the affected hemisphere were graded by using a score described by Menon et al¹² and were used in different dynamic CTA studies.¹⁵ Briefly, this approach uses a 20-point score that is obtained by summing up 10 single scores for 10 MCA territory regions that were defined by the Alberta Stroke Program Early CT Score.²⁰ For each of the 10 regions, the collateral vessels of the affected hemisphere are compared with those on the contralateral hemisphere and are assigned a score from 0 to 2: 0, no collateral filling; 1, less than the contralateral hemisphere; 2, equal or greater than the contralateral hemisphere.

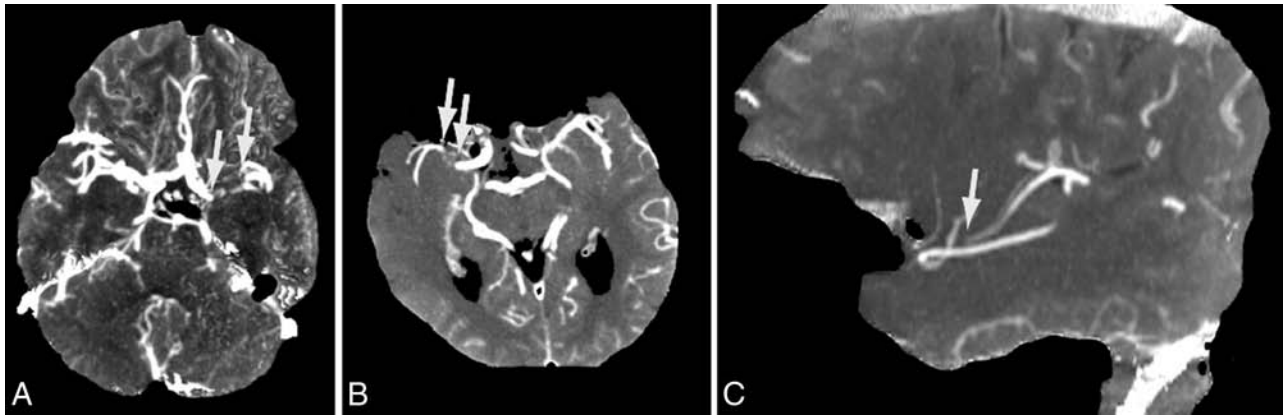


FIG 1. Occlusion-length measurement. Temporal MIP images show the occluding thrombus as a filling defect. *A*, Axial temporal MIP image of a left-sided carotid T occlusion. *B* and *C*, Axial and sagittal images of a right-sided M1 occlusion.

Collateral Blood Flow Time Delay

The time delay distal to the occlusion was measured as described previously by Beyer et al.¹⁷ Briefly, the time delay was defined as the mean difference between time-to-peak contrast enhancement of the M2 segment distal to the occlusion and the corresponding M2 segment of the contralateral side. We used the delay of enhancement of the M2 segment as a surrogate marker for the collateral blood flow. The time-attenuation curves of all ROIs were interpolated by using cubic spline interpolation to improve temporal resolution as previously practiced with CT perfusion time-attenuation curves.²¹ Delay was defined as the difference of the mean of all M2 TTP measurements and the averaged TTP measurements of the contralateral M2 segment.

Endovascular Recanalization Procedure

Endovascular recanalization procedures were performed either with the patient under general anesthesia or, whenever deemed appropriate by the interventional neuroradiologist and the anesthesiologist, with the patient under conscious sedation. All procedures were performed in a triaxial fashion by using a distal-access catheter and a microcatheter to deploy a stent retriever device. All stent retrievers used in this cohort were the latest generation devices (Solitaire; Covidien, Irvine, California; pREset; phenox, Bochum, Germany; Trevo; Stryker, Kalamazoo, Michigan). Because these devices are almost identically constructed, we did not include the device type as a separate predictor in our statistical analysis. After affirmation of mainstem recanalization, we removed the catheter material.

Evaluation of Angiographic Data to Determine Technical Therapy Success

Two readers (1 board-certified neuroradiologist with >12 years [H.J.] and 1 radiologist [K.M.T.] with >3 years of experience in stroke imaging) independently evaluated the angiographic images with respect to recanalization and reperfusion. In case of disagreement, a consensus was reached in a separate session. Reperfusion of the corresponding arterial territory was scored by using the modified Thrombolysis in Cerebral Infarction (mTICI) scale,²² by using 50% as the threshold for achieving reperfusion grade 2b or higher: 0, no perfusion; 1, minimal flow past the occlusion with little to no perfusion; 2a, antegrade partial perfusion

of <50% of the downstream ischemic territory; 2b, antegrade partial perfusion of ≥50% of the downstream ischemic territory; and 3, antegrade complete perfusion of the downstream ischemic territory. An mTICI of 3 was defined as a favorable recanalization outcome.

Statistical Analysis

All statistical analyses were performed with SPSS Statistics 20 (IBM, Armonk, New York). Normal distribution was evaluated by using the Kolmogorov-Smirnov test. In case of normal distribution, we used a 2-tailed Student *t* test. In case of non-normal distribution, a Wilcoxon test was performed.

Univariate logistic regression analysis was used to test the association between predictors and outcome variable (angiographic and clinical outcome). Predictors were the following: age, sex, additional internal carotid artery occlusion, additional IVT, time from symptom onset to initial imaging, length of occlusion, collateral blood flow delay, and morphologic collateral extent. Variables significantly associated with a favorable angiographic/clinical outcome ($P < .2$) in the univariate analysis were included in multivariate models.

All metric and normally distributed variables are reported as mean ± SD; non-normally distributed variables are presented as medians (interquartile range). Categorical variables are presented as frequency and percentage. *P* values below .05 indicate statistical significance.

RESULTS

Study Population

From our initial cohort of 2059 patients, 348 patients were excluded due to missing WB-CTP raw datasets. Among the remaining 1711 patients, 179 were found to have an M1 or carotid T occlusion on spCTA. In 76 of these patients, stent retriever recanalization was performed. From these patients, we excluded 3 patients in whom stent retriever thrombectomy was eventually not performed (no evidence of occlusion in the diagnostic angiographic series [1 patient], impassable proximal ICA occlusion [2 patients]). Furthermore, 1 patient was excluded due to nondiagnostic quality of dynamic CTA; and 3 patients, due to failure to

determine the distal thrombus end in dynamic CTA. The remaining 69 patients formed the final study cohort. The selection process of the patients is illustrated in Fig 2.

Patient Characteristics

The mean age of the 69 included patients was 68.4 ± 14.4 years (range, 28–97 years). Thirty-two (46%) patients were male. Fifty

patients had an occlusion of the MCA, and 19 had an occlusion of the carotid T. Fifty-four (78%) were treated with IVT before stent retriever thrombectomy. The mean time from symptom onset to CT was 161 ± 88 minutes ($n = 46$). The mean time from CT to recanalization was 119 ± 82 minutes ($n = 69$).

On admission, the mean National Institutes of Health Stroke Scale score was 15.6 ± 4.7 ($n = 57$). Baseline NIHSS was significantly associated with better angiographic outcome (OR, 0.809; $P = .005$), a better clinical outcome on discharge (OR, 0.787; $P = .008$), and a better clinical outcome at 90 days (OR, 0.774; $P = .015$). The mean baseline Glasgow Coma Scale score on admission was 12.9 ± 2.4 ($n = 69$).

With respect to angiographic outcome, mTICI scores after recanalization were as follows: mTICI = 0, 5 patients; mTICI = 1, 3 patients; mTICI = 2a, 6 patients; mTICI = 2b, 24 patients; mTICI = 3, 31 patients. The results of univariate logistic regression analyses for mTICI scores after recanalization are shown in Table 1.

Regarding clinical patient outcome, modified Rankin Scale scores on discharge were as follows: mRS = 0, 6 patients; mRS = 1, 4 patients; mRS = 2, 7 patients; mRS = 3, 7 patients; mRS = 4, 10 patients; mRS = 5, 27 patients; mRS = 6, 8 patients. The mean mRS score on discharge was 3.8 ± 1.7 . The

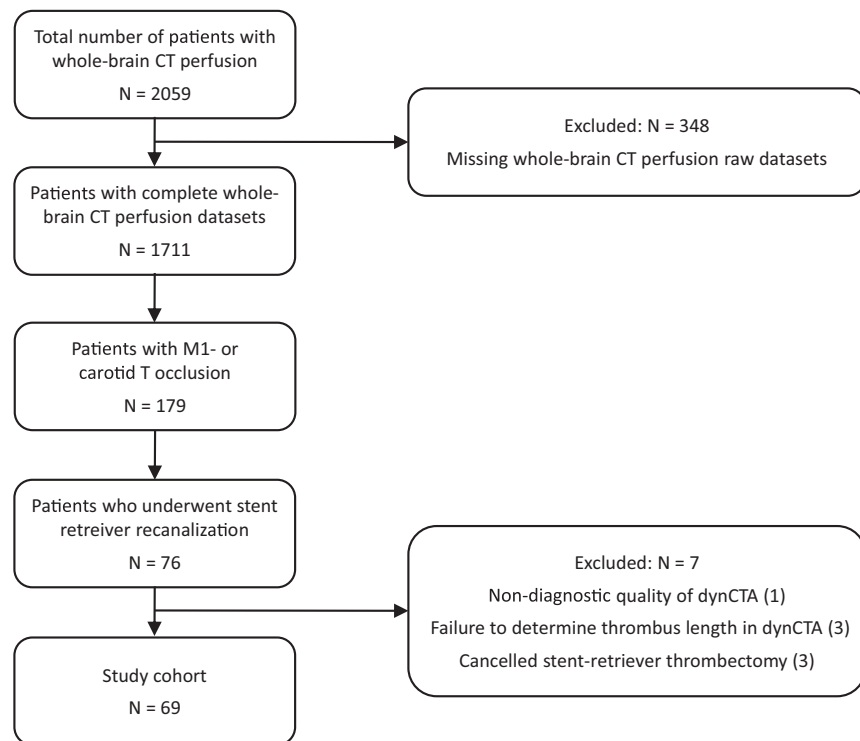


FIG 2. Flow chart of patient selection. dynCTA indicates dynamic CT angiography.

Table 1: Characteristics of patients with favorable (mTICI = 3) and nonfavorable (mTICI < 3) recanalization outcome^a

	Overall (N = 69)	mTICI = 3 (n = 31)	mTICI < 3 (n = 38)	Odds Ratio	P Value
Age (yr)	68.4 ± 14.4	66.7 ± 14.1	69.8 ± 14.5	1.000	.981
Male sex (No.)	32 (46%)	15 (48%)	17 (45%)	1.152	.775
Additional ICA occlusion (No.)	22 (32%)	9 (29%)	13 (34%)	0.708	.485
Carotid T occlusion (No.)	19 (28%)	5 (16%)	14 (37%)	1.768	.274
Time to recanalization (min)	119 ± 82	108 ± 69	127 ± 92	0.859	.389
IVT (No.)	54 (78%)	24 (77%)	30 (79%)	1.094	.878
Occlusion length (mm)	15.6 ± 7.9	12.9 ± 6.8	17.7 ± 8.1	0.409	.018 ^b
Collateralization grade (0–20)	13.8 ± 4.3	13.7 ± 4.5	13.7 ± 4.1	1.003	.958
Time delay (sec)	6.5 ± 2.8	6.2 ± 2.1	6.7 ± 3.2	0.896	.251

^a The last 2 columns show the results of the univariate logistic regression analysis to determine the effect of predictors on recanalization success ($N = 69$).

^b Statistically significant.

Table 2: Characteristics of patients with favorable (mRS_{disc} ≤ 2) and nonfavorable (mRS_{disc} > 2) clinical outcome^a

	Overall (N = 69)	mRS _{disc} ≤ 2 (n = 17)	mRS _{disc} > 2 (n = 52)	Odds Ratio	P Value
Age (yr)	68.4 ± 14.4	65.4 ± 16.5	69.4 ± 13.8	0.982	.380
Male sex (No.)	32 (46%)	7 (41%)	25 (48%)	0.877	.839
Additional ICA occlusion (No.)	22 (32%)	4 (23%)	18 (35%)	0.960	.949
Carotid T occlusion (No.)	19 (28%)	6 (35%)	13 (25%)	1.023	.974
Time to recanalization (min)	119 ± 82	101 ± 77	126 ± 86	0.694	.181 ^b
IVT (No.)	54 (78%)	15 (88%)	39 (75%)	0.202	.142 ^b
Occlusion length (mm)	15.6 ± 7.9	13.6 ± 7.4	16.1 ± 8.2	0.664	.330
Collateralization grade (0–20)	13.8 ± 4.3	13.9 ± 4.5	13.8 ± 4.2	0.996	.953
Time delay (sec)	6.5 ± 2.8	6.7 ± 3.2	6.4 ± 2.8	1.011	.917

Note:—mRS_{disc} indicates mRS at discharge.

^a The last 2 columns show the results of the univariate logistic regression analysis to determine the effect of predictors on clinical outcome ($N = 69$).

^b Below < .2 and therefore included in multivariate analysis.

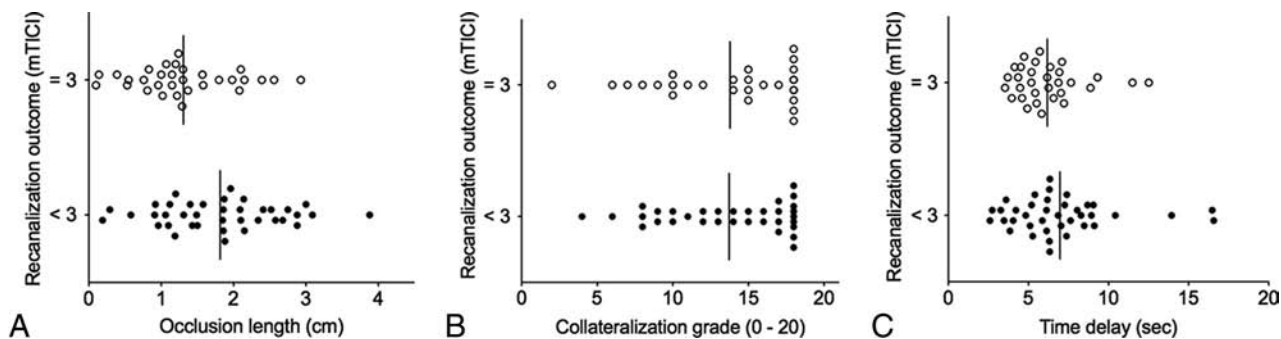


FIG 3. Correlation between dynamic CTA predictors and angiographic outcome. Shorter occlusion length (A) is associated with favorable technical thrombectomy outcome. Both collateralization grade (B) and time delay (C) do not show a significant correlation with angiographic thrombectomy outcome.

results of univariate logistic regression analyses for the modified Rankin Scale score on discharge are presented in Table 2.

mRS after 90 days (mRS₉₀) was available in only 42 patients (61%). Scores of mRS after 90 days in this subgroup were the following: mRS = 0, 4 patients; mRS = 1, 9 patients; mRS = 2, 2 patients; mRS = 3, 6 patients; mRS = 4, 10 patients; mRS = 5, 2 patients; mRS = 6, 9 patients. The mean mRS score after 90 days was 3.1 ± 2.1 .

There were 5 cases of postinterventional hemorrhage, all of which were not space-occupying. The mean values for the dynamic CTA predictors in the cases of hemorrhage were 14.7 ± 5.0 mm for occlusion length, 6.6 ± 2.6 for collateralization grade, and 8.6 ± 2.5 seconds for time delay. With respect to angiographic outcome, 2 of these cases were mTICI 3, and 3 were mTICI 2b. Four of these cases had a nonfavorable functional outcome after 90 days (mRS after 90 days of >2). In 1 case with hemorrhage, the mRS score after 90 days was unknown (mRS score on discharge was favorable in this case).

Association of Predictors with Thrombectomy Outcome

In the univariate analysis for angiographic outcome, occlusion length was significantly associated with recanalization outcome: The mean occlusion length of patients with an mTICI score of 3 ($n = 31$, 12.9 ± 6.8 mm) was significantly shorter than the mean occlusion length in patients with an mTICI score of <3 ($n = 38$, 17.7 ± 8.1 mm; OR, 0.41, $P > .05$). Both collateralization grade (OR, 1.00; $P > .05$) and time delay to peak enhancement (OR, 0.90; $P > .05$) failed to predict a favorable angiographic outcome (Table 1). The correlation between dynamic CTA predictors and favorable angiographic outcome is shown in Fig 3. Age, sex, the presence of an additional ICA occlusion, and additional IV thrombolysis did not show a significant correlation with thrombectomy outcome. Because occlusion length was the only predictor to show an association with angiographic thrombectomy outcome, multivariate analysis was not performed.

In the univariate analyses for clinical outcome on discharge and after 90 days, none of the predictors reached statistical significance. The results for the mRS score on discharge, which was available in all patients, are presented in Table 2. Time to recanalization ($P = .181$) and IV thrombolysis ($P = .142$) were below the P threshold of .2 and were included in a multivariate analysis. In this analysis, neither of these 2 predictors reached statistical significance ($P = .143$ and $P = .108$, respectively).

mRS after 90 days was available in only 42 (61%) patients. In a separate univariate analysis of these 42 patients, none of the predictors were significantly associated with mRS at 90 days. Odds ratios and P values for the 3 imaging parameters were as follows: occlusion length: OR, 0.918, $P = .845$; collateralization grade: OR, 1.016, $P = .833$; time delay: OR, 0.779, $P = .130$.

DISCUSSION

The present study investigated the predictive value of time-resolved dynamic CT angiography on endovascular treatment success. In patients with acute large-vessel occlusion who underwent stent retriever thrombectomy, our study demonstrated a shorter thrombus length as assessed by dynamic CTA associated with a better recanalization success, while collateralization grade and time delay of maximum enhancement distal to the occlusion failed to predict angiographic thrombectomy outcome. None of the imaging parameters were significantly associated with a better clinical outcome.

Occlusion length plays an important role in intravenous thrombolysis and may therefore be considered a potential predictor of endovascular recanalization success.²³ Our observed association between occlusion length and recanalization success is in accordance with animal model studies that have shown longer occlusions to be associated with a lower success rate of endovascular procedures and higher rates of complications.⁸

Previous studies in humans, however, have failed to find an association between thrombus length and success of mechanical recanalization.^{9,11,24} These studies used thin-section nonenhanced CT or spCTA for clot depiction. It has been shown that the nonenhanced CT appearance of clot depends on the thrombus composition, suggesting that some (ie, low-density) portions of clot could be less well-discerned with this technique.^{25,26} In addition, nonenhanced CT is more challenging when vascular calcifications or a high hematocrit cause intra-arterial hyperdensities. On spCTA, visibility of thrombus extent depends on the strength of collateral flow, particularly with state-of-the-art fast-acquisition protocols.²⁷ Dynamic CTA, on the other hand, is more sensitive to delayed contrast arrival and therefore more closely defines thrombus burden than spCTA.¹⁶ It might be reasonably assumed that dynamic CTA is the superior method for clot-length measurement, indicating that, in fact, there is an association between clot length and technical recanalization success.

In contrast to occlusion length, the grading of collateralization did not predict a favorable angiographic outcome of stent retriever recanalization. This finding is not consistent with recently published results of the Interventional Management of Stroke (IMS) III Trial.⁵ This trial showed an association between a more robust collateral grade and both recanalization of the occluded arterial segment and downstream reperfusion. Unlike our study, the IMS III trial used catheter-based angiography to determine the collateralization grade. Possible reasons for the discordant findings could be the imaging technique itself, the method of assessment of collateralization, and the different patient samples.

With respect to thrombectomy recanalization success, an mTICI score of 3, antegrade complete perfusion of the downstream ischemic territory, is, by nature, the most desirable goal for endovascular therapy. Therefore, unlike previous studies that mostly defined a favorable recanalization outcome as an mTICI score of 2b or 3, we restricted the group of favorable outcomes to those with an mTICI score of 3. This approach, at the same time, avoids the problem of group 2b (antegrade partial perfusion of $\geq 50\%$ of the downstream ischemic territory) being quite heterogeneous with respect to functional outcome (depending on the location of the remaining thrombus material).

Clinical outcome, as opposed to angiographic outcome, was not significantly associated with occlusion length or any of the other imaging predictors. The only outcome parameter that was available for all patients in this study was mRS on discharge. The more meaningful outcome, mRS at 90 days, was only available in about 60% of the patients. However, these results should be taken seriously because the actual goal of all reperfusion therapies remains a better clinical outcome for the patients. Nevertheless, as it has already been shown that vascular recanalization is a major prerequisite for a favorable clinical outcome and reduced mortality in acute ischemic stroke,¹⁸ it will remain the first interim goal of endovascular therapy.

There are limitations to our study, which need to be taken into account when interpreting the data. First, the clinical outcome after 90 days was not available in all patients. Second, this is a single-center study with a limited number of patients. In view of the small sample size, some of the nonsignificant findings in this study such as the presence of carotid T occlusion might actually be important predictors of recanalization outcome. Therefore, further studies with larger patient cohorts will need to be conducted, which would also enable a finer graduation of recanalization outcome.

CONCLUSIONS

A shorter occlusion length as determined by dynamic CT angiography is an independent predictor of a favorable outcome of stent retriever thrombectomy in patients with acute ischemic stroke. Given that future studies show a correlation with clinical outcomes as well, dynamic CT angiography may be considered for patient selection.

Disclosures: Felix G. Meinel—UNRELATED: Payment for Lectures (including service on Speakers Bureaus); b.e.imaging (speaker's honoraria). Maximilian F. Reiser—UNRELATED: German Research Society (Deutsche Forschungsgemeinschaft) (November 2006–2016, Principal Investigator, Munich Center of Advanced Photonics, Ludwig-Maximilians-University of Munich-Technical University of Munich, Germany)

“Cluster of Excellence”*; Euro-Biolmaging (December 2010–2016, Principal Site Investigator for Euro-Biolmaging: European Commission, SP4 Capacities, FP7-Infrastructures-2010-1 [GA 262023], Ludwig-Maximilians-University of Munich, Germany)*; German National Cohort (2011–2016 Co-Principal Investigator, German National Cohort, Imaging Working Group, Whole-Body MRI Phenotyping, BMBF/Helmholtz Society, Germany)*; Munich Cluster of Excellence, M4 Imaging (2011–2016 Co-Principal Investigator: Imaging, Personalized Medicine, a new dimension of drug development)*; BMBF German Center for Lung Diseases (2010–2015 Principal Investigator)*; BMBF German Center for Cardiovascular Diseases (2010–2015 Principal Investigator)*; Birgit Ertl-Wagner—UNRELATED: Board Membership: Philips Healthcare, Bracco, Springer Medical Publishing; Consultancy: Munich Medical International, Philips Healthcare; Grants/Grants Pending: Eli Lilly,* Genentech,* Guerbet,* Merck Serono,* Novartis*; Payment for Lectures (including service on Speakers Bureaus): Siemens, Bayer Schering; Payment for Manuscript Preparation: Siemens, Springer Medical Publishing, Thieme Medical Publishers, Bracco; Royalties: Springer Medical Publishing, Thieme Medical Publishers; Payment for Development of Educational Presentations: Siemens, Bracco, Springer, Thieme; Stock/Stock Options: Siemens (stock owned by spouse); Travel/Accommodations/Meeting Expenses Unrelated to Activities Listed: Siemens. *Money paid to the institution.

REFERENCES

- Berkhemer OA, Fransen PS, Beumer D, et al. **A randomized trial of intraarterial treatment for acute ischemic stroke.** *N Engl J Med* 2015; 372:11–20 CrossRef Medline
- Goyal M, Demchuk AM, Menon BK, et al; ESCAPE Trial Investigators. **Randomized assessment of rapid endovascular treatment of ischemic stroke.** *N Engl J Med* 2015;372:1019–30 CrossRef Medline
- Saver JL, Goyal M, Bonafe A, et al; SWIFT PRIME Investigators. **Stent-retriever thrombectomy after intravenous t-PA vs. t-PA alone in stroke.** *N Engl J Med* 2015;372:2285–95 CrossRef Medline
- Campbell BC, Mitchell PJ, Kleinig TJ, et al; EXTEND-IA Investigators. **Endovascular therapy for ischemic stroke with perfusion-imaging selection.** *N Engl J Med* 2015;372:1009–18 CrossRef Medline
- Liebeskind DS, Tomsick TA, Foster LD, et al; IMS III Investigators. **Collaterals at angiography and outcomes in the Interventional Management of Stroke (IMS) III trial.** *Stroke* 2014;45:759–64 CrossRef Medline
- Legrand L, Naggara O, Turc G, et al. **Clot burden score on admission T2*-MRI predicts recanalization in acute stroke.** *Stroke* 2013;44: 1878–84 CrossRef Medline
- Sillanpaa N, Saarinen JT, Rusanen H, et al. **The clot burden score, the Boston Acute Stroke Imaging Scale, the cerebral blood volume ASPECTS, and two novel imaging parameters in the prediction of clinical outcome of ischemic stroke patients receiving intravenous thrombolytic therapy.** *Neuroradiology* 2012;54:663–72 CrossRef Medline
- Gralla J, Burkhardt M, Schroth G, et al. **Occlusion length is a crucial determinant of efficiency and complication rate in thrombectomy for acute ischemic stroke.** *AJNR Am J Neuroradiol* 2008;29:247–52 CrossRef Medline
- Froehler MT, Tateshima S, Duckwiler G, et al; UCLA Stroke Investigators. **The hyperdense vessel sign on CT predicts successful recanalization with the Merci device in acute ischemic stroke.** *J Neurointerv Surg* 2013;5:289–93 CrossRef Medline
- Mokin M, Morr S, Natarajan SK, et al. **Thrombus density predicts successful recanalization with Solitaire stent retriever thrombectomy in acute ischemic stroke.** *J Neurointerv Surg* 2015;7:104–07 CrossRef Medline
- Spiotta AM, Vargas J, Hawk H, et al. **Hounsfield unit value and clot length in the acutely occluded vessel and time required to achieve thrombectomy, complications and outcome.** *J Neurointerv Surg* 2014;6:423–27 CrossRef Medline
- Menon BK, O'Brien B, Bivard A, et al. **Assessment of leptomeningeal collaterals using dynamic CT angiography in patients with acute ischemic stroke.** *J Cereb Blood Flow Metab* 2013;33:365–71 CrossRef Medline
- Calleja AI, Cortijo E, Garcia-Bermejo P, et al. **Collateral circulation on perfusion-computed tomography-source images predicts the response to stroke intravenous thrombolysis.** *Eur J Neurol* 2013;20: 795–802 CrossRef Medline

14. Frölich AM, Wolff SL, Psychogios MN, et al. **Time-resolved assessment of collateral flow using 4D CT angiography in large-vessel occlusion stroke.** *Eur Radiol* 2014;24:390–96 CrossRef Medline
15. Beyer SE, Thierfelder KM, von Baumgarten L, et al. **Strategies of collateral blood flow assessment in ischemic stroke: prediction of the follow-up infarct volume in conventional and dynamic CTA.** *AJNR Am J Neuroradiol* 2015;36:488–94 CrossRef Medline
16. Frölich AM, Schrader D, Klotz E, et al. **4D CT angiography more closely defines intracranial thrombus burden than single-phase CT angiography.** *AJNR Am J Neuroradiol* 2013;34:1908–13 CrossRef Medline
17. Beyer SE, von Baumgarten L, Thierfelder KM, et al. **Predictive value of the velocity of collateral filling in patients with acute ischemic stroke.** *J Cereb Blood Flow Metab* 2015;35:206–12 CrossRef Medline
18. Rha JH, Saver JL. **The impact of recanalization on ischemic stroke outcome: a meta-analysis.** *Stroke* 2007;38:967–73 CrossRef Medline
19. Smit EJ, Vonken EJ, van der Schaaf IC, et al. **Timing-invariant reconstruction for deriving high-quality CT angiographic data from cerebral CT perfusion data.** *Radiology* 2012;263:216–25 CrossRef Medline
20. Pexman JH, Barber PA, Hill MD, et al. **Use of the Alberta Stroke Program Early CT Score (ASPECTS) for assessing CT scans in patients with acute stroke.** *AJNR Am J Neuroradiol* 2001;22:1534–42 Medline
21. Royalty K, Manhart M, Pulfer K, et al. **C-arm CT measurement of cerebral blood volume and cerebral blood flow using a novel high-speed acquisition and a single intravenous contrast injection.** *AJNR Am J Neuroradiol* 2013;34:2131–38 CrossRef Medline
22. Yoo AJ, Simonsen CZ, Prabhakaran S, et al; Cerebral Angiographic Revascularization Grading Collaborators. **Refining angiographic biomarkers of revascularization: improving outcome prediction after intra-arterial therapy.** *Stroke* 2013;44:2509–12 CrossRef Medline
23. Riedel CH, Zimmermann P, Jensen-Kondering U, et al. **The importance of size: successful recanalization by intravenous thrombolysis in acute anterior stroke depends on thrombus length.** *Stroke* 2011;42:1775–77 CrossRef Medline
24. Mokin M, Morr S, Natarajan SK, et al. **Thrombus density predicts successful recanalization with Solitaire stent retriever thrombectomy in acute ischemic stroke.** *J Neurointerv Surg* 2015;7:104–07 CrossRef Medline
25. Liebeskind DS, Sanossian N, Yong WH, et al. **CT and MRI early vessel signs reflect clot composition in acute stroke.** *Stroke* 2011;42:1237–43 CrossRef Medline
26. Kim EY, Heo JH, Lee SK, et al. **Prediction of thrombolytic efficacy in acute ischemic stroke using thin-section noncontrast CT.** *Neurology* 2006;67:1846–48 CrossRef Medline
27. Pulli B, Schaefer PW, Hakimelahi R, et al. **Acute ischemic stroke: infarct core estimation on CT angiography source images depends on CT angiography protocol.** *Radiology* 2012;262:593–604 CrossRef Medline

C-Arm Conebeam CT Perfusion Imaging in the Angiographic Suite: A Comparison with Multidetector CT Perfusion Imaging

 K. Niu,  P. Yang,  Y. Wu,  T. Struffert,  A. Doerfler,  S. Schafer,  K. Royalty,  C. Strother, and  G.-H. Chen



ABSTRACT

BACKGROUND AND PURPOSE: Perfusion imaging in the angiography suite may provide a way to reduce time from stroke onset to endovascular revascularization of patients with large-vessel occlusion. Our purpose was to compare conebeam CT perfusion with multidetector CT perfusion.

MATERIALS AND METHODS: Data from 7 subjects with both multidetector CT perfusion and conebeam CT perfusion were retrospectively processed and analyzed. Two algorithms were used to enhance temporal resolution and temporal sampling density and reduce the noise of conebeam CT data before generating perfusion maps. Two readers performed qualitative image-quality evaluation on maps by using a 5-point scale. ROIs indicating CBF/CBV abnormalities were drawn. Quantitative analyses were performed by using the Sørensen–Dice coefficients to quantify the similarity of abnormalities. A noninferiority hypothesis was tested to compare conebeam CT perfusion against multidetector CT perfusion.

RESULTS: Average image-quality scores for multidetector CT perfusion and conebeam CT perfusion images were 2.4 and 2.3, respectively. The average confidence score in diagnosis was 1.4 for both multidetector CT and conebeam CT; the average confidence scores for the presence of a CBV/CBF mismatch were 1.7 ($\kappa = 0.50$) and 1.5 ($\kappa = 0.64$). For multidetector CT perfusion and conebeam CT perfusion maps, the average scores of confidence in making treatment decisions were 1.4 ($\kappa = 0.79$) and 1.3 ($\kappa = 0.90$). The area under the visual grading characteristic for the above 4 qualitative quality scores showed an average area under visual grading characteristic of 0.50, with 95% confidence level cover centered at the mean for both readers. The Sørensen–Dice coefficient for CBF maps was 0.81, and for CBV maps, 0.55.

CONCLUSIONS: After postprocessing methods were applied to enhance image quality for conebeam CT perfusion maps, the conebeam CT perfusion maps were not inferior to those generated from multidetector CT perfusion.

ABBREVIATIONS: AUC = area under the curve; CBCT = conebeam CT; CBCTP = conebeam CT perfusion; MDCT = multidetector CT; MDCTP = multidetector CT perfusion; PICCS = prior image constrained compressed sensing; VGC = visual grading characteristics

Recent results from several clinical trials¹⁻⁵ provide compelling evidence that in patients with an acute ischemic stroke due to an anterior circulation large-artery occlusion, revascularization improved functional outcomes and reduced mortality, compared

with conventional therapy. The following additional insights were provided by these trials: 1) the critical interplay between the elapsed time from stroke onset to revascularization and functional outcome, and 2) the potential value of multidetector CT perfusion (MDCTP) in patient selection for endovascular treatment. Other studies further document and emphasize the link between outcomes and the elapsed time between stroke onset and revascularization.^{1,2,6-8} Because “time is brain,” our study aimed at comparing the diagnostic utility of dynamic perfusion maps obtained with conebeam CT (CBCT) with ones obtained by using multidetector CT (MDCT). We were motivated to do this because if the CBCT measurements are similar to those obtained by using MDCT, the ability to obtain perfusion measurements in the angiography suite would largely eliminate the delays currently associated with multitechnique imaging protocols.⁹⁻¹¹

While the feasibility of acquiring dynamic conebeam CT per-

Received October 8, 2015; accepted after revision December 9.

From the Departments of Medical Physics (K.N., Y.W., G.-H.C.) and Radiology (P.Y., C.S., G.-H.C.), University of Wisconsin-Madison, Madison, Wisconsin; Department of Neurosurgery (P.Y.), Changhai Hospital, Second Military Medical University, Shanghai, China; University of Erlangen-Nuremberg (T.S., A.D.), Erlangen, Germany; and Siemens Medical Solutions USA (S.S., K.R.), Hoffman Estates, Illinois.

The work was partially supported by a research grant from the National Institutes of Health (U01 EB021183) and a research agreement with Siemens AX.

Please address correspondence to Guang-Hong Chen, PhD, University of Wisconsin-Madison, Department of Medical Physics, L1167, WIMR, Madison, Wisconsin 53705-2275; e-mail: gchen7@wisc.edu

 Indicates open access to non-subscribers at www.ajnr.org

<http://dx.doi.org/10.3174/ajnr.A4691>

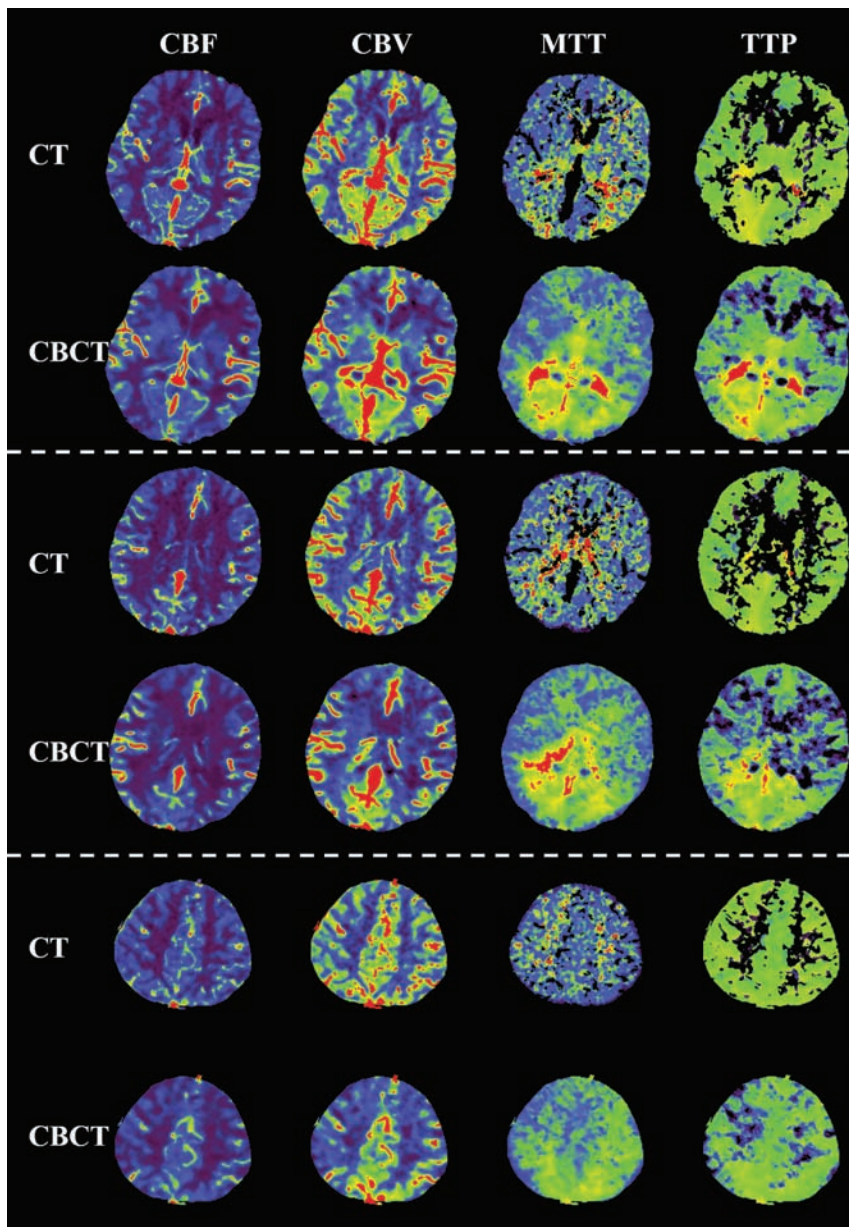


FIG 1. Examples of perfusion parametric maps for both MDCT and CBCT modalities. There are 4 type of maps: CBF, CBV, MTT, and TTP. Three different section locations, separated by using a dashed line, are shown.

fusion maps has been demonstrated both in animals and humans, the poor temporal resolution (4–6 seconds) and poor sampling density (7–10 data points) available with current C-arm angiographic systems still presents significant challenges in acquiring data that are comparable with those obtained with MDCTP.^{11,12} In this study, dynamic perfusion data obtained by using a commercial flat panel detector angiographic system (Axiom Artis zee; Siemens, Erlangen, Germany) were processed by using previously reported novel algorithms which, by reducing noise and also enhancing temporal resolution and temporal sampling, very significantly reduce these limitations.^{13–15} Dynamic CBCT perfusion maps postprocessed by using these algorithms were compared with dynamic perfusion maps from the same subject's conventional MDCTP study.

MATERIALS AND METHODS

Patient Selection

From a group of 17 consecutive patients with acute ischemic stroke who were examined with both C-arm conebeam CT perfusion (CBCTP) and MDCTP or MR perfusion imaging, 7 had both CBCTP and MDCTP before endovascular treatment. Data from these 7 were used for this study. All studies were performed under an approved ethics committee protocol.

Among the 7 cases, 1 was spontaneous thrombus lysis before revascularization therapy. In this instance, the CBCT perfusion maps showed very little abnormality compared with the earlier MDCTP maps. In another case, there was significant truncation in the acquired data, which resulted in a truncated arterial input function. These 2 cases were excluded from quantitative image-quality analysis. Further details of the 2 cases can be found in the "Discussion."

Data Acquisition

MDCTP datasets were acquired by using multisection CT, Somatom Definition AS (Siemens). The total z-direction coverage was 80 mm. Contrast was injected by using a dual-syringe angiographic power injector (Accutron; Medtron, Saarbruecken, Germany) with the following protocol: Thirty-milliliters of contrast medium, Imeron 350 (iopamidol; Bracco, Milan, Italy) was injected into a peripheral vein at a rate of 4 mL/s followed by a 30-mL saline chase.

The interval from performing the MDCTP to arrival in the angiography suite averaged about 30 minutes (range, 20–40 minutes). On arrival in the angiography suite, a dynamic C-arm CBCTP data acquisition was performed by using a prototype data-acquisition mode on a commercial biplane flat detector angiographic system (Axiom Artis zee). Sixty milliliters of contrast medium was injected into a peripheral vein with the use of a dual-syringe power injector (Accutron). For each acquisition, 9 bidirectional rotations (5 forward and 4 reverse) were performed; the contrast medium was injected 5 seconds after the start of the first rotation. Thus, the images from the first 2 rotations did not contain contrast and could be used as the mask images while images from the other 7 captured the bolus passing through the vasculature. These are designated as the "fill" images. The rotation angular range was

Table 1: Results of image-quality and confidence level evaluation for MDCTP and CBCTP parametric maps

Modality and Rating	Reader 1	Reader 2	Cohen κ
MDCTP			
Image quality	2.5 ± 0.7	2.3 ± 0.8	0.45
Confidence level of making stroke diagnosis	1.6 ± 1.2	1.2 ± 0.5	0.42
Confidence level of determining whether there is a mismatch	2.0 ± 1.5	1.4 ± 0.7	0.50
Confidence level of making treatment decisions	1.5 ± 1.1	1.3 ± 0.7	0.79
CBCTP			
Image quality	2.4 ± 0.6	2.1 ± 0.7	0.62
Confidence level of making stroke diagnosis	1.5 ± 0.9	1.3 ± 0.5	0.75
Confidence level of determining whether there is a mismatch	1.6 ± 0.9	1.4 ± 0.5	0.64
Confidence level of making treatment decisions	1.3 ± 0.5	1.3 ± 0.5	0.90

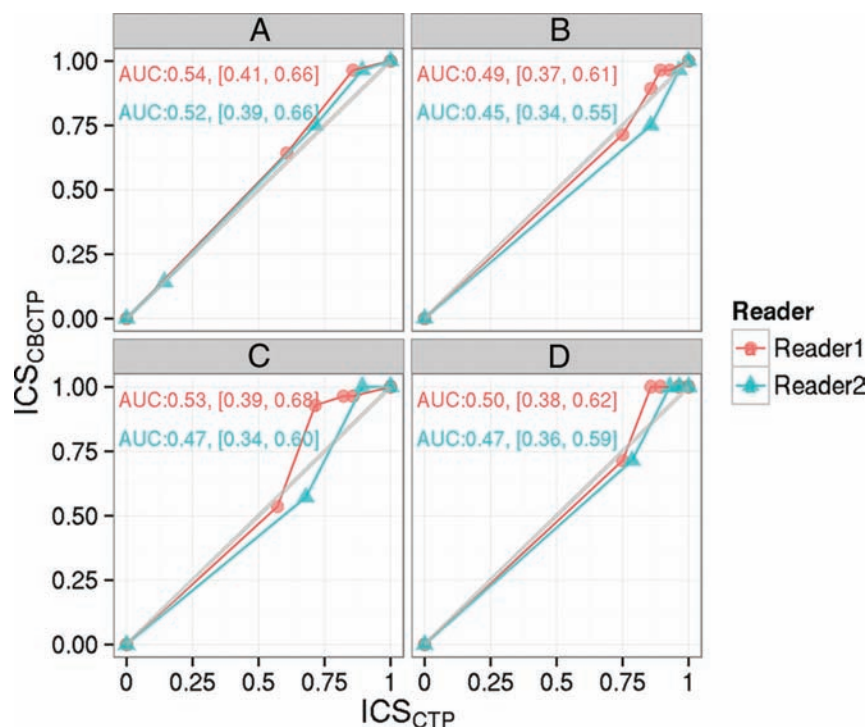


FIG 2. Visual grading characteristic curves of the 2 readers in terms of image quality (A) and confidence level of making a stroke diagnosis (B), determining whether there is a mismatch (C), and making treatment decisions (D), respectively. The area under the curve and its 95% confidence interval are also noted on each subplot. ICS indicates image criteria scores.

200° at approximately 5 seconds for each rotation. Two hundred forty-eight projections were acquired during each rotation. The tube potential was 77 kV(peak), and the dose rate was 0.36 μ Gy/projection. This acquisition protocol resulted in a temporal window to sample the contrast uptake curve of approximately 5 seconds, with 41 seconds of total acquisition duration. In the 9-sweep CBCTP acquisition protocol used in this study, a total radiation dose of 4.6 mSv⁹ was delivered to the patient. The dose from a state-of-the-art diagnostic CTP examination is 5.0 mSv.¹⁶

Image Postprocessing

MDCT Perfusion Maps. The acquired MDCTP projection datasets were reconstructed by using the vendor's commercial software, and the parametric perfusion maps (CBF, CBV, MTT, TTP) were calculated by using the NeroPBV perfusion software pro-

vided by the vendor (Siemens). Final perfusion maps were reformatted into 512 × 512 images with 10-mm thickness.

CBCT Perfusion Maps. To enhance the temporal resolution/temporal sampling density and to reduce noise in the reconstructed CBCTP maps, we postprocessed all of the reconstructed image volumes by using the prior image constrained compressed sensing (PICCS) algorithm^{14,15} to reduce noise and a new technique, temporal resolution and sampling recovery,¹³ to enhance temporal resolution and improve temporal sampling density. The total time needed to process images with PICCS and temporal resolution and sampling recovery is <3 minutes for each clinical case by using a personal computer equipped with a graphics card. After the application of PICCS and temporal resolution and sampling recovery algorithms, we used the postprocessed CBCT image volumes to generate the dynamic perfusion maps (CBF, CBV, MTT, and TTP) by using the same proprietary software used for the MDCTP maps. The CBCT maps were reformatted into 10-mm section thicknesses to match the CTP maps.

A 3D rigid registration algorithm (a commercially available component of the DynaCT [Siemens] application) was also applied to coregister the MDCTP and the CBCTP maps for comparison; no other motion-correction software was used for image postprocessing.

Image Evaluation

Both MDCTP and CBCTP maps were imported into a research workstation

(Nero PBV; Siemens), where CBCTP maps were registered to the corresponding CTP maps. The same color map was applied for both MDCTP and CBCTP datasets. Under the guidance of an experienced clinician, the window and level were adjusted separately for CBCTP and MDCTP to optimize the maps for viewing and analysis.

Qualitative Image-Quality Evaluation. Four consecutive (adjacent) image sections were selected from each case for evaluation. These yielded 56 images (4 × 7 = 28 images for CTP and 28 images for CBCTP) for each of the 4 dynamic perfusion maps (CBF, CBV, MTT, TTP). The 4 maps from the same section were put together on 1 PowerPoint slide (Microsoft, Redmond, Washington). Then, the 56 slides of each map parameter were randomized and anonymized. These randomized slides were presented to the 2 experienced clinicians (P.Y. and

Table 2: Pooled observer results for lesion identification and location by modality^a

Modalities	Left	Right	Bilateral	No. of Lesions	Total	Cohen κ
MDCTP	30	25	0	1	56	0.93
CBCTP	32	17	4	3	56	0.94

^a Cohen κ quantified the interobserver agreement for both modalities.

Table 3: Pooled observer results for mismatch diagnosis by modality^a

Modalities	Mismatch (Yes)	Mismatch (No)	Total	Cohen κ
MDCTP	7	49	56	0.51
CBCTP	16	40	56	0.65

^a Cohen κ quantified the interobserver agreement for both modalities.

Table 4: Sørensen-Dice coefficient and ROI size results for both CBF and CBV maps^a

Maps	Sørensen-Dice Coefficient		ROI Size	
	Mean	SD	MDCTP	CBCTP
CBF	0.81	0.09	1 ± 0.69	0.97 ± 0.44
CBV	0.55	0.23	0.38 ± 0.21	0.45 ± 0.24

^a The ROI size was normalized with respect to mean ROI size of MDCTP CBF maps.

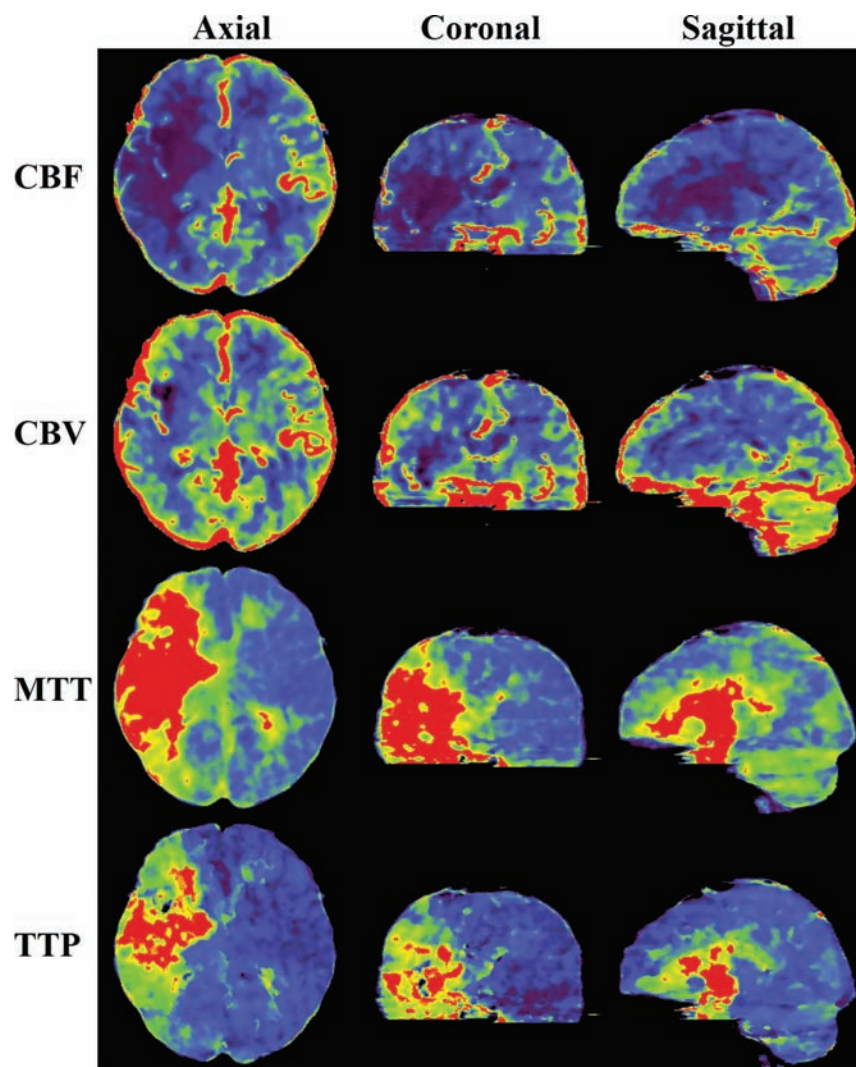


FIG 3. CBCTP-derived parametric maps (CBF, CBV, MTT, TTP) shown on axial, coronal, and sagittal sections. The section thickness is 10 mm for all the images.

C.S.) to score the quality of maps by using the following 5-point scale: 1, excellent image quality, no limitations for clinical use; 2, good image quality, minimal limitations for

presented as mean ± SD.

Because the scores of image quality and confidence level were ordinal categorical, a visual grading characteristics (VGC) analysis

clinical use; 3, sufficient image quality, moderate limitations for clinical use but no substantial loss of information; 4, restricted image quality, relevant limitations for clinical use, clear loss of information; 5, poor image quality, image not usable, loss of information; image must be repeated. For each slide, the readers were also asked to indicate their confidence level in determining whether there was a mismatch between CBV and CBF and in making treatment decisions by using the following 5-point rating scale: 1, definitely can; 2, possibly can; 3, unsure; 4, possibly cannot; 5, definitely cannot. After the evaluation of each slide, the 2 readers were asked to record their diagnosis by using the following annotations: 1) no lesion, 2) left, right, or bilateral lesion. They were also asked to indicate their assessment regarding the existence of a mismatch: yes or no.

No other clinical data were provided to the readers, so the diagnosis made was solely based on the 4 parametric maps of each of the 56 slides.

Quantitative Image-Quality Analysis.

By consensus, the same observers who performed the qualitative analysis drew a ROI on the CBF and CBV maps of the 40 datasets (4 for each of the 5 datasets) to indicate the extent of any abnormality. The similarity of the ROIs between the matching (corresponding MDCTP and CBCTP) maps was then quantitatively analyzed for both CBF and CBV maps. The Sørensen-Dice coefficients were used to quantify the similarity of the corresponding ROIs. If the 2 ROIs have the same size and shape, then the Sørensen-Dice coefficient simply shows what percentage of their ROIs overlap (a coefficient of 1 means 100% overlap of the 2 ROIs, and a coefficient of 0.5 means the 2 ROIs overlap by 50%).

Statistical Analysis

Statistical analysis was performed by using the software package (R, Version 3.2.1, <http://www.r-project.org>). The image quality, confidence level evaluation, and Sørensen-Dice coefficient for ROI similarity analysis are presented

was performed. The 2 axes corresponded to the image criteria scores (ICS) of MDCTP and CBCTP, respectively (ICS_{CTP} versus ICS_{CBCTP}). The similarity analysis of MDCTP and CBCTP in terms of image quality and confidence level was evaluated by using the area under the VGC curve (AUC_{VGC}), in which $AUC_{VGC} = 0.5$ means that the 2 modalities have equivalent performance. Cohen κ coefficients were calculated to evaluate the interobserver agreement for each variable. The interobserver agreement was described as unacceptable ($\kappa < 0$), poor ($0 \leq \kappa < 0.4$), fair ($0.4 \leq \kappa < 0.6$), good ($0.6 \leq \kappa < 0.8$), and excellent ($\kappa \geq 0.8$).

RESULTS

The image quality of the perfusion maps (Fig 1) was judged to be between good and sufficient for both MDCTP (pooled reader rating, 2.4) and CBCTP (pooled reader rating, 2.3) with fair interobserver agreement ($\kappa = 0.45$ and 0.62 for MDCTP and CBCTP, respectively). The 2 reviewers also agreed (κ between 0.42 and 0.90) that they had the confidence (scales from 1.2 to 2.0) of making stroke diagnosis, determining whether there is a mismatch, and making treatment decisions on the basis of the perfusion maps computed from both MDCTP and CBCTP datasets. The detailed results of image-quality and confidence level scores are presented in Table 1.

The VGC curves (Fig 2) demonstrated equivalent performance of MDCTP and CBCTP in terms of image quality ($AUC_{VGC} = 0.54$ for observer 1 and 0.52 for observer 2) and confidence level of making a stroke diagnosis ($AUC_{VGC} = 0.49$ for observer 1 and 0.45 for observer 2), determining whether there is a mismatch ($AUC_{VGC} = 0.53$ for observer 1 and 0.47 for observer 2), and making treatment decisions ($AUC_{VGC} = 0.50$ for observer 1 and 0.47 for observer 2). $AUC_{VGC} > 0.5$ indicates that CBCTP has better performance and $AUC_{VGC} < 0.5$ indicates that MDCTP has better performance. The 95% confidence interval covers 0.5 for both readers.

Table 2 presents the pooled observer reading results for stroke diagnosis. The 2 observers had excellent agreement ($\kappa = 0.93$ and 0.94 for MDCTP and CBCTP maps, respectively) about the lesion identification for both MDCTP and CBCTP maps. The 2 observers also agreed on the mismatch detection on the basis of both MDCTP and CBCTP maps; the detailed results are presented in Table 3.

The statistical results of similarity analysis of abnormal regions for both CBF and CBV are shown in Table 4. For CBF maps, the abnormal regions extracted from CTP and CBCTP maps showed a strong correlation (Sørensen-Dice coefficient = 0.81 ± 0.09), while for CBV maps, the abnormal region just demonstrated a fair correlation (Sørensen-Dice coefficient = 0.55 ± 0.23).

Examples of the parametric maps (CBF, CBV, MTT, and TTP) for both MDCTP and CBCTP are presented in Figs 1 and 3. The parametric maps of CBCTP look quite similar compared with those from MDCTP, especially for the CBF and CBV maps. In the CBF and CBV maps, gray matter and white matter can be differentiated by both modalities. The same observations can be found in Fig 4.

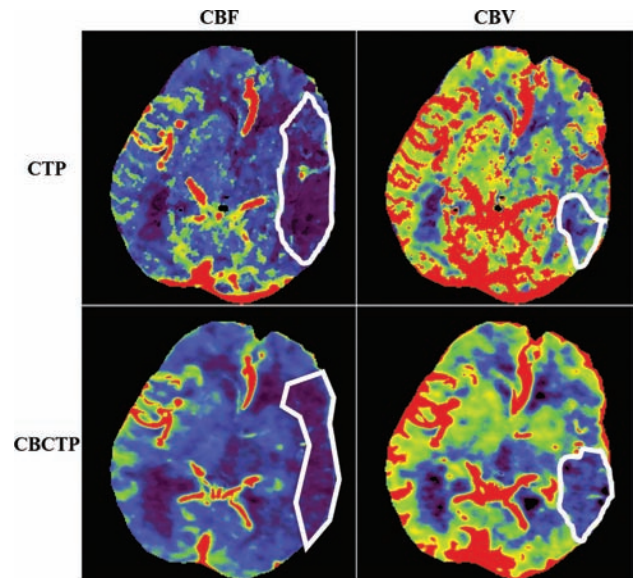


FIG 4. Example of ROI evaluation for CBF and CBV maps from the same patient at same section location. The white ROIs were drawn by the 2 neuroradiologists to indicate the abnormality regions on each map by consensus.

DISCUSSION

In this small feasibility study, parametric perfusion maps (CBF, CBV, MTT, and TTP) made by using data obtained with a commercial biplane flat detector angiographic C-arm system were compared with perfusion maps from conventional MDCT. In terms of image quality, confidence levels of making a diagnosis of a stroke, determining whether there was a mismatch between CBV and CBF, and making treatment decisions, the perfusion maps from CBCTP datasets were judged to have information content equivalent to that of maps obtained from the MDCTP dataset.

In the abnormality shape and size studies, the region of abnormality on the CBV maps was usually much smaller than that on CBF maps ($\sim 40\%$ of CBF ROI sizes, Table 4). Thus, it is harder to manually contour abnormal ROIs on the CBV maps with good precision. This difficulty partially explains why the Sørensen-Dice coefficient is smaller for CBV (Table 4).

The perfusion maps generated from biplane C-arm CBCTP look similar to the maps generated from MDCTP. There was good correlation between the maps in depicting regions of abnormal perfusion. However, because the evolution of ischemic tissue is quite dynamic as time progresses, the shape and location of the penumbra and core may change. The differences in the time between obtaining the MDCTP and CBCTP maps may be 1 reason why these maps may look different. These differences can partially explain the slightly different diagnoses from diagnostic multisession CT and C-arm CBCT (Table 3). The 1 case in this series in which there was spontaneous lysis of a thrombus in the MCA (Fig 5) provides an excellent example of the dynamic nature of the evolution of blood flow and perfusion in acute ischemic stroke. Just as this patient's blood flow and perfusion improved in the MDCTP and CBCTP interval, those of others are perhaps more likely to deteriorate. The potential benefit of being able to measure perfusion parameters at the time when treatment is initiated

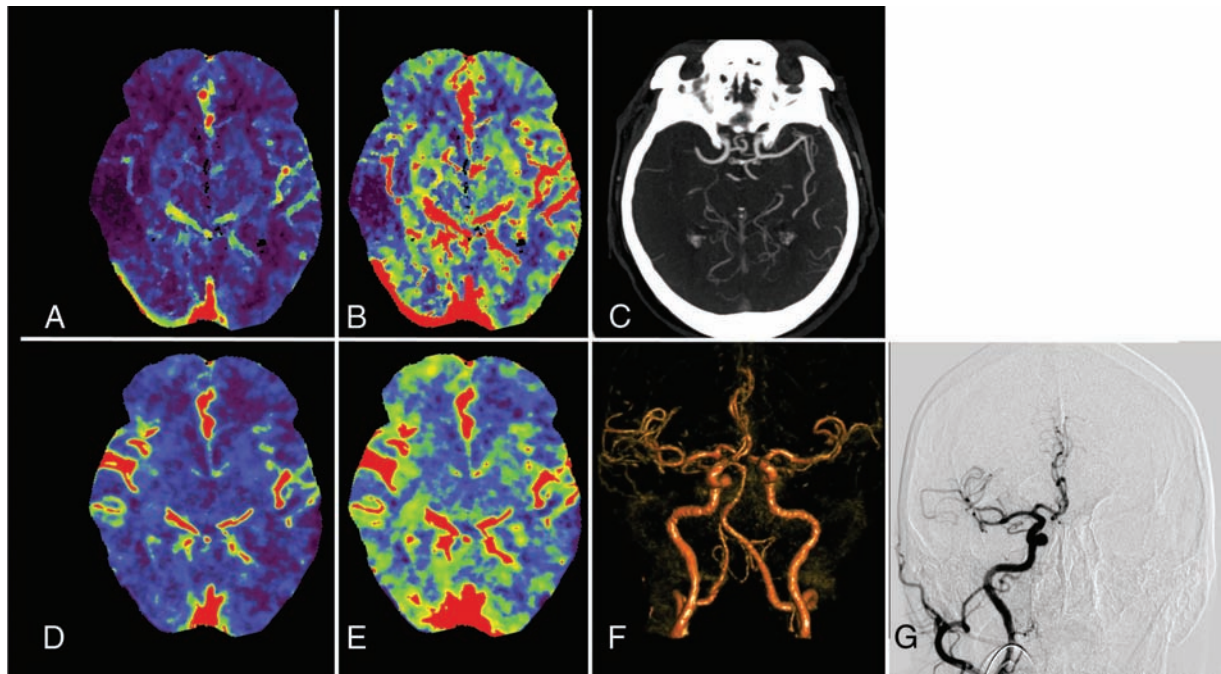


FIG 5. *A*, CBF map from the MDCTP dataset. *B*, CBV map from the MDCTP dataset. *C*, MDCTA image before transfer of the patient to the interventional suite. *D*, CBF map from the CBCTP dataset acquired after the same patient was transferred to the interventional suite. *E*, CBV map from the CBCTP dataset. *F*, Volume-rendered time-resolved CBCTA image derived from the CBCTP dataset. *G*, DSA image in the interventional suite before the treatment started.

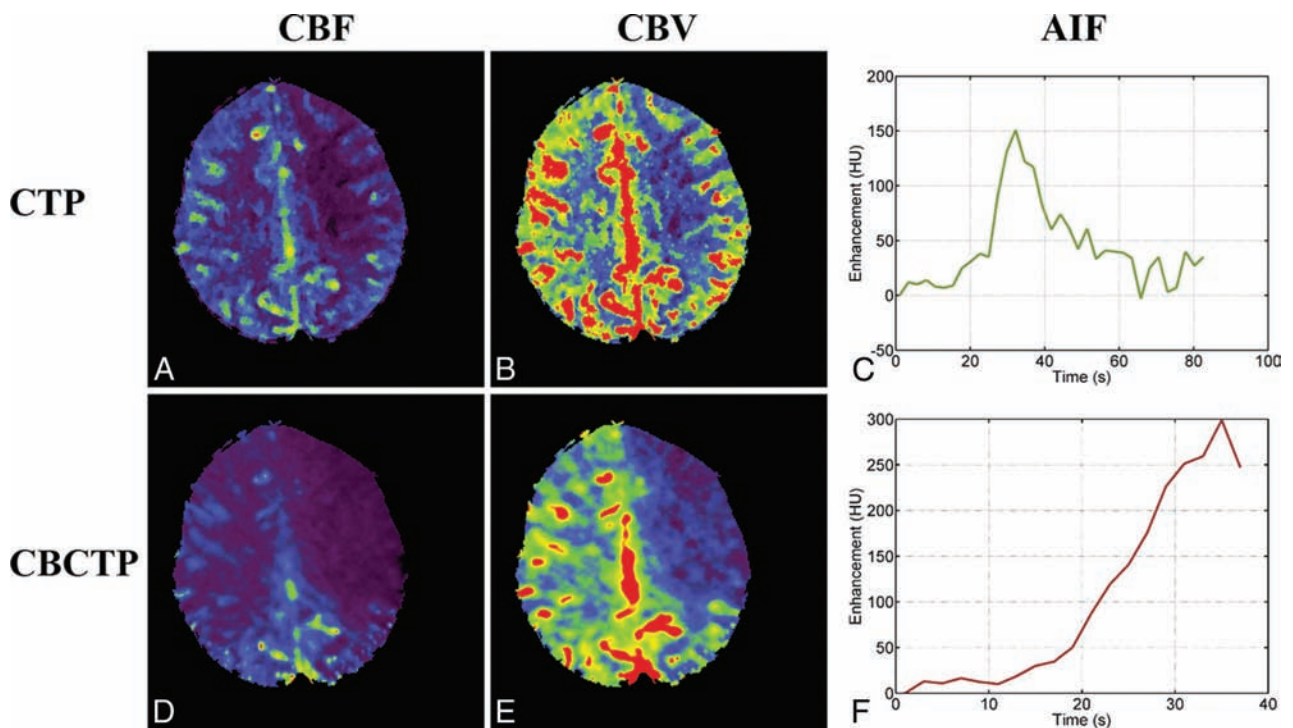


FIG 6. *A*, A CBF map from a CTP dataset. *B*, A CBV map from a CTP dataset. *C*, Arterial input function curve of the CTP dataset used to compute perfusion maps. *D*, A CBF map from the CBCTP dataset of the same patient. *E*, A CBV map from the CBCTP dataset. *F*, Arterial input function curve of the CBCTP dataset used to compute perfusion maps.

seems obvious: By replacing conventional MDCTP imaging in patients with acute stroke with CBCTP imaging, the time between stroke onset and revascularization can be substantially reduced. This reduction could be especially helpful for patients being referred from external hospitals for endovascular therapy.^{17,18} The

contrast dose and radiation dose associated with CBCTP are relatively low so that the concept of performing perfusion measurements more than once in some revascularization procedures is, in our opinion, quite reasonable.

There are several limitations to this study. First, the sample size

is small, and the results only demonstrate the feasibility of the technique. Second, these data acquisitions were performed at a single institution (Department of Neuroradiology, University Erlangen-Nuremberg, Germany) during a short time. A multi-institution study with a larger patient cohort is needed to validate both the reliability and reproducibility of CBCTP perfusion maps. Third, all patients were treated under general anesthesia; how severe patient motion associated with awake patients affects the image quality should be evaluated in future study. Fourth, the software used to enhance temporal resolution/temporal sampling and to reduce noise has not yet been optimized for large-scale deployment, so its functionality in a clinical environment has not been established. Fifth, data-acquisition protocols, including contrast dose, radiation dose, delay time, number of back-and-forth acquisitions, and angular coverage for each conebeam CT acquisition, are also not optimized (Fig 6).

CONCLUSIONS

After postprocessing with novel methods to enhance temporal sampling/resolution and reduce noise, perfusion data obtained by using a commercial biplane flat detector angiographic system was adequate to create clinically usable parametric maps of CBF, CBV, MTT and TTP. These maps were judged noninferior in information content to perfusion maps obtained by using a commercial MDCT. If available in the angiographic suite, this capability would further enrich the environment for diagnosis, triage, and treatment of patients with an acute ischemic stroke due to a large-artery occlusion.

Disclosures: Sebastian Schafer—UNRELATED: Employment: Siemens Medical Solutions USA. Kevin Royalty—UNRELATED: Employment: I am a full-time employee of Siemens Medical Solutions. My role is Director of Research Collaborations Eastern North America. Charles Strother—RELATED: Grant: Siemens.* Comments: Funds were provided under a sponsored research agreement between Siemens and the University of Wisconsin-Madison School of Medicine and Public Health; Provision of Writing Assistance, Medicines, Equipment, or Administrative Support: Angiography equipment was provided under a Master Research Agreement between Siemens and the University of Wisconsin-Madison School of Medicine and Public Health*; UNRELATED: Grants/Grants Pending: Funds were provided for x-ray angiography advanced imaging techniques under a sponsored research agreement between Siemens and the University of Wisconsin-Madison School of Medicine and Public Health*; Patents (planned, pending or issued): Payments were made under a nonexclusive licensing agreement; Travel/Accommodations/Meeting Expenses Unrelated to Activities Listed: reimbursed by Siemens for travel and expenses for Symposium on Quantitative DSA 2015 Taiwan. Guang-Hong Chen—RELATED: Grant: National Institutes of Health,* Siemens Research Contract*; UNRELATED: Patents (planned, pending or issued): I am the inventor of PICCS, a patented technology; Royalties: PICCS-related patents were licensed to GE Healthcare and royalties were received by Wisconsin Alumni Research Foundation (WARF).* However, that has nothing to do with the work presented here. *Money paid to the institution.

REFERENCES

- Berkhemer OA, Fransen PSS, Beumer D, et al. **A randomized trial of intraarterial treatment for acute ischemic stroke.** *N Engl J Med* 2015; 372:11–20 CrossRef Medline
- Campbell BC, Mitchell PJ, Kleinig TJ, et al; EXTEND-IA Investigators. **Endovascular therapy for ischemic stroke with perfusion-imaging selection.** *N Engl J Med* 2015;372:1009–18 CrossRef Medline
- Saver JL, Goyal M, Bonafe A, et al; SWIFT PRIME Investigators. **Stent-retriever thrombectomy after intravenous t-PA vs. t-PA alone in stroke.** *N Engl J Med* 2015;372:2285–95 CrossRef Medline
- Jovin TG, Chamorro A, Cobo E, et al; REVASCAT Trial Investigators. **Thrombectomy within 8 hours after symptom onset in ischemic stroke.** *N Engl J Med* 2015;372:2296–306 CrossRef Medline
- Goyal M, Demchuk AM, Menon BK, et al; ESCAPE Trial Investigators. **Randomized assessment of rapid endovascular treatment of ischemic stroke.** *N Engl J Med* 2015;372:1019–30 CrossRef Medline
- Broderick JP, Palesch YY, Demchuk AM, et al; Interventional Management of Stroke (IMS) III Investigators. **Endovascular therapy after intravenous t-PA versus t-PA alone for stroke.** *N Engl J Med* 2013;368:893–903 CrossRef Medline
- Khatiri P, Yeatts SD, Mazighi M, et al; IMS III Trialists. **Time to angiographic reperfusion and clinical outcome after acute ischaemic stroke: an analysis of data from the Interventional Management of Stroke (IMS III) Phase 3 Trial.** *Lancet Neurol* 2014;13:567–74 CrossRef Medline
- Menon BK, Almekhlafi MA, Pereira VM, et al; STAR Study Investigators. **Optimal workflow and process-based performance measures for endovascular therapy in acute ischemic stroke: analysis of the Solitaire FR thrombectomy for acute revascularization study.** *Stroke* 2014;45:2024–29 CrossRef Medline
- Struffert T, Deuerling-Zheng Y, Kloska S, et al. **Dynamic angiography and perfusion imaging using flat detector CT in the angiography suite: a pilot study in patients with acute middle cerebral artery occlusions.** *AJNR Am J Neuroradiol* 2015;36:1964–70 CrossRef Medline
- Strother CM. **3D imaging in the angiography suite: from vascular anatomy to implant and physiology assessment.** *AJNR Am J Neuroradiol News Digest* November 2013. <http://ajnrdigest.org/3d-imaging-angiography-suite-vascular-anatomy-implant-physiology-assessment/>. Accessed August 26, 2015
- Royalty K, Manhart M, Pulfer K, et al. **C-arm CT measurement of cerebral blood volume and cerebral blood flow using a novel high-speed acquisition and a single intravenous contrast injection.** *AJNR Am J Neuroradiol* 2013;34:2131–38 CrossRef Medline
- Manhart MT, Aichert A, Struffert T, et al. **Denosing and artefact reduction in dynamic flat detector CT perfusion imaging using high speed acquisition: first experimental and clinical results.** *Phys Med Biol* 2014;59:4505–24 CrossRef Medline
- Tang J, Xu M, Niu K, et al. **A novel temporal recovery technique to enable cone beam CT perfusion imaging using an interventional C-arm system.** In: *Proceedings of SPIE Conference on Medical Imaging*, Orlando, Florida. February 9, 2013
- Chen GH, Tang J, Leng S. **Prior image constrained compressed sensing (PICCS): a method to accurately reconstruct dynamic CT images from highly undersampled projection data sets.** *Med Phys* 2008; 35:660–63 CrossRef Medline
- Niu K, Tang J, Royalty K, et al. **Radiation dose reduction and CNR enhancement in C-arm cone beam CT.** In: *Proceedings of SPIE Conference on Medical Imaging*, Orlando, Florida. February 9, 2013
- Manniesing R, Oei MT, van Ginneken B, et al. **Quantitative dose dependency analysis of whole-brain CT perfusion imaging.** *Radiology* 2016;278:190–07 CrossRef Medline
- Hung SC, Lin CJ, Guo WY, et al. **Toward the era of a one-stop imaging service using an angiography suite for neurovascular disorders.** *BioMed Res Int* 2013;2013:e873614 CrossRef Medline
- Doerfler A, Göllitz P, Engelhorn T, et al. **Flat-panel computed tomography (DYNA-CT) in neuroradiology: from high-resolution imaging of implants to one-stop-shopping for acute stroke.** *Clin Neuro-radiol* 2015;25(suppl 2):291–97 CrossRef Medline

Thinner Regions of Intracranial Aneurysm Wall Correlate with Regions of Higher Wall Shear Stress: A 7T MRI Study

 R. Blankena,  R. Kleinloog,  B.H. Verweij,  P. van Ooij,  B. ten Haken,  P.R. Luijten,  G.J.E. Rinkel, and  J.J.M. Zwanenburg



ABSTRACT

BACKGROUND AND PURPOSE: Both hemodynamics and aneurysm wall thickness are important parameters in aneurysm pathophysiology. Our aim was to develop a method for semi-quantitative wall thickness assessment on in vivo 7T MR images of intracranial aneurysms for studying the relation between apparent aneurysm wall thickness and wall shear stress.

MATERIALS AND METHODS: Wall thickness was analyzed in 11 unruptured aneurysms in 9 patients who underwent 7T MR imaging with a TSE-based vessel wall sequence (0.8-mm isotropic resolution). A custom analysis program determined the in vivo aneurysm wall intensities, which were normalized to the signal of nearby brain tissue and were used as measures of apparent wall thickness. Spatial wall thickness variation was determined as the interquartile range in apparent wall thickness (the middle 50% of the apparent wall thickness range). Wall shear stress was determined by using phase-contrast MR imaging (0.5-mm isotropic resolution). We performed visual and statistical comparisons (Pearson correlation) to study the relation between wall thickness and wall shear stress.

RESULTS: 3D colored apparent wall thickness maps of the aneurysms showed spatial apparent wall thickness variation, which ranged from 0.07 to 0.53, with a mean variation of 0.22 (a variation of 1.0 roughly means a wall thickness variation of 1 voxel [0.8 mm]). In all aneurysms, apparent wall thickness was inversely related to wall shear stress (mean correlation coefficient, -0.35 ; $P < .05$).

CONCLUSIONS: A method was developed to measure the wall thickness semi-quantitatively, by using 7T MR imaging. An inverse correlation between wall shear stress and apparent wall thickness was determined. In future studies, this noninvasive method can be used to assess spatial wall thickness variation in relation to pathophysiologic processes such as aneurysm growth and rupture.

ABBREVIATIONS: AWT = apparent wall thickness; MPR-TSE = magnetization-prepared inversion-recovery turbo spin-echo; PC/mag = phase-contrast MR magnitude images; PCMR = phase-contrast MR imaging; WSS = wall shear stress

Intracranial aneurysms may rupture; this rupture leads to subarachnoid hemorrhage. The case fatality of aneurysmal SAH has decreased during the past decades but is still around 30%–40%,

and almost half of the survivors remain permanently disabled.¹ The prevalence of intracranial aneurysms is approximately 3%.² Several risk and trigger factors for rupture have been identified,^{3,4} but these factors explain only a small proportion of the risk of rupture and are insufficient to explain the pathophysiology of rupture.⁵ Thus, we need more risk factors to better predict rupture, and we need to increase knowledge of pathophysiology to better understand rupture.⁶

Hemodynamics play an important role in aneurysm pathophysiology because the endothelial cells are sensitive to mechanical stimuli such as stretch and wall shear stress (WSS, the frictional force on the walls caused by the blood flow).⁷ Time-resolved 3D phase-contrast MR imaging (PCMR) can measure in vivo flow and WSS in aneurysms,⁸ and a recent study showed that the use of 7T MR imaging increases the signal-to-noise ratio and improves flow visualization and quantification.⁹

Aneurysmal wall thickness is another interesting parameter in the pathophysiology of rupture because the wall eventually ruptures. In a previous study, we showed that it is possible to assess

Received September 3, 2015; accepted after revision December 22.

From the Department of Neurology and Neurosurgery (R.B., R.K., B.H.V., G.J.E.R.), Brain Center Rudolf Magnus, Department of Radiology (P.R.L., J.J.M.Z.), and Image Sciences Institute (P.R.L., J.J.M.Z.), University Medical Center Utrecht, Utrecht, the Netherlands; Faculty of Science and Technology (R.B., B.t.H.), Department of Technical Medicine, University of Twente, Enschede, the Netherlands; and Department of Biomedical Engineering and Physics (P.v.O.), Academic Medical Center, Amsterdam, the Netherlands.

R. Kleinloog was supported by a Focus and Mass cardiovascular research grant by Utrecht University, the Netherlands. J.J.M. Zwanenburg received funding from the European Research Council under the Seventh Framework Programme of the European Union (FP7/2007–2013)/European Research Council grant agreement No. 337333.

Please address correspondence to Jaco J.M. Zwanenburg, PhD, Department of Radiology, University Medical Center Utrecht, Heidelberglaan 100, 3584 CX Utrecht, the Netherlands; e-mail: j.j.m.zwanenburg@umcutrecht.nl

 Indicates open access to non-subscribers at www.ajnr.org

 Indicates article with supplemental on-line photo.

<http://dx.doi.org/10.3174/ajnr.A4734>

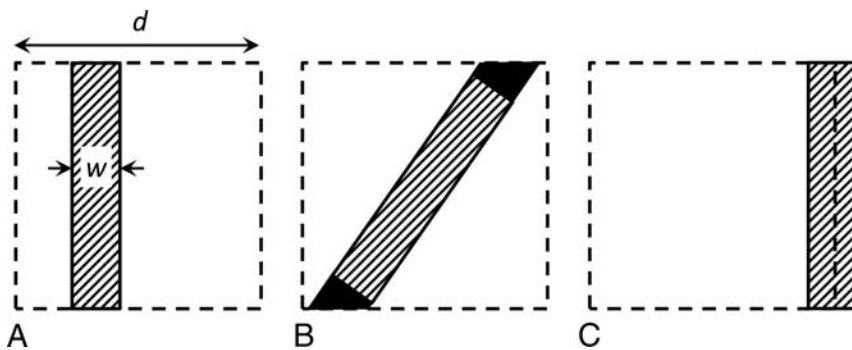


FIG 1. A, Illustration of a voxel (dashed square, size d) partly filled with aneurysm wall (filled rectangle) with thickness w . In case of perfect suppression of the surrounding CSF and blood, the signal from the voxel is directly proportional to the wall thickness w , as given by the equation. B, If the vessel wall is oblique, the filling factor is higher, leading to a different proportionality constant between the wall thickness and the signal obtained from the voxel (extra signal is indicated by black areas). C, If the voxel boundary falls within the vessel wall, the partial volume effect is spread over 2 voxels, leading to apparently thinner walls (less signal compared with A).

the spatial variation in aneurysm wall thickness by using signal intensities of the aneurysm wall on 7T MR imaging.¹⁰ A phantom and histopathologic correlation study validated that there is a linear relation between wall thickness and image intensity.¹⁰ This development has the potential to enable noninvasive assessments of the relation between different pathophysiologic parameters and wall thickness. However, a method to quantitatively assess the wall thickness on in vivo images has not yet been developed. Therefore, we aimed to develop an algorithm to obtain semi-quantitative measurements of the wall thickness to assess the spatial variation of the apparent wall thickness within an aneurysm and to assess the correlation between wall thickness and WSS on 7T images in patients with intracranial aneurysms.

MATERIALS AND METHODS

Patient Selection

From a series of patients (18, with 20 aneurysms in total) with unruptured intracranial aneurysms from a previous study,¹⁰ we selected the patients who underwent both a magnetization-prepared inversion-recovery turbo spin-echo (MPIR-TSE) scan for vessel wall imaging and a time-resolved PCMR scan for wall shear stress assessment. Patients with artifacts in the PCMR scan due to gradient coil hardware problems were excluded as well as patients with motion artifacts on the MPIR-TSE scan. Patients in whom an insufficient amount of aneurysm wall was free from directly bordering brain tissue (<10%, based on subjective estimation) could not be analyzed and were excluded (in total, 4 aneurysms were excluded for this reason). We performed exclusion blinded to the WSS results.

Imaging Sequences

MR imaging was performed on a 7T MR imaging scanner (Achieva; Philips Healthcare, Best, the Netherlands) with a 32-channel receive head coil and a volume-transmit coil (Nova Medical, Wilmington, Massachusetts).

A previously described¹⁰ T1-weighted 3D MPIR-TSE sequence with whole-brain coverage was used to image the aneurysm wall.¹¹ Briefly, the scan parameters were as follows: acquired resolution, $0.8 \times 0.8 \times 0.8 \text{ mm}^3$; FOV, $250 \times 250 \times 190 \text{ mm}^3$ (feet to head \times anterior to posterior \times right to left); scan duration, approximately 11 minutes.

A time-resolved 3D PCMR sequence was used to determine wall shear stress. Briefly, we used the following scan parameters⁹: acquired resolution, $0.5 \times 0.5 \times 0.5 \text{ mm}^3$; FOV, $190 \times 190 \times 200 \text{ mm}^3$ (anterior to posterior \times right to left \times feet to head); velocity-encoding limit, 150 cm/s for each velocity-encoding direction. Five ($n = 1$) or 6 ($n = 10$) cardiac phases were obtained, retrospectively gated, by using a peripheral pulse unit. Acquired temporal resolution ranged between 209 and 286 ms, depending on the heart rate. The scan duration was approximately 13 minutes.

Image Processing

Wall Thickness from Intensity: Theory. For walls thinner than the voxel size, the intensity on the MPIR-TSE images is proportional to the vessel wall thickness.¹⁰ Under idealized circumstances, the observed intensity in MPIR-TSE images could be used to compute the absolute wall thickness, w , by using a simple linear relationship:

$$w = d \times S_w/S_0,$$

where S_w is the signal for a voxel with isotropic voxel size d , containing the vessel wall with surrounding blood and CSF. S_0 is the signal of a voxel completely filled with vessel wall.

To render signal intensity a true reflection of the wall thickness (relative to the voxel size), one should have the following (long) list of requirements for a voxel with a piece of vessel wall inside: First, the partial volume effect should occur only among the vessel wall, blood, and CSF, and the signal from blood and CSF should be perfectly suppressed (Fig 1A). Second, the signal intensity of a voxel that is fully filled with vessel wall (S_0) should be known. Third, there should be no variation of vessel wall signal across the wall due to, for example, heterogeneous tissue composition in combination with the contrast-weighting of the MPIR-TSE sequence. Fourth, the vessel wall should be parallel with one of the sides of the voxel because oblique walls will lead to a higher filling factor than just the proportion of the wall thickness to the voxel size (Fig 1B). Fifth, the partial volume effect of the thin vessel wall should not be divided over 2 voxels; thus, there may be no boundary of 2 voxels within the vessel wall, parallel to the vessel wall (Fig 1C). Last, the nominal acquired resolution of the MPIR-TSE images (0.8 mm) should be equal to the true physical resolution, without blurring due to motion or an imperfect point spread function.

Apparent Wall Thickness Estimation Algorithm

Because the above-mentioned requirements will not be met, in practice, an algorithm was developed to obtain an estimation of the ratio S_w/S_0 from the signal intensities in the vessel wall (MPIR-TSE) images, and this ratio was termed “apparent wall thickness” (AWT). With the limitations of the requirements in mind, one might think of the AWT as a fractional thickness of the vessel wall relative to the voxel size. As a surrogate for the unknown

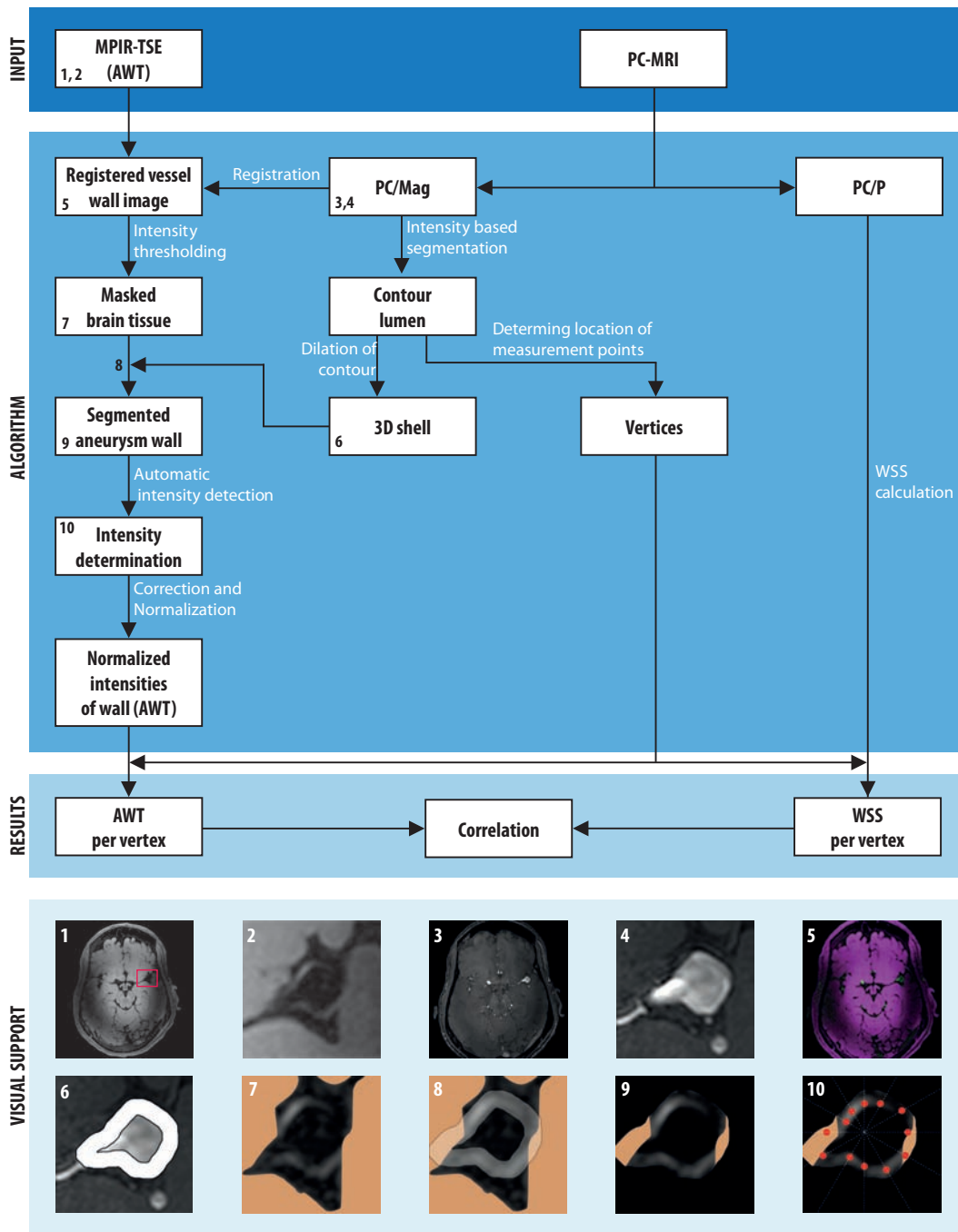


FIG 2. Schematic overview of the algorithm to determine the apparent wall thickness and its correlation to wall shear stress in intracranial aneurysms on 7T MR imaging. *Blocks* represent in- and outputs, and *arrows* represent procedures within the algorithm. The numbers in the boxes refer to the visualizations of several steps at the bottom of the image: 1) MPIR-TSE image (transverse orientation); the *red box* indicates the area of brain tissue that is used for the correction (by fitting a second-order polynomial function to the brain tissue intensities) and normalization of the vessel wall intensities; 2) cropped MPIR-TSE image clearly showing the aneurysm wall and its varying intensity; 3) the PC/mag image used for segmentation of the aneurysm lumen; 4) cropped PC/mag image; 5) registered images: pink is MPIR-TSE; green, PC/mag; 6) 3D shell encompassing the aneurysm wall; 7) brain tissue mask; 8) overlay of the 3D shell on the MPIR-TSE image with tissue mask; 9) segmented aneurysm wall; and 10) radial intensity profiles to sample vessel wall intensities (ie, signal maxima within the 3D shell, indicated by *red dots*). The profiles were rotated by stepping with 1° ; here only a few profiles are shown. The images are taken from aneurysm 1 (Table). PC/P indicates phase-contrast MRI phase images.

intensity of a voxel completely filled with vessel wall, S_0 , the intensity of the adjacent brain tissue, was used. Brain tissue was chosen because the vessel wall has T1 similar to that of brain tissue at 7T¹² and because the MPIR-TSE yields only limited T1-weighted contrast (almost no contrast between gray and white matter, Fig 2). A schematic overview of the analysis

method, including the correlation with WSS measurements, is shown in Fig 2.

First, to be able to relate measurements and segmentations of either images, the MPIR-TSE images were registered to the PCMR magnitude (PC/Mag) images by using a standard rigid body registration in MeVisLab (MeVis Medical Solutions, Bremen, Ger-

many). The registration was performed on the entire image, which leads, in a minority of cases, to slightly suboptimal registration at the location of the aneurysm. Therefore, when automatic registration was not optimal, small manual adjustments were made. After registration, no deviations between the lumen derived from the PC/mag and the lumen of the MPIR-TSE images were observed.

Second, the aneurysm lumen/wall boundary was obtained by segmentation of the PC/Mag by using a level set evolution algorithm.¹³ To obtain the segmentation of the aneurysm wall on MPIR-TSE images, we dilated the contour of the segmented lumen to generate a 3D shell (ROI) that encompassed the aneurysm wall (Fig 2, image panel 6). This step and the remaining postprocessing steps of the analysis method were performed in a custom built Matlab program (MathWorks, Natick, Massachusetts).

Next, the intensities of the wall within the 3D shell were automatically sampled by using radial-intensity profiles crossing the aneurysm wall in the MPIR-TSE images. Maximum intensities along the profiles within the 3D shell (ie, where the profile crossed the aneurysm wall) were saved. The profiles were rotated with a step of 1° through all 2D sections containing the aneurysm, in transversal, sagittal, and coronal planes. Because the aneurysm wall has nearly the same intensity as brain tissue, the wall was indistinguishable from the brain tissue in areas where the aneurysm bordered the brain tissue. Therefore, a brain tissue mask based on an intensity threshold and connected components was used to avoid intensity measurements in the bordering brain tissue. Intensities of parent vessels were manually deleted, as well as intensities that were evidently located outside the wall (errors).

Finally, the AWT was computed by normalizing to the local brain tissue intensity. Care was taken to use only local brain tissue to also correct for intensity inhomogeneity, which is typically present on the 7T images (Fig 2, image panel 1). The inhomogeneity in local brain tissue intensity was corrected for by fitting the intensities to a second-order polynomial function, by using brain signal from a manually drawn box around the aneurysm. The brain signal was selected by removing CSF and blood signal (based on their low intensities) and the aneurysmal wall (based on the segmented 3D shell described above). The resulting fitted brain tissue intensity field was used to normalize the aneurysm wall intensities. The normalized aneurysm wall intensities were used as AWT.

Wall Shear Stress Calculation

Wall shear stress was determined as previously described.¹⁴ After smoothing of the lumen/wall boundary segmentation mentioned above, a spline was fitted through the velocity values derived from PCMR phase images perpendicular to the wall. A blood viscosity of 4.0×10^{-3} Pa \times s, which is commonly used in similar algorithms,¹⁵⁻¹⁷ was used in this algorithm and the wall shear stress during peak systole was used for correlation with the AWT measurements. Peak systole was defined as the cardiac timeframe with the highest average velocity in the aneurysm segmentation.

Comparison of Apparent Wall Thickness and Wall Shear Stress

To obtain common measurement locations for both the AWT and WSS, we divided the aneurysm lumen contour into different faces (individual surfaces) and vertices (corners of faces) by using the isosurface function in Matlab. The amount of vertices was determined by the algorithm used in the isosurface function of Matlab and depended on the size of the aneurysm. At each vertex point, the WSS was computed from the 3D velocity data, and the corresponding AWT was obtained by averaging the AWT samples that were closest to the vertex. Because the amount of vertices was much higher (approximately 10 times) than the amount of voxels on the aneurysm lumen contour, the AWT and WSS values at each vertex cannot be regarded as independent or unique measurements. Accordingly, the resolution of the AWT map (or WSS map) is determined by the resolution of the underlying MPIR-TSE images (or PCMR images), and not by the density of the vertices. Visual comparisons were made for all aneurysms, to illustrate the results of the statistical analysis. The 3D lumen contours of each aneurysm were presented, colored by an interpolated color map representing the WSS and AWT.

Statistical Analyses

Spatial variation in AWT was defined as the interquartile range of the AWT within an aneurysm (ie, the number specifies the range that contains the middle 50% of the AWT). A higher range reflects more variation in wall thickness across the aneurysm. The interquartile range was chosen to avoid the effect of outliers on the AWT variation assessment. A visual estimation of the coverage and the amount of data points were reported to give an impression of the area of the aneurysm wall that was covered by the analysis.

Because the potential relation between WSS and AWT is not necessarily linear, Spearman correlation coefficients were computed to compare AWT and WSS in the aneurysms. The correlation coefficients between AWT and WSS were calculated for each individual aneurysm, after which a 1-sample *t* test was used to test whether the mean correlation coefficient was significantly different from zero, with significance set at $P < .05$. The correlation coefficients were weighted by the amount of measured points, to decrease the influence of aneurysms with fewer data points. We decided to not pool all the data to calculate the overall correlation coefficient because the amount of points were different per aneurysm. If the data were pooled, the observed correlation between WSS and AWT could be dominated by the data of the largest aneurysm. The significance of each individual correlation coefficient was not determined because the artificially high number of data points (from the high number of vertices on the lumen contour) would yield unrealistically low *P* values.

The correlation between AWT and WSS was further visualized with histograms for each aneurysm. To reduce the amount of data in these histograms, the WSS was divided into quartiles, with an equal amount of data points per quartile.

RESULTS

Population

Eighteen patients (with 20 aneurysms in total) underwent both MPIR-TSE scans and PCMR. Four patients were excluded on the

Baseline characteristics and AWT results of 11 unruptured intracranial aneurysms

Aneurysm	Age (yr), Sex	Aneurysm (mm), Largest Diameter (Height × Width in mm)	Location of Aneurysm	Analyzed Points	Coverage ^b	AWT Heterogeneity ^c	Correlation (ρ)
1	50, M ^a	9.1 (5.9 × 6.3)	MCA	864	50%–75%	0.17	−0.4
2	55, M	9.6 (6.1 × 9.6)	MCA	769	50%–75%	0.53	−0.6
3	70, M	9.5 (7.8 × 7.8)	AcomA	714	25%–50%	0.22	−0.1
4	64, M	10.1 (8.8 × 7.7)	MCA	466	25%–50%	0.15	−0.3
5	60, F ^a	6.8 (6 × 4.7)	MCA	428	50%–75%	0.21	−0.5
6	55, F	7.4 (6.0 × 5.8)	MCA	406	50%–75%	0.11	−0.2
7	56, M	12.6 (10.1 × 9.4)	AcomA	298	<25%	0.31	−0.5
8	50, M ^a	6.4 (4.8 × 3.9)	ICA	166	25%–50%	0.21	−0.5
9	74, F	6.1 (6.1 × 5.7)	AcomA	163	25%–50%	0.13	−0.1
10	50, F	12.9 (12.9 × 6.3)	MCA	130	<25%	0.31	−0.3
11	60, F ^a	5.6 (4.5 × 3.9)	Pericallosal artery	33	<25%	0.07	−0.4

Note:—AcomA indicates anterior communicating artery.

^a Two aneurysms in 1 patient.

^b Coverage indicates the visual estimated percentage of the area of the wall that could be analyzed.

^c Heterogeneity is defined as the interquartile range in AWT, and reflects the spatial wall thickness variation.

basis of PCMR artifacts due to a gradient hardware problem; 1 patient, due to motion artifacts on MPR-TSE; and 4, due to an insufficient proportion of visible wall. Thus, 9 patients with, in total, 11 aneurysms were available for analysis. Their mean age was 59 years, and 44% were women. Baseline characteristics are shown in the Table.

Apparent Wall Thickness and Wall Shear Stress

Color maps of the AWT showed spatial variation in almost all aneurysms (Fig 3), which ranged from 0.07 to 0.53, with a mean variation of 0.22 (Table). A variation of 1.0 roughly means a thickness variation of 1 voxel.

A correlation between AWT and WSS was visible in most aneurysms (Fig 3), particularly where the coverage and the spatial variation was high (Table).

In all aneurysms, AWT and WSS were inversely correlated (though sometimes close to zero, Table). The mean correlation coefficient was -0.35 , which was significantly different from zero ($P < .05$).

The inverse relation between AWT and WSS is also visible in the individual and pooled plots, as shown in Fig 4. In the lowest WSS quartile, there was more variety in AWT between different aneurysms than in the highest WSS quartile. In other words, low WSS at thinner walls was present, but high WSS at thicker walls was rarely observed (Fig 4B).

DISCUSSION

On the basis of previous work, a semi-automatic algorithm was developed to measure apparent aneurysm wall thickness from the signal intensity of the wall on 7T MR vessel wall images of patients with unruptured intracranial aneurysms. Semi-quantitative measurements of the wall thickness were obtained, which showed wall thickness variation in all analyzed aneurysms. Furthermore, by calculating WSS from PCMR data, we found an inverse relation between apparent wall thickness and wall shear stress.

Our results are in contrast with the results of a previous study, which found a positive correlation between wall thickness and wall shear stress.¹⁸ The relation between WSS and wall thickness is probably complex and may differ between large, thick-walled aneurysms and small, thin-walled ones.⁶ Kadasi et al¹⁸ studied predominantly smaller aneurysms because 12 of 54 aneurysms (22%)

were >7 mm, and we studied relatively large aneurysms (7 of 11 (63%) were >7 mm), which might partly explain the different observations. However, the different observations can also be related to methodologic differences. Kadasi et al used intraoperative images for a dichotomous visual scoring of wall thickness, while we semi-quantitatively assessed wall thickness on noninvasive MR images. Furthermore, although they did not validate thickness measurements with ex vivo histopathologic assessment, they visually assessed actual wall appearance. On the other hand, while we did validate our thickness assessments with an ex vivo study on 2 samples with heterogeneous composition,¹⁰ we did so in the absence of flowing blood or fluid. Wall shear stress was, in our study, measured by 3D PCMR, while the previous study used computational fluid dynamics simulations, which depend on certain assumptions and boundary conditions such as rigid vessel walls and inflow velocity at the entrance of the simulated vessel segment. However, general WSS patterns should be similar for either method (computational fluid dynamics or PCMR).¹⁴ A clear advantage of our method is the avoidance of invasive methods (such as aneurysm surgery) to obtain information on wall thickness. An elaborate study by using both approaches on small and large aneurysms with ex vivo (postsurgery) validation is warranted to determine the impact of the differences in methodology.

The observed inverse correlation in the present study is consistent with the hypothesis that high WSS is associated with the process of intracranial aneurysm wall remodelling that might cause wall thinning, such as activation of proteases by mural cells, matrix degradation, and apoptosis.⁶ Furthermore, low WSS is associated with increased inflammatory cell infiltration and smooth muscle cell proliferation,^{6,7} which may lead to wall thickening.

The WSS computations require sufficiently high velocity-to-noise ratios. We used a higher velocity-encoding (150 cm/s) than the velocity-encoding of 100 cm/s that was used by van Ooij et al,¹⁴ who showed good qualitative agreement between WSS measured with PCMR and computational fluid dynamics simulations. However, the study of van Ooij et al was performed at 3T, whereas we performed PCMR at 7T, which yields a higher SNR and, therefore, improved accuracy of the velocity vector direction

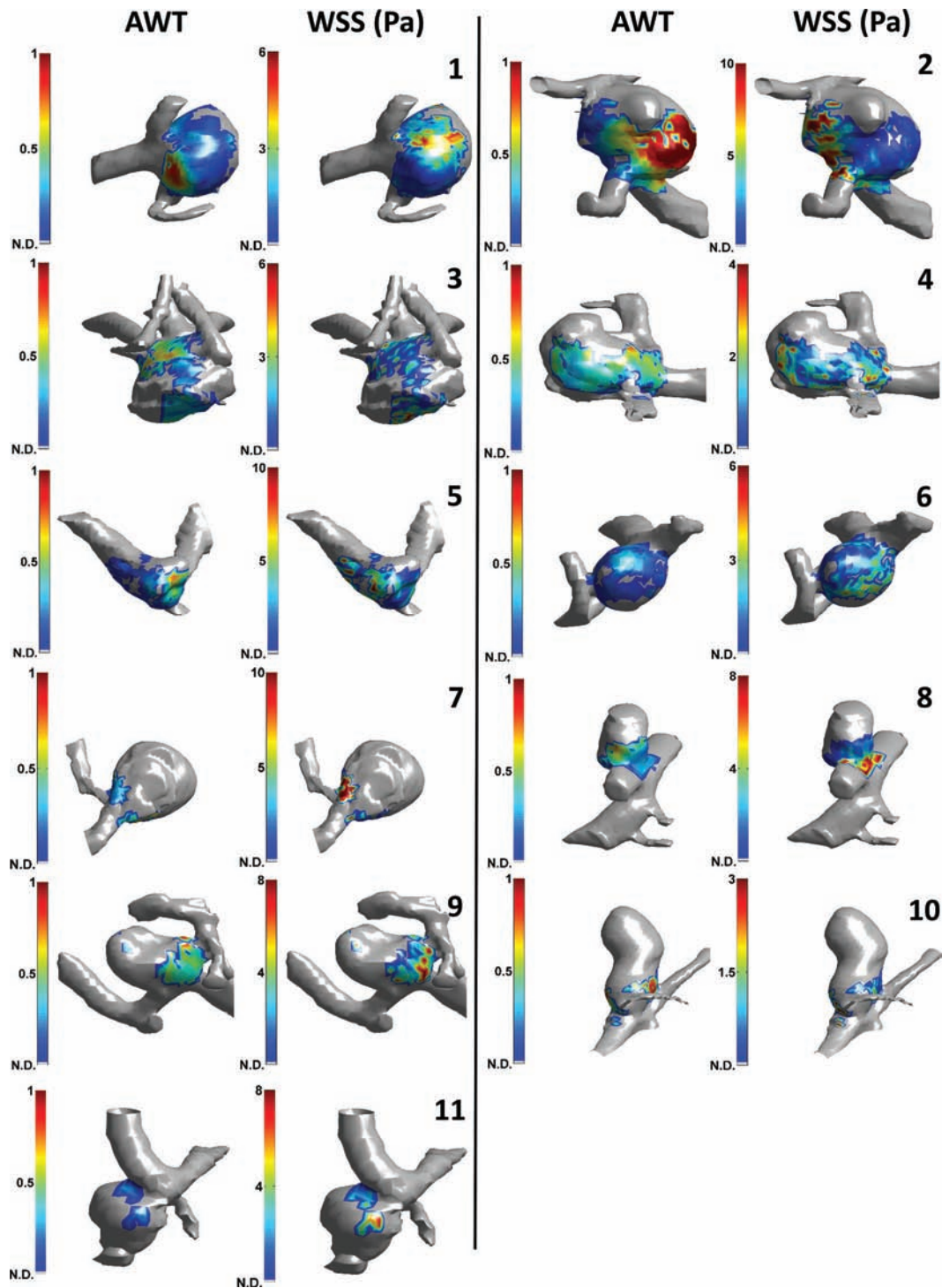


FIG 3. Visual comparison between apparent wall thickness and wall shear stress in intracranial aneurysms on 7T MR imaging. 3D color map with AWT (*left images*) and 3D color map with WSS (*right images*) are shown. The color scaling for all AWT images is equal, while the WSS images were individually scaled as indicated by the *color scale bars*. Parent vessels and wall areas where no AWT data (N.D.) were available are displayed in gray. Numbers correspond to the numbering of the aneurysms in the Table. The other side of the aneurysms is shown in the On-line Figure.

and magnitude.⁹ Thus, we are confident that the low WSS values are of at least comparable reliability with those presented before.¹⁴ The lumen segmentations were performed on the PC/mag images, in which the SNR depends on the blood velocity (inflow effect). The segmentations appear to be robust because no mismatches were observed with the lumens obtained from the MPIR-TSE images. Besides, comparisons of velocity direction and

magnitude obtained from PCMR at 3T and the segmentation algorithm showed good agreement with computational fluid dynamics in regions of both high and low SNR and velocity-to-noise ratio in intracranial aneurysms.¹⁹

This study has several strengths. First, it uses a noninvasive method to quantify wall thickness, which provides a unique means for in vivo quantification of wall thickness variation in

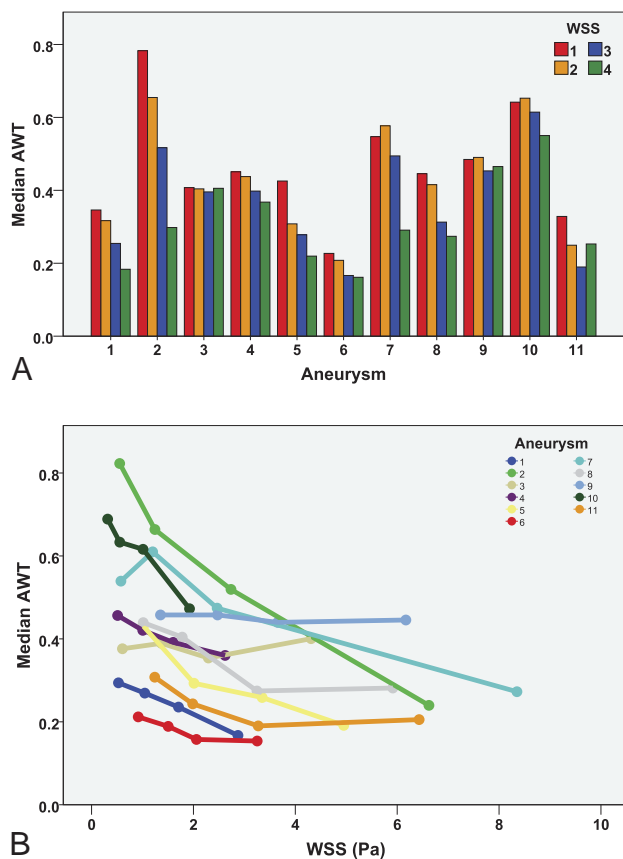


FIG 4. Comparison of apparent wall thickness and wall shear stress in intracranial aneurysms on 7T MR imaging. *A*, Histogram for each aneurysm is sorted from the aneurysm with the highest amount of measurements points ($n = 864$) to the aneurysm with the least amount of measurement points ($n = 33$). The 4 colors represent the WSS, divided into 4 quartiles per aneurysm with increasing WSS (1 = lowest WSS quartile, 4 = highest WSS quartile). *B*, AWT is plotted against WSS in all aneurysms (different colors). The *dots* represent the 4 WSS quartiles.

unruptured aneurysms. Second, the method is based on the relation between aneurysm wall thickness and image intensity, which has been validated by a phantom and histopathologic correlation study.¹⁰ Finally, the analyzed methods for WSS and wall thickness have been shown useful in aneurysms of various sizes, providing that an appropriate signal-to-noise ratio of the MR images is obtained and that the walls are surrounded by CSF.

Some limitations should be mentioned. First, the relation between the aneurysm wall parts bordering brain tissue and WSS could not be analyzed because measurement of thickness in these parts is not possible. Therefore, the association between thickness of wall bordering the parenchyma and WSS remains unknown. Unfortunately, this association frequently concerned the apex of the aneurysm, which is especially of interest because it is known to be the predominant site of rupture. Second, the observed correlation coefficients were relatively weak, which may partly be due to noise. The influence of noise is suggested by the fact that aneurysms with larger variation in wall thickness, and thus a larger dynamic range in the AWT parameter, tended to show a stronger correlation than aneurysms with a more narrow range in AWT. Last, despite the AWT, in theory, being directly related to the

absolute vessel wall thickness, it depends on too many requirements that are not met in practice to claim that we have found a tool to measure absolute wall thickness. The most important requirement is the nulling of CSF and blood. The found inverse correlation may be partly caused by imperfect nulling of blood with very low flow velocities. The MPR-TSE is used to obtain black blood, which is based on the high flow sensitivity of the long turbo spin-echo train with low refocusing angles. However, very slow blood flow may still yield some signal. If that is the case, the wall seems thicker at locations with low velocities and thus low WSS. This feature leads to overestimation of the negative correlation.

We previously validated the correlation between signal intensity and wall thickness with an ex vivo imaging experiment on an aneurysm wall of heterogeneous composition and histopathologic validation, and with a tapering phantom study, in which flow could not affect the wall thickness.¹⁰ However, although these validation experiments show that thickness variation can explain the observed signal variation, they cannot exclude a potential additional confounding role of slow-flowing blood in the in vivo situation. The long turbo spin-echo trains with low reduced refocusing angles are very sensitive to motion, up to diffusion-related motion.²⁰ The refocusing angles of the MPR-TSE sequence used in this work were very low, with a range of 12°–40°. Although we think the low refocusing angles will protect against the effect of low-flow velocities, this should be confirmed in future studies by using a dedicated phantom setup with flow or by performing additional validation studies on postoperative material from patients who have been scanned with the MPR-TSE sequence before an operation.

Future Directions

The conflicting results of our study and a previous study on the relation between aneurysm wall thickness and WSS¹⁸ call for further studies in which both approaches are applied and compared in the same patients. The presented method for in vivo wall thickness determination, in combination with the aneurysm-specific WSS, might provide a valuable means to noninvasively study how wall thickness and hemodynamic parameters are related to aneurysm growth and rupture. This study may yield new insights in the pathophysiology of intracranial aneurysms. Therefore, studies to correlate rupture of aneurysms with WSS and wall thickness may help in the search for new rupture predictors. In particular, the spatial variation in AWT might be an interesting parameter for those future studies. Whether thickness variation indicates higher rupture risks is currently unknown. Nevertheless, it seems plausible that much variation in thickness calls for a pathologic wall, prone to rupture.

CONCLUSIONS

A method was developed to measure the wall thickness semi-quantitatively, using 7T MR imaging. An inverse correlation between wall shear stress and AWT was determined. In future studies, this noninvasive method can be used to assess spatial wall thickness variation in relation to pathophysiologic processes such as aneurysm growth and rupture.

ACKNOWLEDGMENTS

The authors thank Roy Sanders for his assistance with the figures.

Disclosures: Rachel Kleinloog—RELATED: Grant: Focus and Mass cardiovascular grant of Utrecht University.* Jaco J.M. Zwanenburg—RELATED: Grant: European Research Council starting grant, European Union (SmallVesselMRI, No. 337333). *Money paid to the institution.

REFERENCES

1. Nieuwkamp DJ, Setz LE, Algra A, et al. **Changes in case fatality of aneurysmal subarachnoid haemorrhage over time, according to age, sex, and region: a meta-analysis.** *Lancet Neurol* 2009;8:635–42 CrossRef Medline
2. Vlak MH, Algra A, Brandenburg R, et al. **Prevalence of unruptured intracranial aneurysms, with emphasis on sex, age, comorbidity, country, and time period: a systematic review and meta-analysis.** *Lancet Neurol* 2011;10:626–36 CrossRef Medline
3. Greving JP, Wermer MJ, Brown RD Jr, et al. **Development of the PHASES score for prediction of risk of rupture of intracranial aneurysms: a pooled analysis of six prospective cohort studies.** *Lancet Neurol* 2014;13:59–66 CrossRef Medline
4. Vlak MH, Rinkel GJ, Greebe P, et al. **Trigger factors and their attributable risk for rupture of intracranial aneurysms: a case-crossover study.** *Stroke* 2011;42:1878–82 CrossRef Medline
5. Wermer MJ, van der Schaaf IC, Algra A, et al. **Risk of rupture of unruptured intracranial aneurysms in relation to patient and aneurysm characteristics: an updated meta-analysis.** *Stroke* 2007;38:1404–10 CrossRef Medline
6. Meng H, Tutino V. **High WSS or low WSS? Complex interactions of hemodynamics with intracranial aneurysm initiation, growth, and rupture: toward a unifying hypothesis.** *AJNR Am J Neuroradiol* 2014;35:1254–62 CrossRef Medline
7. Nixon AM, Gunel M, Sumpio BE. **The critical role of hemodynamics in the development of cerebral vascular disease.** *J Neurosurg* 2010;112:1240–53 CrossRef Medline
8. Boussel L, Rayz V, Martin A, et al. **Phase-contrast magnetic resonance imaging measurements in intracranial aneurysms in vivo of flow patterns, velocity fields, and wall shear stress: comparison with computational fluid dynamics.** *Magn Reson Med* 2009;61:409–17 CrossRef Medline
9. van Ooij P, Zwanenburg JJ, Visser F, et al. **Quantification and visualization of flow in the Circle of Willis: time-resolved three-dimensional phase contrast MRI at 7 T compared with 3 T.** *Magn Reson Med* 2013;69:868–76 CrossRef Medline
10. Kleinloog R, Korkmaz E, Zwanenburg JJ, et al. **Visualization of the aneurysm wall: a 7.0-Tesla magnetic resonance imaging study.** *Neurosurgery* 2014;75:614–22; discussion 622 CrossRef Medline
11. van der Kolk AG, Hendrikse J, Brundel M, et al. **Multi-sequence whole-brain intracranial vessel wall imaging at 7.0 Tesla.** *Eur Radiol* 2013;23:2996–3004 CrossRef Medline
12. Koning W, Rotte A de, Bluemink J, et al. **MRI of the carotid artery at 7 Tesla: quantitative comparison with 3 Tesla.** *J Magn Reson Imaging* 2015;41:773–80 CrossRef Medline
13. Li C, Xu C, Gui C, et al. **Level set evolution without re-initialization: a new variational formulation.** In: *Proceedings of the 2005 IEEE Computer Society Conference on Computer Vision and Pattern Recognition*, San Diego, California. June 20–26, 2005:430–36 CrossRef
14. van Ooij P, Potters WV, Guédon A, et al. **Wall shear stress estimated with phase contrast MRI in an in vitro and in vivo intracranial aneurysm.** *J Magn Reson Imaging* 2013;38:876–84 CrossRef Medline
15. Cebral JR, Castro MA, Appanaboyina S, et al. **Efficient pipeline for image-based patient-specific analysis of cerebral aneurysm hemodynamics: technique and sensitivity.** *IEEE Trans Med Imaging* 2005;24:457–67 CrossRef Medline
16. Mut F, Löhner R, Chien A, et al. **Computational hemodynamics framework for the analysis of cerebral aneurysms.** *Int J Numer Method Biomed Eng* 2011;27:822–39 CrossRef Medline
17. Shojima M, Oshima M, Takagi K, et al. **Magnitude and role of wall shear stress on cerebral aneurysm: computational fluid dynamic study of 20 middle cerebral artery aneurysms.** *Stroke* 2004;35:2500–05 CrossRef Medline
18. Kadasi LM, Dent WC, Malek AM. **Colocalization of thin-walled dome regions with low hemodynamic wall shear stress in unruptured cerebral aneurysms.** *J Neurosurg* 2013;119:172–79 CrossRef Medline
19. van Ooij P, Schneiders JJ, Marquering HA, et al. **3D cine phase-contrast MRI at 3T in intracranial aneurysms compared with patient-specific computational fluid dynamics.** *AJNR Am J Neuroradiol* 2013;34:1785–91 CrossRef Medline
20. Weigel M, Hennig J. **Diffusion sensitivity of turbo spin echo sequences.** *Magn Reson Med* 2012;67:1528–37 CrossRef Medline

Inflow Jet Patterns of Unruptured Cerebral Aneurysms Based on the Flow Velocity in the Parent Artery: Evaluation Using 4D Flow MRI

 K. Futami,  T. Kitabayashi,  H. Sano,  K. Misaki,  N. Uchiyama,  F. Ueda, and  M. Nakada

ABSTRACT

BACKGROUND AND PURPOSE: Inflow jet characteristics may be related to aneurysmal bleb formation and rupture. We investigated the visualization threshold on the basis of the flow velocity in the parent artery to classify the inflow jet patterns observed on 4D flow MR imaging.

MATERIALS AND METHODS: Fifty-seven unruptured aneurysms (24 bifurcation and 33 sidewall aneurysms) were subjected to 4D flow MR imaging to visualize inflow streamline bundles whose velocity exceeded visualization thresholds corresponding to 60%, 75%, and 90% of the maximum flow velocity in the parent artery. The shape of the streamline bundle was determined visually, and the inflow jet patterns were classified as concentrated, diffuse, neck-limited, and unvisualized.

RESULTS: At the 75% threshold, bifurcation aneurysms exhibited a concentrated inflow jet pattern at the highest rate. At this threshold, the inflow jets were concentrated in 13 aneurysms (group C, 22.8%), diffuse in 18 (group D, 31.6%), neck-limited in 11 (group N, 19.3%), and unvisualized in 15 (group U, 26.3%). In 16 (28.1%) of the 57 aneurysms, the inflow jet pattern was different at various thresholds. Most inflow parameters, including the maximum inflow velocity and rate, the inflow velocity ratio, and the inflow rate ratio, were significantly higher in groups C and D than in groups N and U.

CONCLUSIONS: The inflow jet pattern may depend on the threshold applied to visualize the inflow streamlines on 4D flow MR imaging. For the classification of the inflow jet patterns on 4D flow MR imaging, the 75% threshold may be optimal among the 3 thresholds corresponding to 60%, 75%, and 90% of the maximum flow velocity in the parent artery.

The inflow jets of cerebral aneurysms have been characterized as flow structures composed of strongly directed inflow with higher speeds than in other parts of the aneurysm.^{1,2} Computational fluid dynamics analyses by using human cerebral aneurysm models suggested that inflow jets may be related to bleb formation and aneurysmal rupture.³⁻⁵ Cebal et al³ reported that most blebs formed at sites where the inflow jet impacted the aneurysmal wall, and they qualitatively classified the inflow jets of ruptured and unruptured cerebral aneurysms into concentrated and diffuse inflow jets.³⁻⁵ They found that most ruptured aneurysms featured concentrated inflow jets, while diffuse inflow jets tended to be seen in unruptured an-

eurysms.^{4,5} This finding suggests that bleb formation and aneurysm rupture may be attributable to a degenerative change in the aneurysm wall exposed to the increased hemodynamic stress exerted by the inflow jet. Therefore, the assessment of inflow jet patterns and quantitative estimation of the inflow hemodynamics may contribute to a more precise prediction of the risk for bleb formation and aneurysm rupture.

Computational fluid dynamics analysis uses human aneurysm models based on a number of assumptions and approximations regarding blood properties, vessel wall compliance, and flow conditions.³⁻⁸ For the quantitative evaluation of the hemodynamics in real human cerebral aneurysms, 4D flow MR imaging, which is based on time-resolved 3D cine phase-contrast MR imaging techniques, has been used.⁹⁻²⁰ In this study, we investigated the visualization threshold on the basis of the flow velocity in the parent artery to classify the inflow jet patterns of unruptured cerebral aneurysms on 4D flow MR imaging. We applied different thresholds to visualize the inflow streamlines, evaluated the inflow jet patterns, and examined the relationship between the inflow jet pattern and the inflow hemodynamics.

Received August 7, 2015; accepted after revision December 16.

From the Department of Neurosurgery, Mattoh-Ishikawa Central Hospital (K.F.), Ishikawa, Japan; and Departments of Neurosurgery (T.K., H.S., K.M., N.U., M.N.) and Radiology (F.U.), Kanazawa University School of Medicine, Ishikawa, Japan.

Please address correspondence to Kazuya Futami, MD, Department of Neurosurgery, Mattoh-Ishikawa Central Hospital, 3-8 Kuramitsu, Hakusan, 920-8588 Ishikawa, Japan; e-mail: kfutami@matttoh.com

<http://dx.doi.org/10.3174/ajnr.A4704>

MATERIALS AND METHODS

This study was approved by the ethics committee of Mattoh-Ishikawa Central Hospital. Prior written informed consent was obtained from all patients.

Materials

We acquired 4D flow MR images in 68 patients with 72 unruptured cerebral aneurysms. Excluded from our study were 7 aneurysms whose poor-quality images were inadequate for evaluation due to motion artifacts²¹ during the systole phase of the cardiac cycle and 8 aneurysms with a maximum diameter of <4.0 mm or a neck size of <2.0 mm because the spatial resolution is limited on 4D flow MR imaging.^{20,22} Consequently, this study included 53 patients (22 men, 31 women) ranging in age from 51 to 86 years (mean, 71.6 ± 9.0 years) with 57 unruptured cerebral aneurysms (24 bifurcation and 33 sidewall aneurysms). Of the aneurysms, 4 were located on the cavernous, and 15, on the paraclinoid segment of the ICA; 14, on the ICA segment branching the posterior communicating artery; 1, on the ICA bifurcation; 6, on the bifurcation of the anterior cerebral artery and the anterior communicating artery; 14, on the MCA bifurcation; and 3, on the basilar artery bifurcation. The maximum diameters of the aneurysms and their neck sizes were 6.8 ± 3.1 mm (range, 4.0–17 mm) and 5.0 ± 2.2 mm (range, 2.0–13.7 mm), respectively.

MR Imaging

MR imaging was performed on a 1.5T scanner (Magnetom Avanto; Siemens, Erlangen, Germany) with a slew rate of 125 T/m/s and an 8-channel head array coil. The vascular geometry was assessed on 3D TOF MRA. The scanning parameters were TR/TE/NEX, 35 ms/7.15 ms/average 1; flip angle, 22°; FOV, 150 × 123 mm; z-coverage, 45.6 mm; 0.6-mm thickness; 3 slabs; 30 sections/slab; slab interval, -4.2 mm (ie, overlapping slab acquisition, 4.2 mm); matrix, 256 × 168 (512 × 336 with zero-filling interpolation processing); voxel size, 0.59 × 0.73 × 0.6 mm (0.295 × 0.365 × 0.6 mm with zero-filling); bandwidth, 87 Hz/px; imaging time, 4 minutes 53 seconds; transaxial direction.

Blood flow analysis was performed on 4D flow MR imaging scans. The parameters were TR/TE/NEX, 33.05 ms/5.63 ms/average 1; flip angle, 22°; FOV, 200 × 200 mm; 0.8-mm thickness; 1 slab; 24–26 sections/slab; z-coverage, 19.2 mm; matrix, 192 × 192; no interpolation processing; voxel size, 1.04 × 1.04 × 0.8 mm; velocity-encoding, 80 cm/s; bandwidth, 434 Hz/px; parallel imaging with reduction factor, 2; imaging time, 20–30 minutes depending on the patient's heart rate; transaxial direction; retrospective gating with electrocardiogram; 20 phases. We selected a velocity-encoding of 80 cm/s to visualize streamlines whose velocity exceeded a chosen visualization threshold based on the maximum flow velocity in the parent artery.

On the basis of the 3D TOF MRA datasets, the vascular wall was constructed by using the region-growing method²³ and the "Marching Cubes" method.²⁴ The 3D datasets obtained by 4D flow MR imaging were converted to pixel datasets at a spatial resolution of 0.5 × 0.5 × 0.5 mm by using a function featured on commercially available software (Flova II, Version 2.9.15.0; R'tech, Hamamatsu, Japan) to visualize 3D flow information.

Data Analysis

With a Flova II function, an arbitrary percentage value of the maximum flow velocity in the parent artery can be selected as the visualization threshold. We set 60%, 75%, and 90% as the thresholds to evaluate the role they play in the visualization of the inflow jet patterns. The inflow jet was visualized as a bundle of streamlines whose velocity exceeded the threshold at the aneurysmal orifice. The 57 aneurysms were classified by visual inspection into 4 groups based on the shape of the streamline bundle and the site on the aneurysmal wall impacted by the inflow streams (Fig 1). Group C exhibited a concentrated inflow jet with intrusion into the aneurysmal dome without dispersion in 20% of the width of the streamline bundle at the aneurysmal orifice and an impact at the aneurysm wall at a site half-way up the aneurysm height (Fig 1, Concentrated). Group D comprised aneurysms with a diffuse inflow jet defined as an inflow jet intruding into the aneurysmal dome with dispersion in >20% of the width of the streamline bundle at the aneurysm orifice and an impact on the aneurysmal wall at a site more than half-way up the aneurysm height (Fig 1, Diffuse). The 20% value was chosen to accommodate measurement errors of the width of the inflow streamline bundle. Group N consisted of aneurysms with neck-limited inflow jets defined as inflow streamlines that impacted the aneurysm wall at a site between the neck and the lower half of the aneurysm height irrespective of the shape of the inflow streamline bundle (Fig 1, Neck-limited). Group U aneurysms had unvisualized inflow streamlines (Fig 1, Unvisualized).

The inflow streamline bundles were not visualized during the diastole phase in any of the 57 aneurysms. The inflow jet pattern of each aneurysm was determined by selecting a stable pattern through the systole phase of the cardiac cycle. Three observers (K.F., F.U., and M.N.) independently recorded the inflow jet patterns; disagreements were settled by consensus.

We compared the inflow hemodynamic parameters among the 4 aneurysm groups. The parameters included the maximum inflow velocity, the maximum inflow rate, the inflow velocity ratio (in percentages) (ie, the ratio of the maximum inflow velocity to the maximum flow velocity in the parent artery), and the inflow rate ratio (in percentages) (ie, the ratio of the maximum inflow rate to the maximum flow rate in the parent artery). The maximum inflow velocity and rate were measured on the section plane corresponding to the aneurysmal orifice. The maximum flow velocity and rate in the parent artery were assessed on the section plane in the parent artery just proximal to the aneurysm. All hemodynamic parameters were measured at peak systole by using a function of the Flova II software. Each numeric value was determined as the mean of 3 measurements performed by one of the authors (K.F.).

Statistical analysis was performed with the Mann-Whitney *U* test for continuous variables and the Fisher exact test for categorical variables. Differences of $P < .05$ were statistically significant.

RESULTS

Table 1 shows the inflow jet patterns observed at the different thresholds in the 57 aneurysms. The distribution of the patterns was significantly different at the 60% and 90% thresholds ($P = .0468$). In 16 (28.1%) of the 57 aneurysms, the inflow jet pattern

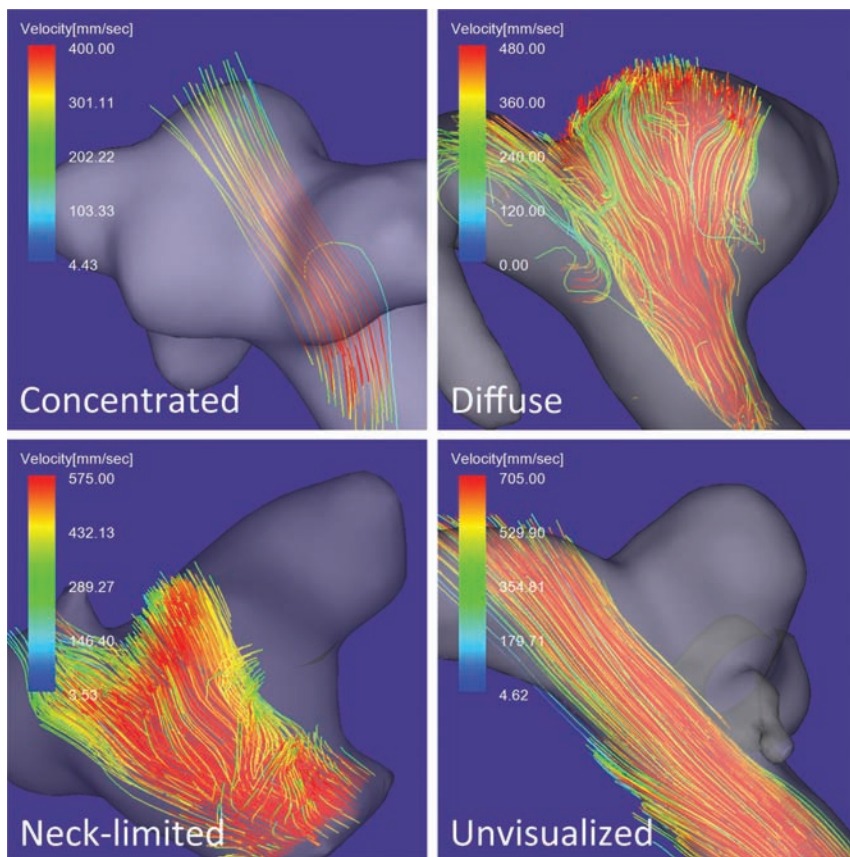


FIG 1. Classification of inflow jet patterns visualized on 4D flow MR images. Concentrated: An aneurysm on the anterior communicating artery with a concentrated inflow jet defined as a bundle of inflow streamlines intruding into the aneurysmal dome without dispersion in 20% of the width of the streamline bundle at the aneurysmal orifice and impacting the aneurysmal wall at a site more than half-way up the aneurysm height. Diffuse: A sidewall aneurysm on the ICA with a diffuse inflow jet defined as inflow streamlines intruding into the aneurysmal dome with dispersion in >20% of the width of the streamline bundle at the aneurysmal orifice and impacting the aneurysmal wall at a site more than half-way up the aneurysm height. Neck-limited: A sidewall aneurysm on the ICA with a neck-limited inflow jet defined as inflow streamlines impacting the aneurysmal wall between the neck and half-way down the aneurysm height. Unvisualized: A sidewall aneurysm on the ICA with unvisualized inflow streamlines defined as no inflow streams into the aneurysm.

Table 1: Inflow jet patterns visualized at the 60%, 75%, and 90% threshold of the maximum velocity in the parent artery^a

Inflow Jet Pattern	No. of Aneurysms (Threshold 60%)	No. of Aneurysms (Threshold 75%)	No. of Aneurysms (Threshold 90%)
Concentrated inflow jet	8 (14.0%)	13 (22.8%)	16 (28.1%)
Diffuse inflow jet	23 (40.4%)	18 (31.6%)	14 (24.6%)
Neck-limited	15 (26.3%)	11 (19.3%)	9 (15.8%)
Unvisualized	11 (19.3%)	15 (26.3%)	18 (31.6%)

^a The distribution of the inflow jet patterns at the 60% and 90% threshold was significantly different ($P = .0468$).

was different at different thresholds (Fig 2). Four of 16 aneurysms classified as group C at the 90% threshold were group D lesions at the 75% threshold; 3 of these 4 aneurysms were sidewall aneurysms. Of the 13 aneurysms classified as group C at the 75% threshold, 5 (38.5%) were group D at the 60% threshold; these 5 were bifurcation aneurysms. Furthermore, 10 of 16 (62.5%) group C and 2 of 14 (14.3%) group D aneurysms at the 90% threshold ($P = .0106$), 10 of 13 (76.9%) group C and 2 of 18 (11.1%) group D aneurysms at the 75% threshold ($P = .0005$), and 6 of 8 (75%) group C and 7 of 23 (30.4%) group D aneurysms at the 60% threshold ($P = .0429$) were bifurcation aneurysms.

Because among the 3 thresholds, at 75%, the rate of bifurcation aneurysms was most significantly higher in the concentrated group (group C) than in the diffuse group (group D), we compared the inflow hemodynamic parameters in the 4 groups at the 75% threshold.

Table 2 shows the maximum inflow velocity and the maximum inflow rate at the 75% threshold for the different aneurysm groups. The maximum inflow velocity was significantly higher in groups C and D than in group U, and the maximum inflow rate was significantly higher than in groups N and U. There was no statistically significant difference in these values between groups C and D and between groups N and U.

In Table 3, we present the inflow velocity ratio and the inflow rate ratio at the 75% threshold for the 4 aneurysm groups. Again, these values were significantly higher in groups C and D than in groups N and U, and there was no statistically significant difference between groups C and D and between groups N and U.

DISCUSSION

4D flow MR imaging makes it possible to assess the flow status in human aneurysms.¹⁰⁻²⁰ The hemodynamics (eg, the velocity distribution, inflow streamlines, and flow patterns) determined on 4D flow MR imaging have been validated by computational fluid dynamics studies in human cerebral aneurysms,^{10,12,14} experimental canine aneurysms,²⁵ and life-size human aneurysm phantoms.^{22,26,27} The feasibility of visualizing the aneurysmal inflow on 4D flow MR imaging has been confirmed.^{9,11,14,17,20,21} We used 4D flow MR imaging to evaluate the inflow jet patterns and the inflow hemodynamic parameters in patients with unruptured aneurysms.

At present there is no accepted robust definition of inflow jets. They have been evaluated by visual inspection and characterized by their strongly directed, high-speed flow structure.^{1,2} Schneiders et al⁷ and Jansen et al⁸ defined the inflow jet as the top 25% of the flow magnitude within an aneurysm. However, there may be a considerable difference in the maximum flow magnitude within an aneurysm. In fact, we found that there was a 3.8-fold difference in the mean value of the maximum inflow rate between group C and U lesions (Table 2). According to Szikora et al²⁸ and Castro et al,⁶ in ruptured aneurysms, the inflow jet tended to enter straight from the parent artery. Their observation suggests that

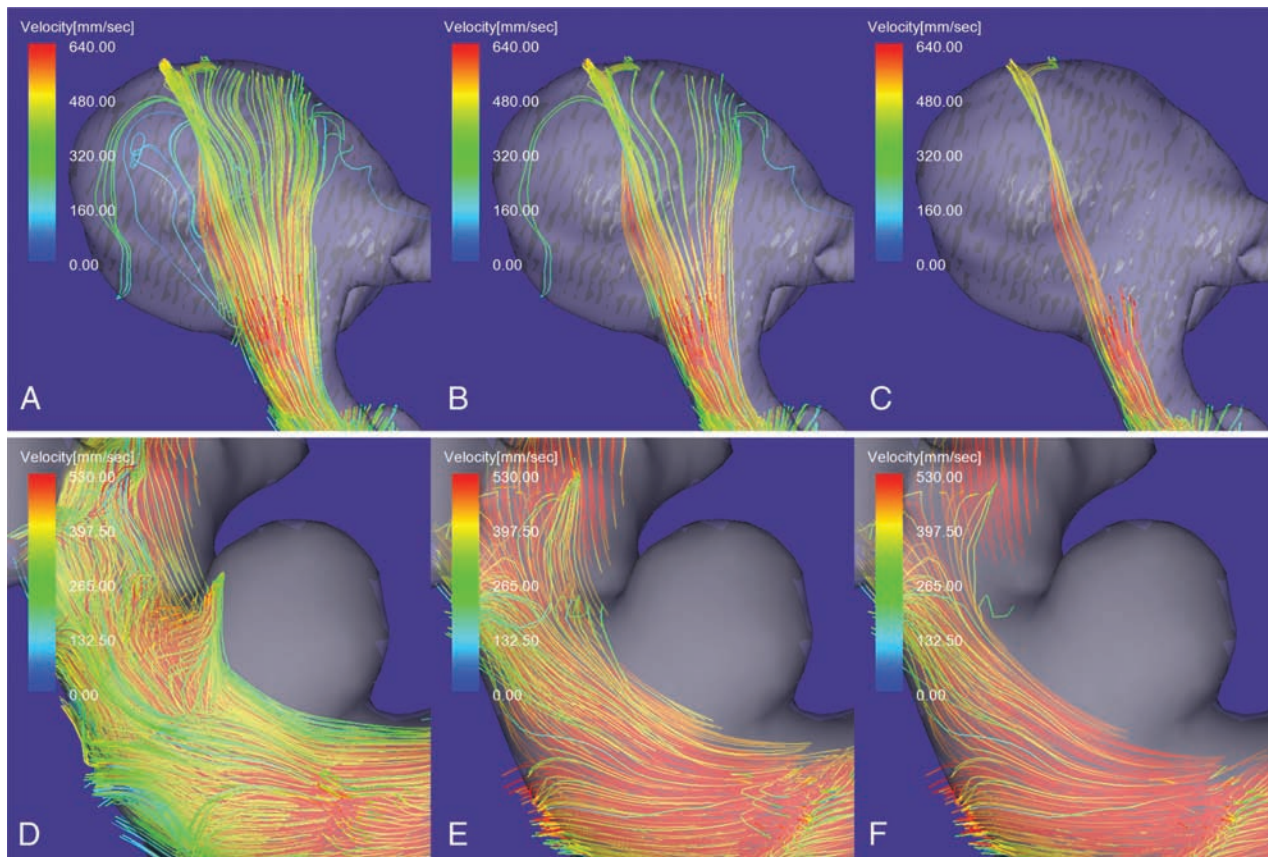


FIG 2. Inflow jet patterns on 4D flow MR images determined by observing the inflow streamline bundle with a velocity exceeding visualization thresholds corresponding to 60% (A and D), 75% (B and E), and 90% (C and F) of the maximum velocity in the parent artery. A–C, An aneurysm on the ICA segment branching the posterior communicating artery. D–F, An aneurysm on the paraclinoid segment of the ICA. A and B, A diffuse inflow jet intruding into the aneurysmal dome. The visualization thresholds are 60% (A) and 75% (B). C, A concentrated inflow jet intruding into the aneurysmal dome without dispersion (visualized at the 90% threshold). D, A neck-limited inflow jet visualized at the 60% threshold. E and F, Unvisualized inflow streams—that is, no inflow streams are observed at the 75% (E) and the 90% (F) thresholds.

Table 2: Maximum inflow velocity and maximum inflow rate in unruptured aneurysms with different inflow jet patterns visualized at the 75% threshold of the maximum velocity in the parent artery^a

Inflow Jet Pattern	Median (IQR)	Concentrated Inflow Jet	Diffuse Inflow Jet	Neck-Limited	Unvisualized
Concentrated inflow jet					
Maximum inflow velocity (mm/s)	572 (206)		.2539 (NS)	.4689 (NS)	.0002 (S)
Maximum inflow rate (mL/s)	2610 (3080)		.8414 (NS)	.0049 (S)	.0006 (S)
Diffuse inflow jet					
Maximum inflow velocity (mm/s)	636 (289)	.2539 (NS)		.0963 (NS)	<.0001 (S)
Maximum inflow rate (mL/s)	2450 (3080)	.8414 (NS)		.0017 (S)	<.0001 (S)
Neck-limited					
Maximum inflow velocity (mm/s)	462 (380)	.4689 (NS)	.0963 (NS)		.2645 (NS)
Maximum inflow rate (mL/s)	890 (424)	.0049 (S)	.0017 (S)		.3637 (NS)
Unvisualized					
Maximum inflow velocity (mm/s)	382 (44.0)	.0002 (S)	<.0001 (S)	.2645 (NS)	
Maximum inflow rate (mL/s)	696 (454)	.0006 (S)	<.0001 (S)	.3637 (NS)	

Note:—IQR indicates interquartile range; S, significant; NS, not significant by the comparison test adjusted for the *P* value.

^a Statistical analysis was performed between a variable in the left column and a variable in the headers.

the inflow jet should be defined on the basis of the flow magnitude in the parent artery. We assessed the inflow jets on 4D flow MR imaging by using thresholds based on the maximum flow velocity in the parent artery and classified the aneurysms on the basis of the inflow jet pattern.

Szikora et al²⁸ reported that concentrated inflow jets were observed in most ruptured aneurysms and that all aneurysms with such inflow jets were bifurcation aneurysms; none were sidewall aneurysms. We showed that individual inflow jet patterns re-

flected the threshold used to visualize the inflow streamlines. Three sidewall aneurysms whose inflow jets were concentrated at the 90% threshold exhibited a diffuse inflow jet at the 75% threshold, while 5 bifurcation aneurysms whose inflow jets were concentrated at the 75% threshold exhibited a diffuse inflow jet at the 60% threshold. The most significant difference in the rate of bifurcation aneurysms between groups C and D was observed at the 75% threshold. However, there is no evidence that the 75% threshold is optimal for evaluating the risk for aneurysmal

Table 3: Inflow velocity ratio and inflow rate ratio in unruptured aneurysms with different inflow jet patterns visualized at the 75% threshold of the maximum velocity in the parent artery^a

Inflow Jet Pattern and Ratio	Median % (IQR)	Concentrated Inflow Jet	Diffuse Inflow Jet	Neck-Limited	Unvisualized
Concentrated inflow jet					
Inflow velocity	94.1 (15.5)		.5222 (NS)	.0138 (S)	<.0001 (S)
Inflow rate	89.9 (52.3)		.1735 (NS)	.0059 (S)	<.0001 (S)
Diffuse inflow jet					
Inflow velocity	101 (31.8)	.5222 (NS)		.0053 (S)	<.0001 (S)
Inflow rate	59.3 (59.9)	.1735 (NS)		.0194 (S)	<.0001 (S)
Neck-limited					
Inflow velocity	69.4 (28.8)	.0138 (S)	.0053 (S)		.0516 (NS)
Inflow rate	29.8 (33.3)	.0059 (S)	.0194 (S)		.1021 (NS)
Unvisualized					
Inflow velocity	59.1 (7.62)	<.0001 (S)	<.0001 (S)	.0516 (NS)	
Inflow rate	21.6 (16.0)	<.0001 (S)	<.0001 (S)	.1021 (NS)	

Note:—IQR indicates interquartile range; S, significant; NS, not significant by the comparison test adjusted for the *P* value; inflow velocity ratio, the ratio of the maximum inflow velocity to the maximum flow velocity in the parent artery; inflow rate ratio, the ratio of the maximum inflow rate to the maximum flow rate in the parent artery.

^a Statistical analysis was performed between a variable shown in the left column and a variable in the headers.

growth, bleb formation, or rupture. Long-term observation studies are needed to identify the optimal visualization threshold.

Among the aneurysms in our study, those in groups C and D manifested significantly higher values in the inflow hemodynamic parameters than did group N and U lesions (Tables 2 and 3). While there was no statistically significant difference in the maximum inflow velocity, the maximum inflow rates, the inflow velocity ratio, and the inflow rate ratio between groups C and D, concentrated inflow jets may exert a stronger impact force on a small area in the aneurysm wall than diffuse inflow jets. Cebral et al^{4,5} reported that the inflow jets of ruptured aneurysms tended to be concentrated, while unruptured aneurysms manifested diffuse inflow jets that impacted larger areas. However, it remains unclear at what degree of inflow hemodynamic force aneurysmal rupture is likely. On the other hand, others^{29,30} have associated aneurysmal rupture with low-flow conditions as seen in our group N and U aneurysms. Our classification of inflow jet patterns and our quantitative estimation of the inflow hemodynamics may be the foundation for further studies investigating risk factors for aneurysmal rupture.

Our study has some limitations. In aneurysms with a low height and a wide neck, the inflow streamline bundle is usually short and wide. This may render it difficult to determine the extent of inflow jet dispersion by visual inspection. To identify risky inflow jet patterns computationally and to avoid subjective judgments, studies to establish numeric values for inflow hemodynamic parameters representing risk factors are needed. 4D flow MR imaging may yield poor-quality images due to motion artifacts attributable to a relatively long acquisition time²¹ and limited spatial resolution.^{9-14,17,20,22,25-27} Because flow quantification by using 4D flow MR imaging requires at least 16 isotropic voxels over the vessel lumen area,³¹ a spatial resolution of 1.0 mm in the isotropic voxel dimensions is needed to evaluate the flow conditions in aneurysms with a diameter of 4.0 mm.²² Although only 1.5T MR imaging scanners are available at our institution, high-resolution MR imaging on greater than 3T instruments may make it possible to evaluate the inflow jets of aneurysms smaller than 4.0 mm.^{12-14,17,22} While contrast-enhanced 3D cine phase-contrast MR imaging may improve the spatial and temporal resolution, its efficacy for the evaluation of inflow hemodynamics remains to be established. In addition, computational fluid dy-

namics analysis can be performed on the basis of the accurate vascular geometry with a motion-free acquisition. Additional studies are needed to understand the effects of novel techniques applied to 3D cine phase-contrast MR imaging and to validate the evaluation of small aneurysms on 1.5T scanners by computational fluid dynamics analysis.

CONCLUSIONS

The inflow jet pattern may depend on the threshold applied to visualize the inflow streamlines on 4D flow MR images. Because of the significant difference in the rate of bifurcation aneurysms and in the values of inflow hemodynamic parameters, for a classification of the inflow jet patterns on 4D flow MR imaging, the 75% threshold may be optimal within the 3 thresholds corresponding to 60%, 75%, and 90% of the maximum flow velocity in the parent artery.

REFERENCES

- Gasteiger R, Lehmann DJ, van Pelt R, et al. **Automatic detection and visualization of qualitative hemodynamic characteristics in cerebral aneurysms.** *IEEE Trans Vis Comput Graph* 2012;18:2178–87 CrossRef Medline
- Neugebauer M, Gasteiger R, Janiga G, et al. **Effective visual exploration of hemodynamics in cerebral aneurysms.** In: *Proceedings of the Conference of the European Association for Computer Graphics*, Geona, Spain; May 6–10, 2013
- Cebral JR, Sheridan M, Putman CM. **Hemodynamics and bleb formation in intracranial aneurysms.** *AJNR Am J Neuroradiol* 2010;31:304–10 CrossRef Medline
- Cebral JR, Castro MA, Burgess JE, et al. **Characterization of cerebral aneurysms for assessing risk of rupture by using patient-specific computational hemodynamics models.** *AJNR Am J Neuroradiol* 2005;26:2550–59 Medline
- Cebral JR, Mut F, Weir J, et al. **Association of hemodynamic characteristics and cerebral aneurysm rupture.** *AJNR Am J Neuroradiol* 2011;32:264–70 CrossRef Medline
- Castro MA, Putman CM, Sheridan MJ, et al. **Hemodynamic patterns of anterior communicating artery aneurysms: a possible association with rupture.** *AJNR Am J Neuroradiol* 2009;30:297–302 Medline
- Schneiders JJ, Marquering HA, Antiga L, et al. **Intracranial aneurysm neck size overestimation with 3D rotational angiography: the impact on intra-aneurysmal hemodynamics simulated with computational fluid dynamics.** *AJNR Am J Neuroradiol* 2013;34:121–28 CrossRef Medline
- Jansen IG, Schneiders JJ, Potters WV, et al. **Generalized versus pa-**

- tient-specific inflow boundary conditions in computational fluid dynamics simulations of cerebral aneurysmal hemodynamics. *AJNR Am J Neuroradiol* 2014;35:1543–48 CrossRef Medline
9. Meckel S, Stalder AF, Santini F, et al. **In vivo visualization and analysis of 3-D hemodynamics in cerebral aneurysms with flow-sensitized 4-D MR imaging at 3 T.** *Neuroradiology* 2008;50:473–84 CrossRef Medline
 10. Boussel L, Rayz V, Martin A, et al. **Phase-contrast magnetic resonance imaging measurements in intracranial aneurysms in vivo of flow patterns, velocity fields, and wall shear stress: comparisons with computational fluid dynamics.** *Magn Reson Med* 2009;61:409–17 CrossRef Medline
 11. Hope TA, Hope MD, Purcell DD, et al. **Evaluation of intracranial stenoses and aneurysms with accelerated 4D flow.** *Magn Reson Imaging* 2010;28:41–46 CrossRef Medline
 12. Isoda H, Ohkura Y, Kosugi T, et al. **Comparison of hemodynamics of intracranial aneurysms between MR fluid dynamics using 3D cine phase contrast MRI and MR-based computational fluid dynamics.** *Neuroradiology* 2010;52:913–20 CrossRef Medline
 13. Isoda H, Ohkura Y, Kosugi T, et al. **In vivo hemodynamic analysis of intracranial aneurysms obtained by magnetic resonance fluid dynamics (MRFD) based on time-resolved three-dimensional phase-contrast MRI.** *Neuroradiology* 2010;52:921–28 CrossRef Medline
 14. Naito T, Miyachi S, Matsubara N, et al. **Magnetic resonance fluid dynamics for intracranial aneurysms: comparison with computed fluid dynamics.** *Acta Neurochir (Wien)* 2012;154:993–1001 CrossRef Medline
 15. Kawaguchi T, Nishimura S, Kanamori M, et al. **Distinctive flow pattern of wall shear stress and oscillatory shear index: similarity and dissimilarity in ruptured and unruptured cerebral aneurysm blebs.** *J Neurosurg* 2012;117:774–80 CrossRef Medline
 16. Kecskemeti S, Johnson K, Wu Y, et al. **High resolution three-dimensional cine phase contrast MRI of small intracranial aneurysms using a stack of stars k-space trajectory.** *J Magn Reson Imaging* 2012;35:518–27 CrossRef Medline
 17. van Ooij P, Schneiders JJ, Marquering HA, et al. **3D cine phase-contrast MRI at 3T in intracranial aneurysms compared with patient-specific computational fluid dynamics.** *AJNR Am J Neuroradiol* 2013;34:1785–91 CrossRef Medline
 18. Schnell S, Ansari SA, Vakil P, et al. **Three-dimensional hemodynamics in intracranial aneurysms: influence of size and morphology.** *J Magn Reson Imaging* 2014;39:120–31 CrossRef Medline
 19. Berg P, Stucht D, Janiga G, et al. **Cerebral blood flow in a healthy circle of Willis and two intracranial aneurysms: computational fluid dynamics versus four-dimensional phase-contrast magnetic resonance imaging.** *J Biomech Eng* 2014;136 CrossRef Medline
 20. Futami K, Sano H, Misaki K, et al. **Identification of the inflow zone of unruptured cerebral aneurysms: comparison of 4D flow MRI and 3D TOF MRA data.** *AJNR Am J Neuroradiol* 2014;35:1363–70 CrossRef Medline
 21. Futami K, Sano H, Kitabayashi T, et al. **Parent artery curvature influences inflow zone location of unruptured sidewall cerebral aneurysms.** *AJNR Am J Neuroradiol* 2015;36:342–48 70 CrossRef Medline
 22. Hollnagel DI, Summers PE, Poulidakos D, et al. **Comparative velocity investigations in cerebral arteries and aneurysms: 3D phase-contrast MR angiography, laser Doppler velocimetry and computational fluid dynamics.** *NMR Biomed* 2009;22:795–808 CrossRef Medline
 23. Lorensen WE, Cline HE. **Marching cubes: a high resolution 3D surface construction algorithm.** *ACM Siggraph Computer Graphics* 1987;21:163–69 CrossRef
 24. Shimai H, Yokota H, Nakamura S, et al. **Extraction from biological volume data of a region of interest with nonuniform intensity.** In: *Proceedings of the Society of Photo-Optical Instrumentation Engineers 6051, Optomechatronic Machine Vision*, Kauhiko, Sumi, Japan. December 6, 2005; 6051:605115
 25. Jiang J, Johnson K, Valen-Sendstad K, et al. **Flow characteristics in a canine aneurysm model: a comparison of 4D accelerated phase contrast MR measurements and computational fluid dynamics simulations.** *Med Phys* 2011;38:6300–12 CrossRef Medline
 26. van Ooij P, Guedon A, Poelma C, et al. **Complex flow patterns in a real-size intracranial aneurysm phantom: phase contrast MRI compared with particle image velocimetry and computational fluid dynamics.** *NMR Biomed* 2012;25:14–26 CrossRef Medline
 27. van Ooij P, Potters WV, Guédon A, et al. **Wall shear stress estimated with phase contrast MRI in an in vitro and in vivo intracranial aneurysm.** *J Magn Reson Imaging* 2013;38:876–84 CrossRef Medline
 28. Szikora I, Paal G, Ugron A, et al. **Impact of aneurysmal geometry on intraaneurysmal flow: a computerized flow simulation study.** *Neuroradiology* 2008;50:411–21 CrossRef Medline
 29. Xiang J, Yu J, Snyder KV, et al. **Hemodynamic-morphological discriminant models for intracranial aneurysm rupture remain stable with increasing sample size.** *J Neurointerv Surg* 2016;8:104–10 CrossRef Medline
 30. Yasuda R, Strother CM, Taki W, et al. **Aneurysm volume-to-ostium area ratio: a parameter useful for discriminating the rupture status of intracranial aneurysms.** *Neurosurgery* 2011;68:310–17 CrossRef Medline
 31. Tang C, Blatter CC, Paker DL. **Accuracy of phase-contrast flow measurements in the presence of partial-volume effects.** *J Magn Reson Imaging* 1993;3:377–85 CrossRef Medline

The Impact of Middle Turbinate Concha Bullosa on the Severity of Inferior Turbinate Hypertrophy in Patients with a Deviated Nasal Septum

C.M. Tomblinson, M.-R. Cheng, D. Lal, and J.M. Hoxworth

ABSTRACT

BACKGROUND AND PURPOSE: Inferior turbinate hypertrophy and concha bullosa often occur opposite the direction of nasal septal deviation. The objective of this retrospective study was to determine whether a concha bullosa impacts inferior turbinate hypertrophy in patients who have nasal septal deviation.

MATERIALS AND METHODS: The electronic medical record was used to identify sinus CT scans exhibiting nasal septal deviation for 100 adult subjects without and 100 subjects with unilateral middle turbinate concha bullosa. Exclusion criteria included previous sinonasal surgery, tumor, sinusitis, septal perforation, and craniofacial trauma. Nasal septal deviation was characterized in the coronal plane by distance from the midline (severity) and height from the nasal floor. Measurement differences between sides for inferior turbinate width (overall and bone), medial mucosa, and distance to the lateral nasal wall were calculated as inferior turbinate hypertrophy indicators.

RESULTS: The cohorts with and without concha bullosa were similarly matched for age, sex, and nasal septal deviation severity, though nasal septal deviation height was greater in the cohort with concha bullosa than in the cohort without concha bullosa (19.1 ± 4.3 mm versus 13.5 ± 4.1 mm, $P < .001$). Compensatory inferior turbinate hypertrophy was significantly greater in the cohort without concha bullosa than in the cohort with it as measured by side-to-side differences in turbinate overall width, bone width, and distance to the lateral nasal wall ($P < .01$), but not the medial mucosa. Multiple linear regression analyses found nasal septal deviation severity and height to be significant predictors of inferior turbinate hypertrophy with positive and negative relationships, respectively ($P < .001$).

CONCLUSIONS: Inferior turbinate hypertrophy is directly proportional to nasal septal deviation severity and inversely proportional to nasal septal deviation height. The effect of a concha bullosa on inferior turbinate hypertrophy is primarily mediated through influence on septal morphology, because the nasal septal deviation apex tends to be positioned more superior from the nasal floor in these patients.

ABBREVIATIONS: CB+ = cohort with concha bullosa; CB- = cohort without concha bullosa; ITH = inferior turbinate hypertrophy; NSD = nasal septal deviation; Δ = side-to-side difference in inferior turbinate measurements

Nasal airway obstruction is a challenging problem that can arise from multiple etiologies, which include structural abnormalities such as nasal septal deformity and turbinate hypertrophy. Inferior turbinate hypertrophy (ITH) has received much attention in the literature in the debate over optimal surgical management of nasal obstruction.¹ Although the term “hypertrophy” is most accurately reserved for the overall enlargement of an organ because of increasing cell size, its use is widely accepted in the setting of turbinate enlargement secondary to greater thick-

ness of soft-tissue and/or bone components.²⁻⁵ Although limited normative data has been published on inferior turbinate size by using CT, ITH remains a clinical diagnosis.⁶

ITH has been commonly described as occurring contralateral to the direction of nasal septal deviation (NSD) or, alternatively phrased, along the concave side of the septum.^{2,3,7-14} Because of this association, it has been speculated that ITH is compensatory, to create physiologically favorable nasal airflow turbulence and to protect the mucosa from excessive drying and crusting with increased air flow. In other words, the inferior turbinate may have progressively enlarged to fill the void in the nasal cavity created by the shifted midline with the undesirable result of a smaller-than-expected cross-sectional area for air passage.² Using septoplasty to correct NSD without addressing the ITH may have the unintended consequence of worsening symptomatic nasal obstruction.⁷

Concha bullosa is an anatomic variant of ethmoid air cell development in which pneumatization most commonly extends

Received September 25, 2015; accepted after revision December 21.

From the Departments of Radiology (C.M.T., J.M.H.), Biostatistics (M.-R.C.), and Otolaryngology (D.L.), Mayo Clinic, Phoenix, Arizona.

Paper presented in preliminary form at: Annual Meeting of the American Society Head and Neck Radiology, September 10-14, 2014; Seattle, Washington.

Please address correspondence to Joseph M. Hoxworth, MD, 5777 E Mayo Blvd, Phoenix, AZ 85054; e-mail: hoxworth.joseph@mayo.edu

<http://dx.doi.org/10.3174/ajnr.A4705>

into the middle turbinate. This can be limited to the vertical lamella, extend into the bulbous portion, or extensively involve the vertical lamella and bulbous segment of the middle turbinate.¹⁵ If one allowed some outlier data, the prevalence is likely in the range of 21%–53%.^{15–27} Some of the reported variability can be attributed to differences in the populations being evaluated, the type of evaluation (ie, CT versus surgery), and the definition of concha bullosa (ie, whether to include small lamellar types). Similar to ITH, a preponderance of published reports support a strong association between the presence of concha bullosa and NSD, in which the nasal septum typically bows toward the contralateral side and may increasingly do so when middle turbinate pneumatization is greatest.^{23,24,27–30} Moreover, in bilateral cases, the nasal septum is usually near midline when the conchae bullosa are balanced in size but usually deviates away from an asymmetrically enlarged dominant concha bullosa.

When one controls for the shape and severity of a deviated nasal septum, it has yet to be determined whether a concha bullosa significantly influences the presence of ipsilateral ITH. Logically, an interaction may exist between the structures because the concha bullosa and ITH both commonly develop along the concave side of a deviated nasal septum within a secondarily widened nasal cavity. The objective of this study was to assess patients with NSD on CT in an attempt to identify whether the presence or absence of a concha bullosa influences ipsilateral ITH.

MATERIALS AND METHODS

This retrospective study, which is compliant with the Health Insurance Portability and Accountability Act, was approved by the institutional review board at the authors' institution, and the need for informed consent was waived. The radiology information management system was used to identify patients who underwent noncontrast sinus CT between January 1, 2011, and July 1, 2014. All sinus CT scans were acquired with a 64-detector scanner (LightSpeed VCT or Discovery CT750 HD; GE Healthcare, Milwaukee, Wisconsin), and the same CT protocol was used for all studies (120 kV[peak], 180 mA, 0.5-second rotation time, 0.531 pitch, and 0.625-mm section collimation). No topical intranasal vasoconstrictors were administered at the time of imaging.

The sinus CT scans and corresponding electronic medical records were evaluated in consecutive reverse-chronologic fashion to determine study eligibility. We specifically excluded patients with a Lund-Mackay score greater than zero, prior sinonasal surgery, CT or clinical findings of sinonasal polyposis, a history of head and neck tumor or irradiation, nasal septal perforation, and a documented history of craniofacial trauma. Inclusion required that patients were at least 18 years of age at the time of imaging and that the sinus CT was of diagnostic quality. Additionally, all patients were required to have unilateral NSD without a minimum threshold for severity. Subjects with S-shaped or other complex bidirectional nasal septal deformities were excluded. In total, we enrolled 200 patients with NSD: 100 with a unilateral middle turbinate concha bullosa (CB+) and 100 without a concha bullosa (CB−). As previously published, concha bullosa was defined as >50% pneumatization of the vertical height of the middle turbinate, thereby excluding very small conchae bullosa or pneumatization of the vertical lamella only.²⁴

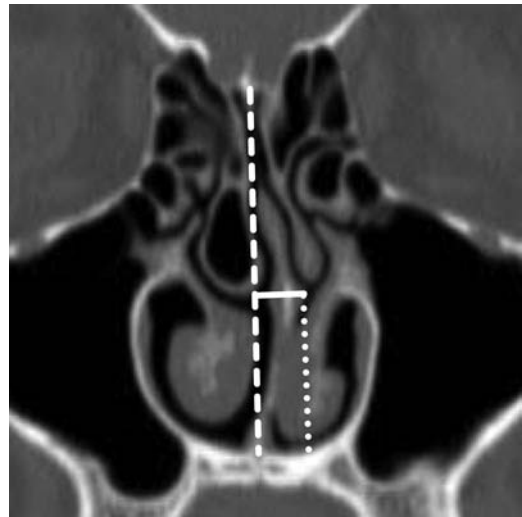


FIG 1. Coronal reformatted image from noncontrast sinus CT demonstrates the measurements of NSD. The midline is defined by a *dashed line* extending from the crista galli to the nasal crest. NSD severity (*solid line*) is measured to the point of maximal NSD orthogonal to the midline. NSD height is determined by measuring the distance from the point of maximal NSD to the floor of the nasal cavity parallel to the midline (*dotted line*).

Image assessment was performed by a board-certified neuro-radiologist by using a PACS. The following measurements were performed on 1.25-mm coronal reformations that were rendered in a bone algorithm and viewed at window level and width of 450 HU and 2500 HU, respectively:

Concha Bullosa. The maximum transverse width and craniocaudal length of the middle turbinate concha bullosa (CB+ group only).

NSD. Using the image on which the NSD was most severe, we drew a line from the crista galli to the nasal crest to define the midline. An orthogonal measurement was taken from the midline to the apex of maximal nasal septal deviation (NSD severity). The vertical distance from the apex to the floor of the nasal cavity was measured parallel to midline (NSD height), and the direction of septal deviation was recorded (Fig 1).

Inferior Turbinate. Because no standard definition exists for ITH on CT, 4 measurements were acquired to document the width of the inferior turbinate and the degree to which it projected into the nasal cavity.

1) Lateral offset (Fig 2A) represents the maximum transverse distance from the most medial aspect of the inferior turbinate bone to the lateral nasal wall.

2) Width (Fig 2A) was determined by the maximum transverse width of the pendulous portion of the inferior turbinate inclusive of soft tissue and bone.

3) Bone width (Fig 2B) represents the maximum transverse width of the inferior turbinate bone.

4) Medial mucosa width (Fig 2B) was a transverse measurement at the point of maximal soft-tissue thickness along the medial aspect of the inferior turbinate.

For consistency, these measurements were all performed by the same neuroradiologist at the level of the ostiomeatal complex

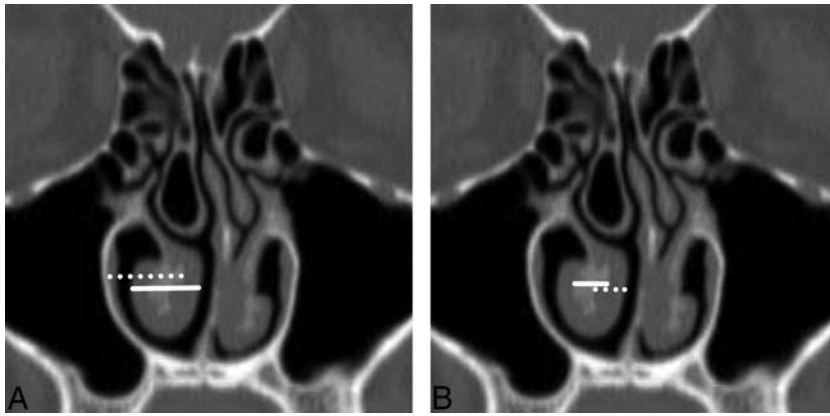


FIG 2. Coronal reformatted image from noncontrast sinus CT demonstrates the measurements of inferior turbinate size. A, The maximum transverse distance from the most medial aspect of the inferior turbinate conchal bone to the lateral nasal wall (lateral offset) is defined by the *dotted line*. The maximum transverse width of the pendulous portion of the inferior turbinate inclusive of soft tissue and bone (width) is depicted by the *solid line*. B, The greatest width of the inferior turbinate bone (bone width) is demarcated with a *solid line*, while the thickest transverse dimension of the soft tissue along the medial aspect of the inferior turbinate (medial mucosa width) is identified with a *dotted line*.

Table 1: Comparison between CB groups for patient characteristics and measurements^a

Variable	CB- (n = 100)	CB+ (n = 100)	Entire Cohort (N = 200)	P Value
Age (yr)	52.6 (16.6)	54.2 (17.4)	53.4 (17.0)	.50 ^b
Sex (female)	54 (54.0%)	59 (59.0%)	113 (56.5%)	.48 ^c
NSD severity (mm)	7.1 (1.6)	7.3 (2.0)	7.2 (1.8)	.25 ^b
NSD height (mm)	13.5 (4.1)	19.1 (4.3)	16.3 (5.1)	<.001 ^b
ΔLateral offset (mm)	2.7 (1.8)	1.9 (2.0)	2.3 (1.9)	<.01 ^b
ΔWidth (mm)	3.4 (2.0)	2.5 (2.3)	2.9 (2.2)	<.01 ^b
ΔBone width (mm)	1.3 (0.7)	0.9 (0.8)	1.1 (0.8)	<.01 ^b
ΔMedial mucosa width (mm)	1.0 (1.5)	0.7 (1.5)	0.8 (1.5)	.13 ^b

^a All values are displayed as mean (SD) except for sex, which is presented as count (%).

^b Two-sample *t* test was used to compare the CB+ and CB- groups.

^c χ^2 tests were used to compare the CB+ and CB- groups.

on the posterior-most coronal image on which the primary maxillary sinus ostium was visible. As an indicator of ITH for each patient, side-to-side differences (Δ) in inferior turbinate measurements were calculated by subtracting the side ipsilateral to the apex of the NSD from the contralateral side. In other words, a positive value for this difference would support the hypothesis that the inferior turbinate on the concave side of the nasal septum was larger than the one on the opposite side.

To assess the potentially confounding influence of vasocongestion related to the normal nasal cycle, we recorded the maximal mucosal thickness along the inferior aspect of the middle turbinate for the concave and convex sides of the deviated nasal septum.

Patient characteristics and side-to-side differences for the inferior turbinate measurements were compared between the presence and absence of the concha bullosa by using the 2-sample *t* test for continuous variables and the χ^2 test for categorical variables. Pearson correlation coefficients were also used to assess the strength and direction of linear relationships for the inferior turbinate measurement differences relative to NSD severity and NSD height for all 200 subjects, in addition to being stratified by CB+ and CB- groups. Multiple linear regression models were conducted for predicting the side-to-side differences in inferior turbinate measurements, controlling for CB+, NSD severity, NSD height, and potential interaction terms. A paired *t* test was used to

compare the middle turbinate mucosa thickness on the concave side of the deviated nasal septum with that on the convex side. Potential correlations between the concha bullosa width, concha bullosa length, NSD severity, and NSD height were examined by using Pearson correlation coefficients, and simple linear regressions were used for modeling the relationships. All analyses were performed with SAS 9.4 (SAS Institute, Cary, North Carolina). All hypothesis tests were 2-sided, and statistical significance was defined as $P < .05$.

RESULTS

The CB+ and CB- cohorts were similarly matched in age, sex, and NSD severity (Table 1). The mean (SD) transverse width and craniocaudal length of the middle turbinate conchae bullosa were 7.5 mm (2.2 mm) and 15.5 mm (3.8 mm), respectively, in the CB+ group, and the NSD height was significantly greater in the presence of a contralateral middle turbinate concha bullosa (mean, 19.1 \pm 4.3 mm versus 13.5 \pm 4.1 mm; $P < .001$). Concha bullosa width showed statistically significant moderate correlations for NSD height (Pearson $r = 0.30$, $P < .01$) and NSD severity (Pearson $r = 0.20$, $P = .04$). However, concha bullosa height was not significantly correlated with NSD

height or NSD severity. Because concha bullosa height and width were highly correlated (Pearson $r = 0.53$, $P < .001$), simple linear regression was performed by using only concha bullosa width as the predictor. There were statistically significant positive relationships between NSD height and concha bullosa width (β coefficient = 0.61, standard error = 0.20, $P < .01$) and NSD severity and concha bullosa width (β coefficient = 0.19, standard error = 0.09, $P < .04$).

Bivariate analysis was initially undertaken to evaluate the indicators of ITH related to concha bullosa status. No significant relationships were identified on the basis of age or sex. As seen in Table 1, the values for Δ lateral offset, Δ width, and Δ bone width were greater in the CB- group compared with CB+, but the results for Δ medial mucosa width did not reach significance. However, this comparison does not correct for the potentially confounding influence of NSD severity and NSD height. Pearson correlation coefficients were examined to determine the strength and direction of potential relationships between the side-to-side differences in inferior turbinate measurements and NSD severity and NSD height (Table 2). When we evaluated the data in aggregate and divided into CB+ and CB- groups, Δ lateral offset, Δ width, and Δ bone width showed strong potential as indicators of ITH as correlated to NSD severity and NSD height, while the level of strength for Δ medial mucosa width was again not as strong.

Table 2: Pearson correlation coefficients (*P* value) between side-to-side differences in inferior turbinate measurements and risk factors by concha bullosa group

Variable	CB- (<i>n</i> = 100)		CB+ (<i>n</i> = 100)		Entire Cohort (<i>N</i> = 200)	
	Septal Deviation Severity	Septal Deviation Height	Septal Deviation Severity	Septal Deviation Height	Septal Deviation Severity	Septal Deviation Height
ΔLateral offset	0.31 ^a (<.01)	-0.13 (.20)	0.36 ^a (<.001)	-0.17 (.10)	0.31 ^a (<.001)	-0.24 ^a (<.001)
ΔWidth	0.23 ^a (.02)	-0.22 ^a (.03)	0.23 ^a (.02)	-0.13 (.21)	0.20 ^a (<.01)	-0.26 ^a (<.001)
ΔBone width	0.43 ^a (<.001)	-0.24 ^a (.02)	0.56 ^a (<.001)	-0.31 ^a (<.01)	0.47 ^a (<.001)	-0.35 ^a (<.001)
ΔMedial mucosa width	-0.03 (.76)	-0.21 ^a (.04)	-0.08 (.43)	-0.03 (.79)	-0.07 (.35)	-0.16 ^a (.03)

^a Pearson correlation coefficients that were significant at the *P* < .05 level.

Table 3: Multiple linear regression models predicting side-to-side inferior turbinate measurement differences

Dependent Variable/Predictor	β Coefficient (Standard Error)	<i>P</i> Value
ΔLateral offset		<.001 ^a
NSD height	-0.10 (0.02)	<.001
NSD severity	0.36 (0.07)	<.001
ΔWidth		<.001 ^a
NSD height	-0.12 (0.03)	<.001
NSD severity	0.28 (0.08)	<.001
ΔBone width		<.001 ^a
NSD height	-0.06 (0.01)	<.001
NSD severity	0.22 (0.02)	<.001
ΔMedial mucosa width		.06 ^a
NSD height	-0.05 (0.02)	.03
NSD severity	-0.04 (0.06)	.45

^a Overall model *P* value.

Regression models were constructed with Δlateral offset, Δwidth, Δbone width, and Δmedial mucosa width as the dependent variables, respectively, while NSD severity, NSD height, CB+, and appropriate statistical interaction terms were the independent variables. No statistically significant interactions were identified, so these terms were removed. Because CB+ was highly associated with NSD height (*P* < .001), these variables essentially conveyed the same information so that both could not achieve significance within the same model. Because the models containing NSD height and NSD severity had the best overall statistical significance, CB+ was removed from the regression models. The regression models for Δlateral offset, Δwidth, and Δbone width reached significance (*P* < .001), with all of these variables showing an inverse relationship with NSD height and a positive relationship with NSD severity (Table 3). The model for Δmedial mucosa width approached, but did not reach, statistical significance (*P* = .06). In other words, as the nasal septum further deviates, the inferior turbinate on the concave side of the septum becomes asymmetrically enlarged, but the degree of enlargement is abated as the apex of the NSD moves farther away from the floor of the nasal cavity. This relative increase in inferior turbinate size can be explained with this model as greater projection of the turbinate bone more medially into the nasal cavity (Δlateral offset) and an increase in the width of the pendulous portion of the inferior turbinate (Δwidth), with the latter driven by thickening of bone more than mucosa.

Middle turbinate mucosal thickness did not differ significantly between the concave (mean, 2.2 ± 0.7 mm) and convex (mean, 2.2 ± 0.6 mm) sides of the deviated nasal septum (*P* = .99, paired *t* test).

DISCUSSION

Concordant with previous reports, the current study supports the association between NSD and contralateral ITH.^{2,3,7-14} NSD severity and NSD height best predicted the severity of ITH without significant contribution from the presence or absence of the concha bullosa. Although some of the prior reports did not objectively measure the severity of NSD, 1 study found that inferior turbinate bone thickness on the side opposite the NSD positively correlated with NSD severity as measured by septal angle and volume.¹³ In contrast, Akoğlu et al⁹ attempted to associate the angle of the deviated septum with the cross-sectional areas for hypertrophied inferior turbinate bone, mucosa, and overall size, but no significant correlation was found. This may be because a septal angle eliminates some useful information. When one measures the angle from the region of the crista galli, severe NSD centered closer to the floor of the nasal cavity and a milder NSD positioned more superiorly can yield the same septal angle but have a different impact on septal morphology and surrounding structures. Therefore, NSD in the current study was characterized by 2 variables, NSD severity and NSD height.

The elimination of the concha bullosa from the regression model does not mean that it is irrelevant, because the bivariate analysis clearly showed significant associations between the concha bullosa and the indicators of ITH (ie, side-to-side measurement differences in inferior turbinate bone width, overall width, and the degree of intranasal projection). Instead, it merely indicates that the presence of a concha bullosa did not provide additional statistical significance in a multiple regression model because it presumably conveys much of the same information as the parameters of NSD. On the basis of the current results, the severity of ITH correlates directly with NSD severity and inversely with NSD height. This correlation effectively accounts for the observation that the apex of maximal NSD tends to be located more superiorly in the presence of a unilateral concha bullosa.

Prior studies have documented the presence of ITH in NSD in a variety of different ways. Some of the earliest work on ITH used acoustic rhinometry to indirectly evaluate the extent of ITH by estimating the cross-sectional area of the nasal cavity as a function of the distance from the nostrils.^{2,7} Because of an incomplete response following topical nasal decongestant application, it was concluded that ITH must result from combined mucosal and skeletal hypertrophy. CT has been used as an alternative form of in vivo assessment for ITH associated with NSD by acquiring different measurements of bone and soft-tissue components of the inferior turbinate and comparing these results internally with the contralateral side or exter-

nally with a control population.^{8,9,11-13} In general, these CT data support the findings of acoustic rhinometry that compensatory ITH arises from increased bone and mucosal thickness. Additionally, as measured by distance or angle, the inferior turbinate on the concave side of a deviated septum projects farther medially into the nasal cavity.^{11,14} Histopathologically, Berger et al³ compared resected inferior turbinate specimens in patients undergoing surgery for NSD with ITH and compared them with freshly harvested postmortem specimens. The conchal bone in the ITH group showed a 2-fold increase in thickness, which accounted for approximately 75% of the difference in overall turbinate thickness compared with the cadaveric controls, with no significant difference in bone type (lamellar versus compact). The mucosal contribution to ITH was much less, though the appropriateness of comparing surgically resected turbinates with postmortem specimens has been questioned.⁵ When viewed in aggregate, this previously published work supports compensatory ITH arising from both bone and mucosal thickening. The tendency of the bone findings to be slightly more reproducible across studies may relate to the inherent variability in mucosal thickening introduced by normal mucosal cycling. In the current study, the lack of a difference in middle turbinate mucosal thickness along the concave and convex sides of the deviated nasal septum argues against the presence of a systematic bias from the nasal cycle. However, the multivariable model for Δ medial mucosal width showed that there was no statistically significant difference ($P = .06$), and this might be attributable to the added variability introduced by the nasal cycle. In contrast, the 3 ITH variables that included osseous structures were all highly significant.

The choice of representative measurements in the current study was grounded in the previously published body of literature.^{2,3,7-9,11-14} Inferior turbinate width (total and bone only) and the distance that the inferior turbinate projects into the nasal cavity were selected as appropriate representations of ITH. Because the medial mucosal layer of the inferior turbinate tends to be the widest because it contains the thickest lamina propria, it was also chosen for measurement.³ We chose the coronal image used for assessment through the level of the maxillary sinus ostium to include the concha bullosa, while noting that the contributions of bone and mucosa to ITH have been validated for the middle third of the inferior turbinate.^{8,9,12}

The precise mechanism underlying the development of compensatory ITH in NSD remains unclear, but there is evidence to suggest a long-standing acquired process. Aslan et al¹² stratified adult (mean age, 40.2 ± 12.4 years) and pediatric (mean age, 10.9 ± 3.8 years) cohorts into those who had NSD versus those with a straight or nearly straight septum and calculated interturbinate ratios to determine relative size differences in bone and soft-tissue components of the inferior turbinates (ie, an increased ratio suggested ITH). For bone more than soft-tissue structures, the adults with NSD had significantly higher interturbinate ratios compared with the adults with a straight septum, thereby indicating ITH. In contrast, the interturbinate ratios did not significantly differ between the pediatric groups on the basis of the presence of NSD, and the adults with NSD had significantly higher interturbinate ratios than the children with NSD. The results were inter-

preted as ITH being an acquired compensatory process in NSD rather than a congenital abnormality.

A separate study compared patients with NSD and stratified them as to whether the NSD was thought posttraumatic or congenital.¹⁴ Inferior turbinate measurements were compared between the convex and concave sides of the septum to delineate ITH. In the congenital group, the bone of the inferior turbinates on the concave side of the septum projected more medially into the nasal cavity on the basis of the distance and angle relative to the lateral nasal wall. The authors concluded that the conchal bone plays a much greater role in ITH in congenital NSD, underscoring the much longer time needed to acquire osseous-versus-soft-tissue changes. The notion that the mucosal component of compensatory ITH is more dynamic is also supported by a study that evaluated patients who underwent septoplasty without a turbinate operation and then underwent repeat CT at least 1 year postoperatively.¹⁰ On average, the medial mucosa of the hypertrophied inferior turbinate on the concave side of the septum preoperatively became thinner by approximately 1 mm after the septal deformity was corrected. This finding was presumed to represent the mucosal response to narrowing of the adjacent air channel caused by moving the septum back to midline. In contrast, the turbinate skeletal structure was unchanged.

While long-standing NSD appears to lead to the development of ITH, the precise relationship between NSD and concha bullosa continues to be debated. A significant body of evidence not only associates NSD and concha bullosa but also indicates that the NSD is typically directed away from the concha bullosa when unilateral or the dominant concha bullosa when bilateral.^{16,23,24,28,29} The severity of NSD tends to be greater in larger or more extensively pneumatized conchae bullosa; conversely, the prevalence of a concha bullosa correlates positively with the severity of NSD.^{23,24,28,29} The current results further strengthen the intimate relationship between concha bullosa and NSD by demonstrating that the apex of maximum NSD is positioned more superiorly when a unilateral concha bullosa is present and that the severity of NSD increases in direct proportion to concha bullosa width. However, causation remains uncertain. Because a number of studies have documented a preserved air channel between the medial aspect of the concha bullosa and the nasal septum, it is unlikely that an enlarging concha bullosa directly pushes the septum.^{16,23,24}

It has been previously suggested that concha bullosa and NSD represent 2 incidental and potentially unrelated developmental anomalies that tend to appear concomitantly or that a concha bullosa develops to fill in vacant space created by a preexisting NSD, termed the "e vacuo" hypothesis.³¹ However, a study comparing dizygotic and monozygotic twins found that the intrapair similarities were virtually identical for the presence of a deviated nasal septum (23% versus 25%), but monozygotic twins had an intrapair similarity for concha bullosa of 70% compared with 25% for dizygotic twins, suggesting a genetic influence in the presence of a concha bullosa.³² Thus, a high probability of congenital coexistence of NSD and concha bullosa seems questionable. In addition, the concha bullosa would be more apt to precede NSD because of a stronger genetic link, thereby contradicting the e vacuo hypothesis.

Additional observations have further disputed these prevailing hypotheses.^{2,3} Not all individuals with septal deviation have concha bullosa, while most cases with a large or dominant concha bullosa have septal deviation. Moreover, there are instances of medium-to-large bilateral conchae bullosa in the setting of a straight nasal septum. Consequently, it is difficult to establish a purely congenital association between the 2 anatomic variants, and the compensatory growth of a concha bullosa to fill in the space vacated by a deviated nasal septum also seems implausible. In fact, Sazgar et al^{2,3} recently hypothesized that it is the NSD that is more likely to be compensatory for a concha bullosa by synthesizing this idea with the prevailing literature and substantiating it with a discussion of fluid dynamics.

The limitations of the current study are primarily related to the generalizability of the results regarding the relationship of NSD, concha bullosa, and ITH. In an attempt to eliminate confounding variables, the strict inclusion criteria eliminated patients with active inflammatory sinus disease, posttraumatic sinonasal deformity, bilateral conchae bullosa, and small lamellar conchae bullosa. Moreover, the study population consisted of patients with a clear unilateral pattern of septal deflection, and it has been recognized that different patterns of concomitant turbinal hyperplasia and concha bullosa vary on the basis of NSD morphology.^{3,3} Last, ITH and NSD were exclusively defined by CT appearance with no correlate as to the presence of clinically significant nasal obstruction. Because the study population was limited to subjects with clear sinuses on CT, the overwhelming majority never underwent a thorough rhinologic evaluation, thereby limiting the ability to make meaningful imaging-clinical correlations. In reality, symptomatic nasal obstruction from ITH and NSD is best determined clinically. The CT-based measurements performed in this study were a tool to identify anatomic features that contribute to the development of ITH, not a recommended form of clinical assessment.

CONCLUSIONS

The degree of compensatory ITH increases in proportion to the severity of NSD and decreases as the NSD apex moves farther superiorly from the nasal floor. Although the presence of a unilateral middle turbinate concha bullosa is associated with less severe ITH, this effect is primarily attributed to the higher apex of the NSD seen with concha bullosa, as opposed to an independent relationship between concha bullosa and ITH, both of which are commonly found along the concave side of a deviated septum.

REFERENCES

- Jackson LE, Koch RJ. **Controversies in the management of inferior turbinate hypertrophy: a comprehensive review.** *Plast Reconstr Surg* 1999;103:300–12 CrossRef Medline
- Hilberg O, Grymer LF, Pedersen OF, et al. **Turbinate hypertrophy: evaluation of the nasal cavity by acoustic rhinometry.** *Arch Otolaryngol Head Neck Surg* 1990;116:283–89 CrossRef Medline
- Berger G, Hammel I, Berger R, et al. **Histopathology of the inferior turbinate with compensatory hypertrophy in patients with deviated nasal septum.** *Laryngoscope* 2000;110:2100–05 CrossRef Medline
- Berger G, Gass S, Ophir D. **The histopathology of the hypertrophic inferior turbinate.** *Arch Otolaryngol Head Neck Surg* 2006;132:588–94 CrossRef Medline
- Eccles R. **Query, concerning mechanism of inferior turbinate enlargement.** *Arch Otolaryngol Head Neck Surg* 2007;133:624; author reply 624–25 Medline
- Balbach L, Trinkel V, Guldner C, et al. **Radiological examinations of the anatomy of the inferior turbinate using digital volume tomography (DVT).** *Rhinology* 2011;49:248–52 CrossRef Medline
- Grymer LF, Illum P, Hilberg O. **Septoplasty and compensatory inferior turbinate hypertrophy: a randomized study evaluated by acoustic rhinometry.** *J Laryngol Otol* 1993;107:413–17 CrossRef Medline
- Egeli E, Demirci L, Yazıcı B, et al. **Evaluation of the inferior turbinate in patients with deviated nasal septum by using computed tomography.** *Laryngoscope* 2004;114:113–17 CrossRef Medline
- Akoğlu E, Karazincir S, Balci A, et al. **Evaluation of the turbinate hypertrophy by computed tomography in patients with deviated nasal septum.** *Otolaryngol Head Neck Surg* 2007;136:380–84 CrossRef Medline
- Kim DH, Park HY, Kim HS, et al. **Effect of septoplasty on inferior turbinate hypertrophy.** *Arch Otolaryngol Head Neck Surg* 2008;134:419–23 CrossRef Medline
- Jun BC, Kim SW, Cho JH, et al. **Is turbinate surgery necessary when performing a septoplasty?** *Eur Arch Otorhinolaryngol* 2009;266:975–80 CrossRef Medline
- Aslan G, Uzun L, Ugur MB, et al. **Unilateral inferior turbinate bone hypertrophy: is it compensatory or congenital?** *Am J Rhinol Allergy* 2013;27:255–59 CrossRef Medline
- Orhan I, Aydin S, Ormeci T, et al. **A radiological analysis of inferior turbinate in patients with deviated nasal septum by using computed tomography.** *Am J Rhinol Allergy* 2014;28:e68–72 CrossRef Medline
- Korkut AY, Islim F, Gulseven Ciftci S, et al. **Evaluation of inferior turbinate hypertrophy in patients with congenital and traumatic nasal septum deviation.** *J Laryngol Otol* 2012;126:784–88 CrossRef Medline
- Bolger WE, Butzin CA, Parsons DS. **Paranasal sinus bony anatomic variations and mucosal abnormalities: CT analysis for endoscopic sinus surgery.** *Laryngoscope* 1991;101:56–64 Medline
- Bhandary SK, Kamath PS. **Study of relationship of concha bullosa to nasal septal deviation and sinusitis.** *Indian J Otolaryngol Head Neck Surg* 2009;61:227–29 CrossRef Medline
- Javadrashid R, Naderpour M, Asghari S, et al. **Concha bullosa, nasal septal deviation and paranasal sinusitis; a computed tomographic evaluation.** *B-ENT* 2014;10:291–98 Medline
- Kayalioglu G, Oyar O, Govsa F. **Nasal cavity and paranasal sinus bony variations: a computed tomographic study.** *Rhinology* 2000;38:108–13 Medline
- Lam WW, Liang EY, Woo JK, et al. **The etiological role of concha bullosa in chronic sinusitis.** *Eur Radiol* 1996;6:550–52 CrossRef Medline
- Nadas S, Duvoisin B, Landry M, et al. **Concha bullosa: frequency and appearances on CT and correlations with sinus disease in 308 patients with chronic sinusitis.** *Neuroradiology* 1995;37:234–37 CrossRef Medline
- Nouraei SA, Elisay AR, Dimarco A, et al. **Variations in paranasal sinus anatomy: implications for the pathophysiology of chronic rhinosinusitis and safety of endoscopic sinus surgery.** *J Otolaryngol Head Neck Surg* 2009;38:32–37 Medline
- Ozcan KM, Selcuk A, Ozcan I, et al. **Anatomical variations of nasal turbinates.** *J Craniofac Surg* 2008;19:1678–82 CrossRef Medline
- Sazgar AA, Massah J, Sadeghi M, et al. **The incidence of concha bullosa and the correlation with nasal septal deviation.** *B-ENT* 2008;4:87–91 Medline
- Stallman JS, Lobo JN, Som PM. **The incidence of concha bullosa and its relationship to nasal septal deviation and paranasal sinus disease.** *AJNR Am J Neuroradiol* 2004;25:1613–18 Medline

25. Unlü HH, Akyar S, Caylan R, et al. **Concha bullosa.** *J Otolaryngol* 1994;23:23–27 Medline
26. Uygur K, Tüz M, Dogru H. **The correlation between septal deviation and concha bullosa.** *Otolaryngol Head Neck Surg* 2003;129:33–36 CrossRef Medline
27. Yiğit O, Acioglu E, Cakir ZA, et al. **Concha bullosa and septal deviation.** *Eur Arch Otorhinolaryngol* 2010;267:1397–401 CrossRef Medline
28. Elahi MM, Frenkiel S, Fageeh N. **Paraseptal structural changes and chronic sinus disease in relation to the deviated septum.** *J Otolaryngol* 1997;26:236–40 Medline
29. Aktas D, Kalcioğlu MT, Kutlu R, et al. **The relationship between the concha bullosa, nasal septal deviation and sinusitis.** *Rhinology* 2003; 41:103–06 Medline
30. Hatipoglu HG, Cetin MA, Yuksel E. **Nasal septal deviation and concha bullosa coexistence: CT evaluation.** *B-ENT* 2008;4:227–32 Medline
31. Stammberger H. *Functional Endoscopic Sinus Surgery: The Messerklinger Technique.* Philadelphia: B.C. Decker; 1991:156–68
32. Chaiyasate S, Baron I, Clement P. **Analysis of paranasal sinus development and anatomical variations: a CT genetic study in twins.** *Clin Otolaryngol* 2007;32:93–97 CrossRef Medline
33. Baumann I, Baumann H. **A new classification of septal deviations.** *Rhinology* 2007;45:220–23 Medline

Vestibular Aqueduct Measurements in the 45° Oblique (Pöschl) Plane

A.F. Juliano, E.Y. Ting, V. Mingkwansook, L.M. Hamberg, and H.D. Curtin



ABSTRACT

BACKGROUND AND PURPOSE: The 45° oblique (Pöschl) plane allows reliable depiction of the vestibular aqueduct, with virtually its entire length often visible on 1 CT image. We measured its midpoint width in this plane, aiming to determine normal measurement values based on this plane.

MATERIALS AND METHODS: We retrospectively evaluated temporal bone CT studies of 96 pediatric patients without sensorineural hearing loss. Midvestibular aqueduct widths were measured in the 45° oblique plane by 2 independent readers by visual assessment (subjective technique). The vestibular aqueducts in 4 human cadaver specimens were also measured in this plane. In addition, there was a specimen that had undergone CT scanning before sectioning, and measurements made on that CT scan and on the histologic section were compared. Measurements from the 96 patients' CT images were then repeated by using findings derived from the radiologic-histologic comparison (objective technique).

RESULTS: All vestibular aqueducts were clearly identifiable on 45° oblique-plane CT images. The mean for subjective measurement was 0.526 ± 0.08 mm (range, 0.337–0.947 mm). The 97.5th percentile value was 0.702 mm. The mean for objective measurement was 0.537 ± 0.077 mm (range, 0.331–0.922 mm). The 97.5th percentile value was 0.717 mm.

CONCLUSIONS: Measurements of the vestibular aqueduct can be performed reliably and accurately in the 45° oblique plane. The mean midpoint width was 0.5 mm, with a range of 0.3–0.9 mm. These may be considered normal measurement values for the vestibular aqueduct midpoint width when measured in the 45° oblique plane.

ABBREVIATIONS: LVA = large vestibular aqueduct; OPA = optimal percentage attenuation

Valvassori and Clemis^{1,2} reported in 1978 that the vestibular aqueduct may be considered enlarged when its width at midpoint measures >1.5 mm on hypocycloidal polytomography. CT has since replaced tomography as the technique of choice for temporal bone evaluation. In 2007, Boston et al³ proposed a new definition of an enlarged vestibular aqueduct based on axial CT studies. The criteria they established, referred to as the Cincinnati criteria, defined large vestibular aqueduct (LVA) as a vestibular aqueduct with width of ≥ 2 mm at the operculum and/or ≥ 1 mm at the midpoint as measured on axial images.

Current scanners allow CT source images to be reformatted in

any plane with near-identical spatial resolution.^{4,5} This feature is used in temporal bone imaging for optimizing visualization of various anatomic structures. In particular, the 45° oblique (Pöschl) plane has been shown to depict the vestibular aqueduct more reliably than the axial plane because this plane is parallel to the longitudinal axis of the vestibular aqueduct, and this plane allows depiction of virtually the entire length of this structure.^{6,7} Evaluation of the vestibular aqueduct in this plane allows accurate identification of its midpoint and determination of its true cross-sectional width without overestimation related to obliquity (Fig 1).

In this study, we aimed to determine normal measurements for the vestibular aqueduct midpoint width based on the 45° oblique plane.

MATERIALS AND METHODS

Part 1: CT Measurements, with Caliper Placement Based on Visual Assessment of Bony Margins (Subjective Technique)

Subjects. Temporal bone CT studies of 96 children (192 vestibular aqueducts) referred from the pediatric otolaryngology service were reviewed retrospectively in accordance with guidelines from the Massachusetts Eye and Ear Infirmary institutional re-

Received October 8, 2015; accepted after revision December 18.

From the Department of Radiology (A.F.J., H.D.C.), Massachusetts Eye and Ear Infirmary, and Department of Radiology (L.M.H.), Brigham and Women's Hospital, Harvard Medical School, Boston, Massachusetts; Department of Diagnostic Imaging (E.Y.T.), National University Health System, Singapore; and Department of Radiology (V.M.), Thammasat University Hospital, Pathumthani, Thailand.

Please address correspondence to Amy F. Juliano, MD, Department of Radiology, Massachusetts Eye and Ear Infirmary, 243 Charles St, Boston, MA 02114; e-mail: amy_juliano@meei.harvard.edu; @amyjuliano

Indicates open access to non-subscribers at www.ajnr.org

<http://dx.doi.org/10.3174/ajnr.A4735>

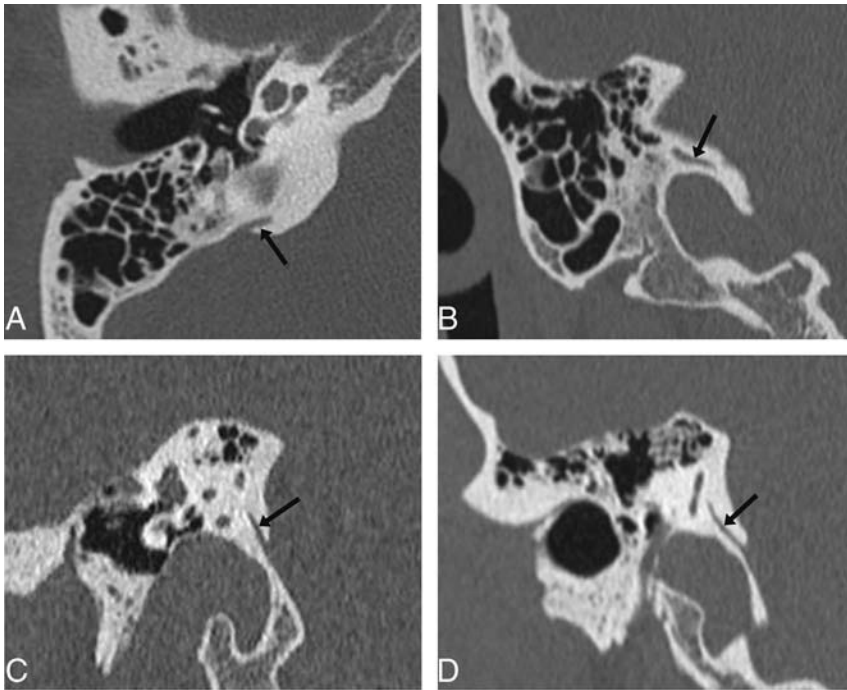


FIG 1. The vestibular aqueduct as seen on axial (A), coronal (B), sagittal (C), and the 45° oblique (Pöschl) (D) planes (arrows). It can be seen along its entire longitudinal length on the 45° oblique plane, but only partially on the other planes. It also appears wider on the axial, coronal, and sagittal planes, due to the oblique orientation of its cross-section relative to these planes, which may lead to overestimation of its width when measurement is made in these planes.

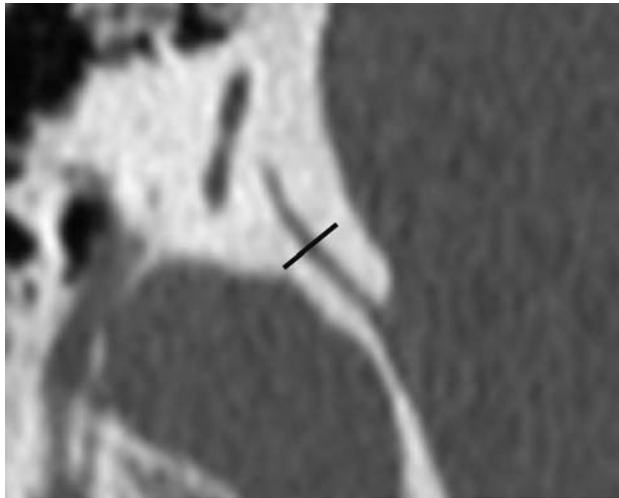


FIG 2. CT image of the vestibular aqueduct in the 45° oblique plane. The midpoint of the vestibular aqueduct is identified, and a line (shown in black) is drawn perpendicular to its wall. The width is measured along this line.

view board. Patients with sensorineural hearing loss were excluded from the study.

CT Scanning and Processing. All patients underwent dedicated temporal bone CT without intravenous contrast on a 40-section multidetector CT scanner (Somatom Sensation 40; Siemens, Erlangen, Germany). Images were obtained with 0.6-mm collimation, 0.6-mm thickness, and a 0.2-mm increment at 320 mAs and 120 kV(peak). Data were reconstructed separately for each temporal bone in the axial plane by using a bone algorithm; this was

performed routinely in all cases by the CT technologist. However, 45° oblique reformations were not routinely produced in all cases. Thus, for this study, the dataset from each case was transferred to a workstation for postprocessing by using a commercially available 3D reformatting software (Voxar 3D; Barco, Edinburgh, Scotland). On this software, images in the 45° oblique plane were produced for each temporal bone by selecting the plane parallel to the superior semicircular canal and by using that as the landmark image. These reformatted images were then analyzed. The image section demonstrating the entire length of the vestibular aqueduct was selected, enlarged, and exported at full resolution to an open-source software, ImageJ (National Institutes of Health, Bethesda, Maryland), for performing measurements and statistical analyses.

CT Image Evaluation and Measurement: Visual Assessment Technique. Two neuroradiologists (E.Y.T. and V.M.) independently reviewed the exported images, which were magnified approximately 15 times and viewed at high resolution with a small FOV in bone window settings (width, 4000 HU; level, 700 HU).

For each image, the vestibular aqueduct width was measured at the midpoint of the postisthmic segment (Fig 2). Because object edges do not appear absolutely sharp on images, especially when magnified, we paid careful attention to the placement of electronic calipers at the perceived edge of the bony canal of the vestibular aqueduct, aiming to locate the point along the gray zone between white (bone) and dark gray (soft tissue) that best represented the transition from bone to soft-tissue attenuation. Each radiologist measured each vestibular aqueduct twice, with a 1-month time interval between the 2 measurements.

Part 2: Cadaveric Specimen Measurement

Cadaveric Specimen Preparation. Temporal bones from patients with normal hearing in life were selected from the cadaveric collection at the Otopathology Laboratory at the Massachusetts Eye and Ear Infirmary. All temporal bones were processed in the standard manner for light microscopy,⁸ including serial sectioning at a thickness of 20 μ m and staining of every tenth section by using hematoxylin-eosin. The stained sections were mounted onto glass slides. Only those specimens aligned and sectioned in the plane of the superior semicircular canal could be used, to replicate the 45° oblique plane. This feature limited the number of available specimens to 4.

Cadaveric Specimen Evaluation and Measurement. Each slide-mounted section that best displayed the entire length of the vestibular aqueduct was reviewed by light microscopy. Measurements were taken at the midpoint of the vestibular aqueduct.

Part 3: Correlation between Measurements Made on Histologic Sections and Measurements Made on CT Images of the Same Cadaveric Specimen

One cadaveric specimen from a patient with normal hearing in life underwent CT scanning before histologic preparation, by using the same CT technique as that for clinical patients. To increase spatial resolution and accuracy, we stained every fifth section through the region of the vestibular aqueduct rather than every tenth. The microtome section that best displayed the entire length of the vestibular aqueduct was paired to the corresponding CT image and reformatted in the 45° oblique plane (Fig 3), and their midpoint widths were measured and compared.

A graph was created by placing calipers on the magnified CT image and recording the CT attenuation (in Hounsfield units) at each pixel along a line drawn through the midpoint of the vestibular aqueduct perpendicular to its wall. The x-axis represented the

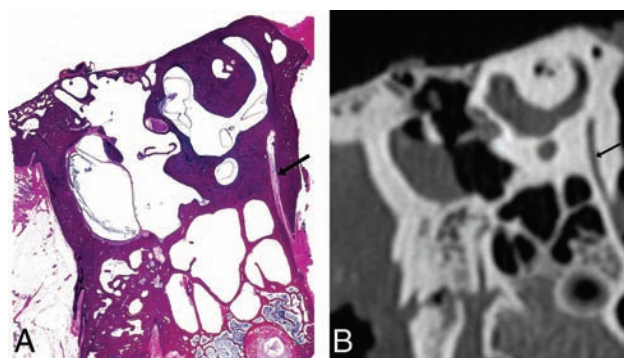


FIG 3. The vestibular aqueduct of a cadaveric temporal bone displayed in the 45° oblique plane (arrow), in a histologically processed microtome section (A) and in a CT image (B).

distance along this line, and the y-axis represented the CT attenuation (Fig 4). This yielded a “CT attenuation curve,” which, instead of being a step function at each bone–soft tissue interface on either end (such as when object edges are absolutely sharp), is a curve. The maximum y-values forming plateaus on either end of the curve (y-max) represent the CT attenuation of bone, and the minimum y-value at the nadir of the curve (y min) represents the CT attenuation in the center of the vestibular aqueduct. For each y-value, the difference between the 2 corresponding x-values (x_1 and x_2) gives the width of the vestibular aqueduct ($x_2 - x_1$, full width). We divided the difference between the maximum and minimum y-values ($y\text{-max} - y\text{-min}$) into 10 percentiles. At each percentile, we calculated the corresponding width of the vestibular aqueduct. The percentile at which the vestibular aqueduct width most closely matched the width as measured on the sectioned specimen was noted. This percentile is referred to as the optimal percentage attenuation (OPA) (Fig 4), the point at which placement of electronic calipers on a CT image would lead to a vestibular aqueduct width value that best correlates with the measurement performed on the histologic specimen (best radiologic-histologic correlation).

Part 4: CT Measurements, with Caliper Placement Based on Optimal Percentage Attenuation (Objective Technique)

The CT images from the 96 children that best displayed the vestibular aqueduct and were exported to ImageJ were again reviewed by the 2 neuroradiologists. These images were magnified approximately 15 times and again viewed at high resolution with a small FOV in bone window settings (width, 4000 HU; level, 700 HU). However, instead of placing electronic calipers at the perceived edges by subjective visual assessment, we applied the OPA

CT attenuation along a line drawn through the mid vestibular aqueduct of a cadaveric specimen

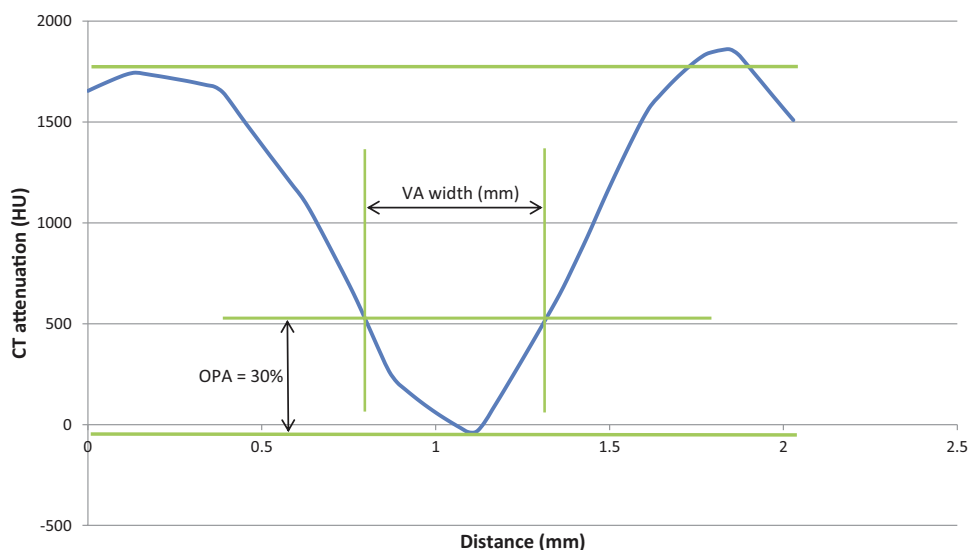


FIG 4. A graph of the distance along a line drawn through the midpoint of the vestibular aqueduct (x-axis) plotted against CT attenuation in Hounsfield units at each point along this line (y-axis). The optimal percentage attenuation is denoted on the graph. Through radiologic-histologic correlation by using the cadaveric temporal bone specimen, the OPA was found to be 30%.

Table 1: Vestibular aqueduct width obtained using the subjective and objective techniques^a

Measurement Technique	Mean VA Width (range) (mm) (n = 192)	VA Width at the 95th Percentile	VA Width at the 97.5th Percentile
Subjective (visual assessment) technique	0.527 ± 0.08 (0.353–0.887)	0.666	0.702
Objective (OPA) technique	0.537 ± 0.077 (0.331–0.922)	0.658	0.717

Note:—VA indicates vestibular aqueduct.

^aUnits are in millimeters.

Table 2: Pearson correlation coefficients to determine the precision of various measurements made

	Pearson Correlation Coefficient
Intraobserver	
Reader 1	0.538
Reader 2	0.648
Interobserver	
First measurement of reader 1 vs 2nd measurement of reader 2	0.506
Second measurement of reader 1 vs 1st measurement of reader 2	0.522
Subjective (visual assessment) vs objective (OPA) technique	
Reader 1	0.499
Reader 2	0.566

technique. First, the Hounsfield unit of bone was measured. Then the Hounsfield unit of the desired pixels (HU Desired Pixel) on which to place the calipers was determined by the following equation: $[(\text{HU Bone} - \text{HU Desired Pixel}) / \text{HU Bone}] \times 100\% = \text{OPA}$. The 2 pixels on either side of the vestibular aqueduct having this Hounsfield unit were selected, and calipers were placed on them for measurement of the vestibular aqueduct width.

Statistical Analysis

Each vestibular aqueduct was measured 5 times (twice for each radiologist using the visual assessment technique, once using the OPA technique).

The measurements made by each radiologist by using the visual assessment technique were analyzed; we calculated the mean, SD, and range for each radiologist (Table 1).

Pearson correlation coefficients (*r*) were used to assess the precision of the measurements (Table 2). We calculated them for correlation among the following:

1) Each radiologist's measurement by using the visual assessment technique and his or her own measurement by using the same technique obtained 1 month later (intraobserver correlation)

2) One radiologist's measurement using the visual assessment technique and the other radiologist's measurement using the same technique (interobserver correlation)

3) Each radiologist's measurement using the visual assessment technique (averaged between the 2 measurements obtained 1 month apart) and the measurement obtained by using the OPA technique

4) The two radiologists' combined measurement (averaged among the 4 values obtained by the 2 radiologists) by using the visual assessment technique and the measurement obtained by using the OPA technique.

Interobserver correlation was obtained by using the first mea-

surement of radiologist A with the second measurement of radiologist B, and the second measurement of radiologist A with the first measurement of radiologist B, to reduce potential bias. Statistical analyses were performed by using SPSS Statistics for Windows (IBM, Armonk, New York).

RESULTS

The 96 patients (51 male and 45 female) had a mean age of 11.0 ± 4.5 years (range, 2–21 years). All vestibular aqueducts were readily identified on the 45° oblique reformations.

For measurements made by using the visual assessment (subjective) technique, the mean midpoint width of the postisthmic segment of the vestibular aqueduct was 0.527 ± 0.08 mm (left side only: 0.524 ± 0.083 mm; right side only: 0.529 ± 0.080 mm). The range was 0.353–0.887 mm. The value at the 95th percentile was 0.666 mm. The value at the 97.5th percentile was 0.702 mm (Table 1).

The optimal percentage attenuation was found to be 30% (Fig 4). In other words, the pixel with the CT attenuation value that is 30% of the difference between the CT attenuation of the center of the vestibular aqueduct and the CT attenuation of the bony margin is the best location for caliper placement on either edge of the vestibular aqueduct that would yield the measurement value closest to that obtained when measuring the actual anatomic structure.

For measurements made by using the OPA technique, the mean midpoint width of the postisthmic segment was 0.537 ± 0.077 mm. The range was 0.331–0.922 mm. The value at the 95th percentile was 0.658 mm. The value at the 97.5th percentile was 0.717 mm (Table 1).

The mean midpoint width of the cadaveric specimens was 0.441 ± 0.134 mm.

Intraobserver, Interobserver, and Intertechnique Reliability

A Pearson correlation coefficient of >0.70 indicates a very strong positive relationship, and a value between 0.40 and 0.69 indicates a strong positive relationship. The measurements made before and after a 1-month interval for the same radiologist (intraobserver reliability) did not demonstrate much variability (*r* = 0.538 and *r* = 0.648 for the 2 radiologists). There was also good interobserver correlation (*r* = 0.506 and *r* = 0.522). Correlation between measurements made with the 2 techniques showed a strong positive relationship as well (*r* = 0.566) (Fig 5 and Table 2).

DISCUSSION

CT and MR imaging are important components in the evaluation of congenital sensorineural hearing loss for excluding structural abnormalities.⁹ Abnormal imaging findings can be seen in 32%–39% of children with sensorineural hearing loss,¹⁰ the most common of which is a large vestibular aqueduct. LVA typically has a flared morphology and is often associated with other inner ear malformations,¹¹ including modiolar deficiency with or without incomplete partition type II.¹² In 1978, Valvassori and Clemis²

Comparison between subjective and objective techniques in measuring the midpoint VA width

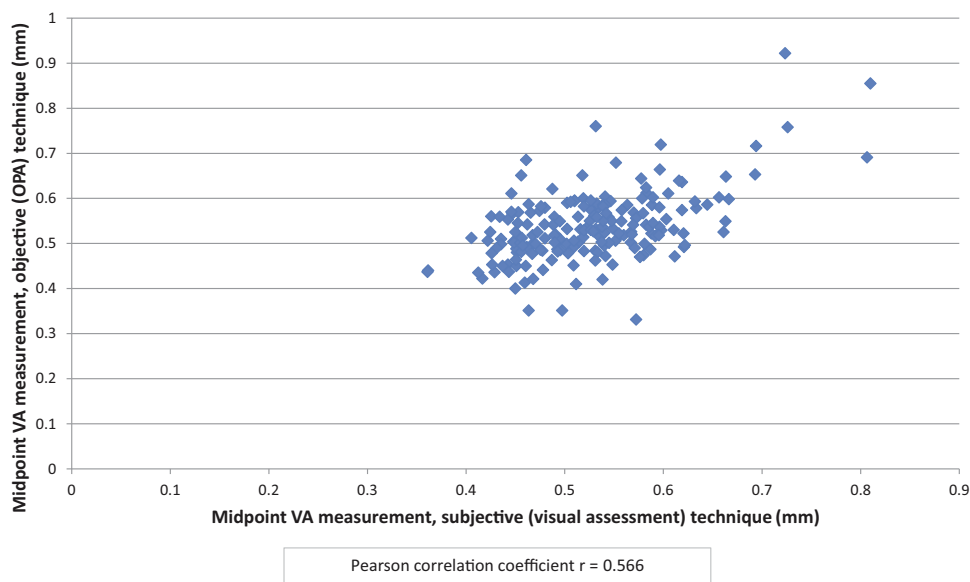


FIG 5. Scatterplot showing comparison between the subjective and objective techniques. Each point denotes the midpoint vestibular aqueduct measurement made by using the subjective (visual assessment) technique (x-axis) plotted against that made by using the objective (modified full width at half maximum/OPA) technique (y-axis). The Pearson correlation coefficient is $r = 0.566$.

coined the term “large vestibular aqueduct syndrome” to describe children with sensorineural hearing loss, often progressive, with LVA.

The goal of this study was to determine normal measurement values for the normal vestibular aqueduct midpoint width in the 45° oblique plane. This plane was chosen because it allows more reliable and accurate depiction of the vestibular aqueduct along its longitudinal axis compared with the axial plane.⁶ This follows the basic geometric principle that the optimal planes for displaying a symmetric structure are planes parallel and perpendicular to its main axes of symmetry. Because the vestibular aqueduct is a channel oriented essentially 45° from the sagittal and coronal planes, running from posteroinferior to anterosuperior, the 45° oblique (Pöschl) plane is ideal for displaying the entire length of this structure. In this plane, its midpoint width can be more easily and accurately identified and measured compared with any other plane (eg, axial and coronal). In fact, the 45° oblique plane is the CT counterpart to the transverse pyramidal plane emphasized by Valvassori,¹ Valvassori and Clemis,² Valvassori et al,¹³ and Becker et al¹⁴ as the ideal plane for assessing the vestibular aqueduct tomographically.

The anatomy and development of the vestibular aqueduct have been well-described in the literature.^{2,15-19} During fetal development, the vestibular aqueduct initially describes a straight course, paralleling the common crus. The aqueduct develops its adult form with the downward pull of the endolymphatic system by the sigmoid sinus and adjacent dura during growth of the posterior fossa. This process results in the originally straight vestibular aqueduct adopting an inverted *J* shape when viewed in profile. The narrow proximal (superior, anterior, medial) segment (termed “isthmus”) ascends over a short distance, representing the short limb of the *J*. In our experience, this portion is not

well-visualized by CT due to its small size relative to CT voxel size and partial volume effect. The longer distal or postisthmic segment descends toward its external aperture (inferior, posterior, lateral), representing the long limb of the *J*. This segment is shaped like a thick triangular slab, with the apex at its junction with the isthmus and the broad base at the external aperture.²⁰ The long axis of symmetry runs almost exactly parallel to the 45° oblique plane; in this plane, the vestibular aqueduct can be seen along its entire postisthmic length and demonstrates a fairly uniform width (thickness of the triangular slab) with only minor undulation. On the other hand, the axial, coronal, and sagittal planes pass at varying obliquities through the vestibular aqueduct; measurements made in these planes may therefore result in overestimation of its width. In addition, the ability to view the entire postisthmic segment in the 45° oblique plane allows us to accurately define its midpoint, while this point can only be estimated when in the axial, coronal, and sagittal planes.

While other authors have suggested measuring the vestibular aqueduct at both the midpoint and external aperture, we chose to limit our assessment to the midpoint. Being able to visualize the entire length of the postisthmic segment in the 45° oblique plane allows reliable identification of the midpoint. In this plane, the walls of the normal vestibular aqueduct run parallel to each other and the width is fairly constant; these features allow us to identify and measure the midpoint width with a high degree of certainty and reproducibility. In contrast, the flared configuration of the normal vestibular aqueduct at the external aperture creates difficulty with defining the exact point at which a measurement there should be made, and it is virtually impossible to determine a width perpendicular to the bony margins without a large degree of uncertainty and very limited reproducibility.

Our study shows that the vestibular aqueduct can be accu-

rately measured in the 45° oblique plane on CT images with excellent interobserver and intraobserver reliability. With this method, the normal vestibular aqueduct midpoint width falls within the range of 0.3–0.9 mm. The mean value of 0.5 mm is statistically independent of age or sex. The 97.5th percentile value is 0.7 mm.

One major source of interobserver variation was likely related to the difficulty in determining the edge of the vestibular aqueduct. At low magnification, the edge of the vestibular aqueduct appears fairly distinct; however, at increasing degrees of magnification, it becomes clear that the edge is actually a blur of gray-scale densities. The width of this gray zone is particularly significant relative to the submillimeter size of the vestibular aqueduct. We sought to minimize this edge error by comparing measurements performed by caliper placement using subjective visual assessment with those performed using a modified full width at half maximum technique, which we termed the “optimal percentage attenuation technique.” Given that there is no criterion standard for defining the “true” edge on a pixelated image, we attempted to provide a standard by comparing a midpoint measurement made on a 45° oblique plane CT image of a cadaveric temporal bone with a midpoint measurement made in that same plane on a histologic section of that specimen. Comparison of these 2 measurements helped establish an objective method of CT caliper placement that would yield a measurement that best correlated with the actual anatomic structure. We found that the best correlation occurred when the full width was measured at 30% of the maximum difference in CT attenuation across the vestibular aqueduct (OPA = 30%) (Fig 4).

We repeated the measurements made on the CT images of our patient population by using this modified full width at half maximum/OPA technique, by using the 30% CT attenuation to help us choose the pixels for caliper placement. We found that the results obtained by using this objective technique did not differ significantly from the results obtained by using the subjective technique of visually estimating the perceived edge of the vestibular aqueduct. This finding reassured us that the visual estimation technique is adequate for making measurements on CT images on a practical basis.

One limitation of this study was the small number of histologic specimens available for comparison. Many factors limit their availability, including logistics related to postmortem and histologic processing, incomplete clinical histories and data,⁸ and the limited number of specimens that had undergone CT scanning before histologic processing to allow radiologic-histologic comparisons (though currently every temporal bone specimen designated for histologic processing at our Otopathology Laboratory undergoes imaging beforehand). In addition, the specimens included were procured specifically to be sectioned in a plane as close as possible to the 45° oblique plane, and preparation time for each specimen was approximately 2 years. Vestibular aqueduct measurements in microdissection specimens have been performed by others and reported in the literature.^{16,18,21–24} Of these, only Sando and Ikeda²⁴ measured the midpoint width of the vestibular aqueduct. They reported the midvestibular aqueduct measurements in 27 normal temporal bones (28–102 years of age; mean, 66 years) with a mean of 0.48 ± 0.17 mm, similar to the

range we obtained from our specimens. Although specimens are subject to various primary and secondary artifacts during their preparation,⁸ we believe that by using the best available equipment and technique for preparation, we were able to derive important information from even a small number of histologic specimens in terms of the range of measurements to expect and for developing the modified full width at half maximum/OPA technique.

At Massachusetts Eye and Ear Infirmary, we consider vestibular aqueducts measuring 0.8 mm (above the 97.5th percentile value) at midpoint in the 45° oblique plane as borderline to slightly enlarged. Of note, however, there has never been direct correlation between minor enlargement and clinical findings.

CONCLUSIONS

The 45° oblique plane allows visualization of the vestibular aqueduct along its longitudinal axis, which, in turn, allows the midpoint and width of the vestibular aqueduct to be readily and accurately identified and measured. We present 2 different measurement techniques in the 45° oblique plane, their corresponding normal range of values, and the results of radiologic-histologic comparison measurements. The mean midpoint width of the vestibular aqueduct was 0.527 ± 0.08 mm when measured by using the subjective visual assessment technique and 0.537 ± 0.077 mm when measured by using the objective 30% optimal percentage attenuation technique. The 95th percentile values were 0.666 and 0.658 mm, respectively, and the 97.5th percentile values were 0.702 and 0.717 mm, respectively. These may be considered normal measurement values of the normal vestibular aqueduct midpoint width when measured in the 45° oblique plane.

Disclosures: Hugh D. Curtin—UNRELATED: Payment for Lectures (including service on Speakers Bureaus); Continuing Medical Education activities (nothing with industry; both paid and unpaid); Royalties: Elsevier (textbook royalties).

REFERENCES

1. Valvassori GE. L'aqueduc du vestibule et les affections du type vertige de Ménière. In: Vignaud J, ed. *Traité de Radiodiagnostic*. Paris: Masson; 1974:355–60
2. Valvassori GE, Clemis JD. The large vestibular aqueduct syndrome. *Laryngoscope* 1978;88:723–28 Medline
3. Boston M, Halsted M, Meinzen-Derr J, et al. The large vestibular aqueduct: a new definition based on audiologic and computed tomography correlation. *Otolaryngol Head Neck Surg* 2007;136:972–77 CrossRef Medline
4. Swartz JD, Russell KB, Wolfson RJ, et al. High resolution computed tomography in evaluation of the temporal bone. *Head Neck Surg* 1984;6:921–31 CrossRef Medline
5. Venema HW, Phoa SS, Mirck PG, et al. Petrosal bone: coronal reconstructions from axial spiral CT data obtained with 0.5-mm collimation can replace direct coronal sequential CT scans. *Radiology* 1999;213:375–82 CrossRef Medline
6. Ozgen B, Cunnane ME, Caruso PA, et al. Comparison of 45 degrees oblique reformats with axial reformats in CT evaluation of the vestibular aqueduct. *AJNR Am J Neuroradiol* 2008;29:30–34 CrossRef Medline
7. Hwang M, Marovich R, Shin SS, et al. Optimizing CT for the evaluation of vestibular aqueduct enlargement: inter-rater reproducibility and predictive value of reformatted CT measurements. *J Otol* 2015;10:13–17 CrossRef
8. Merchant SN, Nadol JB Jr. *Schuknecht's Pathology of the Ear*. 3rd ed. Shelton, Conn.: People's Medical Publishing House USA; 2010

9. Juliano AF, Ginat DT, Moonis G. **Imaging review of the temporal bone: part II. Traumatic, postoperative, and noninflammatory nonneoplastic conditions.** *Radiology* 2015;276:655–72 CrossRef Medline
10. Vijayasekaran S, Halsted MJ, Boston M, et al. **When is the vestibular aqueduct enlarged? A statistical analysis of the normative distribution of vestibular aqueduct size.** *AJNR Am J Neuroradiol* 2007;28:1133–38 CrossRef Medline
11. Davidson HC, Harnsberger HR, Lemmerling MM, et al. **MR evaluation of vestibulocochlear anomalies associated with large endolymphatic duct and sac.** *AJNR Am J Neuroradiol* 1999;20:1435–41 Medline
12. Glastonbury CM, Davidson HC, Harnsberger HR, et al. **Imaging findings of cochlear nerve deficiency.** *AJNR Am J Neuroradiol* 2002;23:635–43 Medline
13. Valvassori G, Hanafee WN, Carter BL, et al. *Radiology of the Ear, Nose and Throat.* Philadelphia: W.B. Saunders; 1982
14. Becker TS, Vignaud J, Sultan A, et al. **The vestibular aqueduct in congenital deafness: evaluation by the axial projection.** *Radiology* 1983;149:741–74 CrossRef Medline
15. Dimopoulos PA, Smedby O, Wilbrand HF. **Anatomical variations of the human vestibular aqueduct, part I: a radioanatomical study.** *Acta Radiol Suppl* 1996;403:21–32 Medline
16. Kodama A, Sando I. **Dimensional anatomy of the vestibular aqueduct and the endolymphatic sac (rugose portion) in human temporal bones: statistical analysis of 79 bones.** *Ann Otol Rhinol Laryngol Suppl* 1982;96:13–20 Medline
17. Kraus EM, Dubois PJ. **Tomography of the vestibular aqueduct in ear disease.** *Arch Otolaryngol* 1979;105:91–98 CrossRef Medline
18. Wilbrand HF, Rask-Andersen H, Gilstring D. **The vestibular aqueduct and the para-vestibular canal: an anatomic and roentgenologic investigation.** *Acta Radiol Diagn (Stockh)* 1974;15:337–55 Medline
19. Gulya AJ. *Gulya and Schuknecht's Anatomy of the Temporal Bone with Surgical Implications.* 3rd ed. New York: Informa Healthcare; 2007
20. Lo WW, Daniels DL, Chakeres DW, et al. **The endolymphatic duct and sac.** *AJNR Am J Neuroradiol* 1997;18:881–87 Medline
21. Anson BJ. **The endolymphatic and perilymphatic aqueducts of the human ear: developmental and adult anatomy of their parietes and contents in relation to otological surgery.** *Acta Oto-Laryngologica* 1965;59:140–53 CrossRef
22. Ogura Y, Clemis JD. **A study of the gross anatomy of the human vestibular aqueduct.** *Ann Otol Rhinol Laryngol* 1971;80:813–25 CrossRef Medline
23. Yuen SS, Schuknecht HF. **Vestibular aqueduct and endolymphatic duct in Menière's disease.** *Arch Otolaryngol* 1972;96:553–55 CrossRef Medline
24. Sando I, Ikeda M. **The vestibular aqueduct in patients with Meniere's disease: a temporal bone histopathological investigation.** *Acta Otolaryngol* 1984;97:558–70 CrossRef Medline

Brain Injury in Neonates with Complex Congenital Heart Disease: What Is the Predictive Value of MRI in the Fetal Period?

M. Brossard-Racine, A. du Plessis, G. Vezina, R. Robertson, M. Donofrio, W. Tworetzky, and C. Limperopoulos



ABSTRACT

BACKGROUND AND PURPOSE: Brain injury in neonates with congenital heart disease is an important predictor of adverse neurodevelopmental outcome. Impaired brain development in congenital heart disease may have a prenatal origin, but the sensitivity and specificity of fetal brain MR imaging for predicting neonatal brain lesions are currently unknown. We sought to determine the value of conventional fetal MR imaging for predicting abnormal findings on neonatal preoperative MR imaging in neonates with complex congenital heart disease.

MATERIALS AND METHODS: MR imaging studies were performed in 103 fetuses with confirmed congenital heart disease (mean gestational age, 31.57 ± 3.86 weeks) and were repeated postnatally before cardiac surgery (mean age, 6.8 ± 12.2 days). Each MR imaging study was read by a pediatric neuroradiologist.

RESULTS: Brain abnormalities were detected in 17/103 (16%) fetuses by fetal MR imaging and in 33/103 (32%) neonates by neonatal MR imaging. Only 9/33 studies with abnormal neonatal findings were preceded by abnormal findings on fetal MR imaging. The sensitivity and specificity of conventional fetal brain MR imaging for predicting neonatal brain abnormalities were 27% and 89%, respectively.

CONCLUSIONS: Brain abnormalities detected by in utero MR imaging in fetuses with congenital heart disease are associated with higher risk of postnatal preoperative brain injury. However, a substantial proportion of anomalies on postnatal MR imaging were not present on fetal MR imaging; this result is likely due to the limitations of conventional fetal MR imaging and the emergence of new lesions that occurred after the fetal studies. Postnatal brain MR imaging studies are needed to confirm the presence of injury before open heart surgery.

ABBREVIATIONS: BCH = Boston Children's Hospital; CHD = congenital heart disease; CNMC = Children's National Medical Center; GA = gestational age; GMH-IVH = germinal matrix hemorrhage and intraventricular hemorrhage; NHPI = nonhemorrhagic parenchymal injury; pWMI = punctate white matter injury; SNAP = Scores for Neonatal Acute Physiology

Preoperative brain injury in neonates with complex congenital heart disease (CHD) is prevalent, ranging from 26% to 41%¹⁻⁷ and is associated with neurodevelopmental disabilities.⁸ Delayed brain maturation in infants with CHD before

neonatal surgical repair has also been reported, suggesting an antenatal onset.^{2,5,9}

More recently, our findings¹⁰ are in line with others¹¹ who reported that conventional fetal MR imaging identifies acquired and developmental brain anomalies in up to 39% of fetuses with CHD. Using quantitative MR imaging, our group has shown that fetuses with CHD demonstrate progressive disturbances in brain growth and delayed cortical gyrification in the third trimester.^{12,13} The extent to which these fetal brain findings are transient or persist in the postnatal preoperative period remains to be determined. Using a prospective longitudinal design, we sought to examine the value of conventional fetal MR imaging for predicting preoperative abnormalities on neonatal MR imaging in neonates with complex CHD. Specifically, we aimed to evaluate the sensitivity and specificity of conventional fetal brain MR imaging as a clinical tool to accurately detect postnatal preoperative brain abnormalities. As a secondary objective, we also examined the relationship between clinical risk factors and newly identified postnatal brain findings.

Received September 14, 2015; accepted after revision January 5, 2016.

From the Advanced Pediatric Brain Imaging Research Laboratory (M.B.-R., C.L.), Division of Diagnostic Imaging and Radiology (M.B.-R., G.V., C.L.), Fetal and Transitional Medicine (M.B.-R., A.d.P., C.L.), and Division of Cardiology (M.D.), Children's National Health System, Washington DC; and Divisions of Radiology (R.R.) and Cardiology (W.T.), Children's Hospital Boston and Harvard Medical School, Boston, Massachusetts.

This work was supported by the Canadian Institutes of Health Research (MOP-81116) and the National Institutes of Health (ROIHL116585, IDDC, grant P30HD40677). Dr Marie Brossard-Racine was financially supported by the Canadian Institutes of Health Research at the time of manuscript preparation.

Please address correspondence to Catherine Limperopoulos, PhD, Advanced Pediatric Brain Imaging Research Laboratory, Division of Diagnostic Imaging and Radiology/Fetal and Transitional Medicine, Children's National Medical Center, 111 Michigan Ave NW, Washington DC 20010; e-mail: climpero@childrensnational.org

Indicates open access to non-subscribers at www.ajnr.org

<http://dx.doi.org/10.3174/ajnr.A4716>

MATERIALS AND METHODS

Subjects

In this longitudinal observational study, pregnant women with a fetal diagnosis of complex CHD confirmed by echocardiography were consecutively recruited and prospectively followed. Complex CHD included diagnoses that would require corrective or palliative neonatal open heart surgery. Recruitment took place between February 2007 and December 2010 at Boston Children's Hospital (BCH) and from June 2011 to October 2014 at Children's National Medical Center (CNMC). Subjects with multiple pregnancies, extracardiac anomalies on fetal sonography, congenital infection, documented fetal or neonatal chromosomal anomalies, and/or multiorgan dysmorphic conditions were excluded. Written informed consent was obtained by all study participants. The study was approved by BCH Committee on Clinical Investigation and the institutional review board of CNMC, in compliance with the Health Insurance Portability and Accountability Act.

A fetal echocardiogram was performed by one of the experienced fetal cardiologists at each center. Fetal CHD diagnoses were subsequently categorized as cyanotic versus acyanotic, single- versus 2-ventricle physiology, and with or without aortic obstruction as determined by anatomic classification and prediction of in utero physiology based on the structural defect. Enrolled pregnant women completed fetal MR imaging during the second or the third trimester of pregnancy. Gestational age of the fetuses was estimated from the first-trimester-dating sonography. At the end of 2013, a second fetal MR imaging (ie, 2 fetal MR imaging studies) was added to our study protocol to serially examine fetal brain structure and development during the second and the third trimesters. For this subset ($n = 19$), only the second MR imaging was included in our analyses because the MR imaging results did not differ between the 2 scans. Once medically stable after delivery, neonates underwent preoperative brain MR imaging. Antenatal, perinatal, and postnatal clinical data and demographic information for each neonate was collected through maternal questionnaires and medical record review and were entered into a Research Electronic Data Capture tool (REDCap; <http://www.project-redcap.org/>) hosted at CNMC.¹⁴ Only subjects who completed both fetal and neonatal MR imaging were kept in the analyses.

Fetal MR Imaging Acquisition Protocol

Each fetal MR imaging was performed on a 1.5T scanner either on an Achieva (Philips Medical Systems, Best, the Netherlands) device by using a 5-channel phased array coil (BCH cohort) or on a Discovery scanner (GE Healthcare, Milwaukee, Wisconsin) with an 8-channel phased array coil (CNMC cohort). Two-millimeter multiplanar single-shot fast spin-echo T2-weighted sequences and 4-mm diffusion-weighted images were obtained by using standard clinical parameters.¹⁰ Diffusion images were assessed at $b=0$ for susceptibility changes and at $b=800$ for diffusion abnormalities; apparent diffusion coefficient maps were also reviewed. Total scan time was approximately 45–60 minutes, and no contrast or sedation was used for any of the fetal MRIs. All studies were reviewed for the presence of developmental malformations, maturation status, and acquired abnormalities by the experienced

fetal neuroradiologist at each center following the clinical guidelines in place at the time of the study. Mild ventriculomegaly was diagnosed when the maximum width of the lateral ventricles at the level of the atrium measured between 10 and 15 mm.¹⁵ Increased extra-axial space was diagnosed when the distance between the inner margin of the cranium and the outer margin of the frontal, temporal, parietal, and/or occipital region was considered enlarged for gestational age.^{16,17} Given that the T2 signal of normal periventricular white matter in third-trimester fetuses is often slightly hyperintense compared with the subcortical white matter, T2 signal greater than the background signal of normal-appearing white matter was considered abnormal.¹⁸ Vermian hypoplasia was diagnosed when there was partial absence of the posterior portion of the vermis in the presence of normally shaped cerebellar hemispheres.¹⁹ Finally, sulcation was considered delayed if ≥ 2 weeks from the expected published normative data.²⁰

Neonatal MR Imaging Acquisition Protocol

Unless clinically indicated, no sedation or contrast was used during the neonatal MR imaging. The nonsedated neonatal MRIs were performed with the patient under natural sleep after feeding and swaddling. All neonates were immobilized by using an Infant Vacuum Immobilizer (Newmatic Medical, Caledonia, Michigan) and were provided with a double ear protection: ear plugs (Mighty Plugs; Beneficial Products, Ashland, Oregon) and Neonatal Noise Guards (Natus Medical, Seattle, Washington). The neonatal brain MRIs were performed on either a 1.5T scanner (Achieva, Philips Healthcare) using a 32-channel receive-only head coil (BCH cohort) or on a 3T Discovery scanner (GE Healthcare) with an 8- or 32-channel receive-only head coil (CNMC cohort). The MR imaging sequences used for clinical diagnosis included 3D-T1WI gradient-echo (fast-field echo) and T2WI dual-echo turbo spin-echo at BCH, 3D-T1WI gradient-echo (echo-spoiled gradient echo) and 3D-T2WI fast spin-echo (Cube; GE Healthcare) at CNMC, and diffusion-weighted images at both centers. Susceptibility-weighted images were also acquired for the CNMC cohort only because it was not the standard of practice at the time of the MR imaging study at BCH. Total scan time was approximately 45–60 minutes.

All neonatal brain MR imaging studies were reviewed by one of the pediatric neuroradiologists at each center, blinded to the subject's clinical information with the exception of age at the time of the MR imaging. MR imaging findings were classified as developmental or acquired injury. Developmental malformations included ex vacuo ventriculomegaly, increased extra-axial space, and delayed maturation based on gyral and sulcal development. Neonatal vermian hypoplasia was diagnosed when the length of the vermis (ie, superior-inferior extent) was smaller for the expected age in the presence of a normally shaped cerebellar hemisphere.¹⁹ The corpus callosum was considered hypoplastic when the length was shorter than expected (ie, incomplete development) by using the tectal plate of the midbrain as a reference point for the posterior aspect of the corpus callosum.²¹

Acquired injury was categorized as 1 of the following: 1) punctate white matter injury (pWMI) seen as foci of T1 hyperintensity and/or T2 hypointensity; 2) hemorrhage, parenchymal and non-

Table 1: CHD diagnoses distribution (n = 103)

Diagnosis	Distribution (%)	Abnormal Findings on Fetal MRI (%)	Abnormal Findings on Preop MRI (%)
Dextro-transposition of the great arteries	31 (30.1)	5 (29.4)	9 (27.3)
Hypoplastic left-heart syndrome	20 (19.4)	3 (17.6)	9 (27.3)
Double-outlet right ventricle	13 (12.6)	2 (11.8)	2 (6.1)
Tetralogy of Fallot	11 (10.7)	2 (11.8)	2 (6.1)
Atrioventricular septal defect	8 (7.8)	3 (17.6)	1 (3.0)
Tricuspid atresia	4 (3.9)	1 (5.9)	3 (12.1)
Ventricular septal defect	4 (3.9)	0 (0.0)	2 (6.1)
Pulmonary atresia	3 (2.9)	0 (0.0)	2 (6.1)
Ebstein anomaly	2 (1.9)	0 (0.0)	1 (3.0)
Pulmonary stenosis	2 (1.9)	0 (0.0)	1 (3.0)
Aortic stenosis	1 (1.0)	0 (0.0)	0 (0.0)
Severe coarctation of the aorta	2 (1.9)	0 (0.0)	0 (0.0)
Hypoplastic right-heart syndrome	1 (1.0)	0 (0.0)	0 (0.0)
Truncus arteriosus	1 (1.0)	1 (5.9)	1 (3.0)
Total	103 (100)	17 (100)	33 (100)

Note:—Preop indicates preoperative.

parenchymal (excluding birth-related subarachnoid and subdural hemorrhages); and 3) nonhemorrhagic parenchymal injury (NHPI). To differentiate mild pWMI from moderate/severe pWMI, we used a cutoff of ≥ 3 lesions and < 2 mm as commonly used in imaging studies of at-risk neonates.^{6,22} We could confirm the hemorrhagic nature of the punctate lesions when susceptibility-weighted images were acquired (ie, CNMC cohort) and corresponding hypointense foci on the T2*-weighted images were detected. A larger parenchymal hemorrhage was considered mild when the intracerebral hemorrhage volume corresponded to $< 2\%$ of the total brain volume.²³

Nonparenchymal hemorrhages included choroid plexus hemorrhage, germinal matrix hemorrhage, and intraventricular hemorrhage (GMH-IVH) graded according to the Papile classification.²⁴ NHPIs were further classified as the following: 1) focal infarction of various etiologies (eg, vaso-occlusive, embolic, hypoperfusion) that appeared as hyperintense on T2-weighted images and/or a hyperintense focal area on diffusion images; 2) diffuse injury (ie, diffuse excessive high signal intensity when the T2 signal exceeded the signal of the corresponding normal-appearing white matter); and 3) cysts.

Statistical Analysis

Descriptive statistics using means, SDs, and frequencies were used to characterize the sample and the nature of the brain abnormalities described by conventional MR imaging. The relative risks with 95% confidence intervals were calculated to assess the association between abnormal findings on ante- and postnatal brain MR imaging studies. The sensitivity and specificity of fetal brain MR imaging were then calculated. Positive and negative predictive values were also calculated to characterize the accuracy of fetal brain MR imaging. Maternal and subject characteristics and clinical factors in newly injured-versus-noninjured neonates were compared by using an independent samples *t* test for continuous parametric variables, the Mann-Whitney *U* test for continuous nonparametric and ordinal variables, and the Fisher exact test for categorical variables. All analyses were executed by using SPSS, Version 17 (IBM, Armonk, New York).

RESULTS

Sample Characteristics

A total of 150 pregnant women completed fetal MR imaging as part of our prospective study. As described in our “Materials and Methods” section, a subset ($n = 19$) of women completed 2 fetal MR imaging studies, resulting in 169 MR images obtained at a mean gestational age (GA) of 31.57 ± 3.86 weeks (range, 17.71–38.57 weeks). Of the 150 subjects with CHD, 2 died in utero and 9 died in the early postnatal period before MR imaging could be performed. Twelve families declined the neonatal MR imaging. Eight families had moved out of state or had changed contact information and could not be located.

Lastly, 16 neonates did not undergo a neonatal MR imaging because they were deemed too unstable medically by the treating team. Subject characteristics of the subset of neonates did not significantly differ from the rest of the sample with respect to sex, CHD diagnosis, frequency of fetal MR imaging abnormality, birth weight, gestational age at birth, Apgar score, and Scores for Neonatal Acute Physiology (SNAP) score. However, neonates that completed the preoperative MR imaging were more likely to be born via vaginal delivery ($P = .01$).

The final sample consisted of 103 fetuses (61 males) with CHD who completed a fetal MR imaging at a mean GA of 32.71 ± 3.61 weeks (median, 33.71 weeks; range, 23.86–38.57 weeks) and then a neonatal MR imaging study at mean age of 6.8 ± 12.2 days (median, 3 days; range, 0–76 days). Of note, all except 5 infants were scanned before 26 days of life. The neonatal MR imaging was performed, on average, 6.8 weeks (range, 1–21 weeks) after the last fetal MR imaging. The sample included 48 neonates from the Boston cohort and 55 from CNMC. The 4 most common cardiac diagnoses in our sample were transposition of the great arteries (30%), hypoplastic left-heart syndrome (19%), double-outlet right ventricle (13%), and tetralogy of Fallot (11%). The complete distribution of the CHD diagnoses is presented in Table 1. The frequency of abnormal MR imaging studies for both fetal and postnatal MR imaging for each CHD diagnosis is also reported in Table 1. Subsequent classification by cardiac diagnosis of our sample resulted in 74 cyanotic versus 29 acyanotic physiology; 46 with single-ventricle versus 57 with 2-ventricle physiology, and 33 with aortic obstruction versus 70 without.

The BCH and CNMC cohorts did not differ with respect to the maternal and neonatal subjects’ characteristics, except for gestational diabetes, which was present in 7 cases (4 on medication and 3 diet-controlled), all from the CNMC cohort ($P = .014$). A higher proportion of neonates with CHD were intubated at birth in the CNMC cohort (16 versus 3; $P < .001$), while a significantly higher percent of neonates from the Boston cohort underwent a cardiac catheterization before neonatal MR imaging (9 versus 2; $P = .012$). No other differences in clinical practice were found between the 2 centers. The antenatal, in-

trapartum, and perinatal characteristics of the sample are presented in Table 2.

Brain Abnormalities Detected by Conventional Brain MR Imaging

On conventional fetal MR imaging, brain abnormalities were detected in 17 cases (16.3%) and included the following: isolated mild ventriculomegaly (6/17) (Fig 1A), increased extra-axial spaces (4/17) (Fig 1B), white matter cysts (2/17), isolated inferior vermian hypoplasia (2/17), and white matter signal hyperintensity on T2-weighted images (1/17). Of note, one of the fetuses with ventriculomegaly also had a single frontal subependymal cyst. Two fetuses presented with an immature brain appearance based on sulcal-gyral development.

Thirty-two neonates (32.0%) had abnormal findings on conventional preoperative brain MR imaging. Acquired injury was

present in 27 (26.2%) neonates. An isolated developmental anomaly (ie, without acquired injury) was detected in 5 neonates, while 5 others presented with both developmental and acquired findings. Hemorrhagic and nonhemorrhagic pWMI were present in 15 neonates (5 mild, 10 moderate/severe), most commonly observed in the periventricular white matter, the centrum semiovale (Fig 2), and the frontal white matter. NHPI was the second most frequently acquired injury and was detected in 13 neonates. Of these, 7 presented with diffuse abnormal T2 signal prolongation (isolated in 2) in the periventricular white matter and 3 with focal infarctions in the deep gray matter (isolated in 1) (Fig 3). Three neonates presented with cysts: One had an isolated right germinal matrix cyst, 1 had a single cyst in the periventricular white matter, and 1 had multiple cysts in the bilateral frontal white matter.

Nonparenchymal hemorrhages were reported in 11 neonates (isolated in 3 cases) and included the following: intraventricular hemorrhage in 1, GMH-IVH grade-I in 1, GMH-IVH grade-II in 5, GMH-IVH grade-III in 1, and choroid plexus hemorrhage in 3. Mild parenchymal hemorrhages were observed in 2 neonates, 1 in the cerebellum (Fig 4) and the other in the left globus pallidus.

Developmental brain malformations were described in 10 (9.7%) neonates. Three neonates presented with isolated congenital malformation such as mild vermian hypoplasia (1/3) and hypoplasia of the corpus callosum (2/3). Delayed maturation was reported in 1 neonate, which manifested as delayed opercular closure. The other 6 neonates presented with a mild global atrophy of the cerebral white matter (isolated in 2 cases), qualitatively described by a mild degree of ventricular enlargement and/or extra-axial space in the intracranial cavity.

Sensitivity and Specificity of Conventional Fetal Brain MR Imaging

The relative risk of presenting with abnormal findings on postnatal brain MR imaging after abnormal findings on fetal brain MR imaging was 1.90 (95% CI, 1.08–3.33; $P = .03$). This translated into a sensitivity of 27.3% and a specificity of 88.6% (Table 3). The positive and the negative predictive values of conventional fetal MR imaging for identifying persisting neonatal brain abnormality were 52.9% and 72.1%, respectively.

The distribution of prenatal brain abnormalities and how they manifested postnatally is presented in Table 4. Of the 17 fetuses with abnormal findings on prenatal brain MR imaging, 9 also presented with abnormal findings on neonatal MR imaging, while 8 had normal findings on a neonatal study. The fetal brain abnormalities that resolved or normalized by the time of the neonatal MR imaging included mild extracerebral space (2/8), mild unilateral ventriculomegaly (3/8), immature brain appearance (2/8), vermian hypoplasia (1/8), and single frontal subependymal cyst (1/8). Gestational age at fetal MR imaging of the fetuses who had transient fetal

Table 2: Clinical characteristics of the cohort (n = 103)

Antenatal	Mean \pm SD/Median (Range)/No. (%)
Pregnancy-induced diabetes	7 (6.8%)
Group B streptococcus	13 (13.3%)
Hyperthyroidism	3 (2.9%)
Hypothyroidism	8 (7.8%)
Pregnancy-induced hypertension	3 (2.9%)
Placenta previa	3 (2.9%)
Placenta abruption	2 (1.9%)
Preterm labor	3 (2.9%)
Chorioamnionitis	1 (1.0%)
Intrapartum	
Induced labor	48 (52.7%)
Emergency cesarean delivery	22 (21.8%)
Gestational age at birth (wk)	38.5 \pm 1.3
Birth weight (g)	3173 \pm 552
Apgar score 1 min/5 min	8 (1–9)/8(5–9)
Intubation at birth	18 (19%)
SNAP-II score	5 (0–68)
Perinatal (prior to MRI)	
Lowest pH	7.318 \pm 0.062
Lowest pO ₂	38.63 \pm 23.72
Highest pCO ₂	47.65 \pm 12.00
Cardiac catheterization	11 (10.9%)
Balloon atrial septostomy	15 (14.6%)

Note:—pCO₂ indicates carbon dioxide partial pressure; pO₂, oxygen partial pressure.

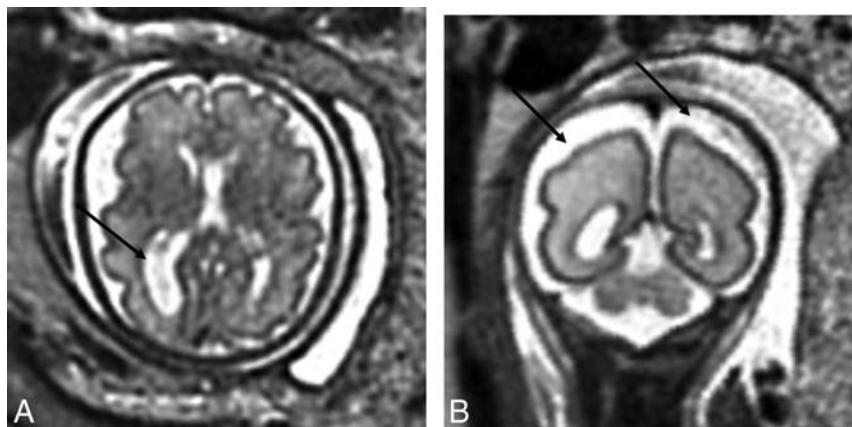


FIG 1. A, T2-weighted axial view of the brain of a 32-week-old fetus with CHD with unilateral ventriculomegaly. B, T2-weighted axial view of the brain of a 27.29-week-old fetus with CHD with extra-axial spaces. Reprinted from Brossard-Racine et al.¹⁰



FIG 2. T2-weighted axial view of a neonate with CHD with punctate white matter injury.



FIG 3. T2-weighted axial view of a neonate with CHD with bilateral deep gray matter infarcts.

brain findings was not significantly different from those fetuses without abnormalities or those with findings on both fetal and neonatal MR imaging. However, fetuses with abnormal fetal MR imaging findings and cyanotic CHD were significantly more likely to present with brain abnormalities on neonatal MR imaging (8 versus 1, $P = .05$). This association was not found when comparing single-ventricle and 2-ventricle physiology or aortic obstruction.

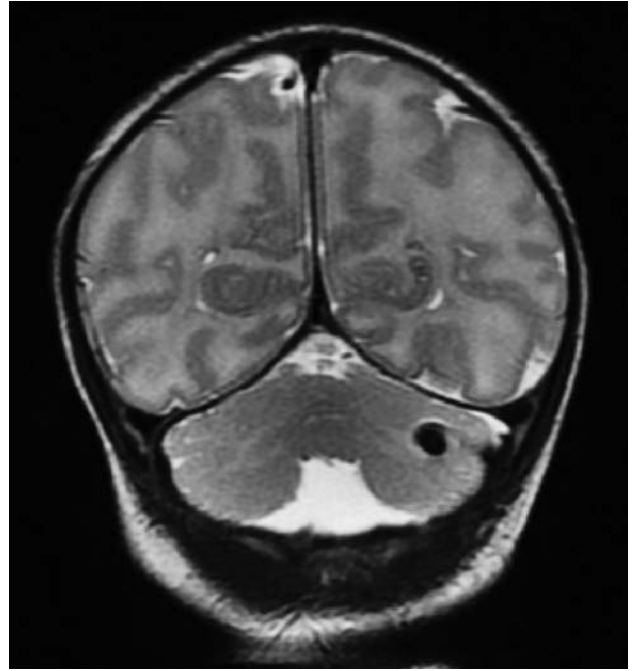


FIG 4. T2-weighted coronal view of a neonate with CHD with unilateral cerebellar hemorrhage.

Of the 9 cases with CHD that presented with brain abnormalities on both the fetal and neonatal scans, 5 neonatal findings were already seen on the fetal MR imaging. These included 2 neonates with white matter cysts, 1 of the 2 neonates with vermis hypoplasia and 1 with sustained mild ventricular enlargement. Of note, the 2 fetal cases that had persisting white matter cysts also presented with other parenchymal injury on the neonatal MR imaging. In 4 other cases, abnormalities were reported on both the fetal and neonatal brain MR imaging, but the nature of the findings had evolved between fetal and neonatal scans. These included 2 cases of mild extra-axial space on the fetal MR imaging that then presented with moderate/severe pWMI on neonatal MR imaging; 1 fetus with an additional choroid plexus hemorrhage and 1 fetus with mild ventriculomegaly presenting with solely diffuse NHPI on the neonatal MR imaging. Last, the fetus with isolated increased T2 signal presented with a grade II intraventricular hemorrhage on neonatal MR imaging.

New Postnatal Brain MR Imaging Findings

New brain abnormalities on neonatal MR imaging were detected in 24 (27.9%) neonates who had previous normal findings on fetal MR imaging. These included 20 neonates with newly acquired injuries, 4 of whom also presented with cerebral atrophy. New isolated developmental anomalies were detected in 4 neonates and included 2 cases with hypoplasia of the corpus callosum, delayed opercular closure in one and isolated global cerebral atrophy in another.

Newly acquired brain injury identified by neonatal MR imaging (ie, detected after a normal findings on fetal MR imaging) included 13 of the 15 postnatal cases with pWMI, 10 of the 11 postnatal cases with nonparenchymal hemorrhages, 8 of the 14 postnatal cases with neonatal NHPI, and 1 case with mild cerebellar parenchymal hemorrhage. These new NHPIs presented as fo-

cal infarctions in 2 neonates, diffuse injuries in 5 neonates, and isolated germinal matrix cyst in 1.

Determinants of Newly Acquired Postnatal Brain MR Imaging Abnormalities

Neonates with newly detected brain findings were not significantly different from neonates with normal findings on postnatal brain MR imaging with respect to their ante- and perinatal characteristics. However, although there was no significant difference in GA at birth or in days of life at neonatal MR imaging, the 20 neonates with newly acquired brain MR imaging findings were imaged postnatally at a significantly younger GA than the noninjured neonates (GA = 38.74 versus 39.73 weeks; $t = 2.49$, $P = .015$) and had their neonatal MR imaging performed earlier following the fetal MR imaging (5.11 versus 7.08 weeks; $P = .011$). Newly acquired brain lesions were significantly more frequent in neonates with single-ventricle CHD (15 versus 5; $P = .002$) and in those who underwent cardiac catheterization before the MR im-

aging ($P = .006$). Most interesting, neonates with newly detected lesions were more frequently born by vaginal delivery than those without new lesions, but the association was not significant ($P = .082$). No other patient-specific or clinical characteristics were associated with newly diagnosed brain injuries. Group differences are presented in Table 5.

DISCUSSION

This study reports, for the first time, the relationship between serial prenatal and postnatal preoperative conventional brain MR imaging studies in a large cohort of fetuses diagnosed with complex CHD. Brain abnormalities were detected in 17% prenatally and in almost twice as many (32%) postnatally before open heart surgery. Noteworthy, CHD cases with abnormal conventional fetal MR imaging findings had a 90% increased risk of presenting with abnormal neonatal brain MR imaging findings. Although conventional fetal MR imaging was shown to have good specificity, it lacked sensitivity for predicting postnatal brain abnormalities.

As previously reported, the most common fetal abnormalities detected on conventional fetal MR imaging in our cohort consisted of enlargement of the ventricular and extra-axial CSF spaces, which are thought to be markers of delayed brain development in fetuses with CHD.¹⁰ These qualitative fetal brain findings are consistent with quantitative MR imaging studies, which have reported cerebral parenchymal growth disturbances, increased CSF volume,¹³ and delayed cortical maturation¹² in fetuses with CHD. However, one of the new findings in the current study is that almost half (8/17) of the fetal brain abnormalities were transient and no longer seen on conventional neonatal MR imaging performed an average of 7 weeks after the fetal study. To our knowledge, there are very few studies that have examined the accuracy of fetal brain MR

Table 3: Fetal MRI sensitivity, specificity, and positive and negative predictive value

Abnormal Fetal MRI Findings	Abnormal Neonatal MRI Findings			Predictive Value
	Yes	No	Total	
Yes	9	8	17	Positive, 9/17 = 52.9% Negative, 62/86 = 72.1%
No	24	62	86	
Total	33	70	$n = 103$	
	Sensitivity, 9/33 = 27.3%	Specificity, 62/70 = 88.6%		

Table 4: Fetal and neonatal preoperative brain MRI findings^a

	Normal	pWMI	Hemorrhage	NHPI	Dev. Abn. ^b	Total
Normal	62	11	6	3	4	86
Extracerebral space	2	2	0	0	0	4
Ventriculomegaly	3	0	0	2	1	6
WM abn.	1	0	1	1	0	3
Immature brain	2	0	0	0	0	2
Vermis hypoplasia	0	1	0	0	1	2
Total	70	14	7	6	6	103

Note:—Dev. Abn. indicates developmental abnormalities.

^a Cases with multiple abnormalities were included only once in the table on the basis of the most severe finding.

^b Developmental anomaly includes congenital malformation, delayed maturation, and cerebral atrophy (extra-axial space and/or ventricular enlargement).

Table 5: Clinical characteristics of neonates with CHD with and without newly acquired brain injury^a

	Neonates without Injury (n = 62)	Neonates with New Injury (n = 20)	P Value
Induced labor	28 (45.2%)	10 (50.0%)	.570
Vaginal delivery	29 (46.8%)	15 (65.0%)	.082
Gestational age at birth (wk)	38.93 (33.86–40.71)	38.71 (36.00–40.00)	.134
Birth weight (g)	3300 (1077–4276)	3085 (2240–4220)	.525
Apgar score 1 min/5 min	8 (1–9)/8 (5–9)	8 (5–9)/8 (7–9)	.816/.266
Intubation at birth	14 (22.5%)	3 (12.5%)	.373
SNAP-II score	5 (0–43)	5 (0–28)	.471
Lowest pH prior to MRI, (mean)	7.320 (7.174 ± 7.490)	7.326 (7.220 ± 7.454)	.567
Lowest pO ₂ prior to MRI	34.85 (20–214)	33.75 (22–78)	.673
Highest pCO ₂ prior to MRI	46.50 (22–83)	46.25 (24–61)	.794
Cardiac catheterization prior to MRI	3 (4.8%)	6 (30.0%)	.006
Balloon atrial septostomy prior to MRI	10 (16.1%)	4 (20.0%)	.612
Age at MRI (days)	3.0 (1.0–76.0)	3.0 (1.0–12.0)	.063
Time between fetal and neonatal MRI (wk)	6.00 (1.28–20.85)	4.86 (1.00–10.43)	.011

^a Values are median (range) or No. (%).

imaging by comparing findings with postnatal imaging. Although fetal MR imaging is thought to be reliable in detecting congenital malformations of the central nervous system,^{25,26} available evidence suggests that some of the variability is attributable to differences in defining normal variants. Isolated mild unilateral ventriculomegaly, for example, has been shown to normalize after birth in 40% of clinical referrals.^{27,28} Similarly, prenatal isolated mild vermis hypoplasia has been shown to normalize in 32% by the time of postnatal MR imaging evaluation.²⁹ Together these findings call for extra caution when interpreting mild prenatal brain findings of unknown etiology on conventional MR imaging because a high proportion of these subtle markers of delayed brain development may normalize by the end of the pregnancy.

The 26% prevalence of preoperatively acquired injury in our cohort with a predominance of pWMI is in agreement with that in previous reports.^{2,5,9,30,31} An important finding of this study is that more than two-thirds (24/33) of the postnatal brain abnormalities identified by conventional MR imaging were diagnosed following a fetal MR imaging study with normal findings. The presence of pWMI, hemorrhages, and ischemic infarctions on neonatal MR imaging were new findings that were not seen on the fetal MR imaging studies. This discrepancy between the fetal-versus-postnatal MR imaging studies may be explained, in part, by the current limitations of fetal MR imaging (ie, fetal and maternal motion, image resolution) and the limited acquisition protocol repertoire available for fetal imaging (ie, lack of robust T1-weighted and susceptibility-weighted sequences), which might have diminished our ability to detect acute white matter injury in utero.^{32,33} Moreover, it is possible that the third-trimester fetal MR imaging studies were performed before these injuries had occurred or consolidated or were below the threshold for lesion detection by conventional MR imaging.

Delayed brain growth and maturation have been reported postnatally in neonates with hypoplastic left-heart syndrome and dextro-transposition of the great arteries⁹ and have been found to be associated with a greater likelihood of brain injury on preoperative brain MR imaging in neonates with CHD.^{1,2,4} Our results corroborate the finding that delayed brain growth and brain immaturity already evident prenatally are associated with an increased vulnerability to acquired injury. In our cohort, more than one-third (10/27) of the acquired neonatal brain injuries were seen concomitantly with qualitative markers of immaturity either on fetal MR imaging or neonatal MR imaging. Our prospectively collected longitudinal data of ante- and postnatal imaging suggest that these newly acquired injuries may result from the cumulative effect of brain dysmaturity, with hemodynamic insults occurring in the perinatal period or during the complex and potentially hazardous transition from fetal to postnatal circulation.³⁴ In fact, we found that the cases with abnormal fetal MR imaging findings (ie, fetal immaturity) and a cyanotic cardiac defect (ie, hemodynamic) were significantly more likely to present with brain abnormalities on neonatal MR imaging. Although the current data did not highlight a single birth-related risk factor for brain lesions, the borderline significant association found between new injury and vaginal delivery raises the question of optimal delivery management for fetuses with complex CHD. Future research is needed to address this important question.

Our data show that preoperative brain injury was significantly more frequent in neonates who underwent a cardiac catheterization before their preoperative MR imaging study. Neonates that required cardiac catheterization in our study all had cyanotic lesions, and most (7/9) had single-ventricle CHD, indicating greater CHD and illness severity among this subset of neonates. Previous studies have reported an association between balloon atrial septostomy and preoperative stroke in neonates with transposition of the great arteries.^{3,4,6} Taken together, these data suggest that cardiac procedures in neonates with CHD with significant hypoxemia and hemodynamic instability are more likely to be associated with brain injury before surgery.

Most interesting, neonates with newly acquired injury had their neonatal MR imaging at a significantly earlier gestational age and sooner after the fetal MR imaging than the noninjured ones. However, we were unable to identify any clinical factors that could explain why these children were scanned earlier. The finding that acquired injury was documented less frequently in neonates scanned at a later time may be explained, in part, by potential resolution of the more subtle injury (eg, pWMI) in the weeks after birth and by the limited time window when diffusion imaging reveals acute/cytotoxic cerebral injury due to subsequent pseudonormalization.³⁵ Additionally, we might have missed microhemorrhages in the BCH cohort, given that susceptibility-weighted imaging was not a standard of practice at the time of the data collection.

Moreover, and in line with other reports, we did not find significant associations between brain injury and other perinatal clinical factors such as birth asphyxia or other markers of illness severity.^{1,2,5,7,31} Nevertheless, earlier age at MR imaging may reflect greater hemodynamic compromise that has not been captured in the current study. Postoperative follow-up MR imaging studies are currently underway and will, hopefully, provide additional insight into this initial observation.

Although this study includes the largest sample reporting serial imaging performed ante- and postnatally, our study limitations deserve mention. First, our current sample size may have been underpowered to identify less frequent clinical risk factors for brain injury. Moreover, given that we carefully excluded cases with chromosomal or genetic conditions, as well as dysmorphic features a priori, it is possible that the true prevalence of brain abnormalities in the overall CHD population has been underestimated in the current sample because structural abnormalities are more frequent in neonates with CHD and other congenital malformations.^{36,37} Also, approximately 11% of our sample was deemed by the clinical team as not medically stable enough to undergo a preoperative MR imaging. We may have missed brain injury in this subset of more severely ill neonates.

Nevertheless, this is the first study to provide prospective serial fetal and preoperative neonatal MR imaging data in subjects with complex CHD. Our large CHD sample was not confined to the most severe cardiac diagnoses but rather included a representative range of CHD. Second, although we did not find a significant difference in GA at fetal MR imaging between fetuses with CHD with and without brain abnormalities, it is possible that the timing of our fetal MR imaging limited our ability to detect delayed brain development. For example, it has been reported that GA estima-

tion based on cortical gyrification can only be made accurately after 28 weeks.³⁸ Although only 7 fetuses were scanned during the late second trimester (ie, 24–27 weeks), we did not identify any structural brain abnormalities in fetuses younger than 32 weeks in our cohort. However, our evaluation of the fetal brain was carefully made and took in account a number of gestational-age-appropriate developmental landmarks. Nevertheless, more studies are needed to determine how GA influences the predictive value of fetal MR imaging postnatally. Finally, our overall goal was to evaluate the sensitivity and specificity of conventional fetal MR imaging for predicting postnatal brain abnormalities in neonates with complex CHD before open heart surgery. Another limitation is that we did not perform repeat blinded MR imaging interpretations to assess intra- and interreader reliability. However, our study was conducted in 2 major referral centers for complex neonatal CHD repair, and all MR imaging studies were reviewed by an experienced pediatric neuroradiologist following clinical best practice standards. Consequently, we are confident that the findings reported in this study are representative of the current findings in clinical settings.

CONCLUSIONS

This study reports, for the first time, that abnormal findings on conventional fetal brain MR imaging are associated with an increased incidence of brain abnormalities in neonates with complex CHD before open heart surgery. Although conventional fetal brain MR imaging had high specificity, it lacked sensitivity in predicting postnatal brain abnormalities. In addition to prenatal brain immaturity, our findings suggest that other currently unidentified clinical and birth-related factors may predispose these neonates to the hazards of cerebral hypoxemia, hypoperfusion, and hemodynamic instability that can occur during the demanding third trimester and the complex circulatory transition surrounding birth.

ACKNOWLEDGMENTS

We thank the families who participated in the study as well as Lauren Crowder and Samantha Bauer for their assistance in the management of the clinical data.

Disclosures: Marie Brossard-Racine—RELATED: Other: postdoctoral fellowship support from Canadian Institutes of Health Research. Adre du Plessis—RELATED: Grant: National Heart, Lung, and Blood Institute.* Comments: I am coinvestigator on this grant. Catherine Limperopoulos—RELATED: Grant: Canadian Institutes of Health,* National Institutes of Health.* *Money paid to the institution.

REFERENCES

- Andropoulos DB, Hunter JV, Nelson DP, et al. **Brain immaturity is associated with brain injury before and after neonatal cardiac surgery with high-flow bypass and cerebral oxygenation monitoring.** *J Thorac Cardiovasc Surg* 2010;139:543–56 CrossRef Medline
- Beca J, Gunn J, Coleman L, et al. **New white matter brain injury after infant heart surgery is associated with diagnostic group and the use of circulatory arrest.** *Circulation* 2013;127:971–79 CrossRef Medline
- Block AJ, McQuillen PS, Chau V, et al. **Clinically silent preoperative brain injuries do not worsen with surgery in neonates with congenital heart disease.** *J Thorac Cardiovasc Surg* 2010;140:550–57 CrossRef Medline
- Dimitropoulos A, McQuillen PS, Sethi V, et al. **Brain injury and development in newborns with critical congenital heart disease.** *Neurology* 2013;81:241–48 CrossRef Medline
- Mahle WT, Tavani F, Zimmerman RA, et al. **An MRI study of neurological injury before and after congenital heart surgery.** *Circulation* 2002;106(12 suppl 1):I109–14 Medline
- McQuillen PS, Hamrick SE, Perez MJ, et al. **Balloon atrial septostomy is associated with preoperative stroke in neonates with transposition of the great arteries.** *Circulation* 2006;113:280–85 CrossRef Medline
- Miller SP, McQuillen PS, Hamrick S, et al. **Abnormal brain development in newborns with congenital heart disease.** *N Engl J Med* 2007;357:1928–38 CrossRef Medline
- Gaynor JW, Stopp C, Wypij D, et al; International Cardiac Collaborative on Neurodevelopment (ICCON) Investigators. **Neurodevelopmental outcomes after cardiac surgery in infancy.** *Pediatrics* 2015;135:816–25 CrossRef Medline
- Licht DJ, Shera DM, Clancy RR, et al. **Brain maturation is delayed in infants with complex congenital heart defects.** *J Thorac Cardiovasc Surg* 2009;137:529–36; discussion 536–37 CrossRef Medline
- Brossard-Racine M, du Plessis AJ, Vezina G, et al. **Prevalence and spectrum of in utero structural brain abnormalities in fetuses with complex congenital heart disease.** *AJNR Am J Neuroradiol* 2014;35:1593–99 CrossRef Medline
- Mlczoch E, Brugger P, Ulm B, et al. **Structural congenital brain disease in congenital heart disease: results from a fetal MRI program.** *Eur J Paediatr Neurol* 2013;17:153–60 CrossRef Medline
- Clouchoux C, du Plessis AJ, Bouyssi-Kobar M, et al. **Delayed cortical development in fetuses with complex congenital heart disease.** *Cereb Cortex* 2013;23:2932–43 CrossRef Medline
- Limperopoulos C, Tworetzky W, McElhinney DB, et al. **Brain volume and metabolism in fetuses with congenital heart disease: evaluation with quantitative magnetic resonance imaging and spectroscopy.** *Circulation* 2010;121:26–33 CrossRef Medline
- Harris PA, Taylor R, Thielke R, et al. **Research electronic data capture (REDCap): a metadata-driven methodology and workflow process for providing translational research informatics support.** *J Biomed Inform* 2009;42:377–81 CrossRef Medline
- Wax JR, Bookman L, Cartin A, et al. **Mild fetal cerebral ventriculomegaly: diagnosis, clinical associations, and outcomes.** *Obstet Gynecol Surv* 2003;58:407–14 Medline
- Girard NJ, Raybaud CA. **Ventriculomegaly and pericerebral CSF collection in the fetus: early stage of benign external hydrocephalus?** *Childs Nerv Syst* 2001;17:239–45 CrossRef Medline
- Watanabe Y, Abe S, Takagi K, et al. **Evolution of subarachnoid space in normal fetuses using magnetic resonance imaging.** *Prenat Diagn* 2005;25:1217–22 CrossRef Medline
- Raybaud C, Ahmad T, Rastegar N, et al. **The premature brain: developmental and lesional anatomy.** *Neuroradiology* 2013;55(suppl 2):23–40 CrossRef Medline
- Tarui T, Limperopoulos C, Sullivan NR, et al. **Long-term developmental outcome of children with a fetal diagnosis of isolated inferior vermian hypoplasia.** *Arch Dis Child Fetal Neonatal Ed* 2014;99:F54–58 CrossRef Medline
- Garel C. *MRI of the Fetal Brain: Normal Development and Cerebral Pathologies.* Berlin: Springer; 2004
- Paul LK. **Developmental malformation of the corpus callosum: a review of typical callosal development and examples of developmental disorders with callosal involvement.** *J Neurodev Disord* 2011;3:3–27 CrossRef Medline
- Miller SP, Cozzio CC, Goldstein RB, et al. **Comparing the diagnosis of white matter injury in premature newborns with serial MR imaging and transfontanel ultrasonography findings.** *AJNR Am J Neuroradiol* 2003;24:1661–69 Medline
- Beslow LA, Ichord RN, Gindville MC, et al. **Pediatric intracerebral hemorrhage score: a simple grading scale for intracerebral hemorrhage in children.** *Stroke* 2014;45:66–70 CrossRef Medline
- Barkovich AJ. *Pediatric Neuroimaging.* 4th ed. Philadelphia: Williams & Wilkins; 2005

25. Blaicher W, Bernaschek G, Deutinger J, et al. **Fetal and early postnatal magnetic resonance imaging: is there a difference?** *J Perinat Med* 2004;32:53–57 Medline
26. Pugash D, Brugger PC, Bettelheim D, et al. **Prenatal ultrasound and fetal MRI: the comparative value of each modality in prenatal diagnosis.** *Eur J Radiol* 2008;68:214–26 CrossRef Medline
27. Lam SJ, Kumar S. **Evolution of fetal ventricular dilatation in relation to severity at first presentation.** *J Clin Ultrasound* 2014;42:193–98 CrossRef Medline
28. Parazzini C, Righini A, Doneda C, et al. **Is fetal magnetic resonance imaging indicated when ultrasound isolated mild ventriculomegaly is present in pregnancies with no risk factors?** *Prenat Diag* 2012;32:752–57 CrossRef Medline
29. Limperopoulos C, Robertson RL, Estroff JA, et al. **Diagnosis of inferior vermian hypoplasia by fetal magnetic resonance imaging: potential pitfalls and neurodevelopmental outcome.** *Am J Obstet Gynecol* 2006;194:1070–76 CrossRef Medline
30. McQuillen PS, Barkovich A, Hamrick S, et al. **Temporal and anatomic risk profile of brain injury with neonatal repair of congenital heart defects.** *Stroke* 2007;38:736–41 CrossRef Medline
31. Petit CJ, Rome JJ, Wernovsky G, et al. **Preoperative brain injury in transposition of the great arteries is associated with oxygenation and time to surgery, not balloon atrial septostomy.** *Circulation* 2009;119:709–16 CrossRef Medline
32. Glenn OA, Barkovich AJ. **Magnetic resonance imaging of the fetal brain and spine: an increasingly important tool in prenatal diagnosis, part 1.** *AJNR Am J Neuroradiol* 2006;27:1604–11 Medline
33. Chung R, Kasprian G, Brugger PC, et al. **The current state and future of fetal imaging.** *Clin Perinatol* 2009;36:685–99 CrossRef Medline
34. Friedman AH, Fahey JT. **The transition from fetal to neonatal circulation: normal responses and implications for infants with heart disease.** *Semin Perinatal* 1993;17:106–21 Medline
35. McKinstry RC, Miller JH, Snyder AZ, et al. **A prospective, longitudinal diffusion tensor imaging study of brain injury in newborns.** *Neurology* 2002;59:824–33 CrossRef Medline
36. Hartman RJ, Rasmussen SA, Botto LD, et al. **The contribution of chromosomal abnormalities to congenital heart defects: a population-based study.** *Pediatr Cardiol* 2011;32:1147–57 CrossRef Medline
37. Miller A, Riehle-Colarusso T, Alverson CJ, et al. **Congenital heart defects and major structural noncardiac anomalies, Atlanta, Georgia, 1968 to 2005.** *J Pediatr* 2011;159:70–78.e72 CrossRef Medline
38. Garel C, Chantrel E, Brisse H, et al. **Fetal cerebral cortex: normal gestational landmarks identified using prenatal MR imaging.** *AJNR Am J Neuroradiol* 2001;22:184–89 Medline

Whole-Brain DTI Assessment of White Matter Damage in Children with Bilateral Cerebral Palsy: Evidence of Involvement beyond the Primary Target of the Anoxic Insult

F. Arrigoni, D. Peruzzo, C. Gagliardi, C. Maghini, P. Colombo, F. Servodio Iammarrone, C. Pierpaoli, F. Triulzi, and A.C. Turconi



ABSTRACT

BACKGROUND AND PURPOSE: Cerebral palsy is frequently associated with both motor and nonmotor symptoms. DTI can characterize the damage at the level of motor tracts but provides less consistent results in nonmotor areas. We used a standardized pipeline of analysis to describe and quantify the pattern of DTI white matter abnormalities of the whole brain in a group of children with chronic bilateral cerebral palsy and periventricular leukomalacia. We also explored potential correlations between DTI and clinical scale metrics.

MATERIALS AND METHODS: Twenty-five patients (mean age, 11.8 years) and 25 healthy children (mean age, 11.8 years) were studied at 3T with a 2-mm isotropic DTI sequence. Differences between patients and controls were assessed both voxelwise and in ROIs obtained from an existing DTI atlas. Clinical metrics included the Gross Motor Function Classification System, the Manual Ability Classification System, and intelligence quotient.

RESULTS: The voxel-level and ROI-level analyses demonstrated highly significant ($P < .001$) modifications of DTI measurements in patients at several levels: cerebellar peduncles, corticospinal tracts and posterior thalamic radiations, posterior corpus callosum, external capsule, anterior thalamic radiation, superior longitudinal fasciculi and corona radiata, optic nerves, and chiasm. The reduction of fractional anisotropy values in significant tracts was between 8% and 30%. Statistically significant correlations were found between motor impairment and fractional anisotropy in corticospinal tracts and commissural and associative tracts of the supratentorial brain.

CONCLUSIONS: We demonstrated the involvement of several motor and nonmotor areas in the chronic damage associated with periventricular leukomalacia and showed new correlations between motor skills and DTI metrics.

ABBREVIATIONS: AD = axial diffusivity; CP = cerebral palsy; CST = corticospinal tract; FA = fractional anisotropy; GMFCS = Gross Motor Function Classification System; HC = healthy control; IQ = intelligence quotient; MACS = Manual Ability Classification System; MD = mean diffusivity; PVL = periventricular leukomalacia; RD = radial diffusivity; SCP = superior cerebellar peduncle

Cerebral palsy (CP) is one of the leading causes of disabilities in children in Western countries, affecting 1–2.5 per 1000 live births.¹ The term CP includes a heterogeneous spectrum of non-

progressive brain disorders manifesting with motor, sensory, and cognitive deficits.² Even if motor impairment often represents the most remarkable manifestation of the disorder, disturbances of sensation, perception, cognition, communication, and behavior commonly affect patients' quality of life.

Conventional MR imaging helps determine the gross brain pathology associated with CP: Periventricular leukomalacia (PVL) is the most common pattern of injury demonstrated by MR imaging in preterm children (low birth weight or very low birth weight) with CP.³ PVL is characterized by a dilation of the lateral ventricles, in particular at the level of the occipital horns, reduction of WM volume, hyperintense signal of the residual periventricular WM on T2-weighted and FLAIR images, and thinning of the corpus callosum. These findings reflect the loss of neuronal cells and gliosis demonstrated by pathology.³

More recently, diffusion-weighted MR imaging and DTI have been used to understand the microstructural changes occurring in the brains of patients with CP both in the acute and chronic

Received October 12, 2015; accepted after revision January 5, 2016.

From the Neuroimaging Lab (F.A., D.P.), Functional Neurorehabilitation Unit (C.G., C.M., F.S.I., A.C.T.), and Child Psychopathology Unit (P.C.), Scientific Institute IRCCS Eugenio Medea, Bosisio Parini, Italy; National Institutes of Health (C.P.), Bethesda, Maryland; and Department of Neuroradiology (F.T.), Fondazione IRCCS Ca' Granda, Ospedale Maggiore Policlinico, Milano, Italy.

This work was supported by the Italian Ministry of Health (Ricerca Corrente 2012 to A.C. Turconi).

Paper previously presented as an electronic poster at: Annual Meeting of the European Society of Neuroradiology, September 17–20, 2015; Naples, Italy.

Please address correspondence to Filippo Arrigoni, MD, Scientific Institute IRCCS Eugenio Medea, Via don L. Monza 20, 23842, Bosisio Parini (Lecco), Italy; e-mail: filippo.arrigoni@bp.lnf.it

Indicates open access to non-subscribers at www.ajnr.org

Indicates article with supplemental on-line appendix and tables.

Indicates article with supplemental on-line photos.

<http://dx.doi.org/10.3174/ajnr.A4717>

phases. Quantitative measurements derived from DTI,⁴ mostly fractional anisotropy (FA) and mean diffusivity (MD), have been successfully used to demonstrate structural modifications of the corticospinal tract (CST) and ascending sensorimotor tracts (including the posterior thalamic radiations) of patients with CP.⁵ However, a quantification of the impairment of different tracts measured by DTI is lacking. Most studies⁵ focus on reporting the significant differences between patients and controls but not on the magnitude of the differences, which could instead provide valuable information about the severity of damage to each tract. More detailed descriptions of the characteristics and amount of the damage could contribute to a more precise clinical definition and could help in targeting more specific rehabilitation interventions, thus improving their efficacy.

Moreover, despite the presence of important nonmotor symptoms, the evidence of the involvement of cerebral commissures and association tracts and of the frontal, temporal, and occipital lobes is not consistent.⁵ Data on corpus callosum and association tracts such as the superior and inferior longitudinal fasciculi are conflicting, with some studies showing FA reductions in patients with CP^{6,7} and others showing no differences compared with controls.⁸⁻¹⁰

Given these premises, in this article, we applied a standardized pipeline of analysis of DTI data to a group of children with PVL and bilateral CP to do the following:

- 1) Assess the pattern of WM abnormalities in the whole brain, extending beyond motor areas.
- 2) Quantify the severity of the alterations in terms of FA modifications to detect the most affected tracts.
- 3) Correlate diffusion metrics with cognitive and clinical features.

MATERIALS AND METHODS

The study took place at Scientific Institute IRCCS Eugenio Medea. This study was approved by the local ethics committee, and written informed parental consent was obtained for all participants.

Patients

Twenty-five children (16 males, mean age, 11.8 ± 3.1 years; age range, 7.7–16.8 years; 20 right-handed) with a diagnosis of spastic bilateral CP were included in the study. Children were selected from the clinical database of the Functional Neurorehabilitation Unit of Eugenio Medea Institute and underwent a clinical and radiologic protocol developed as part of a research study on CP. Subject selection criteria were the following:

- Preterm birth (<37 weeks of gestation).
- Diagnosis of spastic bilateral CP with a known history of anoxic or hypoxic injuries associated with labor and delivery.
- PVL as described on the MR imaging report of previous examinations.
- Age older than 7 years to perform MR imaging without sedation.
- Visual Acuity more than three-tenths (Snellen Letter Acuity Test), corresponding to normal or mildly reduced visual acuity, not consistent with a severe visual impairment.

Table 1: Demographic and clinical characteristics of patients with CP and HCs

	Patients with Bilateral CP	Healthy Controls	Statistics	
Participants (No.)	25	25		
Sex (M/F)	16:09	17:08	$\chi^2 = 0.62$	$P < .43$
Age at MRI (yr)	11.8 ± 3.1	11.8 ± 2.8	$t = 0.027$	$P > .97$
Gestational age (wk)	31.8 ± 3.1	38.8 ± 1.3	$U = 197$	$P < .001$
IQ	68.8 ± 19.6	121 ± 18.7	$U = 18.5$	$P < .001$
MACS (I, II, III)	9, 10, 6	–		
GMFCS (I, 2, 3, 4)	9, 4, 8, 4	–		

- Mild-to-moderate gross motor and upper limb functional impairment.

The recruited participants were classified according to the Classification of Cerebral Palsy and the Surveillance of Cerebral Palsy in Europe algorithms. Their motor function was assessed according to the Gross Motor Function Classification System (GMFCS),¹¹ while handling of objects in daily activities was classified according to the Manual Ability Classification System (MACS).¹² General intelligence abilities were assessed by the age-appropriate Wechsler Scale.¹³

Twenty-five healthy controls (HCs) (8 females; mean age, 11.8 ± 2.8 years; age range, 7.6–16.8 years; 20 right-handed) with no history of psychiatric or neurologic illness, learning disabilities, or hearing or visual loss were recruited to be matched with patients with CP. HCs showed average school performances in language, and reading and had an intelligence quotient (IQ) of at least 85 on the Cattell's Culture Fair Intelligence Test, a nonverbal culture-free test to measure the analytic and reasoning ability in abstract and novel situations with a fair correlation index with the IQ in the Wechsler Scales.¹⁴

Emotional and behavioral problems were assessed by the Child Behavioral Checklist and Youth Self Report.¹⁵ None of the healthy subjects exceeded the clinical cutoff ($T = 63$) in the Total Problems Scale.

Demographic details of the entire group are shown in Table 1.

MR Imaging and DTI Protocol

All the examinations were performed on the same 3T scanner (Achieva; Philips Healthcare, Best, the Netherlands) equipped with a 32-channel head coil and included both conventional MR imaging and DTI sequences.

Conventional MR imaging included a 3D T1-weighted sequence (TR = 8.2 ms, TE = 3.8 ms, flip angle = 8° , FOV = 210×210 mm², acquired matrix = $210 \times 210 \times 170$, voxel size = $1 \times 1 \times 1$ mm) and a 2D T2-weighted turbo spin-echo sequence with a high in-plane resolution on the axial plane (TR = 4100 ms, TE = 82 ms, flip angle = 90° , FOV = 230×230 mm, acquired matrix = 550×420 , section thickness = 3 mm, reconstructed voxel size = $0.22 \times 0.22 \times 3$ mm).

DTI data were acquired with the same sequence in all subjects. We used a multishell 2D T2-weighted EPI sequence (TR = 8645 ms, TE = 63 ms, flip angle = 90° , FOV = 224×224 mm², acquired matrix = 112×112 , section thickness = 2 mm, final voxel size = $2 \times 2 \times 2$ mm³), including 15 directions at $b=300$ s/mm², 53 directions at $b=1100$ s/mm², and 8 volumes at $b=0$

s/mm² (see the On-line Appendix for a detailed explanation of the DTI acquisition scheme).

Moreover, a T2-weighted structural volume was acquired with a fat-suppressed TSE sequence to correct DTI data for susceptibility-induced EPI distortion artifacts as described by Wu et al¹⁶ (TR = 3000 ms, TE = 100 ms, FOV = 224 × 224 mm², acquired matrix = 112 × 112, section thickness = 1.7 mm, voxel size = 2 × 2 × 1.7 mm).

Morphologic Damage

T1- and T2-weighted images of each patient were reviewed by the same experienced neuroradiologist (F.A., with 8 years of experience in pediatric neuroradiology), blinded to clinical data, to confirm the presence of PVL diagnosed in previous examinations and to assess and quantify, on a visual scale, the severity of the cerebral damage. To assess the homogeneity of our cohort in terms of WM damage, 3 parameters were taken into account: ventricular dilation, WM involvement (thinning and hyperintense abnormal signal on T2-weighted images), and corpus callosum thinning. Each structure was visually classified as mildly, moderately, or severely involved according to its appearance on morphologic sequences. A global assessment of WM damage was obtained combining the appearance of the 3 structures (the overall damage was considered moderate or severe if at least 2 or 1 structure, respectively, was moderately or severely involved; otherwise the pattern of injury was considered mild) (On-line Fig 1). Brain injury at the level of gray matter structures such as the basal ganglia and thalami was evaluated separately.

DTI Processing

DTI processing was performed by using the TORTOISE software (<http://tortoisedi.nichd.nih.gov/stbb/login.html>).¹⁷ The preprocessing pipeline included a motion-correction step, a correction of image distortions (eg, eddy current, B0 susceptibility, EPI distortion) by using the nondistorted T2-weighted volume as a reference,^{16,18} a realignment to the anterior/posterior commissure plane, and an upsampling to a final voxel resolution of 1.5 × 1.5 × 1.5 mm.

Data were then visually inspected to detect remaining artifacts and/or wrong preprocessing results. Corrupted volumes were discarded from the subsequent analysis.

The DTI tensor was computed by using the nonlinear least squares method described by Chang et al,¹⁹ and FA, MD, axial diffusivity (AD), and radial diffusivity (RD) maps were then calculated for each subject.

A study DTI template was built from all subject tensors (patients and controls) with the DTI-ToolKit software package (<http://software.incf.org/software/dti-toolkit-dti-tk>),²⁰ which uses a spatial registration algorithm based on the diffusion tensor similarity to achieve a better alignment of WM structures. All subject tensors were moved to the template space performing only 1 interpolation operation, and scalar diffusion maps were subsequently derived in the template space for the voxel-level statistical analysis.

ROIs for the ROI-level analysis were derived from the Johns Hopkins atlases of WM included in FSL (<http://www.fmrib.ox.ac.uk/fsl>). More precisely, the 20 ROIs representing the most important WM tracts of the brain included in the Johns Hopkins

University WM tractography atlas^{21,22} were integrated with ROIs derived from the ICBM-DTI-81 atlas (http://www.loni.usc.edu/atlas/Atlas_Detail.php?atlas_id=15),²³ to obtain an extensive coverage of both the supra- and infratentorial WM. The warp field between the Johns Hopkins University template and the DTI study template was computed and combined with the subject-DTI study template warp field to move the ROIs from the Johns Hopkins University template to the single subject space. For each ROI, the mean FA, MD, AD, and RD values were computed for the statistical analysis.

Statistical Analysis

Differences in clinical measures between the HC and the CP groups were investigated with the χ^2 for sex, the *t* test for age at MR imaging, and the Mann-Whitney test for gestational age and IQ.

For all DTI comparisons, significance was set at $P \leq .001$ (corrected for multiple comparisons), to be very conservative and detect the most relevant differences between groups. Statistical analysis at the voxel level was performed by using the permutation test implemented by Winkler et al,²⁴ with the threshold-free cluster enhancement method. Statistical analysis at the ROI level was performed by using Matlab (MathWorks, Natick, Massachusetts), and the significance threshold was set to $P < .001$, corrected for multiple comparisons (false discovery rate).

The General Linear Model was used to model the data both at the voxel and ROI levels by using age as the predictor. Moreover, the Pearson correlation coefficients between the diffusion values and the clinical variables (GMFCS, MACS, IQ) were computed.

RESULTS

Descriptive Results and Clinical Features

All participants (HCs and patients with CP) completed the study protocol (MR imaging and clinical evaluations). HCs and patients with CP differed in gestational age and IQ, but not for mean age at MR imaging and sex distribution (Table 1). Gross motor function, manipulation, and general cognitive ability scales showed a large range of values in the CP group. Considering gross motor functions, mild or moderate impairment (class I and II at GMFCS) was present in 13 patients (52%), while severe impairment (class IV at GMFCS) was present only in 4 (16%). As to handling and manipulation abilities measured by MACS, mild impairment (MACS I and II) was noted in 19 patients (76%), while no patients had severe impairment (MACS IV). Full IQ ranged from 38 to 109, with a mean of 68.8 ± 19.6 (Table 1). Mild cognitive impairment (IQ = 50–70) was noted in 9 children (36%), moderate cognitive impairment (IQ < 50) was noted in 4 children (16%), whereas 12 children (48%) had no cognitive impairment (IQ > 70). Mean gestational age at birth was 31.8 ± 3.1 weeks, ranging from 27 to 37 weeks.

No correlation was found between the level of impairment by MACS and GMFCS and IQ score or gestational age, but GMFCS scores were correlated to MACS scores ($r = 0.82$).

Pattern of Damage at Conventional MR Imaging

The results of the classification of cerebral WM damage based on the visual inspection of T1- and T2-weighted imaging is reported

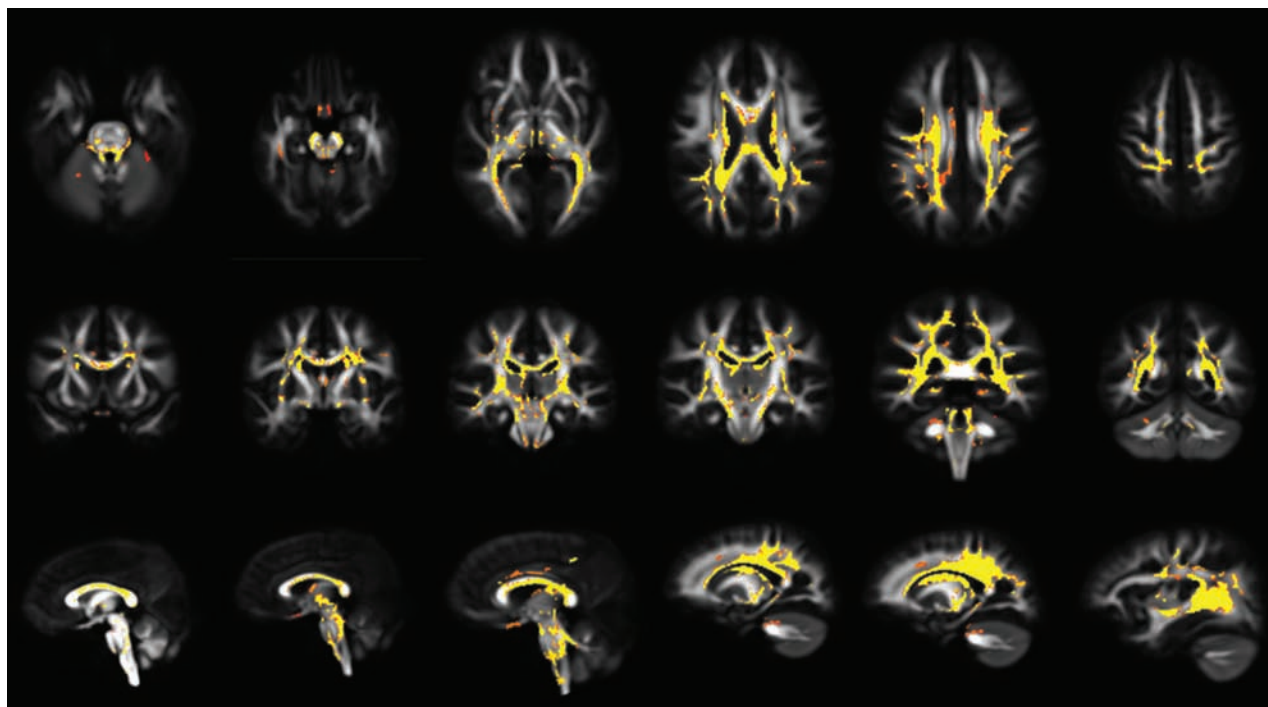


FIG 1. Axial (first row), coronal (second row), and sagittal (third row) MR images show voxelwise FA group differences between patients with CP and HCs (FA patients < FA controls). Results are overlaid on the FA template obtained from all subjects, at a significance level of $P < .001$, corrected for multiple comparisons.

in On-line Table 1. In 16/25 cases (64%), the severity of PVL was mild, and it was moderate in 7 (28%). Severe WM damage was found in only 2 patients (8%). Thalamic or basal ganglia atrophy was found in 8 cases (32%).

Voxel-based DTI results for the whole-brain voxel-based analysis demonstrated significant differences ($P < .001$) of FA values between patients with CP and HCs: Visual group comparison detected a diffuse reduction of FA values in both the supratentorial and infratentorial WM (Fig 1). The areas affected were bilaterally located in the superior and inferior cerebellar peduncles (including decussation), motor and sensory tracts in the brain stem, posterior limbs of internal capsules, peritrigonal WM (including the optic and thalamic radiations), external capsules, centrum semiovale, corpus callosum (with a prevalent involvement of its central portion), fornix, cingulum, chiasm, and optic tracts. The same regions in the supratentorial WM showed increased MD, AD, and RD values at the same significance level ($P < .001$) (On-line Fig 2). No significant differences were detected for MD, AD, and RD in the brain stem and cerebellum, except for an RD increase at the level of cerebellar and cerebral peduncles (On-line Fig 2). No regions in the brain showed increased FA or decreased MD, AD, and RD in patients with CP compared with controls.

ROI-Level DTI Results

In On-line Table 2, we show mean FA values in the 43 tracts derived from the DTI atlas for both patients with CP and HCs. Mean MD, AD, and RD values are reported in On-line Table 3. When we set a conservative threshold of $P < .001$, differences in FA and other DTI metrics emerged in motor areas (like CSTs and thalamic radiations), but also in nonmotor pathways such as the middle and posterior parts of the corpus callosum, optic radia-

tions, superior longitudinal fasciculi, cingulum, and cerebellar peduncles.

The magnitude of the differences of FA mean values for significant tracts ($P < .001$) is reported in Fig 2, where percentage differences of patients with CP versus HCs (Δ FA) and corresponding z scores are also shown. The magnitude of the differences varied among tracts. In patients with CP, posterior corona radiata, thalamic radiations, corpus callosum, cingulum, and superior cerebellar peduncles showed a large FA reduction, between 15% and 30%. Other significant tracts showed a less pronounced FA reduction, between 8% and 15%.

On-line Tables 4 and 5 summarize the correlations between the level of impairment of motor skills (by GMFCS and MACS) and DTI measures. With a significance threshold of .001, no correlations emerged, while some correlations were significant when the threshold was set at $< .05$. In particular, FA values in the corticospinal tracts, posterior thalamic radiations, corona radiata, and superior longitudinal fasciculus showed significant negative correlations with both GMFCS and MACS. FA mean values of the inferior cerebellar peduncle, inferior fronto-occipital fasciculus, inferior longitudinal fasciculus, and uncinate fasciculus were negatively correlated with GMFCS, but not with MACS. Few tracts showed positive correlations between other DTI measures (MD, AD, RD) and GMFCS or MACS.

No significant correlations were found between IQ score and DTI measures in the ROIs at both $P < .05$ and $< .001$.

DISCUSSION

In this study, we assessed abnormal findings on diffusion MR imaging associated with PVL in preterm children affected by bi-

FA differences

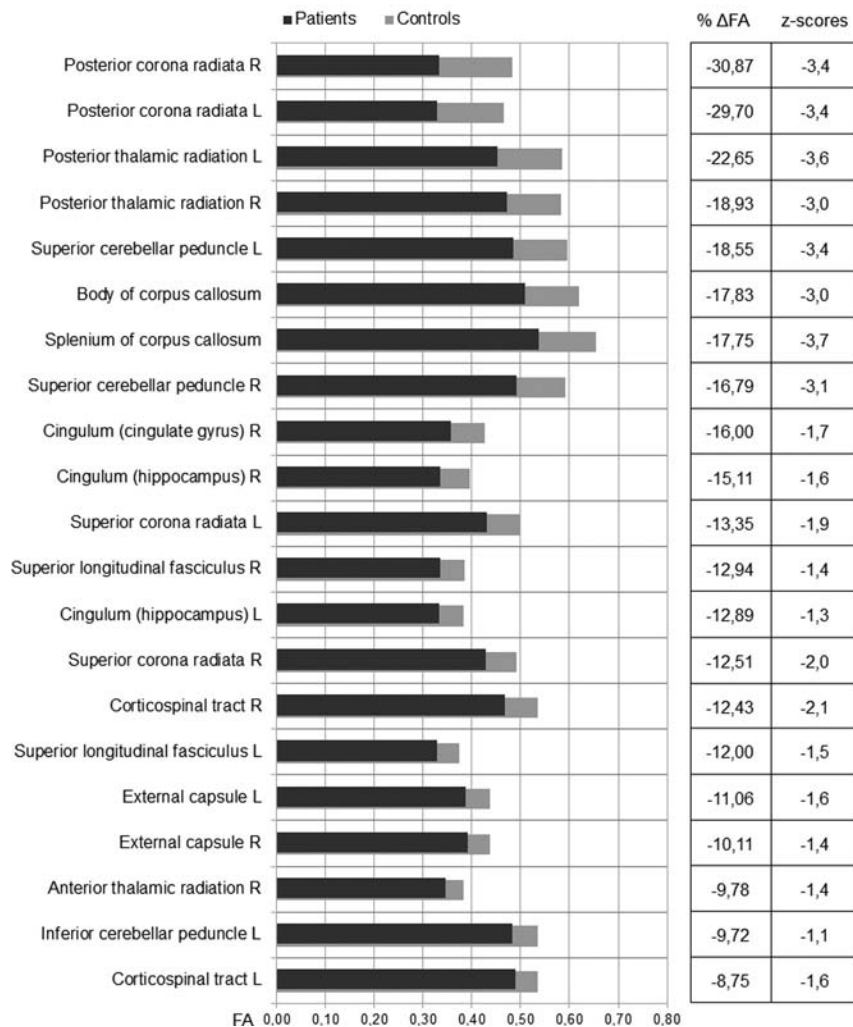


FIG 2. The bar graph shows the mean FA values for patients with CP and HC in tracts that showed significant ($P < .001$) differences. Tracts are listed according to the percentage differences (Δ FA) between patients with CP and HCs, reported in the right column. Z scores for each tract are also shown. R indicates right; L, left.

lateral cerebral palsy. Through both a voxel-level and an atlas-based ROI approach, we extended our investigation beyond the analysis of corticospinal and sensory-motor tracts that were extensively investigated in previous studies.^{8,25-30} Our analysis took into account, with a standardized and non-operator-dependent method, a large number of WM tracts and areas extensively covering both the supratentorial and infratentorial brain and the cerebellum.

Moreover, we did not limit our observations to significance maps and averaged values, but we also examined the magnitude of the differences of DTI measures between patients with CP and HCs and correlated these data with clinical cognitive and motor indices.

We focused on WM organization and damage, both in motor and nonmotor areas. We hypothesized that the alteration of cerebral organization and connections in CP could involve multiple tracts and areas, thus mirroring the complex clinical features.

Recent literature^{8,25-30} has extensively documented, through

DTI, the damage occurring to cortico-spinal and sensory-motor tracts in patients with CP. Less attention has been paid to the severity of the alterations and to the different degrees of involvement that can affect WM tracts.

The distribution of WM abnormalities measured by DTI confirmed, in our patients with PVL, a prevalent involvement of CSTs, the posterior part of corpus callosum, posterior corona radiata, and thalamic radiations, with a less severe involvement of anterior brain regions.

These findings indicate that the atlas-based ROI approach we used provided results consistent with the non-atlas-based methods that have been used in previous studies.^{7,31} Moreover, we extended our observation to the severity of DTI modifications, discovering that FA was less reduced in CSTs (8.75%, 12.43%) than in the posterior thalamic radiations (approximately 20%); thus, these findings testified to the well-known importance of sensory integration in the determinism of the multilevel damage in CP. The FA difference between HCs and participants with CP was also quite relevant (approximately 17%) in the cerebellar peduncles and corpus callosum. The involvement of cerebellar peduncles could be the result of a secondary degeneration due to WM damage. These alterations can contribute to the motor impairment observed in patients with CP, given that cerebrocerebellar connections between the cerebellum and thalami through the superior cerebellar peduncles (SCPs) are necessary for motor functions.³² The same mechanisms may be valid for the corpus callosum, whose integrity is fundamental for coordination and movement, but also for cognition.

Therefore, as we observed, even in patients with milder forms of bilateral spastic CP and PVL, the impairment of the descending pyramidal fibers could be a relatively minor feature, whereas the damage of other parts of the neuronal network involved in motor control (such as the corpus callosum and cerebellum) may have a larger impact.⁶

Moreover, as we showed, the complex PVL damage affects many projections and associative tracts far beyond those involved in motor planning and control, thus contributing to the complex clinical pattern that characterizes bilateral CP.^{5,32,33} We found a severe involvement of optic tracts, optic radiations, and posterior corona radiata that could affect the integrity of the afferent sensory visual tracts with much more evidence than previously described.^{32,34} Although our recruitment criteria excluded children

with major visual problems, visual perceptual difficulties characterize the cognitive profile in children with PVL³⁵ and can be linked to damage to the visual afferent pathways and visual processing. The diffuse damage in the anteroposterior associative and commissural tracts may explain the impairment in problem solving and executive functions.

Different from Wang et al,³² we failed to find a correlation between mean FA values in WM tracts and cognitive competences. This failure could be explained by the different ages of the 2 cohorts: Wang et al studied very young children, with a mean age of 16 months, while we studied older patients (mean age, 11.8 years). Brain maturation and growth could affect WM structures and DTI measures and explain the different correlations found, as recently demonstrated in the meta-analysis by Li et al.³⁶ Also the different methodology used in cognitive assessment (developmental quotient versus IQ) may have played a role.

This study has limitations. First, the parenchymal damage in subjects with CP, with loss of WM volume and ventricular enlargement, may influence the creation of a common DTI template between patients and HCs and affect DTI results. However, our cohort showed only mild ventricular enlargement in 68% of patients, and the effects of the distortions applied by the transformation used to build the template and the results of single-subject registrations were carefully inspected and corrected to prevent possible errors.

Second, the use of noncontinuous scales such as the GMFCS and MACS for correlations with WM damage is suboptimal; however, this method has been used in previous studies in patients with CP.³²

CONCLUSIONS

Our study demonstrates that the structural WM damage affecting children with CP affects not only structures that are the primary target of the anoxic insult in the preterm, such as thalamic radiations and periventricular WM, but it also strongly affects other distant tracts and pathways like the SCPs, optic nerves and tracts, and long associative fasciculi. These elements can help to better understand the pattern of clinical impairment in CP and can be a prerequisite for the developing targeted rehabilitation-training programs that could improve the performance of such patients. In particular, the magnitude of tract injury, as measured by DTI metrics, may be used in the future as a biomarker for monitoring the effect of cognitive and motor rehabilitative programs.

Disclosures: Filippo Arrigoni—RELATED: Grant: Ministero della Salute (RC 2012).* UNRELATED: Grants/Grants Pending: Ministero della Salute (RC 2013).* Chiara Gagliardi, Cristina Maghini, Anna Carla Turconi—RELATED: Grant: Ministero della Salute-Italia (RC 2012).* *Money paid to the institution.

REFERENCES

1. Reid SM, Carlin JB, Reddihough DS. Rates of cerebral palsy in Victoria, Australia, 1970 to 2004: has there been a change? *Dev Med Child Neurol* 2011;53:907–12 CrossRef Medline
2. Rosenbaum P, Paneth N, Leviton A, et al. A report: the definition and classification of cerebral palsy April 2006. *Dev Med Child Neurol Suppl* 2007;109:8–14 Medline
3. Volpe JJ. Brain injury in premature infants: a complex amalgam of destructive and developmental disturbances. *Lancet Neurol* 2009;8:110–24 CrossRef Medline
4. Basser PJ, Pierpaoli C. Microstructural and physiological features of tissues elucidated by quantitative-diffusion-tensor MRI. *J Magn Reson B* 1996;111:209–19 CrossRef Medline
5. Scheck SM, Boyd RN, Rose SE. New insights into the pathology of white matter tracts in cerebral palsy from diffusion magnetic resonance imaging: a systematic review. *Dev Med Child Neurol* 2012;54:684–96 CrossRef Medline
6. Koerte I, Pelavin P, Kirmess B, et al. Anisotropy of transcallosal motor fibres indicates functional impairment in children with periventricular leukomalacia. *Dev Med Child Neurol* 2011;53:179–86 CrossRef Medline
7. Yoshida S, Hayakawa K, Yamamoto A, et al. Quantitative diffusion tensor tractography of the motor and sensory tract in children with cerebral palsy. *Dev Med Child Neurol* 2010;52:935–40 CrossRef Medline
8. Murakami A, Morimoto M, Yamada K, et al. Fiber-tracking techniques can predict the degree of neurologic impairment for periventricular leukomalacia. *Pediatrics* 2008;122:500–06 CrossRef Medline
9. Thomas B, Eyssen M, Peeters R, et al. Quantitative diffusion tensor imaging in cerebral palsy due to periventricular white matter injury. *Brain* 2005;128:2562–77 CrossRef Medline
10. Nagae LM, Hoon AH Jr, Stashinko E, et al. Diffusion tensor imaging in children with periventricular leukomalacia: variability of injuries to white matter tracts. *AJNR Am J Neuroradiol* 2007;28:1213–22 CrossRef Medline
11. Palisano RJ, Rosenbaum P, Bartlett D, et al. Content validity of the expanded and revised Gross Motor Function Classification System. *Dev Med Child Neurol* 2008;50:744–50 CrossRef Medline
12. Eliasson AC, Krumlinde-Sundholm L, Rösblad B, et al. The Manual Ability Classification System (MACS) for children with cerebral palsy: scale development and evidence of validity and reliability. *Dev Med Child Neurol* 2006;48:549–54 CrossRef Medline
13. Wechsler D. *Manual for the Wechsler Intelligence Scale for Children-Revised*. New York: Psychological Corporation; 1974
14. Cattell R. *Culture Free Intelligence Test, Scale 2, Handbook*. Champaign: Institute of Personality and Ability Testing; 1949
15. Achenbach TM, Rescorla LA. *Manual for the ASEBA School-Age Forms and Profiles*. Burlington: University of Vermont, Research Center for Children, Youth, and Families; 2001
16. Wu M, Chang LC, Walker L, et al. Comparison of EPI distortion correction methods in diffusion tensor MRI using a novel framework. *Med Image Comput Assist Interv* 2008;11:321–29 Medline
17. Pierpaoli C, Walker L, Irfanoglu MO, et al. TORTOISE: an integrated software package for processing of diffusion MRI data. In: *Proceedings of the International Society for Magnetic Resonance in Medicine*, Stockholm, Sweden; May 1–7, 2010: 1597
18. Rohde GK, Barnett AS, Basser PJ, et al. Comprehensive approach for correction of motion and distortion in diffusion-weighted MRI. *Magn Reson Med* 2004;51:103–14 CrossRef Medline
19. Chang LC, Jones DK, Pierpaoli C. RESTORE: robust estimation of tensors by outlier rejection. *Magn Reson Med* 2005;53:1088–95 CrossRef Medline
20. Zhang H, Yushkevich PA, Rueckert D, et al. Unbiased white matter atlas construction using diffusion tensor images. *Med Image Comput Assist Interv* 2007;10:211–18 Medline
21. Wakana S, Caprihan A, Panzenboeck MM, et al. Reproducibility of quantitative tractography methods applied to cerebral white matter. *Neuroimage* 2007;36:630–44 CrossRef Medline
22. Hua K, Zhang J, Wakana S, et al. Tract probability maps in stereotaxic spaces: analyses of white matter anatomy and tract-specific quantification. *Neuroimage* 2008;39:336–47 CrossRef Medline
23. Mori S, Oishi K, Jiang H, et al. Stereotaxic white matter atlas based on diffusion tensor imaging in an ICBM template. *Neuroimage* 2008;40:570–82 CrossRef Medline
24. Winkler AM, Ridgway GR, Webster MA, et al. Permutation infer-

- ence for the general linear model. *Neuroimage* 2014;92:381–97 CrossRef Medline
25. Bleyenheuft Y, Grandin CB, Cosnard G, et al. **Corticospinal dysgenesis and upper-limb deficits in congenital hemiplegia: a diffusion tensor imaging study.** *Pediatrics* 2007;120:e1502–11 CrossRef Medline
 26. Glenn OA, Ludeman NA, Berman JI, et al. **Diffusion tensor MR imaging tractography of the pyramidal tracts correlates with clinical motor function in children with congenital hemiparesis.** *AJNR Am J Neuroradiol* 2007;28:1796–802 CrossRef Medline
 27. Trivedi R, Agarwal S, Shah V, et al. **Correlation of quantitative sensorimotor tractography with clinical grade of cerebral palsy.** *Neuroradiology* 2010;52:759–65 CrossRef Medline
 28. Chang MC, Jang SH, Yoe SS, et al. **Diffusion tensor imaging demonstrated radiologic differences between diplegic and quadriplegic cerebral palsy.** *Neurosci Lett* 2012;512:53–58 CrossRef Medline
 29. Cho HK, Jang SH, Lee E, et al. **Diffusion tensor imaging-demonstrated differences between hemiplegic and diplegic cerebral palsy with symmetric periventricular leukomalacia.** *AJNR Am J Neuroradiol* 2013;34:650–54 CrossRef Medline
 30. Lennartsson F, Holmström L, Eliasson AC, et al. **Advanced fiber tracking in early acquired brain injury causing cerebral palsy.** *AJNR Am J Neuroradiol* 2015;36:181–87 CrossRef Medline
 31. Rha DW, Chang WH, Kim J, et al. **Comparing quantitative tractography metrics of motor and sensory pathways in children with periventricular leukomalacia and different levels of gross motor function.** *Neuroradiology* 2012;54:615–21 CrossRef Medline
 32. Wang S, Fan G, Xu K, et al. **Potential of diffusion tensor MR imaging in the assessment of cognitive impairments in children with periventricular leukomalacia born preterm.** *Eur J Radiol* 2013;82:158–64 CrossRef Medline
 33. Yoshida S, Faria AV, Oishi K, et al. **Anatomical characterization of athetotic and spastic cerebral palsy using an atlas-based analysis.** *J Magn Reson Imaging* 2013;38:288–98 CrossRef Medline
 34. Lee JD, Park HJ, Park ES, et al. **Motor pathway injury in patients with periventricular leukomalacia and spastic diplegia.** *Brain* 2011;134:1199–210 CrossRef Medline
 35. Melhem ER, Hoon AH Jr, Ferrucci JT Jr, et al. **Periventricular leukomalacia: relationship between lateral ventricular volume on brain MR images and severity of cognitive and motor impairment.** *Radiology* 2000;214:199–204 CrossRef Medline
 36. Li K, Sun Z, Han Y, et al. **Fractional anisotropy alterations in individuals born preterm: a diffusion tensor imaging meta-analysis.** *Dev Med Child Neurol* 2015;57:328–38 CrossRef Medline

Decreased Superior Sagittal Sinus Diameter and Jugular Bulb Narrowing Are Associated with Poor Clinical Outcome in Vein of Galen Arteriovenous Malformation

G. Saliou, P. Dirks, R.H. Sacho, L. Chen, K. terBrugge, and T. Krings

ABSTRACT

BACKGROUND AND PURPOSE: Few clinical and imaging findings are known to be associated with poor outcome in neonates and infants with vein of Galen arteriovenous malformations. In the present consecutive series of 35 patients, we evaluated both the diameter of the superior sagittal sinus at onset and the diameter of the jugular bulb on follow-up as potential factors related to poor outcome.

MATERIALS AND METHODS: Thirty-five consecutive neonates and infants who were prospectively collected in a single-center data base were included in this review. Outcome was assessed by using the Bicêtre Outcome Score. Both the absolute diameter of the superior sagittal sinus and its ratio to the biparietal diameter were measured at onset, compared with age-matched controls, and correlated to patient outcome.

RESULTS: The diameter of the superior sagittal sinus at onset and its ratio to the biparietal diameter were significantly smaller in the vein of Galen arteriovenous malformation population compared with the matched population ($P = .0001$) and were correlated significantly with a risk of poor clinical outcome ($P = .008$). Development of jugular bulb narrowing was also related to poor clinical outcome ($P < .0001$).

CONCLUSIONS: Decreased superior sagittal sinus diameter may reflect a decrease of cerebral blood flow due to cerebral arterial steal and intracranial hydrovenous disorders. This finding may be considered cerebral blood flow deterioration and thus taken into consideration in the management decisions for patients with vein of Galen arteriovenous malformations. Likewise, our data suggest that progressive jugular bulb narrowing may indicate earlier intervention to prevent severe narrowing.

ABBREVIATIONS: SSS = superior sagittal sinus; VGAM = vein of Galen arteriovenous malformation

Vein of Galen aneurysmal malformations are rare congenital choroidal arteriovenous malformations.¹ In true Vein of Galen arteriovenous malformations (VGAMs), arteriovenous fistulas drain into an aberrantly persistent fetal median prosencephalic vein, coined the “vein of Markowski,”² which constitutes an embryonic precursor of the vein of Galen, thus

forcing the deep venous system to drain through persistent alternative embryonic routes, mainly the lateromesencephalic and lateropontine veins and the superior petrosal sinus.³ VGAMs are supposed to be associated with high morbidity and mortality.^{4–8} Lasjaunias et al^{9,10} proposed a neonatal scoring system for these malformations, a multiorgan evaluation, to decide the indication and timing of treatment. Certain clinical and imaging findings, such as a low neonatal score,^{9,10,11} encephalomalacia,^{10–12} intraparenchymal calcifications,¹⁰ and the angioarchitecture of the VGAM (choroidal type nidus and jugular stenosis without cavernous drainage), have been associated with a poorer prognosis.

In the present series, we tried to determine additional signs identifiable on cross-sectional imaging that may be associated with poor clinical outcome. Anecdotally, we have observed that the diameter of the superior sagittal sinus (SSS) in babies with VGAM appeared smaller compared with children without cere-

Received May 28, 2015; accepted after revision December 16.

From the Department of Neuroradiology (G.S., R.H.S., L.C., K.T., T.K.), Toronto Western Hospital and University Health Network, Toronto, Ontario, Canada; Department of Neuroradiologie (G.S.), Centre Hospitalier Universitaire Bicêtre, Le Kremlin-Bicêtre, France; and Division of Neurosurgery (P.D.), The Hospital for Sick Children, Toronto, Ontario, Canada.

Guillaume Saliou was responsible for conception and design, acquisition of data and drafting the article, statistical analysis, and analysis and interpretation of data. Peter Dirks was responsible for conception and design, acquisition of data and drafting the article, and analysis and interpretation of data. Raphael H. Sacho was responsible for acquisition of data and drafting the article and analysis and interpretation of data. Long Chen was responsible for statistical analysis, drafting the article, and analysis and interpretation of data. Karel terBrugge was responsible for acquisition of data and drafting the article and analysis and interpretation of data. Timo Krings was responsible for conception and design, acquisition of data and drafting the article, and analysis and interpretation of data.

Paper previously presented in part at: ABC-WIN Conference, January 18–23, 2015; Val d'Isère, France.

Please address correspondence to Guillaume Saliou, MD, PhD, Department of Neuroradiology, Toronto Western Hospital and University Health Network, 3MCL-429, 399 Bathurst St, Toronto, ON, M5T 2S8 Canada; e-mail address: guillaume.saliou@bct.aphp.fr

<http://dx.doi.org/10.3174/ajnr.A4697>

bral arteriovenous malformations and that on angiography, a delayed and decreased cortical venous drainage through the SSS was present. We presumed that these findings were related to the downstream venous hypertension induced by the arteriovenous shunt; therefore, it could be an indirect marker for high-flow angiopathy, venous congestion, and arterial steal, which, in turn, may be associated with poor clinical outcome. Therefore, in the present series, we wanted to evaluate, in a consecutive series, whether a smaller diameter of the superior sagittal sinus, which can already be present at birth in babies with VGAM, can predict outcome. In addition, we evaluated whether jugular bulb stenosis or occlusion, which are more likely to appear during the first year of life, can predict outcome.

MATERIALS AND METHODS

Patient Population

The patient cohort was extracted from a data base of vein of Galen malformations managed at a single center (The Hospital for Sick Children, Toronto, Canada). Thirty-five consecutive children with vein of Galen aneurysmal malformation were included in this study from January 2004 to June 2014 after institutional ethics board approval was obtained. Only “true” VGAMs were included (ie, pediatric patients with pial AVMs that drained into the vein of Galen were not included).

All patients who were treated with embolization were treated with intra-arterial *N*-butyl cyanoacrylate injection by the 2 senior authors with the patient under general anesthesia. Embolization was performed in an attempt to control heart failure or hydrodynamic disorder in the neonatal period or to enable normal psychomotor development as previously proposed.^{9,10}

Clinical Features

We retrospectively reviewed the following clinical data: sex, scoring (Bicêtre neonatal score),^{9,10} and hemodynamic parameters at clinical presentation (cardiac failure and suprasystemic pulmonary hyperpressure). The follow-up outcome for all patients was assessed by using the Bicêtre Outcome Score (Appendix).^{9,10} Poor outcome was defined as a Bicêtre Outcome Score of 0 or 1.

Radiologic Features

Imaging review included conventional MR imaging and digital subtraction angiography. For the purpose of this study, we focused on first imaging (onset) and follow-up MR imaging performed between 12 and 24 months of age.

The following angioarchitectural features were studied on DSA before embolization: type of VGAM (ie, mural or choroidal) and type of flow (high or low) and superior sagittal sinus reflux. A VGAM associated with cardiac failure was considered high-flow. The following features were studied on first MR imaging: superior sagittal sinus diameter and encephalomalacia. The measurement of the SSS diameter was performed by the same operator (G.S.), who had >10 years' experience in neuroradiology. The maximal transverse diameter was measured. If a cortical vein reached the sinus at this level, the measurements were performed in an adjacent region of the sinus without cortical veins, to avoid measurement errors. In vein of Galen malformation, the normal triangular shape of the sinus was often not present and was replaced with

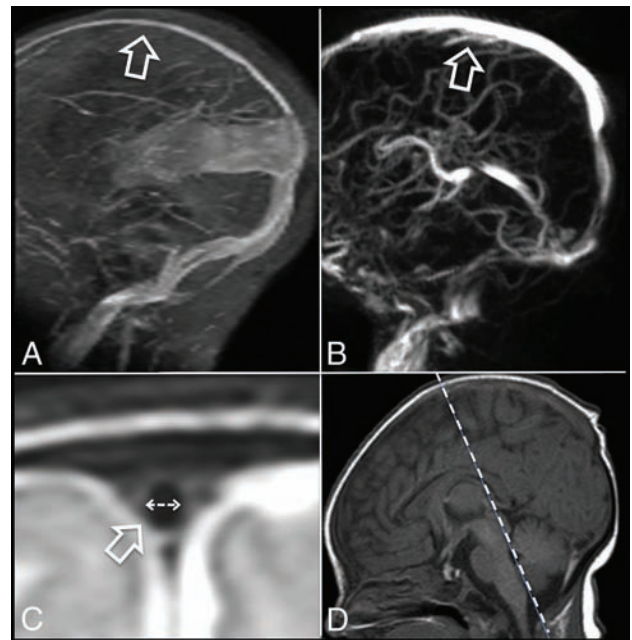


FIG 1. Decreased diameter of the superior sagittal sinus in a patient with a vein of Galen aneurysmal malformation at onset (A, arrow) compared with an age-matched control (B, arrow). The width of the superior sagittal sinus was assessed on a T2-TSE-weighted sequence (flow void; C, arrow) in the coronal view crossing the posterior part of the brain stem (D, dotted line) and indicates significant reduction in the vein of Galen aneurysmal malformation.

an ovoid sinus. “Encephalomalacia” was defined as any focal or regional cerebral white and gray matter change with atrophy on imaging.

Because the size of the skull and every organ grows according to the infant’s age, we related the SSS diameter, as measured on coronal T2-TSE sequences, to the biparietal diameter. Thus, the SSS index was calculated as the width of the flow void in the sagittal sinus on coronal T2 spin-echo/biparietal diameter \times 100. The SSS width was always assessed on a coronal view in a section passing through the tectum (Fig 1), and care was taken that in all cases, a similar coronal angulation was used. We also measured the SSS index in an age-matched population of 35 children without VGAM who underwent MR imaging for a reason other than vascular disease after institutional ethics board approval was obtained. The MRIs were performed for psychomotor delay (19 patients), seizure (11 patients), and suspicion of encephalitis (5 patients). All these MRI findings were considered normal. These patients were chosen because they were the same age as those in our population study: fewer than 5 days difference for the patients younger than 2 months of age; 15 days, for those younger than 6 months of age; 1 month, for those younger than 1 year of age; and 2 months, after 1 year of age. We considered that an SSS index inferior or equal to the 10th percentile of the matched population reflected a decrease in the SSS diameter.

The percentage of jugular bulb narrowing was assessed on CTA or DSA as the smallest diameter of the jugular bulb divided by the diameter of the jugular veins 2 cm below the jugular foramen (Fig 2). We considered bilateral narrowing of >75% severe. Bilateral narrowing of <75% or unilateral narrowing was not considered a severe narrowing.

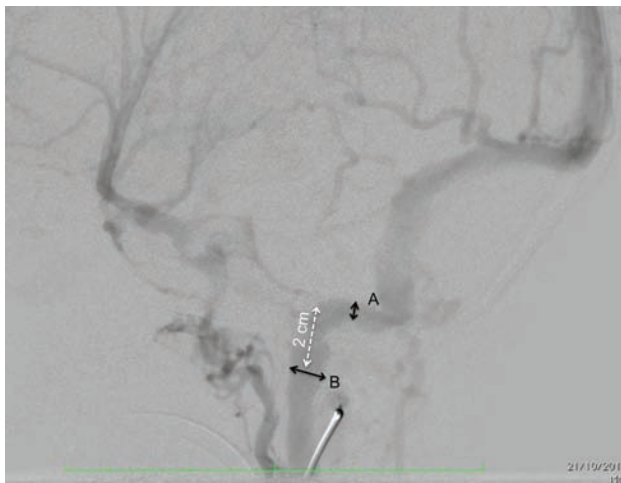


FIG 2. Method of assessment of jugular bulb stenosis at angiography. A corresponds to the maximal stenosis of the jugular bulb. B corresponds to the maximal diameter of the jugular vein at a point 2 cm (white dotted arrow) below its exit from the jugular foramina. The percentage of stenosis was calculated as $A/B \times 100$.

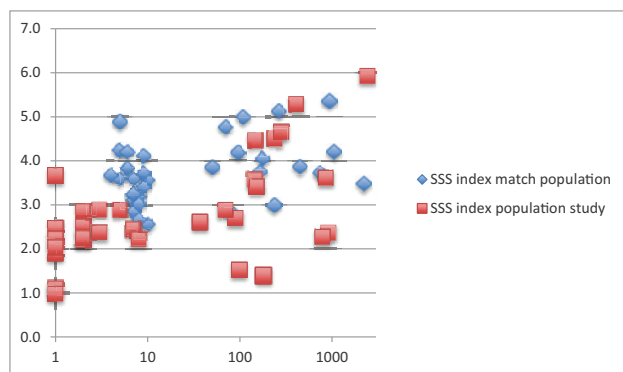


FIG 3. SSS index in the study population (red squares) and the matched population (blue diamonds) according to the age of the patient (days).

Statistical Analysis

Descriptive statistics were performed to summarize the distribution of clinical features across patients with and without decreased SSS diameter (Table). The distribution of categorical variables was described by frequencies and percentages; continuous and normally distributed variables, by means and SDs; and continuous and non-normally distributed variables, by medians and interquartile ranges. Univariate statistics were performed via χ^2 or Fisher exact tests (comparison of categorical variables) to assess the associations among clinical features, SSS index, and jugular bulb stenosis. To evaluate whether the SSS index in VGAM was decreased due only to an increase of the biparietal diameter (for instance in case of hydrocephalus, frequently observed in VGAM), we also compared the absolute number of the diameter of the SSS in the VGAM population with the matched population, without taking into account the biparietal diameter. A Student *t* test was performed to assess a difference between the population with a VGAM and the matched population regarding the SSS index. A *P* value $< .05$ was statistically significant.

RESULTS

Between January 2000 and June 2014, 35 consecutive children were identified who fulfilled our inclusion criteria. We had a median clinical follow-up of 356 days (interquartile range, 10.5–195.5 days). There were 12 (34%) females and 23 (66%) males. The median age at diagnosis was 5 days (interquartile range, 1.5–150.5 days). There was no statistical difference with the control group, in which the median age was 9 days (interquartile range, 7–136.5 days).

On the basis of the control group, we determined the 10th percentile of the SSS index to be 3. Consequently, we considered that an SSS index of ≤ 3 indicated a decreased SSS diameter. Twenty-one (60%) patients had an SSS index of ≤ 3 on their first MR imaging. Overall, 6 patients had bilateral jugular bulb stenosis of $>75\%$. However, only 1 of 20 patients who were scanned in their first month of life exhibited this bilateral stenosis, whereas in this subgroup of 20 patients, 16 already had an SSS index of <3 .

The SSS index was significantly smaller in the VGAM population study group compared with the matched population ($P = .0001$) (Fig 3). The comparison of the absolute numbers of the diameter of the SSS in the VGAM population with those in the matched population, without taking into account the biparietal diameter, also showed significant ($P = .03$) differences (median, 2.35 mm; interquartile range, 2–3 mm; and median, 3.6 mm; interquartile range, 2.9–4.45 mm in the VGAM group and matched population, respectively).

Factors associated with a risk of poor clinical outcome were presentation with cardiac failure ($P = .043$), an SSS index of ≤ 3 at onset ($P = .008$), and presentation with encephalomalacia ($P = .004$).

As only 1 child presented with bilateral jugular bulb narrowing, no statistical relevance was found between this feature and poor outcome at onset; however, bilateral jugular bulb stenosis at 1–2 years of age was associated with poor clinical outcome ($P < .0001$).

Main findings on statistical analysis are summarized in the Table.

DISCUSSION

Multiple factors have been associated with poor clinical outcome in babies with vein of Galen arteriovenous malformation.^{10–12} Among them, a Bicêtre neonatal score of <12 , parenchymal changes or calcifications as a sign of manifest brain damage, arterial steal with visible diffusion abnormalities before treatment, cardiac failure, and multiorgan failure have been described. To our knowledge, this is the first series to report that decreased diameter of the SSS in VGAM at diagnosis and evolution of jugular bulb narrowing with time are also associated with poor clinical outcome.

In the present series, the overall population with a VGAM tended to have a smaller superior sagittal sinus diameter, and within the group of patients with VGAM, a decreased diameter was associated with poor clinical outcome. In addition, patients who were seen to develop jugular bulb narrowing also had an unfavorable clinical outcome.

Three aspects distinguish the jugular bulb narrowing from the SSS diameter narrowing: Unlike the focal jugular bulb narrowing,

Summary of the statistical results

Summary	P Value
SSS index decreased at onset (ie, <10th percentile of matched population)	
Superior sagittal sinus reflux on angiography at onset	.357
Type of the vein of Galen malformation at onset (high-flow vs slow-flow)	.072
Poor clinical outcome (last clinical assessment)	.004
Risk of bilateral jugular bulb stenosis >75% at 1–2 years	.757
Angioarchitecture at onset	
Bilateral jugular bulb stenosis at onset	.757
Encephalomalacia at onset	.008
Type of the vein of Galen malformation at onset (high-flow vs slow-flow)	.043
Bilateral jugular bulb stenosis at 1–2 years on MRI	<.0001
SSS index in the present series and matched population	.0001

the decreased diameter of the SSS was noted along the entire length of the SSS. Second, while the SSS diameter decrease was typically present at onset, jugular bulb narrowing almost always developed later during the course of the disease. Third, while the arterialized blood flow from the VGAM shunt did use the jugular bulbs as an outflow pathway, it did not use the superior sagittal sinus (with the exception made for rare cases where SSS reflux was noted).

Although at present the cause and nature of the venous diameter reduction remain unclear, the above-mentioned considerations make it likely that different causes may be present. While there are no pathologically proved concepts of why the SSS diameter is decreased or why this is associated with poor clinical outcome, one may, however, propose the following hypotheses: First, the decreased diameter is related to decreased volume of venous flow and thus a collapse of the SSS. Because the SSS drains most cortical veins, the increase of intracranial pressure, the high-flow cardiac failure, and the arterial steal toward the shunt may lead to a decreased blood flow through the brain and thus into the sinuses. Second, an increase in intracranial pressure may be responsible for external compression of the SSS. Given these 2 hypotheses, SSS narrowing may be secondary to cerebral blood flow deterioration and thus explain why those patients had a worse outcome. Because patients with chronic hydrovenous disorders and high-flow cardiac failure^{10–12} are known to be at risk of psychomotor delay, the apparent narrowing of the SSS may therefore not be an independent predictor but rather an imaging correlate of the underlying pathologic mechanism. One may, however, presume that the SSS narrowing has already occurred early in the course of the disease and thus may represent an imaging correlate that indicates an early intervention. Thus, we believe that the described imaging findings may be an important decision-making tool in the discussion of the optimal treatment window.

Alternatively, the narrowing of the SSS may be related to a true stenosis, similar to the believed cause of the jugular bulb narrowing. This may be related to in utero reflux, though we have not observed this in this retrospective series. It is unlikely that both findings have the same underlying cause: Only a few patients had bilateral jugular bulb stenosis at onset (6 patients, 17%). However, 66% already had decreased SSS diameter.

Therefore, we hypothesize that the decreased flow in the SSS was a secondary reflection of a combination of increased intracranial pressure, arterial steal, and low cardiac output. Thus, it may represent an important imaging correlate that may help predict

outcome in the initial imaging work-up of babies with VGAM. This can be of particular importance when contemplating a more urgent treatment to control cerebral blood flow and/or early hydrovenous disorders. Conversely, a normal SSS diameter may support delayed treatment.

Jugular bulb stenosis or occlusion has previously been called “dysmaturation of the jugular bulbs.”⁹ In our experience, this progressive narrowing is commonly observed in patients with VGAM. The influence of abnormal skull

base growth maturation caused by macrocrania as opposed to a venous high-flow angiopathy has been put forward as a potential cause.^{9,13} Jugular bulb narrowing may protect the heart by decreasing the venous pressure arising in the right heart. If the jugular bulb stenosis is severe, drainage of the VGAM and the brain may compete and venous congestion can be present,⁹ leading to chronic venous ischemia, delayed calcifications, and the so-called “pseudophlebitic” appearance of the cortical veins.

CONCLUSIONS

Decreased diameter of the superior sagittal sinus at presentation or jugular bulb narrowing or occlusion in 1- and 2-year-old children is associated with poor clinical outcome in patients with VGAM. The first may reflect a decrease of the cerebral blood flow due to cerebral arterial steal and intracranial hydrovenous disorders. At presentation, this finding could be considered a manifestation of cerebral blood flow deterioration and taken into consideration in the management decisions for patients with VGAM, even if the patients still have a good psychomotor development. The second may lead to pial venous congestion.

APPENDIX

Bicêtre Outcome Score

0. Death (D)

1. Severe neurologic symptoms, mental retardation of more than 20% (SNS), specialized school, and/or cardiac failure unstable despite treatment
2. Permanent minor neurologic symptoms, mental retardation of up to 20%, nonpermanent neurologic symptoms under treatment (MNS), normal school with support, and/or cardiac failure stabilized with treatment
3. Transient neurologic symptoms, not treated (TNS), and/or asymptomatic cardiac overload under treatment
4. Minimal non-neurologic symptoms, not treated (MS), and/or asymptomatic enlargement of the cardiac silhouette
5. Normal (N).

REFERENCES

1. Alvarez H, Garcia Monaco R, Rodesch G, et al. **Vein of Galen aneurysmal malformations.** *Neuroimaging Clin N Am* 2007;17:189–206 CrossRef Medline
2. Markowski J. **Entwicklung der Sinus durae matris und der Hirnvenen des Menschen.** *Bulletin International de l'Academie des Sci-*

ences et des Lettres. *Classe des Sciences Mathe' matiques et Naturelles. Serie B: Sciences Naturelles* 1921;1–269

3. Lasjaunias P, Garcia-Monaco R, Rodesch G, et al. **Deep venous drainage in great cerebral vein (vein of Galen) absence and malformations.** *Neuroradiology* 1991;33:234–38 CrossRef Medline
4. Berenstein A, Masters LT, Nelson PK, et al. **Transumbilical catheterization of cerebral arteries.** *Neurosurgery* 1997;41:846–50 CrossRef Medline
5. Dahdah NS, Alesseh H, Dahms B, et al. **Severe pulmonary hypertensive vascular disease in two newborns with aneurysmal vein of Galen.** *Pediatr Cardiol* 2001;22:538–41 CrossRef Medline
6. Frawley GP, Dargaville PA, Mitchell PJ, et al. **Clinical course and medical management of neonates with severe cardiac failure related to vein of Galen malformation.** *Arch Dis Child Fetal Neonatal Ed* 2002;87:F144–49 CrossRef Medline
7. Johnston IH, Whittle IR, Besser M, et al. **Vein of Galen malformation: diagnosis and management.** *Neurosurgery* 1987;20:747–58 CrossRef Medline
8. Jones BV, Ball WS, Tomsick TA, et al. **Vein of Galen aneurysmal malformation: diagnosis and treatment of 13 children with extended clinical follow-up.** *AJNR Am J Neuroradiol* 2002;23:1717–24 Medline
9. Lasjaunias PL, Berenstein A, terBrugge KG. **Vein of Galen aneurysmal malformation.** In: Lasjaunias PL, Berenstein A, terBrugge KG. *Surgical Neuroangiography: Clinical and Interventional Aspects in Children.* 2nd ed. Berlin: Springer-Verlag; 2006:105–226
10. Lasjaunias PL, Chng SM, Sachet M, et al. **The management of vein of Galen aneurysmal malformations.** *Neurosurgery* 2006;59(5 suppl 3):S184–94; discussion S3–13 Medline
11. Geibprasert S, Krings T, Armstrong D, et al. **Predicting factors for the follow-up outcome and management decisions in vein of Galen aneurysmal malformations.** *Childs Nerv Syst* 2010;26:35–46 CrossRef Medline
12. Li AH, Armstrong D, terBrugge KG. **Endovascular treatment of vein of Galen aneurysmal malformation: management strategy and 21-year experience in Toronto.** *J Neurosurg Pediatr* 2011;7:3–10 CrossRef Medline
13. Raybaud CA, Hald JK, Strother CM, et al. **Aneurysms of the vein of Galen: angiographic study and morphogenetic considerations [in French].** *Neurochirurgie* 1987;33:302–14 Medline

Development of the Fetal Vermis: New Biometry Reference Data and Comparison of 3 Diagnostic Modalities—3D Ultrasound, 2D Ultrasound, and MR Imaging

 E. Katorza,  E. Bertucci,  S. Perlman,  S. Taschini,  R. Ber,  Y. Gilboa,  V. Mazza, and  R. Achiron



ABSTRACT

BACKGROUND AND PURPOSE: Normal biometry of the fetal posterior fossa rules out most major anomalies of the cerebellum and vermis. Our aim was to provide new reference data of the fetal vermis in 4 biometric parameters by using 3 imaging modalities, 2D ultrasound, 3D ultrasound, and MR imaging, and to assess the relation among these modalities.

MATERIALS AND METHODS: A retrospective study was conducted between June 2011 and June 2013. Three different imaging modalities were used to measure vermis biometry: 2D ultrasound, 3D ultrasound, and MR imaging. The vermian parameters evaluated were the maximum superoinferior diameter, maximum anteroposterior diameter, the perimeter, and the surface area. Statistical analysis was performed to calculate centiles for gestational age and to assess the agreement among the 3 imaging modalities.

RESULTS: The number of fetuses in the study group was 193, 172, and 151 for 2D ultrasound, 3D ultrasound, and MR imaging, respectively. The mean and median gestational ages were 29.1 weeks, 29.5 weeks (range, 21–35 weeks); 28.2 weeks, 29.05 weeks (range, 21–35 weeks); and 32.1 weeks, 32.6 weeks (range, 27–35 weeks) for 2D ultrasound, 3D ultrasound, and MR imaging, respectively. In all 3 modalities, the biometric measurements of the vermis have shown a linear growth with gestational age. For all 4 biometric parameters, the lowest results were those measured by MR imaging, while the highest results were measured by 3D ultrasound. The inter- and intraobserver agreement was excellent for all measures and all imaging modalities. Limits of agreement were considered acceptable for clinical purposes for all parameters, with excellent or substantial agreement defined by the intraclass correlation coefficient.

CONCLUSIONS: Imaging technique–specific reference data should be used for the assessment of the fetal vermis in pregnancy.

ABBREVIATIONS: AP = anteroposterior; ICC = intraclass correlation coefficient; SA = surface area; SI = superoinferior; US = ultrasound; VCI = volume contrast imaging

Imaging of the fetal posterior fossa is considered a routine part of the fetal sonographic examination. Normal sonographic biometry and normal morphology of the posterior fossa rule out most major anomalies of the fetal cerebellum and vermis.¹ However, in case of an abnormal posterior fossa, evaluation of the vermian biometry and morphology is of paramount im-

portance, considering the wide clinical spectrum of this imaging finding.²

Fetal posterior fossa anomalies range from benign asymptomatic conditions to severe abnormalities associated with neurologic impairment.^{3–6} The most frequent of these anomalies, Blakes pouch cyst, vermian hypoplasia, and Dandy-Walker malformation, have a similar imaging appearance^{7,8} but different vermian biometry and, therefore, different prognoses.⁹

Many anomalies of the posterior fossa can be depicted with sonography alone.¹⁰ Although the standard axial imaging planes may detect most anomalies of the posterior fossa, the diagnosis of the exact type of abnormality might be challenging because a clear visualization of the midsagittal plane is essential. Subtle changes in the morphology of the vermis are hidden by this axial view, and this feature can lead to false-positive diagnoses of vermian pathologies.^{11,12}

Our group has proposed using the transabdominal sagittal plane for visualization of the fetal vermis,¹³ while Malinger et al¹⁴

Received August 27, 2015; accepted after revision January 5, 2016.

From the Antenatal Diagnostic Unit (E.K., S.P., R.B., Y.G., R.A.), Department of Obstetrics and Gynecology, Haim Sheba Medical Center, Sackler School of Medicine, Tel Aviv University, Israel; and Prenatal Medicine Unit (E.B., S.T., V.M.), Department of Obstetrics and Gynecology, Modena Hospital, Modena, Italy.

E. Katorza and E. Bertucci contributed equally to this study.

Please address correspondence to Sharon Perlman, MD, Antenatal Diagnostic Unit, Department of Obstetrics and Gynecology, Sheba Medical Center, Tel HaShomer, Ramat Gan, Israel; e-mail: drsharonperlman@gmail.com; sharoni5@yahoo.com

 Indicates article with supplemental on-line tables.

<http://dx.doi.org/10.3174/ajnr.A4725>

reported their experience with the transvaginal approach. Vinals et al¹⁵ used volume contrast imaging (VCI) on plane C to construct nomograms for the normal fetal vermis. Our group used this same VCI on plane C technique to compare normal and abnormal fetal vermis measurements, and we concluded that the 3D sonographic technique has many advantages in the detection of posterior fossa anomalies.¹⁶ It allows off-line evaluation and reconstruction of images, even with abnormal angles when the midsagittal plane is difficult to obtain.

MR imaging is a well-known complementary tool in the prenatal diagnosis of fetal brain abnormalities. The challenges described above in achieving a good visualization of the midsagittal

plane in prenatal sonography led to frequent use of this tool to assess, more accurately, the structures of the posterior fossa and improve prenatal diagnosis.

Various nomograms have been developed to establish normal biometric measures of the fetal vermis by using ultrasound (US) or MR imaging.¹⁷⁻¹⁹ None of these nomograms provided data regarding all 4 vermian biometric parameters. Moreover, there were no comparisons among all 3 imaging modalities.²⁰

The aims of our study were the following: to provide normal reference biometric data of the fetal vermis in 4 biometric parameters for 3 imaging modalities, to evaluate the reproducibility of the vermian biometry, and to compare the measurements obtained by 2D sonography, 3D sonography, and MR imaging.

MATERIALS AND METHODS

Population

A retrospective study was conducted between June 2011 and June 2013.

All sonographic examinations were performed during routine pregnancy follow-up and were in addition to the standard axial views. MR imaging examinations were performed due to increased risk of suspected cerebral pathology, including suspected infectious fetopathy, suspected sonographic cerebral abnormality, positive family history, a previous pregnancy with CNS abnormality, decreased fetal movements, polyhydramnios, and extracranial anomalies such as club foot, cleft lip, and/or palate. However, there was no evidence of intracranial abnormalities.

The inclusion criteria for the 3 groups were the following: singleton pregnancy, good dating, estimated fetal weight within the 10th to 90th percentiles, normal obstetric course (no evidence of intra-uterine growth restriction or macrosomia or pregnancy-related hypertensive disorders or gestational diabetes mellitus), absence of maternal disease (healthy women without any background illness such as hypercoagulability state, hypertension, diabetes, or other systemic disease), clinically normal fetus at birth (normal Apgar scores at birth, normal neonate physical examination findings), and no known neurologic family history. A detailed sonographic scan was performed to rule out fetal malformations. Only 1 measurement was used for each patient with each gestational week in each imaging technique.

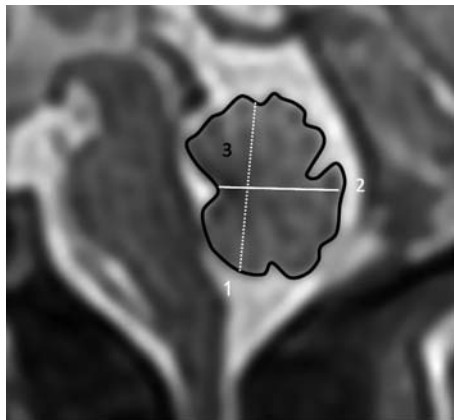


FIG 1. Magnification of the fetal posterior fossa and vermis and demonstration of biometric parameters. 1) Maximum superoinferior diameter. 2) Anteroposterior diameter. 3) Perimeter and surface area.

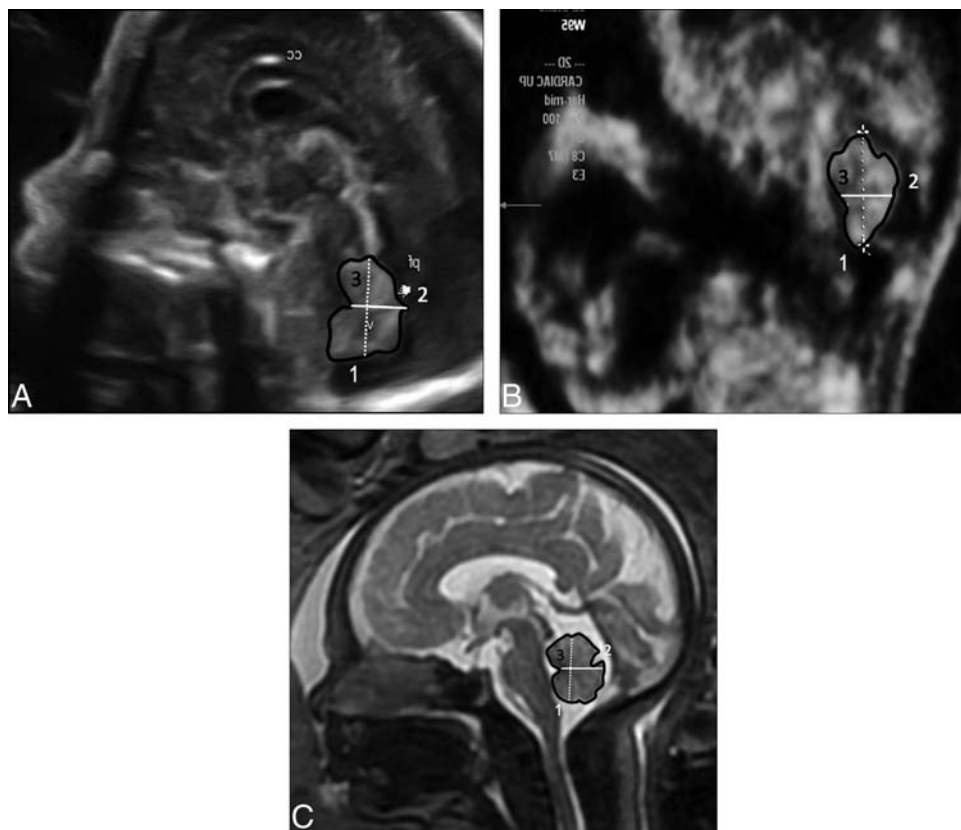


FIG 2. Midsagittal view of the fetal brain demonstrating the vermis. A, 2D US. B, 3D US. C, MR imaging.

Table 1: Median, 5th, and 95th percentiles for SI measurements

Gestational Age (wk)	Imaging Modality								
	US 2D			US 3D			MRI		
	%5	Median	%95	%5	Median	%95	%5	Median	%95
21	10.69	11.95	12.57	11.10	12.30	14.60			
22	10.42	12.72	14.40	11.50	13.60	14.90			
23	11.71	12.79	13.84	13.00	14.40	16.50			
24	13.33	13.79	14.82	13.40	15.35	17.50			
25	13.85	15.17	16.66	14.50	16.00	17.80			
26	13.75	16.09	18.45	15.60	16.80	19.50			
27	14.05	17.07	18.78	16.70	18.70	20.20	13.30	14.13	15.05
28	16.08	17.09	19.72	16.30	18.80	23.80	13.66	14.58	15.73
29	17.29	18.72	20.33	18.10	20.00	22.20	13.25	16.02	17.54
30	17.83	18.56	19.62	18.40	20.50	23.60	15.77	17.38	20.76
31	18.03	19.34	20.75	18.10	21.30	23.80	16.16	18.02	19.34
32	17.68	19.33	20.59	19.00	21.40	26.60	16.75	18.67	20.12
33	16.78	20.93	22.94	20.70	22.70	24.50	18.37	19.48	21.21
34	19.11	20.38	23.34	20.40	22.30	28.50	17.90	19.56	21.30
35	19.62	21.75	24.29	20.90	22.00	27.00	18.27	19.83	23.29

Note:—%5 indicates 5th percentile; %95, 95th percentile.

Table 2: Median, 5th, and 95th percentiles for AP measurements

Gestational Age (wk)	Imaging Modality								
	US 2D			US 3D			MRI		
	%5	Median	%95	%5	Median	%95	%5	Median	%95
21	7.08	7.79	8.71	5.70	8.10	10.30			
22	7.51	9.51	10.62	7.40	9.15	12.40			
23	7.27	8.72	10.25	6.30	8.80	11.00			
24	8.96	9.49	10.64	8.60	9.85	11.00			
25	9.58	10.73	13.17	9.90	10.50	14.60			
26	8.76	11.28	14.17	8.10	11.30	12.80			
27	10.06	11.44	12.69	9.30	12.50	14.80	9.11	9.33	11.10
28	10.75	12.32	14.94	9.20	12.30	15.90	8.90	9.97	12.04
29	10.09	12.61	15.01	11.20	12.80	14.40	8.93	11.05	13.28
30	11.06	13.36	14.94	10.70	13.70	16.80	10.39	11.92	15.01
31	12.69	14.01	15.81	11.80	14.60	18.00	11.07	12.30	13.96
32	11.93	13.87	17.38	10.70	15.20	18.40	11.40	13.04	13.90
33	12.63	15.11	17.83	11.80	13.05	19.70	11.91	13.26	15.22
34	12.36	15.94	17.82	12.00	15.60	21.40	11.18	13.77	15.10
35	13.84	16.40	17.40	12.60	15.75	18.90	12.70	14.83	17.17

Note:—%5 indicates 5th percentile; %95, 95th percentile.

Table 3: Median, 5th, and 95th percentiles for perimeter measurements

Gestational Age (wk)	Imaging Modality								
	US 2D			US 3D			MRI		
	%5	Median	%95	%5	Median	%95	%5	Median	%95
21	36.20	40.94	44.80	37.20	41.70	54.60			
22	37.04	46.80	48.64	40.60	47.30	49.40			
23	41.20	45.07	49.39	41.50	46.90	55.20			
24	48.10	49.89	51.80	45.00	49.20	56.70			
25	46.74	52.41	62.86	48.80	53.30	63.30			
26	50.00	57.87	65.98	50.80	58.30	68.60			
27	48.97	59.08	67.10	51.40	64.00	69.30	50.05	50.67	57.75
28	53.26	60.42	69.40	57.60	66.20	82.60	48.22	53.30	58.16
29	58.58	65.42	69.37	58.80	66.40	77.20	50.58	56.85	61.09
30	60.08	64.98	70.36	57.80	70.20	82.80	55.07	61.10	72.13
31	61.18	65.67	71.97	64.10	71.10	82.40	59.38	66.21	71.93
32	62.13	67.31	77.88	65.30	74.60	96.10	61.20	68.11	73.79
33	68.13	71.38	76.83	73.70	77.95	82.50	64.98	70.90	78.33
34	67.05	73.97	80.43	66.50	80.10	92.80	67.21	71.06	83.00
35	70.20	75.19	79.16	68.50	79.70	100.20	69.44	75.93	86.11

Note:—%5 indicates 5th percentile; %95, 95th percentile.

Table 4: Median, 5th, and 95th percentiles for SA measurements

Gestational Age (wk)	Imaging Modality								
	US 2D			US 3D			MRI		
	%5	Median	%95	%5	Median	%95	%5	Median	%95
21	82.41	99.27	112.76	70.00	98.00	126.00			
22	92.43	114.88	131.10	95.00	125.00	141.00			
23	100.38	125.18	146.12	92.00	119.00	164.00			
24	130.89	138.14	154.26	118.00	140.50	175.00			
25	135.91	170.76	198.12	127.00	155.00	233.00			
26	139.84	189.49	234.09	150.00	193.00	215.00			
27	158.35	198.22	234.51	176.00	223.00	255.00	127.08	143.50	152.34
28	182.56	222.26	293.91	177.00	218.00	376.00	132.66	157.32	176.64
29	215.82	246.64	293.68	199.00	235.00	319.00	140.89	175.90	204.92
30	228.12	255.40	282.77	223.00	286.00	330.00	170.35	196.48	251.86
31	240.25	268.21	299.06	219.00	298.00	355.00	181.44	214.24	239.03
32	241.17	282.90	330.94	263.00	297.00	412.00	202.60	229.60	272.65
33	274.90	325.12	370.45	295.00	308.00	383.00	207.49	246.18	266.11
34	283.93	340.38	405.17	256.00	327.00	540.00	224.95	246.21	322.73
35	302.87	350.00	392.47	280.00	323.00	478.00	242.75	279.97	363.32

Note:—%5 indicates 5th percentile; %95, 95th percentile.

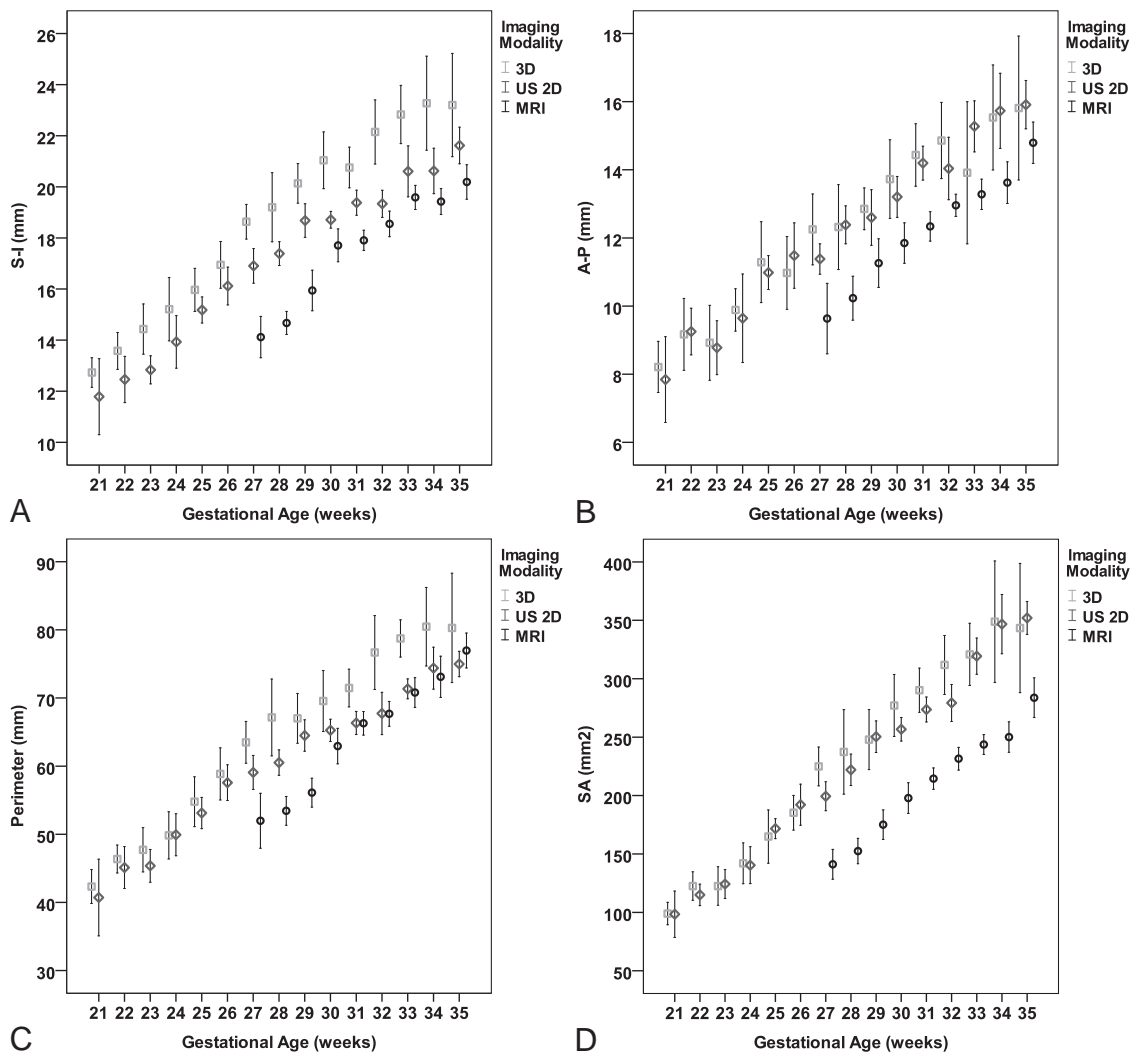


FIG 3. Comparison of measurements (mean \pm SD, 95% CI) obtained by 2D US, 3D US, and MR imaging. A, S-I. B, AP. C, Perimeter. D, SA.

The measurements of vermian parameters were performed according to the following anatomic landmarks: 1) The maximum superoinferior (SI) diameter, the greatest height of the vermis, which is generally parallel to the axis of the brain stem; 2) maximum anteroposterior (AP) diameter from the peak of the fourth ventricle, the fastigium, to the maximal AP diameter; 3) perimeter, the track line that follows vermian fissures; and 4) surface area, the same peripheral line that calculates surface area. All 4 parameters of the fetal vermis were measured at the same landmarks for each technique (Fig 1).

For each study group, all measurements were performed by a single operator. To evaluate the reproducibility of measurements, an arbitrary sample of 50 fetuses was evaluated twice by the first operator and then by a second operator. Each operator was unaware of the results obtained by the other.

Imaging Technique and Measurements

Sonography. All patients were scanned by using a Voluson 730 Expert or a Voluson E8 (GE Medical Systems, Kretz Ultrasound, Zipf, Austria) with a transabdominal transducer of 4–8 MHz or a 5- to 9-MHz transvaginal probe.

2D Technique. The fetal brain was scanned in a midsagittal plane by using the transfontanel approach. A true midsagittal image of the entire vermis is defined as a plane of a section that passes

through the rostral and caudal convexities at the levels of the superior, middle, and inferior portion of the vermis. The fastigium should be visualized in this plane.

According to Achiron et al,¹³ the midsagittal view includes the corpus callosum, the cavum septi pellucidi, and the brain stem–vermis plane. At the brain stem–vermis level, attention was paid to include the rostral part of the thalamus, the midbrain, the pons, the medulla oblongata, the fourth ventricle, and the cerebellar vermis (Fig 2A).

3D Technique. After a standard 2D examination, 3D volumes were acquired for off-line computer evaluation.¹⁰ Before we acquired the volume, the contrast of the 2D image was optimized by activating the harmonic function with high frequency, low gain, and high contrast, to enhance tissue interfaces. The 3D image was acquired during fetal rest in the absence of fetal movements, and the standard volume sweep angle was 55°. The starting image was in the axial plane at the level of the transverse cerebellar diameter. The static VCI on plane C was rebuilt, and a perfect midsagittal view was obtained. Subsequently, the volume measurements were stored, and analysis was performed off-line with 4D View, Version 7.0 software (GE Healthcare, Kretz Ultrasound).

After obtaining a measurement of the volume of the fetal brain in the axial plain, we placed the reference dot in the A reference image in the middle of the vermis. Afterward, the skull was rotated along the z-axis until the midline was horizontal, and the dot of interest was placed in the middle of the vermis in the B reference image. Finally, the skull was rotated again along the z-axis until the midline was again horizontal. The image was magnified to the maximal size available, and biometric measurements were performed (Fig 2B).

MR Imaging. Scans were obtained by using a 1.5T system (Optima; GE Healthcare). Single-shot fast spin-echo T2-weighted sequences in 3 orthogonal planes were performed with the following parameters: section thickness, 3 mm; no gap; flexible coil (8-channel cardiac coil); matrix, 320/224; TE, 90 ms; and TR, 1298 ms. The FOV was determined by the size of the fetal head and was 24 cm for the smaller fetuses and up to 30 cm for the larger fetuses. T1 fast spoiled gradient-echo sequences were performed only in the axial plane with a larger FOV (400 mm); section thickness, 3 mm; gap, 0.5 mm; TR, 160 ms; TE, 2.3 ms. Then diffusion-weighted sequences in the axial plane were performed with an FOV, 40 cm; b-value, 0 and 1000 ms; section thickness, 3 mm; and no gap.

Table 5: Linear association between gestational age and biometric measurements

	Linear Regression Coefficient		Model Summary
	Unstandardized β^a	Standardized β	Adjusted R^2
SI			
US 2D	0.693	0.916	0.839
US 3D	0.833	0.899	0.806
MRI	0.742	0.811	0.656
AP			
US 2D	0.559	0.871	0.757
US 3D	0.574	0.800	0.637
MRI	0.606	0.791	0.624
Perimeter			
US 2D	2.340	0.912	0.831
US 3D	2.989	0.889	0.790
MRI	3.243	0.843	0.708
SA			
US 2D	18.487	0.948	0.897
US 3D	19.670	0.897	0.804
MRI	17.587	0.844	0.711

^a $P < .001$ for all coefficients.

Table 6: Comparison of imaging modalities for each biometric measurement: estimated marginal means 95% CI

	SI		AP		Perimeter		SA	
	Mean	95% CI	Mean	95% CI	Mean	95% CI	Mean	95% CI
At gestational age 29.6 wk ^a								
US 2D	18.10	17.91–18.30	12.99	12.80–13.19	63.34	62.60–64.08	247.45	243.13–251.77
US 3D	19.80	19.58–20.01	13.18	12.97–13.39	67.77	66.97–68.5	258.43	253.77–263.10
MRI	16.47	16.23–16.70	11.40	11.17–11.64	60.68	59.80–61.55	181.04	175.90–186.1
For examinations performed at ≥ 27 wk of gestation: mean gestational age, 31.3 wk								
US 2D	19.28	19.05–19.51	13.88	13.64–14.11	67.20	66.31–68.10	276.99	271.53–282.45
US 3D	17.80	17.57–18.03	12.36	12.13–12.59	65.34	64.48–66.20	212.94	207.68–218.20
MRI	21.34	21.08–21.61	14.20	13.93–14.46	73.28	72.28–74.29	294.12	288.00–300.23

^a Mean gestational age for all populations (516 fetuses).

Table 7: Intraobserver reproducibility of measurements

Vermian Measurement	Differences in Measurements of Vermian Biometry	
	Mean (95% CI of the Difference)	ICC (95% CI)
US 2D, intraobserver variability		
SI	-0.34 ± 0.73 (-0.54 to -0.13)	0.94 (0.91 to 0.97)
AP	0.71 ± 1.02 (0.42 to 1.00)	0.85 (0.75 to 0.91)
Perimeter	0.93 ± 2.7 (0.16 to 1.7)	0.93 (0.88 to 0.96)
SA	2.2 ± 14.4 (2.04 to -1.81)	0.97 (0.95 to 0.98)
US 3D, interobserver variability		
SI	-0.47 ± 1.5 (-0.89 to -0.43)	0.95 (0.92 to 0.97)
AP	-0.26 ± 0.55 (-0.41 to -0.10)	0.98 (0.98 to 0.99)
Perimeter	1.05 ± 10.66 (-1.97 to 4.08)	0.81 (0.7 to 0.89)
SA	-1.2 ± 2.6 (-1.95 to -0.44)	0.999 (0.99 to 1.0)
MRI, intraobserver variability		
SI	0.60 ± 0.66 (0.42 to 0.79)	0.94 (0.91 to 0.97)
AP	0.55 ± 1.05 (0.25 to 0.85)	0.79 (0.66 to 0.88)
Perimeter	1.2 ± 4.05 (0.05 to 2.3)	0.88 (0.81 to 0.93)
SA	-0.36 ± 10.1 (-3.2 to 2.5)	0.97 (0.96 to 0.98)

Table 8: Interobserver reproducibility of measurements

Vermian Measurement	Differences in Measurements of Vermian Biometry	
	Mean (95% CI of the Difference)	ICC (95% CI)
US 2D, interobserver variability		
SI	-0.07 ± 1.15 (-0.40 to 0.25)	0.86 (0.77 to 0.92)
AP	0.92 ± 1.32 (0.54 to 1.2)	0.71 (0.54 to 0.82)
Perimeter	2.4 ± 4.6 (1.15 to 3.81)	0.81 (0.69 to 0.88)
SA	8.3 ± 31.18 (-0.47 to 17.25)	0.86 (0.76 to 0.91)
US 3D, interobserver variability		
SI	-0.07 ± 1.15 (-0.40 to 0.25)	0.86 (0.77 to 0.92)
AP	0.92 ± 1.32 (0.54 to 1.2)	0.71 (0.54 to 0.82)
Perimeter	2.4 ± 4.6 (1.15 to 3.81)	0.81 (0.69 to 0.88)
SA	8.3 ± 31.18 (-0.47 to 17.25)	0.86 (0.76 to 0.91)
MRI, interobserver variability		
SI	-0.47 ± 1.5 (-0.89 to -0.43)	0.95 (0.92 to 0.97)
AP	-0.26 ± 0.55 (-0.41 to -0.10)	0.98 (0.98 to 0.99)
Perimeter	1.05 ± 10.66 (-1.97 to 4.08)	0.81 (0.7 to 0.89)
SA	-1.2 ± 2.6 (-1.95 to -0.44)	0.99 (0.99 to 1.0)

The biometric parameters of the fetal vermis were measured in the midsagittal plane by using single-shot fast spin-echo T2-weighted sequences (Fig 2C).

Statistical Analysis

Statistical analysis was performed with the SPSS software, Version 22.0 (IBM, Armonk, New York). Gestational age was described as mean, median, and range. Biometric measurements of the vermis are described for each gestational age as median and 5th and 95th percentiles and as mean ± SD and 95% CI of the mean. Linear regression models were used to assess the relationship between gestational age and vermian biometric measurements.

Comparison among the 3 imaging modalities for each biometric measurement adjusted for gestational age was performed by using a general linear model with the Bonferroni multiple comparison test. Because MR imaging was not performed before 27 weeks' gestational age, a sensitivity analysis was added considering MR imaging, US 2D, and US 3D measurements at the gestational age of ≥27 weeks. Estimates of the intraclass correlation coefficient (ICC) were used to explore inter- and intra-agreement between the radiologists. Agreement was considered slight with

ICC ≤ 0.2, fair with 0.2 < ICC ≤ 0.4, moderate with 0.4 < ICC ≤ 0.6, substantial with 0.6 < ICC ≤ 0.8, and almost perfect with ICC > 0.8.

Ethics Approval

The study was approved by the institutional review board of the Sheba Medical Center.

RESULTS

Normal Biometric Reference Data

The study groups included 516 fetuses with a normal posterior fossa: 193 in the US 2D group (range, 21–35 weeks of gestation; mean, 29.1 weeks; median, 29.5 weeks), 172 in the US 3D group (range, 21–35 weeks of gestation; mean, 28.2 weeks; median, 29.05 weeks), and 151 fetuses in the MR imaging group (range, 27–35 weeks of gestation, mean, 32.1 weeks; median, 32.6 weeks).

Biometric measurements of the vermis are described for each parameter, imaging modality, and gestational age as median and 5th and 95th percentiles (Tables 1–4) and as mean ± SD and 95% CI of the mean (Fig 3 and On-line Tables 1–4). For all 3 imaging

modalities, the biometric measurements of the vermis have shown a linear growth with gestational age. Results from linear regression models are presented in Table 5.

When we compared the effect of imaging technique controlled for gestational age in the general linear model, the lowest results were those measured by MR imaging, while the highest results were measured by 3D US. All the differences (Bonferroni comparison) were significant ($P < .001$) except AP and surface area (SA) measurements by 2D and 3D US ($P = .601$ and $.02$) (Table 6 and On-line Tables 5 and 6).

Reproducibility of Measurements

Reproducibility of measurement was excellent for all measures and all imaging modalities (Tables 7 and 8). The limits of agreement were considered acceptable for clinical purposes for all parameters, with excellent or substantial agreement defined by ICC.

DISCUSSION

The differential diagnosis of vermian pathology is quite challenging. Biometric parameters allow assessment of the integrity of the

vermis, especially in cases in which the main anatomic landmarks cannot be well demonstrated.

This study provides vermian biometric data from a large cohort of fetuses from 21 to 35 weeks of gestation assessed by 3 imaging modalities. So far, although various nomograms have been developed by using 2D and 3D sonography and MR imaging,¹⁷⁻¹⁹ none has provided data regarding all 4 vermian parameters (maximum superoinferior diameter, maximum anteroposterior diameter, perimeter, and surface area) or compared measurements obtained by the 3 modalities. Moreover, it was not clear whether measurements obtained by different modalities can be compared for clinical purposes.

Biometric analysis of the vermis has a major role in the evaluation of an abnormal posterior fossa for precise prenatal diagnosis. With this study, we provide new reference data for 3 imaging modalities for the biometric parameters.

2D US is the major tool used in customary clinical work and serves as an excellent screening tool for the diagnosis of an abnormal posterior fossa.¹ However, at advanced gestation, acoustic shadow from the bony fetal skull and the bony maternal pelvis make the transabdominal visualization and measurement of the vermis challenging; therefore, transvaginal US is frequently needed for clear imaging of the fetal vermis. This approach is obviously not relevant in breech presentations.

3D US imaging has 3 major advantages. The first is the ability to easily reconstruct the relevant midsagittal plane from the axial plane independent of fetal lie and position. The second is the ability to store data and perform postprocessing off-line analysis. This feature allows filter application such as static VCI to achieve improved tissue contrast and better visualization of anatomic landmarks.^{11,21} The third advantage is the ability to depict posterior fossa anomalies during early gestational ages.²²

MR imaging has an advantage in brain imaging at advanced gestational age. Unlike 2D US and 3D US, MR imaging provides high-resolution images almost independent of maternal body habitus and fetal position. Moreover, MR imaging provides the opportunity of diagnosing associated brain abnormalities, such as migration disorders, white matter abnormalities, and so forth.

In this study for all 3 imaging modalities, the biometric measurements of the vermis have shown a linear growth with gestational age.

Statistically significant differences among imaging modalities justify applying a technique-specific reference value for fetal vermian measurements. The differences between measurements can be explained by a clearer image of the fetal vermian borders obtained by MR imaging, in comparison with the relatively blurred borders obtained by 3D US.

Reproducibility of measurements, expressed by inter- and intraobserver variability and the ICC, is not always evaluated in articles providing reference data for fetal brain measurements.^{23,24} Our study showed high intraobserver reproducibility (range, 0.79–0.99) and high agreement between 2 radiologists (range, 0.71–1) for all biometric measurements in the 3 imaging modalities. Similar results were reported by Tilea et al¹⁸ and by Ber et al²⁵ for MR imaging measurements of the posterior fossa.

CONCLUSIONS

Overall, our study provides normal biometric data of the fetal vermis in a large cohort of fetuses from 21 to 35 weeks of gestation in 3 imaging modalities. Statistical analysis revealed high inter- and intraobserver reproducibility of measurements. Differences in biometric measurements between imaging modalities justify applying technique-specific reference values for fetal vermian measurements. The nomograms developed in this study may have a role in the multidisciplinary clinically challenging prenatal classification of an abnormal posterior fossa.

ACKNOWLEDGMENTS

The authors acknowledge Estela Derazne from the Sackler School of Medicine, Tel Aviv University, Israel, for her assistance with statistical analysis

REFERENCES

1. International Society of Ultrasound in Obstetrics & Gynecology Education Committee. **Sonographic examination of the fetal central nervous system: guidelines for performing the 'basic examination' and the 'fetal neurosonogram'**. *Ultrasound Obstet Gynecol* 2007;29:109–16 CrossRef Medline
2. Guibaud L, des Portes V. **Plea for an anatomical approach to abnormalities of the posterior fossa in prenatal diagnosis**. *Ultrasound Obstet Gynecol* 2006;27:477–81 CrossRef Medline
3. Barkovich AJ, Millen KJ, Dobyns WB. **A developmental and genetic classification for midbrain-hindbrain malformations**. *Brain* 2009;132:3199–230 CrossRef Medline
4. Gandolfi Colleoni G, Contro E, Carletti A, et al. **Prenatal diagnosis and outcome of fetal posterior fossa fluid collections**. *Ultrasound Obstet Gynecol* 2012;39:625–31 CrossRef Medline
5. Limperopoulos C, Robertson RL, Estroff JA, et al. **Diagnosis of inferior vermian hypoplasia by fetal magnetic resonance imaging: potential pitfalls and neurodevelopmental outcome**. *Am J Obstet Gynecol* 2006;194:1070–76 CrossRef Medline
6. Zalel Y, Gilboa Y, Gabis L, et al. **Rotation of the vermis as a cause of enlarged cisterna magna on prenatal imaging**. *Ultrasound Obstet Gynecol* 2006;27:490–93 CrossRef Medline
7. Tilea B, Delezoide AL, Khung-Savatovski S, et al. **Comparison between magnetic resonance imaging and fetopathology in the evaluation of fetal posterior fossa non-cystic abnormalities**. *Ultrasound Obstet Gynecol* 2007;29:651–59 CrossRef Medline
8. Carroll SG, Porter H, Abdel-Fattah S, et al. **Correlation of prenatal ultrasound diagnosis and pathologic findings in fetal brain abnormalities**. *Ultrasound Obstet Gynecol* 2000;16:149–53 CrossRef Medline
9. Bolduc ME, Limperopoulos C. **Neurodevelopmental outcomes in children with cerebellar malformations: a systematic review**. *Dev Med Child Neurol* 2009;51:256–67 CrossRef Medline
10. Filly RA, Cardoza JD, Goldstein RB, et al. **Detection of fetal central nervous system anomalies: a practical level of effort for a routine sonogram**. *Radiology* 1989;172:403–08 CrossRef Medline
11. Paladini D, Volpe P. **Posterior fossa and vermian morphometry in the characterization of fetal cerebellar abnormalities: a prospective three-dimensional ultrasound study**. *Ultrasound Obstet Gynecol* 2006;27:482–89 CrossRef Medline
12. Pilu G, Segata M, Ghi T, et al. **Diagnosis of midline anomalies of the fetal brain with the three-dimensional median view**. *Ultrasound Obstet Gynecol* 2006;27:522–29 CrossRef Medline
13. Achiron R, Kivilevitch Z, Lipitz S, et al. **The development of the human fetal pons: in utero ultrasonographic study**. *Ultrasound Obstet Gynecol* 2004;24:506–10 CrossRef Medline
14. Malinger G, Ginath S, Lerman-Sagie T, et al. **The fetal cerebellar vermis: normal development as shown by transvaginal ultrasound**. *Prenat Diagn* 2001;21:687–92 CrossRef Medline

15. Vinals F, Muñoz M, Naveas R, et al. **The fetal cerebellar vermis: anatomy and biometric assessment using volume contrast imaging in the C-plane (VCI-C).** *Ultrasound Obstet Gynecol* 2005;26:622–27 Medline
16. Bertucci E, Gindes L, Mazza V, et al. **Vermian biometric parameters in the normal and abnormal fetal posterior fossa: three-dimensional sonographic study.** *J Ultrasound Med* 2011;30:1403–10 Medline
17. Ginath S, Lerman-Sagie T, Haratz Krajden K, et al. **The fetal vermis, pons and brainstem: normal longitudinal development as shown by dedicated neurosonography.** *J Matern Fetal Neonatal Med* 2013; 26:757–62 CrossRef Medline
18. Tilea B, Alberti C, Adamsbaum C, et al. **Cerebral biometry in fetal magnetic resonance imaging: new reference data.** *Ultrasound Obstet Gynecol* 2009;33:173–81 CrossRef Medline
19. Parazzini C, Righini A, Rustico M, et al. **Prenatal magnetic resonance imaging: brain normal linear biometric values below 24 gestational weeks.** *Neuroradiology* 2008;50:877–83 CrossRef Medline
20. Robinson JA, Blaser S, Toi A, et al. **The fetal cerebellar vermis: assessment for abnormal development by ultrasonography and magnetic resonance imaging.** *Ultrasound Q* 2007;23:211–23 CrossRef Medline
21. Viñals F, Muñoz M, Naveas R, et al. **Transfrontal three-dimensional visualization of midline cerebral structures.** *Ultrasound Obstet Gynecol* 2007;30:162–68 Medline
22. Garcia-Flores J, Recio M, Uriel M, et al. **Fetal magnetic resonance imaging and neurosonography in congenital neurological anomalies: supplementary diagnostic and postnatal prognostic value.** *J Matern Fetal Neonatal Med* 2013;26:1517–23 CrossRef Medline
23. Chitty LS, Altman DG, Henderson A, et al. **Charts of fetal size, 2: head measurements.** *Br J Obstet Gynaecol* 1994;101:35–43 CrossRef Medline
24. Kurmanavicius J, Wright EM, Royston P, et al. **Fetal ultrasound biometry: 1. Head reference values.** *Br J Obstet Gynaecol* 1999;106: 126–35 CrossRef Medline
25. Ber R, Bar-Yosef O, Hoffmann C, et al. **Normal fetal posterior fossa in MR imaging: new biometric data and possible clinical significance.** *AJNR Am J Neuroradiol* 2015;36:795–802 CrossRef Medline

A Novel Methodology for Applying Multivoxel MR Spectroscopy to Evaluate Convection-Enhanced Drug Delivery in Diffuse Intrinsic Pontine Gliomas

D.I. Guisado, R. Singh, S. Minkowitz, Z. Zhou, S. Haque, K.K. Peck, R.J. Young, A.J. Tsiouris, M.M. Souweidane, and S.B. Thakur

ABSTRACT

BACKGROUND AND PURPOSE: Diffuse intrinsic pontine gliomas are inoperable high-grade gliomas with a median survival of less than 1 year. Convection-enhanced delivery is a promising local drug-delivery technique that can bypass the BBB in diffuse intrinsic pontine glioma treatment. Evaluating tumor response is critical in the assessment of convection-enhanced delivery of treatment. We proposed to determine the potential of 3D multivoxel ¹H-MR spectroscopy to evaluate convection-enhanced delivery treatment effect in these tumors.

MATERIALS AND METHODS: We prospectively analyzed 3D multivoxel ¹H-MR spectroscopy data for 6 patients with nonprogressive diffuse intrinsic pontine gliomas who received convection-enhanced delivery treatment of a therapeutic antibody (Phase I clinical trial NCT01502917). To compare changes in the metabolite ratios with time, we tracked the metabolite ratios Cho/Cr and Cho/NAA at several ROIs: normal white matter, tumor within the convection-enhanced delivery infusion site, tumor outside of the infused area, and the tumor average.

RESULTS: There was a comparative decrease in both Cho/Cr and Cho/NAA metabolite ratios at the tumor convection-enhanced delivery site versus tumor outside the infused area. We used MR spectroscopy voxels with dominant white matter as a reference. The difference between changes in metabolite ratios became more prominent with increasing time after convection-enhanced delivery treatment.

CONCLUSIONS: The comparative change in metabolite ratios between the convection-enhanced delivery site and the tumor site outside the infused area suggests that multivoxel ¹H-MR spectroscopy, in combination with other imaging modalities, may provide a clinical tool to accurately evaluate local tumor response after convection-enhanced delivery treatment.

ABBREVIATIONS: CED = convection-enhanced delivery; DIPG = diffuse intrinsic pontine glioma; MRSI = MR spectroscopic imaging; preCED = 1 week prior to CED treatment; postCED1 = 1 day after CED treatment; postCED2 = 1 month after CED treatment; postCED3 = 2 months after CED treatment

Diffuse intrinsic pontine gliomas (DIPGs) are inoperable high-grade gliomas that account for 10%–15% of pediatric primary CNS tumors and 75%–80% of pediatric brain stem tumors.^{1,2} The current standard of care for DIPG is radiation therapy; despite much effort, median survival is <1 year. Effective

drug delivery to these brain tumors is an obstacle.³ The relatively intact blood-brain barrier presents a major hurdle in drug delivery to DIPGs. Convection-enhanced delivery (CED) is a local drug-delivery technique that bypasses the BBB and uses hydraulic pressure to deliver agents directly to the brain tumor. CED allows enhanced and uniform drug distribution, optimized therapeutic indices, and greatly reduced systemic toxicity to patients.⁴⁻⁶

There is currently no standard method for evaluating treatment response at the CED infusion site that is different from evaluating the whole-tumor treatment response. In this study, we used MR spectroscopic imaging (MRSI), a noninvasive imaging technique that provides information on the tissue metabolites.⁷ Due to the unique metabolic characteristics of tumors, MRSI has been used to aid in diagnosing various cancers and evaluating intratumoral heterogeneity and treatment response in both ani-

Received August 21, 2015; accepted after revision January 5, 2016.

From the Weill Medical College of Cornell University (D.I.G., R.S.), New York, NY; Departments of Radiology (S.M., A.J.T.) and Neurological Surgery (Z.Z., M.M.S.), Weill Medical College of Cornell University, New York, New York; and Departments of Radiology (S.H., K.K.P., R.J.Y., S.B.T.), Neurosurgery (M.M.S.), and Medical Physics (K.K.P., S.B.T.), Memorial Sloan Kettering Cancer Center, New York, New York.

This work was partly supported by the Memorial Sloan Kettering Cancer Center Summer Fellowship, the American Association of Neurological Surgeons Medical Student Summer Fellowship, Perry's Promise Fund, The Cristian Rivera Foundation, Solving Kids' Cancer, The Cure Starts Now Foundation, The Lyla Nsouli Foundation, the Dana Foundation, St. Baldrick's Foundation, Pediatric Brain Tumor Foundation, McKenna Claire Foundation, and Ian's Friends Foundation. This research was partially supported by the Memorial Sloan Kettering Cancer Center Support Grant/Core Grant (P30 CA008748).

Memorial Sloan Kettering has exclusively licensed the 8H9 used in this trial to Y-mAbs Therapeutics.

Please address correspondence to Sunitha Thakur, PhD, 300 East 66th St, Breast Imaging Center, Memorial Sloan Kettering Cancer Center, New York, NY 10065; e-mail: thakurs@mskcc.org

<http://dx.doi.org/10.3174/ajnr.A4713>

mals and humans.⁸ MRSI allows the analysis of many different metabolites in tumor and normal tissue regions of the brain. Some of the major metabolites of interest in examining brain tissue are choline compounds, creatine, and *N*-acetylaspartate.^{7,8} Cho represents the sum of choline compounds, which are components of cell membrane and increase with cellular proliferation. Cr is a biomarker of energy metabolism and is generally stable, functioning primarily as a standard comparison of the other metabolites, though it can vary within certain tumors.⁹ NAA is used as a biomarker for neuronal and axonal integrity and will decrease with neuronal damage or loss. The metabolite ratios of Cho/Cr and Cho/NAA were the parameters of interest in this study.

In the current descriptive study, we used multivoxel proton ¹H-MR spectroscopy to compare metabolic changes at the CED infusion site with tumor outside the CED-infused area. We used voxels filled with dominant normal white matter as a reference. We hypothesized that multivoxel ¹H-MR spectroscopy would show a difference in the change of metabolites at the CED-infused area compared with the non-CED infused area.

MATERIALS AND METHODS

Participants

We prospectively analyzed MR spectroscopy data from 6 patients diagnosed with DIPG who received CED of a therapeutic antibody in a Phase I clinical trial (NCT01502917), which was approved by the Memorial Sloan Kettering Cancer Center review board. The median age of patients was 7 years (range, 3–17 years). Patients were diagnosed with DIPG on the basis of clinical presentation and MR imaging findings. Before CED treatment, they all completed standard external beam radiation therapy (54–60 Gy) for at least 9 weeks, but for no more than 14 weeks. MR spectroscopic imaging was performed at ≥ 3 time points for each patient: 1 week before treatment (preCED), 1 day after treatment (postCED1), and 1 month after treatment (postCED2). All patients were required to have imaging at 1 month after CED (postCED2). Some patients had additional scans at 1-month intervals afterward (postCED3 and 3 months after CED treatment) if they were able to return more frequently due to their close proximity or willingness to travel for additional scans.

MRI/MRSI Methods

The MR imaging/MRSI studies were performed by using a whole-body 3T Discovery MR750 scanner (GE Healthcare, Milwaukee, Wisconsin) with a quadrature head coil as the transceiver. The MR imaging protocol included precontrast sagittal and axial T1-weighted, axial T2-weighted, axial T2 FLAIR, axial diffusion-weighted, and postcontrast T1-weighted sequences in axial, sagittal, and coronal planes. The precontrast T2 FLAIR images were obtained by using a fast spin-echo sequence (TI/TE/TR = 2250/120/9000 ms, FOV = 24 cm). The 3-mm section thickness with no spacing between sections (320 × 256 acquisition matrix size) served as scouts for placement of the volume of interest for the 3D MRSI data acquisition. MRSI data acquisition was performed following the precontrast MR imaging acquisition, but before gadolinium contrast administration. The 3D MRSI VOI encompassed the lesion (hyperintense area on T2 FLAIR images) and surround-

ing normal-appearing brain tissue. Outer volume saturation bands were applied to avoid signal contaminations caused by subcutaneous lipid, bone, and varying magnetic susceptibility effects that might compromise the quality of the spectra. A point-resolved spectroscopy sequence with water suppression by using chemical shift selective suppression was used to collect the 3D ¹H-MRSI datasets with TE = 144 ms, TR = 1000 ms, FOV = 8 cm, section thickness = 10 mm, 3D spatial-encoding (8 × 8 × 8 matrix size, resulting in 1-cm³ nominal MRSI voxel size), 5000-Hz spectral width, and 4096 data points. The acquisition time for 3D MRSI was approximately 9 minutes, including the prescan for magnetic field shimming. The MRSI VOI location, size, and acquisition parameters were kept the same for each patient during follow-up studies by using anatomic landmarks. The axial postcontrast T1WI MR images were collected with the same section number, location, and thickness as the axial T2 FLAIR images.

MR Spectroscopy Data Processing

Multivoxel ¹H-MR spectroscopy data were analyzed with FuncTool software (Advantage Workstation, Version 11.3–4.2; GE Healthcare). The MRSI sections were interpolated to 3 mm to match the FLAIR images and generate overlay images of the MRSI grid onto the corresponding T2-FLAIR image. ROIs were equivalent to 1 MR spectroscopy voxel (nominal size of 1 cubic centimeter) and were selected by using the overlaid T2-FLAIR images for anatomic reference. Major resonance peaks of NAA (2.0 ppm), Cr (3.0 ppm), and Cho (3.2 ppm) for each MRSI voxel were assigned and numerically integrated to estimate peak areas. Peak area ratios were calculated and color maps were generated for Cho/NAA and Cho/Cr.

ROI Selection

Several ROIs were chosen to analyze MR spectroscopic data: a voxel at the CED infusion, a voxel that was within the tumor but outside the CED infusion, additional voxels that were within the tumor to calculate the average tumor metabolites, and normal tissue voxels as controls. A radiologist with a Certificate of Added Qualification in radiology (S.H., 11 years of experience) and a physicist (S.B.T., 12 years of experience in brain MR spectroscopy) oversaw all ROI voxel selections. The CED infusion voxel was selected by using the postCED1 scans because the infusion site was visible as hyperintense signal on the T2-FLAIR images (Fig 1A–D). The CED infusion site voxels for preCED, postCED2, and, when applicable, postCED3 were selected by matching the section numbers and location by using anatomic landmarks to the postCED1 infusion site voxel. The tumor non-CED infusion site voxel was chosen at least 2 sections away from the CED infusion site and was verified by the radiologist (S.H.) to be outside of the CED infused volume of distribution (Fig 1E–H).

Color metabolite maps were used to observe the relative intensity of each metabolite and metabolite ratio in and around the CED infusion site. Anatomic landmarks and section numbers were used to best match equivalent tumor non-CED infusion site voxels for the remaining scans. Additional tumor voxels were selected on the basis of MR imaging and spectra that were characteristic of tumor (high Cho and low NAA peak compared with unaffected tissue and metabolite ratios: Cho/Cr of >1.5 and Cho/

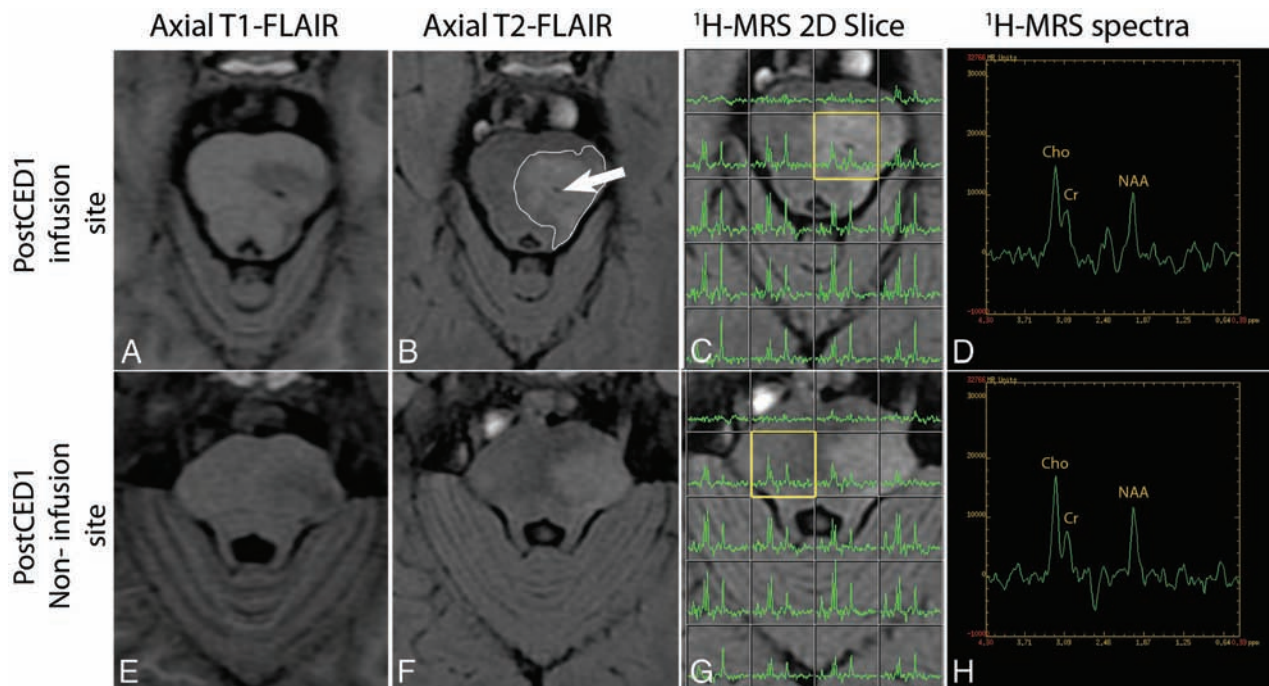


FIG 1. ROI selection. *A*, Axial T1-weighted FLAIR image shows regional hypointensity at the CED infusion site. *B*, The CED infusion site (white arrow) is also visible on the axial T2 FLAIR image with surrounding T2-hyperintense signal (outlined in white) indicative of the CED infusion volume of distribution. *C*, The corresponding axial T2-FLAIR with multivoxel MR spectroscopy is shown with the selected CED infusion site voxel (yellow box). *D*, Enlarged view of the MR spectra for the selected CED infusion site voxel. *E* and *F*, The axial T1-weighted FLAIR and axial T2-FLAIR images of the noninfusion site section. *G*, The selected tumor non-CED infusion site voxel (yellow box) is outside the CED infusion volume of distribution. *H*, The enlarged view of the MR spectra for the selected tumor non-CED infusion site voxel.

NAA of >1). An average of the tumor metabolite ratios was calculated for each scan by taking an average of the Cho/Cr and Cho/NAA ratios from the following voxels of tumor: the CED infusion site, the tumor non-CED infusion site, and the other additional tumor voxels. Normal tissue voxels were chosen in the white matter cerebellum or cerebrum away from the tumor and had spectra characteristic of normal white matter with metabolite ratios of Cho/Cr of ~ 0.7 – 1 and Cho/NAA of ~ 0.5 – 1 .^{10–12}

Statistical Analysis

Statistical analysis was performed on metabolite ratios, which were treated as data with unknown distributions. Exploratory data analysis included group means/medians with time and graphing individual measurements with time. To test the trend of changes in metabolite ratios, we performed paired difference tests by using the Wilcoxon signed rank test in R (<http://www.r-project.org>).

RESULTS

The metabolite ratios Cho/Cr and Cho/NAA for the CED infusion site, tumor non-CED infusion site, average tumor, and normal-tissue ROIs were compared during the course of treatment. Color metabolite maps demonstrated the higher intensity of Cho, Cho/Cr, and Cho/NAA and lower intensity of NAA in the area of the pons with tumor (Fig 2).

The metabolite ratios for normal tissue remained stable and within the normal range for each patient throughout the course of treatment (Fig 3). In 4 patients, Cho/Cr and Cho/NAA decreased at the CED infusion site with time, while the

ratios for the tumor non-CED infusion site generally decreased by a lesser degree or increased with time (Fig 4A–D). In 2 patients, Cho/Cr and Cho/NAA increased at the infusion site with time, but a more substantial increase occurred in Cho/Cr and Cho/NAA at the tumor non-CED infusion site and for the average tumor (Fig 4E, –F). In 2 patients, Cho/Cr and Cho/NAA in the CED infusion site ROI at postCED1 were high (Fig 4B, –E).

Statistical analysis was performed to assess the change in Cho/Cr and Cho/NAA at the CED infusion site compared with the tumor non-CED infusion site in all patients (Fig 5). There was a relative difference in the percentage change in both Cho/Cr and Cho/NAA for the CED infusion site compared with the tumor non-CED infusion site. The mean and *P* value decreased for both Cho/Cr and Cho/NAA metabolite ratios with time when comparing preCED with postCED1, preCED with postCED2, and preCED with postCED3. The mean (SD) for the change in Cho/Cr between infusion and non-CED infusion sites was similar between postCED1 and postCED2 compared with preCED: 1.20 (0.53) and 1.21 (0.43), respectively; but it decreased at postCED3 to 0.66 (0.06). The mean (SD) change in Cho/NAA between the infusion and non-CED infusion sites decreased from 1.11 (0.66) to 0.93 (0.97) to 0.82 (0.29) at postCED1, postCED2, and postCED3, respectively. The *P* value for the change in Cho/Cr at the CED infusion site compared with the tumor non-CED infusion site decreased from 0.84 at postCED1 to 0.25 at postCED3. The *P* value for the change in Cho/NAA decreased from 1.00 at postCED1 to 0.50 at postCED3.

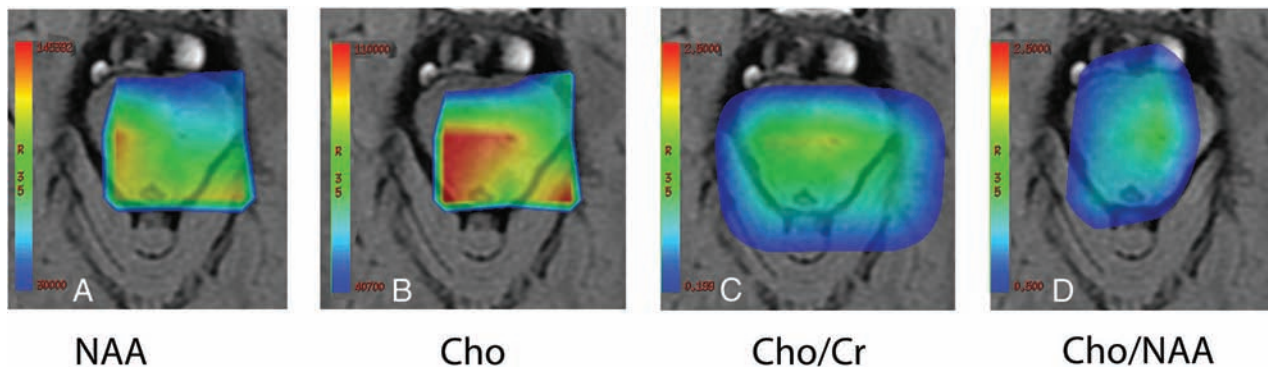


FIG 2. Color metabolite maps. Relative intensities of metabolites NAA (A), Cho (B), Cho/Cr (C), and Cho/NAA (D) are shown in this postCED1 infusion section. The CED infusion site is visible and is located in the area of the pons with a higher intensity signal of Cho, Cho/Cr, and Cho/NAA and lower NAA intensity.

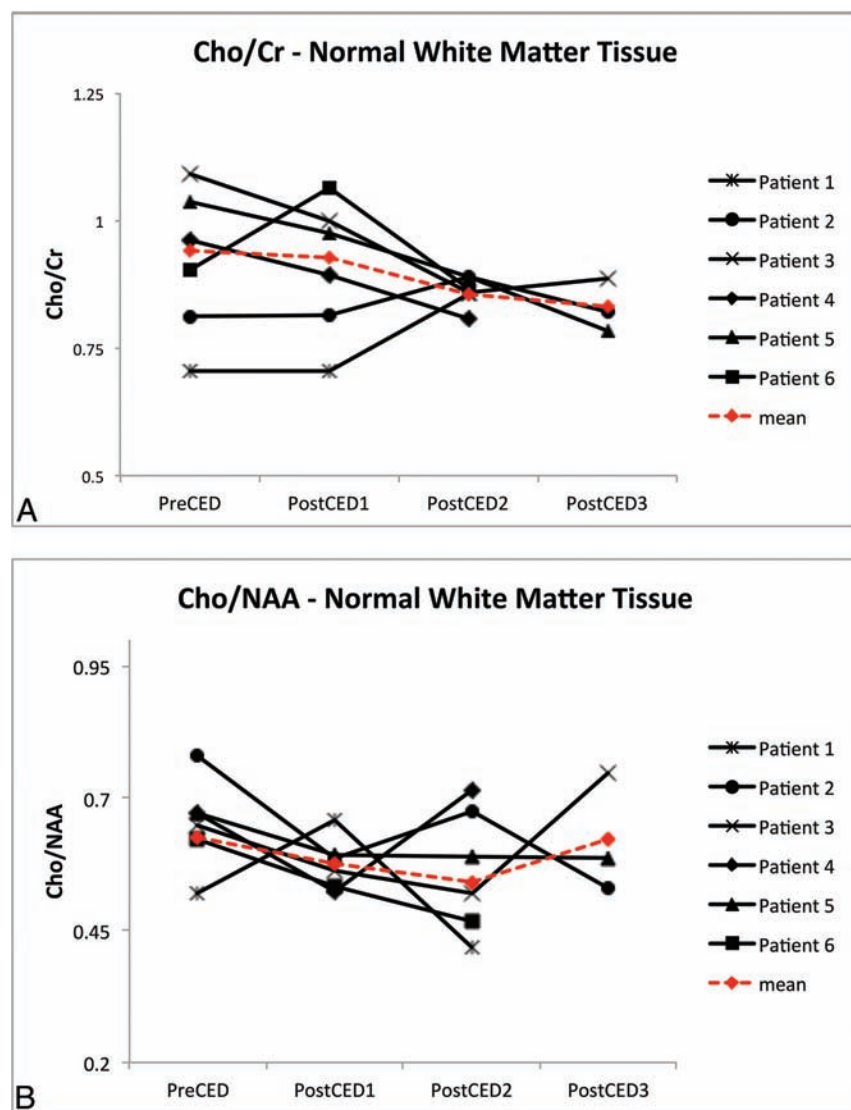


FIG 3. Metabolite ratios for normal white matter. Cho/Cr (A) and Cho/NAA (B) ratios for normal cerebellar or cerebral white matter for each patient are shown throughout the course of treatment, and the mean value at each time point is shown in red. Both metabolite ratios for each patient remained stable and in the expected normal range.

DISCUSSION

Despite much therapeutic effort, patients with DIPG continue to have a poor prognosis with a median survival of <1 year. Radia-

tion therapy is the standard of care because most chemotherapeutic agents do not prolong survival. CED is a promising technique that allows direct localized delivery of therapeutic agents to the tumor. In this study, patients with non-progressive DIPG received CED treatment with a therapeutic antibody in a Phase I clinical trial (NCT01502917). Evaluating local treatment response at the CED infusion site is critical because it may suggest that there is some treatment effect when whole-tumor response may be undetectable. A CED therapeutic agent may be falsely deemed ineffective if whole-tumor response is assessed without evaluating the response at the local infusion site.

Evaluating DIPG treatment response with conventional MR imaging alone is inadequate due to nonspecific changes on imaging that can arise from recurrent tumor, inflammatory responses, and necrotic changes from treatment.^{12,13} Furthermore, conventional MR imaging results alone have not been shown to correlate with survival in patients with DIPG.¹⁴ Diffusion tensor imaging and diffusion-weighted imaging have been studied in patients with DIPG, but the diffuse infiltration of DIPG has made using these techniques difficult. The pattern and amount of tract involvement varies among patients, and the significance of diffusion properties in DIPG varies anatomically.^{15,16} Perfusion-weighted MR imaging has been used to assess the angiogenesis of the tumor, but relative tumor blood volume has a weaker correlation to disease progression than increased choline levels with ¹H-MR spectroscopy.¹⁷

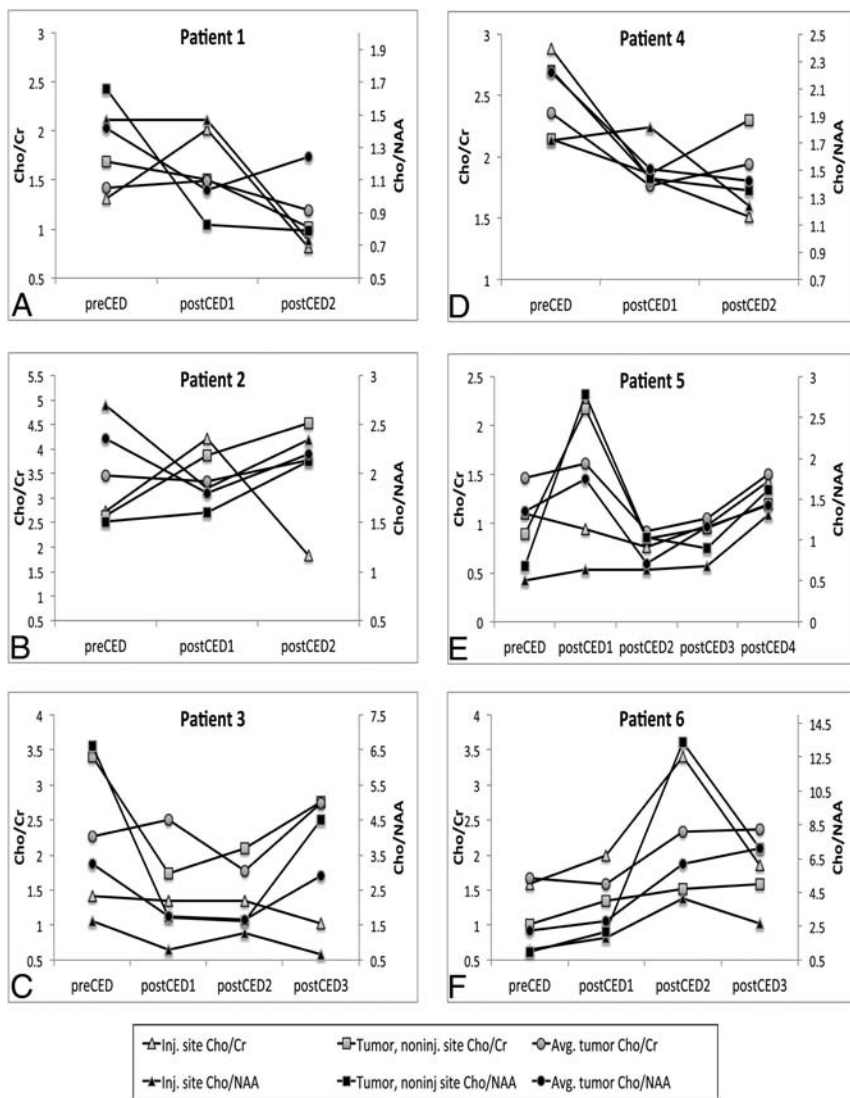


FIG 4. Metabolite ratios for CED infusion site, tumor non-CED infusion site, and average tumor for individual patients. A–D, Patients 1–4 show a similar trend with a comparative decrease in Cho/Cr and Cho/NAA with time for the CED infusion site compared with the tumor non-CED infusion site and average tumor voxels. E and F, Patients 5 and 6 show a slight increase in Cho/Cr and Cho/NAA for the CED infusion site and a comparatively larger increase in both ratios for the tumor non-CED infusion site and the average tumor.

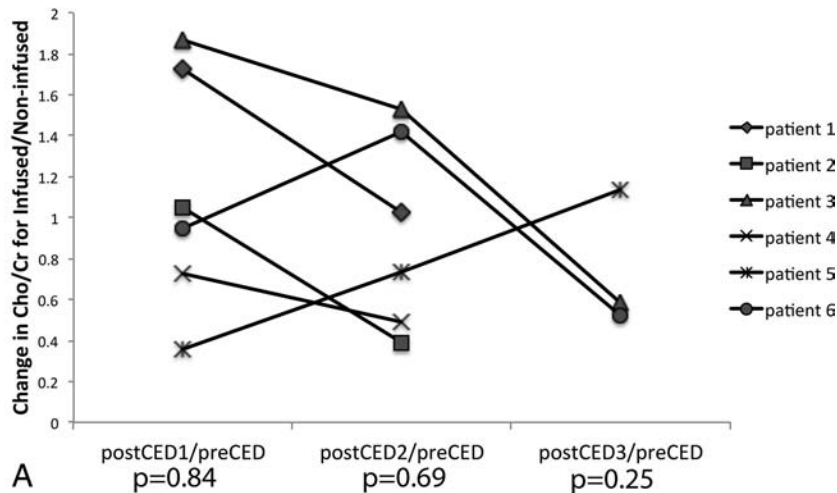
¹H-MR spectroscopy is effective in providing clinically important information in brain tumors and has increased diagnostic sensitivity, specificity, and accuracy when used with MR imaging.⁸ ¹H-MR spectroscopy uses the radiofrequency signal from protons when a magnetic field is applied to determine metabolite concentrations by displaying a spectrum of peaks corresponding to different metabolites. The area under the curve of the peak is then used to calculate the concentration and ratios of the metabolites.⁷ Due to the abnormal metabolism characteristic of tumor cells, MR spectroscopy can be used to identify tumorous tissue with good accuracy. Cho, Cr, and NAA are some of the most common metabolites analyzed for brain tumors. Increases in Cho correspond to increased membrane turnover or cellular density and thus make Cho a biomarker for tumor tissue.⁷ Cr is usually stable because it is a biomarker of energy metabolism, but it can vary within certain tumors, and a decrease in Cr can signify tissue

necrosis.^{7,9} Decreasing levels of NAA signify a decrease in neuronal integrity.⁷ Cho/Cr and Cho/NAA ratios have often been used to identify the metabolic changes in tumor tissue.^{11,12} Increases in both Cho/Cr and Cho/NAA indicate tumor because Cho increases, Cr generally stays stable or decreases, and NAA decreases in tumor tissue.

Single-voxel ¹H-MR spectroscopy has been used to assess prognosis and overall treatment response to radiation therapy and chemotherapeutics in DIPG tumors.^{8,18,19} However, multivoxel ¹H-MR spectroscopy allows the interrogation of local changes in metabolism within different regions of the tumor.¹³ A previous study used multivoxel ¹H-MR spectroscopy to look at DIPG during radiation therapy and compared changes in tumor versus normal brain tissue. This study showed a correlation with low Cho/Cr and Cho/NAA during response to radiation therapy and high Cho/Cr and Cho/NAA with relapse.¹² Other studies have also shown increases in Cho/Cr and Cho/NAA ratios in DIPG tumors corresponding to prognosis and relapse after treatment.^{20,21} In our study, we wanted to evaluate the utility of using multivoxel ¹H-MR spectroscopy for assessing CED treatment. We prospectively analyzed the multivoxel ¹H-MR spectroscopy data from 6 patients with DIPG receiving CED treatment. We compared the Cho/Cr and Cho/NAA ratios across time at the CED infusion site with the tumor non-CED infusion site outside the CED infused volume of distribution.

Based on the MR spectroscopy data for these patients, there is a comparative reduction in Cho/Cr and Cho/NAA after CED treatment at the CED infusion site compared with the tumor non-CED infusion site. This reduction becomes more pronounced with increasing time after CED treatment. These MR spectroscopic changes, when combined with findings from other modalities, such as DWI, DTI, PWI, and PET and compared with patient outcomes, may reflect CED treatment response. In 2 patients, metabolite ratios for the CED infusion site ROI at postCED1 were high compared with their baseline metabolite ratios at preCED. Patient 2 had Cho/Cr = 4.22 for the CED infusion site and 3.88 for the tumor noninfusion site, respectively, at postCED1 (Fig 4B). Patient 5 had Cho/NAA = 2.78 and Cho/Cr = 2.17 for the tumor noninfusion site at postCED1 (Fig 4E). Because postCED1 is 1 day after CED treatment, there may be an influence of the infused CED volume on the MR spectroscopic readings. The infusate may produce susceptibility arti-

Change in Cho/Cr from baseline: Infused/ Non-infused



Change in Cho/NAA from baseline: Infused/ Non-infused

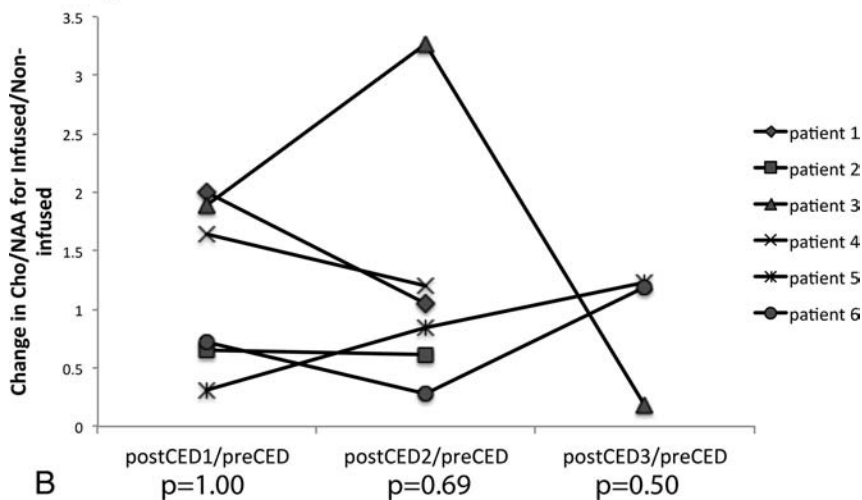


FIG 5. CED infusion site versus tumor non-CED infusion site Cho/Cr and Cho/NAA comparison. The change in metabolite ratios Cho/Cr (A) and Cho/NAA (B) from the baseline preCED scan to postCED1, postCED2, and postCED3 scans is calculated for the group of patients at both the CED infusion site and tumor non-CED infusion site. The change in Cho/Cr and Cho/NAA at the CED infusion site compared with the tumor non-CED infusion site is calculated by using the Wilcoxon signed rank test. While no statistical claims can be made, the decreasing *P* values for both metabolite ratios suggest that a comparative reduction in the ratios becomes more pronounced with time.

facts that could result in poor shimming and hence broader line widths. This result could lead to inaccurate quantification of metabolites at postCED1. Despite this limitation, we were able to see a difference in metabolite ratios at the infusion site versus the noninfused tumor by using our methodology with multivoxel $^1\text{H-MR}$ spectroscopy. Our methodology for ROI selection to assess CED treatment response can also be used in parallel to analyze results from other imaging modalities such as DWI and PWI, which may provide additional biomarkers to help evaluate the response in CED treatment.

The study is limited in that a reduced metabolite ratio trend without statistical significance was observed on the basis of the small number of patients analyzed with only a few scans. Additionally, the patients started with different tumor volumes and with different metabolite ratios from their baseline

preCED scan. These variables may influence the response to CED treatment. It may be of interest for future studies to derive absolute measures of metabolites that could provide an accurate way to study the local changes with treatment and to standardize the patient's tumor size and baseline metabolic ratios.

CONCLUSIONS

Our methodology for analysis of multivoxel $^1\text{H-MR}$ spectroscopy highlighted a trend of decreasing *P* values for the metabolite ratios Cho/Cr and Cho/NAA after CED treatment at the CED infusion site compared with the tumor non-CED infusion site. Although statistical tests were not significant with the small number of patients, the results are encouraging, and if confirmed, MRSI could be used to obtain early markers of tumor response in individual patients. Our methodology may also be applicable to other imaging modalities, with some optimization for determining ROI size and placement. When combined with other imaging techniques, such as PET, DTI, DWI, and PWI, our methodology may provide a clinical tool to more accurately evaluate local tumor response after CED treatment.

Disclosures: Mark M. Souweidane—UNRELATED: Consultancy: Aesculap Neuro-Endoscopy Advisory Council; Payment for Lectures (including service on Speakers Bureaus): Aesculap Neuro-Endoscopy Advisory Council, Comments: annual endoscopic practical course; Travel/Accommodations/Meeting Expenses Unrelated to Activities Listed: Aesculap Neuro-Endoscopy Advisory Council, Comments: annual endoscopic practical course.

REFERENCES

- Jansen MH, van Vuurden DG, Vandertop WP, et al. Diffuse intrinsic pontine gliomas: a systematic update on clinical trials and biology. *Cancer Treat Rev* 2012;38:27–35 CrossRef Medline
- Warren KE. Diffuse intrinsic pontine glioma: poised for progress. *Front Oncol* 2012;2:205 CrossRef Medline
- Jain RK. The next frontier of molecular medicine: delivery of therapeutics. *Nat Med* 1998;4:655–57 CrossRef Medline
- Sandberg DI, Edgar MA, Souweidane MM. Convection-enhanced delivery into the rat brainstem. *J Neurosurg* 2002;96:885–91 CrossRef Medline
- Song DK, Lonser RR. Convection-enhanced delivery for the treatment of pediatric neurologic disorders. *J Child Neurol* 2008;23:1231–37 CrossRef Medline
- Bobo RH, Laske DW, Akbasak A, et al. Convection-enhanced delivery of macromolecules in the brain. *Proc Natl Acad Sci U S A* 1994; 91:2076–80 CrossRef Medline

7. Gujar SK, Maheshwari S, Björkman-Burtscher I, et al. **Magnetic resonance spectroscopy.** *J Neuroophthalmol* 2005;25:217–26 CrossRef Medline
8. Glunde KB, Bhujwala ZM. **Metabolic tumor imaging using magnetic resonance spectroscopy.** *Semin Oncol* 2011;38:26–41 CrossRef Medline
9. Kinoshita Y, Yokota A. **Absolute concentrations of metabolites in human brain tumors using in vitro proton magnetic resonance spectroscopy.** *NMR Biomed* 1997;10:2–12 Medline
10. Soares DP, Law M. **Magnetic resonance spectroscopy of the brain: review of metabolites and clinical applications.** *Clin Radiol* 2009;64:12–21 CrossRef Medline
11. Howe FA, Barton SJ, Cudlip SA, et al. **Metabolic profiles of human brain tumors using quantitative in vivo 1H magnetic resonance spectroscopy.** *Magn Reson Med* 2003;49:223–32 CrossRef Medline
12. Laprie A, Pirzkall A, Haas-Kogan DA, et al. **Longitudinal multivoxel MR spectroscopy study of pediatric diffuse brainstem gliomas treated with radiotherapy.** *Int J Radiat Oncol Biol Phys* 2005;62:20–31 CrossRef Medline
13. Yang I, Huh NG, Smith ZA, et al. **Distinguishing glioma recurrence from treatment effect after radiochemotherapy and immunotherapy.** *Neurosurg Clin N Am* 2010;21:181–86 CrossRef Medline
14. Hargrave D, Chuang N, Bouffet E. **Conventional MRI cannot predict survival in childhood diffuse intrinsic pontine glioma.** *J Neurooncol* 2008;86:313–19 CrossRef Medline
15. Helton KJ, Phillips NS, Khan RB, et al. **Diffusion tensor imaging of tract involvement in children with pontine tumors.** *AJNR Am J Neuroradiol* 2006;27:786–93 Medline
16. Chen HJ, Panigrahy A, Dhall G, et al. **Apparent diffusion and fractional anisotropy of diffuse intrinsic brain stem gliomas.** *AJNR Am J Neuroradiol* 2010;31:1879–85 CrossRef Medline
17. Tzika AA, Astrakas LG, Zarifi MK, et al. **Spectroscopic and perfusion magnetic resonance imaging predictors of progression in pediatric brain tumors.** *Cancer* 2004;100:1246–56 CrossRef Medline
18. Meisamy S, Bolan PJ, Baker EH, et al. **Neoadjuvant chemotherapy of locally advanced breast cancer: predicting response with in vivo (1)H MR spectroscopy: a pilot study at 4 T.** *Radiology* 2004;233:424–31 CrossRef Medline
19. Steffen-Smith EA, Venzon DJ, Bent RS, et al. **Single- and multivoxel proton spectroscopy in pediatric patients with diffuse intrinsic pontine glioma.** *Int J Radiat Oncol Biol Phys* 2012;84:774–79 CrossRef Medline
20. Laprie A, Catalaa I, Cassol E, et al. **Proton magnetic resonance spectroscopic imaging in newly diagnosed glioblastoma: predictive value for the site of postradiotherapy relapse in a prospective longitudinal study.** *Int J Radiat Oncol Biol Phys* 2008;70:773–81 CrossRef Medline
21. Hipp SJ, Steffen-Smith E, Hammoud D, et al. **Predicting outcome of children with diffuse intrinsic pontine gliomas using multiparametric imaging.** *Neuro Oncol* 2011;13:904–09 CrossRef Medline

Imaging Signs in Spontaneous Intracranial Hypotension: Prevalence and Relationship to CSF Pressure

 P.G. Kranz,  T.P. Tanpitukpongse,  K.R. Choudhury,  T.J. Amrhein, and  L. Gray

ABSTRACT

BACKGROUND AND PURPOSE: Patients with spontaneous intracranial hypotension often exhibit low CSF pressure and changes on brain MR imaging and/or evidence of CSF leak on myelography. We investigated whether individual imaging signs of spontaneous intracranial hypotension correlate with measured CSF pressure and how frequently these 2 markers of spontaneous intracranial hypotension were concordant.

MATERIALS AND METHODS: We performed a retrospective, cross-sectional study of 99 subjects with spontaneous intracranial hypotension. Prevalence of brain and myelographic imaging signs of spontaneous intracranial hypotension was recorded. CSF pressure among subjects with or without individual imaging signs was compared by using a 2-tailed *t* test and ANOVA. Concordance between low CSF pressure (≤ 6 cm H₂O) and imaging was defined as the presence of the sign in a subject with low CSF pressure or absence of the sign when pressure was not low.

RESULTS: Dural enhancement, brain sagging, and venous distension sign were present in 83%, 61%, and 75% of subjects, respectively, and myelographic evidence of CSF leak was seen in 55%. Marginal correlations between CSF pressure and brain sagging ($P = .046$) and the venous distension sign ($P = .047$) were found. Dural enhancement and myelographic evidence of leak were not significantly correlated with CSF pressure. Rates of concordance between imaging signs and low CSF pressure were generally low, ranging from 39% to 55%.

CONCLUSIONS: Brain and myelographic signs of spontaneous intracranial hypotension correlate poorly with CSF pressure. These findings reinforce the need to base the diagnosis of spontaneous intracranial hypotension on multiple diagnostic criteria and suggest the presence of patient-specific variables that influence CSF pressure in these individuals.

ABBREVIATIONS: P_{CSF} = CSF pressure; SIH = spontaneous intracranial hypotension

Low CSF pressure (P_{CSF}) is a well-known feature of spontaneous intracranial hypotension (SIH) and is one of several diagnostic criteria for the disorder.^{1,2} The fact that SIH is categorized by the International Classification of Headache Disorders, 3rd edition, as a “headache attributed to low cerebrospinal fluid pressure”² underlines the historical strength of the association between SIH and abnormally low pressure.

Given this association, it would be expected that low CSF pres-

sure would also be associated with other diagnostic criteria of SIH, including typical brain imaging findings and the presence of CSF leak on myelography.¹ There is some evidence to the contrary, however. Previous investigators have recognized that patients with brain imaging findings of SIH or myelographic evidence of CSF leak may not exhibit low CSF pressure.^{3,4} This observation would seem to call into question whether low CSF pressure is the fundamental cause of SIH and has prompted the alternate hypothesis that SIH is actually primarily a disorder of low CSF volume rather than low pressure.⁵ To our knowledge, the frequency of discordance between imaging and CSF pressure and, by inference, the likelihood of this alternate hypothesis have not been previously explored.

The purpose of this investigation is to describe the prevalence of brain imaging and myelographic signs of SIH from a large retrospective series of patients with confirmed SIH and to determine the correlation between these imaging signs and CSF pres-

Received October 19, 2015; accepted after revision November 27.

From the Department of Radiology, Duke University Medical Center, Durham, North Carolina.

Paper previously presented in part at: American Society of Neuroradiology Annual Meeting and the Foundation of the ASNR Symposium, April 25–30, 2015; Chicago, Illinois.

Please address correspondence to Peter G. Kranz, MD, Department of Radiology, DUMC Box 3808, Duke University Medical Center, Durham, NC 27710; e-mail: peter.kranz@duke.edu; @PeterGKranz

<http://dx.doi.org/10.3174/ajnr.A4689>

Table 1: Diagnostic criteria for SIH from Schievink et al¹

Criteria
A) Orthostatic headache
B) The presence of at least 1 of the following: <ol style="list-style-type: none"> 1) Low opening pressure (≤ 60 mm H₂O) 2) Sustained improvement of symptoms after epidural blood patching 3) Demonstration of an active spinal CSF leak 4) Cranial MRI changes of intracranial hypotension (eg, brain sagging or pachymeningeal enhancement)
C) No recent history of dural puncture
D) Not attributable to another disorder

sure measurements, with a particular focus on reporting how commonly imaging signs of SIH and low CSF pressure are concordant or discordant.

MATERIALS AND METHODS

This investigation is a retrospective cross-sectional study of patients with SIH treated at our institution between January 2006 and October 2014. The investigation was approved by our local institutional review board and is compliant with Health Insurance Portability and Accountability regulations.

Subjects

Subjects were identified through review of departmental procedure logs of patients evaluated for possible SIH. Standard initial diagnostic work-up for suspected SIH at our institution includes lumbar puncture followed immediately (ie, within 1–3 minutes after contrast injection) by CT myelography of the cervical, thoracic, and lumbar spine.⁶ CSF opening pressure was recorded from this initial evaluation. All pressures were measured with the patient in the lateral decubitus position, with legs extended, and resting quietly. Demographic information was recorded from the patient's electronic medical record.

Subjects were included if they satisfied the diagnostic criteria for SIH previously outlined by Schievink et al (Table 1).¹ Patients were excluded if preprocedural brain MR imaging was not available.

Image Analysis

Brain MR imaging was reviewed to evaluate imaging findings of SIH. Abnormal dural enhancement was evaluated on postcontrast axial and/or coronal T1-weighted images in subjects with available postcontrast brain imaging. Brain sagging was considered present if downward sloping of the third ventricular floor resulting in descent of the mammillary bodies to the level of the dorsum sella was present on either sagittal T1- or T2-weighted images. A "venous distension" sign was considered present if there was a convex inferior border of the dominant transverse venous sinus at its midportion (approximated by a section containing the lens of the eye) on sagittal T1- or T2-weighted images.⁷ Pituitary hyperemia, another imaging sign reported in association with SIH,⁸ was not assessed in this investigation because it was thought to be too subjective and not a principal sign of the condition.

CT-myelograms were reviewed to evaluate the presence of a CSF leak, defined by the presence of contrast outside of the thecal sac in the epidural space. If present, CSF leaks were further classified as either high-flow leaks, denoted by the presence of a pool

of epidural contrast extending over >1 vertebral segment, or low-flow leaks, in which contrast leakage did not extend over >1 vertebral segment.⁹

Initial image review was performed by a board-certified radiologist in the second year of a neuroradiology fellowship. Equivocal or borderline cases were reviewed by a second board-certified radiologist who holds a Certificate of Added Qualification in neuroradiology and has 12 years' experience interpreting brain MR imaging, including extensive experience in evaluating patients with SIH.

Concordance or discordance of the individual brain imaging signs with low CSF pressure (defined as P_{CSF} of ≤ 6 cm H₂O) was also assessed. Individual signs were considered concordant if the sign was present in a subject with low CSF pressure or absent when the pressure was >6 cm H₂O. Conversely, a sign was considered discordant if it was present but the subject's CSF pressure was >6 cm H₂O or if the sign was absent but the subject's CSF pressure was low.

Statistical Analysis

Descriptive statistics regarding the prevalence of individual imaging signs and the concordance/discordance of those signs with CSF pressure were calculated. For individual brain MR imaging signs, differences in CSF pressure between groups with or without the sign present were compared by using a 2-tailed *t* test. For individual leak patterns on CT myelography (ie, no leak, high-flow leaks, and low-flow leaks), CSF pressure between groups was compared by using ANOVA. Additionally, CSF pressure in the group showing any evidence of leak (either high-flow or low-flow) was compared with the group with no leak by using a 2-tailed *t* test. Analysis was performed by using R statistical and computing software, Version 3.0.2 (<http://www.r-project.org>). For all comparisons, a *P* value $< .05$ was considered statistically significant.

RESULTS

A total of 106 patients with SIH were identified. Of these, 7 were excluded due to the absence of any available preprocedural brain MR imaging, with a final study population of 99 subjects (33 men, 66 women). Of these subjects with available preprocedural brain imaging, 6 brain MRIs were performed without contrast; the remaining studies (93 subjects, 94%) were performed with and without contrast. The mean age for the final study population was 47.8 ± 13.4 years.

Prevalence of Imaging Signs

Of the 93 subjects with available postcontrast brain MR images, 83% (77 subjects) showed abnormal dural enhancement. Among all 99 subjects, 61% (60 subjects) showed evidence of brain sagging and 75% (74 subjects) showed a venous distension sign.

Of all 99 subjects, 93% (92 subjects) showed at least 1 of the 3 imaging signs. All 3 signs were present in 43% of subjects; 2 signs, in 33%; 1 sign, in 16%; and zero signs (ie, brain MR imaging negative for signs of SIH), in 7%. Of the 6 subjects with noncontrast images only, 5 showed at least 1 imaging sign (ie, brain sagging or venous distension sign); the remaining patient had normal brain imaging findings but met the criteria for the diagnosis

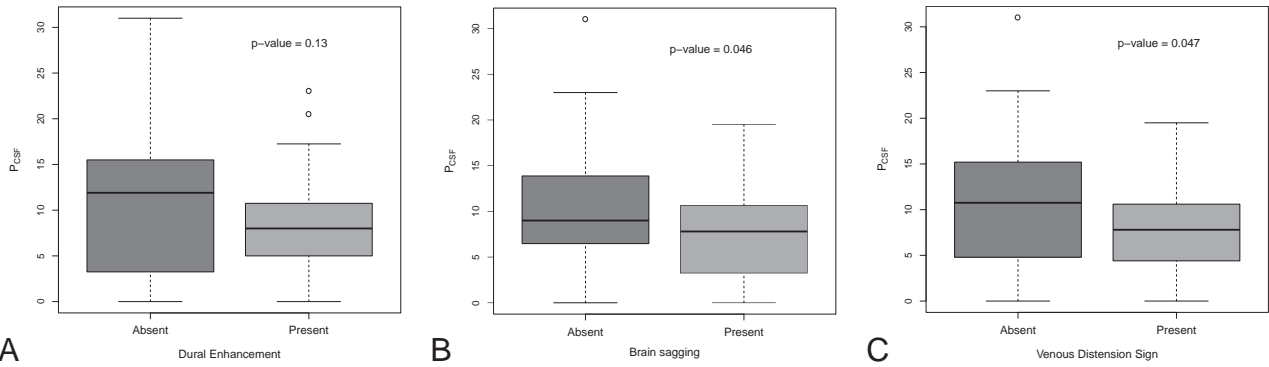


FIG 1. Box-and-whisker plots comparing P_{CSF} (cm H_2O) with the presence or absence of individual brain imaging signs of SIH.

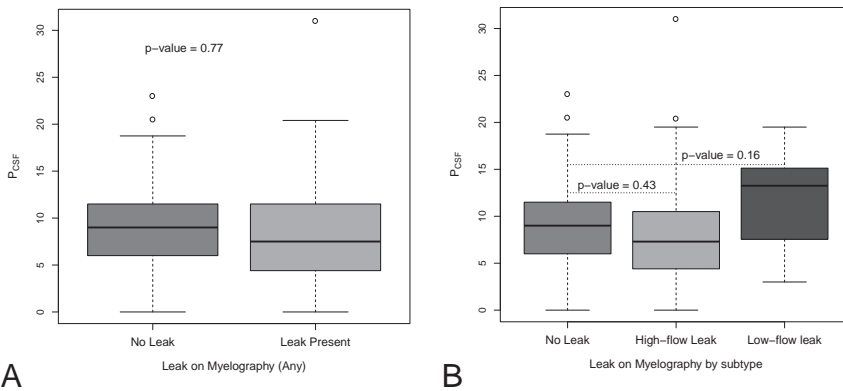


FIG 2. Box-and-whisker plots comparing P_{CSF} (cm H_2O) with the presence or absence of various myelographic patterns in SIH.

of SIH by having a CSF pressure of 0 cm H_2O and evidence of a high-flow leak on myelography.

On CT myelography, 55% of subjects showed a leak of any type. Of these subjects with a leak, most (46 subjects, 85%) had a high-flow leak, and the remainder (8 subjects, 15%) had a low-flow leak.

Correlation of Imaging Signs and CSF Pressure

The distribution of CSF pressure in subjects with and without individual brain imaging signs is shown in Fig 1. For all signs, there was substantial overlap in the distribution of CSF pressures between groups.

No significant difference in CSF pressure was observed between subjects with and without dural enhancement (mean P_{CSF} , 7.8 ± 4.8 versus 11.3 ± 8.4 ; $P = .13$). Marginally significant differences in CSF pressure were seen for brain sagging (mean P_{CSF} , 7.4 ± 4.9 versus 10.1 ± 7.0 ; $P = .046$) and for the venous distension sign (mean P_{CSF} , 7.5 ± 4.7 versus 11.1 ± 8.1 ; $P = .047$).

The distribution of CSF pressure in subjects with various myelographic leak types is shown in Fig 2. As with brain imaging, there was substantial overlap of CSF pressures between groups. When all patients with any subtype of leak (high-flow or low-flow) were considered together, there was no difference in CSF pressure for patients with leak versus without leak (mean P_{CSF} , 8.3 ± 6.2 versus 8.6 ± 5.5 ; $P = .77$). Furthermore, when individual subtypes of leaks were analyzed separately, again no difference in CSF pressure was observed between groups (mean P_{CSF} , $8.6 \pm$

5.5 for no leak versus 7.7 ± 6.2 for high-flow leak versus 11.8 ± 5.6 for low-flow leak; $P \geq .16$).

Rates of Discordance between Imaging Signs and CSF Pressure

The rates of concordance/discordance between individual imaging signs and the presence of low CSF pressure are shown in Table 2. Only brain sagging and leak on myelography were found to be concordant in more than half of cases, and no sign was concordant >55% of the time. For the cases of discordance, it was much more common that the sign was present but the CSF pressure was >6 cm H_2O , though for all signs, the sign was absent despite the finding of low pressure in at least some cases.

DISCUSSION

Spinal CSF leaks in SIH, which can be detected by myelography in some cases, cause loss of CSF volume, which some investigators believe results in the changes seen on brain imaging.^{10,11} Given the known relationship between pressure and volume in a closed system, one would expect that these imaging signs of SIH would also be correlated with low CSF pressure, another common finding in SIH. To the contrary, however, our investigation shows that while the presence of ≥ 1 brain imaging sign is relatively common in patients with SIH, there is weak correlation between individual brain or myelographic imaging signs and a patient's CSF pressure. As a result, discordance between the expected imaging signs and the finding of low CSF pressure is routinely encountered.

This discordance indicates that the imaging findings associated with SIH are not uniformly accompanied by a low-pressure state. Furthermore, it reinforces the need to pursue the diagnosis by using a combination of CSF pressure measurement, brain imaging, and spinal imaging rather than any single test when the diagnosis is suspected.

Our investigation is not the first to describe the variability of CSF pressure and imaging findings in patients with SIH.¹² Mokri⁵ previously reported a case series of patients with SIH who demonstrated discordant pressure and imaging and suggested that decreased CSF volume rather than decreased pressure was a more

Table 2: Prevalence of imaging signs and concordance with low P_{CSF}^a

	Overall Prevalence		Concordant Sign and P _{CSF}		Discordant Sign and P _{CSF}			
					Sign Absent, P _{CSF} ≤ 6		Sign Present, P _{CSF} > 6	
	%	No./Total	%	No./Total	%	No./Total	%	No./Total
Dural enhancement	83	77/93	39	36/93	5	5/93	56	52/93
Brain sagging	61	60/99	55	54/99	9	9/99	36	36/99
Venous distension sign	75	75/99	42	42/99	8	8/99	49	49/99
Leak on myelogram	55	54/99	55	54/99	12	12/99	33	33/99

^a Concordance is defined as the presence of the imaging sign when P_{CSF} is low (≤ 6 cm H₂O) or absence of the sign when P_{CSF} is not low.

appropriate conception of the disease. Since then, other authors have made similar observations, though predominantly in single case reports or small case series.¹³⁻¹⁵ Our data, however, confirm that this variability is common in a large proportion of patients with the disease, rather than in a small subset.

Despite previous reports on this discordance between symptoms and CSF pressure, the concept that low CSF pressure (ie, ≤ 6 cm H₂O) is the fundamental pathology underpinning SIH remains entrenched in both the literature and professional societies. For example, the International Classification of Headache Disorders, 3rd edition² published in 2013 classifies SIH as “headache attributed to low cerebrospinal fluid pressure.” Similarly, a review published in 2015 states that “a decrease in CSF pressure defines spontaneous intracranial hypotension.”¹⁶ In our experience, these definitions lead to confusion among clinicians seeking to evaluate patients for the condition, often leading to the misconception that CSF pressure measurement alone is sufficient to diagnose or exclude SIH.

Having established that discordance between imaging (which likely principally reflects CSF volume) and CSF pressure is common in SIH, one must next consider why this seemingly paradoxical state occurs, because a loss in CSF volume would be expected to result in decreased CSF pressure. To answer this question, it is useful to briefly consider normal CSF physiology. In the steady-state, CSF pressure is greater than systemic venous pressure, a fact that permits reabsorption of CSF at the level of the arachnoid granulations.¹⁷ Maintenance of this steady-state CSF pressure occurs via balancing of CSF production and absorption.¹⁷ Thus, if CSF volume decreases and CSF pressure falls below venous pressure, CSF absorption will decrease; this decrease allows CSF volume to re-accumulate and restore normal CSF pressure, a process termed “dynamic equilibrium.”¹⁸ It is possible, however, to disrupt the homeostatic mechanisms that maintain a constant CSF pressure if the buffering capacity of the system is overwhelmed.¹⁷

On the basis of our data, it is clear that some patients with CSF leaks are able to maintain the steady-state CSF pressure while others are not, though the ability to maintain the CSF pressure does not necessarily prevent headache in these patients. Furthermore, it seems that this ability to maintain CSF pressure is not solely a function of a slower rate of CSF leakage because we observed no difference in CSF pressures between patients who had evidence of a high-flow CSF leak and those with no leak seen. These observations suggest 2 conclusions: First, that headache in patients with SIH is not primarily determined by low CSF pressure; and second, compensatory mechanisms exist in some indi-

viduals that help maintain CSF pressure despite active CSF volume loss.

One potential compensatory mechanism that may vary from person to person is compliance of the thecal sac, which may be influenced by body habitus or dilation of epidural veins. For example, in a recent investigation, Tain et al¹⁹ demonstrated that the compliance of the spinal canal was less in patients with obesity with idiopathic intracranial hypertension (pseudotumor cerebri) than in healthy controls, noting that MR imaging of the thecal sac showed a reduced cross-sectional area of the spinal CSF spaces in these patients.^{19,20} In SIH, dilation of the epidural venous plexus has been observed in some cases,²¹ which would reduce cross-sectional area of the spinal canal, thereby compensating for CSF volume loss and increasing CSF pressure, in a manner analogous to pseudotumor cerebri. Moreover, cervical venous dilation is known to change between supine and upright posture in healthy individuals but has been observed to demonstrate person-to-person variability,²² a finding that may be more significant in the setting of orthostatic changes in CSF pressure associated with SIH. These compensatory mechanisms would share in common the ability to, at least partially, preserve the overall volume within the enclosed craniospinal canal, allowing CSF pressure to be maintained despite decreased CSF volume due to a spinal fluid leak. In so doing, these proposed mechanisms would satisfy the requirements of the Monro-Kellie hypothesis.¹¹ Further investigation into what compensatory mechanisms are engaged in the setting of SIH could potentially help elucidate the underlying physiology of the CSF pressure/volume relationship in these patients and could help guide novel therapies.

Our study has limitations. First, it is possible that there is variability in CSF pressure that could decrease the accuracy of any single pressure measurement. Second, it is possible that our location at a tertiary care center could result in referral bias, leading to an atypical cohort of subjects with SIH, though all subjects satisfied established diagnostic criteria for SIH and most patients had not been treated previously at other centers.

CONCLUSIONS

The presence of ≥ 1 brain imaging and myelographic imaging sign of SIH is common in those with the condition, but individual signs generally correlate poorly with CSF pressure measurements. These findings emphasize the need to base the diagnosis of SIH on multiple criteria rather than any single imaging finding or CSF pressure measurement. Furthermore, our results reinforce the

notion that low CSF pressure is not the only factor that results in the condition and that patient-specific variables may influence the pathophysiology of the disease.

REFERENCES

1. Schievink WI, Dodick DW, Mokri B, et al. **Diagnostic criteria for headache due to spontaneous intracranial hypotension: a perspective.** *Headache* 2011;51:1442–44 CrossRef Medline
2. Headache Classification Committee of the International Headache Society (IHS). **The International Classification of Headache Disorders, 3rd edition (beta version).** *Cephalalgia* 2013;33:629–808 CrossRef Medline
3. Mokri B, Hunter SF, Atkinson J, et al. **Orthostatic headaches caused by CSF leak but with normal CSF pressures.** *Neurology* 1998;51:786–90 CrossRef Medline
4. Chung SJ, Kim JS, Lee MC. **Syndrome of cerebral spinal fluid hypovolemia: clinical and imaging features and outcome.** *Neurology* 2000;55:1321–27 CrossRef Medline
5. Mokri B. **Spontaneous cerebrospinal fluid leaks: from intracranial hypotension to cerebrospinal fluid hypovolemia—evolution of a concept.** *Mayo Clin Proc* 1999;74:1113–23 CrossRef Medline
6. Kranz PG, Gray L, Taylor JN. **CT-guided epidural blood patching of directly observed or potential leak sites for the targeted treatment of spontaneous intracranial hypotension.** *AJNR Am J Neuroradiol* 2011;32:832–38 CrossRef Medline
7. Farb RI, Forghani R, Lee SK, et al. **The venous distension sign: a diagnostic sign of intracranial hypotension at MR imaging of the brain.** *AJNR Am J Neuroradiol* 2007;28:1489–93 CrossRef Medline
8. Alvarez-Linera J, Escribano J, Benito-León J, et al. **Pituitary enlargement in patients with intracranial hypotension syndrome.** *Neurology* 2000;55:1895–97 CrossRef Medline
9. Kranz PG, Luetmer PH, Diehn FE, et al. **Myelographic techniques for the detection of spinal CSF leaks in spontaneous intracranial hypotension.** *AJR Am J Roentgenol* 2016;206:8–19 CrossRef Medline
10. Fishman RA, Dillon WP. **Dural enhancement and cerebral displacement secondary to intracranial hypotension.** *Neurology* 1993;43:609–11 CrossRef Medline
11. Mokri B. **The Monro-Kellie hypothesis: applications in CSF volume depletion.** *Neurology* 2001;56:1746–48 CrossRef Medline
12. Schievink WI. **Spontaneous spinal cerebrospinal fluid leaks and intracranial hypotension.** *JAMA* 2006;295:2286–96 CrossRef Medline
13. Schievink WI, Tourje J. **Intracranial hypotension without meningeal enhancement on magnetic resonance imaging: case report.** *J Neurosurg* 2000;92:475–77 CrossRef Medline
14. Schoffer KL, Benstead TJ, Grant I. **Spontaneous intracranial hypotension in the absence of magnetic resonance imaging abnormalities.** *Can J Neurol Sci* 2002;29:253–57 CrossRef Medline
15. Schievink WI, Maya MM, Louy C. **Cranial MRI predicts outcome of spontaneous intracranial hypotension.** *Neurology* 2005;64:1282–84 CrossRef Medline
16. Ducros A, Bioussé V. **Headache arising from idiopathic changes in CSF pressure.** *Lancet Neurol* 2015;14:655–68 CrossRef Medline
17. Marmarou A, Shulman K, Rosende RM. **A nonlinear analysis of the cerebrospinal fluid system and intracranial pressure dynamics.** *J Neurosurg* 1978;48:332–44 CrossRef Medline
18. Ryder HW, Espey FF, Kimbell FD, et al. **The mechanism of the change in cerebrospinal fluid pressure following an induced change in the volume of the fluid space.** *J Lab Clin Med* 1953;41:428–35 Medline
19. Tain RW, Bagci AM, Lam BL, et al. **Determination of cranio-spinal canal compliance distribution by MRI: methodology and early application in idiopathic intracranial hypertension.** *J Magn Reson Imaging* 2011;34:1397–404 CrossRef Medline
20. Hogan QH, Prost R, Kulier A, et al. **Magnetic resonance imaging of cerebrospinal fluid volume and the influence of body habitus and abdominal pressure.** *Anesthesiology* 1996;84:1341–49 CrossRef Medline
21. Yousry I, Förderreuther S, Moriggl B, et al. **Cervical MR imaging in postural headache: MR signs and pathophysiological implications.** *AJNR Am J Neuroradiol* 2001;22:1239–50 Medline
22. Alperin N, Lee SH, Sivaramakrishnan A, et al. **Quantifying the effect of posture on intracranial physiology in humans by MRI flow studies.** *J Magn Reson Imaging* 2005;22:591–96 CrossRef Medline

The “Hyperdense Paraspinal Vein” Sign: A Marker of CSF-Venous Fistula

P.G. Kranz, T.J. Amrhein, W.I. Schievink, I.O. Karikari, and L. Gray

ABSTRACT

SUMMARY: CSF-venous fistula is a recently reported cause of spontaneous intracranial hypotension that may occur in the absence of myelographic evidence of CSF leak. Information about this entity is currently very limited, but it is of potential importance given the large percentage of cases of spontaneous intracranial hypotension associated with negative myelography findings. We report 3 additional cases of CSF-venous fistula and describe the “hyperdense paraspinal vein” sign, which may aid in its detection.

ABBREVIATION: SIH = spontaneous intracranial hypotension

Spontaneous intracranial hypotension is thought to result from leakage of CSF from the spinal thecal sac, but in approximately half of cases, no leak is seen on myelography.^{1,2} Patients may be treated with prolonged bed rest or nontargeted lumbar epidural blood patch, but these therapies may not be successful in a substantial proportion of patients.^{1,3} In cases in which targeted treatment is desired (such as when nontargeted lumbar epidural blood patch fails), these cases of SIH with no myelographic evidence of CSF leak can be very challenging, and the inability to determine the site of the leak may preclude effective treatment. It has been previously presumed that these cases may be the result of intermittent or very slow-flow CSF leaks.

Recently, it has been recognized that direct fistulas between CSF and paraspinal veins can be a cause of SIH with negative findings on myelography. In a series of 3 patients, Schievink et al⁴ reported the presence of such CSF-venous fistulas, diagnosed by using digital subtraction myelography. Two of these cases had negative findings on CT myelography, meaning that they occurred with no concomitant epidural leak of CSF. Presently, it is unclear how frequently this phenomenon occurs and to what extent it may account for some of the cases of SIH in patients with negative findings on myelography. Furthermore, these lesions were identified with digital subtraction myelography, which is not

performed at all institutions, is more commonly used in the setting of high-flow CSF leaks, and typically covers only a portion of the total length of the spine.^{5,6} Thus, it would be helpful to identify, from clues on cross-sectional imaging, which patients might benefit from a digital subtraction myelogram and where that imaging should be focused to detect these uncommonly recognized, often subtle lesions.

In this Brief Report, we present 3 additional cases of CSF-venous fistulas in patients with SIH and describe a novel imaging sign, the “hyperdense paraspinal vein,” which may assist in CSF-venous fistula localization.

Cases

Case 1. A 34-year-old woman had new-onset orthostatic headache and back pain. Brain MR imaging showed dural enhancement, brain sagging, and a venous distention sign. Opening pressure measured 0 cm H₂O. A blind epidural blood patch improved her symptoms for 2 weeks, but her headaches recurred. CT myelography revealed a focal leak of contrast at the left T8 nerve root (Fig 1). Additionally, a hyperattenuated paraspinal vein was seen at this level, measuring 83–126 HU. The same vein on nonmyelographic CT images measured 27–34 HU. Targeted patching by using blood and fibrin glue was performed at this level but did not result in durable relief. A dynamic myelogram was then obtained, whereby the patient was placed in the left lateral decubitus position with the table tilted feet-down, contrast was injected into the thecal sac, the patient was then slowly tilted head-down, and the contrast passage was monitored by using intermittent fluoroscopy and spot radiographs. This study demonstrated no epidural fluid collection, but there was evidence of a CSF-venous fistula, with myelographic contrast identified in the adjacent paraspinal vein. The patient was taken to the operating room, where a hemi-

Received October 28, 2015; accepted after revision December 4.

From the Departments of Radiology (P.G.K., T.J.A., L.G.) and Neurosurgery (I.O.K.), Duke University Medical Center, Durham, North Carolina; and Department of Neurosurgery (W.I.S.), Cedars-Sinai Medical Center, Los Angeles, California.

Please address correspondence to Peter G. Kranz, MD, Department of Radiology, DUMC Box 3808, Duke University Medical Center, Durham, NC 27710; e-mail: peter.kranz@duke.edu; @PeterGKranz

<http://dx.doi.org/10.3174/ajnr.A4682>

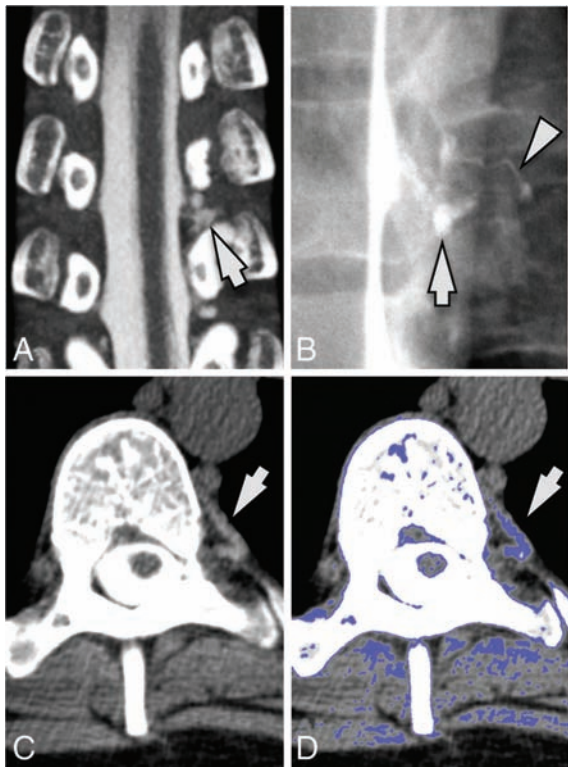


FIG 1. A 34-year-old woman with SIH. *A*, Coronal image from a CT myelogram shows a low-flow CSF leak inferior to the left T8 nerve root (arrow). *B*, A subsequent dynamic myelogram obtained with the patient in the left lateral decubitus position shows the area of the leak (arrow) with a fistula to an adjacent paraspinal vein (arrowhead). *C*, Axial image from her original CT myelogram reveals a hyperattenuated paraspinal vein (arrow). *D*, Postprocessed image with thresholded color overlay depicting attenuation values from 60 to 140 HU helps improve the conspicuity of this hyperattenuated vein.

laminectomy was performed to expose the nerve root. No free epidural CSF leakage was seen, but an abnormal enlarged vein was seen connecting to a CSF-filled diverticulum of the nerve root, which was coagulated and divided. Following the operation, the positional headache immediately resolved and had not recurred at 4-month follow-up.

Case 2. A 56-year-old man with new-onset positional headaches associated with neck and interscapular pain. Brain MR imaging showed dural enhancement, brain sagging, a venous distention sign, and bilateral subdural collections. Opening pressure measured 3 cm H₂O. Nontargeted lumbar epidural blood patch only helped his symptoms for a few hours. CT myelogram revealed a small focus of CSF leakage adjacent to the right nerve root sleeve at T10–11 (Fig 2). A hyperattenuated paraspinal vein was seen at this level, measuring 93–146 HU. The same vein on nonmyelographic CT images measured 14–32 HU. Targeted patching by using blood and fibrin glue was performed, which only provided 5 days of relief. He re-presented with new subdural hemorrhages and underwent repeat targeted patching 2 additional times during the next month, again without durable relief. He was then taken to the operating room, where a hemilaminectomy was performed to expose the nerve root. No dural defect or CSF leak was seen; however, prominent veins surrounding the nerve root were identified

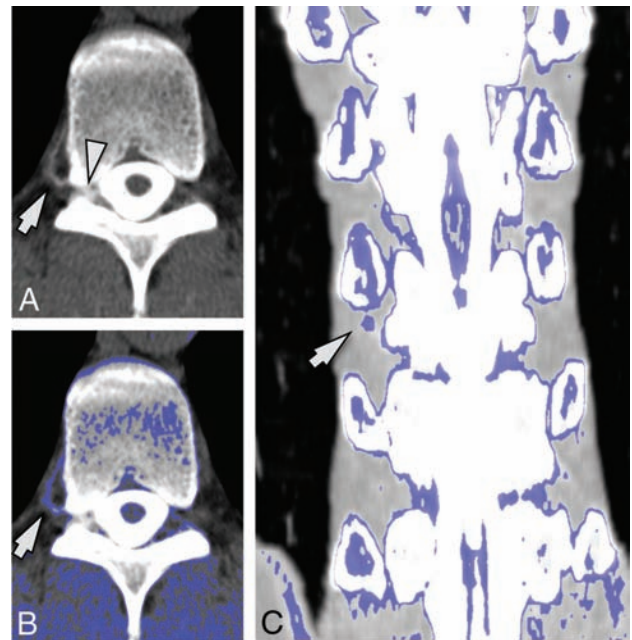


FIG 2. A 56-year-old man with SIH. *A*, Axial image from a CT myelogram shows a low-flow CSF leak in the right neural foramen at T10–11 (arrowhead). An adjacent hyperattenuated paraspinal vein (arrow) is seen. *B*, Postprocessed image with thresholded color overlay depicting attenuation values from 60 to 140 HU improves the conspicuity of this hyperattenuated vein (arrow). *C*, Coronal image with thresholded color overlay demonstrates that only the vein at the level and side of the fistula (arrow) shows increased attenuation.

and coagulated. Following surgery, the positional headaches immediately resolved and had not recurred at 2-year follow-up.

Case 3. A 59-year-old woman presented with 5 years of positional headache, neck and bilateral upper extremity pain, and tinnitus. Brain MR imaging showed dural enhancement, brain sagging, and a venous distention sign. Opening pressure measured 10.2 cm H₂O. A previous blind epidural blood patch did not produce durable relief. CT myelography revealed extensive nerve root sleeve diverticula but no evidence of a CSF leak. A hyperattenuated paraspinal vein was present on the right at T6–7, measuring 85–101 HU (Fig 3). The same vein on nonmyelographic CT images measured 29 HU. She underwent epidural patching by using blood and fibrin glue targeted at multiple nerve root sleeve diverticula on 3 occasions, but her symptoms recurred each time. A digital subtraction myelogram was then obtained, by using the technique previously described,⁶ revealing a CSF-venous fistula on the right at T6–7. At the operation, a very thin-walled cyst was encountered, to which was attached an extensive venous plexus. The plexus was carefully dissected free and then cauterized. No dural defect was seen intraoperatively. Her positional headaches resolved after surgery and had not recurred at 15-month follow-up.

DISCUSSION

In this report, we present radiologic and surgical confirmation of the presence of CSF-venous fistulas as an etiology for SIH, first reported in a recent small case series of 3 patients by Schievink et al.⁴ Confirmation of this entity is important in that it identifies an alternative mechanism of CSF volume loss leading to the clinical

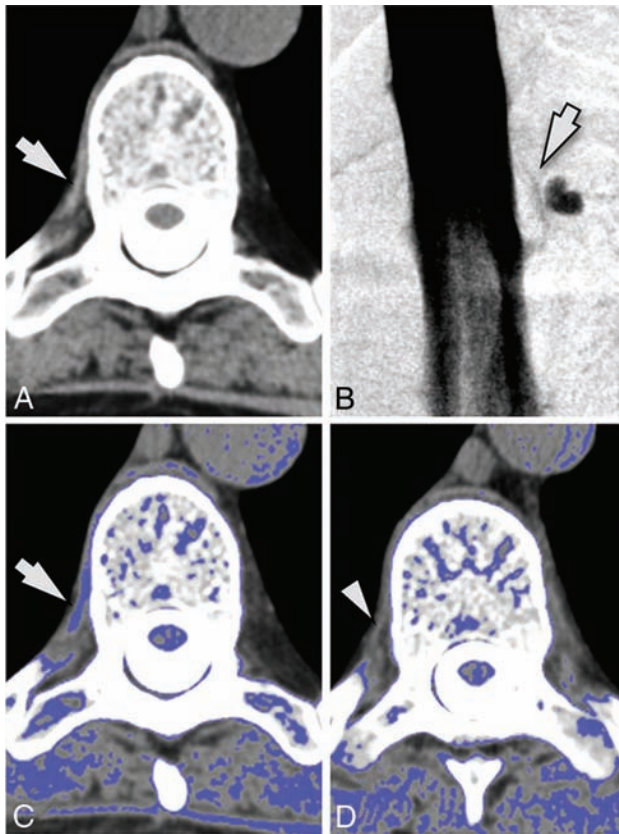


FIG 3. A 59-year-old woman with SIH. *A*, Axial image from a CT myelogram shows a hyperattenuated paraspinal vein (arrow) at T6–7 on the right. *B*, A subsequent digital subtraction myelogram shows a CSF-venous fistula at this location (arrow). *C*, Postprocessed image with thresholded color overlay depicting attenuation values from 60 to 140 HU again helps with the identification of this finding (arrow). *D*, Axial image from an adjacent level (T8–9) where there was no fistula is provided for comparison. Note that the paraspinal vein is not hyperattenuated (arrowhead) and is not identified on the thresholded color overlay.

syndrome of SIH. For the estimated 46%–55% of patients with SIH with no evidence of CSF leakage on myelography,^{1,2} the identification of a fistula may provide the opportunity for targeted treatment. On the basis of our limited experience with CSF-venous fistulas, we have found them to be generally unresponsive to epidural patching, ultimately requiring surgical intervention to obliterate the fistula and its draining veins.

Our series also suggests that CT myelography may provide some clues as to the presence and location of the fistula. In all 3 of our cases, after intrathecal contrast was administered, a hyperattenuated paraspinal vein was identified in close proximity to the site where the CSF fistula was ultimately localized. The average attenuation of the hyperattenuated vessel on postmyelographic CT measured 105.7 ± 23.0 HU, compared with attenuation values of 27.5 ± 6.4 HU for the same vessel on nonmyelographic CT (ie, CT performed without intrathecal myelographic contrast).

The conspicuity of this sign was improved by the use of image postprocessing with commercially available software (Aquarius iNtuition, Version 4.4.11; TeraRecon, San Mateo, California).

Image thresholding with color overlay was used to highlight CT attenuation values of 60–140 HU; this range was selected empirically on the basis of observed attenuation values in the hyperattenuated-appearing veins compared with normal-appearing paraspinal veins at other levels.

This “hyperdense paraspinal vein” sign presumably represents rapid passage of myelographic contrast into the venous system through the fistula. Under normal conditions, CSF reabsorption into the bloodstream happens at the level of spinal nerve roots, driven by a pressure gradient across arachnoid villi by means of vacuoles that traverse the wall of the villus in a unidirectional manner.^{7–9} CSF-venous fistulas may represent focal rupture or failure of these villi, resulting in persistent, unregulated CSF loss.

Identification of this sign not only suggests that a fistula is present but also aids in its localization. This finding is potentially important because the subtle imaging appearance associated with many of the reported cases of CSF-venous fistula may make them difficult to detect on conventional myelography or digital subtraction myelography unless their presence is suspected, and not all patients with SIH will undergo digital subtraction myelography because its use has previously been generally restricted to a limited number of medical centers where it is typically used for the localization of high-flow CSF leaks.⁵ As future cases of CSF-venous fistulas are identified, it will be useful to determine the sensitivity of this imaging sign, whether there are false-positive causes of hyperattenuated paraspinal veins, whether this entity is ever seen outside of the context of SIH, and whether other imaging techniques or image postprocessing may aid in its detection.

REFERENCES

1. Sencakova D, Mokri B, McClelland RL. **The efficacy of epidural blood patch in spontaneous CSF leaks.** *Neurology* 2001;57:1921–23 CrossRef Medline
2. Luetmer PH, Schwartz KM, Eckel LJ, et al. **When should I do dynamic CT myelography? Predicting fast spinal CSF leaks in patients with spontaneous intracranial hypotension.** *AJNR Am J Neuroradiol* 2012;33:690–94 CrossRef Medline
3. Chung SJ, Kim JS, Lee MC. **Syndrome of cerebral spinal fluid hypovolemia: clinical and imaging features and outcome.** *Neurology* 2000;55:1321–27 CrossRef Medline
4. Schievink WI, Moser FG, Maya MM. **CSF-venous fistula in spontaneous intracranial hypotension.** *Neurology* 2014;83:472–73 CrossRef Medline
5. Hoxworth JM, Trentman TL, Kotsenas AL, et al. **The role of digital subtraction myelography in the diagnosis and localization of spontaneous spinal CSF leaks.** *AJR Am J Roentgenol* 2012;199:649–53 CrossRef Medline
6. Hoxworth JM, Patel AC, Bosch EP, et al. **Localization of a rapid CSF leak with digital subtraction myelography.** *AJNR Am J Neuroradiol* 2009;30:516–19 CrossRef Medline
7. Levine JE, Povichock JT, Becker DP. **The morphological correlates of primate cerebrospinal fluid absorption.** *Brain Res* 1982;241:31–41 CrossRef Medline
8. Cutler RW, Page L, Galicich J, et al. **Formation and absorption of cerebrospinal fluid in man.** *Brain* 1968;91:707–20 CrossRef Medline
9. Edsbacke M, Tisell M, Jacobsson L, et al. **Spinal CSF absorption in healthy individuals.** *Am J Physiol Regul Integr Comp Physiol* 2004;287:R1450–55 CrossRef Medline

Celebrating 35 Years of the AJNR

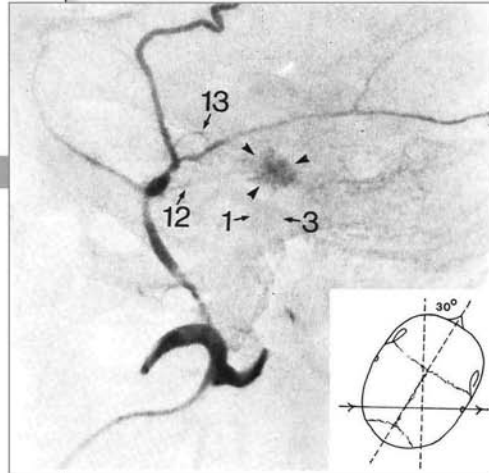
July 1981 edition

Selective Arteriography of Glomus Tympanicum and Jugulare Tumors: Techniques, Normal and Pathologic Arterial Anatomy

John R. Hessolink¹
Kenneth R. Davis
Juan M. Tavoras

Glomus tympanicum and jugulare tumors arise within the middle ear and jugular fossa, respectively, but often extend into the adjacent areas of the skull base and posterior fossa. Multiple branches of the external carotid, internal carotid, and vertebral arteries may contribute to the vascular supply of these lesions. The arteriograms of 15 patients with glomus tumors were correlated with the surgical findings to determine if selective arteriography could define precisely the involvement within the middle ear, jugular fossa, and mastoid. The arteriographic mapping correlated well with the surgical findings in nine of 13 cases that had surgery, but a few important limitations were found. Therefore, a new arteriographic projection, called a transcanalicular view, is proposed that separates the middle ear from the jugular fossa, allowing for better visualization and assessment of the tumor blush.

Glomus tympanicum and jugulare tumors arise from paraganglionic glomus tissue within the middle ear and jugular fossa. Improved microsurgical techniques in association with preoperative embolization have allowed complete resection of these vascular tumors in many cases with minimal blood loss [1, 2]. Previous reports have described successful embolization of glomus tumors [3-7]. Selective arteriography is mandatory to define precisely the location and extent of these tumors for such treatment. In this report, we describe the arteriographic techniques, propose the optimum radiographic positions, review the complex arterial anatomy of the region, and evaluate the arterial pedicles of glomus tympanicum and jugulare tumors.



Received December 31, 1980; accepted after revision March 10, 1981.

Presented at the annual meeting of the Radiological Society of North America, Dallas, TX, November 1980.

This work was supported in part by the Mallinckrodt Company, St. Louis, MO.

All authors: Department of Radiology, Section of Neurosurgery, Harvard Medical School, and Massachusetts General Hospital, Boston, MA 02114. Address reprint requests to J. R. Hessolink.

AJNR 2:389-397, July/August 1981
0195-8108/81/0204-0389 \$05.00
© American Roentgen Ray Society

Myelography of Sacral Agenesis

Betty Sue Brooks¹
Taher El Gammal²
Patricia Hartlage²
Wayne Beveridge³

In the past, neurologic deficits found in association with sacral agenesis were thought to be unamenable to surgical therapy. Recent experience and a careful review of autopsy and case reports from the literature have demonstrated that this assumption is unwarranted. Four cases of sacral agenesis are reported with description of the myelographic findings of each case. Surgical confirmation was obtained in three of these patients. Dural sac stenosis treated with duraplasty resulted in striking improvement in the neurologic status of two patients, while in the third, a 2-month-old infant, adhesive arachnoidal bands in the distal thecal sac were found at surgery and a fat and thickened filum terminale was transected. The fourth patient had a low-lying spinal cord and a posterior meningocele. The myelographic findings appear to be divisible into two categories. One group of patients may have high termination of the subarachnoid space with a dural sac stenosis and will benefit from duraplasty, while in the other, findings may include a widened or normal subarachnoid space and low-lying tethered spinal cord. It is emphasized that treatment of dural sac stenosis, tethered cord, and intrathecal or extrathecal masses that occur in some of these patients may afford significant improvement in their neurologic condition. These children deserve careful baseline neurologic evaluation and follow-up and a more aggressive approach toward adequate myelographic assessment.

Myelograms have been obtained infrequently in children with sacral agenesis. In the past, emphasis has been on management of the more clinically apparent orthopedic and genitourinary tract problems that usually accompany this condition [1-8]. Accompanying neurologic deficits have received less attention, and surgical exploration has been infrequently attempted.

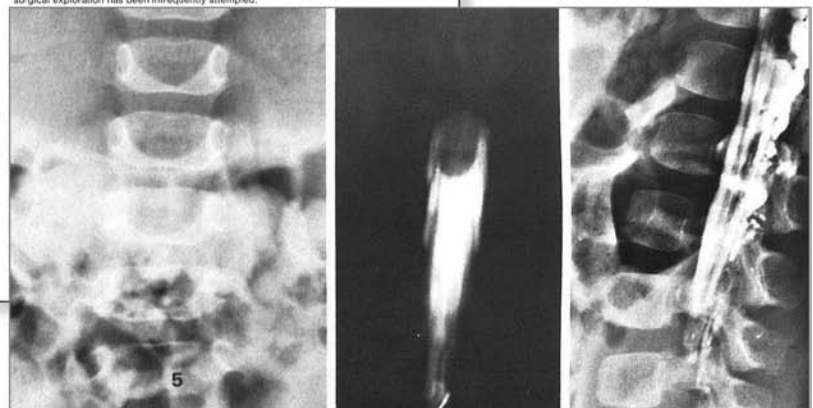
Received October 31, 1980; accepted after revision February 25, 1981.

¹Department of Radiology, Section of Neurosurgery, Medical College of Georgia, Augusta, GA 30912. Address reprint requests to B. S. Brooks.

²Department of Pediatric Neurology, Medical College of Georgia, Augusta, GA 30912.

³Department of Neurosurgery, Medical College of Georgia, Augusta, GA 30912.

AJNR 2:319-323, July/August 1981
0195-8108/81/0204-0319 \$05.00
© American Roentgen Ray Society



ON-LINE APPENDIX

Interscanner Platform Calibration and Validation

QSM measurements on the Philips Achieva and Siemens Verio platforms were cross-validated by using a ferumoxytol phantom (see Tan et al¹ for details). The QSM imaging protocols were identical to those used clinically. The purpose of this phantom experiment was to ensure that no bias was introduced when combining data from both platforms for analysis.

Susceptibility values in the ferumoxytol phantom were calculated and compared between the 2 platforms by using ROIs. Quantitative results from both platforms were correlated by using linear regression.

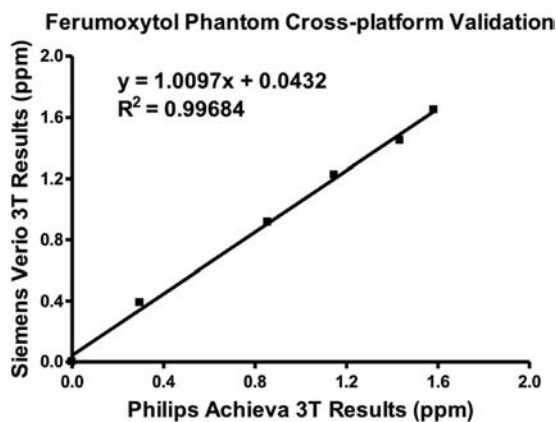
Cross-Platform Validation Results

The ferumoxytol phantom result is shown in the On-line Fig. QSM was able to clearly differentiate various ferumoxytol

concentrations with the data acquired on both Siemens and Philips 3T platforms. A strong positive correlation was found between the measurements made in Siemens and Philips platforms with a correlation coefficient of 0.998 ($P < .01$, $R^2 > 0.99$). This result provided confidence that QSM produced comparable measurements across those 2 instruments. The comparable results between the 2 hardware platforms supported the feasibility of multicentered trials by using QSM as an outcome measure.

REFERENCE

1. Tan H, Liu T, Wu Y, et al Evaluation of iron content in human cerebral cavernous malformation by using quantitative susceptibility mapping. *Invest Radiol* 2014;49:498–504



ON-LINE FIG. Cross-platform validation between Siemens Verio and Philips Achieva systems by using a ferumoxytol phantom.

ON-LINE APPENDIX

Data Acquisition

All imaging experiments were performed on a 3T MR imaging system with a maximum gradient strength of 45 mT/m and a maximum single-direction slew rate of 200 mT/m/ms (Tim Trio, Siemens) by using a twice-refocused balanced spin-echo diffusion echo-planer imaging pulse sequence¹ with fat suppression. Each session included independent DSI and DKI acquisitions, with the DTI data being taken as a subset of the DKI acquisition. Each volunteer was scanned during 2 separate sessions, resulting in 6 complete DSI and DKI datasets to quantify variability for each DWI method. The DWI protocols were optimized, to maximize the SNR rather than minimize the acquisition times, to facilitate the assessment of the accuracy of the DKI and DTI fiber-orientation estimates relative to those of DSI.

Acquisition parameters common to both DSI and DKI acquisitions were the following: voxel size = $2.7 \times 2.7 \times 2.7$ mm³, matrix = 82×82 , number of sections = 45, bandwidth = 1356 Hz/pixel, and a 32-channel head coil with an acceleration factor of 2 by using generalized autocalibrating partially parallel acquisition² and adaptive combine coil mode.³ Additional parameters for the DSI acquisition were TR/TE = 8300/151 ms and 515 diffusion-encoding gradient directions over a Cartesian grid with a maximum b-value of 6000 s/mm², which was optimized for diffusion sensitivity and gradient performance,⁴ resulting in a total acquisition time of 71.7 minutes. For the DKI acquisitions, additional parameters were TR/TE = 6100/102 ms, 64 diffusion-encoding gradient directions at b-values of 1000 s/mm² and 2000 s/mm², and 20 independent acquisitions without diffusion-weighting (b0 images), resulting in a total acquisition time of 15.6 minutes. In both cases, the TE was minimized to maximize SNR. DTI data were also analyzed by using the 0 and 1000 s/mm² b-value images from the DKI dataset. During each session, an additional T1-weighted magnetization-prepared rapid acquisition of gradient echo image with $1.0 \times 1.0 \times 1.0$ mm³ voxel dimensions was also acquired for anatomic reference. If one assumes 80% of the maximum gradient strength (45 mT/m), ie, 36 mT/m, was used to achieve the minimum TE, δ and Δ can be estimated at 32 and 74 ms for the DSI scan and 22.5 and 50 ms for the DKI scan, respectively.

dODF Reconstructions

Each scan for each subject was coregistered to the subject's initial DSI scan by using a 12-parameter affine transformation with SPM12 (<http://www.fil.ion.ucl.ac.uk/spm/software/spm12>). Following coregistration, we applied spatial smoothing to all diffusion-weighted images to reduce the effects of signal noise by using a Gaussian smoothing kernel of 1.25 times the voxel dimensions.⁵

The intravoxel DSI dODF was reconstructed by using DSI Studio (dsi-studio.labsolver.org) with a Hanning filter, width 17, applied to the q -space data. DKI-derived diffusion and kurtosis tensors were calculated by using a constrained weighted linear least squares algorithm,⁵ and the DKI dODF was calculated by using the closed-form solution derived by Jensen et al.⁶ The DTI-derived diffusion tensor was obtained by using weighted linear least squares.⁷ Following previous studies, the radial weighting power was set to $\alpha = 2$ for DSI^{8,9} and $\alpha = 4$ for DKI.^{6,10,11} For visual-

ization of DTI dODFs, the radial weighting power was set to $\alpha = 4$; however, this had no effect on the DTI-derived orientation estimates.^{6,10} All orientations were corrected for rotations of the image volume that occurred during image acquisition and coregistration.¹² The kurtosis dODF reconstruction was performed by using the Diffusional Kurtosis Estimator Fiber Tractography Module (<https://www.nitrc.org/projects/dke/>), and the DTI dODF was reconstructed by using in-house software.

Data Analysis

Angular variability of the dODFs was calculated by the absolute voxelwise angular difference for each reconstruction between the principal orientation (the orientation corresponding to the global maxima pair) from the first scan and the nearest orientation from the second scan. Angular errors in the DKI and DTI dODFs were calculated by using the absolute angular differences between the principal orientation from the corresponding DSI scan and the nearest dODF maximum from the respective reconstruction. For angular difference measures, the nearest orientation in the second scan was chosen as opposed to the global maximum from the second scan because small fluctuations in dODF magnitudes in voxels with multiple orientation estimates could vary which orientation was identified as the global maximum, resulting in artificially large angular differences.¹⁰ Angular error estimates include intrinsic variability in the reconstruction techniques and hence combine both random and systematic error. In addition, because absolute differences are used, these measures are positively biased by noise and will consequently overestimate the true systematic differences.

To quantify angular variability and angular error, we defined ROIs for each subject. These included an inclusive WM ROI, which was defined as voxels with FA > 0.1; a conservative WM ROI, which was defined as voxels with FA > 0.3; a single-fiber-bundle ROI, which was defined as voxels within the inclusive WM ROI with the estimated number of fiber directions = 1 in the DSI scan; 2 crossing-fibers ROI, which was defined as voxels within the inclusive WM ROI with the number of fiber directions = 2 in the DSI scan; and a ≥ 3 crossing-fibers ROI, which was defined as voxels within the inclusive WM ROI with the number of fiber directions ≥ 3 in the DSI scan. To reduce CSF partial volume effects, we excluded voxels within each ROI with a mean diffusivity of $> 1.5 \mu\text{m}^2/\text{ms}$ from quantitative analyses.^{6,10} To help reduce the occurrence of spurious peaks in the DSI reconstruction, we used a quantitative anisotropy threshold of 0.1 to filter the DSI orientations.¹³

To visualize group differences in the angular variability and angular error measures, we normalized parameter maps from each subject to the International Consortium for Brain Mapping WM template¹⁴ by using SPM12 with nonlinear registration, and we constructed average, group-wise parameter maps.

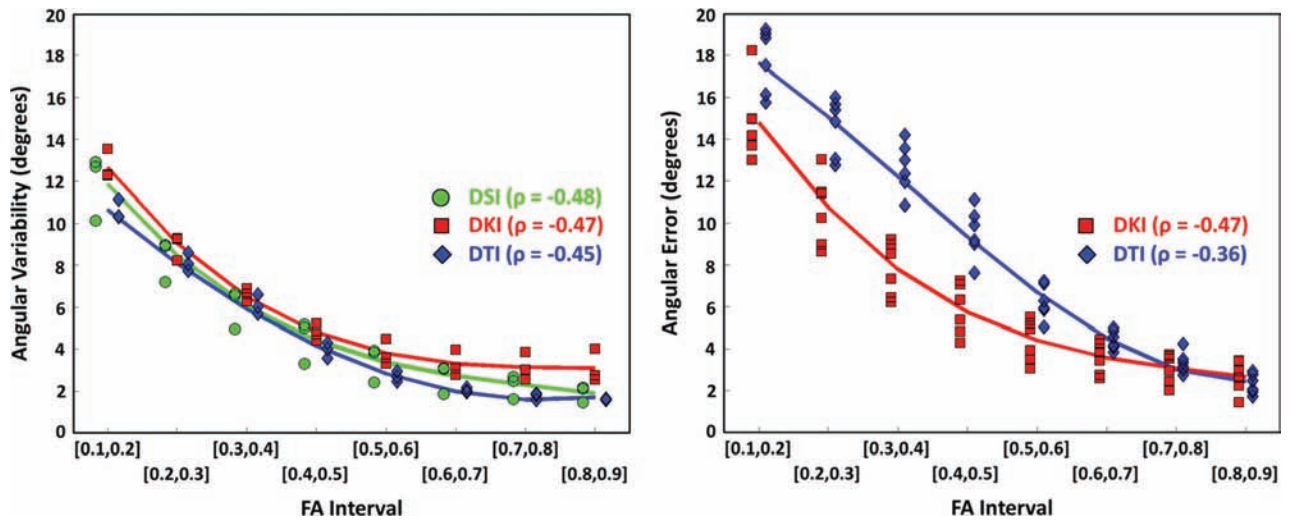
Tractography

WM fiber tractography was performed with DSI Studio by using the Euler method¹⁵ with a step size of 1.35 mm, a minimum track length of 20 mm, and a maximum track length of 450 mm. For direct and qualitative comparisons across the 3 techniques, we defined a common WM tracking ROI to include

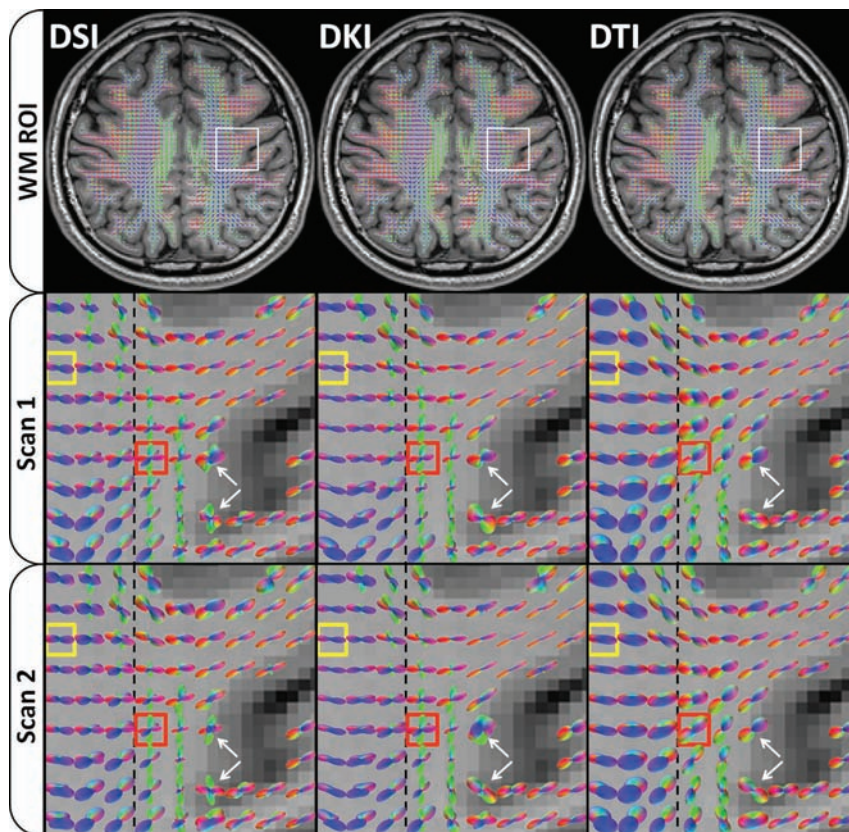
regions in the inclusive WM ROI with quantitative anisotropy of >0.1 in the DSI scan. The fiber-tracking algorithm was seeded with 200,000 random seed points within the WM tracking ROI. WM fiber tracts were visualized by using TrackVis (<http://www.trackvis.org>).

REFERENCES

1. Reese TG, Heid O, Weisskoff RM, et al. **Reduction of eddy-current-induced distortion in diffusion MRI using a twice-refocused spin echo.** *Magn Reson Med* 2003;49:177–82 CrossRef Medline
2. Griswold MA, Jakob PM, Heidemann RM, et al. **Generalized auto-calibrating partially parallel acquisitions (GRAPPA).** *Magn Reson Med* 2002;47:1202–10 CrossRef Medline
3. Walsh DO, Gmitro AF, Marcellin MW. **Adaptive reconstruction of phased array MR imagery.** *Magn Reson Med* 2000;43:682–90 Medline
4. Kuo LW, Chen JH, Wedeen VJ, et al. **Optimization of diffusion spectrum imaging and q-ball imaging on clinical MRI system.** *Neuroimage* 2008;41:7–18 CrossRef Medline
5. Tabesh A, Jensen JH, Ardekani BA, et al. **Estimation of tensors and tensor-derived measures in diffusional kurtosis imaging.** *Magn Reson Med* 2011;65:823–36 CrossRef Medline
6. Jensen JH, Helpert JA, Tabesh A. **Leading non-Gaussian corrections for diffusion orientation distribution function.** *NMR Biomed* 2014; 27:202–11 CrossRef Medline
7. Basser PJ, Mattiello J, Le Bihan D. **Estimation of the effective self-diffusion tensor from the NMR spin echo.** *J Magn Reson* 1994;103: 247–54 CrossRef Medline
8. Wedeen VJ, Hagmann P, Tseng WY, et al. **Mapping complex tissue architecture with diffusion spectrum magnetic resonance imaging.** *Magn Reson Med* 2005;54:1377–86 CrossRef Medline
9. Wedeen VJ, Wang RP, Schmahmann JD, et al. **Diffusion spectrum magnetic resonance imaging (DSI) tractography of crossing fibers.** *Neuroimage* 2008;41:1267–77 CrossRef Medline
10. Glenn GR, Helpert JA, Tabesh A, et al. **Optimization of white matter fiber tractography with diffusional kurtosis imaging.** *NMR Biomed* 2015;28:1245–56 CrossRef Medline
11. Neto Henriques R, Correia MM, Nunes RG, et al. **Exploring the 3D geometry of the diffusion kurtosis tensor: impact on the development of robust tractography procedures and novel biomarkers.** *Neuroimage* 2015;111:85–99 CrossRef Medline
12. Leemans A, Jones DK. **The B-matrix must be rotated when correcting for subject motion in DTI data.** *Magn Reson Med* 2009;61: 1336–49 CrossRef Medline
13. Yeh FC, Verstynen TD, Wang Y, et al. **Deterministic diffusion fiber tracking improved by quantitative anisotropy.** *PLoS One* 2013;8: e80713 CrossRef Medline
14. Mori S, Wakana S, Nagae-Poetscher LM, et al. *MRI Atlas of Human White Matter.* Amsterdam: Elsevier; 2005
15. Basser PJ, Pajevic S, Pierpaoli C, et al. **In vivo fiber tractography using DT-MRI data.** *Magn Reson Med* 2000;44:625–32 Medline



ON-LINE FIG 1. The performance of dODF-derived orientation estimates depends on FA, with angular variability and angular error decreasing with increasing FA. Data points for each group are averaged over the indicated interval and are separated in the horizontal direction within each interval for legibility. The Spearman rank correlation coefficient for the voxelwise performance measure relative to FA is indicated by ρ .



ON-LINE FIG 2. For each reconstruction, dODFs within the inclusive WM ROI are overlaid on the MPRAGE image for anatomic reference. The dODF reconstructions are qualitatively consistent between repeat scans, but DTI cannot detect crossing fibers (red box); this feature may increase angular error relative to DSI. DSI is more sensitive than DKI at detecting crossing fibers (yellow box). The inclusive WM ROI may include partial volume effects (white arrows), which may increase variability and error in orientation estimates.

On-line Table: dODF performance statistics in the FA- and NFD-defined WM ROIs^a

	No.	Angular Variability			Angular Error		Systematic Error ^b	
		DSI	DKI	DTI	DKI	DTI	DKI	DTI
Inclusive WM ROI (FA > 0.1)								
Subject 1	33303	8.7 (9.7)	8.2 (9.4)	7.6 (9.9)	9.9 (10.4)	13.7 (13.8)	1.7	6.1
Subject 2	34087	9.5 (9.7)	9.9 (9.9)	7.7 (9.7)	11.4 (12.3)	14.0 (14.0)	1.4	6.3
Subject 3	35340	6.4 (7.6)	8.3 (9.3)	7.4 (9.3)	10.0 (10.4)	13.8 (14.1)	1.7	6.5
Mean	34243	8.2 (9.0)	8.8 (9.5)	7.6 (9.7)	10.4 (11.0)	13.8 (14.0)	1.6	6.3
Conservative WM ROI (FA > 0.3)								
Subject 1	13692	5.3 (5.7)	4.8 (5.6)	4.4 (5.8)	6.2 (6.6)	10.1 (10.7)	1.4	5.7
Subject 2	11418	5.4 (5.4)	5.8 (5.4)	4.3 (5.6)	6.2 (7.1)	9.4 (10.1)	0.4	5.2
Subject 3	16144	3.7 (4.6)	5.2 (5.7)	4.8 (6.3)	6.3 (6.9)	9.9 (10.7)	1.1	5.0
Mean	13751	4.8 (5.2)	5.3 (5.6)	4.5 (5.9)	6.2 (6.9)	9.8 (10.5)	1.0	5.3
Single-fiber ROI (NFD = 1)								
Subject 1	18808	8.3 (8.3)	7.8 (8.2)	6.4 (7.6)	9.0 (8.7)	10.2 (9.7)	1.2	3.8
Subject 2	18814	8.8 (8.2)	9.2 (8.4)	6.0 (6.4)	10.0 (9.9)	10.5 (9.7)	0.9	4.6
Subject 3	23573	6.3 (7.0)	8.0 (8.4)	6.2 (7.4)	9.4 (9.2)	10.9 (10.8)	1.4	4.7
Mean	20398	7.8 (7.8)	8.3 (8.4)	6.2 (7.1)	9.5 (9.3)	10.6 (10.1)	1.2	4.4
Two crossing-fiber ROIs (NFD = 2)								
Subject 1	11258	9.2 (10.9)	8.7 (10.3)	8.8 (11.5)	10.7 (11.7)	17.4 (16.2)	2.0	8.6
Subject 2	11404	10.0 (10.9)	10.5 (10.8)	9.3 (11.5)	12.4 (13.7)	17.4 (16.2)	1.9	8.1
Subject 3	9824	6.6 (8.6)	8.6 (10.4)	9.2 (11.6)	10.8 (11.8)	18.2 (16.7)	2.2	9.0
Mean	10829	8.6 (10.1)	9.3 (10.5)	9.1 (11.5)	11.3 (12.4)	17.7 (16.4)	2.1	8.6
Three or more crossing fibers (NFD ≥ 3)								
Subject 1	3237	9.7 (12.3)	9.0 (11.7)	10.4 (14.1)	12.6 (14.1)	22.4 (18.9)	3.5	12.0
Subject 2	3869	11.3 (12.4)	12.0 (13.1)	11.4 (14.5)	14.9 (16.6)	21.7 (19.4)	2.9	10.3
Subject 3	1943	7.7 (10.0)	10.1 (12.3)	11.6 (14.0)	13.2 (14.3)	24.8 (19.8)	3.0	13.2
Mean	3016	9.6 (11.6)	10.4 (12.4)	11.1 (14.2)	13.5 (15.0)	23.0 (19.4)	3.2	11.8

Note:—NFD indicates number of fiber directions as determined with DSI.

^a The number of voxels in each ROI is indicated by "No.," and values for angular variability and angular error represent the mean (\pm SD) of the voxelwise performance measures throughout the ROI. All values are given in degrees.

^b Defined as the difference between the mean angular error and the mean angular variability over each ROI for the respective reconstructions.

ON-LINE APPENDIX

Supplemental Methods

For whole-brain CT perfusion/dynamic CTA, first a contrast bolus of 50 mL of iomeprol (Iomeron 400; Bracco, Milan, Italy) was injected using a Stellant CT Injector (Medrad, Indianola, Pennsylvania) with a flow rate of 4.5–5.5 mL/s, followed by 35–50 mL of saline with a flow rate of 3.5–5.0 mL/s, depending on the weight of the patient. Seven seconds after contrast injection, the first volume was imaged with a full dose of 310 mA. Three seconds later, 4 volumes were obtained every 2 seconds with 160 mA,

intended to visualize the early arterial phase. Subsequently, 6 volumes were imaged with 300 mA, to visualize the mid-arterial phase, followed by 3 volumes with 160 mA to visualize the late arterial phase. These volumes were also obtained every 2 seconds. Finally, 5 volumes were imaged at 130 mA every 5 seconds to image the venous phase. In total, 19 volumes were obtained during 1 minute, with a maximum total effective dose of 8.4 mSv. Postprocessing was performed on a Vitrea fx, Version 1.0, workstation (Vital Images, Minnetonka, Minnesota).

On-line Table 1: Baseline characteristics (N = 61)

	No. (%) ^a
Baseline:	
Age (yr) (mean) (SD)	67 (13)
Female sex	27 (44%)
NIHSS score (median) (IQR)	15 (12–19)
Premorbid mRS score of 0–2	58 (95%)
History of stroke/TIA	8 (13%)
History of hypertension	28 (46%)
History of diabetes mellitus	9 (15%)
Stroke onset to study CT time (min) (median) (IQR)	64 (40–110)
Occlusion site:	
MCA, M1 segment	39 (64%)
MCA, M2 segment	8 (13%)
Tandem occlusion (MCA + ICA)	14 (23%)
Treatment:	
No intravenous thrombolysis, no endovascular treatment	7 (11%)
IV thrombolysis alone	37 (61%)
Mechanical thrombectomy alone	3 (5%)
IV thrombolysis and mechanical thrombectomy	14 (23%)

Note:—IQR indicates interquartile range.

^aAll values are given as No. (%), unless otherwise indicated.

On-line Table 2: Risk of poor radiologic outcome at follow-up (infarct volume ≥ 70 mL) in relation to other clinical and radiologic parameters (N = 61)

Characteristics	Poor Outcome/Characteristic Present (n/N) (%)	Poor Outcome/Characteristic Absent (n/N) (%)	Risk Ratio (95% CI)
Age 60 years or older	28/46 (61%)	5/15 (33%)	1.8 (0.8–3.9)
Female sex	11/27 (41%)	22/34 (65%)	0.6 (0.4–1.1)
NIHSS score > 15	16/29 (55%)	17/32 (53%)	1.0 (0.7–1.6)
M1 MCA segment	21/39 (54%)	12/22 (55%)	1.0 (0.6–1.6)
M2 MCA segment	3/8 (38%)	30/53 (57%)	0.7 (0.3–1.7)
Middle cerebral and internal carotid arteries ^a	9/14 (64%)	24/47 (51%)	1.3 (0.8–2.0)
IVT only	19/37 (51%)	14/24 (58%)	0.9 (0.6–1.4)
IA treatment	9/17 (53%)	24/44 (55%)	1.0 (0.6–1.6)
No treatment	5/7 (71%)	28/54 (52%)	1.4 (0.8–2.4)
ASPECTS ^b ≤ 5	7/8 (88%)	26/53 (49%)	1.8 (1.2–2.6)
Clot burden score ^c < 7	23/37 (62%)	10/24 (42%)	1.5 (0.9–2.6)

Note:—IVT indicates intravenous thrombolysis; IA, intra-arterial.

^aCarotid terminus or tandem occlusion.

^bASPECTS is an imaging measure of the extent of ischemic stroke. Scores range from 0 to 10, with lower scores indicating a larger infarct core.

^cThe clot burden score is a grading system of the extent of arterial occlusion in patients with acute anterior circulation ischemic stroke. Scores range from 0 to 10, with lower scores indicating more occluded vessel segments.

On-line Table 3: Number of patients with poor or good collaterals on dynamic CTA among patients receiving IA treatment (either with or without IVT) or non-IA treatment (IVT only or no treatment) (N = 61)^a

	Poor Collaterals	Good Collaterals
IA treatment (No.)	6	11
Non-IA treatment (No.)	11	33
Total (No.)	17	44

Note:—IA indicates intra-arterial.

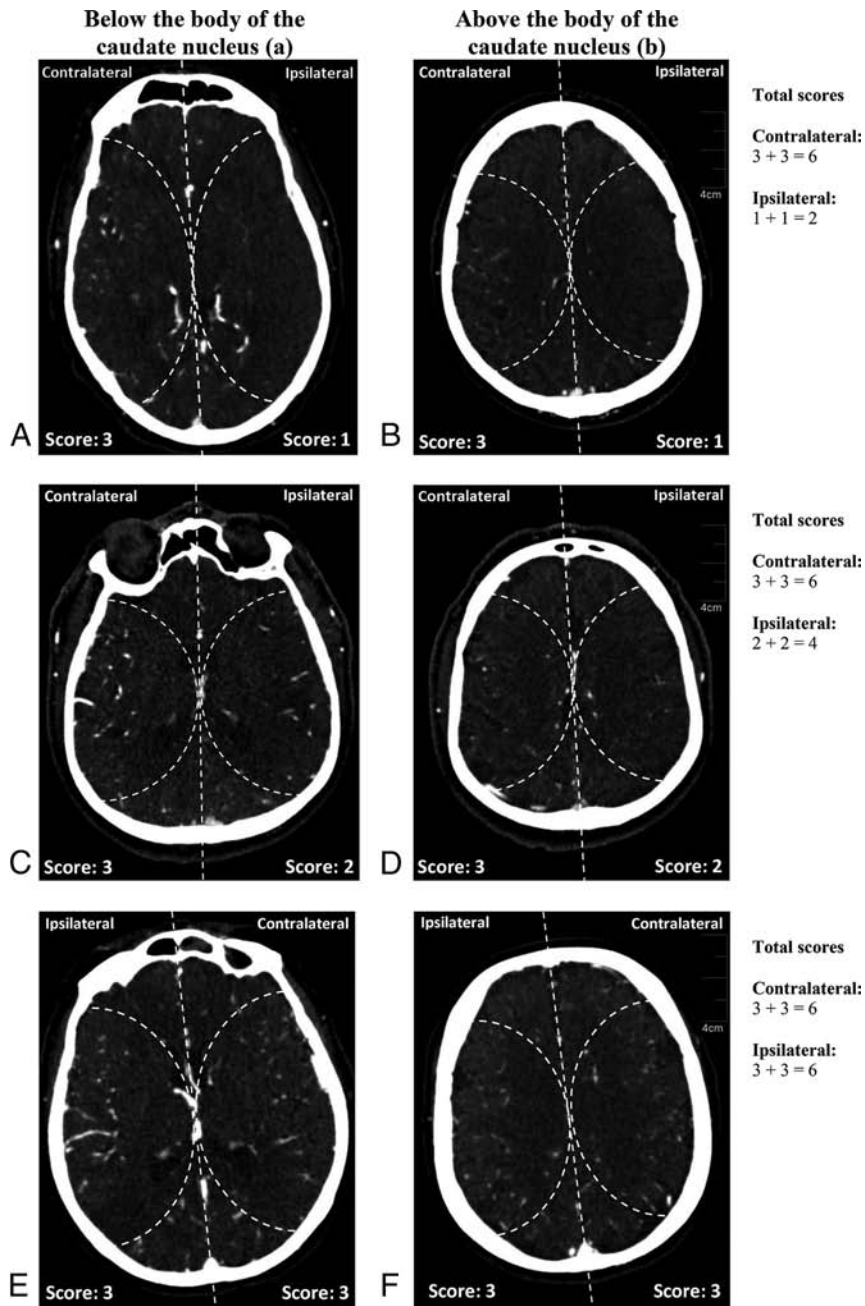
^aThe relative risk of receiving IA treatment given poor-versus-good collateral status is 1.4 (95% CI, 0.6–3.2).

On-line Table 4: Number of patients with poor or good collaterals on dynamic CTA among patients with poor or good reperfusion after receiving IA treatment (either with or without IVT) (n = 17)^a

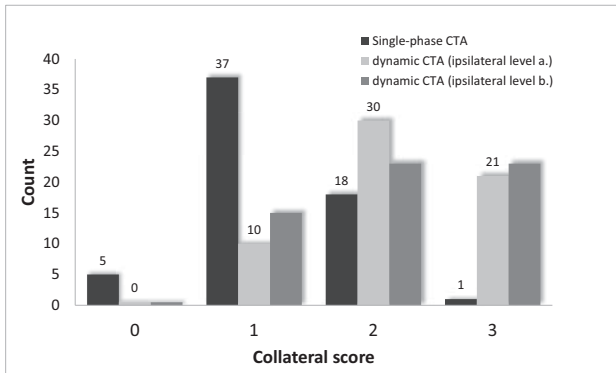
	Poor Collaterals	Good Collaterals
Poor reperfusion (No.)	4	7
Good reperfusion (No.)	2	4
Total (No.)	6	11

Note:—IA indicates intra-arterial.

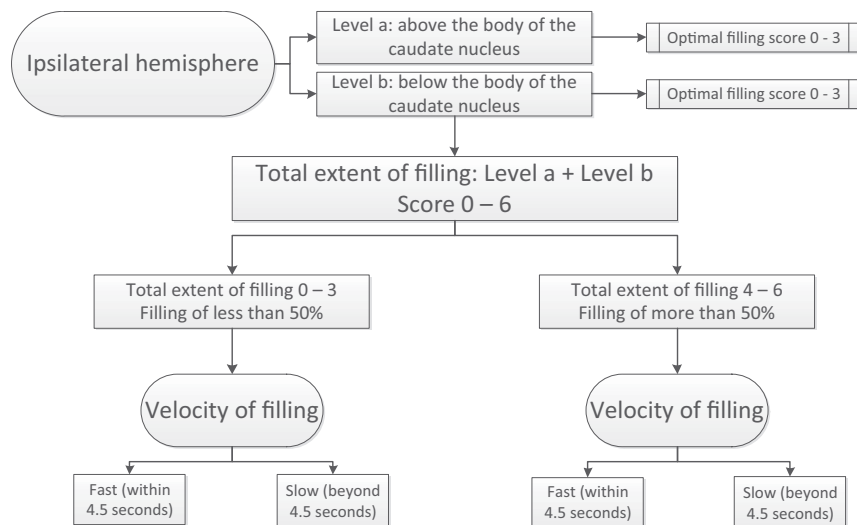
^aThe risk ratio for poor reperfusion status given poor-versus-good collateral status is 1.1 (95% CI, 0.5–2.2).



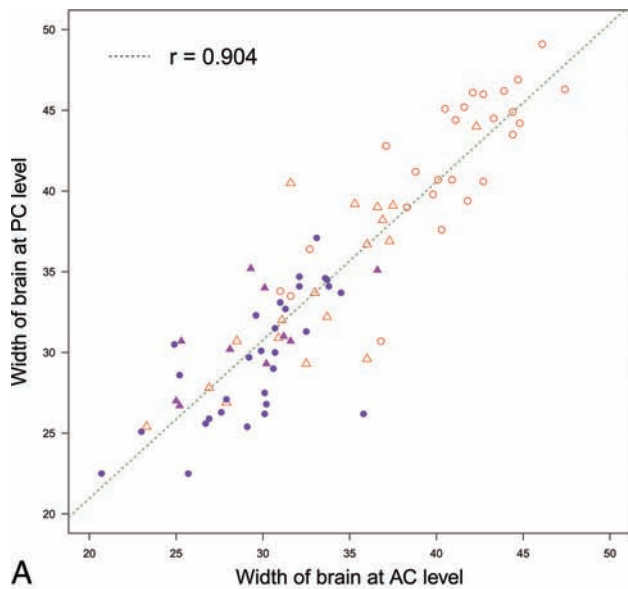
ON-LINE FIG 1. Examples of different extents of collateral filling on dynamic CT angiography. Examples of dynamic CTA volume sections (0.5 mm) with optimal filling in the unaffected (ie, contralateral) hemisphere, but different collateral flow grades in the affected (ie, ipsilateral) hemisphere in patient 1 (A and B), patient 2 (C and D), and patient 3 (E and F). All volumes were derived from patients with proximal middle cerebral artery M1 segment occlusions. Examples in the first column (A, C, and E) show the level below the body of the caudate nucleus (lower level *a*). Examples in the second column (B, D, and F) show the level above the body of the caudate nucleus (upper level *b*). Each level in each hemisphere is rated with a score of 0–3, depending on the amount of vessels filling in the MCA territory (bordered by *dashed lines*). The last column shows the total score for each hemisphere, calculated by adding the score of the lower level to that of the upper level.



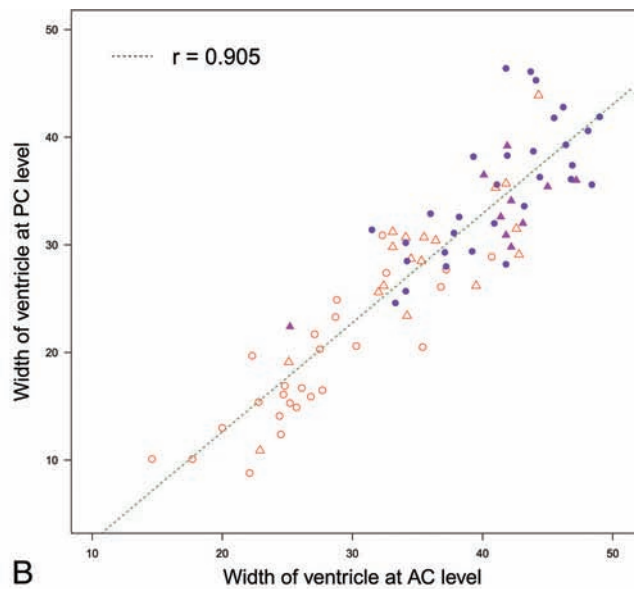
ON-LINE FIG 2. Collateral filling scored on single-phase CTA with a collateral score by Tan et al,¹⁵ and collateral filling scored on dynamic CTA at 2 different levels (*a*, below the body of the caudate nucleus; *b*, above the body of the caudate nucleus) of the ipsilateral (ie, affected) hemisphere. Most cases received collateral scores of 1 or 2 when graded by using single-phase CTA, while the same cases received collateral scores 2 or 3 when graded by using dynamic CTA.



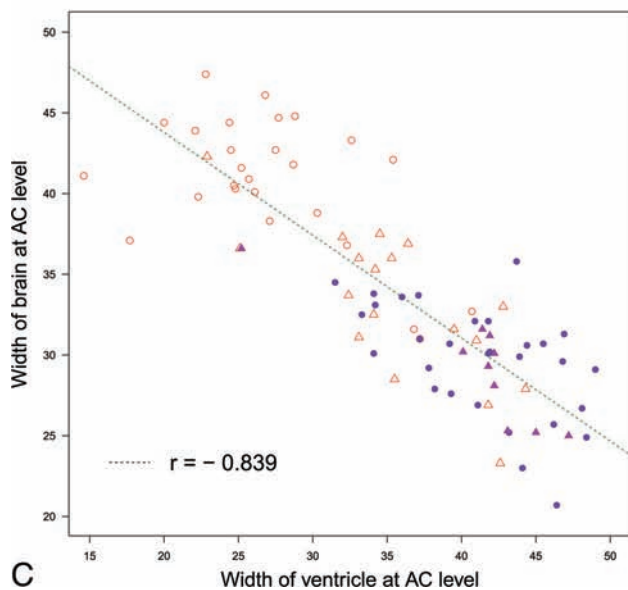
ON-LINE FIG 3. The flow chart shows 4 different patient groups by the extent of filling and the velocity of filling. The ipsilateral hemisphere was graded for 2 levels separately. Optimal filling of level *a*, with a score ranging from 0 to 3, included the area above the body of the caudate nucleus; and optimal filling of level *b* included the area below the body of the caudate nucleus. The total extent of filling was obtained by adding the score of level *a* to the score of level *b*, resulting in a score ranging from 0 to 6. This was divided into poor filling of <50% of the ischemic area, which included a total extent of filling of 0–3, and a good filling of >50%, including a total extent of filling from 4 to 6. The difference between the time (in seconds) until contralateral filling reached its maximal extent and until ipsilateral filling reached its maximal extent was calculated to assess the velocity of filling. When the difference between the ipsilateral and the contralateral hemispheres was <4.5 seconds, the velocity of filling was fast, and when this difference was ≥ 4.5 seconds, the velocity of filling was slow. The extent and velocity of filling resulted in 4 groups.



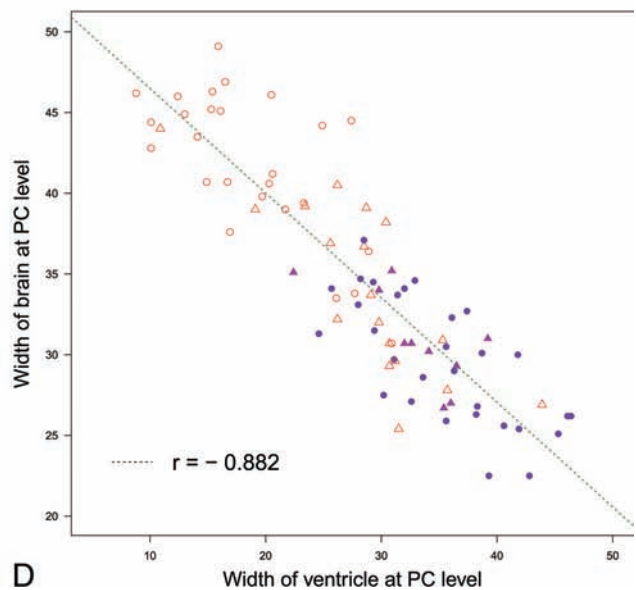
A



B



C



D

ON-LINE FIGURE. Scatterplots and receiver operating characteristic curves for the differential diagnosis of idiopathic normal pressure hydrocephalus and Alzheimer disease. These 4 diagrams show the scatterplots and linear regressions for the correlation between the widths of the brain and ventricle at the anterior and posterior commissure levels. The *purple circle* indicates iNPH, the *purple triangle* indicates iNPH concurrent with Alzheimer disease, the *open red triangle* indicates AD, and the *open red circle* indicates controls.

On-line Table: Demographic and clinical features in 8 patients with atypical SIH

Case No.	Sex	Age at Onset/ Symptom Duration	Follow-Up (mo)	Orthostatic Headache	Dysarthria	Dysphagia	Gait Disturbance	Movement Disorder	Cognitive Deficit	Behavior	Hypersomnia	Treatment
1	M	51yr/48 mos	No	No	No	No	No	No	Executive and verbal memory impairments, less impairment in spatial memory	Moderate disinhibition, impulsivity, attention deficit	Yes	No follow-up
2	M	48 yr/12 mos	25	Mild	No	No	No	Face and upper body tics	Deficits in speed of information processing, cognitive efficiency, and executive functions	Disinhibition and apathy	Yes	Died from MI; postmortem findings negative for FTD
3	M	57 yr/36 mos	46	Mild	Yes, severe	Yes, severe	Yes, gait ataxia, imbalance	Tics, facial grimacing	Nonfocal deficits in mental efficiency (processing speed, attention/concentration, and acquisition)	Disinhibition	Yes	Transient improvement with spinal patches and saline infusions, resolved with spinal operation
4	F	67 yr/24 mos	50	Yes	Yes, scanning speech	No	Yes, unsteady	Facial grimacing	Short-term memory symptoms	Disinhibition, inappropriate laughter	Yes	Transient improvement with thoracic cyst ligation, decreased stable
5	M	30 yr/18 mos	58	Yes	Yes	Yes	Wide-based staggering gait, falls	Resting tremor, right UE and head	No	Normal	No	Chiari decompression, stable
6	M	64 yr/24 mos	7	Yes	No	No	No	No	Severe impairment of anterograde verbal and visual memory	Normal	Yes	Improved with targeted blood patches
7	F	76 yr/1 mo	1	Yes, severe	No	Yes	Yes, falls	No	Anterograde memory deficit; confusion	Nonresponsiveness, fluctuating	Yes	Deceased
8	F	51yr/2 wk	111	Yes	No	No	Yes, falls	No	Severely impaired on phonemic fluency, confrontation naming, verbal memory, and perceptual discrimination	Normal	Yes	Improved after burr-hole with resolution of sagging

Note:—UE indicates upper extremity; FTD, frontotemporal dementia; MI, myocardial infarction.

On-line Table 1: MR imaging acquisition parameters of 3D-T1WI FSE

	1.5T	3T
No. of channels	8	12
TR (ms)	500	600
TE (ms)	Minimum	Minimum
FOV (cm)	25.6	25.6
Matrix	256 × 256 × 176	256 × 256 × 176
Voxel size (mm ³) (interpolated)	0.5 × 0.5 × 0.5	0.5 × 0.5 × 0.5
Section thickness (mm)	1.0/zero	1.0/zero
Bandwidth (kHz)	83.3	62.5
Echo-train length	28	22
Scan time	3 min 36 sec	3 min 41 sec

On-line Table 2: MR imaging acquisition parameters of 3D-TOF

	1.5T	3T
TR (ms)	29	25
TE (ms)	6.8	3.3
FOV (cm)	20	20
Matrix	352 × 160	512 × 224
Voxel size (mm ³) (interpolated)	0.4 × 0.4 × 0.6	0.4 × 0.4 × 0.5
Section thickness (mm) (interpolated)	0.6	0.5
No. of slabs	3	1
Bandwidth (kHz)	19.2	50.0
Scan time	4 min 55 sec	4 min 27 sec

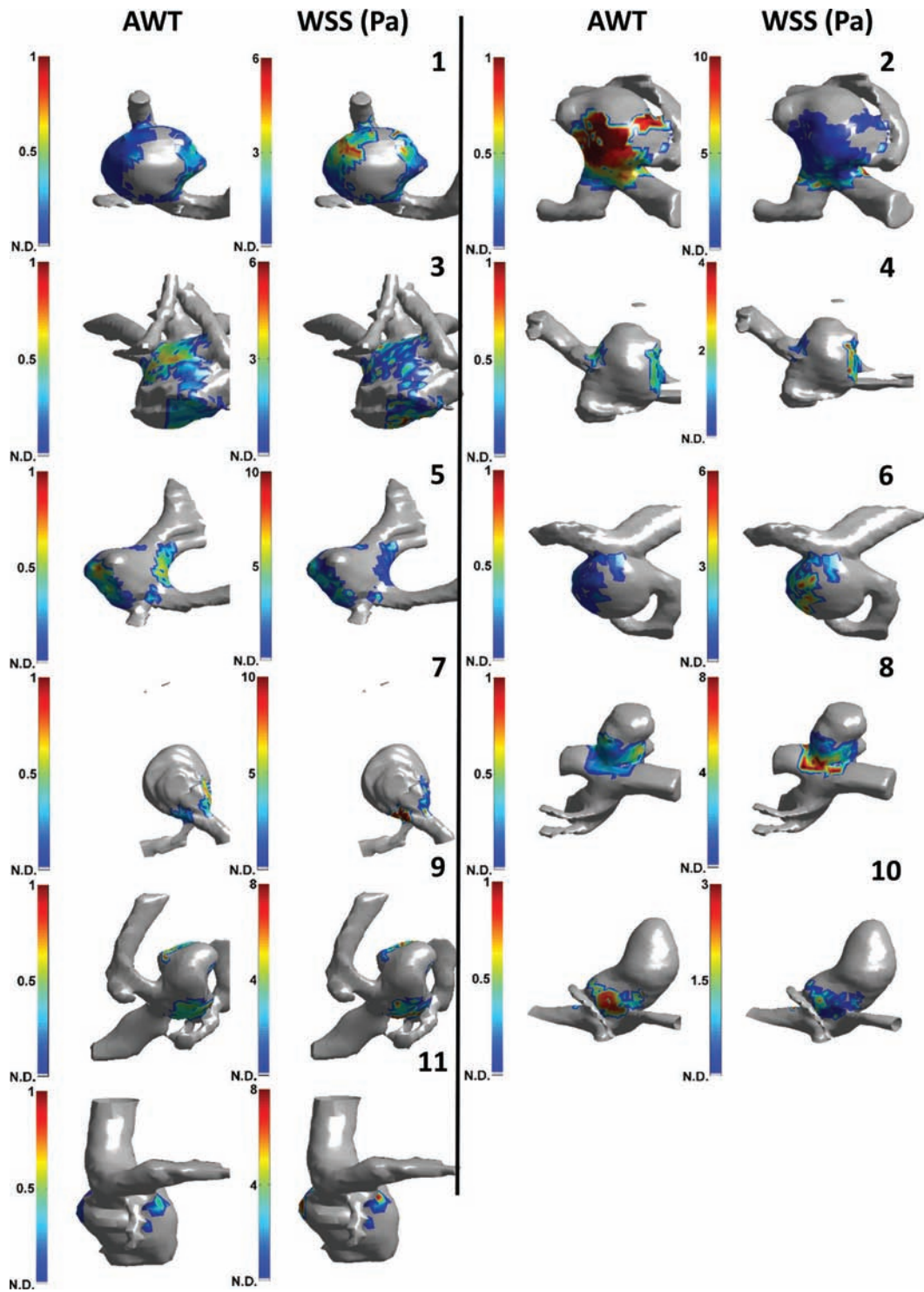
On-line Table 1: Exclusion criteria

Criteria
1) Refractory to general anesthesia; patients were not amenable to general anesthesia even though they have been pretreated with medical therapy
2) Any condition that precludes proper angiographic assessment
3) Tandem extracranial or intracranial stenosis (70%–99%) or occlusion that is proximal or distal to the target intracranial lesion
4) Bilateral intracranial vertebral artery stenosis of 70%–99% and uncertainty about which lesion is symptomatic (eg, if the patient has pontine, midbrain, temporal, and occipital lobar symptoms)
5) Presence of a previously placed intravascular stent or graft in the ipsilateral distribution within 1 month
6) Previous treatment of the target lesion with a stent, angioplasty, or other mechanical device or a plan to perform staged angioplasty followed by stent placement in target lesion
7) Severe vascular tortuosity or anatomy that would preclude the safe introduction of a guiding catheter, guiding sheath, or stent placement
8) Plan to perform concomitant angioplasty or stenting of an extracranial vessel tandem to an ipsilateral intracranial stenosis
9) Presence of intraluminal thrombus proximal to or at the target lesion
10) Any aneurysm proximal to or distal to an intracranial stenotic artery
11) Intracranial tumors or any intracranial vascular malformations
12) CT or angiographic evidence of severe calcification at the target lesion
13) Thrombolytic therapy within 24 hours before enrollment
14) Evolving stroke or progressive neurologic signs within 24 hours before enrollment
15) Stroke of sufficient size (>5 cm on CT or MRI) to place the patient at risk of hemorrhagic transformation during the procedure; hemorrhagic transformation of an ischemic stroke within the past 15 days
16) Previous spontaneous intracerebral (parenchymal) or other intracranial (subarachnoid, subdural, or epidural) hemorrhage within 1 month
17) Untreated chronic subdural hematoma of >5 mm in thickness
18) Other cardiac sources of emboli such as left ventricular aneurysms, intracardiac filling defect, cardiomyopathy, aortic or mitral prosthetic heart valve, calcified aortic stenosis, endocarditis, mitral stenosis, atrial septal defect, atrial septal aneurysm, and left atrial myxoma
19) Myocardial infarction within the previous 30 days
20) Chronic atrial fibrillation; any episode of paroxysmal atrial fibrillation within the past 6 months or history of paroxysmal atrial fibrillation requiring chronic anticoagulation
21) Intolerance or allergic reaction to any medical therapy, including aspirin, clopidogrel, heparin, and local or general anesthetics
22) History of life-threatening allergy to contrast medium; if not life-threatening and can be effectively pretreated, patient can be enrolled at physician's discretion
23) Recent gastrointestinal bleeding that would interfere with antiplatelet therapy
24) Active bleeding diathesis or coagulopathy; active peptic ulcer disease; major systemic hemorrhage within 30 days, active bleeding diathesis, platelet count < 125,000, hematocrit level < 30, Hgb level < 10 g/dL, uncorrected INR > 1.5, bleeding time >1 minute beyond upper limit normal; or heparin-associated thrombocytopenia that increases the risk of bleeding; uncontrolled severe hypertension (systolic BP > 180 mm hg or diastolic BP > 115 mm hg); severe liver impairment (AST or ALT > 3 times normal, cirrhosis); serum creatinine level > 265.2 μ mol/L (unless on dialysis)
25) Major surgery (including open femoral, aortic, or carotid surgery) within previous 30 days or planned in the next 90 days after enrollment
26) Indication for warfarin or heparin beyond enrollment (note: exceptions allowed the use of systemic heparin during the stent-placement procedure or subcutaneous heparin for deep venous thrombosis prophylaxis while hospitalized)
27) Inability to understand and cooperate with study procedures or sign an informed consent
28) Severe dementia or psychiatric problems that prevent the patient from following an outpatient follow-up program reliably
29) Pregnancy or childbearing potential and unwilling to use contraception for the duration of this study
30) Actively participating in another drug or device trial that has not completed the required protocol follow-up period

Note:—Hgb indicates hemoglobin; INR, international normalized ratio; BP, blood pressure; AST, aspartate transaminase; ALT, alanine aminotransferase.

On-line Table 2: Clinical and procedural characteristics of 2 patients with 1-month stroke and/or death within the single-arm trial

Case No.	Age (yr)/Sex	Location of Stenotic Artery	Events	Preprocedure Stenosis	Postprocedure Stenosis	Mechanism of Stroke	mRS at Event	mRS at 30 Days
2	42/Female	Mid-basilar artery	Presented with right-sided hemiparesis and ataxia within 24 hours after basilar artery stent placement	90%	10%	Perforating artery ischemic stroke; left pontine infarction on MRI	2	0
8	50/Female	Mid-basilar artery	Presented with left-sided hemiplegia and central facial paralysis 72 hours after basilar artery stent placement	75%	5%	Perforating artery ischemic stroke; right pontine infarction on MRI	4	1



ON-LINE FIGURE. Visual comparison between apparent wall thickness and wall shear stress in intracranial aneurysms on 7T MR imaging. The aneurysms are the same as those in Fig 3 but shown from the back side.

ON-LINE APPENDIX

DTI Acquisition Scheme

The main goal of using multiple b-values when acquiring DTI data is to exploit their complementary information in the diffusion tensor estimation. In particular, low b-values (ie, $b=300 \text{ s/mm}^2$) are characterized by a high signal-to-noise ratio while at high b-values, images have a more important diffusion-weighting. Thus, combining low and high b-values results in a better characterization of the diffusion tensor and consequently allows a more precise estimate of the diffusion parameters (ie, FA, MD, AD, RD). Due to software limitations, we acquired the multiple b-value data using 3 independent sequences that share the same FOV and geometric parameters. In particular, we acquired the following sequences:

Sequence 1: 6 directions with $b=0 \text{ s/mm}^2$ and 6 directions with $b=1100 \text{ s/mm}^2$.

Sequence 2: 1 direction with $b=0 \text{ s/mm}^2$, 15 directions with $b=300 \text{ s/mm}^2$, 15 directions with $b=1100 \text{ s/mm}^2$.

Sequence 3: 1 direction with $b=0 \text{ s/mm}^2$, 32 directions with $b=1100 \text{ s/mm}^2$.

On-Table 1: Pattern of damage for patients with CP at conventional MRI

	Ventricular Enlargement	WM Damage	CC Thinning	Global Brain Damage
Mild	17	12	17	16
Moderate	7	12	8	7
Severe	1	1	0	2

Note:—CC indicates corpus callosum.

One possible problem with this acquisition protocol is that there could be a difference in the signal intensity among sequences due to a different gain setup of the receiver amplifiers. To limit this issue, we managed to concatenate the sequence acquisition and turn off the amplifier gain optimization step in sequences 2 and 3. Moreover, we included multiple volumes with the same b-value (ie, $b=1100 \text{ s/mm}^2$) in each sequence to check and, eventually, correct for it. After the acquisition and intensity check, the data can be merged and elaborated as they are acquired with a single sequence.

On-line Table 2: Mean FA values in the 43 tracts for patients with CP and HCs

	FA (Mean)	
	Patients	Controls
Cerebellar peduncles-inferior		
ICP R	0.495 ± 0.041	0.539 ± 0.047
ICP L	0.484 ± 0.040 ^a	0.536 ± 0.048 ^a
Cerebellar peduncles-middle		
MCP	0.502 ± 0.024	0.524 ± 0.033
Cerebellar peduncles-superior		
SCP R	0.491 ± 0.040 ^a	0.590 ± 0.032 ^a
SCP L	0.485 ± 0.042 ^a	0.595 ± 0.033 ^a
Corticospinal tract		
CST R	0.468 ± 0.043 ^a	0.535 ± 0.032 ^a
CST L	0.489 ± 0.042 ^a	0.536 ± 0.030 ^a
Internal capsule		
ALIC R	0.519 ± 0.053	0.557 ± 0.036
ALIC L	0.511 ± 0.052	0.537 ± 0.034
PLIC R	0.626 ± 0.034	0.655 ± 0.036
PLIC L	0.641 ± 0.035	0.658 ± 0.034
External capsule		
EC R	0.393 ± 0.031 ^a	0.437 ± 0.032 ^a
EC L	0.388 ± 0.029 ^a	0.437 ± 0.030 ^a
Thalamic radiations		
ATR R	0.346 ± 0.038 ^a	0.384 ± 0.027 ^a
ATR L	0.363 ± 0.044	0.395 ± 0.026
PTR R	0.473 ± 0.082 ^a	0.583 ± 0.037 ^a
PTR L	0.452 ± 0.090 ^a	0.584 ± 0.036 ^a
Forceps		
FOMa	0.418 ± 0.083	0.504 ± 0.037
FOMi	0.370 ± 0.033	0.407 ± 0.027
Inferior occipital fasciculus		
IFO R	0.401 ± 0.042	0.440 ± 0.031
IFO L	0.411 ± 0.046	0.452 ± 0.032
Inferior longitudinal fasciculus		
ILF R	0.384 ± 0.036	0.415 ± 0.030
ILF L	0.357 ± 0.043	0.393 ± 0.026
Superior longitudinal fasciculus		
SLF R	0.335 ± 0.038 ^a	0.384 ± 0.035 ^a
SLF L	0.329 ± 0.037 ^a	0.374 ± 0.030 ^a
SLF-T R	0.420 ± 0.057	0.482 ± 0.039
SLF-T L	0.392 ± 0.050	0.447 ± 0.035
Uncinate fasciculus		
UF R	0.389 ± 0.027	0.409 ± 0.037
UF L	0.394 ± 0.029	0.423 ± 0.032
Corpus callosum		
CC-G	0.565 ± 0.056	0.613 ± 0.038
CC-B	0.508 ± 0.080 ^a	0.618 ± 0.036 ^a
CC-S	0.537 ± 0.097 ^a	0.653 ± 0.032 ^a
Cingulum		
CING-G R	0.358 ± 0.051 ^a	0.426 ± 0.040 ^a
CING-G L	0.389 ± 0.052	0.435 ± 0.043
CING-H R	0.336 ± 0.032 ^a	0.396 ± 0.038 ^a
CING-H L	0.333 ± 0.025 ^a	0.382 ± 0.039 ^a
Fornix		
FOR	0.478 ± 0.050	0.523 ± 0.042
Corona radiata		
ACR R	0.410 ± 0.047	0.445 ± 0.042
ACR L	0.402 ± 0.051	0.442 ± 0.042
SCR R	0.430 ± 0.058 ^a	0.491 ± 0.031 ^a
SCR L	0.431 ± 0.051 ^a	0.497 ± 0.035 ^a
PCR R	0.334 ± 0.087 ^a	0.483 ± 0.043 ^a
PCR L	0.328 ± 0.081 ^a	0.467 ± 0.041 ^a

Note:—ICP indicates inferior cerebellar peduncle; MCP, middle cerebellar peduncle; ALIC, anterior limb of internal capsule; PLIC, posterior limb of internal capsule; EC, external capsule; ATR, anterior thalamic radiation; PTR, posterior thalamic radiation; FOMa, forceps major; FOMi, forceps minor; IFO, inferior fronto-occipital fasciculus; ILF, inferior longitudinal fasciculus; SLF, superior longitudinal fasciculus; SLF-T, temporal part of the superior longitudinal fasciculus; UF, uncinate fasciculus; CC-G, genu of the corpus callosum; CC-B, body of the corpus callosum; CC-S, splenium of the corpus callosum; CING-G, cingulate gyrus; CING-H, hippocampal portion of cingulate gyrus; FOR, fornix; ACR, anterior corona radiata; SCR, superior corona radiata; PCR, posterior corona radiata; R, right; L, left.

^aSignificant values ($P < .001$).

On-line Table 3: Mean MD, AD, and RD values in the 43 tracts for patients with CP and HCs

	MD (Mean)		AD (Mean)		RD (Mean)	
	Patients	Controls	Patients	Controls	Patients	Controls
Cerebellar peduncles inferior						
ICP R	2.438 ± 0.442	2.199 ± 0.166	1.175 ± 0.148	1.114 ± 0.057	0.632 ± 0.150	0.543 ± 0.060
ICP L	2.172 ± 0.126	2.112 ± 0.140	1.155 ± 0.060	1.174 ± 0.048	0.508 ± 0.046	0.469 ± 0.055
Cerebellar peduncles-middle						
MCP	2.861 ± 0.574	2.271 ± 0.149	1.446 ± 0.173	1.315 ± 0.062	0.708 ± 0.206	0.478 ± 0.050
Cerebellar peduncles-superior						
SCP R	2.869 ± 0.495	2.538 ± 0.226	1.400 ± 0.150	1.369 ± 0.079	0.735 ± 0.185 ^a	0.584 ± 0.078 ^a
SCP L	2.202 ± 0.300	2.176 ± 0.152	1.056 ± 0.090	1.097 ± 0.049	0.573 ± 0.109 ^a	0.539 ± 0.057 ^a
Corticospinal tract						
CST R	2.312 ± 0.146 ^a	2.302 ± 0.147 ^a	1.122 ± 0.053	1.139 ± 0.057	0.595 ± 0.049 ^a	0.581 ± 0.051 ^a
CST L	1.997 ± 0.139	1.952 ± 0.146	1.227 ± 0.051	1.234 ± 0.056	0.385 ± 0.047 ^a	0.359 ± 0.049 ^a
Internal capsula						
ALIC R	3.731 ± 1.272	2.214 ± 0.191	1.615 ± 0.392	1.143 ± 0.074	1.058 ± 0.441	0.536 ± 0.065
ALIC L	2.122 ± 0.106	2.063 ± 0.139	1.134 ± 0.037	1.127 ± 0.049	0.494 ± 0.037	0.468 ± 0.047
PLIC R	3.034 ± 0.388	2.968 ± 0.398	1.568 ± 0.120	1.590 ± 0.122	0.733 ± 0.138	0.689 ± 0.142
PLIC L	2.991 ± 0.662	2.299 ± 0.164	1.471 ± 0.192	1.330 ± 0.060	0.760 ± 0.239	0.484 ± 0.056
External capsula						
EC R	3.019 ± 0.622	2.471 ± 0.209	1.589 ± 0.170	1.497 ± 0.085	0.715 ± 0.230	0.487 ± 0.067
EC L	2.238 ± 0.240	2.081 ± 0.146	1.098 ± 0.064	1.088 ± 0.054	0.570 ± 0.091	0.497 ± 0.051
Thalamic radiations						
ATR R	3.297 ± 0.621	2.589 ± 0.189	1.750 ± 0.147	1.599 ± 0.074	0.773 ± 0.244	0.495 ± 0.062
ATR L	2.418 ± 0.368	2.182 ± 0.154	1.179 ± 0.123	1.109 ± 0.057	0.620 ± 0.126	0.537 ± 0.056
PTR R	2.431 ± 0.186 ^a	2.168 ± 0.131 ^a	1.259 ± 0.072	1.202 ± 0.051	0.586 ± 0.066 ^a	0.483 ± 0.045 ^a
PTR L	2.354 ± 0.180 ^a	2.157 ± 0.131 ^a	1.244 ± 0.067	1.196 ± 0.056	0.555 ± 0.064 ^a	0.480 ± 0.042 ^a
Forceps						
FOMa	2.264 ± 0.158	2.224 ± 0.195	1.041 ± 0.058	1.087 ± 0.074	0.611 ± 0.054	0.568 ± 0.065
FOMi	3.322 ± 0.245	3.083 ± 0.260	1.704 ± 0.074	1.732 ± 0.099	0.809 ± 0.092	0.676 ± 0.084
Inferior fronto-occipital fasciculus						
IFO R	2.035 ± 0.175	2.038 ± 0.144	1.117 ± 0.045	1.148 ± 0.052	0.459 ± 0.070	0.445 ± 0.049
IFO L	3.411 ± 0.304	3.057 ± 0.268	1.731 ± 0.106	1.726 ± 0.095	0.840 ± 0.107	0.666 ± 0.091
Inferior longitudinal fasciculus						
ILF R	3.718 ± 1.200	2.248 ± 0.187	1.617 ± 0.368	1.176 ± 0.071	1.051 ± 0.417	0.536 ± 0.065
ILF L	2.230 ± 0.128	2.144 ± 0.138	1.170 ± 0.065	1.185 ± 0.047	0.530 ± 0.043	0.479 ± 0.054
Superior longitudinal fasciculus						
SLF R	2.273 ± 0.188	2.219 ± 0.144	1.062 ± 0.055	1.075 ± 0.050	0.606 ± 0.070	0.572 ± 0.049
SLF L	2.182 ± 0.216	2.094 ± 0.150	1.037 ± 0.064	1.055 ± 0.052	0.573 ± 0.080	0.520 ± 0.052
SLF-T R	2.264 ± 0.174	2.219 ± 0.143	1.083 ± 0.063	1.092 ± 0.049	0.590 ± 0.060	0.563 ± 0.049
SLF-T L	2.273 ± 0.158	2.271 ± 0.152	1.103 ± 0.056	1.132 ± 0.057	0.585 ± 0.054	0.569 ± 0.052
Uncinate fasciculus						
UF R	2.109 ± 0.131	2.131 ± 0.152	1.013 ± 0.050	1.071 ± 0.057	0.548 ± 0.044	0.530 ± 0.050
UF L	2.128 ± 0.129	2.124 ± 0.146	1.027 ± 0.044	1.068 ± 0.053	0.550 ± 0.046	0.528 ± 0.049
Corpus callosum						
CC-G	2.470 ± 0.328	1.974 ± 0.151	1.227 ± 0.112	1.043 ± 0.066	0.622 ± 0.113	0.465 ± 0.047
CC-B	2.169 ± 0.180	2.171 ± 0.164	1.016 ± 0.060	1.086 ± 0.054	0.577 ± 0.069 ^a	0.543 ± 0.060 ^a
CC-S	2.235 ± 0.169 ^a	2.233 ± 0.191 ^a	1.031 ± 0.067	1.080 ± 0.070	0.602 ± 0.054 ^a	0.577 ± 0.064 ^a
Cingulum						
CING-G R	2.371 ± 0.185	2.362 ± 0.137	1.126 ± 0.057 ^a	1.162 ± 0.045 ^a	0.622 ± 0.066	0.600 ± 0.048
CING-G L	2.546 ± 0.353	2.425 ± 0.199	1.461 ± 0.118	1.466 ± 0.071	0.543 ± 0.120	0.479 ± 0.067
CING-H R	2.297 ± 0.214	2.201 ± 0.150	1.126 ± 0.065	1.127 ± 0.049	0.586 ± 0.079	0.537 ± 0.052
CING-H L	2.253 ± 0.205	2.196 ± 0.133	1.008 ± 0.064	1.028 ± 0.044	0.622 ± 0.072	0.584 ± 0.046
Fornix						
FOR	1.959 ± 0.132	1.939 ± 0.139	1.224 ± 0.049	1.227 ± 0.057	0.368 ± 0.046	0.356 ± 0.045
Corona radiata						
ACR R	2.444 ± 0.390	1.980 ± 0.152	1.209 ± 0.141	1.050 ± 0.064	0.617 ± 0.127	0.465 ± 0.049
ACR L	2.019 ± 0.150	2.011 ± 0.142	1.120 ± 0.040	1.156 ± 0.053	0.450 ± 0.061	0.428 ± 0.049
SCR R	2.273 ± 0.200 ^a	2.175 ± 0.136 ^a	1.025 ± 0.061 ^a	1.030 ± 0.041 ^a	0.624 ± 0.071 ^a	0.573 ± 0.050 ^a
SCR L	2.381 ± 0.232 ^a	2.243 ± 0.132 ^a	1.159 ± 0.077 ^a	1.138 ± 0.045 ^a	0.611 ± 0.082 ^a	0.552 ± 0.046 ^a
PCR R	2.562 ± 0.539 ^a	2.275 ± 0.159 ^a	1.173 ± 0.166 ^a	1.095 ± 0.054 ^a	0.695 ± 0.187 ^a	0.590 ± 0.054 ^a
PCR L	2.554 ± 0.434 ^a	2.308 ± 0.150 ^a	1.158 ± 0.132 ^a	1.096 ± 0.05 ^a	0.698 ± 0.15 ^a	0.606 ± 0.051 ^a

Note:—ICP indicates inferior cerebellar peduncle; MCP, middle cerebellar peduncle; ALIC, anterior limb of internal capsule; PLIC, posterior limb of internal capsule; EC, external capsule; ATR, anterior thalamic radiation; PTR, posterior thalamic radiation; FOMa, forceps major; FOMi, forceps minor; IFO, inferior fronto-occipital fasciculus; ILF, inferior longitudinal fasciculus; SLF, superior longitudinal fasciculus; SLF-T, temporal part of the superior longitudinal fasciculus; UF, uncinate fasciculus; CC-G, genu of the corpus callosum; CC-B, body of the corpus callosum; CC-S, splenium of the corpus callosum; CING-G, cingulate gyrus; CING-H, hippocampal portion of cingulate gyrus; FOR, fornix; ACR, anterior corona radiata; SCR, superior corona radiata; PCR, posterior corona radiata; R, right; L, left.

^aSignificant values ($P < .001$).

On-line Table 4: Correlations between GMFCS and DTI metrics in WM tracts

Tract	FA		MD		AD		RD	
	r	P	r	P	r	P	r	P
Cerebellar peduncles-inferior								
ICP R	-0.50	.01 ^a	0.04	.86	-0.30	.14	0.20	.35
ICP L	-0.37	.07	-0.23	.28	-0.45	.02 ^a	0.01	.98
Cerebellar peduncles-middle								
MCP	0.01	.97	-0.16	.44	-0.14	.50	-0.21	.32
Cerebellar peduncles-superior								
SCP R	0.01	.97	-0.25	.24	-0.34	.10	-0.19	.36
SCP L	0.03	.89	-0.33	.10	-0.42	.04 ^a	-0.26	.20
Corticospinal tract								
CST R	-0.52	.01 ^a	0.23	.27	-0.08	.72	0.29	.16
CST L	-0.51	.01 ^a	0.32	.11	0.17	.42	0.37	.07
Internal capsule								
ALIC R	-0.28	.18	0.18	.38	-0.03	.88	0.28	.17
ALIC L	-0.25	.23	0.21	.31	0.12	.57	0.27	.20
PLIC R	-0.30	.15	0.27	.19	0.20	.34	0.30	.15
PLIC L	-0.06	.78	0.11	.59	0.12	.57	0.08	.71
External capsule								
EC R	-0.45	.02 ^a	0.25	.24	0.02	.91	0.33	.11
EC L	-0.36	.08	0.13	.54	-0.13	.53	0.16	.44
Thalamic radiations								
ATR R	-0.35	.09	0.18	.40	0.17	.40	0.16	.46
ATR L	-0.39	.06	0.29	.17	0.28	.18	0.27	.20
PTR R	-0.48	.02 ^a	0.35	.09	0.32	.12	0.36	.08
PTR L	-0.52	.01 ^a	0.49	.01 ^a	0.46	.02 ^a	0.48	.02 ^a
Forceps								
FOMa	-0.37	.07	0.29	.16	0.07	.74	0.34	.10
FOMi	-0.45	.02 ^a	0.19	.36	-0.03	.90	0.21	.30
Inferior fronto-occipital fasciculus								
IFO R	-0.43	.03 ^a	0.31	.13	0.23	.26	0.32	.12
IFO L	-0.42	.04 ^a	0.40	.05	0.32	.12	0.40	.05 ^a
Inferior longitudinal fasciculus								
ILF R	-0.50	.01 ^a	0.42	.04 ^a	0.32	.12	0.46	.02 ^a
ILF L	-0.40	.05	0.41	.04 ^a	0.36	.08	0.40	.05 ^a
Superior longitudinal fasciculus								
SLF R	-0.57	.00 ^a	0.37	.07	0.33	.10	0.39	.06
SLF L	-0.48	.01 ^a	0.32	.12	0.22	.29	0.39	.06
SLF-T R	-0.56	.00 ^a	0.48	.01 ^a	0.45	.02 ^a	0.49	.01 ^a
SLF-T L	-0.53	.01 ^a	0.38	.06	0.21	.31	0.45	.02 ^a
Uncinate fasciculus								
UF R	-0.24	.25	0.25	.23	0.31	.14	0.22	.29
UF L	-0.50	.01 ^a	0.28	.18	0.08	.72	0.33	.11
Corpus callosum								
CC-G	-0.20	.33	0.11	.62	0.04	.84	0.14	.49
CC-B	-0.46	.02 ^a	0.37	.07	0.25	.23	0.39	.05
CC-S	-0.43	.03 ^a	0.38	.06	0.22	.29	0.38	.06
Cingulum								
CING-G R	-0.37	.07	0.35	.09	0.11	.60	0.40	.05 ^a
CING-G L	-0.47	.02 ^a	0.42	.04 ^a	0.22	.29	0.46	.0 ^a
CING-H R	-0.26	.21	0.00	.99	-0.16	.44	0.15	.48
CING-H L	-0.13	.54	-0.08	.71	-0.13	.55	0.02	.94
Fornix								
FOR	-0.22	.30	0.15	.48	0.12	.55	0.13	.55
Corona radiata								
ACR R	-0.41	.04 ^a	0.45	.02 ^a	0.46	.02 ^a	0.45	.02 ^a
ACR L	-0.52	.01 ^a	0.48	.02 ^a	0.38	.06	0.49	.01 ^a
SCR R	-0.59	.00 ^a	0.66	.00 ^a	0.48	.02 ^a	0.69	.00 ^a
SCR L	-0.59	.00 ^a	0.61	.00 ^a	0.55	.01 ^a	0.64	.00 ^a
PCR R	-0.46	.02 ^a	0.39	.06	0.32	.12	0.38	.06
PCR L	-0.48	.02 ^a	0.37	.07	0.34	.10	0.36	.08

Note:—ICP indicates inferior cerebellar peduncle; MCP, middle cerebellar peduncle; ALIC, anterior limb of internal capsule; PLIC, posterior limb of internal capsule; EC, external capsule; ATR, anterior thalamic radiation; PTR, posterior thalamic radiation; FOMa, forceps major; FOMi, forceps minor; IFO, inferior fronto-occipital fasciculus; ILF, inferior longitudinal fasciculus; SLF, superior longitudinal fasciculus; SLF-T, temporal part of the superior longitudinal fasciculus; UF, uncinate fasciculus; CC-G, genu of the corpus callosum; CC-B, body of the corpus callosum; CC-S, splenium of the corpus callosum; CING-G, cingulate gyrus; CING-H, hippocampal portion of cingulate gyrus; FOR, fornix; ACR, anterior corona radiata; SCR, superior corona radiata; PCR, posterior corona radiata; R, right; L, left.

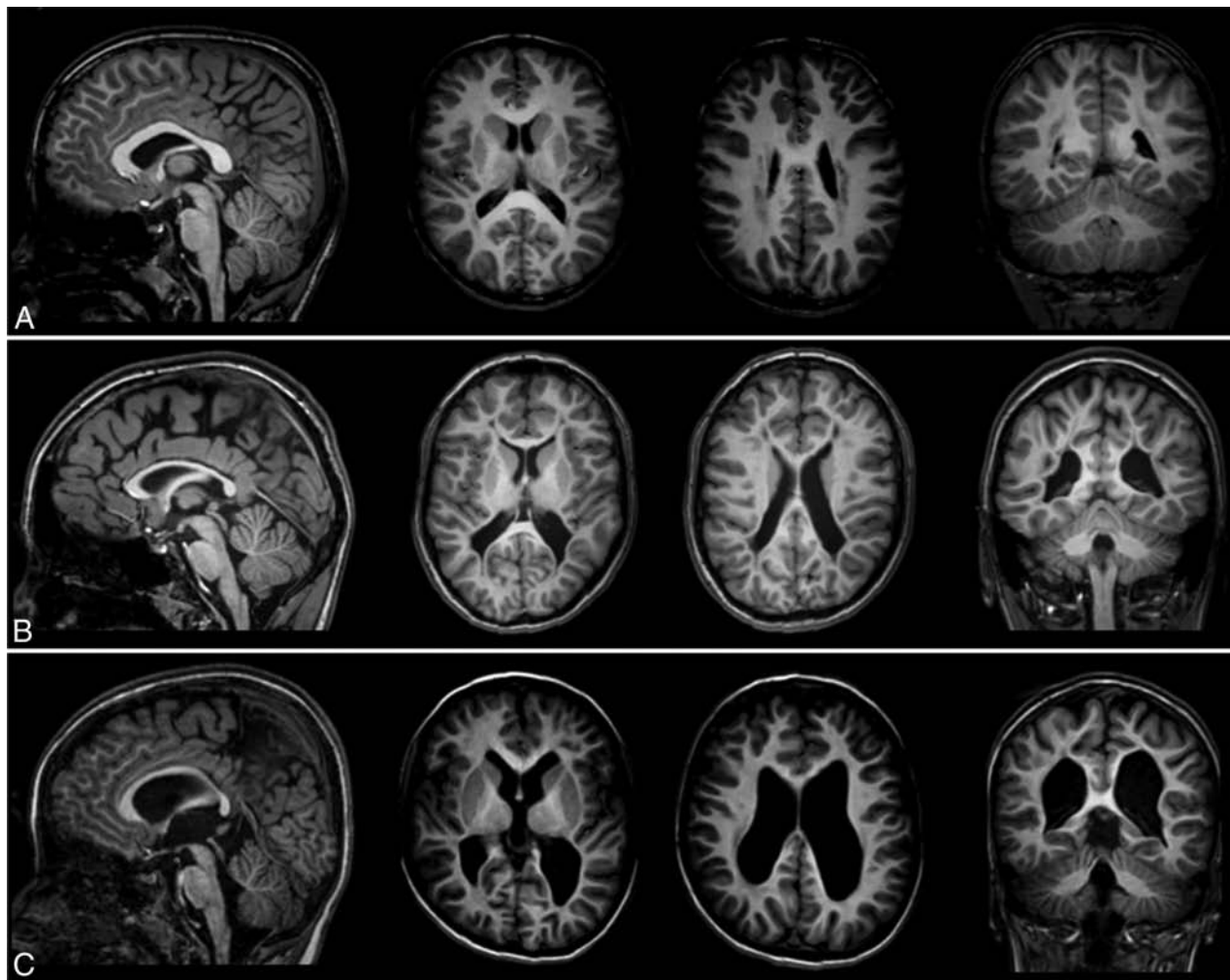
^aP < .05.

On-line Table 5: Correlations between MACS and DTI metrics in WM tracts

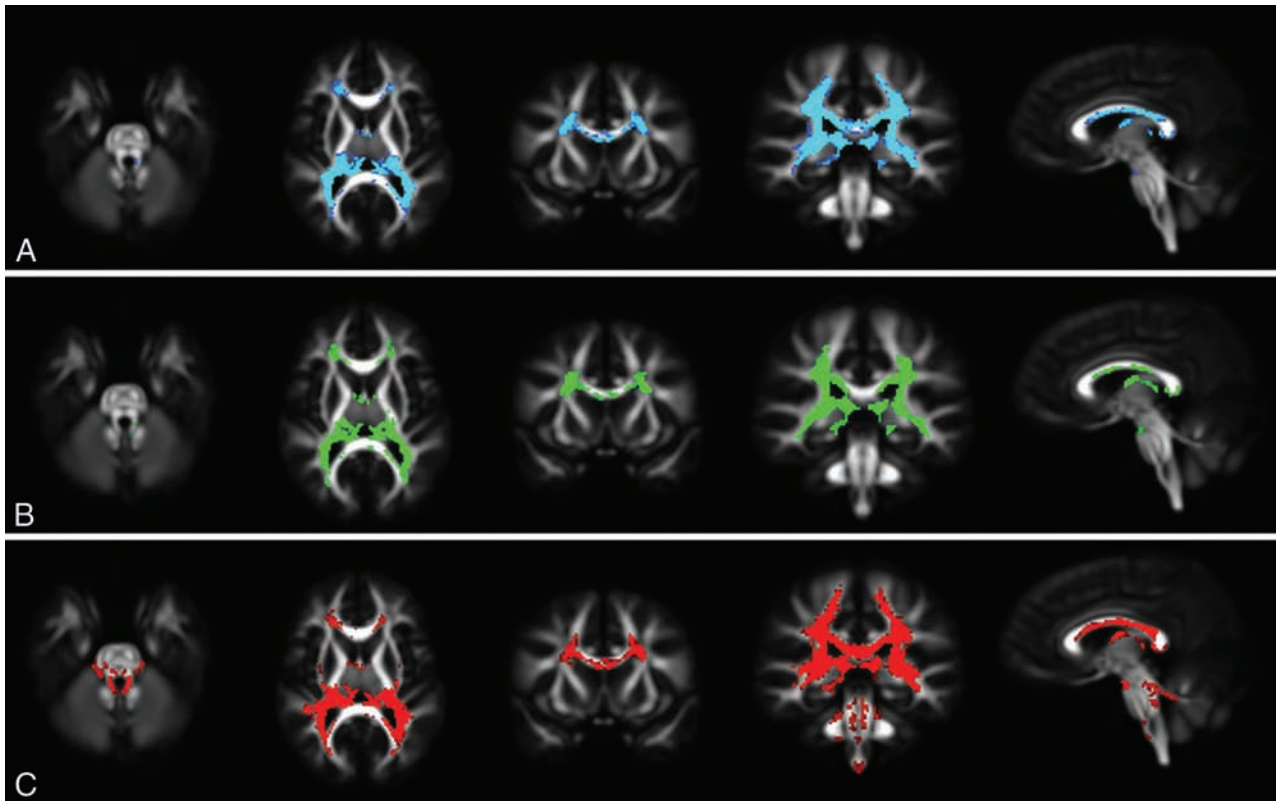
Tract	FA		MD		AD		RD	
	r	P	r	P	r	P	r	P
Cerebellar peduncles-inferior								
ICP R	-0.39	.06	-0.02	.91	-0.26	.22	0.12	.56
ICP L	-0.28	.18	-0.31	.13	-0.44	.03 ^a	-0.12	.58
Cerebellar peduncles-middle								
MCP	0.04	.85	-0.17	.41	-0.22	.28	-0.23	.26
Cerebellar peduncles-superior								
SCP R	0.13	.53	-0.22	.28	-0.22	.29	-0.23	.27
SCP L	0.11	.61	-0.23	.27	-0.31	.13	-0.17	.43
Corticospinal tract								
CST R	-0.35	.09	0.00	.99	-0.22	.30	0.10	.64
CST L	-0.50	.01 ^a	0.24	.26	0.05	.83	0.30	.15
Internal capsule								
ALIC R	-0.23	.27	0.10	.64	-0.19	.37	0.17	.41
ALIC L	-0.20	.33	0.13	.53	-0.05	.83	0.17	.41
PLIC R	-0.08	.71	0.07	.76	0.06	.77	0.07	.73
PLIC L	-0.04	.86	0.07	.73	0.01	.96	0.03	.89
External capsule								
EC R	-0.27	.19	0.07	.75	-0.10	.64	0.13	.55
EC L	-0.13	.52	0.00	.99	-0.18	.40	-0.04	.87
Thalamic radiations								
ATR R	-0.28	.17	0.17	.43	0.13	.53	0.16	.43
ATR L	-0.39	.05	0.33	.11	0.28	.17	0.31	.14
PTR R	-0.45	.02 ^a	0.29	.17	0.24	.24	0.30	.15
PTR L	-0.50	.01 ^a	0.48	.02 ^a	0.46	.02 ^a	0.48	.02 ^a
Forceps								
FOMa	-0.30	.14	0.17	.41	-0.03	.87	0.24	.25
FOMi	-0.45	.03 ^a	0.16	.46	-0.05	.82	0.19	.36
Inferior fronto-occipital fasciculus								
IFO R	-0.35	.09	0.22	.29	0.09	.67	0.25	.24
IFO L	-0.23	.28	0.21	.31	0.18	.40	0.23	.27
Inferior longitudinal fasciculus								
ILF R	-0.30	.14	0.21	.31	0.16	.46	0.27	.20
ILF L	-0.28	.17	0.30	.15	0.20	.35	0.29	.15
Superior longitudinal fasciculus								
SLF R	-0.40	.05 ^a	0.32	.12	0.26	.21	0.34	.09
SLF L	-0.36	.08	0.27	.20	0.15	.48	0.34	.10
SLF-T R	-0.45	.02 ^a	0.40	.05 ^a	0.35	.09	0.40	.05 ^a
SLF-T L	-0.42	.04 ^a	0.26	.21	0.13	.53	0.35	.09
Uncinate fasciculus								
UF R	-0.10	.63	0.02	.92	0.05	.81	0.00	.99
UF L	-0.26	.22	0.03	.90	-0.16	.44	0.09	.66
Corpus callosum								
CC-G	-0.17	.41	0.10	.65	0.04	.85	0.15	.48
CC-B	-0.29	.16	0.23	.27	0.15	.48	0.27	.19
CC-S	-0.33	.11	0.27	.20	0.02	.94	0.29	.15
Cingulum								
CING-G R	-0.23	.26	0.19	.37	-0.12	.56	0.24	.25
CING-G L	-0.40	.05 ^a	0.27	.19	-0.01	.98	0.31	.13
CING-H R	-0.12	.58	-0.23	.28	-0.37	.07	-0.08	.70
CING-H L	0.01	.96	-0.26	.21	-0.24	.24	-0.19	.36
Fornix								
FOR	-0.18	.40	0.12	.56	0.09	.66	0.14	.49
Corona radiata								
ACR R	-0.29	.16	0.34	.10	0.40	.05	0.35	.09
ACR L	-0.45	.02 ^a	0.42	.04 ^a	0.27	.19	0.46	.02 ^a
SCR R	-0.32	.12	0.40	.05	0.30	.15	0.43	.03 ^a
SCR L	-0.43	.03 ^a	0.51	.01 ^a	0.49	.01 ^a	0.54	.01 ^a
PCR R	-0.44	.03 ^a	0.34	.10	0.27	.19	0.33	.11
PCR L	-0.50	.01 ^a	0.39	.06	0.36	.08	0.40	.05

Note:—ICP indicates inferior cerebellar peduncle; MCP, middle cerebellar peduncle; ALIC, anterior limb of internal capsule; PLIC, posterior limb of internal capsule; EC, external capsule; ATR, anterior thalamic radiation; PTR, posterior thalamic radiation; FOMa, forceps major; FOMi, forceps minor; IFO, inferior fronto-occipital fasciculus; ILF, inferior longitudinal fasciculus; SLF, superior longitudinal fasciculus; SLF-T, temporal part of the superior longitudinal fasciculus; UF, uncinate fasciculus; CC-G, genu of the corpus callosum; CC-B, body of the corpus callosum; CC-S, splenium of the corpus callosum; CING-G, cingulate gyrus; CING-H, hippocampal portion of cingulate gyrus; FOR, fornix; ACR, anterior corona radiata; SCR, superior corona radiata; PCR, posterior corona radiata; R, right; L, left.

^aP < .05.



ON-LINE FIG 1. Mild (row A), moderate (row B), and severe (row C) patterns of PVL are shown on T1-weighted images. A progression in corpus callosum thinning, ventricular enlargement, and WM gliosis is evident from mild-to-severe damage.



ON-LINE FIG 2. Axial (first 2 columns), coronal (third and fourth columns), and sagittal (last column) MR images show voxelwise MD (row A), AD (row B), and RD (row C) differences between patients with CP and HCs. For all 3 variables, measured values in patients were higher than those in controls. Results are overlaid on the FA template obtained from all participants, at a significance level of $P < .001$, corrected for multiple comparisons.

On-line Table 1: Mean, SD, and CI for SI measurements

Gestational Age wk	US 2D			US 3D			MRI		
	No.	Mean ± SD	95% CI	No.	Mean ± SD	95% CI	No.	Mean ± SD	95% CI
21	4	11.8 ± 0.94	10.30–13.28	15	12.7 ± 1.04	12.16–13.31			
22	10	12.5 ± 1.27	11.55–13.37	10	13.6 ± 1.01	12.86–14.30			
23	8	12.8 ± 0.66	12.29–13.38	9	14.4 ± 1.28	13.45–15.42			
24	4	13.9 ± 0.65	12.91–14.96	8	15.2 ± 1.48	13.97–16.45			
25	16	15.2 ± 0.96	14.67–15.69	9	16.0 ± 1.10	15.12–16.81			
26	13	16.1 ± 1.23	15.38–16.86	11	17.0 ± 1.36	16.03–17.86			
27	16	16.9 ± 1.27	16.23–17.58	12	18.6 ± 1.07	17.96–19.31	5	14.1 ± 0.65	13.31–14.93
28	18	17.4 ± 0.94	16.92–17.85	11	19.2 ± 2.01	17.85–20.55	10	14.7 ± 0.63	14.22–15.12
29	12	18.7 ± 1.03	18.02–19.34	11	20.1 ± 1.15	19.36–20.91	13	15.9 ± 1.32	15.15–16.74
30	21	18.7 ± 0.71	18.39–19.04	11	21.0 ± 1.65	19.93–22.15	16	17.7 ± 1.21	17.06–18.35
31	22	19.4 ± 1.10	18.89–19.87	23	20.8 ± 1.84	19.96–21.55	26	17.9 ± 0.98	17.51–18.30
32	12	19.3 ± 0.83	18.81–19.87	15	22.2 ± 2.26	20.89–23.40	27	18.6 ± 1.27	18.05–19.05
33	14	20.6 ± 1.72	19.61–21.60	8	22.8 ± 1.23	21.69–23.97	16	19.6 ± 0.88	19.11–20.06
34	10	20.6 ± 1.25	19.73–21.51	11	23.3 ± 2.74	21.43–25.11	15	19.4 ± 0.92	18.92–19.93
35	13	21.6 ± 1.19	20.90–22.33	8	23.2 ± 2.42	21.18–25.22	23	20.2 ± 1.56	19.52–20.86

On-line Table 2: Mean, SD, and CI for AP measurements

Gestational Age (wk)	US 2D			US 3D			MRI		
	No.	Mean ± SD	95% CI	No.	Mean ± SD	95% CI	No.	Mean ± SD	95% CI
21	4	7.8 ± 0.79	6.58–9.10	15	8.2 ± 1.35	7.46–8.96			
22	10	9.3 ± 0.96	8.57–9.94	10	9.2 ± 1.48	8.11–10.23			
23	8	8.8 ± 0.95	7.99–9.57	9	8.9 ± 1.43	7.82–10.02			
24	4	9.6 ± 0.82	8.34–10.94	8	9.9 ± 0.74	9.27–10.51			
25	16	11.0 ± 0.93	10.49–11.48	9	11.3 ± 1.54	10.10–12.48			
26	13	11.5 ± 1.59	10.52–12.44	11	11.0 ± 1.59	9.90–12.04			
27	16	11.4 ± 0.84	10.94–11.83	12	12.3 ± 1.64	11.21–13.29	5	9.6 ± 0.83	8.60–10.67
28	18	12.4 ± 1.12	11.83–12.94	11	12.3 ± 1.86	11.07–13.57	10	10.2 ± 0.90	9.59–10.88
29	12	12.6 ± 1.28	11.78–13.41	11	12.9 ± 0.91	12.24–13.47	13	11.3 ± 1.18	10.55–11.97
30	21	13.2 ± 1.32	12.60–13.80	11	13.7 ± 1.72	12.57–14.88	16	11.9 ± 1.11	11.26–12.44
31	22	14.2 ± 1.12	13.70–14.69	23	14.4 ± 2.12	13.52–15.35	26	12.3 ± 1.06	11.91–12.77
32	12	14.0 ± 1.44	13.12–14.95	15	14.9 ± 2.02	13.74–15.98	27	13.0 ± 0.83	12.63–13.28
33	14	15.3 ± 1.30	14.53–16.02	8	13.9 ± 2.49	11.83–16.00	16	13.3 ± 0.84	12.84–13.73
34	10	15.7 ± 1.54	14.63–16.83	11	15.5 ± 2.29	14.00–17.08	15	13.6 ± 1.10	13.01–14.23
35	13	15.9 ± 1.17	15.20–16.62	8	15.8 ± 2.52	13.70–17.92	23	14.8 ± 1.41	14.19–15.40

On-line Table 3: Mean, SD, and CI for perimeter measurements

Gestational Age (wk)	US 2D			US 3D			MRI		
	No.	Mean ± SD	95% CI	No.	Mean ± SD	95% CI	No.	Mean ± SD	95% CI
21	4	40.7 ± 3.53	35.09–46.34	15	42.3 ± 4.49	39.84–44.81			
22	10	45.1 ± 4.29	42.05–48.18	10	46.4 ± 2.86	44.32–48.42			
23	8	45.4 ± 2.88	42.96–47.77	9	47.7 ± 4.22	44.48–50.96			
24	4	49.9 ± 1.93	46.84–53.00	8	49.8 ± 4.15	46.37–53.30			
25	16	53.1 ± 4.31	50.82–55.41	9	54.8 ± 4.76	51.12–58.44			
26	13	57.6 ± 4.33	54.95–60.19	11	58.9 ± 5.68	55.04–62.67			
27	16	59.1 ± 4.67	56.58–61.56	12	63.5 ± 4.83	60.43–66.56	5	52.0 ± 3.25	47.95–56.01
28	18	60.5 ± 3.74	58.65–62.37	11	67.2 ± 8.40	61.50–72.79	10	53.4 ± 2.96	51.32–55.55
29	12	64.5 ± 3.61	62.20–66.79	11	67.0 ± 5.42	63.37–70.65	13	56.1 ± 3.50	54.00–58.23
30	21	65.3 ± 3.57	63.63–66.88	11	69.6 ± 6.66	65.08–74.03	16	62.9 ± 4.88	60.34–65.54
31	22	66.3 ± 3.82	64.63–68.02	23	71.5 ± 6.41	68.69–74.24	26	66.3 ± 4.28	64.56–68.01
32	12	67.7 ± 4.90	64.62–70.84	15	76.7 ± 9.79	71.25–82.10	27	67.7 ± 4.58	65.86–69.49
33	14	71.3 ± 2.52	69.89–72.80	8	78.7 ± 3.27	76.01–81.47	16	70.8 ± 4.09	68.62–72.98
34	10	74.4 ± 4.30	71.30–77.46	11	80.5 ± 8.58	74.70–86.23	15	73.1 ± 5.45	70.09–76.13
35	13	75.0 ± 3.09	73.12–76.85	8	80.3 ± 9.60	72.26–88.32	23	77.0 ± 5.93	74.40–79.53

On-line Table 4: Mean, SD, and CI for SA measurements

GA (wk)	US 2D			US 3D			MRI		
	No.	Mean ± SD	95% CI	No.	Mean ± SD	95% CI	No.	Mean ± SD	95% CI
21	4	98.4 ± 12.46	78.59–118.26	15	99.0 ± 17.38	89.37–108.63			
22	10	115.0 ± 12.79	105.82–124.12	10	122.5 ± 17.01	110.33–134.67			
23	8	124.3 ± 14.78	111.89–136.60	9	122.6 ± 21.52	106.02–139.10			
24	4	140.4 ± 9.92	124.58–156.14	8	142.0 ± 20.92	124.51–159.49			
25	16	171.7 ± 16.06	163.12–180.23	9	164.9 ± 29.64	142.11–187.67			
26	13	192.1 ± 29.18	174.51–209.78	11	185.3 ± 22.08	170.44–200.11			
27	16	199.4 ± 23.20	187.02–211.74	12	224.9 ± 26.14	208.31–241.53	5	141.2 ± 10.29	128.40–153.94
28	18	222.0 ± 27.07	208.56–235.49	11	237.4 ± 53.87	201.17–273.56	10	152.5 ± 15.17	141.61–163.32
29	12	250.4 ± 21.27	236.85–263.89	11	247.9 ± 38.21	222.24–273.58	13	175.1 ± 20.87	162.46–187.68
30	21	256.7 ± 22.05	246.70–266.78	11	277.1 ± 39.49	250.56–303.62	16	197.8 ± 24.66	184.70–210.98
31	22	273.6 ± 24.11	262.95–284.33	23	290.2 ± 43.78	271.24–309.10	26	214.5 ± 22.54	205.41–223.62
32	12	279.3 ± 24.93	263.44–295.12	15	311.8 ± 45.62	286.54–337.06	27	231.6 ± 24.45	221.90–241.25
33	14	319.3 ± 26.86	303.81–334.83	8	320.9 ± 31.83	294.26–347.49	16	243.7 ± 15.91	235.21–252.17
34	10	346.8 ± 35.43	321.42–372.10	11	348.8 ± 77.43	296.80–400.84	15	250.1 ± 23.53	237.02–263.09
35	13	352.0 ± 23.32	337.94–366.12	8	343.4 ± 66.15	288.07–398.68	23	283.8 ± 39.22	266.79–300.71

Note:—GA indicates gestational age.

On-line Table 5: Bonferroni multiple comparison of estimated marginal means between 3 imaging modalities for SI and AP

Imaging Modality	SI			AP		
	Mean Difference	P	95% CI of the Difference	Mean Difference	P	95% CI of the Difference
US 2D vs MRI	1.636	<.001	1.259 to 2.012	1.589	<.001	1.212 to 1.967
US 2D vs US 3D	−1.694	<.001	−2.042 to −1.345	−0.186	.601	−0.535 to 0.163
MRI vs US 3D	−3.329	<.001	−3.727 to −2.932	−1.776	<.001	−2.174 to −1.378

On-line Table 6: Bonferroni multiple comparison between estimated marginal means between 3 imaging modalities for perimeter and SA

Imaging Modality	Perimeter			SA		
	Mean Difference	P	95% CI of the Difference	Mean Difference	P	95% CI of the Difference
US 2D vs MRI	2.661	<.001	1.238 to 4.085	66.408	<.001	58.084 to 74.732
US 2D vs US 3D	−4.435	<.001	−5.751 to −3.119	−10.984	.002	−18.677 to −3.290
MRI vs US 3D	−7.096	<.001	−8.597 to −5.595	−77.392	<.001	−86.166 to −68.617